Design and Synthesis of Stimuli Activated Near-Infrared Dyes to Target Cellular Organelle

THESIS SUBMITTED FOR

THE DEGREE OF DOCTOR OF PHILOSOPHY (SCIENCE)

OF

JADAVPUR UNIVERSITY

October, 2023

By

AYAN MUKHERJEE, M.Sc.

DEPARTMENT of CHEMISTRY

INDEX NO: 74/19/Chem./26

DATE OF REGISTRATION: 06th SEPTEMBER, 2019

JADAVPUR UNIVERSITY,

KOLKATA-700032 WEST BENGAL, INDIA

I would like to dedicate this thesis to my beloved parents and my PhD Supervisor.

17th October, 2023

CERTIFICATE FROM THE SUPERVISOR

This is to certify that the thesis entitled ":Design and Synthesis of Stimuli Activated Near-Infrared Dyes to Target Cellular Organelle " submitted by Sri Ayan Mukherjee, who got his name registered on 06th September, 2019 for the award of Ph. D. (Science) degree of Jadavpur University, is absolutely based upon his own work under the supervision of Dr. SAMIT GUHA and that neither this thesis nor any part of it has been submitted for either any degree/diploma or any other academic award anywhere before.

Samit Guha 17th October 2023

(Signature of the Supervisor)

Dr. Samit Guha
Assistant Professor
Department of Chemistry
Jadavpur University
Kolkata-700032, India

Design and Synthesis of Stimuli Activated Near-Infrared Dyes to Target Cellular Organelle

INDEX NO: 74/19/Chem./26

Abstract: We demonstrated ratiometric acidic pH-activatable visible to NIR switchable fluorescent dye that we synthesised. An organic cell-permeable probe with an acidic pH-activatable oxazolidine moiety and lysosome-targeting morpholine activity makes up the design. Through ring opening of the oxazolidine moiety at acidic pH, the visible closed oxazolidine form (abs418 nm) can be changed to the highly conjugated NIR Cy-7 form (abs780 nm). The pH can be used to influence the ratiometric fluorescent probe's switching, which is very reversible. Spectroscopies for NMR, UV/vis, and fluorescence allowed for the observation of the probe's pH switching behaviour. We have shown how to efficiently synthesise acidic pH-triggered visible to NIR interchangeable ratiometric fluorescent pH sensors using crystal structures. This bioresponsive probe has reversible pH-sensitive absorption/emission characteristics, low cytotoxicity, a huge bathochromic spectral shift at 322 nm with enhanced quantum yield from neutral to acidic pH, high sensitivity and selective targeting of live cell lysosomes with ideal pKa, off-to-on narrow NIR absorption/fluorescence signals with high molar absorption coefficient at acidic lysosomal lumen, and in situ live Using a dual channel confocal laser scanning microscope, selective labelling and ratiometric pH imaging in human cancer live cell lysosomes are observed. The pH-activatable organic fluorescent dye used in this experiment has a morpholine moiety for lysosome targeting and an acidic pH. We have designed and synthesized acidic pH-activatable dual targeting ratiometric fluorescent probe-peptide conjugate using SPPS protocol on Rink amide AM resin for living carcinoma cell specific active targeting successively cell penetration and selective staining of lysosomes alongside real-time monitoring, 3D, and multicolor live-cell imaging. The design consists of a RGDS peptide residue to target cancer cell surface overexpressed receptor

$\alpha_V\beta_3$ integrin, live-cell penetrating organic Changsha chromophore comprising a lysosome targeting morpholine group, and acidic pH openable spiro-lactam ring for visible-to-NIR switchable ratiometric response. The fluorescent probe-peptide conjugate exhibits intramolecular spirolactamization at physiological and basic pH through Arg amide NH of the RGDS peptide residue. The visible spirolactam state (NIR OFF) can be switched to the highly conjugated push-pull NIR open amide state (NIR ON) through spiro-lactam ring opening triggered by acidic pH with huge bathochromic shift ($\Delta\lambda_{abs}$ = 336 nm, $\Delta\lambda_{em}$ = 265 nm) and displays dynamic pH-sensitive ratiometric optical switching. This bioresponsive *in situ* acidic cancer cell lysosome activatable functional fluorophore-peptide conjugate shows enormous bathochromic fluorescence shift of 265 nm from physiological to acidic pH, OFF-to-ON narrow NIR abs/em bands with augmented molar absorptivity, respectable quantum yield, and ultra-brightness at acidic lysosomal pH; negligible cytotoxicity, and dual targeted ratiometric imaging capability of living cancer cell lysosomes with perfect pK_a.

Acknowledgements

I would like to offer my profound gratitude and appreciation to my supervisor, Dr. Samit Guha, Department of Chemistry at Jadavpur University, for his helpful advice, enlightening talks, and helpful suggestions. The thesis could not have been finished without his direction and passion. In addition, Dr. Samit Guha has been a wonderful human being to me during this difficult path in addition to being a fantastic supervisor. The experience of finishing a research project can be greatly improved by developing a good working relationship with a supervisor. The scientific discussions I had with my supervisor greatly pushed me. In addition to being a great boss, He also assisted me in developing my writing abilities.

I am grateful to our collaborator Dr. Arunima Sengupta (Department of Life Sciences and Biotechnology, Jadavpur University) for their spontaneous help related to my research work.

I also acknowledged my friends Abhisek Gupta (Department of Organic Chemistry, IACS), Monotosh Bhakat (Department of Organic Chemistry, IACS), Dr. Paramita Saha (Department of Inorganic Chemistry, IACS), Dr. Sanu Saha (Department of Organic Chemistry, IACS), Hasina Mamtaj Begum (Department of Organic Chemistry, IICB), Bhaswati Paul (Department of Organic Chemistry, IICB), Sarat Chatterjee (Department of Organic Chemistry, IICB), Israful Haque (Department of Organic Chemistry, IICB).

I am grateful to Jadavpur University's administration and the department of chemistry for providing me with a lab, library, and a conducive environment to do my research. I would also like to express my gratitude to all of the instructors in the organic chemistry division, Jadavpur University, and the department's support personnel.

I would like to express my gratitude to Dr. Nayim Sepay for his assistance and helpful advice he gave me throughout my research.

I am also appreciative that the Bose Institute and the Indian Institute of Chemical Biology (CSIR-1ICB, Kolkata) allowed me to use confocal microscopy equipment for my research.

I'm proud to acknowledge the kindness and support of my group's members, Mr. Pranab Chandra Saha, Mr. Rabi Sankar Das, Mr. Tapas Bera, Mr. Samiran Kar and Mr. Aniruddha Mondal.

Additionally, Mr. Deepak Kumar Bhunia and the Project Students are to be thanked for their assistance with my research.

I am also grateful to the West Bengal government's Swami Vivekanda Merit Cum Means Fellowship for providing me with financial support while I was conducting my research.

I would like to thank all the faculties of chemistry department, Jadavpur University. Mr. Prantik Saha (confocal microscopy section, Bose Institute), Dr. Arnab Biswas, and all the fellow friends of Department of chemistry, Jadavpur University for their overwhelming help and support throughout my research work.

I believe this is the ideal chance to send my sincere thanks to all of my teachers.

I'd want to thank all of my friends for their spontaneous assistance with my research, especially Gopal Rana, Prabhat Kumar Ghorai, and Sourav Sarkar.

Last but not least, I take great pleasure in expressing my gratitude to and my parents (Mr. Lob and Mrs. Sarbani Mukherjee) and my wife (Mrs. Shila Mukherjee) for their invaluable support, encouragement, and mental support. My decision-making in life is always aided by their blessings and well wishes.

October, 2023 ……..

Department of Chemistry *(Ayan Mukherjee)*

Jadavpur University,

188, Raja S.C. Mallick Road,

Jadavpur, Kolkata, West Bengal-700032

PREFACE

The study described in the current thesis, "Design and Synthesis of Stimuli Activated Near-Infrared Dyes to Target Cellular Organelle," focuses on the synthesis, characterization, and application of near-infrared (NIR) symmetrical and unsymmetrical cyanine-7 molecules, Changsha dye, and their conjugates for the selective targeting and imaging of cellular Lysosomes in live cells using confocal laser scanning microscopy. Additionally, it is discovered that these fluorophores are helpful for cellular imaging.

Under the guidance of Dr. Samit Guha, Department of Chemistry, Organic Section, Jadavpur University, Kolkata-700032, India, the author conducted the current investigation detailed in this thesis at the university during the months of September 2019 through October 2023.

The six chapters that described the thesis are as follows:

Chapter-1: In Chapter 1, there is a brief overview of the literature-reported synthetic methods of ratiometric fluorescence probe uses. The importance of intracellular pH as a biological parameter for controlling cellular activity and function is highlighted. The importance of NIR chromophore in comparison to UV and visible probes. The emphasis of this chapter has been on cyanine dyes, with a special emphasis on Cy-7 dyes. There has been discussion of structural scaffolds for ratiometric pH sensing. The significance of lysosomes as a cellular organelle has been highlighted. Multicolor cellular imaging, confocal laser scanning microscopy for live cell imaging, and lysosome targeting structural scaffolds have also been discussed.

Chapter-2: explains the substances used and the experimental methods needed to finish the entire project covered in this chapter.

Chapter-3: For the purpose of precisely targeting live-cell lysosomes, Chapter 3 discusses the design and manufacturing of acidic pH-activatable visible to NIR switchable ratiometric probes. An organic cell-permeable probe with an acidic pH-activatable oxazolidine moiety and lysosome targeting morpholine functionality makes up the design. Through ring opening of the oxazolidine moiety at acidic pH, the visible closed oxazolidine form (abs 418 nm) can be changed to the highly conjugated NIR Cy-7 form (abs 780 nm). The pH can be used to influence the ratiometric fluorescent probe's switching, which is very reversible. Spectroscopies for NMR, UV/vis, and

fluorescence allowed for the observation of the probe's pH switching behaviour. This bioresponsive in situ acidic organelle-activated fluorophore exhibited reversible pH-switchable ratiometric optics, high photostability, a large bathochromic emission shift at 320 nm from basic to acidic pH, narrow NIR absorption, and emission regions with higher molar extinction. coefficient lysosomal pH, good quantum yield, low cytotoxicity and targeted imaging capability, ideal pKa of living cell lysosomes. The report showed ratiometric imaging with improved acid lysosomal specificity while minimizing signals in the NIR region of non-target neutral or basic organelles in human carcinoma HeLa and A549 and healthy rat H9c2 (2-1) cells monitored by confocal laser scanning microscopy techniques.

Chapter-4: In Chapter 4 the design, effective synthesis method, and crystal structures for the creation of acidic pH-triggers visible to NIR interchangeable ratiometric fluorescent pH sensors are described. In situ live cell pH-activated ratiometric imaging, off-to-on narrow NIR absorption/fluorescence signals with high molar absorption coefficient at acidic lysosomal lumen, pH-sensitive reversible absorption/emission features, low cytotoxicity, 322 nm huge bathochromic spectral shift with augmented quantum yield from neutral to acidic pH, high sensitivity and selective targeting ability of live cell lysosomes with ideal pKa. By combining a dual channel confocal laser scanning microscope with a pH-activatable organic fluorescent dye that includes a morpholine moiety for lysosome targeting and an acidic pH openable oxazolidine ring, it is possible to monitor selective staining and ratiometric pH imaging in live human carcinoma cell lysosomes. The synthesised pH-activatable probe has also been used for live cell imaging in 3D, multicolor, and real-time lysosome tracking.

Chapter-5: describes the design and synthesis of a RGDS peptide conjugated ratiometric pH sensitive NIR fluorophore to target cancer cell lysosomes. Herein, we've presented a NIR OFF/ON functional dyes based on ring closing and opening mechanism. We have designed and synthesized a type of Changsha NIR fluorophores, a novel class of NIR functional fluorescent dyes with large extinction coefficients, high fluorescence quantum yields, high brightness, and pH sensitive property. Remarkably, the new NIR dyes outperform the conventional rhodamine dyes with both NIR absorption and emission while keeping the rhodamine-like ON-OFF switching mechanism for their fluorescence. We have conjugated RGDS peptide in this NIR dye to target the cancer cells and morpholine unit to target specifically the lysosomes.

Chapter-6: The introduction contains a synopsis of all the research discussed in this thesis. This chapter also looks at the findings of the investigation's applicability.

Chapter 3-5: begins with a brief introduction, then moves on to Experimental Methodology, Results & Discussion, and Conclusions.

The list of Publications has been incorporated at the end of this thesis.

Abbreviations

Abbreviations used for amino acids, peptides, amino acid derivatives, substituents, reagents are largely in accordance with the recommendations of IUPAC–IUB commission on Biochemical Nomenclature, 1974, Pure and Applied Chemistry, 40, 315–331. Other symbols and nomenclature, etc. are based on the list in J. Biol. Chem. 1989, 669–671. Standard three letter coding is used for all the amino acids. Additional abbreviations used in this thesis are listed below–

A	Absorbance
ACN	Acetonitrile
APN	Amino Peptidase N
CLSM	Confocal laser scanning microscopy
CPP	Cell Penitrating Peptide
2-CTC	2-chloro tritylchloride
Cy-7	Cyanine-7
DBU	1,8-diazabicyclo[5.4.0]undec-7-en
DCM	Dichloromethane
DIPEA	N,N-Diisopropylethylamine
DMSO	Dimethyl sulfoxide
DMEM	Dulbecco's Modified Eagle Medium

DMF	N, N – dimethylformamide
DQF COSY	Double Quantum Filtered Correlation Spectroscopy
d	doublet
ESIPT	Exited-State Intramolecular Proton Transfer
FBS	Fetal Bovine Serum
Fl	Fluorescence
Fmoc	9-Fluorenylmethoxycarbonyl
FRET	Forster resonance electron transfer
GSH	Glutathione
HATU	1-Bis(dimethylamino)methylene]-1H-1,2,3-triazolo[4,5-b]pyridinium 3-oxide hexafluorophosphate
HRMS	High-resolution mass spectrometry
HRMS-ESI	High-resolution electrospray ionisation mass spectrometry
HOBT	1- hydroxybenzotriazole
J	Coupling constant m Multiplate
LTG	Lyso Tracker Green
MeOH	Methanol
MTDR	Mitotracker Deep Red FM
MTG	MitoTracker Green FM
MTT	3-(4,5-dimethyl-2-thiazolyl)-2,5-diphenyltetrazolium bromide
MW	Microwave
NMR	Nuclear Magnetic Resonance
NIR	Near-infrared

PDT	Photodynamic therapy
PEG	Poly ethylene glycol
PET	Photo Induced Electron Transfer
PMT	Photo Multiplier Tube
PTT	Photothermal therapy
QDs	Quantum Dots
ROS	Reactive oxygen species
S	Singlet
SPPS	Solid phase peptide synthesis
t	triplet
TCSPC	Time-correlated single photon counting
TLC	Thin layer chromatography

Contents

Chapter No.	Chapter Title	Page No.
Chapter 1	General Introduction	1-53
Chapter 2	Materials and Methods	54-58
Chapter 3	Acidic pH-Triggered Live-Cell Lysosome Specific Tracking, Ratiometric pH Sensing and Multicolor Imaging by Visible to NIR Switchable Cy-7 Dyes	59-121
Chapter 4	Acidic pH-Triggered Live-Cell Lysosome Specific Tracking, Ratiometric pH Sensing, and Multicolor Imaging by Visible to NIR Switchable Cy-7 Dyes	122-225
Chapter 5	Dual Targeting Acidic pH-Activatable NIR Convertible Ratiometric Fluorescent Probe-Peptide Conjugate for Living Cancer Cell Specific Active Targeting Subsequently Selective Tracking of Lysosomes	226-302
Chapter 6	Summery and Outlook	303-304
	List of Publications	305
	Presentation/Participation in International/National Symposium/Conferences	306
		306

Chapter 1

General Introduction

NIR Dyes:

The majority of molecular imaging probes display UV/Vis wavelength region absorption and emission. Owing to the strong absorbance and autofluorescence of biological molecules in the UV/Vis area, this makes them challenging for applications in bioimaging.[1-4] Near-infrared (NIR) region (700-900 nm) can be effectively used to study in vivo targets (Figure 1).[5] Additionally, they are spectrally segregated from the autofluorescence of tissue components like collagen and fluorescence signals resulting from other body absorbers, molecular imaging probes operating in the NIR region have enhanced signal-to-noise ratios.[6] Moreover, NIR light has deep tissue penetration and cause little photodamage to biological samples. Molecular imaging probes with NIR region (700-900 nm) absorption and emission can be

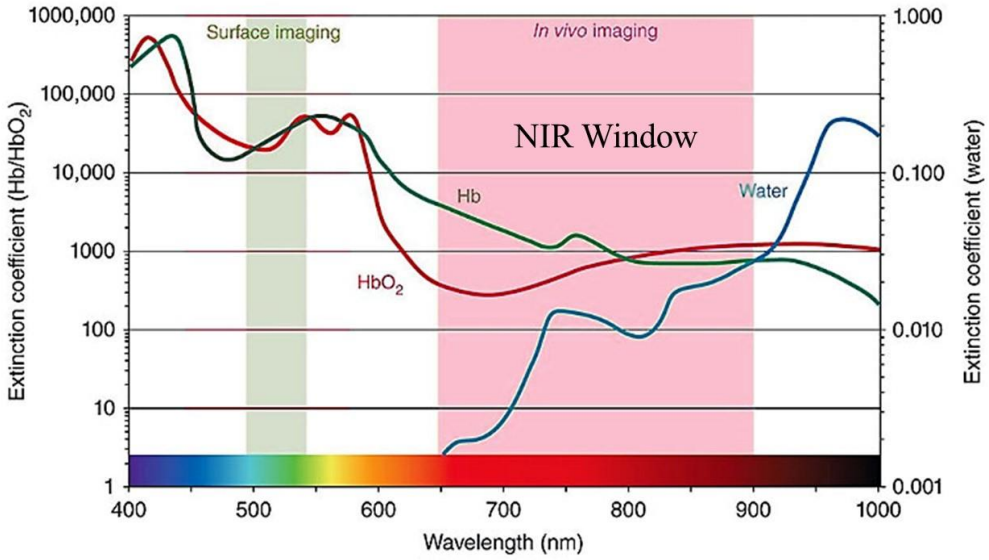

Figure 1. NIR Window.[5]

effectively used to investigate cellular organelle tracking.[7] Molecular imaging probes that are currently used in bioimaging are non-targeting and targeting. Non-targeting probes are currently using in clinical applications for assessing blood flow and clearance, which include a range of NIR fluorescent cyanine dyes including ICG.[8] The NIR light can penetrate 5 to 10 mm, however it is typically depends on the type of tissue being examined.[9,10] Due to the fact that cancer cells frequently overexpress particular surface receptors, the targeting probes are primarily used for functional imaging of tumour tissues. In this method, the fluorophore is generally coupled to a ligand that binds to a particular overexpressed receptor.[11] While the unbound probes are taken out of circulation, the targeted probes bind to the cancer cell surface receptor and remain at the target spot. Activatable targeting fluorescent probes are another class of the targeting probes.[12,13]

Cyanine Dyes:

By reacting N-amyl quinolinium iodide and N-amyl lepidinium iodide in NH_3 under heating condition to create a "magnificent blue colored" probe, C. H. G. Williams synthesised the first cyanine dye[14] in 1856 (Figure 2). The common term for cyanine dye is derived from the Latin word cyanos, which means blue.[14] Due to the existence of two heterocyclic residues that can play both electron acceptors and donors form the push pull colored cyanine system. More than any other class of dyes that has been found, cyanine dyes exhibit a broad range of absorption. Cosco and colleagues devised an approach that involved rationally modifying the molecular stucture of fluorescent chromophores employed for visible and NIR optical imaging. These delocalized cationic compounds known as Cyanine dye,[9] have two

heterocyclic moieties (rings containing heteroatom) linked by 3, 5, 7, 9 or 11 methine units (=CH- groups; Figure 2).[15-18] They are particularly good light absorbers, which contributes to their excellent emitters in response to light irradiation.

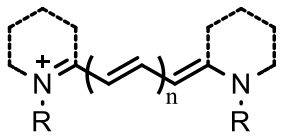

Figure 2. General structure of carbocyanine dyes.[15-18]

Cyanine dyes have the property of huge molar absorption coefficients and long range of wavelengths. Between the terminal heterocyclic groups of the polymethine chain, each vinyl unit addition causes a 100 nm bathochromic shift in the absorption/emission wavelength. The dyes absorb at longer wavelengths due to the cation's delocalization on the terminal heterocyclic ring. The photodegradation of NIR cyanine dyes (λ_{max} > 700 nm) is a common incidence.[19] This is crucial for all practical cyanine dye applications including emission spectroscopy, where high sensitivity or a high signal-to-noise ratio are required. Fluorescence of cyanine dye can be fine-tuned by alteration of polymethine chain,[20] substitution at the terminal aromatic rings,[21] and the structures of the chromophores.[22]

The number of methine units in the polymethine chain determines the common names of cyanine probes. Mono-, tri-, penta-, and hepta-methine cyanines, for instance, are compounds with (n=1,2,3,5,7……) respectively. A wide variation of polymethine cyanine derivatives was created. A process of stepwise condensation between two nucleophilic aza-heterocycles comprising an active methyl functionality and a precursor to a polyene chain, such as an

unsaturated bisaldehyde or its comparable, is used to synthesise these cyanine molecules. Variations in the polyene chain, functionalization in polymethine backbone, functionalization at the heterocyclic nitrogen, and modification of the heterocycles are used to create a wide range of symmetrical and unsymmetrical cyanine dyes.

Functional groups like carboxylic acid, free amine, sulphonic acids are inert to the reagents used for condensation reaction and the reaction condition. These attached functional group are very useful for post synthetic modification to target specific part of cell. For *in vivo* imaging[23] and DNA sequencing applications[24], certain functional groups, such as carboxylic acid and amino groups connected to heptamethine cyanine dyes have been used (figure 3).

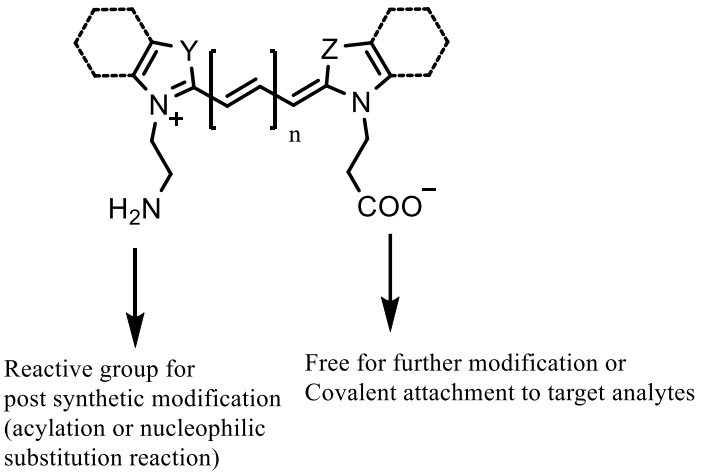

Figure 3. Reactive groups for post-synthetic modifications.[18-23]

The manufacture and uses of polymethine chromophore as non-covalent labelling agent for detection of nucleic acid have recently been extensively

reported.[25] These dyes cover the visible and near-infrared spectrums when labelling non-covalent nucleic acids, these are mono-, tri-, and pentamethine cyanine dyes. The monomethine and trimethine cyanines can be made in a variety of ways, but in order to create the pentamethine and heptamethine cyanine dyes, methyl-substituted quaternized heterocycles are frequently combined with dialdehyde or its' analogue.[26-29]

Pentamethine cyanine dyes:

Our group has reported the following Cy-5 dye. A microwave-assisted Fmoc solid phase peptide synthesis technique on the Wang resin has been utilized to create unsymmetrical visible Cy-5 chromophore peptide conjugate where mitochondria targeting functional Cy-5 probe is conjugated with a Phe-Phe dipeptide (Figure 4).

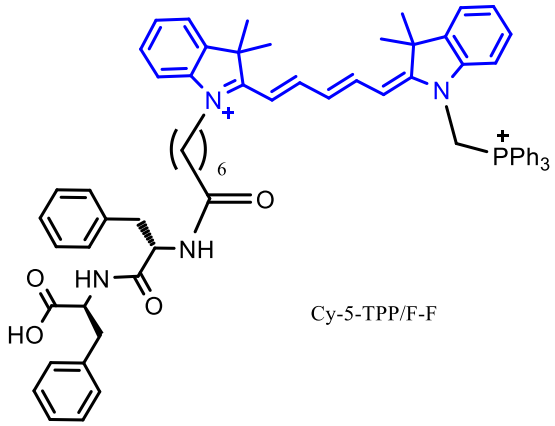

Figure 4. Chemical Structure of Cy-5-TPP/F-F.

As fluorogenic probes for proteins (both native and denatured) and nucleic acids, a series of pentamethine cyanine dyes containing cyclohexene or

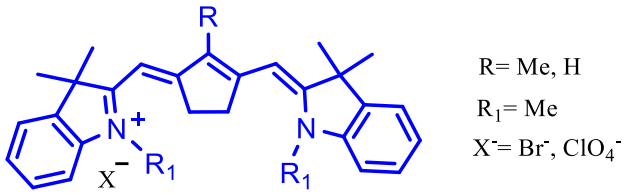

Figure 5. Structure of cyclopentene ring containing Cy-5 dye.

cyclopentene groups in the polymethine chain, presumed to be DNA groove-binders, were examined (Figure 5).[30] It was found that the development of dye-DNA fluorescent complexes is inhibited by the occurrence of methyl/dimethyl residues in the cyclohexene ring, whereas the presence of methyl substituents in the position 2 boosts the fluorescence intensity of the dye-DNA complex. [31]

Heptamethine cyanine dyes:

Indocyanine green (ICG) dye is one of the most significant heptamethine cyanine dyes (Figure 6).[32] The U.S. Food and Drug Administration (FDA) gave endorsement to ICG as a contrast agent for clinical use, and it is well known for being used clinically to identify liver function.

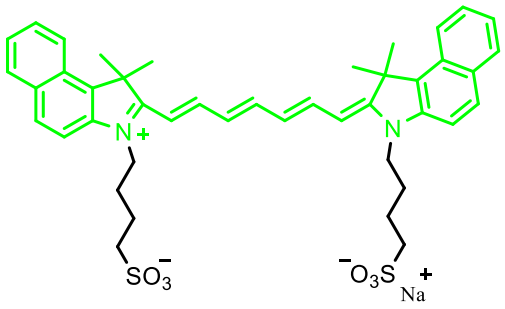

Figure 6. Structure of ICG.[32]

According to Nagao and co-workers descriptions of the construction of a fluorescent labelling probe, an ICG analogue, was synthesised in this circumstances as a general pH sensor (Figure 7). [34]

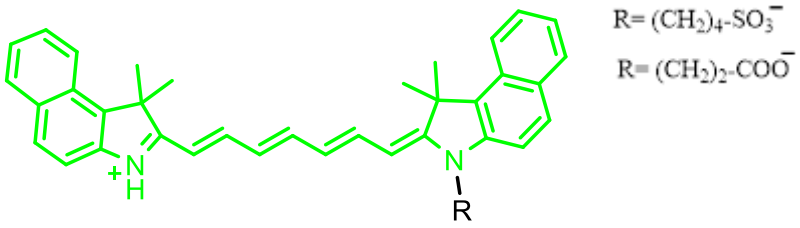

Figure 7. pH switchable Cy-7 dye.

The existence of chlorine, an electron-withdrawing group, at the meso carbon of the cyclohexene ring causes absorbance to shift to even longer wavelengths

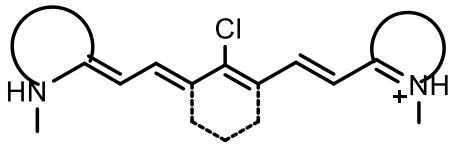

Figure 8. Skeleton of cyanine 7 dye.

by removing electrons from the polymethine chain (Figure 8). A blue shift was detected when chlorine is substituted by electron-donating groups, like amines.

The photostability of the dyes can be significantly improved by substituting the central chlorine of the cyclohexene ring by an electron-donating group (Figure 9). To achieve more sophisticated photochemical and photophysical

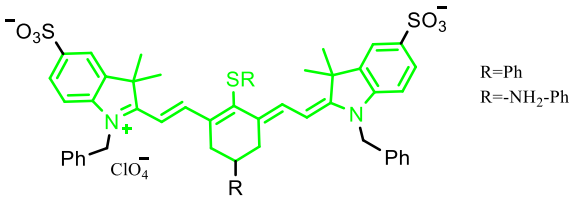

Figure 9. Substituted cyanine-7 dye.[35]

capabilities, the heptamethine cyanine dyes have undergone numerous chemical synthesis modifications.[35]

Synthesis of New Generation Cyanine-7 Dye:

Under benign conditions, Petr Klan group reported the direct conversion of Zincke salts to cyanine dyes, along with the integration of a derivatized pyridine part in the heptamethine residue (Figure 10).[36] This effort is the first generic strategy, which enables the outline of various derivatives and various

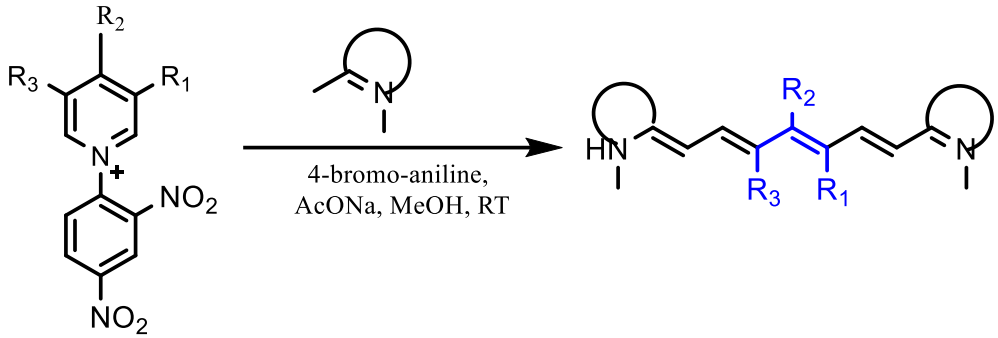

Figure 10. Design for the synthesis of substituted cyanine dyes.[36]

patterns of substitution at the chain's C3′–C5′ locations. This approach is a potent method for gaining access to a new generation of cyanine derivatives.

The usage of pyridinium benzoxazole (PyBox) as cy-7 dye is described by Schnermann group (Figure 11).[37] This technique offers access to newly undiscovered chromophore capabilities and is straightforward to use. They used this technique to make compounds to tackle two unmet NIR fluorescence imaging goals. First, they developed compounds for protein-targeted tumour imaging using an iterative methodology.

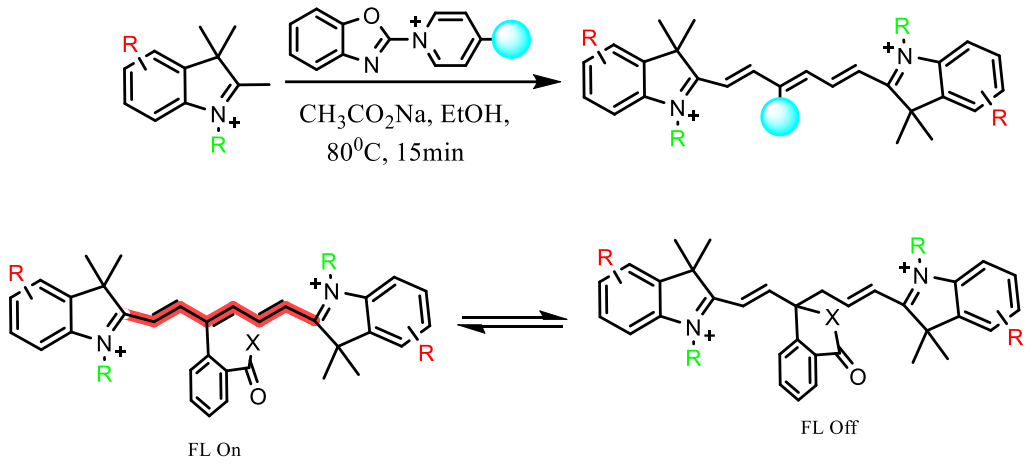

Figure 11. Design and synthesis of heptamethine indocyanines.[37]

The optimised probe improves the tumour selectivity of monoclonal antibody and nanobody conjugates as compared to typical NIR fluorophores.[37] Second, in order to enhance cellular absorption and fluorogenic characteristics, they created cyclizing heptamethine indocyanines. They showed the ring opening/ ring closing which is sensitive to solvents may also be altered using a broad range of electrophiles and nucleophiles. Then, utilising organelle-targeted Halo-Tag self-labelling proteins, they demonstrated a chloroalkane derivative of a substance with tunable cyclization capabilities undergoes exceptionally effective live cell imaging. Overall, the chemistry described here increases the range of chromophore activity that is accessible, which, in turn, makes it possible to find NIR probes with promising features for high-end imaging applications.

pH Switchable NIR Dyes:

NIR light absorbing organic chromophores have been regarded as potent guns against many diseases due to their extraordinary efficacy in phototherapeutic mode. However, the inadequate disease-targeting

effect of NIR chromophores remains a barrier to therapeutic use since they may produce NIR damage to healthy tissues. Given the acidic circumstances caused by harsh microenvironments in certain unhealthy tissues, producing "turn-on" NIR fluroscence in acidic pH-sensitive photophysical characteristics could be a viable strategy for enhancing disease specificity. Based on a consideration of their photophysical relaxation processes, strategies for building pH-sensitive NIR organic chromophores are summarised here, comprising the augmentation of internal conversion and intersystem crossing of those dyes in presence of low pH.

Samuel Achilefu group designed photostable NIR pH sensors with high

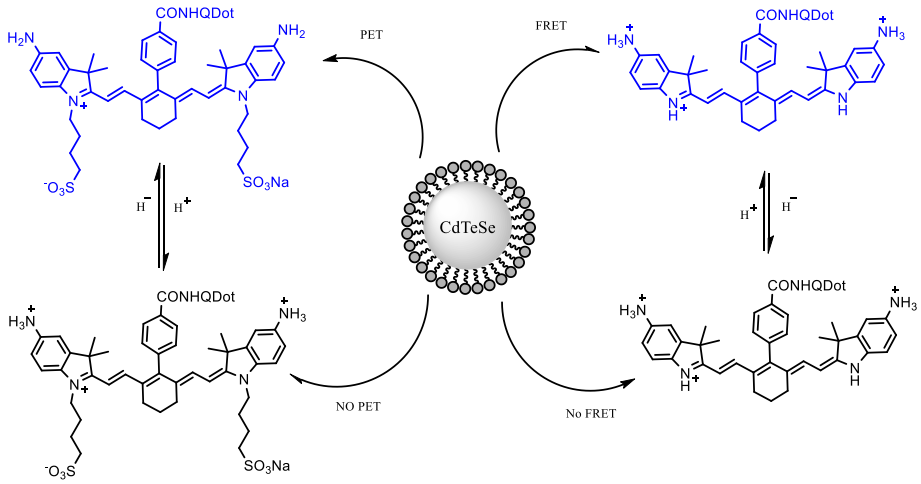

Figure 12. The mechanism for QD-based pH sensing caused by pH-responsive organic dyes.[38]

dynamic pH detecting capacity (Figure 12).[38] The hybrid structures containing quantum dots' (QDs') exhibits strong photophysical capabilities with pH sensitivity of NIR organic probes.

Shangguan et al. developed HQO, a pH activatable cyanine dye, to measure pH variations for gaining a better knowledge of the mitophagy process in live cells by real-time monitoring of mitochondria and autolysosomes

(Figure 13).[39] HQO (ex/em = 530/650 nm) was particularly integrated inside the mitochondria; however, when pH was decreased, it transitioned to the red-shifted protonated $HQOH^+$ state (ex/em = 710/750 nm) when defective mitochondria fused with lysosomes and transformed into autolysosomes. With the ability to differentiate autolysosomes from other lysosomes, this pH switchable HQO molecule proved ideal for studying mitophagy.

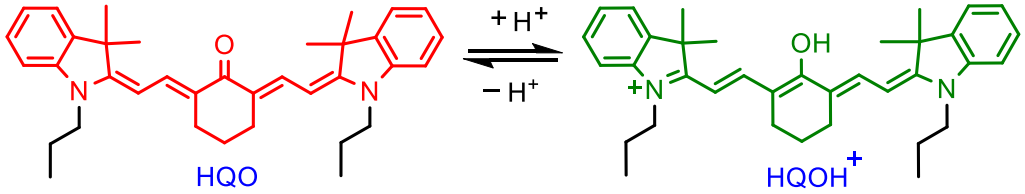

Figure 13. The pH sensitive structural change of HQO and $HQOH^+$.[39]

Maged Henary presented a benzothiazole carbocyanine probes having a meso-pyridyl residue. When the nitrogen lone pair interacts with a free proton, the pyridyl nitrogen acts as a pH-sensitive functionality which is **Figure**

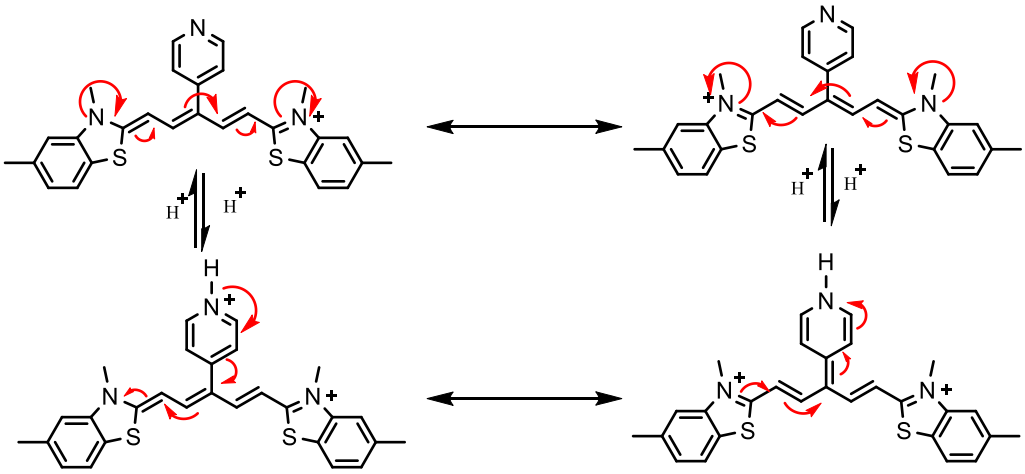

14. An alternative process for protonated meso-pyridine pentamethine dye is proposed.[40]

directly conjugated with the probe and alters the molecular orbital distribution and absorption band gap of the dye (Figure 14).[40]

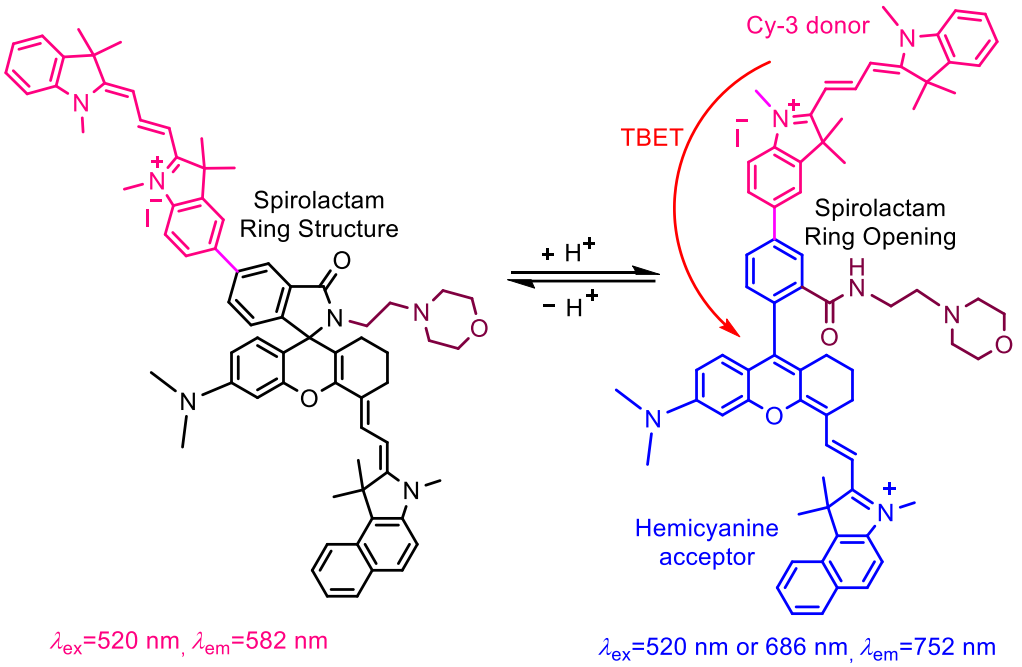

Figure 15. A ratiometric dye based on TBET for monitoring pH alterations in mitochondria during the mitophagy process.[41]

Liu and colleagues synthesized a ratiometric NIR fluorophore with a significant Stokes shift that can detect changes of mitochondrial pH via very efficient through-bond energy transfer (TBET) from a Cy-3 donor to an NIR hemi-cyanine acceptor coupled by a spiro-lactam ring structure (Figure 15).[41] The probe emits in Cy-3 region at basic or neutral pH (ex 520 nm, ex 582 nm). However, in acidic pH spiro-lactam ring opening was detected, resulting in prolonged conjugation and a new NIR fluorescence peak at 752 nm (ex 520 nm or 686 nm) is observed. This results in ratiometric fluorescence responses of the

probe to pH changes denoted by decrease in donor fluorescence and increase in acceptor fluorescence upon donor ex at 520 nm owing to a very effective TBET from the donor to the acceptor. The probe emits as a Cy-3 donor inside the mitochondria (pH 8.0). Nonetheless, during the mitophagy process, the probe showed respectable fluorescence decrease for the Cy-3 donor and significant fluorescence increases for the hemicyanine acceptor (ratiometric fluorescence responses to pH variations).

Tetsuo Nagano group synthesised a pH activatable cyanine probe.[42] On the basis of aminocyanine containing a diamine moiety, novel ratiometric, NIR fluorescent pH dyes with varying pK_a values were devised and synthesised, and their photochemical properties were investigated (Figure 16). These pH dyes exhibited a 46-83 nm bathochromic shift of the λ_{max} under acidic circumstances.

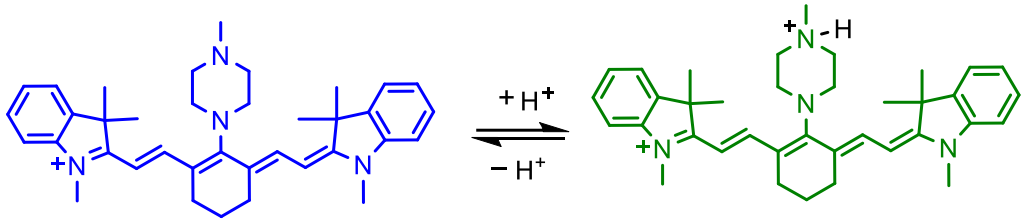

Figure 16. pH switchable Cy-7 dye.[42]

Activatable NIR Probe: Hao Wang group modularly constructed peptide-cyanine conjugates that self-assemble intracellularly into 1D column like superstructures.[43] After entering the cell the peptide sequence is cleaved by caspase-3/7. When the two cyanine dyes are attached with self assembling conjugated cyanine dyes were H-aggregated in P helical style (Figure 17). And this phenomena helps this cyanine dye to increase its' photothermal conversion

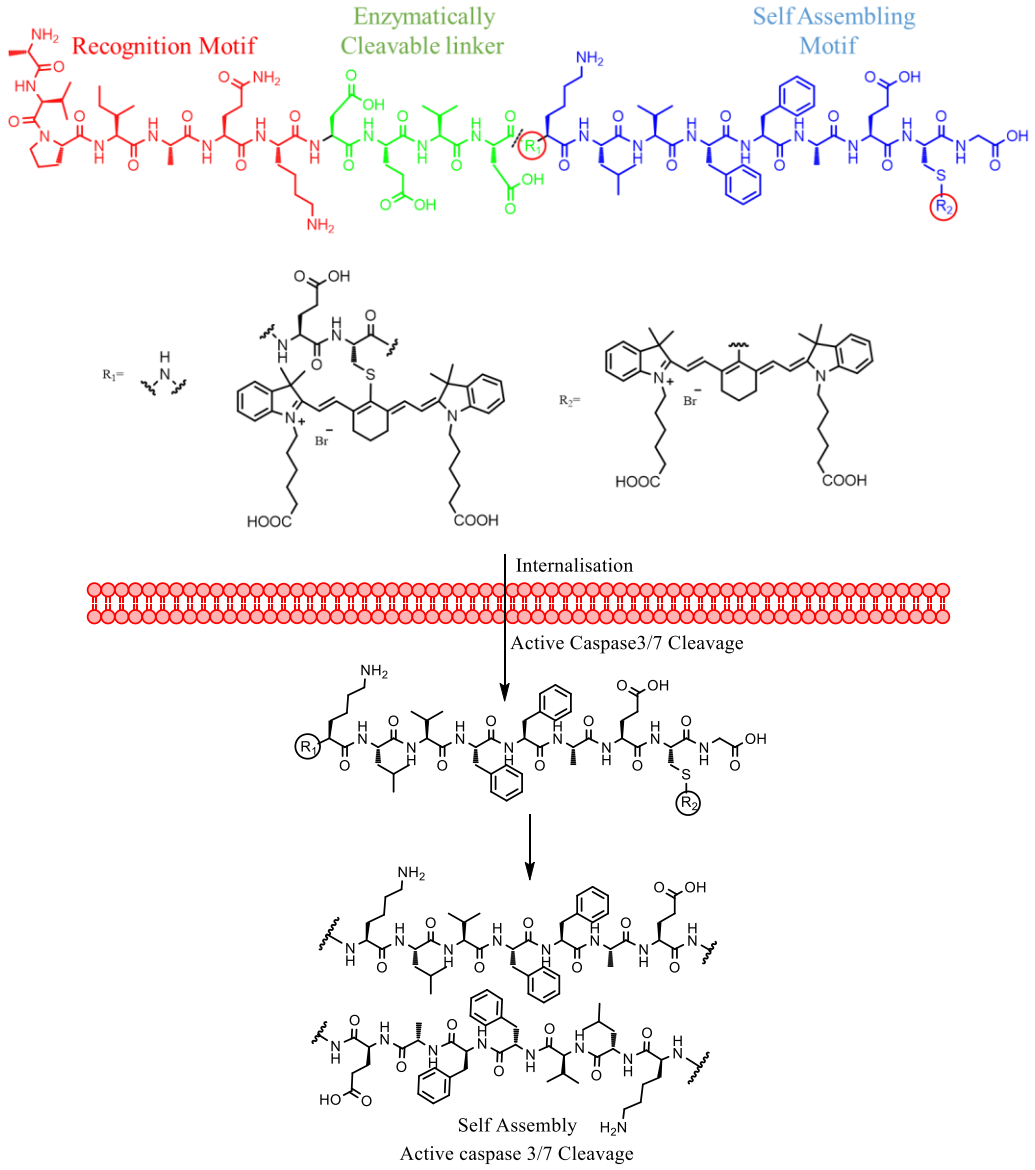

Figure 17. Illustration of how peptide is cleaved and this cyanine molecule is activated in presence of caspase3/7 enzyme.[43]

efficiency by 3,4 fold compared to free cyanine one. When the self assembled peptide substituted with one cyanine dye it gives undefined structure with very good fluorescence property which helps to use it in fluorescence imaging. Peptides combined with functional compounds to achieve bio-applications are desired.

Based on the methylene blue (MB) fluorophore, a gal-activated probe, MB-β-gal, was developed to detect and remove aged cells.[44] The probe showed no fluorescence in the absence of β-gal, and its $^1O_2$ generation efficiency was decreased at the same time. on contrary MB-β-gal might be particularly stimulated in the high amount β-gal in senescent cells,

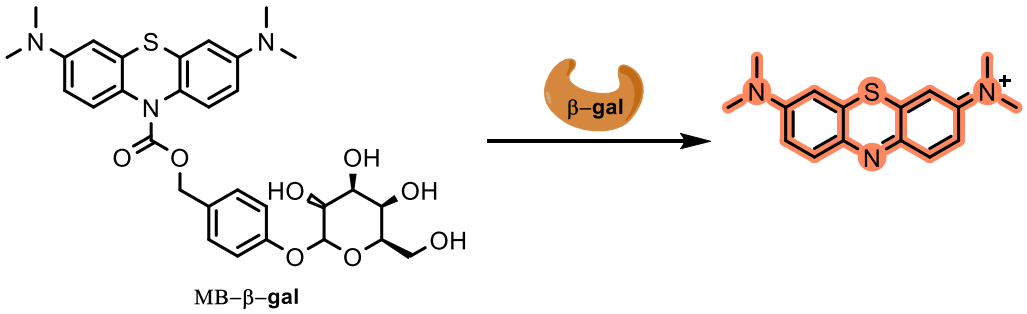

Figure 18. Mechanistic of MB-β-gal activated by β-gal gal.

with NIR fluorescence and high $^1O_2$ generation efficacy when exposed to light (Figure 18). MB-gal was later utilised to image and destroy senescent cells since it had a rapid reaction, high sensitivity, and outstanding selectivity when it came to detecting -gal in an aqueous solution. In both mouse embryonic fibroblast cells and aged HeLa cells, the dual actions of MB-gal were effectively established.

In order to detect BC in living mice using real-time NIRF imaging and urinalysis, a macromolecular reporter (CyP1) was created. Due to its high renal clearance and cancer marker (APN=aminopeptidase N) selectivity, CyP1 may be effectively transferred to the bladder and specifically turn on its NIR emission to report the finding of BC in alive mice (Figure 19).[45] Furthermore, CyP1 might be employed for optical urinalysis, allowing for ex vivo tumour progression monitoring for therapy assesment and straightforward translation of CyP2 as an in vitro diagnostic test.

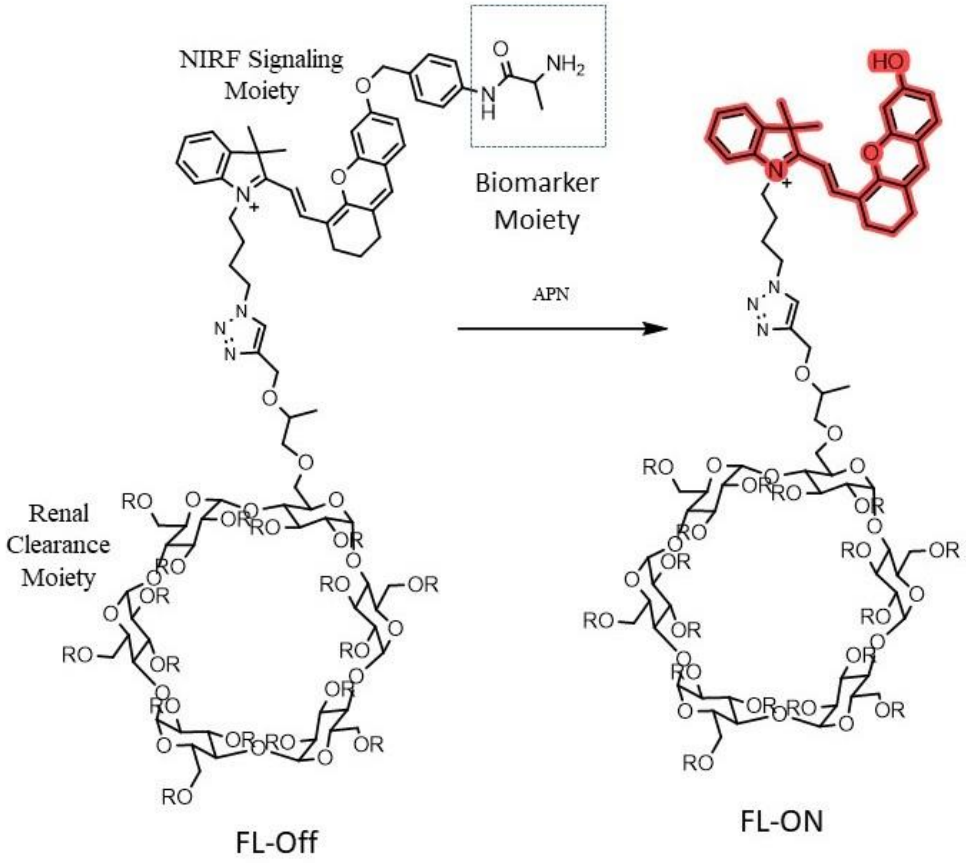

Figure 19. Compound CyP1 and its activated state in presence of APN (R=H or $CH_2CHOHCH_3$).

Utilising the receptor-induced binding and retention consequence as well as enzyme-stimulated emission activation, the Deju Ye group developed a "one-pot sequential click reaction" technique to synthesise an activatable NIR probe (1-DPA2) (Figure 20).[46]

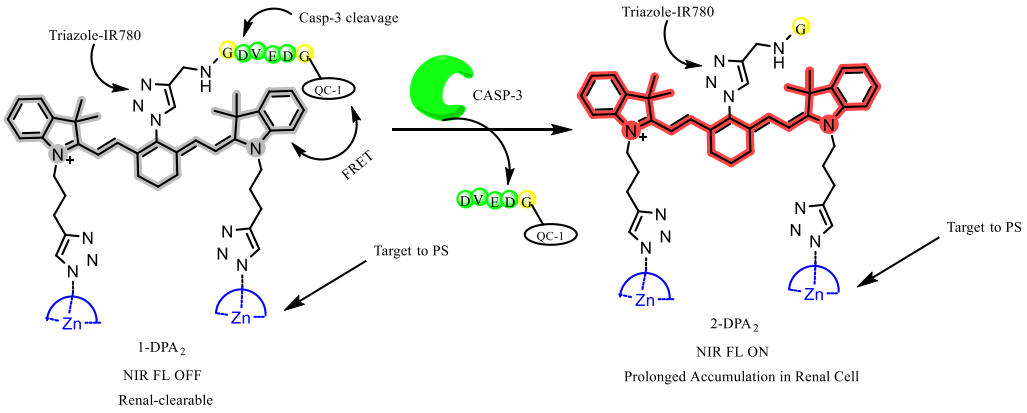

Figure 20. Molecular structure of 1-DPA$_2$ and caspase-3-triggered proteolysis of 1-DPA$_2$ turned into fluorescent compound, 2-DPA$_2$.

In order to detect the onset of cisplatin-triggered AKI in mice as early as 24 hours after cisplatin incubation, 1-DPA$_2$ can target both externalised phosphatidylserine and active caspase-3 markers of apoptosis. This results in augemented 808 nm NIR emission and a high signal-to-noise ratio. Using real-time fluorescence imaging by 1-DPA$_2$, they have documented the incremental restoration of kidney function in AKI mice after N-acetyl-L-cysteine (NAC) therapy in addition to tracking the steady activation of Casp-3 in the mouse kidney.

Lysosome:

Lysosome is an essential cell organelle in eukaryotic animal cells. Because of their peculiar purpose, they are frequently referred to as the "suicide bags" of the cell.

Christian de Duve recieved the 1974 Nobel Prize in Physiology or Medicine for the discovery of lysosome.

Let's take a closer look at the lysosome's structure, uses, and disorders that are related to it. The hydrolytic enzymes found in lysosomes, which are sphere-shaped sacs, can degrade a wide variety of biomolecules. To put it another way, lysosomes are membrane organelles whose sole purpose is to ingest and break down cellular waste and debris using hydrolytic enzymes (Figure 21).

Figure 21. Image of a human cell along with all the organelles.

As lysosomes are membrane-bound organelles, the hydrolytic enzymes and other cellular waste are found in the lumen, an area inside the membrane. The lysosomal lumen has pH between 4.0 and 5.0, which is fairly acidic in nature. It almost serves the same purpose as the stomach's natural acids. In addition to dissolving biological polymers, lysosomes also play a role in the counting of discharged materials, energy metabolism, cell signaling, and plasma membrane repair. Lysosomes are generally spherical in shape and sizes vary between 0.1 to 0.6 μm. The largest lysosomes measure more than 1.2 μm in length.

Lysosomes are acidic organelles that are membrane-bound and present in all mammalian cells. They include a range of enzymes that can be broken down and are active at acidic pH levels. Degradation of lipids, proteins, nucleic acids, and carbohydrates is carried out by lysosomes. They also participate in exocytosis.[47] Lysosomes play an important role not only in biopolymer breakdown, but also in a variety of cell mechanisms such as plasma membrane repair, apoptosis, cell signalling, and energy metabolism. The proton-pump vacuolar ATPases in lysosomes are able to maintain the interior's acidic pH 4–5 environment. Lysosome dysfunction, which results in lysosomal storage disorders, neurological disorders, cancer, and apoptosis, is caused by abnormalities in lysosomes.[48]

Lysosomes can be taken over during viral infections by viruses that make use of the local viral proteins must be cleaved into their mature forms by lysosome proteases in order for a viral infection to be successful.[49] In two separate papers published in Science, researchers used genetic screening to find a membrane protein that is crucial for lysosomal protease trafficking, which in turn affects the lysosome's capacity to carry out its many duties. This protein, formerly known as TMEM251, was given the new name LYSET (lysosomal enzyme trafficking factor) by the two groups.[50,51].Pancreatic adenocarcinoma cells were used by Pechincha et al. to identify the genes necessary for the catabolism of extracellular proteins in the lysosome, which frequently takes place in nutrient-poor environments, such as the microenvironments of tumours, to obtain amino-acid nutrients.[50] In a related work, Richards, Jabs, and Qiao et al. looked into variables that support the infectiousness of viruses like SARS-CoV-2, which mature with the lysosomal enzyme cathepsin.[51] These two investigations provide evidence for LYSET's generalizable role in lysosomal transport, confirming its critical function in trafficking and marking.

Lysosomal Hydrolases:

Over 50 distinct degradative enzymes, including those that can hydrolyse DNA, RNA, protiens lipids and polysacharides, are found in lysosomes. More than 30 different human genetic illnesses, also known as lysosomal storage diseases because they cause undegraded material to build up in the lysosomes of affected individuals, are instigated by mutations in the genes that encode these enzymes. Single lysosomal enzyme deficits are the primary cause of the majority of these illnesses. For instance, a mutation in the gene encoding a lysosomal enzyme necessary for the denature of glycolipids causes Gaucher's disease, the most prevalent of these illnesses. I-cell illness is an unusual exception, which is brought on by a lack of the enzyme necessary for the Golgi apparatus' initial step in the tagging of lysosomal enzymes with mannose-6-phosphate.[52]

Although lysosomes are kept at an acidic pH of around 4-5, all of its enzymes are acid hydrolases that are inactive in neutral pH 7,2. Lysosomes must actively concentrate H^+ ions in order to maintain their acidic internal pH. The lysosomal membrane contains a proton pump that actively moves protons from the cytoplasm into the lysosome to achieve this.

Endocytosis and Lysosome Formation:

One of the main role of lysosomes is the digesting of molecules entered by endocytosis. Lysosomes are specifically created when endosomes that comprise molecules picked up by endocytosis at the plasma membrane, and transport vesicles that sprouted from the trans Golgi network join. Hence, the development of lysosomes constitutes a meeting point for the secretory

system, which processes lysosomal proteins, and the endocytic pathway, which transports extracellular molecules to the cell surface. The early endosomes progressively develop into late endosomes that are the ancestors to lysosomes, and membrane components are then recycled to the plasma membrane. Lowering the internal pH of endosomes to around 5.5 during endosome maturation is one of the significant changes that occur. This change is crucial for the transport of lysosomal acid hydrolases from the trans Golgi network.

As previously described, acid hydrolases are directed to lysosomes by mannose-6-phosphate moieties that are recognised by mannose-6-phosphate receptors in the trans Golgi network and packaged into clathrin-coated vesicles. These transport vesicles merge with late endosomes after the clathrin coat is removed, and the internal pH's acidity leads the hydrolases to separate from the mannose-6-phosphate receptor. As a result, the hydrolases are discharged into the endosome's lumen, but the receptors stay in the membrane and ultimately return to the Golgi. After late endosomes have a full complement of acid hydrolases, they develop into lysosomes and begin to break down the molecules that were initially taken up by endocytosis.[53]

Phagocytosis and Autophagy:

Lysosomes digest material produced by phagocytosis and autophagy decide breaking down molecules entered through endocytosis. Specialized cells, such macrophages, capture and break down big particles during phagocytosis, including bacteria, cell debris, and ageing cells, which required to be expelled from the body. Large particles like these are ingested by phagosomes that subsequently combine with lysosomes to breakdown their contents. Given that the size and shape of the lysosomes produced in this manner (phagolysosomes) are influenced by the composition of the material being digested, they can grow to be fairly large and diverse.

The progressive breakdown of a cell's own components is known as autophagy, and it is also carried out by lysosomes. The enclosing of an organelle (such as a mitochondrion) in membrane produced from the ER appears to be the initial stage of autophagy. An autophagosome is created, which is subsequently fused with a lysosome to produce a digestible vesicle. Autophagy is the process that causes the cytoplasmic organelles to gradually degrade.[54]

Lysosomal Diseases:

Lysosomal enzymes support lysosome-dependent processes which are responsible for health and disease. Molecules that used for lysosomal disease are given below (Figure 22).[55]

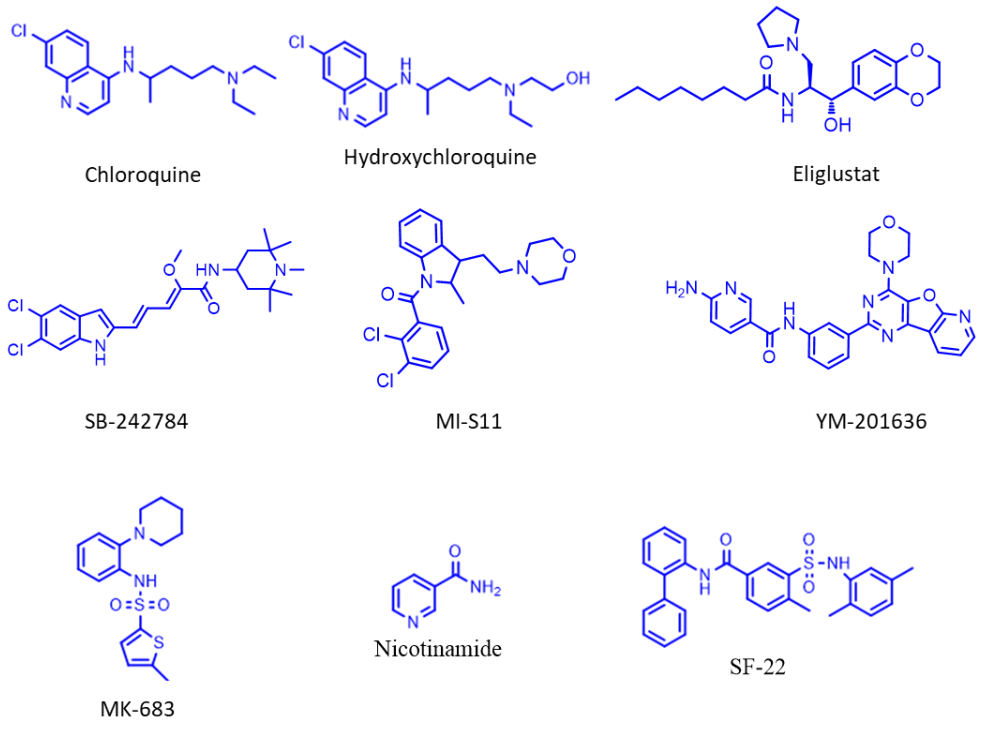

Figure 22. Small molecules for lysosomal disease treatment.

Design of Lysosome targeting functional groups:

With a pK_a range of 4.0–5.0, lysosomes are renowned for their acidic nature. Due to this characteristic, lysosome-targeting groups are designed that can readily bind protons and build up to larger concentrations inside lysosomes. Fluorescence moieties have been added to these functional groups in order to allow fluorescence microscopy imaging of lysosomes inside of living cells.

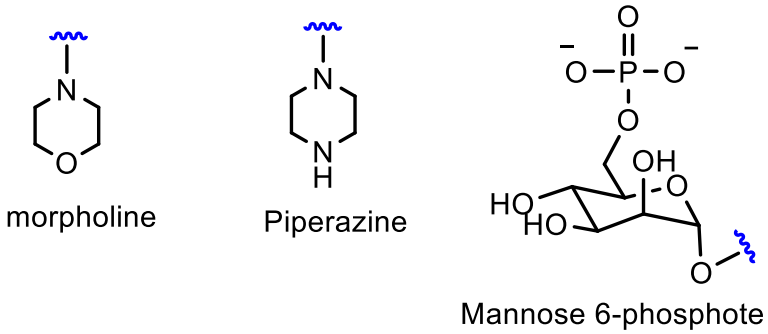

Figure 23. Lysosome targeting scaffolds.

Due to their similar pK_a values to lysosomes, secondary and tertiary amines become excellent candidates to target lysosomes.[56] Such groups include morpholine, piperazine, N-ethyl-N-methyl ethanamine, and mannose 6-phosphate, to name a few (Figure 23). Overall, new areas of investigation into the behaviour and operation of these crucial cellular organelles have been made possible by the capacity to target lysosomes with particular functional groups and fluorescent markers.

Healthy cell:

A healthy cell that is functioning normally and is able to do its fundamental tasks, like metabolism, growth as well as division, in a controlled and regulated way. A healthy cell has the following genetic components:

During cell division, the information contained in the DNA is correctly copied and passed to the daughter cells.[57] In order to preserve tissue homeostasis and prevent the emergence of aberrant growths, such as tumours, healthy cells also have mechanisms to repair any damage to their DNA, proteins, or lipids. This process of programmed cell death is known as apoptosis.[58-60] Overall, a healthy or normal cell is a complex and dynamic creature capable of performing its specific tasks, interacting with other cells to maintain the structures' appropriate functioning, and undergoing programmed organism growth as a whole.

Cancer cell:

Cells that have undergone genetic changes that cause unchecked cell growth and division, resulting in the creation of a tumour or tumours, are referred to as cancer cells. These cells frequently[61-64] have flaws in their DNA repair processes, which can cause a build-up of further mutations and genomic instability. They might also be able to avoid typical cellular processes that ordinarily result in cell death or apoptosis, which would enable them to survive and multiply even in challenging circumstances. Depending on the type of cancer, the properties of cancer cells can change, however, they all have unchecked development and proliferation in common.

There are several key differences between normal cells and cancer cells:

1. Growth and division: A complex network of signalling pathways strictly regulates the process of growth and division in normal cells.[65-67] As a result, they can keep the right number of cells in a tissue or organ. The ability to regulate growth and division has been lost in cancer cells, which causes them to divide uncontrolled even when there is no demand for more cells. The average cell cycle involves three phases: growth, division, and death. Contrarily, cancer cells do not adhere to this cycle. They grow and continue to make new aberrant cells rather than perish.

2. DNA repair mechanisms: Healthy cells have an effective system for repairing DNA damage brought on by regular cellular functions or external stimuli. These repair processes aid in preserving the genome's integrity and halting the accumulation of mutations. On the other hand, cancer cells frequently have flaws in their DNA repair processes, which can cause an increase in mutations and genomic instability.

3. Cell death: The body can get rid of damaged or undesirable cells by allowing normal cells to go through a process called programmed cell death, also known as apoptosis. Contrarily, cancer cells frequently have flaws in the pathways that regulate apoptosis, which allows them to persist and grow despite unfavourable circumstances.[68]

4. Contact inhibition: Normal cells have contact inhibition, which means that when they come into contact with other cells, they stop dividing. This keeps the cells in a tissue or organ's appropriate spatial organisation.[69,70] Cancer cells, on the other hand, frequently lack contact inhibition and continue to divide even in the presence of other cells.

5. Angiogenesis: Angiogenesis, a process that cancer cells have the ability to trigger, assists in supplying the expanding tumour with nutrition and oxygen. Normal cells, however, do not promote angiogenesis.

6. Metastasis: Cancer cells have the capacity to invade adjacent tissues and metastasize (spread to other areas of the body), which can result in the development of additional tumours.[71] Normal cells, in contrast, do not behave in a metastatic manner.

7. At the site of the tumour, specific receptors and enzymes-such as $\alpha_v\beta_3$ integrin, folate, EGFR, leucine aminopeptidase (LAP), and β-galactosidase-are overexpressed.

Cell-penetrating peptides (CPPs): Cell-penetrating peptides (CPPs) can incorporate cells through the cell membrane and deliver a variety of substances, such as proteins, medicines, diagnostic tools, and nucleic acids.[72-75] A well-known CPP is the trans activator of transcription (TAT) peptide. Particularly the TAT peptide (Figure 24), which is generated from the HIV protein, has been thoroughly investigated for its capacity to deliver therapeutic compounds to different cell types.[76, 77] CPPs like TAT enter cells through a variety of methods, including as receptor-mediated endocytosis or direct translocation across the lipid bilayer. CPPs could be used in a variety of biomedical and biotechnological applications. Here are a few illustrations:

1) Drug delivery: When compared to conventional drug delivery techniques, CPPs can be utilised to transport medications directly into cells, potentially increasing their efficacy and minimising negative effects.

2) Gene therapy: Hereditary illnesses and some types of cancer may be treated using CPPs by delivering therapeutic genes into cells..

3) Protein delivery: Therapeutic proteins can be delivered into cells via CPPs, which may help treat a number of diseases, including autoimmune disorders and some types of cancer.

4) Diagnostics: CPPs can be used to transport diagnostic chemicals into cells, which may aid in early illness detection and disease progression monitoring.

Despite their potential, CPPs are still being developed and have numerous obstacles that must be solved, such as increasing their specificity and efficacy and lowering their toxicity. However, there is a lot of promise for the use of CPPs in a range of medical applications in the future as this field of

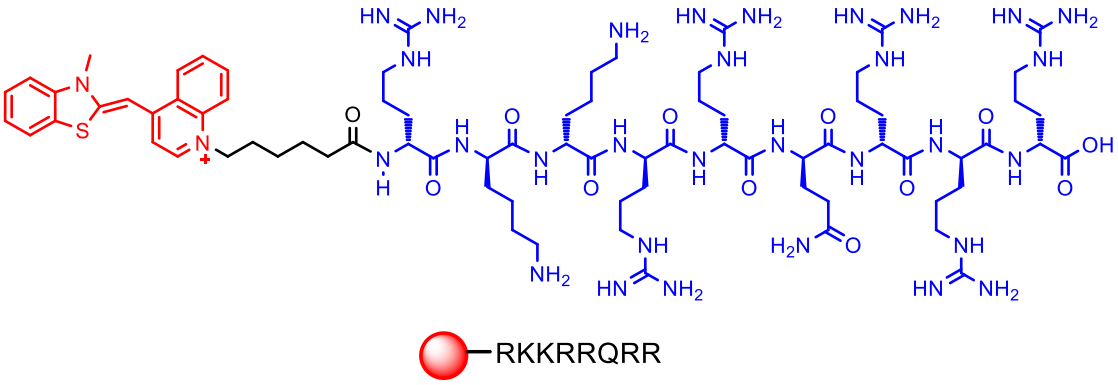

Figure 24. Flurophore conjugated trans activator of transcription (TAT) peptide.[72-75]

study is very active. Many types of receptors that are overexpressed in cancer include: $\alpha_v\beta_3$ integrin, folate, EGFR, and other receptors, among others, are Overexpressed at the tumour site[78,79]. $\alpha_v\beta_3$, integrin is one of numerous receptor subtypes that are overexpressed on cancer cells. The RGD peptide is a particular sequence of amino acids that attaches to the $\alpha_v\beta_3$ integrin in order to function in cell adhesion and migration. $\alpha_v\beta_3$ integrin overexpression in cancer cells contributes to tumour angiogenesis, invasion, and metastasis.[80,81]

The radiopharmaceutical F-fluciclatide, which is utilised for positron emission tomography (PET) imaging of several forms of cancer, is one instance of an RGD-containing drug that targets $\alpha_v\beta_3$ integrin. Another illustration is the medication cilengitide, a peptide with cyclic RGD residue that is being researched as a potential anti-cancer treatment.[82,83] Cilengitide is being explored in clinical tests for the treatment of several cancers, comprising glioblastoma, non-small cell lung cancer, and melanoma. It has been demonstrated to reduce tumour angiogenesis and invasion in preclinical models.

To properly target tumour tissues with therapeutic medicines is a major problem to fight against cancer. Although cancer cells and healthy cells have a lot in common, some receptors—such as integrins, epidermal growth factor receptors, folate receptors, and somatostatin receptors—are overexpressed on the surfaces of cancer cells, providing a way to attach cytotoxic agents to a carrier agent and deliver them to human tumours.[84] This focused anticancer approach can result in medications with less hazardous side effects because of better tumour target specificity, enhanced solubility, biodistribution, and capacity to cross cellular membranes, all of which are important from a therapeutic standpoint. Integrins are one of the receptors that are overexpressed on tumour cells and are therefore interesting targets for pharmaceuticals.[85] These heterodimeric transmembrane cell adhesion glycoproteins play a crucial part in promoting tumour cell motility, invasion, proliferation, and survival. Integrins have also been associated with tumor angiogenesis, which is crucial for the development and metastasis of tumors. The integrins $\alpha_v\beta_3$, $\alpha_v\beta_5$ which are often overexpressed in tumour endothelium cells and in a variety of tumor cells, comprising lung, breast, melanoma, prostate and brain tumors, are particularly intriguing.[86,87] Given that the

consensus tripeptide motif RGD (Arg-Gly-Asp) is recognized by integrins $\alpha_v\beta_3$, $\alpha_v\beta_5$ and with high affinity, it is possible to use carriers based on RGD-peptides or peptidomimetics to transport chemotherapeutic drugs or radionuclides in carcinoma cells or to image tumors.[88,89] Numerous studies have shown that utilizing restricted peptides that embed the RGD sequence within a cyclic structure increases the RGD motif's ability to target angiogenic endothelial cells.[90] Overall, the use of RGD-containing compounds to target the $\alpha_v\beta_3$ integrin is a promising approach for the detection and therapy of cancers.[91]

Confocal Laser Scanning Microscopy: A specialised fluorescence imaging method called confocal laser scanning microscopy (CLSM) is frequently applied in bioimaging applications. In order to create a picture, CLSM uses a concentrated laser beam rather than a lamp or LED lights, following the same principles as a traditional fluorescence microscope. White light lasers or different wavelength laser excitation sources are also employed in CLSM. The small portion of a specimen is illuminated by laser light, and the light that is emitted is sent through a pinhole (located directly in front of the detector), which eliminates out-of-focus light from neighbouring planes to lower background noise and considerably improve the image quality. The fluorescence signal from the specimen was initially detected and amplified by a photomultiplier tube (PMT) in CLSM, but as technology advanced and the HyD hybrid detector was introduced, it now offers higher contrast with superior image quality. Contrary to conventional fluorescence microscopy, CLSM is advantageous for its ability to improve the contrast, sharpness, and optical resolution of the pictures that are captured as well as reduce the impacts of out-of-focus blurring. The main benefit of CLSM is the creation of 3D cellular

pictures using the appropriate colours from a number of Z-stack slices harvested from the specimen at varying depths. This provides more accurate structural information on cellular organelles.

Live cell confocal imaging:

Confocal imaging techniques are widely employed to make sure that a probe is taken up by cells in both fixed cell and live cell settings. However, compared to

Figure 25. Specialized instrumentation for live cell confocal imaging is shown here.

Fixed-cell imaging, live-cell imaging is very different. Cells were grown on a coverslip for fixed cell imaging before being fixed in a 4% paraformaldehyde solution. Cells are largely retained during this process with their original form and composition, making subsequent labelling and imaging procedures considerably simpler than they would be with live cells. However, throughout the fixed cell process, the cell membrane's integrity might be compromised, making fixed cells more permeable to outside chemicals. Furthermore, the images produced following cell fixation lack the dynamic behaviour of the cells, which is crucial biological information. In contrary, in live-cell imaging

cells are active while being imaged over time (time-lapse imaging) at 37°C and 5% CO_2 incubation, illustrating the dynamic nature of cellular organelles. Compared to fixed cell imaging, live cell imaging is more difficult and required unique setup (Figure 25). The fluorophores employed for live cell imaging must, above all, have minimal toxicity and outstanding photophysical characteristics in order to tolerate prolonged laser irradiation.

Multicolor cellular imaging:

To comprehend and view complicated and dynamic biological activities, a multicolor live cell confocal imaging technology has emerged. However, due to a lack of appropriate dyes, it is difficult to simultaneously track multiple cellular organelles of the same cell. Fluorophores coupled with organelle specific functional groups and possessing discrete restricted excitation and emission bands are necessary for multicolor cellular imaging. Multicolor imaging visualises the morphological and structural alterations of multiple organelles that occur under diverse pathogenic events, revealing various cellular events of the same cell in a single image. NIR fluorophores with restricted absorption and emission bands have recently been developed by the Collot and Kai Johnsson groups for multicolor imaging applications.[92-94]

Lysosome Targeting Fluorophores:

Here, Lyso-NINO, a two-photon fluorescent probe containing NO, that targets lysosome is reported based on the photoinduced electron transfer (PET) principle by combining the NO-reactive o-phenylenediamine, the lysosome-specific morpholine, and the effective two-photon probe naphthalimide.[95] Naphthalimide was directly attached to o-phenylenediamine, which served as both a NO trapper and an electron donor (a fluorescence quencher)

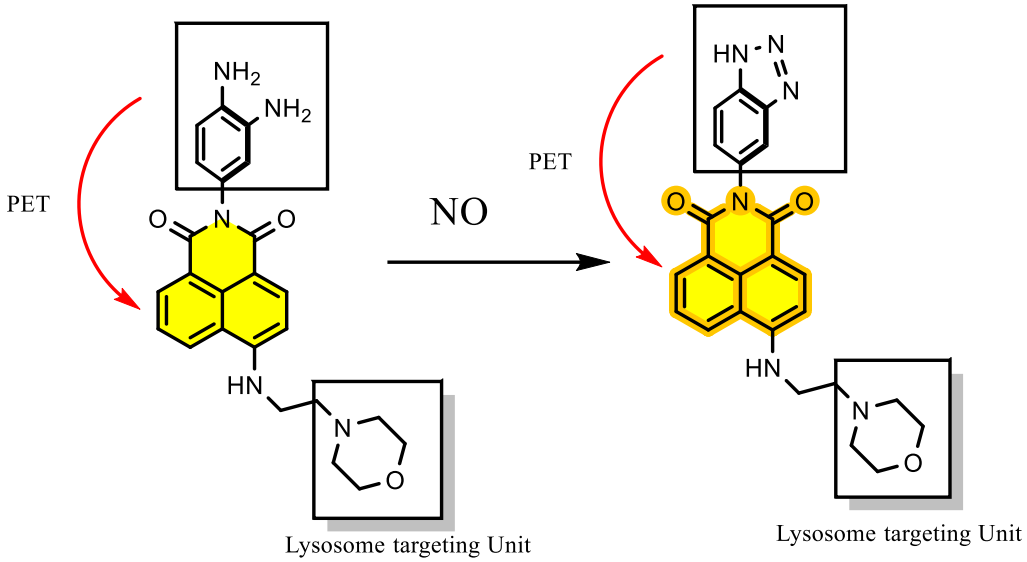

Figure 26. The chemical structure of Lyso-NINO and its capture of NO.[95]

for naphthalimide (Figure 26). Therefore, using 4-(2-aminoethyl)-morpholine, the 4 position of naphthalimide may be retained and further changed. With a lower pK_a value, the alkylmorpholine group specifically targets acid hydrolase-rich lysosomes within the pH domain of 4.0 - 5.0.

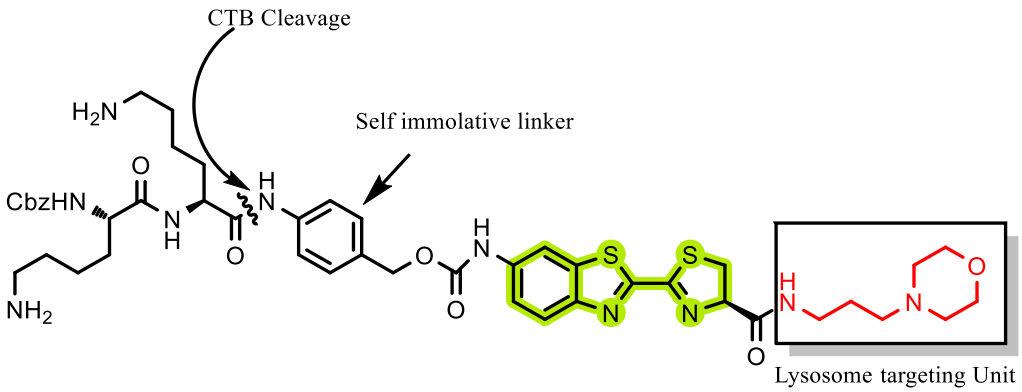

Figure 27. Design of lysosome-targeting CTB activated fluorogenic probe. [96]

Using a CTB-relating peptide substrate called Cbz-Lys-Lys-PABA and lysosome targeting morpholine, they have demonstrated a lysosome-specific fluorophore for imaging of lysosomal CTB in vivo carcinoma cells (Figure 27). They showed that CTB could effectively activate the probe to produce a 73--times increase in fluorescence in the acidic environment (pH 4.0–5.0) of lysosome, enabling greater sensitive and specific detection of CTB.[96] Fluorescence imaging findings demonstrated preferential fluorescence buildup and activation in cancer cells' lysosomes, which were able to report on lysosomal CTB activity in both carcinoma and healthy cells. This results emphasises the scope for developing a sensitive and targeted probe for lysosomal CTB fluorescence imaging in living cells employing a lysosome-targeting group.

For the specific monitoring cellular pH in live-cells, a new lysosome-specific ratiometric fluorescent dye (CQ-Lyso) chromeno quinoline fluorophore is synthesized.[97] The ratiometric fluorescence pH sensor is designed on the

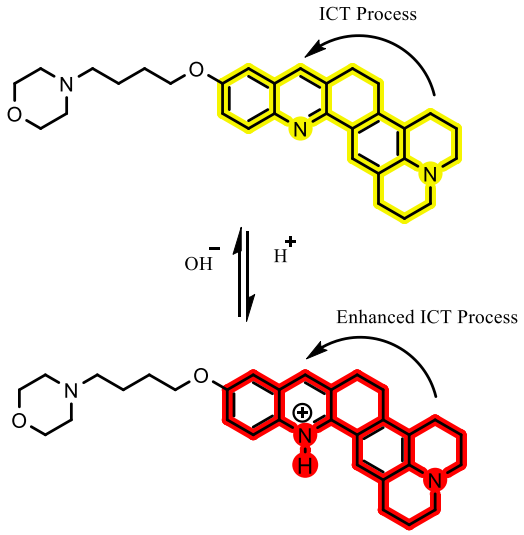

Figure 28. Proposed mechanism for pH measurements in aqueous media.or lysosome

accelerated intramolecular charge transfer (ICT) mechanism that is induced by proton uptake of the quinoline moiety of CQ-Lyso in acidic environments (Figure 28). This process causes substantial bathochromic shifts in both λ_{abs} (104 nm) and λ_{em} (53 nm). With decent Pearson's colocalization coefficients by LysoTracker Deep Red (0.97) and LysoTracker Blue DND-22 (0.95) as benchmarks, this probe effectively stains lysosomes. Significantly, they demonstrate that CQ-Lyso uses single-wavelength excitation to ratiometrically quantify and photograph lysosomal pH levels.

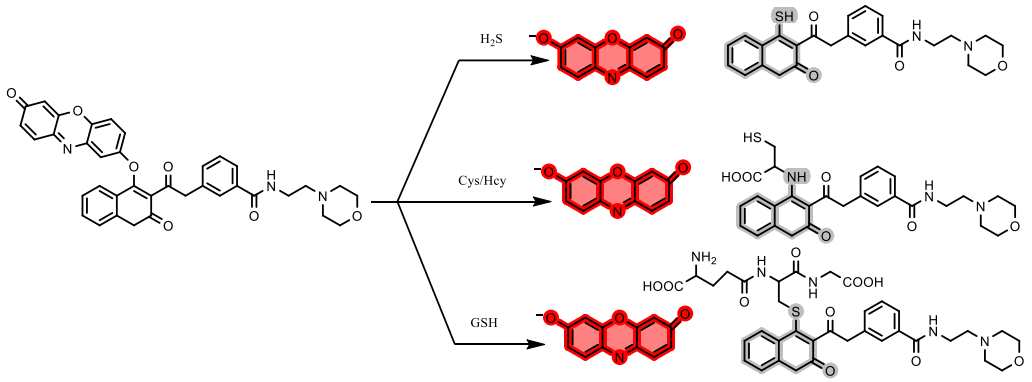

Figure 29. Proposed mechanism for sensing of thiols.

The first fluorescent probe that could target lysosomes, Lyso-RC, was synthesised.[98] It could react to Cys/Hcy, GSH, and H_2S with various sets of signal patterns (Figure 29). Lyso-RC reacts to Cys/Hcy, GSH, and H_2S and produces emission signal patterns of blue-red, green-red, and red, respectively. In HeLa cells, Lyso-RC can distinguish between lysosomal Cys/Hcy, GSH, and H_2S.

Stoddart's group have synthesised a box-like artificial receptor (ExBox·4Cl), which binds a photosensitizer, 5,15-diphenylporphyrin (DPP), to offer photoprotection via controlling light energy.[99] This was motivated by

information of the photoprotective mechanism functioning in photosystem super complexes and bacterial antenna complexes by pigment binding proteins. DPP is made soluble in water by the hydrophilic $ExBox^{4+}$, which also controls DPP's phototoxicity by encasulating in its cavity and releasing it as needed (Figure 30). A pH-sensitive discharge of diprotonated DPP ($DPPH_2^{2+}$) restores the triplet deactivation path, enabling the DPP's capacity to produce reactive oxygen species while trapping blocks access to the DPP triplet state.

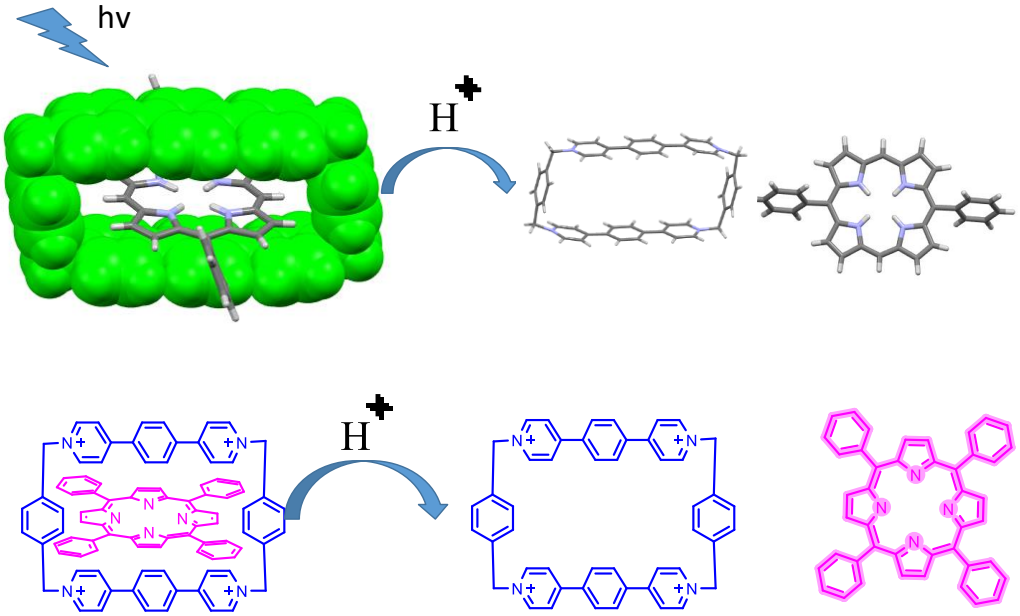

Figure 30. Decomplexation of DPP from $ExBox^{4+}$ at low pH.

For the safe lysomal delivery of DPP they used $ExBox^{4+}$-encapsulated DPP ($ExBox^{4+}$DPP), for the image of cells using the fluorescence of the released $DPPH_2^{2+}$.

In this study, they synthesized a morpholine containg water-soluble complex, triscyclometalated Ir(III) Ir-lyso, which serves as a secure two-photon flurophore for long-time lysosome monitoring (Figure 31).[100] The morpholine moiety in Ir-lyso is essential for both hydrophilicity and specific localisation in lysosomes. Ir-lyso would be kept in the lysosome after morpholine was protonated there because it is more hydrophilic. In acidic lysosomes,

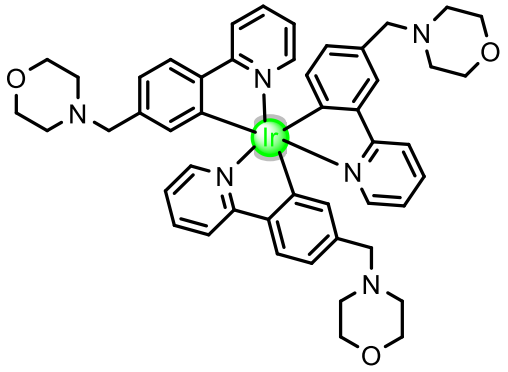

Figure 31. Iridium(III) complex for long term lysosomes tracking.

the protonated morpholine acts as a lock to prevent Ir-lyso from building up. Ir-lyso's ability to respond to pH was inversely related to pH, and even at high pH, it still showed phosphorescence. Ir-lyso illuminated the lysosomes of HeLa cells and 3D tumour spheroids with two-photon properties.

What is the meaning of more that 4. Cross check and write properly

In this work the authors describe a cationic fluorescent probe (PyQPMe) that demonstrates outstanding pH-sensitive fluorescence in

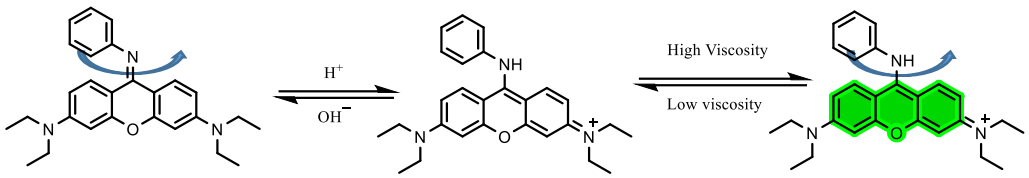

PYQPMe

Figure 32. Chemical structure of probe and the proposed mechanism of pH and viscosity sensing.

endolysosomes at several phases of interest (Figure 32).[101] A detailed photophysical and computational investigation on PyQPMe was conducted to rationalise Zeit's extremely pH-sensitive absorption/ emission. PyQPMe's significant Stokes shift and strong emission signal may substantially reduce background noise induced by excitation light and environments, resulting in a high signal-to-noise ratio for high-resolution imaging of endo-lysosomes. They were able to disclose rate of continuous conversion from early endosomes to late endosomes/lysosomes thoughout autophagy at the submicron level by using PyQPMea as a tiny molecular probe in live cells.

Wei Li et. al.[102] describe an oxazine-based activated molecular assembly

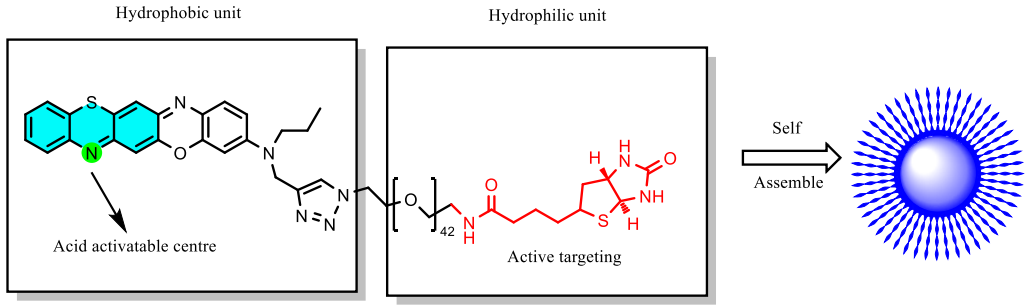

PTO-Biotin

Figure 33. Molecular structure of an activatable NIR probe to image lysosome.

Adjust Figure 32 and caption in the same place.

(ethylene glycol) (PEG) chain was functionalized with a pH-responsive NIR photothermal oxazine molecule to create well-defined nanostructured assemblies inside a single-molecular framework (Figure 33). Due to its increased photothermal activity in the acidic microenvironment, PTO-Biotin NPs has a specific affinity for lysosomal accumulation inside tumour cells. PTO-Biotin NPs caused cytosolic acidification, lysosomal dysfunction, and hindered autophagy upon NIR light activation.

Huimin Ma group synthesized a novel lysosome-targeting NIR ratiometric pH probe by integrating morpholine with a stable

\

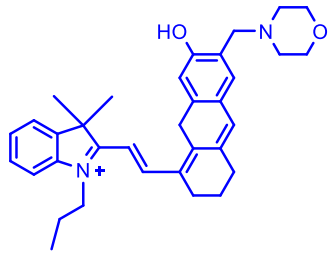

Figure 34. Chemical structure of a NIR flurophore to target lysosome.

hemicyanine skeleton (Figure 34).[103] They showed by fluorescence imaging, that during heat shock, increase in the lysosomal pH value is irreversible which could be due to lysosomal membrane permeabilization. This improved performance allows it for wide use in future in more living cell lysosomal models in elucidating the mechanisms underlying heat-caused disease.

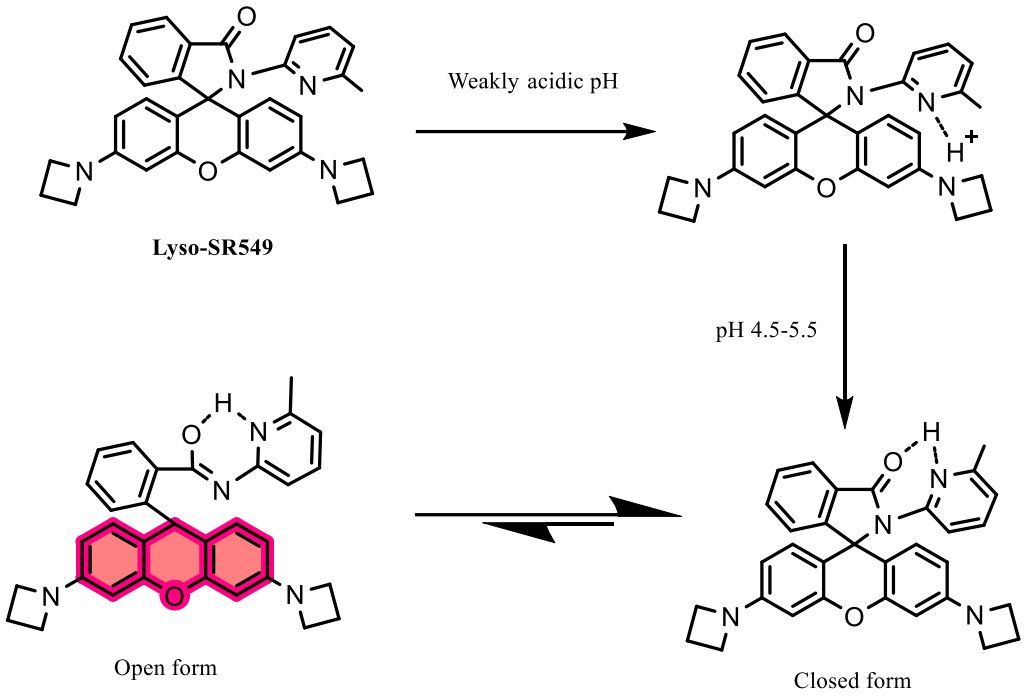

Figure 35. Illustration of mechanism of self-blinking of flurophore in lysosomal pH.[104]

Qinglong Qiao et. al. present a self-blinking fluorophore with high resolution of 12 nm and time resolution of 20 ms in acidic lysosomal conditions. Over 40 minutes, this probe was effectively used in super resolution microscopy of lysosomal dynamics (Figure 35). The dye's pH dependency during blinking rendered the fluorophore sensitive to lysosomal pH. This probe allows to resolve whole-cell lysosome subpopulations based on lysosomal distribution, size, and luminal pH by simultaneously recognising all lysosomes in the whole cell at the single-lysosome resolved level. They also detected a range of lysosomal movement trajectories and distinct sorts of lysosome interactions.

What is Ratiometric Fluorescence?

Ratiometric fluorescence is a technique for detecting alterations in the immediate environment by measuring intensities at two or more wavelengths of an excitation or emission spectrum. A probe that is specifically sensitive to an environmental factor, such as ion concentration, pH, viscosity, or polarity, is typically utilized. By measuring spectra or kinetics, ratiometric dyes can be applied to determine probe-sensitive features like ion concentration.

For the healthy operation of cells in living beings, biological species such as reactive oxygen species (ROS), reactive sulphur species (RSS), reactive nitrogen species (RNS), Pd^{2+}, Cu^{2+}, Hg^{2+}, and others are essential. But their abnormal concentration can lead to a number of deadly illnesses. As a result, it is crucial to keep an eye on biological species in cellular organelles such the nucleus, endoplasmic reticulum, mitochondria, and lysosomes. Ratiometric fluorescence probes have attracted particular interest among the many fluorescent probes for species detection within the organelles as a potential means of getting over the limitations of intensity-based probes. This technique yields an effective result by monitoring the intensity variation of two emission bands (produced by an analyte).

Due to their superior photo-physical properties, high sensitivity, quick reaction, low cost, noninvasiveness, and real-time imaging, fluorescent probes for targeting organelles have recently attracted increased interest.[105] Notably, many single emission probes are susceptible to interference from the surroundings. Ratiometric fluorescence probes could get rid of background noise through an integrated correction of two emissions at various wavelengths.[106] However, using fluorescent probes with single emission features to quantify a target analyte can be challenging due to the interference of various analyte independent factors, including instrumental parameters, local

concentrations of the probe molecules, photobleaching, and microenvironments. The employment of ratiometric techniques is the most efficient method for resolving these problems and ensuring reliability.[107]

Ratiometric fluorophores depends on variations in the intensity of two or more λ_{em} brought on by analytes. The association among the ratio of intensities at two wavelengths and the probes have efficient internal referencing mechanisms that significantly boost their sensitivity and enhance quantification because of the target analyte's concentration. Therefore, this method takes into account environmental elements and gets rid of the majority of uncertainties.

Strategies to Design Ratiometric Fluorescent Probes:

Despite being widely used in labelling, bioimaging, sensing, disease diagnosis, conventional probes like coumarin, naphthalimide, rhodamine, fluorescein, BODIPY, and cyanine still have a number of significant drawbacks. First and foremost, Measurements of fluorescent emission that rely solely on a change in emission intensity at one peak can be affected by methodical faults like environmental variations around the sensor (conc., polarity, pH, temperature, time etc), localization of the dye, actual thickness of the cell in the optical beam, effectiveness of the emission signal, and changes in the laser power. Second, some of the probes' potential applications could still be restricted by certain of their unattractive photophysical characteristics. [108] Ratiometric measurement, an unique technique for simultaneously recording the fluorescence intensities at two channels and calculating their ratio, has been developed to counteract the effects of such circumstances. Numerous methods have been thoroughly studied in the development of ratiometric fluorescence sensing, comprising internal charge transfer (ICT) mechanism, excited-state

intramolecular proton transfer (ESIPT) mechanism, Förster resonance energy transfer (FRET) mechanism, through-bond energy transfer (TBET) mechanism and conjugation modulation mechanism (Figure 36).

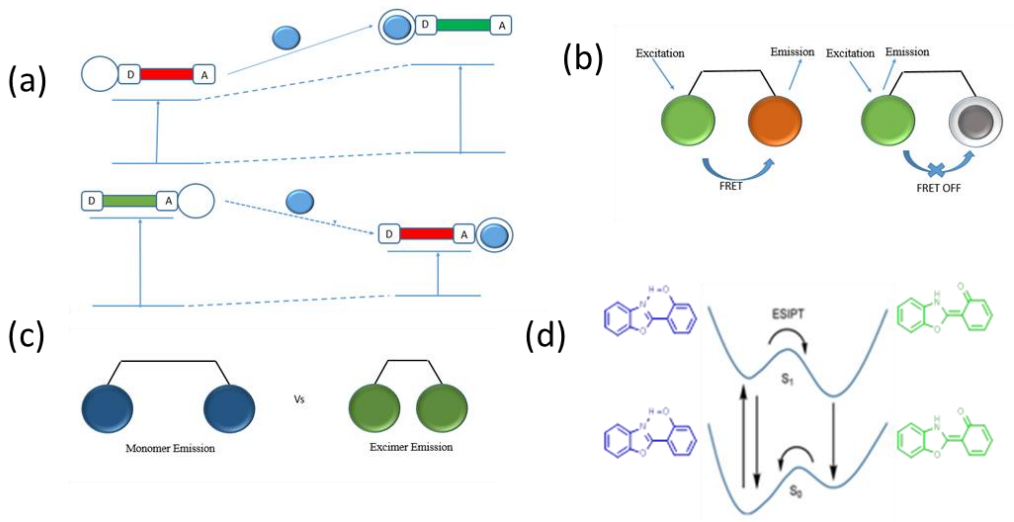

Figure 36. Photophysical processes that cause ratiometric fluorescent changes. (a) ICT (b) FRET (c) monomer–excimer formation, and (d) ESIPT.

Ratiometric Probes:

FRET BASED Ratiometric Probe: Cy3 and Cy5 are both easily

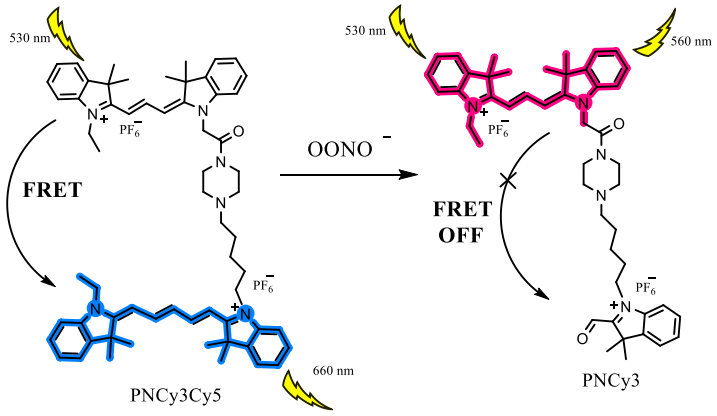

Figure 37. Structure of PNCy3Cy5 and its mechanism for detection of $OONO^-$.

oxidised by $OONO^-$, according to Xuhong Qian.[109] They hypothesised that Cy3, which has a shorter polymethine chain, would be more stable to $OONO^-$. FRET-based ratiometric fluorescent probe (PNCy3Cy5) for detecting $OONO^-$ has been reported in the literature (Figure 37).

ICT and PET Based Ratiometric Probe: Animesh Samanta group designed a one-of-a-kind tiny molecular molecular dye, PM-Mor-OH, based on the lipophilic morpholine -conjugated pyridinium derivate of "IndiFluors" (Figure 38).[110] The morpholine linked dye genrally accumulates

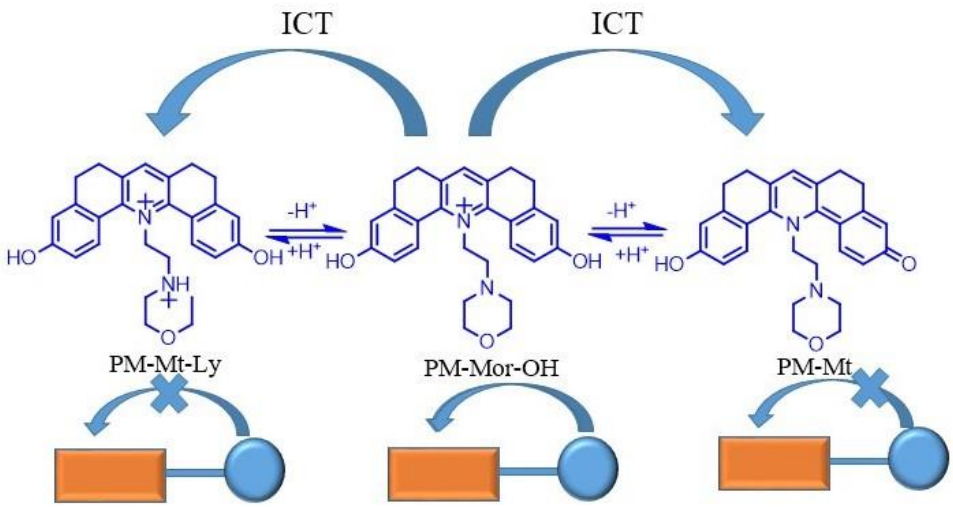

Figure 38. Proposed mechanism for PM-Mor-OH in mitophagy process.

in the lysosome. Though they have detected uncommon phenomena of morpholine-tethered PM-Mor-OH, which localized mitochondria exclusively. The morpholine also showss an important function in tuning optical characteristics via PET during internal pH change (pHi). Lysosomes consume injured mitochondria through the mitophagy process, resulting in pHi, which

may be measured with their dye. It emitted "ratiometric" light at a single wavelength λ_{ex} (ex. 488 nm) and is suited for quantifying the pHi during mitophagy by a confocal microscope. Similarly, the PET process validated the alteration in the fluorescence ratio (green/red) with pH fluctuations. Furthermore, PM-Mor-OH can assess the pH shift caused by rapamycin, mutant A53T-synuclein-induced protein misfolding stress in mitochondria, and malnutrition. Therefore, PM-Mito-OH is a good dye for visualising mitophagy and could be used to diagnose mitochondrial disorders.

ESIPT Based Ratiometric Probe: 3-hydroxyflavones (3-HFs) have been used as fluorescent sensor for the ratiometric sensing of $ONOO^-$ when bound to aggregates, according to research by the teams of Tony D. James and Jonathon L. Sessler. (Figure 39).[111]

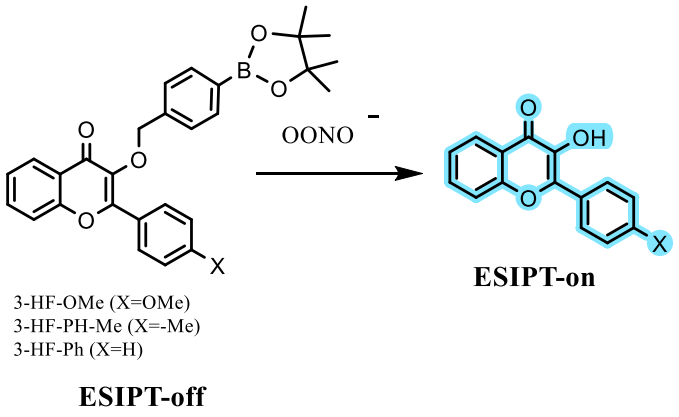

Figure 39. An ESIPT activatable ratiometric probe.

To detect a wide range of analytes, 3-HFs have been widely used as fluorescent probes. Attention is drawn in these systems by the dual emission attributed to the normal (N) and photo tautomeric (T*) states, which result ESIPT. The surroundings of the molecule, notably the solvent's polarity, have an impact on the intensity ratio of these two emission peaks. They have previously shown

that adding a benzyl boronic ester protecting group can hinder the ESIPT process.

Ratiometric Imaging:

Many fundamental cell processes rely on delicate, but dynamic, equilibrium of ions, voltage potentials, and pH among the cell's cytoplasm and the neighbouring extracellular milieu. Alterations in these balances have a major influence on the behaviour and function of a cell. Thus real-time quantification of intracellular ion, voltage, and pH dynamics are of great interest in chemical biology. In many circumstances, though, standard fluorescence methods make precise estimates of real ion concentrations or relative alterations in various locations inside a cell impossible. Because these methods don't take into account the likelihood that changes in cell shape within distinct regions of a single cell or among different cell varieties in cellular networks may affect the quality and amount of transmitted light, this is the cause. This could result in serious misunderstandings when analysing dynamic changes in voltage, pH, or ion concentrations. By analysing fluorophore emission wavelength shifts or contrasting the emission intensity of a fluorophore combination rather than just recording intensity changes, ratiometric imaging methods get around these problems.

The three-dimensional and chronological distribution of native "hot spots" for lively variations in ion concentration, voltage, pH in a cell or cell network is becoming increasingly important in research. Such "hot spots" are frequently found in specialised areas of a cell. Furthermore, in terms of cell metabolism or structure, these zones frequently differ from the remainder of the specimen. Orthodox dyes used to explore vibrant biological conditions modify their emission intensity in response to ion binding, pH change, voltage change. These markers, however, do not account for the fact that alterations in

assembly, diameter, and biomarker uptake might induce variations in the quantity of released light that are unrelated to the actual ion conc., voltage, or pH. To identify alterations in cell structures or distinct cells quantitatively and comparably, a process that is unresponsive to structure diameter and chromophore conc. is required. In comparison to non-ratiometric imaging approaches, ratiometric imaging allows for the reproducible measurement of intracellular ion, voltage, and pH changes regarding cell diameter, probe concentration, and imaging setup photosensitive characteristics. However, ratiometric imaging is dependent on a fast shift in excitation or observed wavelength, a bright light source, efficient optical component transmission, and fast signal detection.

References:

[1] Du, J.; Hu, M.; Fan, J.; Peng, X. *Chem. Soc. Rev*. **2012**, *41*, 4511.

[2] Schnermann, M. J. *Nature* **2017**, *551*, 176–177.

[3] Escobedo, J. O; Rusin, O.; Lim, S., Stongin, R. M. *Curr. Opin. Chem. Biol*. **2010**, *14*, 64-70.

[4] Tung, C. H.; Lin, Y.; Moon, W. K.; Weissleder, R. *Chem. Bio. Chem***. 2002**, *3*, 784-786.

[5] Byron, B.; Lauren A, E.; Alen S, W. *Curr. Med. Chem*. **2005**, *12*, 795-805.

[6] Weissleder, R.; Ntziachristos, V. *Nat. med*. **2003**, *9*, 123-128.

[7] Ntziachristos , V.; Yodh, A. G.; Schnall, M.; Chance, B. *Proc. Nat. Acad. Sci*. **2000**, *97*, 2767-2772.

[8]Chen, W. T.; Mahmood, M.;Weissleder, R.; Tung, C. H. *Arthritis. Res Ther*. **2005**, *7*, 310.

[9] Gorka, A. P.; Nani, R. R.; Schnermann, M. J. *Org. Biomol. Chem.* **2015**, *13*, 7584–7598.

[10] Wyler, H. *Chem. Unserer. Zeit*. **1969**, *3*, 111-115.

[11].Wyler, H. *Chem. Unserer.Zeit*. **1969**, *3*, 146-151.

[12] Nakhaei, E.; Kim, C. W.; Funamoto, D.; Sato, H.; Nakamura, Y.; Kishimura, A.; Mori, T.; Katayama, Y. *Chem. Commun.* **2017**, *8*, 1190–1195.

[13] Chen, W. T.; Mahmood, U.; Weissleder, R.; Tung, C. H. *Arthritis Res. Ther.* **2005**, *7*, 310–317

Please change the color of reference 13

[14] Williams, C. G. *Earth Environ. Sci. Trans. R. Soc. Edinb.* **1857**, *21*, 377–401.

[15] Narayanan, N.; Patonay, G. *J. Org. Chem*. **1995**, *60*, 2391-2395.

[16] Patonay, G.; Salon, J.; Sowell, J.; Strekowski, L. *Molecules* **2004**, *9*, 40–49.

[17] Narayanan, N.; Patonay, G. *J. Org. Chem.* **1995**, *60*, 2391–2395.

[18] Musso, H. *Tetrahedron* **1979**, *35*, 2843–2853.

[19] Lipowska, M.; Patonay, G.; Strekowski, L. *Synth. Commun.* **1993**, *23*, 3087–3094.

[20] Guether, R.; Reddington, M. V. *Tetrahedron Lett.* **1997**, *38*, 6167–6170.

[21] Renikuntla, B. R.; Rose, H. C.; Eldo, J.; Waggoner, A. S.; Armitage, B. A. *Org.Lett.* **2004**, *6*, 909 912.Reichardt,

[22] Mader, O.; Reiner, K.; Egelhaaf, H. J.; Fischer, R.; Brock, R. *Bioconjug. Chem.* **2004**, *15*, 70–78.

[23]Song, F.; Peng, X.; Lu, E.; Wang, Y.; Zhou, W.; Fan, J. *Tetrahedron Lett.* **2005**, *46*, 4817–4820.

[24] Kretschy, N.; Somoza, M. M. *PLOS ONE* **2014**, *9*, e85605.

[25] Warner, I. M.; Soper, S. A.; McGown, L. B. *Anal. Chem.* **1996**, *68*, 73–92

[26] Hammer, F. M. *The Cyanine Dyes and Related Compounds*; *Wiley*, **1964**.

[27]Narayanan, N.; Strekowski, L.; Lipowska, M.; Patonay, G. *J. Org. Chem.* **1997**, *62*, 9387.

[28] Strekowski, L.; Lipowska, M.; Patonay, G. *Synth. Commun.* **1992**, *22*, 2593–2598.

[29] Strekowski, L.; Lipowska, M.; Patonay, G. *J. Org. Chem.* **1992**, *57*, 4578–4580.

[30]Losytskyy, M. Yu.; Volkova, K. D.; Kovalska, V. B.; Makovenko, I. E.; Slominskii, Yu. L.; Tolmachev, O. I.; Yarmoluk, S. M. *J. Fluoresc.* **2005**, *15*, 849–857.

[31]Slominskii, Y. L.; Ephimenko, N. I.; Kachkovskii, A. D.; Kurkina, L. G.; Tolmachev, A. I. *Ukr. Khim. Zh.* **1986**, *52*, 301.

[32]HopeRoss, M.; Yannuzzi, L. A.; Gragoudas, E. S.; Guyer, D. R.; Slakter, J. S.; Sorenson, J. A.; Krupsky,S.; Orlock, D. A.; Puliafito, C. A. *Ophthalmology* **1994**, *101* (3), 529–533.

[33]Hirata, T.; Kogiso, H.; Morimoto, K.; Miyamoto, S.; Taue, H.; Sano, S.; Muguruma, N.; Ito, S.; Nagao, Y. *Bioorg. Med. Chem.* **1998**, *6*, 217.

[34] Zhang, Z.; Achilefu, S. *Chem. Commun.* **2005**, *5887*.

[35] Li, Q.; Tan, J.; Peng, B.-X.*Molecules* **1997**, *2*, 91–98.

[36] Stackova, L.; Stacko, P.; Klan, P. *J. Am. Chem. Soc.* **2019**, 141, 7155.

[37] Usama, S. M.; Marker, S. C.; Li, D.H.; Caldwell, D. R.; Stroet, M.; Patel, N. L.; Tebo, A. G.; Hernot, S.; Kalen, J. D.; Schnermann, *J. Am. Chem. Soc.* **2023**, *145* , 14647–14659.

[38] Tang, R.; Lee, H.; Achilefu, S. *J. Am. Chem. Soc.* **2012**, *134*, 4545–4548.

[39] Liu, Y.; Zhou, J.; Wang, L.; Hu, X.; Liu, X.; Liu, M.; Cao, Z.; Shangguan, D.; and Tan W. *J. Am. Chem. Soc.* **2016**, *138*, 12368−12374.

[40] Lovett, W. R.; Al Hamd, A.; Casa, S.; Henary, M. **2021**, *190*, 109268.

[41] Xia, S.; Wang, J.; Zhang, Y.; Whisman, N.; Bi, J.; Steenwinkel, T. E.; Wan, S.; Medford, J.; Tajiri, M.; Luck, R. L.; Werner, T.; and Liu, H. *J. Mater. Chem. B* **2020**, *8*, 1603-1615.

[42] Myochin, T.; Kiyose, K.; Hanaoka, K.; Kojima, H.; Terai, T.; Nagano, T. *J. Am. Chem. Soc.* **2011**, *133*, 3401–3409.

[43] Zheng, R.; Yang, J.; Mamuti, M.; Hou, D.; An, H.; Zhao, Y.; Wang, H. *Angew. Chem. Int. Ed.* **2021**, *60*, 7809–7819.

[44] Yang, L.; Liu, G.; Chen, Q.; Wan, Y.; Liu, Z.; Zhang, J.; Huang, C.; Xu, Z.; Li, S.; Lee, C. S.; Zhang, L.; Sun, H. *Anal. Chem.* **2022**, *94*, 5425–5431.

[45] Huang, J.; Jiang, Y.; Li, J.; He, S.; Huang, J.; Pu, K. *Angew. Chem. Int. Ed.* **2020**, *59*, 4415–4420.

[46] Weng, J.; Wang, Y.; Zhang, Y.; Ye, D. *J. Am. Chem. Soc.* **2021**, *143* , 18294–18304.

[47] Settembre, C.; Ballabio, A. *Trends Cell Biol.* **2014**, *24*, 743–750.

[48] Bonam, S. R.; Wang, F.; Muller, S. Lysosomes as a Therapeutic Target. *Nat. Rev. Drug Discov.* **2019**, *18*, 923–948.

[49] Scarcella, M.; d'Angelo, D.; Ciampa, M.; Tafuri, S.; Avallone, L.; Pavone, L.M.; De Pasquale, V. *Int. J. Mol. Sci.* **2022**, *23*, 9089.

[50] Catarina Pechincha *et al. Science* **2022,** 378, eabn5637.

[51] Christopher M. Richards et al. *Science* **2022**, *378,* eabn5648.

[52] Wang, S.; Zheng, Y.; Yang, F.; Zhu, L.; Zhu, X. Q.; Wang, Z. F.; Wu, X. L.; Zhou, C. H.; Yan, J. Y.; Hu, B. Y.; Kong, B.; Fu, D. L.; Bruns, C.; Zhao, Y.; Qin, L. X.; Dong, Q. Z. *Signal Transduct. Target. Ther.* **2021**, *6*, 249.

[53] Gruenberg, J. *Nat. Rev. Mol. Cell Biol.* **2001**, *2*, 721–730.

[54] Ferguson, T. A.; Green, D. R. *Autophagy* **2014**, *10*, 165–167.

[55] Mondal, B.; Dutta, T.; Padhy, A.; Das, S.; Sen Gupta, S. *ACS Omega*. **2022**, *7*, 5–16.

[56]Andrew,C. L.; Klemm,A. R.; John, B. L.*Biochim. Biophys. Acta* **1330**, *1997*, 71–82.

[57] Nishitani, H.; Lygerou, Z.*Genes Cells* **2002**, *7*, 523–534.

[58] Salazar, N.; Zabel, B. A. *Front. Immunol.* **2019**, *10*, 147.

[59] Dudley, A.C. *Cold Spring Harb Perspect Med*. **2012**, *2*, a006536.

[60] Aird, W.C. *Cell Tissue Res* **2019**, *335*, 271–281.

[61] Aas, P. A.; Otterlei, M.; Falnes, P. O.; Vågbø, C. B.; Skorpen, F.; Akbari, M.; Sundheim, O.; Bjørås, M.; Slupphaug, G.; Seeberg, E.; Krokan, H.E. *Nature.* **2003**, *421*, 859–863.

[62] Bakkenist, C. J.; Kastan, M. B. *Nature.* **2003**, *421*, 499−506.

[64] Bonate, P. L.; Arthaud, L.; Cantrell, W. R.; Stephenson, K.; Secrist, J. A.; Weitman, S. *Nat. Rev. Drug Discov.* **2006**, *5*, 855–863.

[65] Cerbinskaite, A.; Mukhopadhyay, A.; Plummer, E. R.; Curtin, N. J.; Edmondson, R. J. *Cancer Treat. Rev.* **2012**, *38*, 89–100.

[66] Yang, E.; Zha, J.; Jockel, J.; Boise, L. H.; Thompson, C. B.; Korsmeyer, S. J. *Cell.* **1995**, *80*, 285–91.

[67] Hoeppner, D. J.; Hengartner, M. O.; Schnabel, R. *Nature.* **2001**, *412*, 202–206.

[68] Hitoshi, Y.; Lorens, J.; Kitada, S. I.; Fisher, J.; LaBarge, M.; Ring, H. Z.; Francke, U.; Reed, J. C.; Kinoshita, S.; Nolan, G. P. *Immunity*. **1998**, *8*, 461–71.

[69] Barry, M.; Bleackley, R. C. *Nat Rev Immunol.* **2002**, *2*, 401–9.

[70] Freude, B.; Masters, T. N.; Robicsek, F.; Fokin, A.; Kostin, S.; Zimmermann, R.; Ullmann, C.; Lorenz-Meyer, S.; Schaper, J. *J Mol Cell Cardiol.* **2000**, *32*, 197–208.

[71] Torgovnick, A.; Schumacher, B. *Front Genet.* **2015**, *6*, 157.

[72] Wong, R.S. *J Exp Clin Cancer Res.* **2011**, *30*, 87.

[73] Vikhanskaya, F.; Lee, M. K.; Mazzoletti, M.; Broggini, M.; Sabapathy, K. *Nucl Acids Res.* **2007**, *35*, 2093–2104.

[74] Vucic, D.; Stennicke, H. R.; Pisabarro, M.T.; Salvesen, G. S.; Dixit, V. M. *Curr Biol.* **2000**, *10*, 1359–1366.

[75] Kang, M. H.; Reynolds, C, P. *Clin Cancer Res.* **2009**, *15*, 1126–1132.

[76] Raffo, A. J.; Perlman, H.; Chen, M. W.; Day, M. L.; Streitman, J. S.; Buttyan, R. *Cancer Res.***1995**, *55*, 4438.

[77] Nishida, N.; Yano, H.; Nishida, T.; Kamura, T.; Kojiro, M. *Vasc Health Risk Manag.* **2006**, *2*, 213–219.

[78] Fares, J.; Fares, M. Y.; Khachfe, H. H.; Salhab, H. A.; Fares, Y. *Signal Transduct Target Ther.* **2020**, *5*, 28.

[79] Mäe, M.; Langel, U. *Current Opinion in Pharmacology.* **2006**, *6*, 509–514.

[80] Biswas, S.; Torchilin, V. P. *Adv. Drug Deliv. Rev.* **2014**, *66*, 26–41.

[81] Cai, W.; Chen, X. *Small.* **2007**, *3*, 1840–1854.

[82] Carnevale, K. J. F.; Muroski, M. E.; Vakil, P. N.; Foley, M. E.; Laufersky, G.; Kenworthy, R.; Zorio, D. A. R.; Morgan, T. J. Jr.; Levenson, C. W.; Strouse, G. F. *Bioconjugate Chem.* **2018**, *29*, 3273–3284.

[83] Grunwald, J.; Rejtar, T.; Sawant, R.; Wang, Z.; Torchilin, V. P. *Bioconjugate Chem.* **2009**, *20*, 1531−1537.

[84] Mishra, A.; Lai, G. H.; Schmidt, N. W.; Sun, V. Z.; Rodriguez, A. R.; Tong, R.; Tang, L.; Cheng, J.; Deming, T. J.; Kamei, D. T.; Wong, G. C. *Proc Natl Acad Sci U S A.* **2011**, *108*, 16883−16888.

[85] Liu, S. *Bioconjugate Chem.* **2009**, *20*, 2199−2213.

[86] Dechantsreiter, M. A.; Planker, E.; Matha, B.; Lohof, E.; Holzemann, G.; Jonczyk, A.; Goodman, S. L.; Kessler, H. *J. Med. Chem.* **1999**, *42*, 3033−3040.

[87] Liu, Z.; Yu, L.; Wang, X.; Zhang, X.; Liu, M.; Zeng, W. *Curr Protein Pept Sci.* **2016**, *17*, 570−81.

[88] Danhier, F.; Le Breton, A.; Preat, V. *Mol. Pharmaceutics.* **2012**, *9*, 2961−73.

[89] Ruoslahti, E.; Pierschbacher, M. D. *Science.* **1987**, *238*, 491−497.

[90] Reinmuth, N.; Liu, W.; Ahmad, S. A.; Fan, F.; Stoeltzing, O.; Parikh, A. A.; Bucana, C. D.; Gallick, G. E.; Nickols, M. A.; Westlin, W. F.; Ellis, L. M. *Cancer Res.* **2003**, *63*, 2079−2087.

[91] Chen, X.; Conti, P. S.; Moats, R. A. *Cancer Res.* **2004**, *64*, 8009−8014.

[92] Collot, M.; Fam, T. K.; Ashokkumar, P.; Faklaris, O.; Galli, T.; Danglot, L.; and Klymchenko, A. S. *J. Am. Chem. Soc.* **2018**, *140*, 5401−541.

[94] Nishitani, H.; Lygerou, Z. *Genes to Cells.* **2002**, *7*, 523 –534.

[95] Yu, H.; Xiao, Y.; Jin, L. *J. Am. Chem. Soc.* **2012**, *134* , 17486–17489.

[96] Wang, Y.; Li, J.; Feng, L.; Yu, J.; Zhang, Y.; Ye, D.; Chen, H. Y. *Anal. Chem.* **2016**, *88*, 12403–12410.

[97] Liu, X.; Su, Y.; Tian, H.; Yang, L.; Zhang, H.; Song, X.; Foley, J. W. *Anal. Chem.* **2017**, *89*, 7038–7045.

[98] Zhang, H.; Xu, L.; Chen, W.; Huang, J.; Huang, C.; Sheng, J.; Song, X. *ACS. Sens.* **2018**, *3*, 2513–2517.

[99] Roy, I.; Bobbala, S.; Young, R. M.; Beldjoudi, Y.; Nguyen, M. T.; Cetin, M. M.; Cooper, J. A.; Allen, S.; Anamimoghadam, O.; Scott, E. A.; Wasielewski, M. R.; Stoddart, J. F. *J. Am. Chem. Soc.* **2019**, *141*, 12296–12304.

[100] Qiu, K.; Huang, H.; Liu, B.; Liu, Y.; Huang, Z.; Chen, Y.; Ji, L.; Chao, H. *ACS. Appl. Mater. Interfaces*. **2016**, *8*, 12702–12710.

[101] Song, Y.; Zhang, H.; Wang, X.; Geng, X.; Sun, Y.; Liu, J.; Li, Z. *Anal. Chem.***2021**, *93*, 1786–1791.

[102] Li, W.; Yin, S.; Shen, Y.; Li, H.; Yuan, L.; Zhang, X. B. *J. Am. Chem. Soc.* **2023**, *145* , 3736–3747.

[103] Wan, Q.; Chen, S.; Shi, W.; Li, L.; Ma, H. *Angew. Chem., Int. Ed.* **2014**, *53*, 10916−10920.

[104] Qiao, Q.; Liu, W.; Chen, J.; Wu, X.; Deng, F.; Fang, X.; Xu, N.; Zhou, W.; Wu, S.; Yin, W.; Liu, X.; Xu, Z. *Angew. Chem., Int. Ed.* **2022**, *61*, e202202961.

[105] Goshisht, M. K.; Tripathi, N.; Patra, G. K.; Chaskar, M. *Chem. Sci.* **2023**, *14*, 5842–5871.

[106] Park, S. H.; Kwon, N.; Lee, J. H.; Yoon, J.; Shin, I. *Chem. Soc. Rev.* **2020**, *49*, 143–179.

[107] Huang, X.; Song, J.; Yung, B. C.; Huang, X.; Xiong, Y.; Chen, X. *Chem. Soc. Rev.***2018**, *47* , 2873–2920.

[108] Dave, R.; Terry, D. S.; Munro, J. B.; Blanchard, S. C. *Biophys. J.* **2009**, 96, 2371–2381.

[109] Jia, X.; Chen, Q.; Yang, Y.; Tang, Y.; Wang, R.; Xu, Y.; Zhu, W.; Qian, X. *J. Am. Chem. Soc.* **2016**, *138* , 10778–10781.

[110] Munan, S.; Ali, M.; Yadav, R.; Mapa, K.; Samanta, A. *Anal. Chem.* **2022**, *94*, 11633–11642.

[111] Sedgwick, A. C.; Dou, W. T.; Jiao, J. B.; Wu, L.; Williams, G. T.; Jenkins, A. T. A.; Bull, S. D.; Sessler, J. L.; He, X. P.; James, T. D. *J. Am. Chem. Soc.* **2018**, *140* , 14267–14271.

[112] Mukherjee, A.; Saha, P. C.; Kar, S.; Guha, P.; Das, R. S.; Bera, T.; Guha, S. *ChemBioChem*. **2023**, *24*, e202200641.

Chapter 2

Materials and Methods

Introduction

This chapter provides comprehensive information on fundamental materials and a synopsis of the experimental procedures applied in this thesis to synthesis near infrared dyes for the targeted imaging and targeting of cellular organelle. A number of biological investigations pertinent to this study are also included in the chapter, along with complete information on all spectroscopic measurements and microscopic techniques. Confocal laser scanning microscopy (CLSM) has also received specific attention for imaging live cell organelles, as well as multicolor imaging. Each chapter includes comprehensive details of the biological studies that were relevant to the research study as well as the synthetic procedures related to the compounds that were the subject of this thesis.

Experimental Procedures

General Materials:

3-methyl-2-butanone, 6-bromohexanoic acid, 2-Chloroethanol, N,N-diisopropylethylamine (DIPEA), 4-(2-aminoethyl)morpholine, coumarin 6, 4-hydrazinobenzoic acid, cyclohexanone, and DAPI, HATU (1-Bis(dimethylamino)methylene]-1H-1,2,3-triazolo[4,5-b]pyridinium 3-oxide hexafluorophosphate were obtained from Sigma Aldrich Wang resin LL (100-200 mesh), Fmoc-amino acid building blocks: Fmoc-Arg(Pbf)-OH, Fmoc-Gly-OH, Fmoc-Asp(OtBu)-OH, Fmoc-Ser(tBu)-OH, 2-(1HBenzotriazole-1-yl)-1,1,3,3 tetramethyluroniumhexafluorophosphate (HBTU), 1-Hydroxybenzotriazole (HOBt) hydrate, Ethanol, and TLC silica gel 60 F254 were purchased from Merck. 3-methyl-2-butanone, phenylhydrazine hydrochloride, iodomethane, acetic anhydride**,** 4-(2-aminoethyl)morpholine,

Phosphorus oxychloride, DMF (anhydrous, 99.8%), trifluoroacetic acid (TFA), triisopropylsilane (TIS), D- Glucose, 2-Chloroethanol, BF_3-Et_2O, oleic acid (90%), Bisbenzimide trihydrochloride (Hoechst 33342) and all the HPLC grade solvents used for the spectroscopic experiments were procured from Sigma-Aldrich. indocyanine green (ICG), Rhodamine-B were procured from TCI chemicals. All deuterated NMR solvents were bought from Cambridge Isotope Laboratories, Inc. National Centre for Cell Science in India provided the cell lines Human breast cancer MDA-MB-231 (MD Anderson Metastatic Breast-231), human lung adenocarcinoma A549, and epithelioid cervix carcinoma cell lines, HeLa, HEK293, a healthy human embryonic kidney cell line, and C2C12, a non-cancerous mouse myoblast cell line. The following items were purchased from Himedia: 3-(4,5-dimethyl-2-thiazolyl)-2,5-diphenyltetrazolium bromide (MTT), Dulbecco's modified eagle medium (DMEM), Trypsin EDTA combination. Cell Mask Green (C37608), FM 1-43FX, and the mitochondrial targeting dyes MitoTracker Green FM (M7514) and Mitotracker Red FM (M22425) Thermo Fisher Scientific provided the plasma membrane staining probe, LysoTracker Green DND-26 lysosome targeting probe, Coomassie Brilliant Blue R-250, and protease inhibitor cocktail.

Purification of Reagents required for Synthesis of Cyanine Dyes:

For both symmetrical and asymmetrical NIR dye synthesis using of dry solvents play an important role. All the solvents and reagents were purged with nitrogen before using them. For the synthesis of NIR dye of chapter 5 acetic anhydride is very important reagent. It was made by adding acetyl chloride dropwise to anhydrous sodium acetate in a round bottom flask at 0°C while continually stirring the mixture. After fully incorporating the acetyl chloride,

the liquid was left to cool to room temperature before being distilled to produce pure acetic anhydride.

Microwave Synthesizer: precursor molecules were created manually using a microwave synthesiser (USA-made by CEM Corporation), while CsNIR-peptide conjugates were created manually using a microwave peptide synthesiser and the Fmoc-SPPS technique. Using resin (LL, 0.85 mmol/g loading density), Rink amide resin peptides and Lyso-Changsha-peptide conjugates were synthesised.

Characterization of Cyanine Dyes and their precursors:

Spectroscopic Measurements:

NMR Spectroscopy: All the NIR dyes and their intermediate compounds were characterised using 1D (^{1}H, ^{13}C, ^{31}P) and 2D NMR (^{1}H-^{1}H DQF COSY) spectroscopy. Bruker DPX300 MHz and Bruker DPX400 MHz spectrometers were used for all NMR investigations, which were conducted at room temperature in appropriate deuterated solutions.

Mass spectrometry: High-resolution electrospray ionisation mass spectrometry (HRMS-ESI) was performed using a Q-TofmicroTM (Waters Corporation) mass spectrometer.

Absorption Spectroscopy: Using a Shimadzu UV-1800 spectrometer and a quartz cuvette with a 1 cm path length, absorption spectra were captured.

Fluorescence Spectroscopy: A Horiba Jobin Yvon FluoroMax-4 spectrofluorometer was used to detect the fluorescence.

Time-correlated single photon counting (TCSPC) experiment: The time-correlated single photon counting (TCSPC) method was used to assess the fluorescence lifetime of the cyanine and NIR dyes using a Horiba DeltaFlex lifetime equipment (Horiba Jobin Yvon IBH Ltd, Glasgow, Scotland, UK). The fluorescence lifespan of cyanine and NIR dyes in various solvents was

measured using Delta diode laser excitation sources with 510 nm (Model: DD-510L, Horiba Scientific) and 650 nm (Model: DD-650L, Horiba Scientific) wavelengths. Horiba EzTime decay analysis software was used to gather lifetime measurements and analyse the results.

Single Crystal X-ray diffraction: Single crystal X-ray diffraction technique is used to characterize some of the compounds. In order to produce single crystals appropriate for X-ray diffractions, the vapour diffusion and slow evaporation methods were applied. The diffraction data were obtained using a graded multilayer mirror monochromator (0.71073) at 293 K and a micro focus Single Crystal X-ray Diffraction apparatus (Model: D8 Quest, Make: Bruker). A PHOTON-100 CMOS detector was used. The crystal structure of compound 5 was directly solved using the SHELXT 2014–15 software.Using SHELXL-2018/3 from the Olex2S3 crystallographic collective package, Full-matrix least squares modifications were conducted against F2. The non-hydrogen atoms were improved using anisotropic thermal parameters.

Biological Studies:

Cell culture: In DMEM (pH 7.4) growth medium supplemented with 10% foetal bovine serum (FBS) and antibiotic-(6H, m) antimycotic solution 100 (containing 10,000 units penicillin, 10 mg streptomycin, and 25 g amphotericin B per mL in 0.9% normal saline), both carcinogenic and non-cancerous cell lines were cultured. All cell lines were maintained routinely at 37°C in 5% CO2 passages in an incubator.

Cell viability assay: All cyanine and NIR derivatives were evaluated for their cytotoxicity on carcinogenic and non-cancerous cell lines using the MTT assay.

Cellular uptake and lysosome localization study: Confocal laser scanning microscopy methods were used for multicolor imaging in both living cells as

Chapter 3

Acidic pH-Triggered Live-Cell Lysosome Specific Tracking, Ratiometric pH Sensing and Multicolor Imaging by Visible to NIR Switchable Cy-7 Dyes

Acidic pH-Activatable Visible to Near-Infrared Switchable Ratiometric Fluorescent Probe for Live-Cell Lysosome Targeted Imaging

---

Introduction

A rationally designed pH driven molecular switching inside a complex living cellular organelle is an emerging field of contemporary research.[1–7] Intracellular pH is a crucial biological parameter for guiding the activities and functions of cells such as cellular proliferation, metabolism, apoptosis, enzymatic activity etc.[8,9] Numerous intracellular compartments of cells execute diverse functions with dissimilar pH distributions, e.g., cytoplasm is almost neutral (pH ~7.2), mitochondria is feebly alkaline (pH ~8.0), while the endosomes (pH 5.0–6.0) and lysosomes (pH 4.0–5.0) are acidic.[10–13] Lysosomes are the membrane-bound acidic organelles exist in all mammalian cells, comprise a range of degradable enzymes which are active in acidic pH environments, and accountable for breakdown of carbohydrates, nucleic acids, proteins, as well as lipids and involve in exocytosis.[14,15] Lysosomes are proton-pumping vacuolar ATPases, which is answerable to preserve the interior acidic pH 4–5 environment. Aberrations of the lysosomal pH levels are accountable for the malfunction of lysosomes which leads to lysosomal storage disorders, neurodegenerative diseases, cancer, and apoptosis.[16–18] It is crucial to design *in situ* acidic organelle activatable fluorescent probe for selective targeting and imaging of lysosome.[19–21] However, it is very challenging to perform stimuli responsive chemical reactions inside the intracellular organelle of living cells due to the complexity in biological systems. Moreover, in the live cells, the molecule must conquer numerous barricades to reach the specific organelle. pH responsive lysosome activatable near-infrared (NIR) fluorescent dyes (700−900 nm) have a substantial benefit because cellular or tissue ingredients have insignificant absorption and nominal autofluorescence in the

NIR region; therefore, extremely sensitive, less scattered, and precise imaging of lysosome is conceivable. For effective imaging of live cell lysosomal pH, it is of paramount importance to design *in situ* acid-activatable lysosome targeting ratiometric NIR fluorescence probes where the fluorescence signal should amplify and shift from visible to the NIR region with narrow bandwidth to minimize the cross talk at lysosomal pH environment.[22–29] Due to off to on NIR fluorescence at the targeted acidic lysosomes, negligible NIR fluorescence is anticipated from nontargeted neutral or basic cellular organelles thus intervention from nonspecific background fluorescence outside the region of interest will be minimal. Moreover, it is imperative that the lysosome targeting probe should show decent response with a suitable pK_a value when pH fluctuates from 4.0 to 6.0. However, existing lysosome targeting fluorescence dyes have considerable limitations, like inappropriate pK_a in the lysosomal pH range, lower λ_{ex} and λ_{em} wavelengths, negligible shift between two emission bands ($\Delta\lambda_{FL}$ small, suffered serious spectral overlap) at physiological and lysosomal pH, low fluorescence quantum yield at acid pH, cytotoxicity, and these are not promising for the effective targeted imaging of live cells lysosomal pH.

To overcome these drawbacks and to address these issues, we have designed an unsymmetrical chromophore with an acid-triggered openable oxazolidine moiety and lysosome targeting morpholine functionality to promote the probe selectively inside the lysosome. With its low pK_a value (pK_a 4.8), the synthesized molecule is weakly fluorescent in the NIR region at pH ≥ 7.4, however, highly fluorescent in the acidic milieu of lysosome (pH ≤ 5) and has been successfully applied for selective targeting and confocal laser scanning microscopic (CLSM) imaging of lysosome in human epithelioid cervix carcinoma HeLa, lung adenocarcinoma A549, and rat cardiac myoblast healthy

H9c2(2-1) living cells. The non-NIR emissive closed oxazolidine (visible) form can be switched on to the NIR Cy-7 form through ring opening of oxazolidine moiety via $n_N \rightarrow \sigma^*_{C-O}$ interaction at acidic lysosomal pH.[30–34] The pH switching of these molecules is highly reversible. The synthesized pH sensor relies on fluorescence intensity measurements in two well-differentiated emission wavelengths (λ_{em} 480 and 800 nm) with 320 nm spectral shift which minimize cross talk and allows self-calibration. Consequently changes in intensity due to experimental artifacts such as probe concentration, detector sensitivity, laser power and bleaching are circumvented, yielding more accurate ratiometric fluorescence measurements of lysosomal pH. To the best of our knowledge, this is the first report of a reversible pH switchable with huge spectral shift biocompatible ratiometric organic fluorescent probe for selective targeting and activated NIR imaging as well as real time tracking of live cell lysosomes.

Experimental Methods:

Synthetic procedures:

1-(2-Hydroxyethyl)-2,3,3-trimethyl-3*H*-indoliumchloride (1): 2,3,3-Trimethylindolenine (1.59 g, 10 mmol) and 2-chloroethanol (1.61 g, 20 mmol) were taken in a round bottomed flask and refluxed for 24 hr under an inert N_2 atmosphere. The reaction mixture was cooled and washed with EtOAc for several times (5 × 30 mL). The precipitate was filtered off, washed with EtOAc (3 × 20 mL) and dried under vacuum to afford the pure

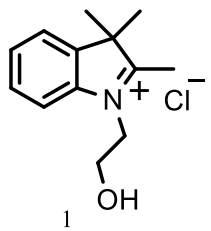

1

compound **1** as a pink solid.

Yield: 1.63 g (68%).

^{1}H NMR (300 MHz, DMSO-d_6, 25°C): δ = 8.00–7.97 (1H, m), 7.87–7.82 (1H, m), 7.65–7.59 (2H, m), 4.61 (2H, t, J = 5.1 Hz), 3.87 (2H, t, J = 5.1 Hz), 3.60 (1H, br), 2.85 (3H, s), 1.56 (6H, s) ppm.

^{13}C NMR (75 MHz, DMSO-d_6, 25°C): δ = 198.3, 142.4, 141.8, 129.8, 129.3, 124.0, 116.3, 58.3, 54.8, 51.1, 22.7, 15.2 ppm.

HRMS (ESI +ve) *m*/*z*: Observed for $C_{13}H_{18}NO^{+}$ $[M]^{+}$ = 204.1428, $[M]^{+}$ calcd = 204.1383.

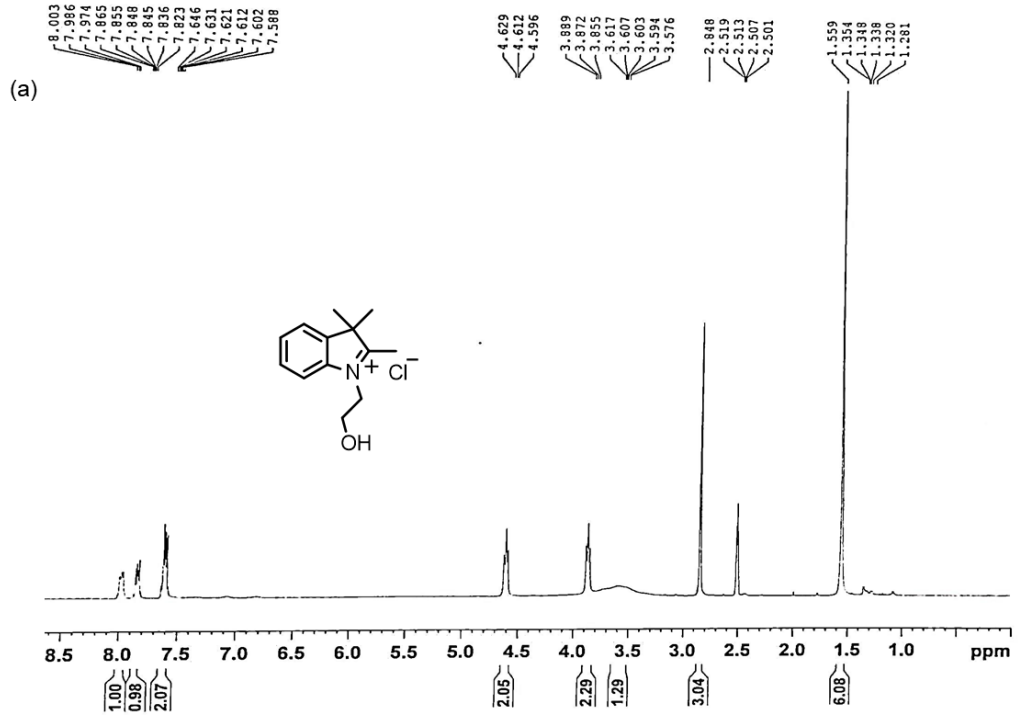

Figure 1a. ^{1}H NMR spectrum (300 MHz, DMSO-d_6, 298 K)

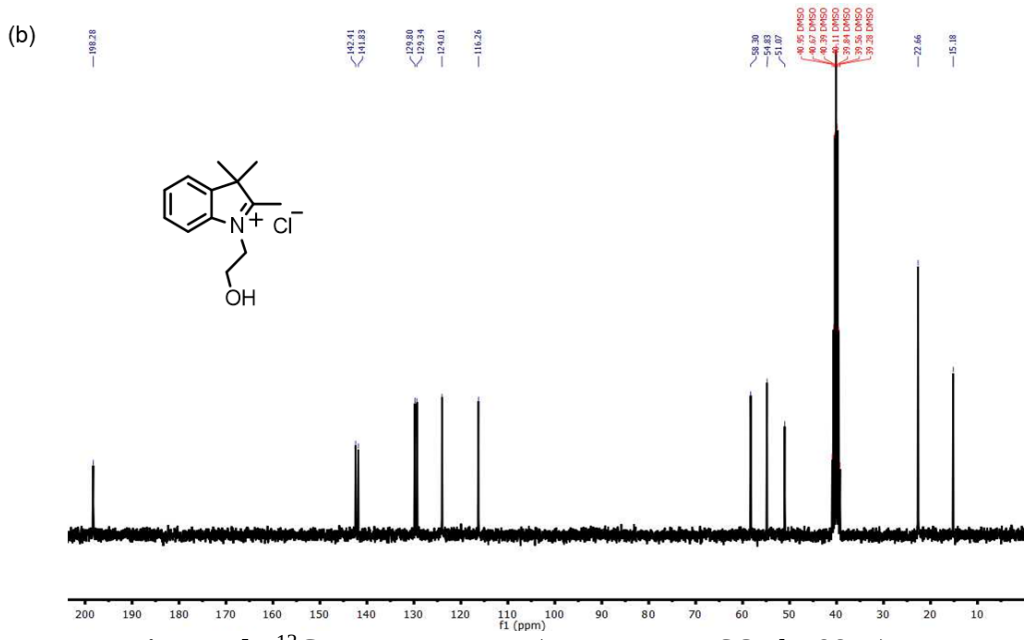

Figure 1b. ^{13}C NMR spectrum (75 MHz, DMSO-*d*, 298 K).

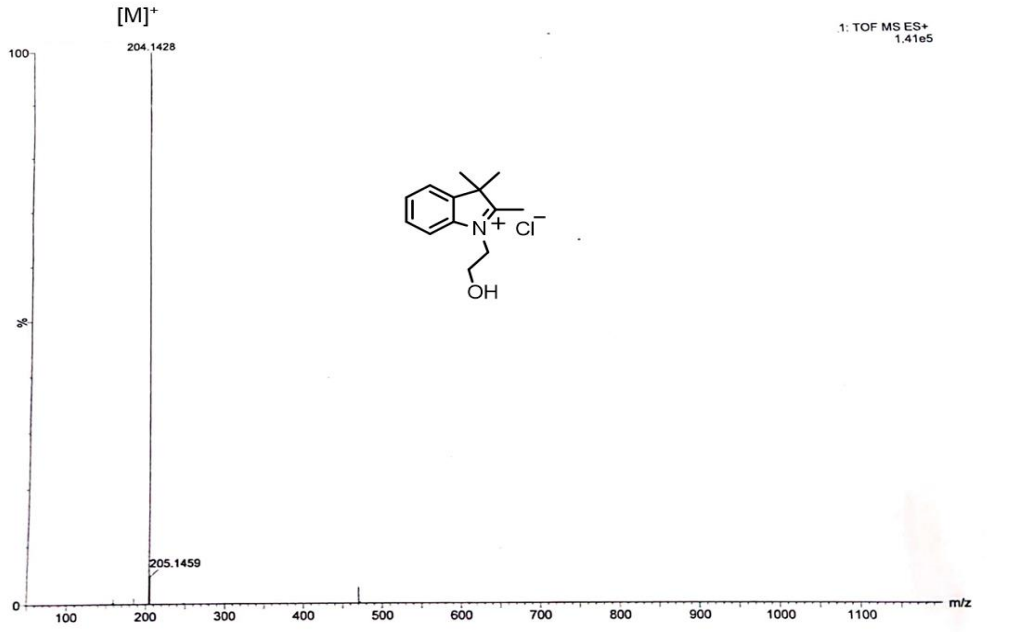

Figure 2. HRMS (ESI +ve) spectrum.

9,9,9a-Trimethyl-2,3,9,9a-tetrahydrooxazolo[3,2-a]indole (2): To a suspension of **1** (0.48 g, 2 mmol) in H_2O (50 mL) an aqueous solution of NaOH (0.6 g NaOH in 30 mL H_2O) was added and the mixture was stirred at 25°C for 30 min. The reaction mixture was extracted with Et_2O (3× 20 mL). The organic layer was washed with H_2O (2× 20 mL), brine (1× 20 mL), dried over anhydrous Na_2SO_4 and concentrated under reduced pressure to obtain the pure compound **2** as a yellow oil.

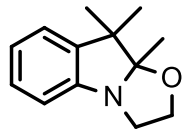

2

Yield: 0.33 g (81%).

^{1}H NMR (300 MHz, $CDCl_3$, 25°C):δ = 7.10–7.05 (2H, m), 6.87–6.78 (2H, m), 3.77–3.68 (2H, m), 3.50–3.43 (1H, m), 3.38–3.30 (1H, m), 1.39 (3H, s), 1.28 (3H, s), 1.10 (3H, s) ppm.

^{13}C NMR (75 MHz, $CDCl_3$, 25°C): δ = 150.6, 140.1, 127.5, 122.4, 121.7, 112.0, 109.0, 63.0, 50.1, 47.0, 28.1, 20.9, 17.6 ppm.

HRMS (ESI +ve) *m*/*z*: Observed for $C_{13}H_{17}NO^+$ $[M+H]^+$ = 204.1610, $[M+H]^+$ calcd = 204.1383.

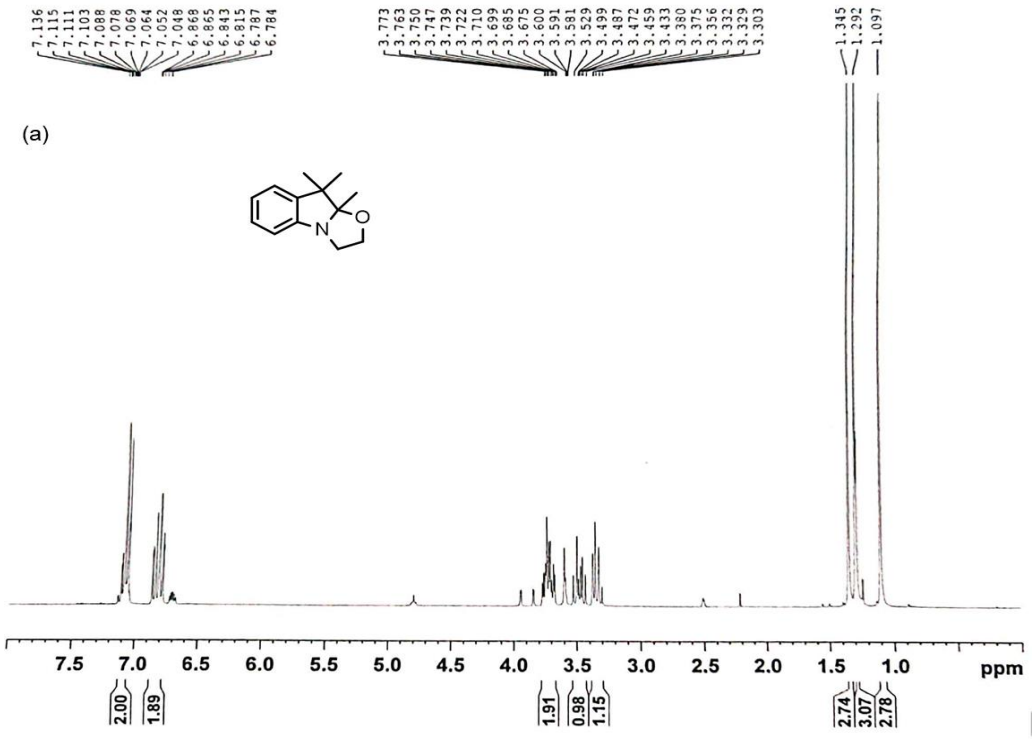

Figure 3a. ^{1}H NMR spectrum (300 MHz, $CDCl_3$, 298 K)

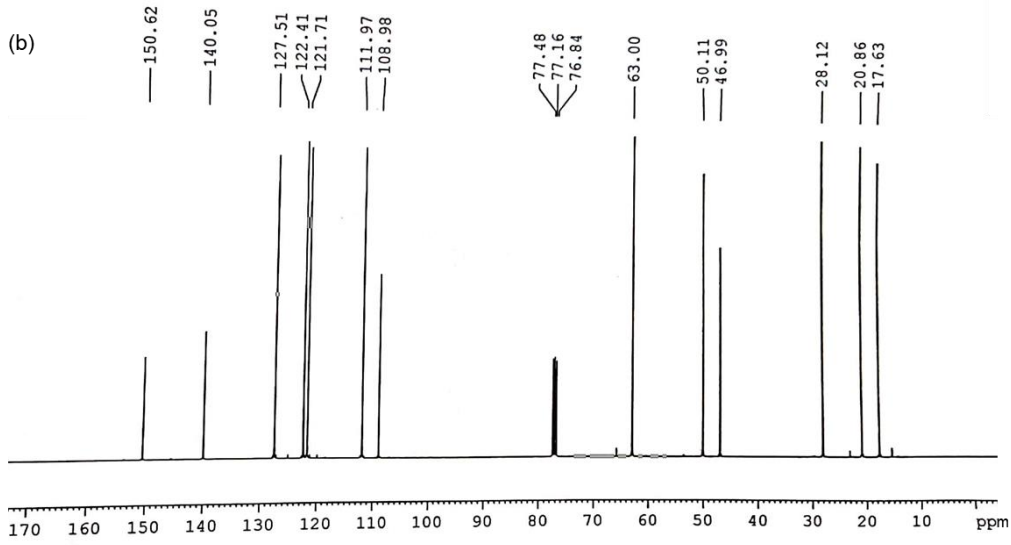

Figure 3b. ^{13}C NMR spectrum (75 MHz, $CDCl_3$, 298 K).

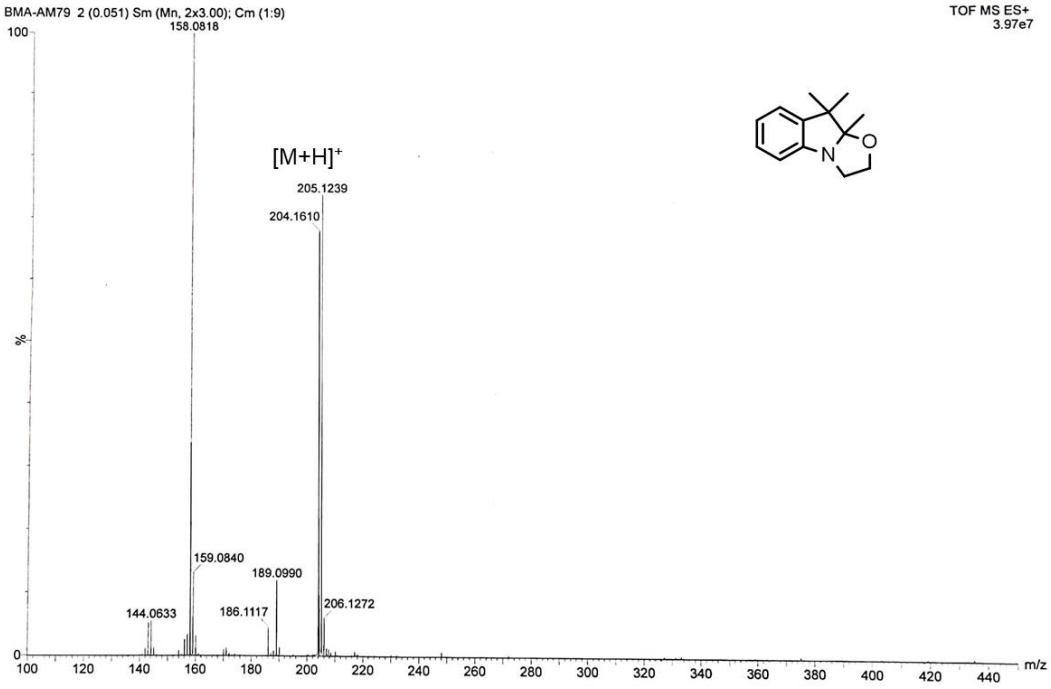

Figure 4. HRMS (ESI +ve) spectrum of compound 2.

(*E*)-2-chloro-3-(hydroxymethylene)cyclohex-1-enecarbaldehyde (3): The compound **3** was synthesized using a literature reported procedure.[35] To a chilled solution of 1:1 DMF:DCM (10 mL each) under N_2 atmosphere, $POCl_3$ (9 mL, 96 mmol) in DCM (1 mL) were added drop wise under an ice bath and stir for 30 min. Cyclohexanone was added (4.45 mL, 43 mmol) and the resulting solution was refluxed for 3 hours at 80ºC. The reaction mixture was cooled and poured into ice cold H_2O and kept it overnight in refrigerator to obtain compound **3** as a yellow solid.

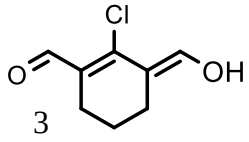

3

Yield: 5.8 g (78%)

2,3,3-trimethyl-3*H*-indole-5-carboxylic acid (4): 4-Hydrazino benzoic acid (1.83 g, 12 mmol) and 3-methyl-2-butanone (2 mL, 32 mmol) were dissolved in glacial AcOH (30 mL). The solution was refluxed for 12 hours, then allowed to cool to room temperature and the solvent was removed under reduced pressure. The crude product was further purified by column chromatography (50% EtOAc/Hexane) to afford the pure compound as a light yellow solid [R_f = 0.4 (50% EtOAc/Hexane)].

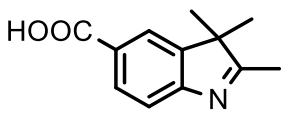

4

Yield: 1.54 g (63%).

^{1}H NMR (300 MHz, DMSO-d_6, 25°C): δ = 12.74 (1H, br), 7.98 (1H, d, J = 1.3 Hz), 7.90 (1H, dd, J = 8.0 Hz, J = 1.7 Hz), 7.49 (1H, d, J = 8.0 Hz), 2.24 (3H, s), 1.26 (6H, s) ppm.

^{13}C NMR (75 MHz, DMSO-d_6, 25°C): δ = 192.1, 168.0, 157.9, 146.6, 130.1, 127.8, 123.2, 119.6, 54.0, 22.8, and 15.8 ppm.

HRMS (ESI +ve) m/z: Observed for $C_{12}H_{13}NO_2$ $[M+H]^+$ = 204.0850, $[M+H]^+$ calcd = 204.1019.

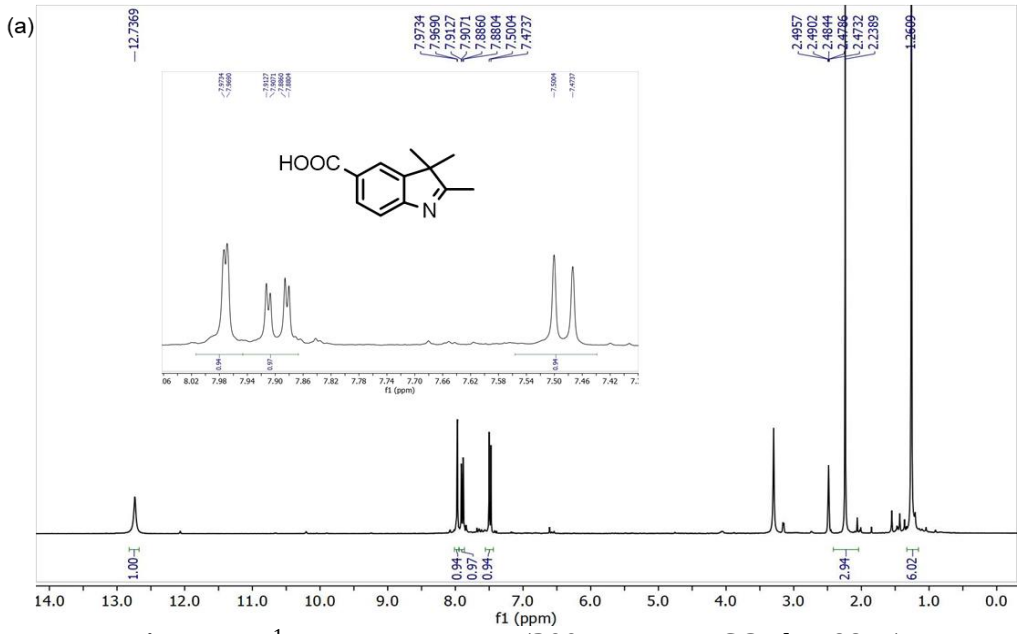

Figure 5a. ^{1}H NMR spectrum (300 MHz, DMSO-d_6, 298 K)

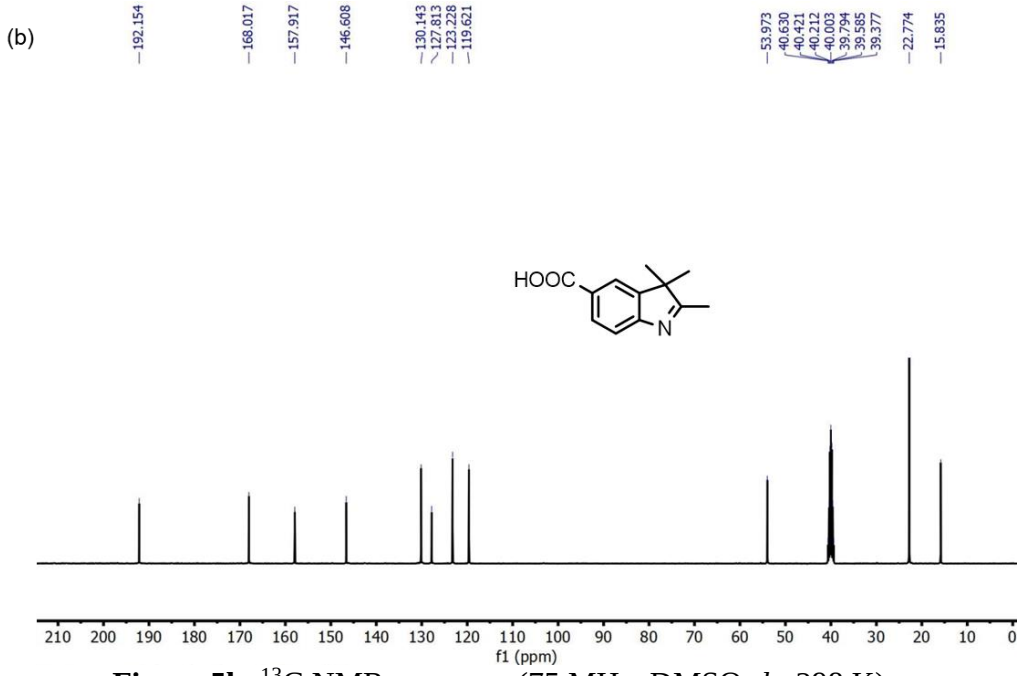

Figure 5b. ^{13}C NMR spectrum (75 MHz, DMSO-d_6, 298 K).

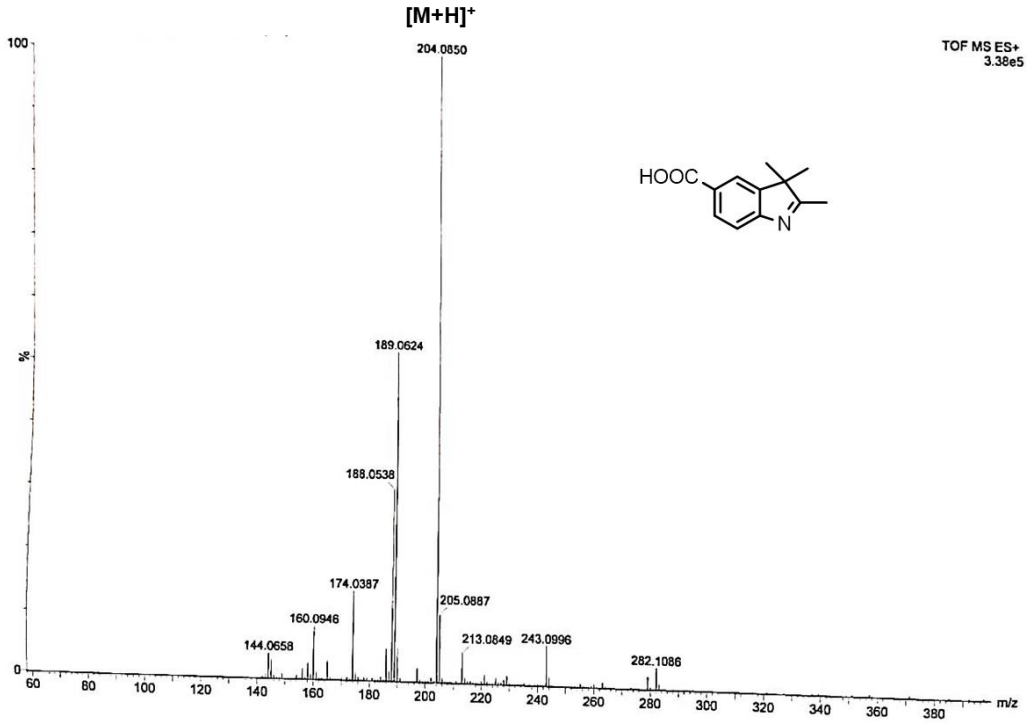

Figure 6. ESI-HRMS spectrum.

5-carboxy-1,2,3,3-tetramethyl-3*H*-indol-1-ium (**5**)**:** Compound 4 (0.5 g, 2.46 mmol) and CH_3I (0.5 mL, 8.0 mmol) were dissolved in CH_3CN (10 mL) and refluxed for 3 hours. After completion of the reaction, the solution mixture was cooled to room temperature and Et_2O was added. A yellow precipitate was observed and it was filtered. The residue was washed with Et_2O for several times to afford a pure light yellow solid product.

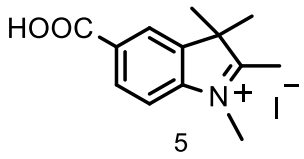

5

Yield: 0.7 g (82%).

^{1}H NMR (300 MHz, DMSO-d_6, 25°C): δ = 8.38 (1H, s), 8.19 (1H, d, J = 8.4 Hz), 8.03 (1H, d, J = 8.4 Hz), 4.00 (3H, s), 2.82 (3H, s), 1.57 (6H, s) ppm.

^{13}C NMR (75 MHz, DMSO-d_6, 25°C): δ = 199.5, 167.0, 145.8, 142.5, 132.1, 130.9, 124.7, 115.9, 54.8, 35.8, 22.1, and 15.5 ppm.

HRMS (ESI +ve) *m*/*z*: Observed for $C_{13}H_{16}NO_2^+$ $[M]^+$ = 218.0895, $[M]^+$ calcd. = 218.1176.

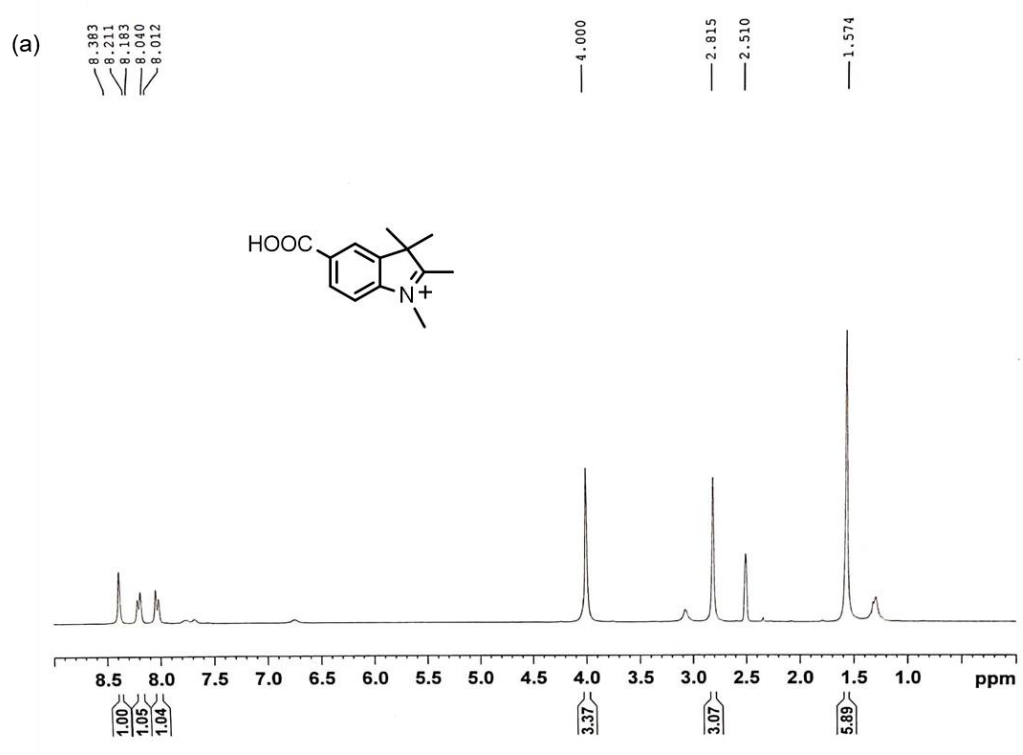

Figure 7a. ^{1}H NMR spectrum (300 MHz, DMSO-d_6, 298 K).

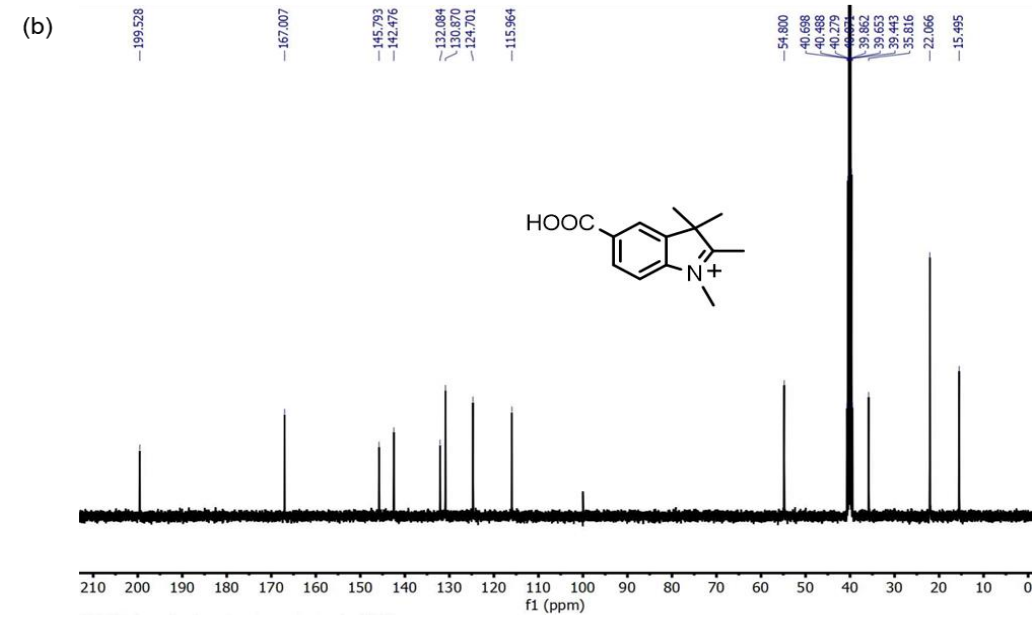

Figure 7b. ^{13}C NMR spectrum (75 MHz, DMSO-d_6, 298 K).

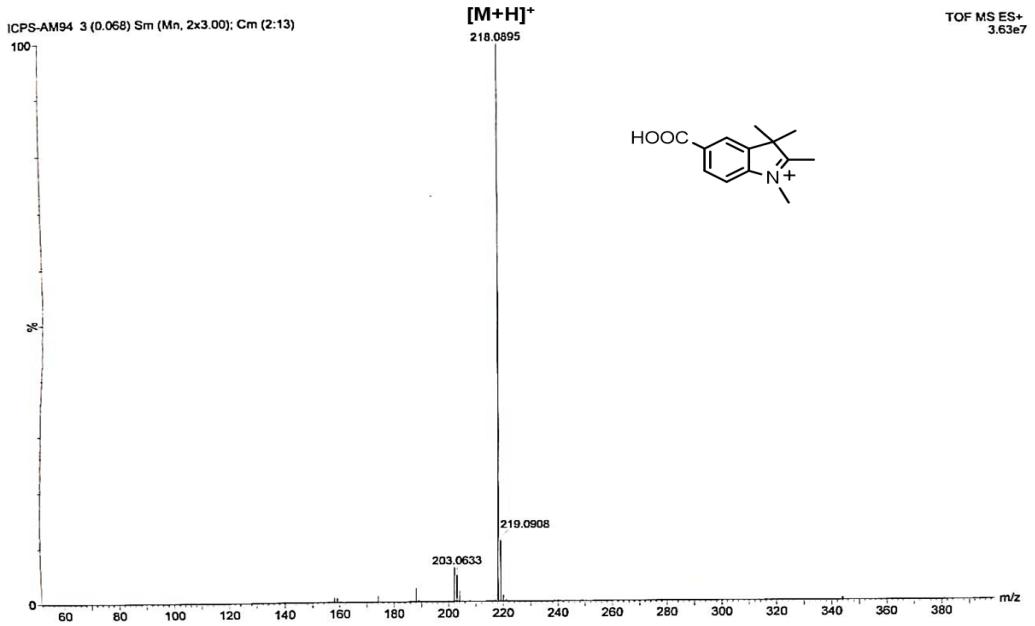

Figure 8. ESI-HRMS spectrum.

1,2,3,3-tetramethyl-5-((2-morpholinoethyl)carbamoyl)-3*H*-indol-1-ium (6):

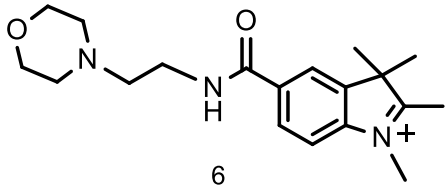

6

Compound 5 (0.79 g, 2.29 mmol) was added to an ice cold DMF (3 mL) under stirring condition. HATU (0.96 g, 2.52 mmol) and DIPEA (0.87 mL, 5 mmol) were added sequentially to the mixture. After 30 min 4-(2-aminoethyl)morpholine (0.65 mL, 5 mmol) was added and the reaction was stirred for 18 hours. After that the cold distilled H_2O was added to the reaction mixture and extracted with DCM. The organic layer was collected and dried over anhydrous Na_2SO_4 and concentrated under reduced pressure. The crude product was purified by column chromatography (6% DCM/MeOH) to get the pure product as a pink gummy solid.

Yield: 0.8 g (76%).

^{1}H NMR (300 MHz, $CDCl_3$, 25°C): δ = 7.55 (s, 1H), 7.55–7.49 (m, 1H), 6.89 (t, *J* = 4.5 Hz, 1H), 6.45 (d, *J* = 9.0 Hz, 1H), 3.65 (t, *J* = 4.5 Hz, 4H), 3.50–3.37 (m, 2H), 3.00 (s, 3H), 2.73 (s, 3H), 2.52 (t, *J* = 6.3 Hz, 2H), 2.43 (t, *J* = 4.3 Hz, 4H), 1.27 (s, 6H) ppm.

^{13}C NMR (75 MHz, $CDCl_3$, 25°C): δ = 167.6, 162.1, 149.00, 137.63, 127.32, 124.4, 121.1, 104.1, 75.4, 66.90, 57.2, 53.3, 43.7, 38.5, 36.2, 31.3, 29.8, 28.8 ppm.

HRMS (ESI +ve) *m*/*z*: Observed for $C_{19}H_{28}N_3O_2^+$ $[M]^+$ = 330.2192, $[M]^+$ calcd = 330.2177.

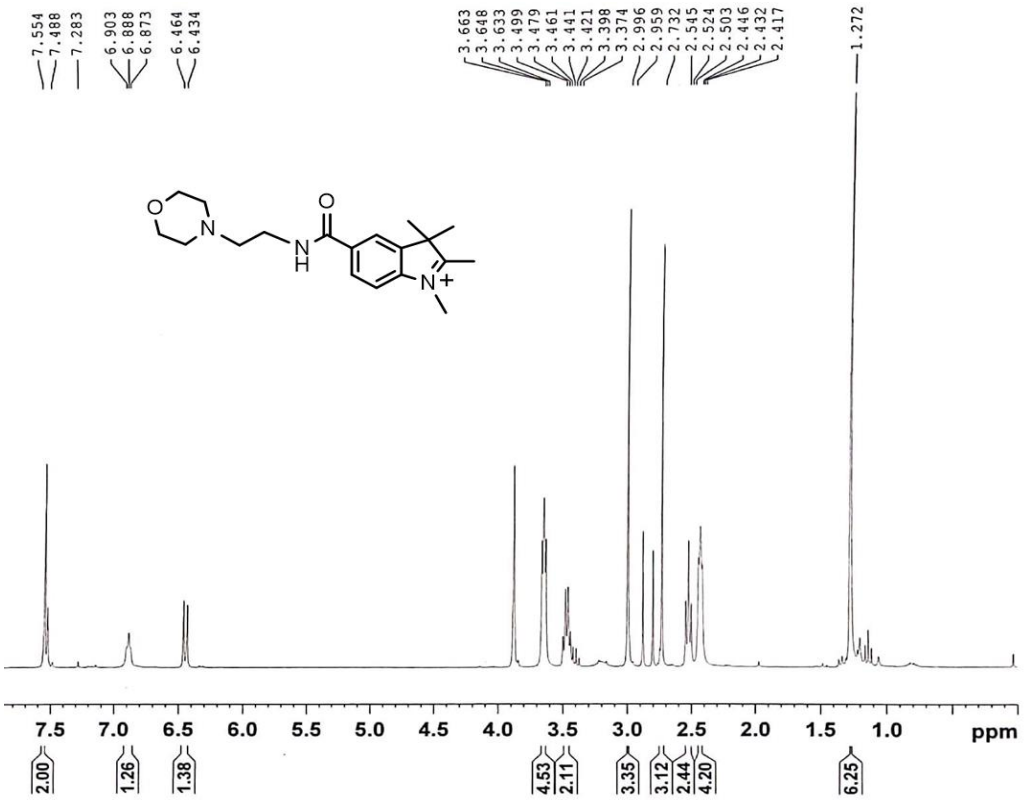

Figure 9. ^{1}H NMR spectrum (300 MHz, $CDCl_3$, 298 K).

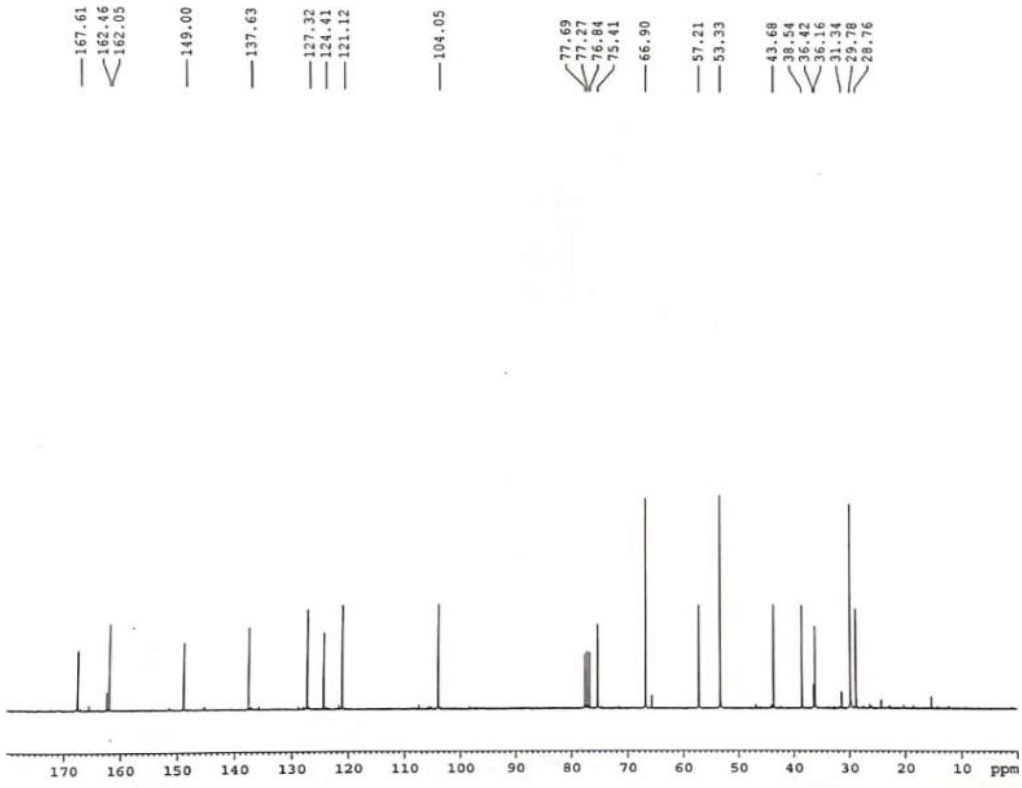

Figure 10. ^{13}C NMR spectrum (75 MHz, $CDCl_3$, 298 K).

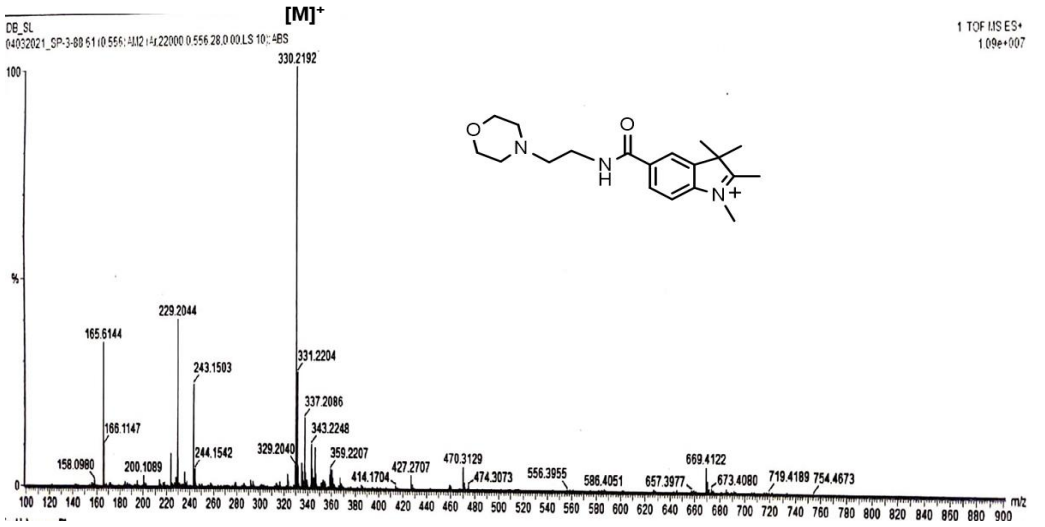

Figure 11. ESI-HRMS spectrum.

Basic closed oxazolidine form [(*E*)-2-((*E*)-2-(2-chloro-3-((*E*)-2-(9,9-dimethyl-2,3,9,9a-tetrahydrooxazolo[3,2-*a*]indol-9a-yl)vinyl)cyclohex-2-en-1-ylidene)ethylidene)-1,3,3-trimethyl-*N*-(2-morpholinoethyl)indoline-5-carboxamide]: Compound **3** (0.074 g, 0.43 mmol) was dissolved in n-BuOH (7 mL) and benzene (3 mL) solvent mixture. The mixture was heated to reflux in a three neck round bottomed flask.

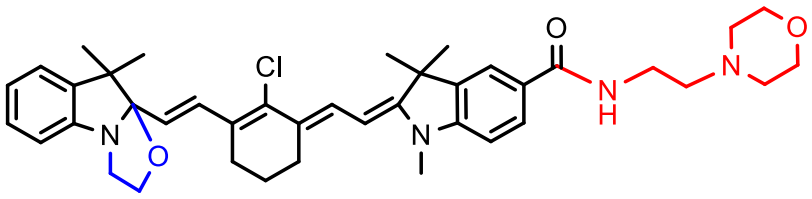

Compounds **1** (0.1 g, 0.43 mmol) and **6** (0.2 g, 0.43 mmol) were dissolved in n-BuOH (7 mL) and benzene (3 mL) mixture individually and taken in two different syringes. After 15 min reflux of compound **3** solution mixtures, compound **6** and compound **1** solution were added drop wise using two different syringes for 3 hours. The color of the reaction mixture was changed towards green from brown. The reaction was monitored using TLC. After 6 hours the solvent was evaporated under reduced pressure. The solid residue was dissolved in MeOH (10 mL). Aqueous NaOH (0.25g NaOH in 10 mL H_2O) solution was added into the methanolic solution of the compound under stirring condition. It was stirred for 12 hours at 25°C. After 12 hours the solvent was evaporated and the residue was extracted with DCM. The organic layer was dried over anhydrous Na_2SO_4, filtered, and concentrated under reduced pressure. The crude product was purified using column chromatography (silica gel mixed with little bit Et_3N) using 1% DCM/MeOH to acquire the desired compound as a yellow solid.

Yield: 0.15 g (52%).

^{1}H NMR (300 MHz, $CDCl_3$, 25°C): δ = 7.62 (s, 1H), 7.58 (d, *J* = 8.2 Hz, 1H) 7.35 (d, *J* = 15.5 Hz, 2H), 7.15 (t, *J* = 7.6 Hz, 1H), 7.07 (d, *J* = 8.7 Hz, 1H), 6.93 (t, *J* = 6.5 Hz, 1H), 6.79 (d, *J* = 7.8 Hz, 1H), 6.71 (t, *J* = 5.0 Hz, 1H)), 6.58 (d, *J* = 8.2 Hz, 1H), 5.81 (d, *J* = 15.8 Hz, 1H), 5.46 (d, *J* = 12.5 Hz, 1H), 3.80–3.67 (m, 6H), 3.66–3.55 (m, 4H), 3.16 (s, 3H), 2.62–2.58 (t, *J* = 6.0 Hz, 4H), 2.56–2.49 (m, 6H), 1.86–1.82 (m, 2H), 1.65 (s, 6H), 1.43 (s, 3H), 1.13 (s, 3H) ppm.

A ^{1}H–^{1}H gCOSY (Gradient-selected Correlation Spectroscopy) experiment established coupling connectivity.

^{13}C NMR (75 MHz, $CDCl_3$, 25°C): δ = 167.5 (C28), 157.5 (C24), 150.8 (C33), 148.0 (C26), 139.9 (C29), 139.3 (C27), 133.1 (C31), 131.3 (C3), 128.9 (C32), 127.6 (C4), 127.3 (C9), 126.5 (C25), 126.3 (C10), 125.6 (C30), 123.6 (C5), 122.5 (C7), 121.7 (C2), 121.1 (C8), 112.1 (C6), 110.3 (C34), 105.1 (C11), 94.5 (C1), 67.1 (C17), 63.6 (C12), 57.2 (C13), 53.5 (C16), 50.2 (C15), 47.9 (C35), 45.4 (C36), 36.2 (C14), 29.4 (C24), 28.2 (C21), 27.8 (C20), 26.5 (C18), 21.7 (C19), 20.5 (C22,C23) ppm.

DEPT 135 (75 MHz, $CDCl_3$, 25°C): δ = 131.3 (C3), 127.6 (C4), 127.3 (C9), 126.3 (C10), 123.6 (C5), 122.5 (C7), 121.7 (C2), 121.1 (C8), 112.1 (C6), 105.1 (C11), 94.5 (C1), 29.4 (C24), 28.2 (C21), 20.5 (C22,C23) ppm $\rightarrow$ +Ve; δ = 67.1 (C17), 63.6 (C12), 57.2 (C13), 53.5 (C16), 50.2 (C15), 36.2 (C14), 27.8 (C20), 26.5 (C18), 21.7 (C19) ppm $\rightarrow$ –Ve; δ = 167.5 (C28), 157.5 (C24), 150.8 (C33), 148.0 (C26), 139.9 (C29), 139.3 (C27), 133.1 (C31), 128.9 (C32), 126.5 (C25), 125.6 (C30), 110.3 (C34), 47.9 (C35), 45.4 (C36) ppm $\rightarrow$ Disappear.

HRMS (ESI +ve) *m*/*z*: Observed for $C_{40}H_{49}ClN_4O_3$ $[M+H]^+$ = 669.3570, $[M+H]^+$calcd = 669.3566

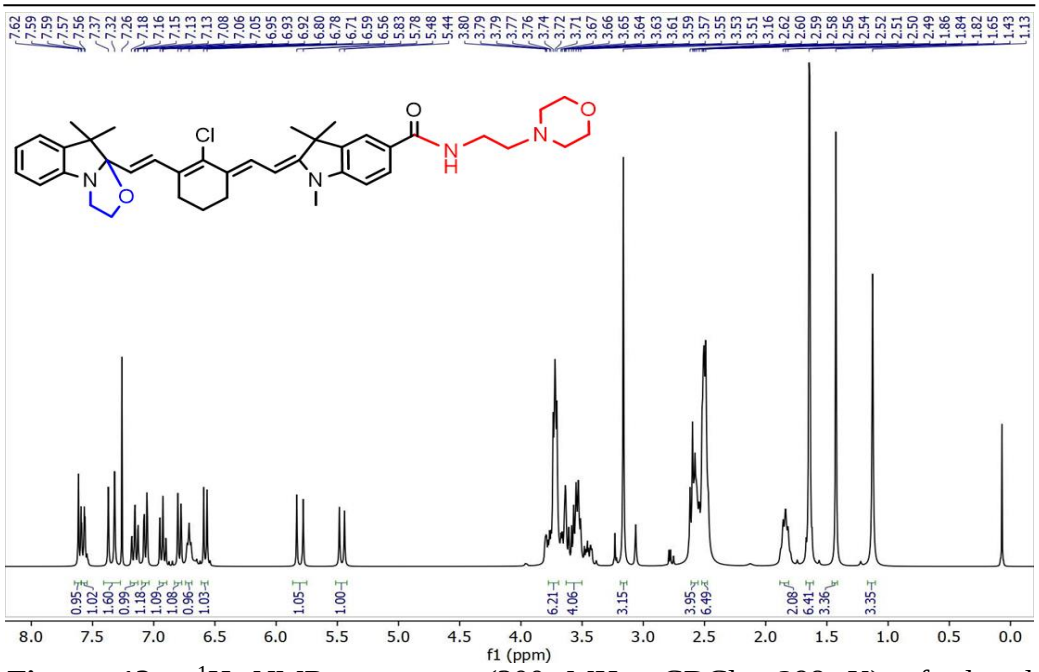

Figure 12a. ^{1}H NMR spectrum (300 MHz, $CDCl_3$, 298 K) of closed oxazolidine form

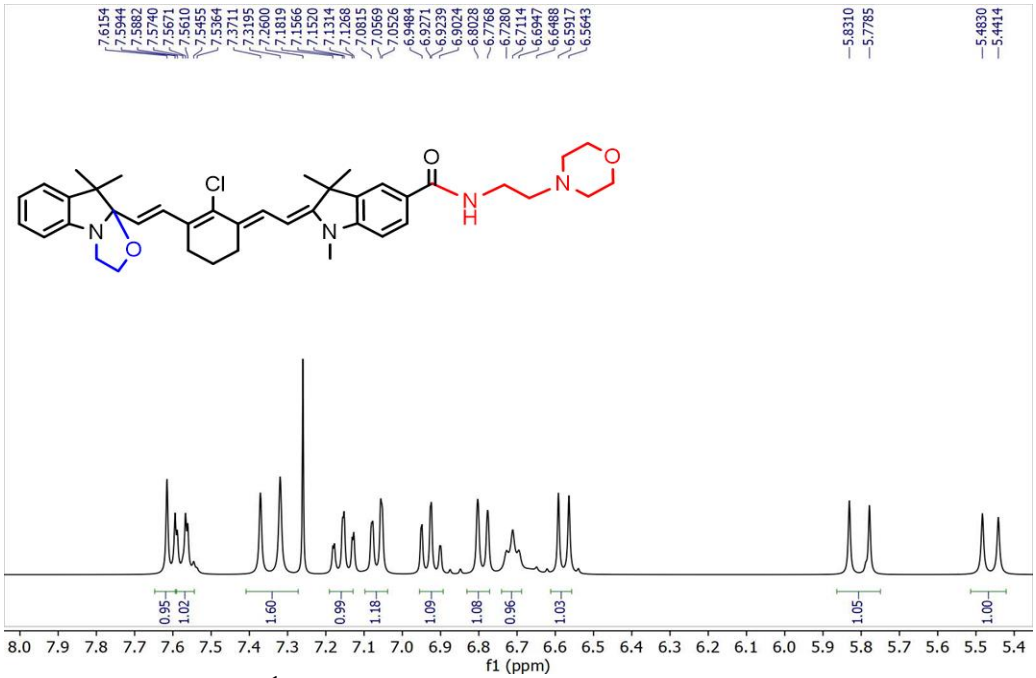

Figure 12b. Partial ^{1}H NMR spectrum (300 MHz, $CDCl_3$, 298 K) of closed oxazolidine form.

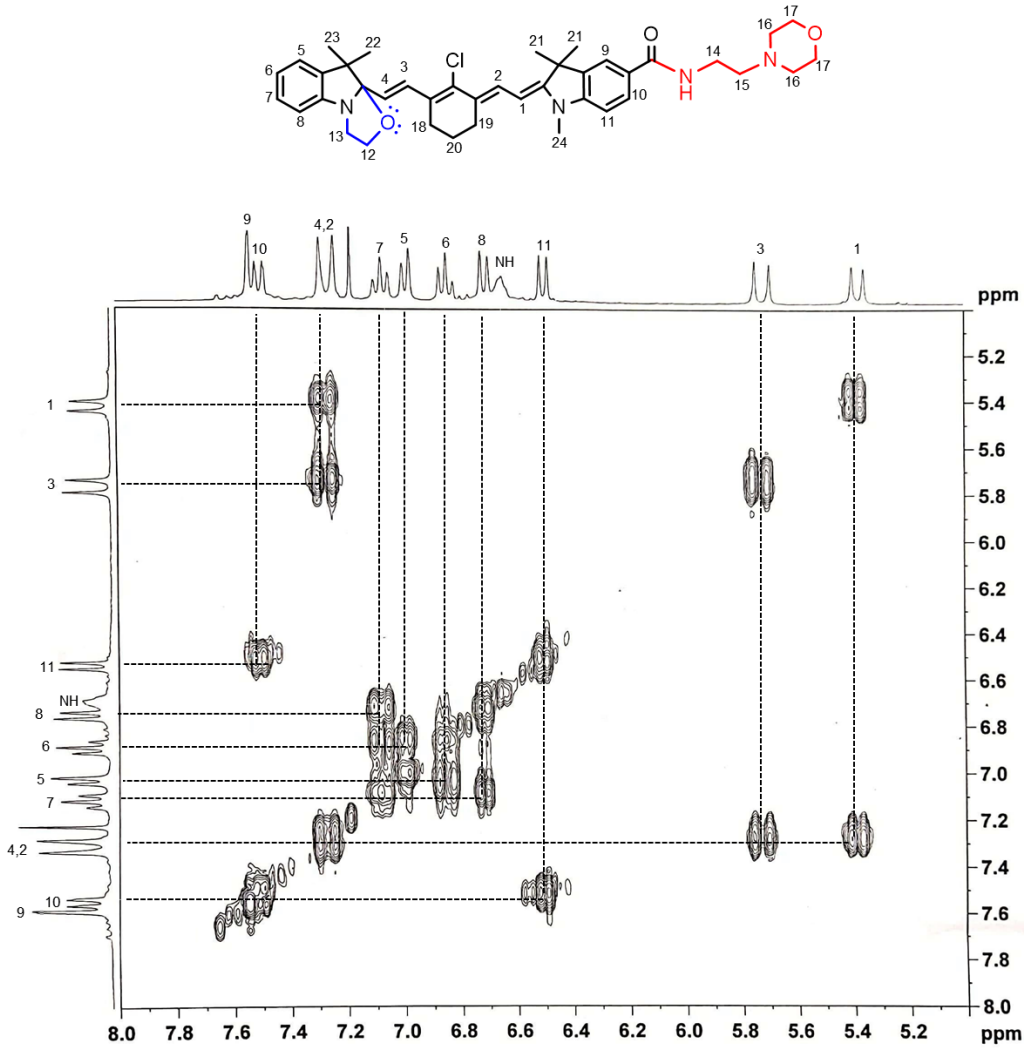

Figure 13. Partial ^{1}H-^{1}H gCOSY (Gradient-selected Correlation Spectroscopy) NMR spectrum (300 MHz, $CDCl_3$, 298 K) of closed oxazolidine form.

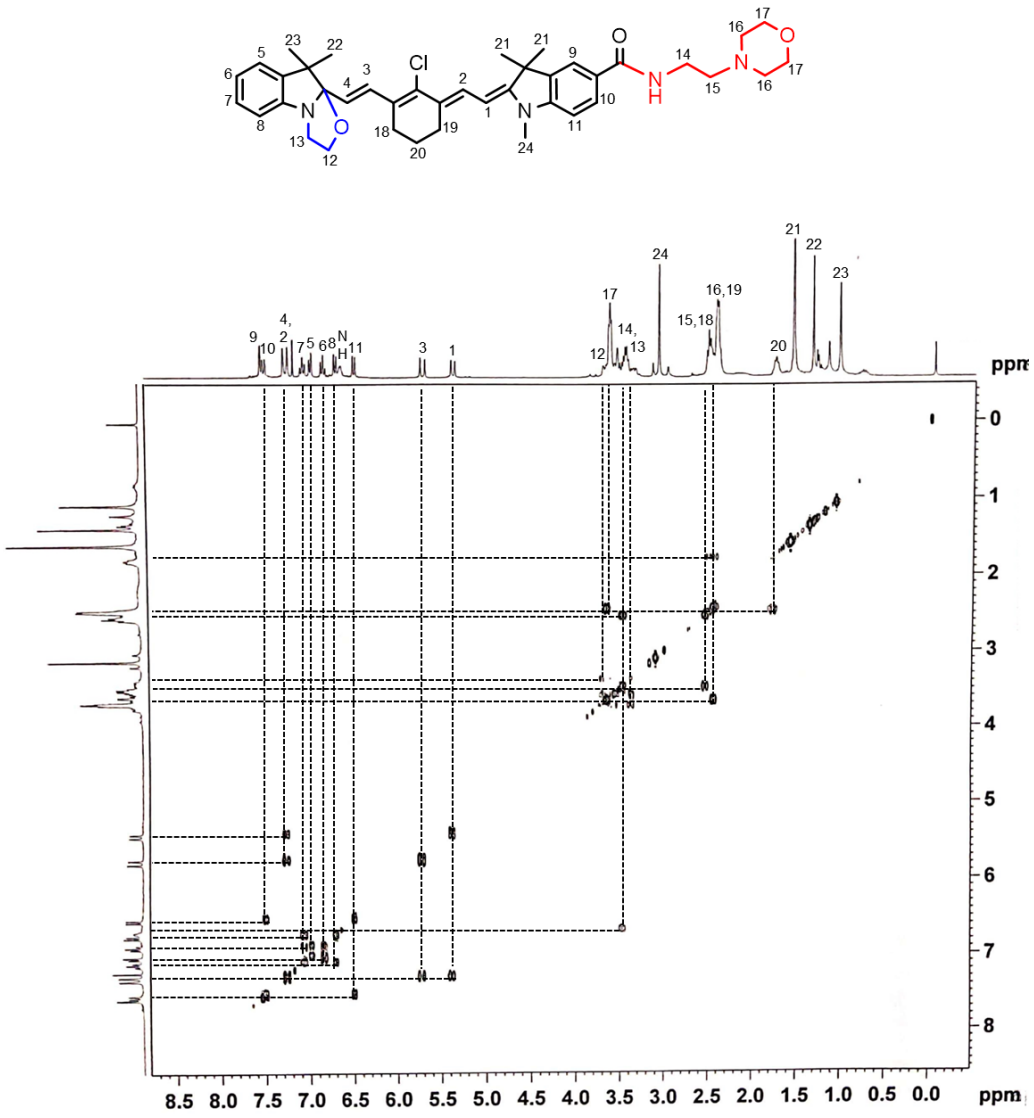

Figure 14. ^{1}H-^{1}H gCOSY (Gradient-selected Correlation Spectroscopy) NMR spectrum (300 MHz, $CDCl_3$, 298 K) of closed oxazolidine form.

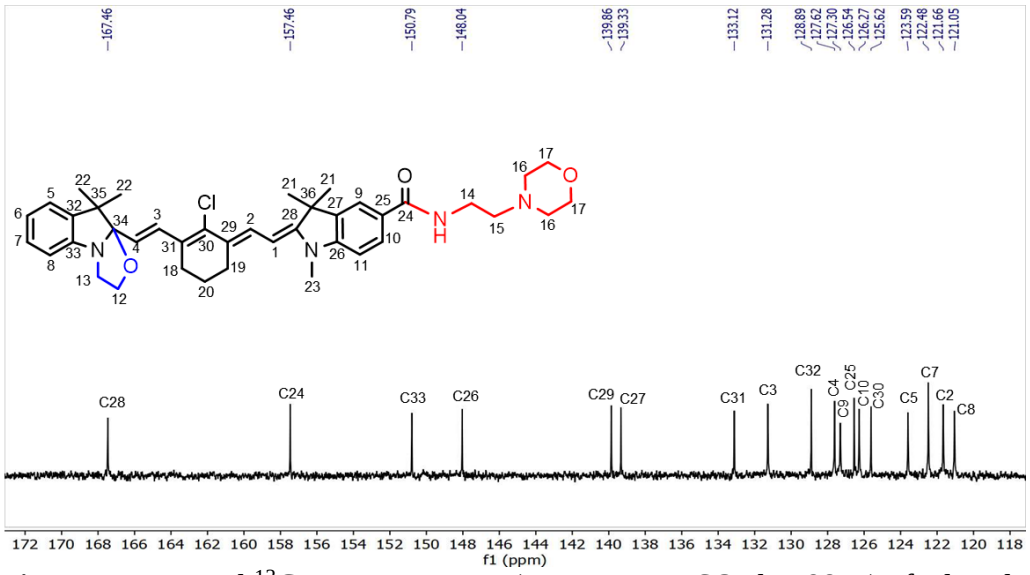

Figure 15a. Partial ^{13}C NMR spectrum (75 MHz, DMSO-d_6, 298 K) of closed oxazolidine form.

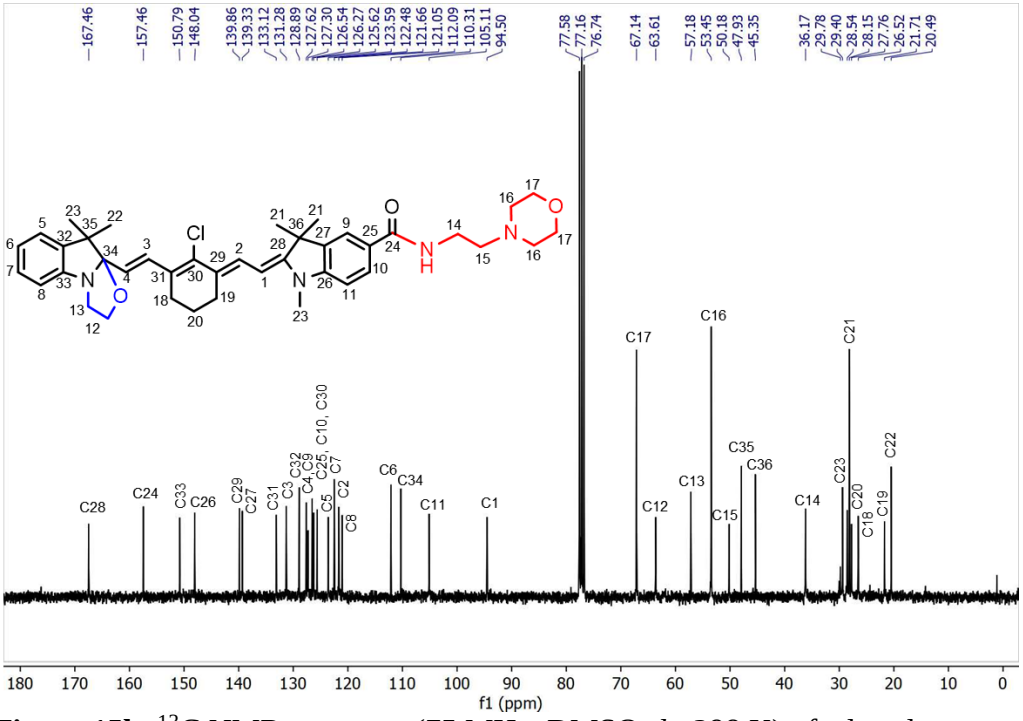

Figure 15b. ^{13}C NMR spectrum (75 MHz, DMSO-d_6, 298 K) of closed oxazolidine molecule.

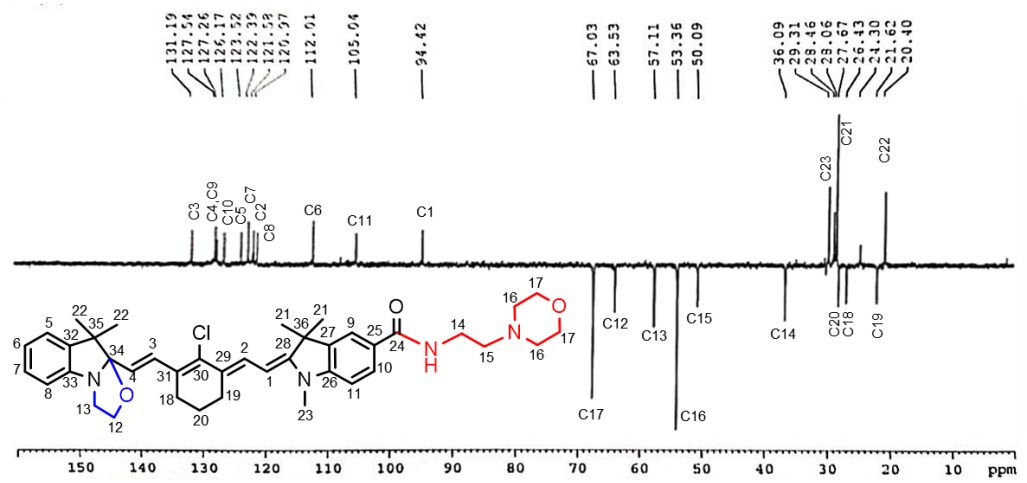

Figure 16. DEPT-135 spectrum (75 MHz, $CDCl_3$, 298 K) of closed oxazolidine form.

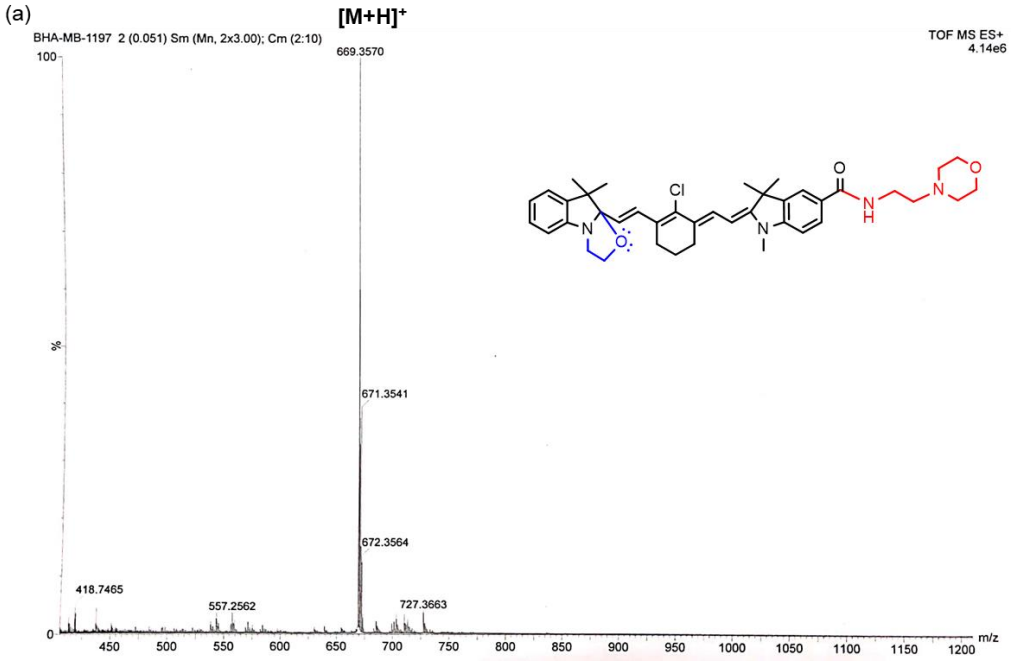

Figure 17a. ESI-HRMS spectrum of closed oxazolidine form.

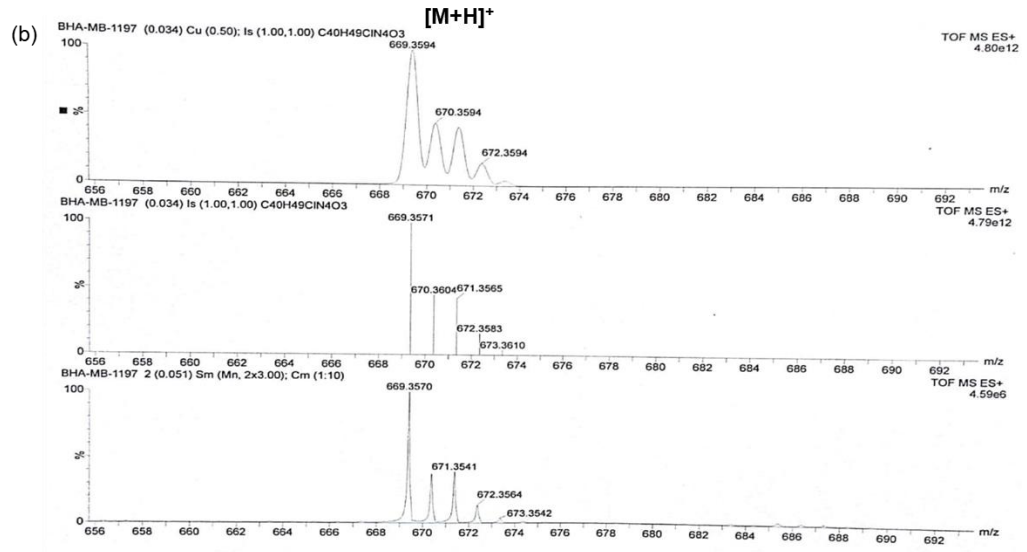

Figure 17b. Isotropic distribution pattern in the ESI-HRMS spectrum of oxazolidine form.

Acidic open Cy-7 form [4-(2-((E)-2-((E)-2-(2-chloro-3-((E)-2-(1-(2-hydroxyethyl)-3,3-dimethyl-3H-indol-1-ium-2-yl)vinyl)cyclohex-2-en-1-ylidene)ethylidene)-1,3,3-trimethylindoline-5-carboxamido)ethyl)morpholin-4-ium]: The yellow colored basic closed oxazolidine compound (0.13 g, 0.2 mmol) was dissolved in MeOH (5 mL).

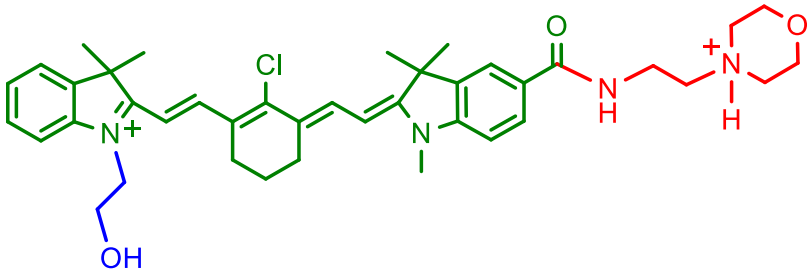

Dilute HCl (1 mL conc. HCl and 5 mL H_2O) was added into the methanolic solution of the oxazolidine compound under stirring condition. It was stirred for 2 hours at 25°C and a green colored solution was observed. After 2 hours the solvent was evaporated under reduced pressure and the green residue was

extracted with DCM. The organic layer was collected, dried over anhydrous Na_2SO_4, filtered, and concentrated under reduced pressure. The crude solid was purified by column chromatogrphy (6% $CHCl_3$/ Acetone) to obtain the pure open Cy-7 compound as a green solid.

Yield: 0.12 g (82%).

^{1}H NMR (300 MHz, $CDCl_3$, 25°C): δ = 9.01 (br, 1H), 8.58 (d, *J* = 14.7 Hz, 1H), 8.29 (s, 1H), 8.16–8.08 (m, 2H), 7.53–7.36 (m, 3H) 7.28-7.23 (m, 1H), 7.05 (d, *J* = 14.4 Hz, 1H), 6.96 (d, *J* = 8.4 Hz, 1H), 5.80 (d, *J* = 13.2 Hz, 1H), 4.62 (t, *J* = 5.7 Hz, 2H), 4.17–4.09 (m, 5H), 3.99–3.93 (m, 4H), 3.57–3.43 (m, 9H), 2.92 (t, *J* = 6.4 Hz, 2H), 2.63 (t, *J* = 6.5 Hz, 2H), 1.99–1.92 (m, 2H), 1.79 (s, 6H), 1.74 (s, 6H) ppm.

A ^{1}H–^{1}H gCOSY experiment provides information on coupling connectivity.

^{13}C NMR (75 MHz, $CDCl_3$, 25°C): δ = 178.5 (C34), 168.4 (C24), 167.0 (C28), 149.8 (C26), 148.9 (C3), 146.1 (C29), 142.2 (C32), 141.8 (C33), 140.0 (C27), 139.1 (C7), 129.9 (C10), 129.2 (C2), 128.2 (C6, C31), 127.3 (C25, C30), 122.2 (C9, C5), 113.1 (C8), 108.1 (C11), 107.7 (C4), 98.0 (C1), 63.7 (C17), 59.1 (C13), 57.8 (C12), 52.4 (16), 50.7 (C35), 48.7 (C15), 47.8 (C36), 34.2 (C14), 30.6 (C23), 28.3 (C22), 28.1 (C21), 27.1 (C20), 26.5 (C18), 20.8 (C19) ppm.

DEPT 135 (75 MHz, $CDCl_3$, 25°C): δ = 148.9 (C3), 139.1 (C7), 129.9 (C10), 129.2 (C2), 128.2 (C6), 122.2 (C9, C5), 113.1 (C8), 108.1 (C11), 107.7 (C4), 98.0 (C1), 30.6 (C23), 28.3 (C22), 28.1 (C21) ppm $\rightarrow$ +Ve; δ = 63.7 (C17), 59.1 (C13), 57.8 (C12), 52.4 (16), 48.7 (C15), 34.2 (C14), 27.1 (C20), 26.5 (C18), 20.8 (C19) ppm $\rightarrow$ –Ve; δ = 178.5 (C34), 168.4 (C24), 167.0 (C28), 149.8 (C26), 146.1 (C29), 142.2 (C32), 141.8 (C33), 140.0 (C27), 128.2 (C31), 127.3 (C25, C30), 50.7 (C35), 47.8 (C36) ppm $\rightarrow$ Disappear.

HRMS (ESI +ve) *m/z*: Observed for $C_{40}H_{51}ClN_4O_3^{2+}$ $[M]^{2+}$ = 335.1819, $[M]^{2+}$calcd = 335.1820;

$[M\text{-}H]^+$ = 669.3558, $[M\text{-}H]^+$calcd = 669.3566

Photophysical properties in DMSO λ_{abs}= 780 nm, λ_{em}= 800 nm, Stokes shift ($\Delta\lambda$) = 20 nm, ε = 4.33 ×10^5 $M^{-1}cm^{-1}$, Φ_f = 0.11 in DMSO [Φ_f of the reference compound ICG in DMSO is 0.12].

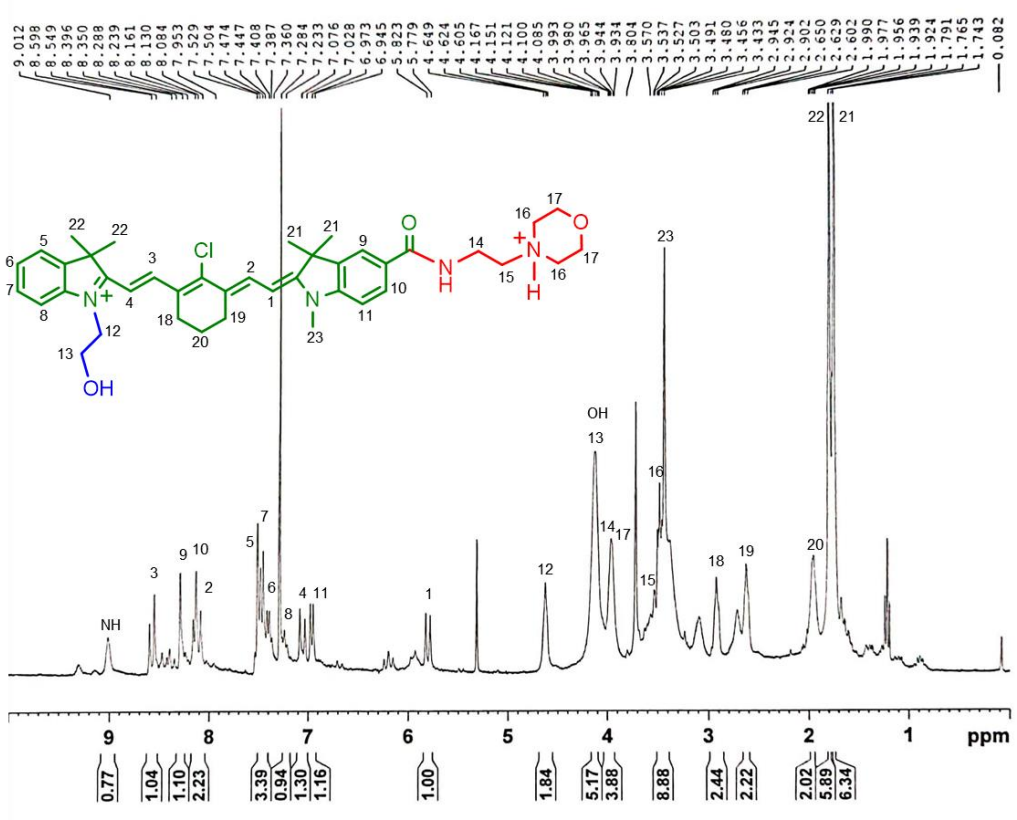

Figure 18. ^{1}H NMR spectrum (300 MHz, $CDCl_3$, 298 K) of open Cy-7 form.

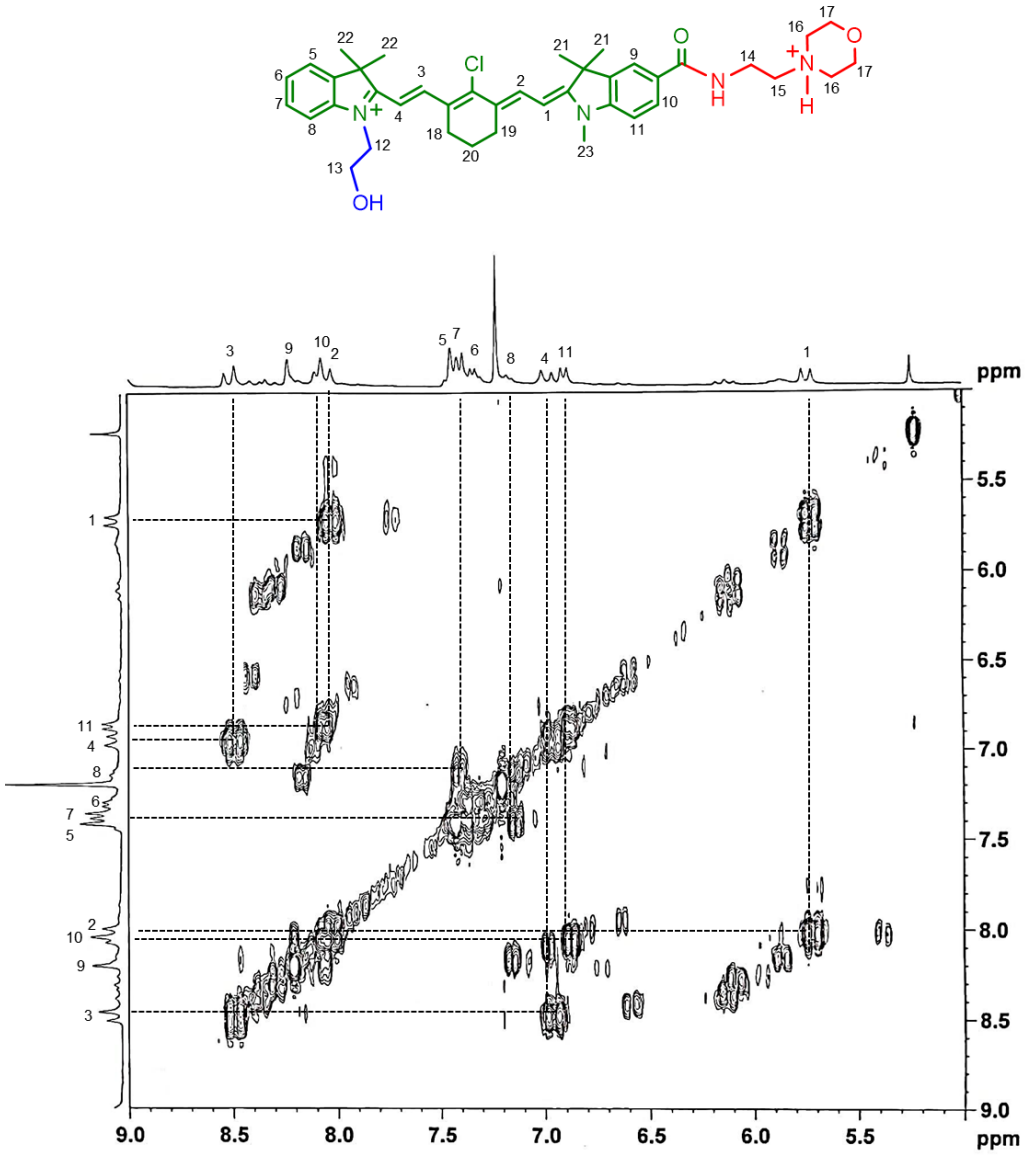

Figure 19. Partial ^{1}H-^{1}H gCOSY (Gradient-selected Correlation Spectroscopy) NMR spectrum (300 MHz, $CDCl_3$, 298 K) of open Cy-7 form.

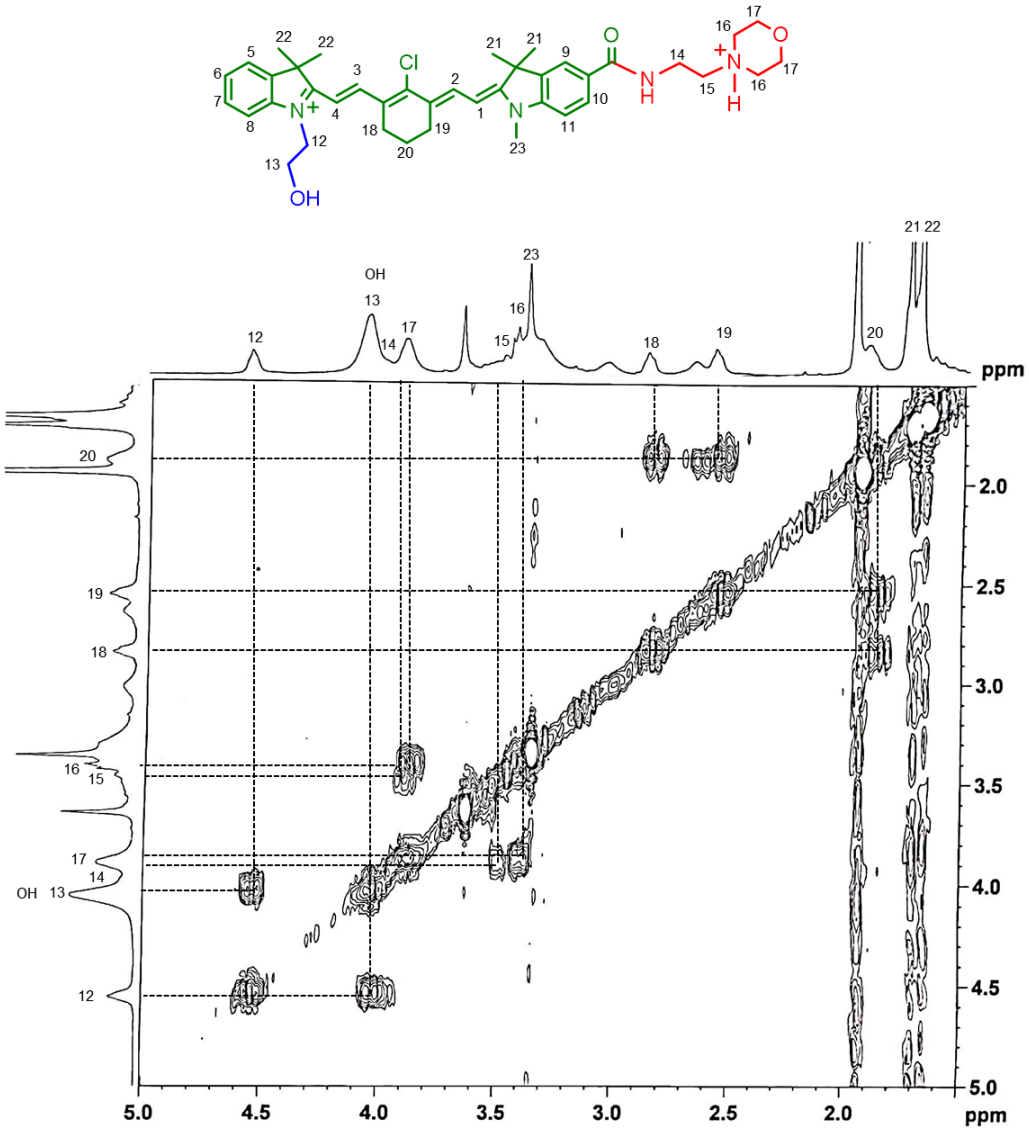

Figure 20. Partial ^{1}H-^{1}H gCOSY (Gradient-selected Correlation Spectroscopy) NMR spectrum (300 MHz, $CDCl_3$, 298 K) of open Cy-7 form.

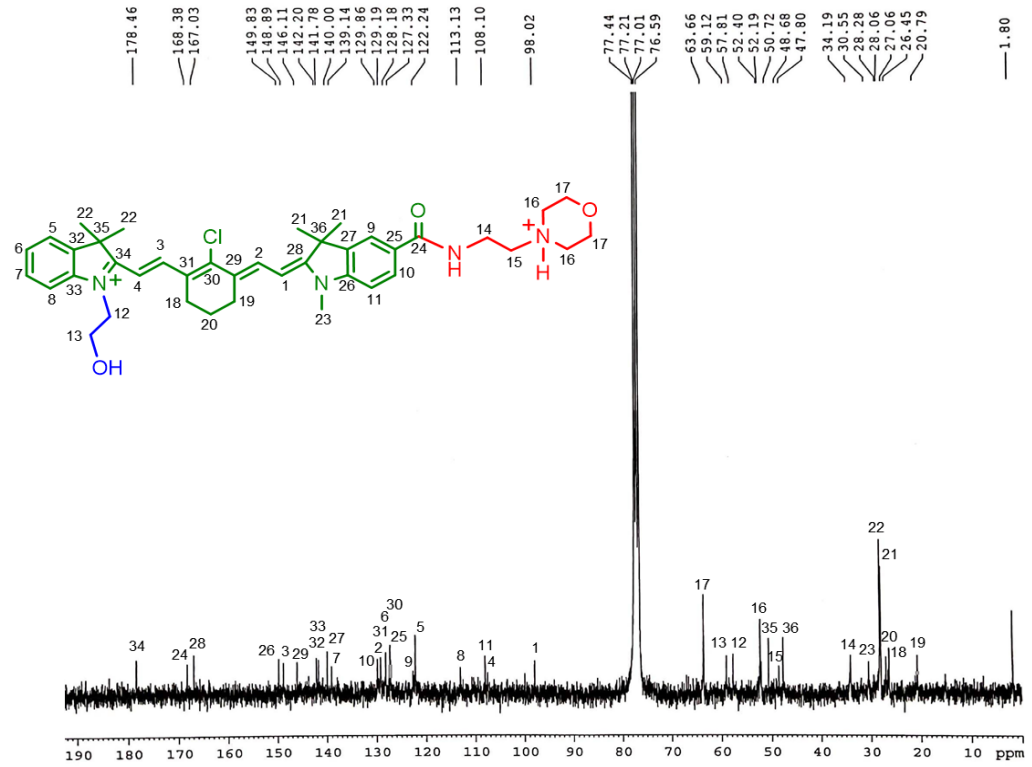

Figure 21a. ^{13}C NMR spectrum (75 MHz, $CDCl_3$, 298 K) of open Cy-7 form.

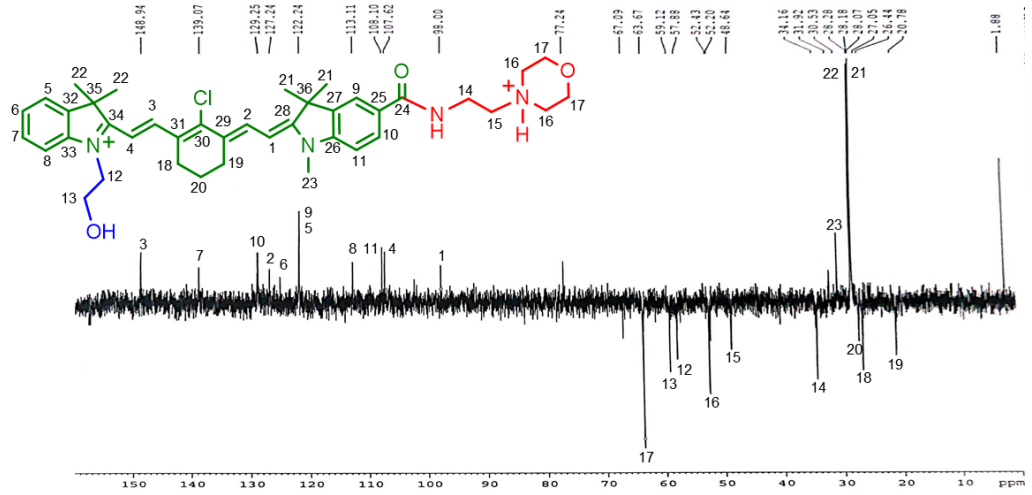

Figure 21b. DEPT-135 spectrum (75 MHz, $CDCl_3$, 298 K) of open Cy-7 form.

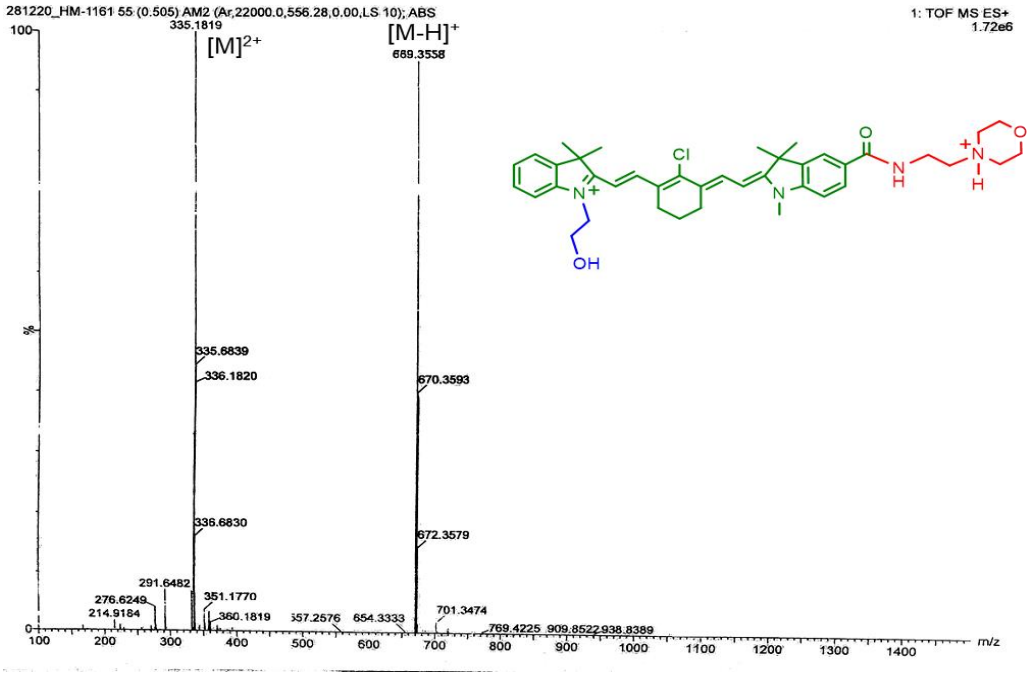

Figure 22. ESI-HRMS spectrum of open Cy-7 form.

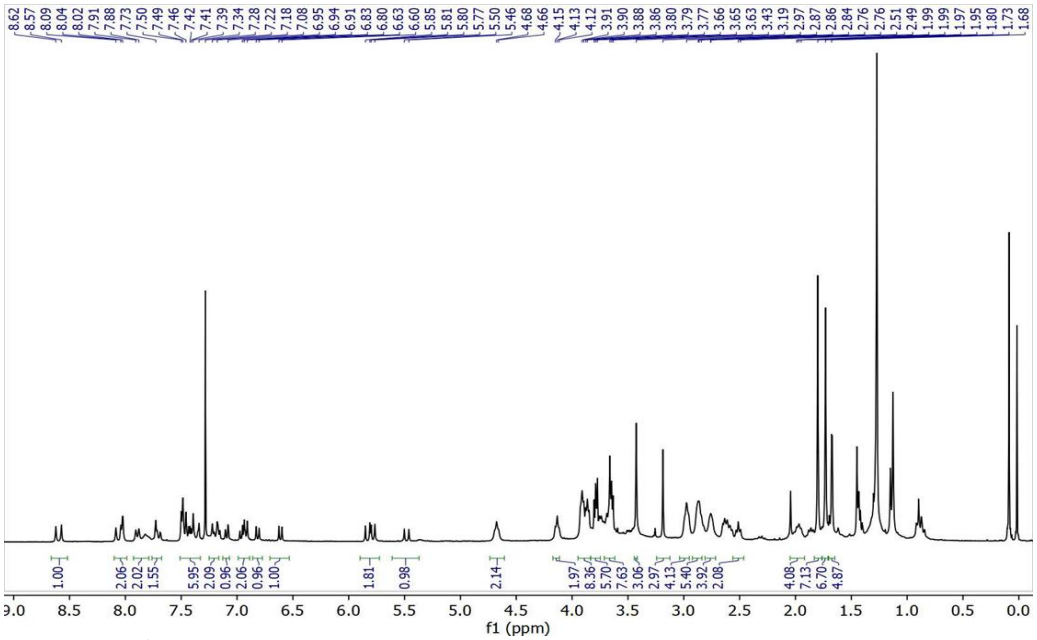

Figure 23. ^{1}H NMR spectrum (300 MHz, $CDCl_3$, 298 K) of the mixture of closed oxazolidine and open Cy-7 form.

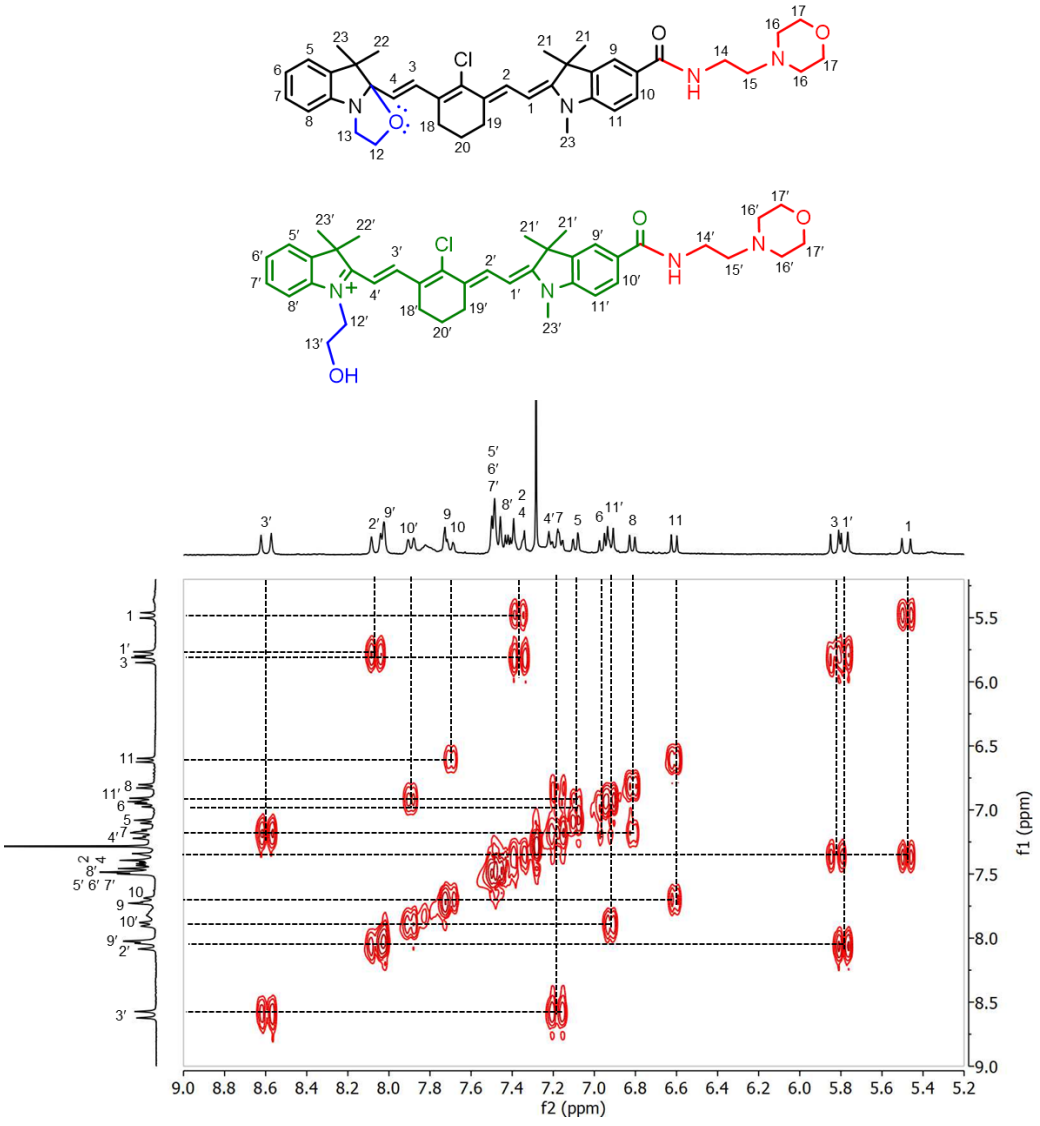

Figure 24. Partial ^{1}H-^{1}H gCOSY NMR spectrum (300 MHz, $CDCl_3$, 298 K) of the closed oxazolidine and open Cy-7 mixture.

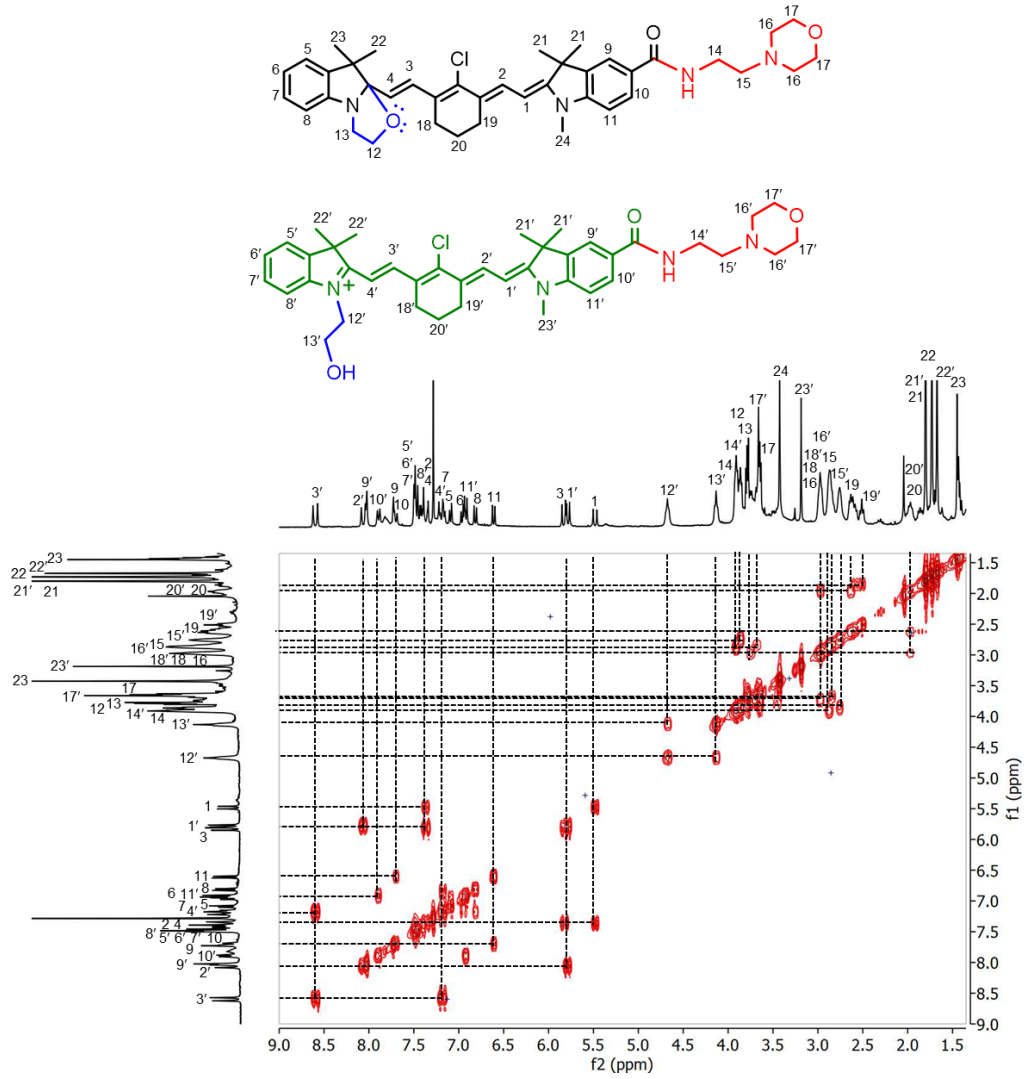

Figure 25. ^{1}H-^{1}H gCOSY NMR spectrum (300 MHz, $CDCl_3$, 298 K) of the closed oxazolidine and open Cy-7 mixture.

.

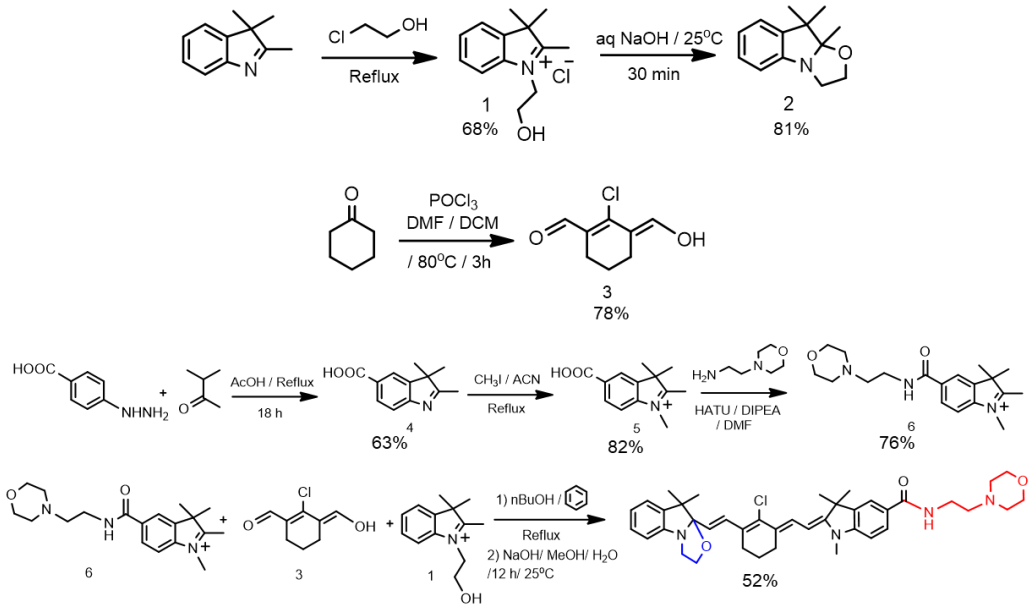

Figure 26. Synthesis of unsymmetrical oxazolidine molecule and their related precursor molecules.

Experimental Section:

Materials: 2-Chloroethanol and TLC silica gel 60 F_{254} were acquired from Merck. 3-Methyl-2-butanone, 1-[Bis(dimethylamino)methylene]-1*H*-1,2,3-triazolo[4,5-*b*]pyridinium 3-oxide hexafluorophosphate (HATU), N,N-diisopropylethylamine (DIPEA), 4-(2-aminoethyl)morpholine, indocyanine green (ICG), coumarin 6, 4-hydrazinobenzoic acid, cyclohexanone, and DAPI were procured from Sigma-Aldrich. $CDCl_3$ and DMSO-d_6 were obtained from Cambridge Isotope Laboratories, Inc. and used for NMR spectroscopy. Spectroscopic grade solvents were used for all the spectroscopic experiments. All the reactions were performed under an inert N_2 atmosphere. Human epithelioid cervix carcinoma HeLa, lung adenocarcinoma A549, and rat cardiomyoblast H9c2(2-1) cell lines were procured from The National Centre for Cell Science, India. Dulbecco's modified eagle medium (DMEM) with and

without phenol red, trypsin EDTA mixture, fetal bovine serum (FBS), antibiotic antimycotic solution, and 3-(4,5-dimethyl-2-thiazolyl)-2,5-diphenyltetrazolium bromide (MTT) were achieved from Himedia. LysoTracker Green DND-26 was acquired from Thermo Fisher Scientific.

METHODS

NMR Spectroscopy: 1D (^{1}H, ^{13}C, DEPT-135) and 2D (^{1}H-^{1}H gCOSY) NMR was recorded at 25°C in suitable deuterated solvents on a Bruker DPX300 MHz spectrometer equipped with a BBO probe. Data were processed by Bruker TopSpin 3.6.2 software.

High-Resolution Electrospray Ionization Mass Spectrometry (HRMS-ESI): HRMS-ESI was acquired on a Q-Tofmicro (Waters Corporation) mass spectrometer. The data were obtained and processed by manufacturers' provided mass application software MassLynx V4.1.

UV/vis Spectroscopy: Absorption spectra were recorded on a JASCO V-730 double-beam spectrophotometer with wavelength range from 200 to 1100 nm by a 1 cm path length quartz cuvette. The data were acquired using a PC and processed by manufacturers' supplied Spectra Manager Version 2 software. The absorption ratio signal (I_{780}/I_{418}) was determined from the absorption intensities at 780 nm and 418 nm.

Fluorescence Spectroscopy: Emission traces were obtained on a FluoroMax-4 spectrofluorometer (Horiba Scientific) operated by FluorEssence Version 3.9.0.1 software. 5 nm excitation and emission slit widths were used. The ratio signal (I_{800}/I_{480}) was measured from the fluorescence intensities at 800 nm and 480 nm.

Fluorescence Lifetime (τ) Measurement: Horiba DeltaFlex lifetime machine (Horiba Jobin Yvon IBH Ltd, UK) was used to accomplish the fluorescence

lifetime (τ) of closed basic oxazolidine form and open acidic Cy-7 form by time-correlated single photon counting (TCSPC) method. Delta diode laser excitation source of 415 nm (Model: DD-415L, Horiba Scientific) and 785 nm (Model: DD-785L, Horiba Scientific) were used to record the fluorescence lifetime of the oxazolidine form and open Cy-7 form, respectively, in DMSO. Horiba EzTime decay analysis software was used to analyses the fluorescence lifetime (τ) data.

pH Titrations: The buffer solutions at various pH were prepared using a Mettler Toledo pH meter. The pH meter was calibrated with the standard buffer solutions of pH 4.01 ± 0.01, 7.00 ± 0.01, and 10.00 ± 0.01 at 25°C. Britton–Robinson universal buffer solution with various pH were prepared and used for the pH titration. All aqueous buffered solutions were freshly prepared and stored in refrigerator (used within one week). A concentrated stock solution of the oxazolidine form (75 μM) in DMSO was prepared. Aliquot of the stock solution was added quantitatively to the aqueous buffer solutions of various pH to obtain the final concentration of the probe of 2.5 μM. The solutions were adequately stirred before spectral measurements. UV/vis as well as fluorescence pH titrations were recorded in triplicate and the outcomes were expressed as the mean ± standard deviation.

Measurement of Fluorescence Quantum Yields of Closed Basic Oxazolidine Form and Open Acidic Cy-7 Form: Fluorescence quantum yields (Φ_f) of basic closed oxazolidine form and acidic open Cy-7 form were determined by relative method. Concentration of the fluorophores was tuned such that absorbance at the λ_{ex} was less than 0.1 to avoid inner filter effect. Here, the integrated fluorescence intensities of oxazolidine form and open

acidic Cy-7 form were compared with emission intensities of reference fluorophores using the subsequent equation (Table S1):

$\Phi_f(y) = \Phi_f(s) \times [(A_s \times F_y \times \eta_y^2) / (A_y \times F_s \times \eta_s^2)]$

$\Phi_f(s)$: Fluorescence quantum yield of the reference fluorophores

$\Phi_f(y)$: Fluorescence quantum yield of the synthesized fluorophores

A_s: Absorbance of reference fluorophore at the λ_{ex}

A_y: Absorbance of synthesized fluorophore at the λ_{ex}

F_s: Integrated emission areas under the corrected fluorescence spectra for the reference molecule

F_y: Integrated fluorescence areas in the corrected emission spectra for the synthesized molecule

η_s and η_y: Refractive indices of the solvents used for the reference and synthesized compounds, respectively [here, $(\eta_y^2 / \eta_s^2) = 1$].

"s" describes to the standard and "y" signifies synthesized compound.

$\Phi_f(s)$ of Coumarin 6= 0.78 in absolute EtOH, which is used as the reference for closed oxazolidine form.

$\Phi_f(s)$ of ICG in DMSO is 0.12 and used as the reference for open Cy-7 form.

Cell Culture: Human cervix adenocarcinoma epithelial HeLa, lung adenocarcinoma A549, and healthy cardiomyoblast H9c2(2-1) cell lines were separately cultured in Dulbecco's modified Eagle medium (DMEM, pH 7.4) supplemented with 10% fetal bovine serum (FBS) and antibiotic-antimycotic solution 100×(containing 10000 units penicillin, 10 mg streptomycin, and 25 μg amphotericin B per mL in 0.9% normal saline) in an air-jacketed incubator of 5% CO_2 at 37°C and was routinely passaged.

MTT Assay: The cytotoxicity of the pH activatable probe on HeLa and A549 cancerous cell lines as well as H9c2(2-1) healthy cell line were verified by 3-(4,5-dimethylthiazol-2-yl)-2,5-diphenyltetrazolium bromide (MTT) assay.

HeLa, A549, and H9c2(2-1) cell lines were separately seeded at a density of ~10^4 cells in a 96-well plate and incubated for 24 h in DMEM. Subsequently 24 h incubation, closed oxazolidine form and open Cy-7 form were separately treated at different concentrations (2, 4, 6, 8, 10, 12, 14, 16, 18, 20, and 25 μM per well) for 24 h at 37°C. HeLa, A549, and H9c2(2-1) cells were then separately incubated with 10 μL MTT solution (5 mg mL^{-1} in PBS) for 4 hour in darkness at 37°C. Formazan crystals (dark blue) were dissolved in DMSO and the absorbance (*A*) at 575 nm was measured (recorded in triplicate) by an ELISA plate reader. The results were described by the following equation:

Cell Viability (%) = (*A* of treated cells / *A* of untreated cells) × 100

Live Cell Lysosome Imaging By Confocal Laser Scanning Microscopy: For live cell confocal microscopy HeLa, A549, and H9c2(2-1) cell lines were separately seeded in a 35 mm glass bottomed cell culture confocal dishes (SPL Lifesciences) at a density of 10^4 cells/mL and permissible to grow in DMEM for 24 h at 37°C in a humidified incubator of 5% CO_2. Subsequently the cells were washed with 1x PBS for three times. After that, live HeLa, A549, and H9c2(2-1) cells were individually incubated with oxazolidine probe (1.0 μM) in media for 30 min in 5% CO_2 atmosphere at 37°C and then rinsed with 1x PBS for three times. According to the manufacturer's protocol the cells were incubated with LysoTracker Green DND-26 (75 nM) at 37°C for 30 min in 5% CO_2 atmosphere. The cell lines were finally incubated with DAPI for 20 min and washed in the similar protocol. Before confocal imaging the cells were washed with 1x PBS for three times and phenol red free media was added. Confocal laser scanning microscopic images were captured by a Leica TCS SP8 microscope with 63x /1.40 (Specification: HC PL APO 63x/1.40 OIL PH3 CS2) oil plan apochromatic objective. All over the live cell confocal laser scanning microscopic imaging process 37°C and 5% CO_2 atmosphere was preserved. A distinct set-up for the live cell confocal imaging

is shown in Figure S40. Confocal microscopic images were analyzed and processed by Leica Application Suite X (LAS X) software.

The live cell CLSM images were captured using different laser excitations: DAPI: laser λ_{ex} 405 nm (blue channel, detection range of emission wavelength 415–480 nm); LysoTracker Green DND-26 (LTG): laser λ_{ex} 488 nm (green channel, detection range of emission wavelength 500–572 nm); pH activatable probe: laser λ_{ex} 670 nm (red channel, detection range of emission wavelength 700–780 nm).

3D Confocal Image: To get the better view of lysosomal staining, Z-stack images of live HeLa cells stained with DAPI and the synthesized acidic pH activatable probe were acquired using a Leica TCS SP8 instrument. For the live cell 3D CLSM image construction, the images were harvested every 0.3 μm on the Z-axis. Eighteen different frames for each channel were collected over a time period of 6 minutes and finally reconstructed with the help of LAS X software to obtain the 3D CLSM image. This 3D reconstructed CLSM image clearly indicates the spherical lysosomal compartment inside the live HeLa cells.

Determination of Pearson's Correlation Coefficient: Pearson's correlation coefficient (PCC) is one of the standard statistical analysis in pattern recognition for matching one confocal microscopic image (green channel defines LysoTracker Green DND-26 staining) with another (red channel designates open Cy-7 staining). PC graph can illustrate the level of overlapping between two patterns in a colocalization image. PCC was measured by the LAS X software using Quantify tool.

PCC was determined (image comprising of red and green channels) by the following equation:

$$PCC = \frac{\sum_i (S1_i - S1_{avg}) * (S2_i - S2_{avg})}{[\sum_i (S1_i - S1_{avg})^2 * \sum_i (S2_i - S2_{avg})^2]^{(1/2)}}$$

S1 = signal intensity of pixels (pixel i) in the green channel

S2 = signal intensity of pixels (pixel i) in the red channel.

$\mathbf{S1_{avg}}$ = mean values of pixels in the green channel

$\mathbf{S2_{avg}}$ = mean values of pixels in the red channel.

PCC is independent of signal levels and background. PCC was measured for colocalization area within the area foreground by LAS X software.

Ratiometric Confocal Microscopic Images: The cultured HeLa cells were incubated with oxazolidine probe (1 μM) for 30 min in 5% CO_2 atmosphere at 37°C in a glass bottomed culture dishes without adding any other staining agent. After washing the cells with 1X PBS, ratiometric confocal microscopic images of live HeLa cells were obtained by dual channel excitation (green channel and red channel), respectively. The exposure times for each filter were kept constant. To get pixel based ratiometric imaging, confocal images acquired by Leica TCS SP8 confocal scanning microscope were processed by ImageJ software (ImageJ 2.1.0; Java 1.8.0_172). At first background subtraction for each channel [channel 1 (red) and channel 2 (green)] was performed before analysis of dual-channel (red/green) ratio images. A region of interest (ROI) in channel 1 (red channel) is determined and with the help of image calculator programme the average emission intensity over that region is

divided by the average emission intensity of ROI in channel 2 (green channel). The constructed pseudocolored ratiometric images (I_{red}/I_{green}) represent the pH values of the exact positions.

Real-Time Tracking of Lysosomes in Live Cells using the Synthesized pH Activatable Probe: Lysosomal movement inside the live HeLa cells was monitored using a Leica TCS SP8 instrument by the synthesized acidic pH activatable lysosome targeting probe over a time course of 5 minutes. 20 frames were collected over 5 minutes to generate a real-time movie using LAS X software.

Synthesis, Purification, and Characterization of closed basic form and open acidic form: Unsymmetrical closed basic oxazolidine form and open acidic Cy-7 form and their precursor molecules were made by an effective method with reasonable yield from easily accessible low-cost starting materials.Analytical TLC (TLC silica gel 60 F_{254}) was executed on silica gel covered aluminium sheets with appropriate solvent mixtures and analyzed by UV lamp or naked eye. The synthesized crude products were purified through column chromatography (silica gel 100-200 mesh). The solvents used for column chromatography were distilled using appropriate drying agents. 2,3,3-Trimethylindolenine was synthesized by the literature reported procedure.[36]

Result and discussion: Synthesis of unsymmetrical chromophore is more challenging than symmetrical chromophore. N of 2,3,3-trimethyl indoleline is covalently linked with hydroxyethyl chain (**1**) which can be further modified to fused oxazolidine ring (**2**) (Figures 1-4). The synthesized 5-carboxy-1,2,3,3-tetramethyl-3*H*-indol-1-ium (**5**) is further conjugated with lysosome targeting 4-(2-aminoethyl)morpholine moiety to get compound **6** (Figures 5-11). The closed oxazolidine probe is prepared by condensation between the **1** and **6** with

(*E*)-2-chloro-3-(hydroxymethylene)cyclohex-1-enecarbaldehyde **(3)** in presence of 1-butanol/benzene (7:3) followed by the treatment with NaOH (Figure 26). The unsymmetrical light yellow closed oxazolidine probe is acquired in good yield and characterized by 1D (^{1}H, ^{13}C, DEPT-135) NMR, 2D (^{1}H-^{1}H gCOSY) NMR, and high-resolution ESIMS (Figures 12-17). The ^{1}H NMR spectrum of the closed form is characterized by the multiplets between 3.6 and 3.8 ppm originating from the methylenic (–CH_2–CH_2–) protons of the fused oxazolidine moiety (Figure 27b). Upon addition of excess dil HCl the full conversion of closed oxazolidine to green colored open Cy-7 form is achieved (Figure 27a, Figures 18-22). After acidification new ^{1}H NMR signals are generated at 4.6 (t, J = 5.7 Hz, 2H) and 4.17–4.09 (m, 2H) ppm (downfield shifted with respect to oxazolidine methylenic protons) which are diagnostic peaks for methylenic protons of pendant hydroxyethyl chain of the open Cy-7 state (Figure 18). ^{1}HNMR spectra confirms switching from the closed oxazolidine state to the open Cy-7 state through intermediate stages where mixtures of both the closed and open forms are identified (Figure 27b, Figures 23-25). The distinct characteristic alternation of the probe structures at acidic pH is observed due to the H^+-triggered ring-opening reaction of the oxazolidine moiety to generate a highly conjugated π electronic push-pull Cy-7 system, which results in the bathochromic shift in the λ_{abs} as well as in λ_{em} from visible to the NIR wavelength (Figure 27). Here $n_N \rightarrow \sigma^*_{C–O}$ interaction induces a rupture of the $\sigma_{C–O}$ bond which trigger ring-opening of the oxazolidine moiety at acidic pH. A reversible, pH-dependent absorption as well as emission spectral shift arises due to the deprotonation of the pendant hydroxyethyl group of indolium moiety to form oxyanion nucleophile which attack at the electron-deficient iminium carbon to form fused oxazolidine ring using 5-endo-trig cyclization in alkaline

solution (Figure 27a). Hence extended conjugation of polymethine system breaks and hypsochromic shift is observed. Surprisingly we observed unusual 5-endo-trig cyclization (generally 5-exo-trig cyclization is preferred according to Baldwin's rules) at alkaline pH through the reaction of oxyanion nucleophile to the iminium carbon.[37,38] At basic and physiological pH the dominating oxazolidine form having shorter π-conjugation exhibits an absorption

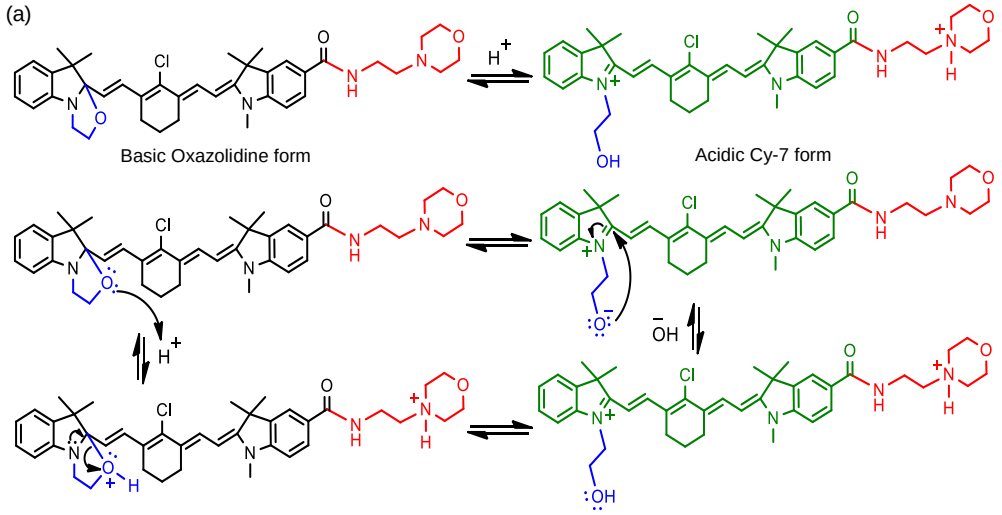

Figure 27a. pH switchable basic closed oxazolidine and acidic open Cy-7 form and their interconversion.

maximum in the visible region (λ_{abs} 418 nm) and light yellow in color (Figure 29a). At acidic pH due to the formation of highly conjugated Cy-7 structure (green color) an absorption peak at 780 nm activated to emerge with associated decrease of the peak at 418 nm with a clear isosbestic point at 460 nm (Figure 2b,c and Figures 27, 28). The dye's absorption profile can be switched reversibly between a basic oxazolidine form and an acidic Cy-7 form for several times (Figure 28c).

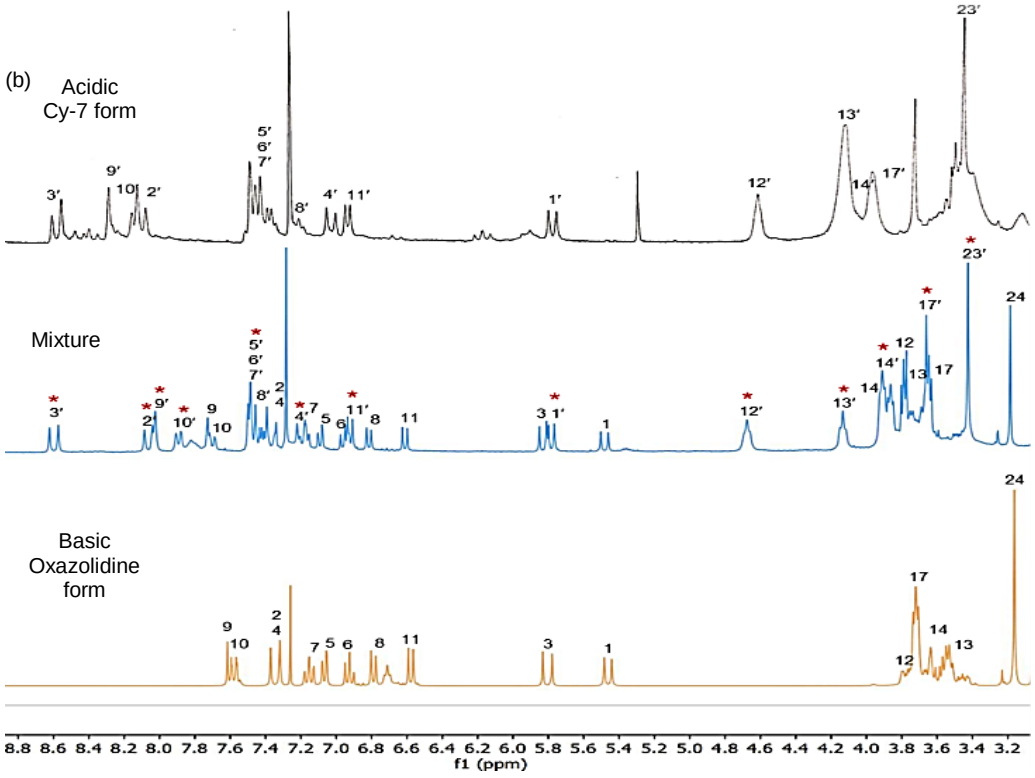

Figure 27b. Partial ^{1}H NMR stacking plot of pure oxazolidine, a mixture of oxazolidine as well as open Cy-7 form and pure open Cy-7 state.

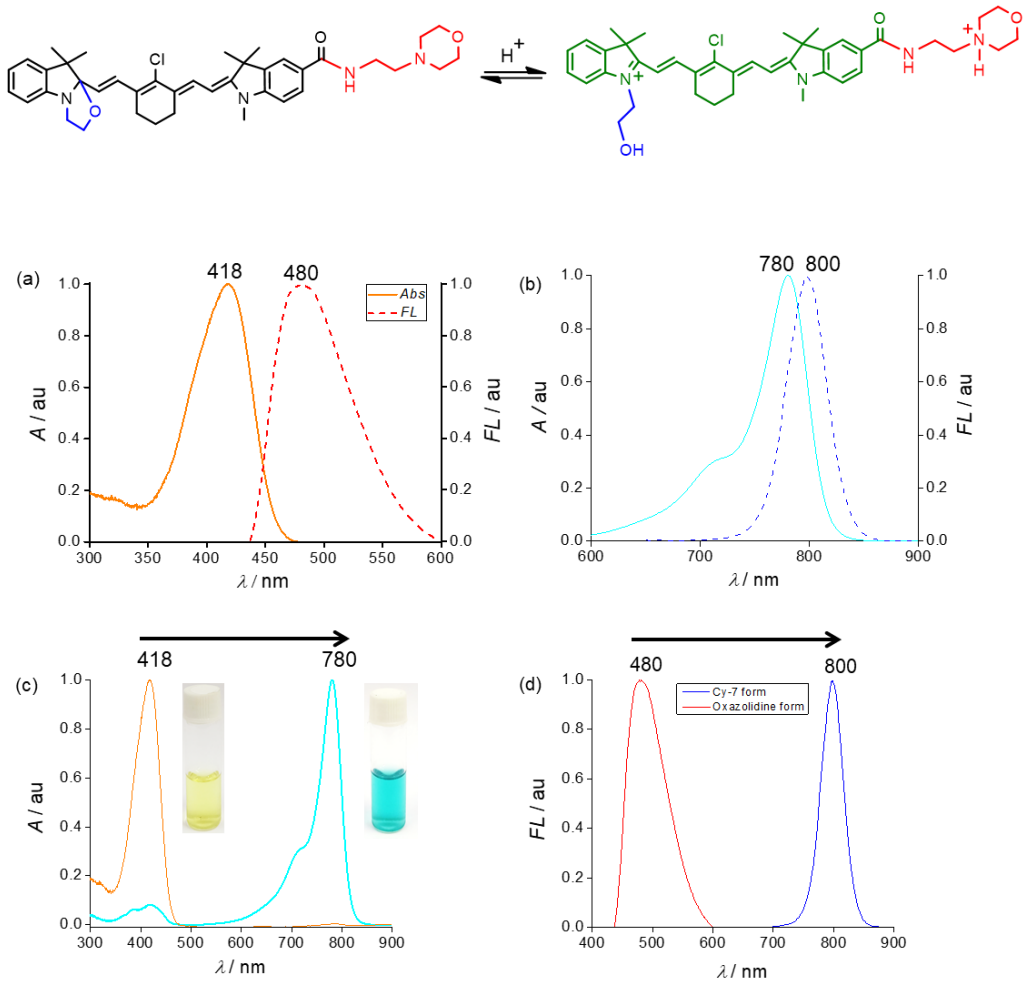

Figure 28. (a) Normalized UV/vis absorption and emission plots of closed oxazolidine (2.5 μM) form in DMSO. (b) Normalized absorption and fluorescence plots of Cy-7 state (2.5 μM) in DMSO. (c) Normalized absorption plot of closed oxazolidine and open Cy-7 form in DMSO shows 362 nm bathochromic shift. (d) Normalized fluorescence plots of closed oxazolidine and open Cy-7 form in DMSO indicates 320 nm bathochromic shift.

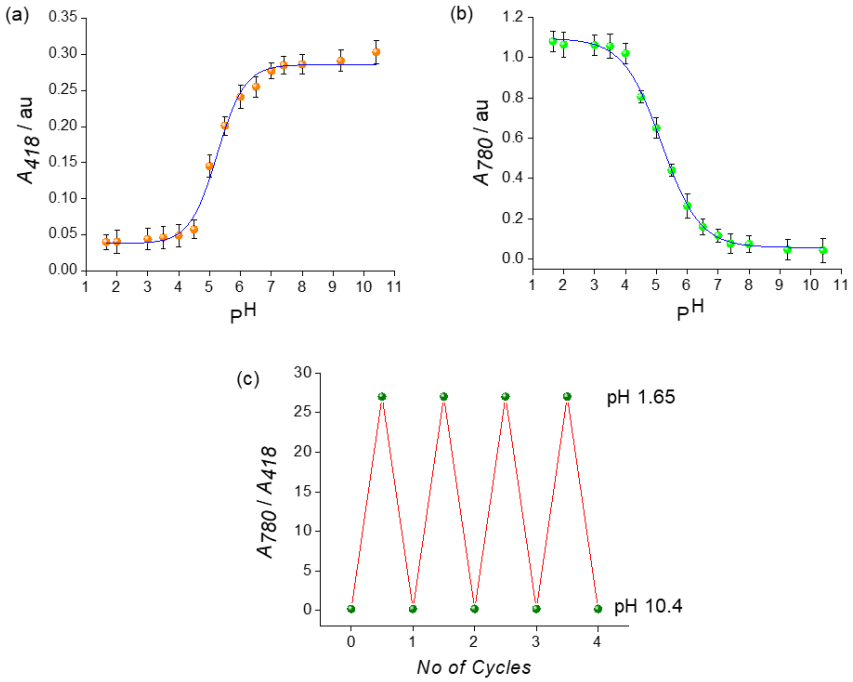

Figure 29. (a) pH vs absorbance intensity at 418 nm plot with sigmoidal curve fitting. Error bars represent the mean±standard deviation of three independent tests. (b) pH vs absorbance intensity at 780 nm plot with sigmoidal curve fitting. Error bars indicate the mean±standard deviation of three independent analyzes. (c) Reversible absorbance switching between pH 10.4 and 1.65 for four cycles.

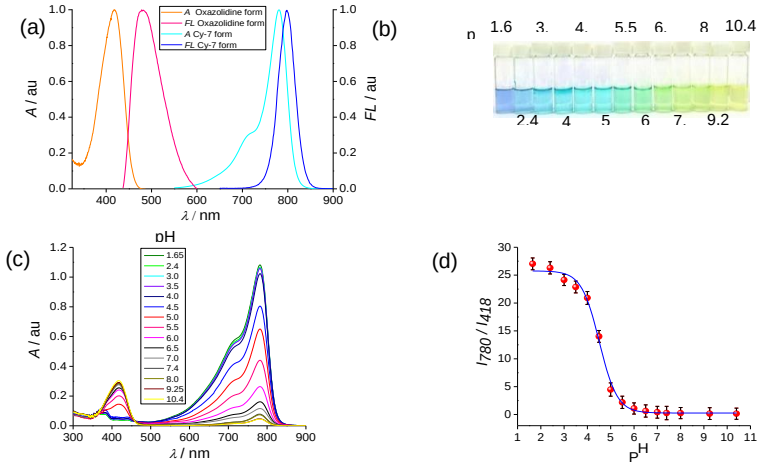

Figure 30. (a) Normalized absorbance and fluorescence plot of oxazolidine and Cy-7 state in DMSO. (b) Color change of the probe in buffer solutions at various pH. (c) UV/vis titration plot of closed oxazolidine (2.5 μM) form in buffer at various pH

values indicates 362 nm bathochromic shifts at acidic pH due to the formation of Cy-7 form. (d) pH vs absorbance intensity ration (I_{780}/I_{418}) plot with sigmoidal curve fitting.

A noteworthy spectral feature is the reasonably narrow absorption bandwidths which permit huge amplitude switching of molar absorptivity at the two wavelengths. The fluorescence emission peak in closed oxazolidine compound and open Cy-7 form are significantly varied. Fluorescence pH titrations are executed in buffered solution with various pH at a probe concentration of 2.5 μM. At basic pH the oxazolidine molecule (closed form) emits at 480 nm (λ_{ex} 418 nm) (Figure 30a). During pH titration the intensity of visible-wavelength emission [$(\lambda_{em})_{basic}$ 480 nm, $(\lambda_{ex})_{basic}$ 418 nm] gradually decreases and a new NIR-wavelength emission band [$(\lambda_{em})_{acidic}$ 800 nm, $(\lambda_{ex})_{acidic}$ 780 nm)] switched on and underwent a concomitant increase with decreasing pH due to the formation of highly conjugated open Cy-7 structure (Figure 31a,b and Figure 32).

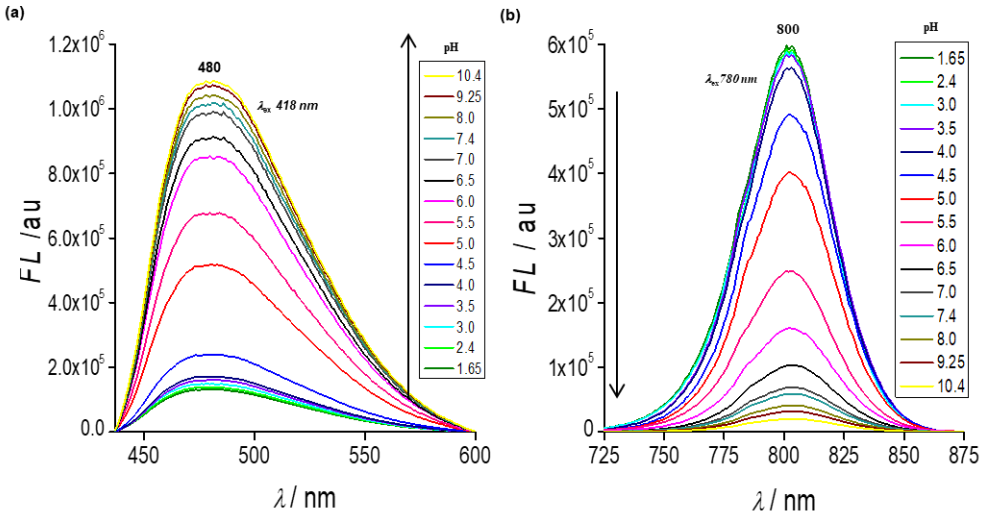

(c)

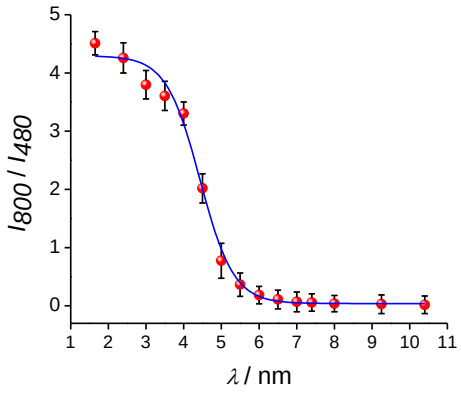

Figure 31. (a) Fluorescence titration plot of pH switchable probe (2.5 μM) at λ_{em} 480 nm (λ_{ex} 418 nm) in buffer solutions at various pH values. (b) Fluorescence pH titration plot of the probe (2.5 μM) at λ_{em} 800 nm (λ_{ex} 780 nm) in different pH.

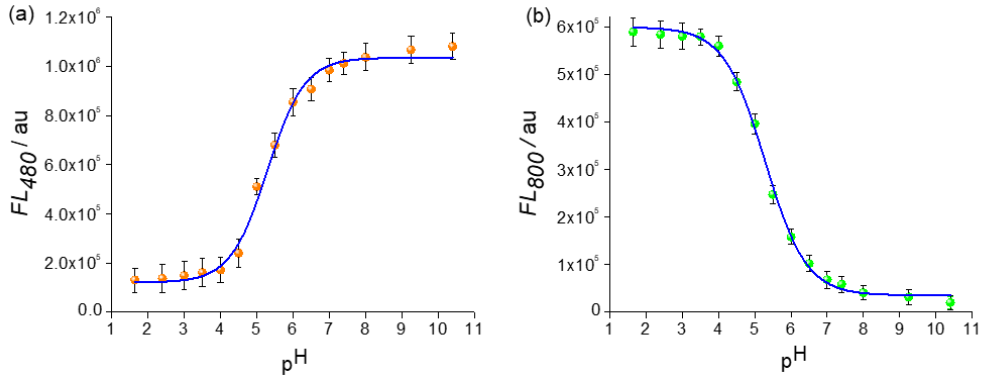

Figure 32. (a) pH vs emission intensity at 480 nm plot with sigmoidal curve fitting. Error bars represent the mean±standard deviation of three independent tests. (b) pH vs λ_{em} at 800 nm plot with sigmoidal curve fitting. Error bars indicate the mean±standard deviation of three independent analyzes.

A huge bathochromic shift of absorption ($\Delta\lambda_{abs}$ 362 nm) as well as emission ($\Delta\lambda_{em}$ 320 nm) is observed from basic closed oxazolidine form to acidic open

Cy-7 form. The pK_a value of the molecule is calculated to be 4.8 which is derived from the sigmoidal curve fitting using the ratiometric data obtained from the absorption (I_{780}/I_{418}) as well as fluorescence (I_{800}/I_{480}) titration at various pH (Figures 30d and 31c). The pK_a value of the molecule is ideal for the imaging of acidic intracellular lysosomal compartments. Moreover, due to off-to-on NIR fluorescence switching of the probe the fluorescence signal at 800 nm increased 30-fold from pH 10.4 to 2.4 (Figure 31b). We observed fully reversible OFF/ON pH- based molecular switching between the closed oxazolidine and open Cy-7 states. Owing to such sharp emission changes arising at two well separated wavelengths (480 nm and 800 nm, $\Delta\lambda_{FL}$ 320 nm) and the turn-on fluorescence at acidic pH in the NIR region of Cy-7 with narrow bandwidth make it a promising candidate for ratiometric fluorescent sensing of pH. Moreover, at acidic pH the conjugated Cy-7 structure exhibits high molar extinction coefficient (ε = 4.33×10^5 $M^{-1}cm^{-1}$) and adequate fluorescence quantum yield (Φ_f = 0.11) (Table 1). Fluorescence lifetime (τ) of the Cy-7 form (τ = 1.05 ns) is found greater than the oxazolidine form (τ = 0.54 ns) in DMSO using time-correlated single photon counting (TCSPC) experiment which suggest that at acidic pH lifetime of the probe increases (Table 1, Figure 33).

Compound (a)	Solvent	λ_{max} (nm)	λ_{em} (nm)	Stokes shift ($\Delta\lambda$)	$\varepsilon \times 10^5$ (M^{-1} cm^{-1})	Quantum Yield in EtOH	Fluorescence lifetime (τ)
Closed Oxazolidine form	DMSO	418	480	62	1.21	0.09	0.54 ns

Compound	Solvent	λ_{max} (nm)	λ_{em} (nm)	Stokes shift ($\Delta\lambda$)	$\varepsilon \times 10^5$ (M^{-1} cm^{-1})	Quantum Yield in DMSO	Fluorescence lifetime (τ)
Open Cy-7 form (b)	DMSO	780	800	20	4.33	0.11	1.05 ns

Table 1. Photophysical data of (a) closed oxazolidine state and (b) open Cy-7 state.

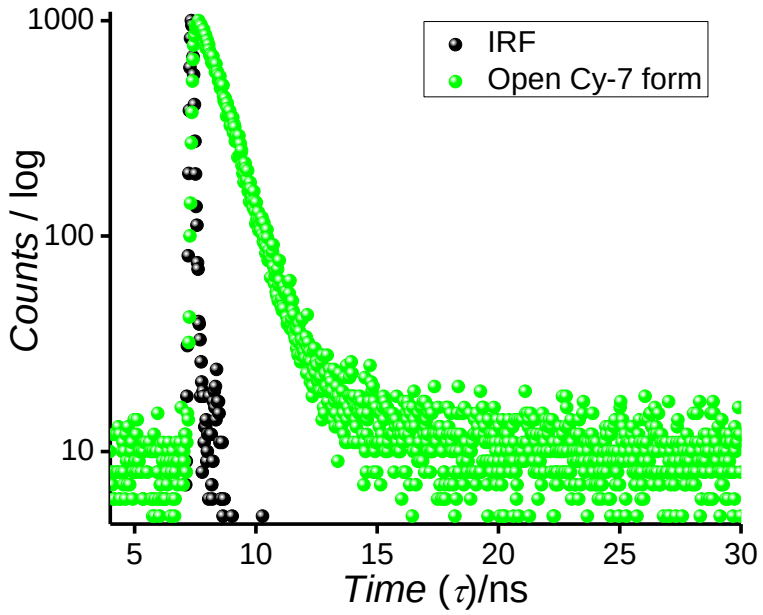

Figure 33. TCSPC plot of open Cy-7 form in DMSO. The fluorescence lifetime (τ) is calculated to be 1.0465±0.0213259 ns (IRF = instrument response function).

Long-term stability of the pH activatable probe is an essential prerequisite for its real applications. The pH-responsive properties and photostability of the probe (2.5 μM) is first verified by determining the fluorescent response over 24 h in pH 2.4, 4.0, 5.0, 7.4, and 10.4 at 37°C. The fluorescence experiment indicates that the ratio of the fluorescence intensities (I_{800} / I_{480}) is stable to the buffer medium over a wide range of pH, time, and light at 37°C (Figure 34).

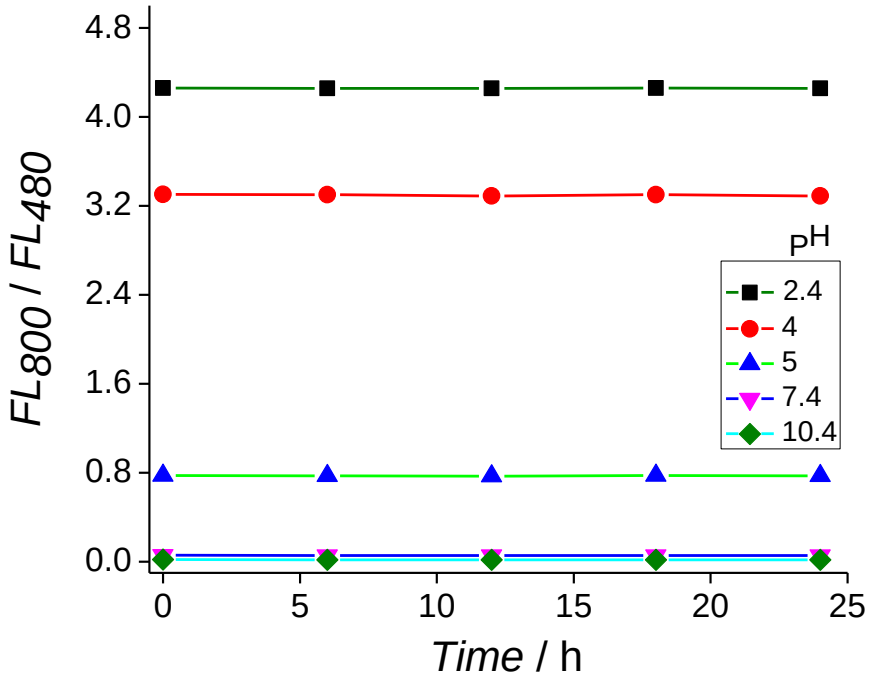

Figure 34. Time course for the ratiometric fluorescence (FL_{800}/FL_{480}) stability of the pH switchable molecule (2.5 μM) in buffer solution at pH 2.4, 4.0, 5.0, and 10.4 at 37°C.

Furthermore, the probe exhibited wonderful reversibility with fast response when the pH is regulated forth and back between 10.4 and 1.65 at least four cycles. The repeatable ON/OFF switching of absorbance (A_{780}/A_{418}) as well as emission (FL_{800}/FL_{480}) are observed without significant change. Moreover, no aggregation or degradation is detected proving the robustness of this pH switching system. The potential interferences of a range of biological analytes are tested. The fluorescence experiment of the pH activatable probe is executed in presence of various crucial metal ions (Na^+, K^+, Ca^{2+}, Mg^{2+}, etc.), anions

(Cl^-, HCO_3^-, NO_3^-, NO_2^-, etc.) as well as bioactive small molecules like glutathione, cysteine, and H_2O_2 at 37°C, pH 7.4 (Figure 36).

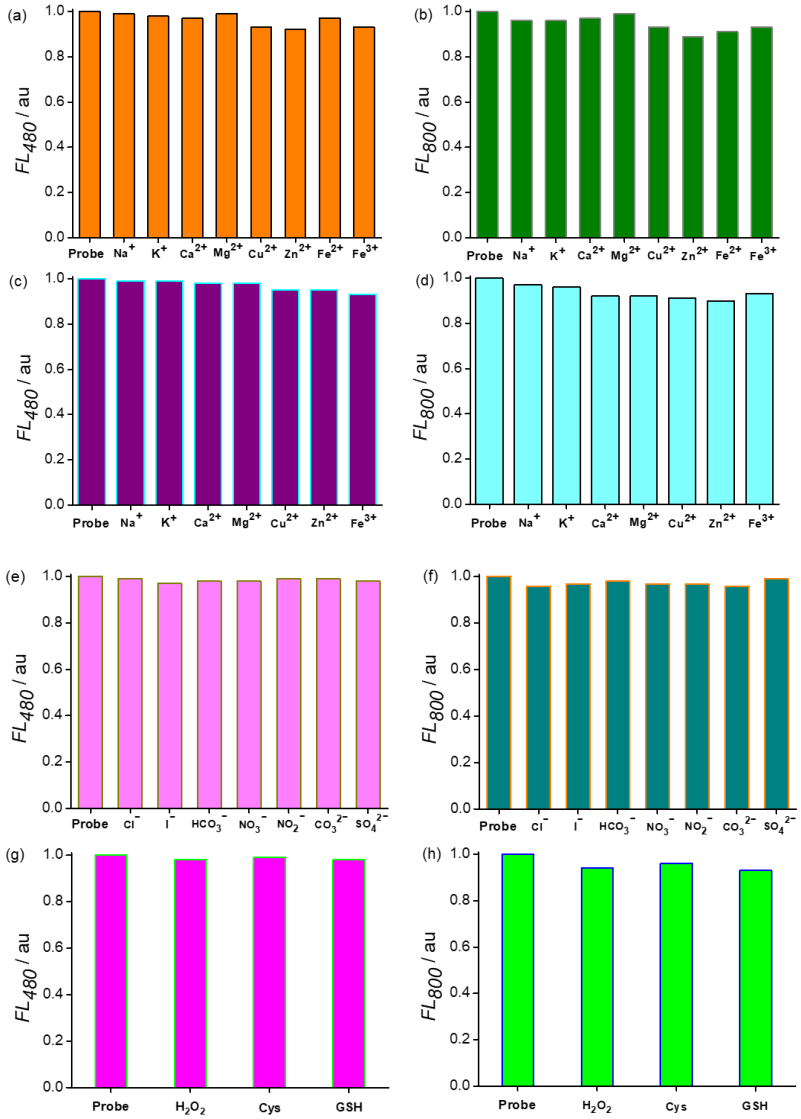

Figure 35. No significant fluctuations are observed in the fluorescence signal of the probe (2.5 μM) at 480 nm and 800 nm in presence of various cations [10 mM Na^+, 10 mM K^+ and 200 μM for Ca^{2+}, Mg^{2+}, Cu^{2+}, Zn^{2+}, Fe^{2+}, and Fe^{3+}] as (a,b) chloride and

(c,d) nitrate salts; (e,f) different anions (200 μM for Cl^-, I^-, HCO_3^-,NO_3^-, NO_2^-, CO_3^{2-}, and SO_4^{2-} as Na^+ salts) as well as (g,h) bioactive small molecules like glutathione (GSH, 5 mM), cysteine (Cys, 5 mM), and H_2O_2 (1 mM) under physiological conditions (37°C, pH 7.4).

No significant variations are observed in the fluorescence spectra of the probe in presence of these probable biological interferents. Cell viability studies using MTT assay display that the probe is less toxic to HeLa, A549, and H9c2 (2-1) cell lines (Figure 36). On this basis, we propose that the probe has the potentiality to be used as a safe fluorescent dye for the live cell acidic lysosomal tracking.

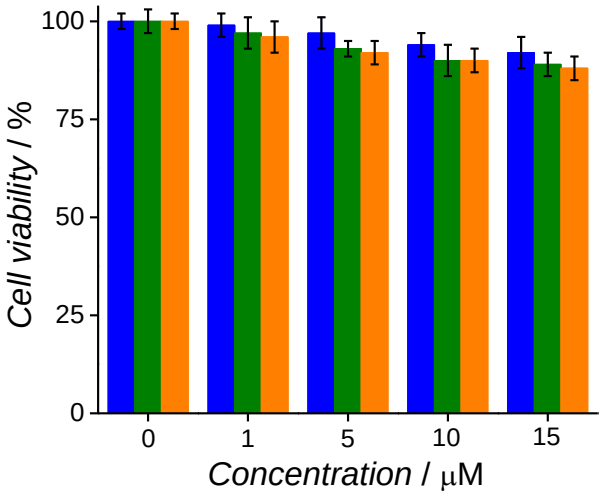

Figure 36. Cell viability of HeLa (blue), A549 (green), and H9c2(2-1) (orange) cell lines incubated with various doses (1, 5, 10, and 15 μM per well) of the pH activatable probe for 24 hours. Error bars specify standard error of mean (SEM, n=5).

CLSM images reveal that, after incubation with the live carcinoma HeLa, A549, and a healthy H9c2(2-1) cell lines for 30 min, the closed oxazolidine

probe with morpholine functionality internalized live cells efficiently, enters into the acidic lysosomal compartment, switched on to the active open NIR Cy-7 structure and exhibited a punctate vesicular pattern. To endorse the lysosomal specificity of the probe, colocalization experiments are executed in live HeLa, A549 carcinoma and a healthy H9c2(2-1) cells with a commercially accessible lysosome specific marker, LysoTracker Green DND-26 (LTG, $\lambda_{ex}/\lambda_{em}$ 504/511) (Figure 37, Figures 37–41).

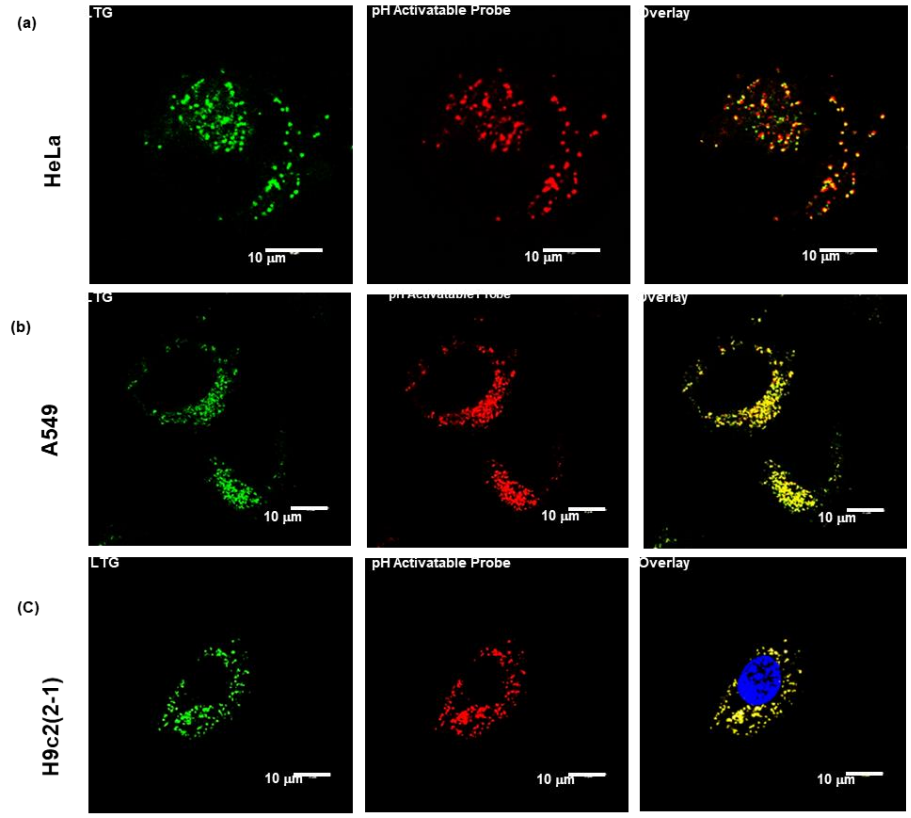

Figure 37. Confocal laser scanning microscopic images of live (a) HeLa carcinoma cells, (b) A549 carcinoma cells, and (c) H9c2(2-1) healthy cells staining with the lysosome targeting pH activatable probe colocalized with LysoTracker Green DND-26 (LTG). Green channel indicates LTG and red channel specifies the pH activatable probe. Overlay images indicate high colocalization inside the live cell lysosomes.

The probe exhibited good colocalization with LTG inside the HeLa, A549 as well as H9c2(2-1) live cells and it is confirmed by CLSM with a high Pearson's correlation coefficient (PCC) of 0.88, 0.85, and 0.91, respectively (Figures 37a, 38a, 39a). CLSM is used to scan various layers of the live cells

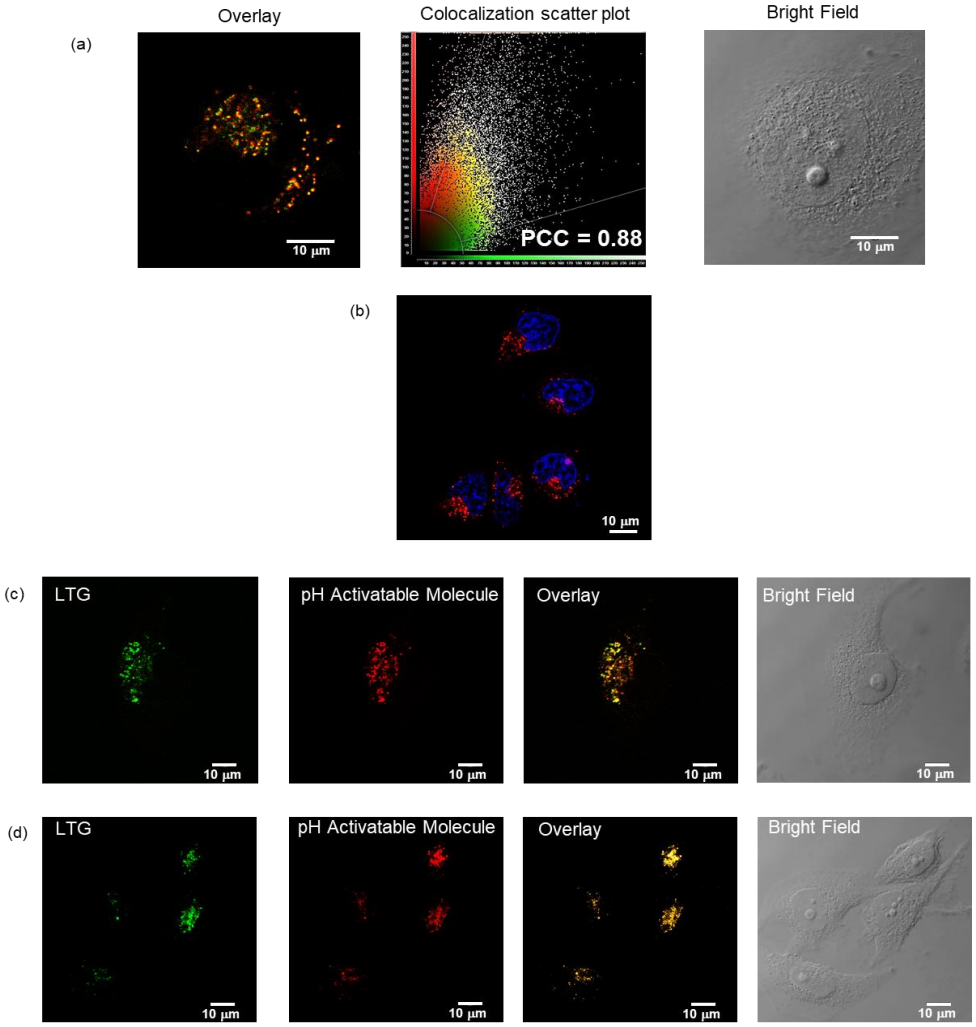

Figure 38. (a) Overlay image indicate high colocalization in live HeLa cell lysosomes. Colocalization scatter plot displays Pearson's correlation coefficient (PCC) of 0.88. (b) CLSM image of live HeLa cells staining with the lysosome targeting pH activatable probe (red color) and nucleus targeting DAPI (blue color). (c,d) CLSM images of live

HeLa carcinoma cells staining with the pH activatable molecule colocalized with LysoTracker Green DND-26 (LTG).

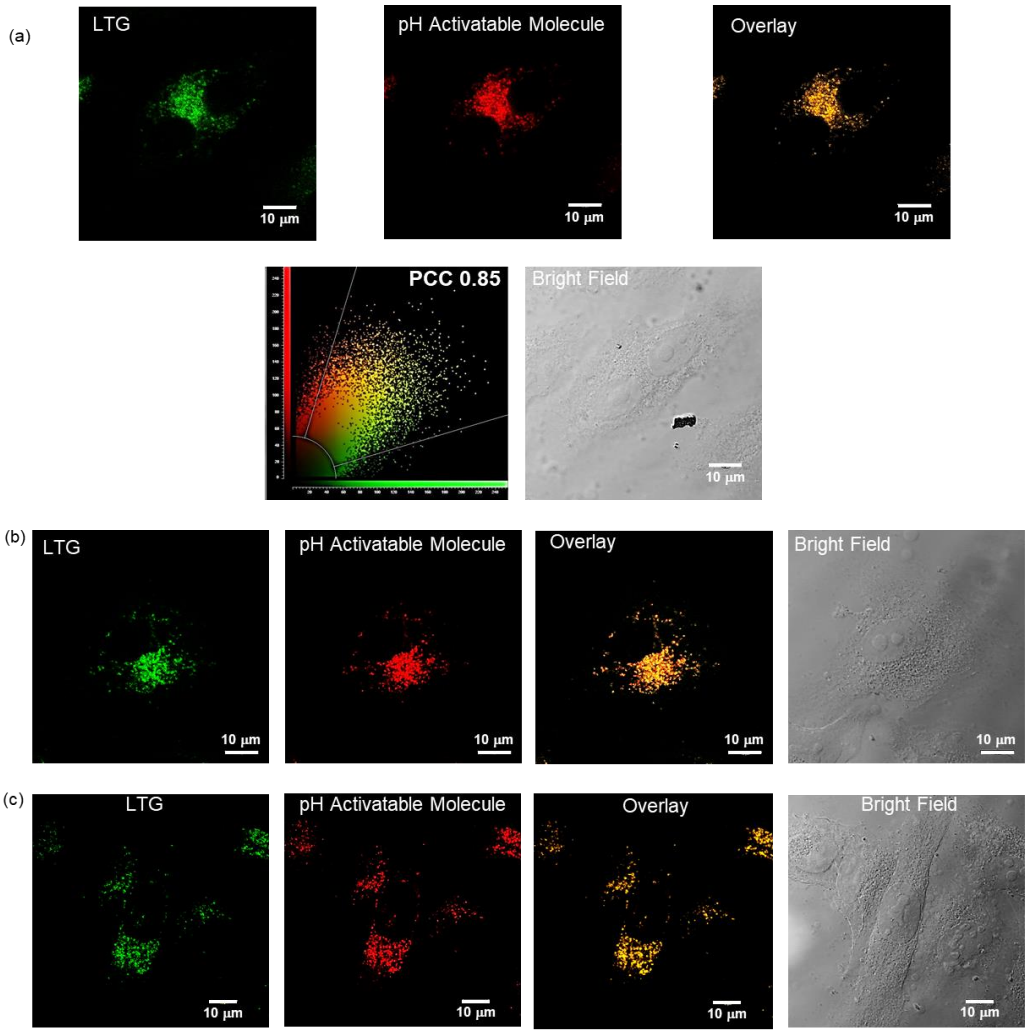

Figure 39. (a–c) CLSM images of live A549 carcinoma cells staining with the pH activatable molecule colocalized with LysoTracker Green DND-26 (LTG). Overlay images indicate high colocalization in lysosomes. Pearson's correlation graph shows PCC of 0.85.

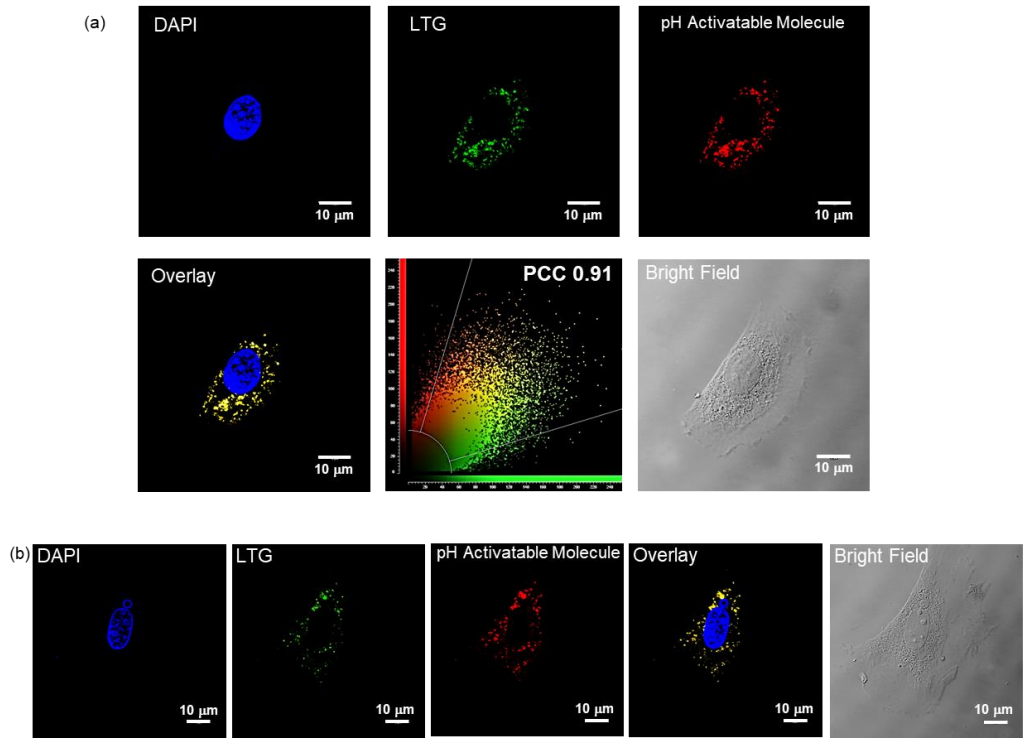

Figure 40. (a and b) CLSM images of live rat cardiac myoblast H9c2 (2-1) healthy cells staining with the pH activatable molecule colocalized with LysoTracker Green DND-26 (LTG). Green channels indicate LTG staining, red channels specify the pH activatable molecule, and blue channels designate DAPI staining. Overlay images indicate high colocalization in lysosome. Colocalization scatter plot displays PCC of 0.91.

It indicates that the oxazolidine molecule has good cell membrane permeability and after internalization through the plasma membrane into the acidic lysosomal lumen, the probe displayed lysosome-specific activation and turned-on fluorescence at NIR region in live cells. Moreover, we have also achieved ratiometric CLSM images in HeLa, A549, and H9c2 (2-1) live cells by dual channel excitation treated with the pH activatable probe. The fluorescence emission intensity in red channel is higher than the fluorescence intensity of

well separated green channel, signifying negligible cross talk between these two channels.

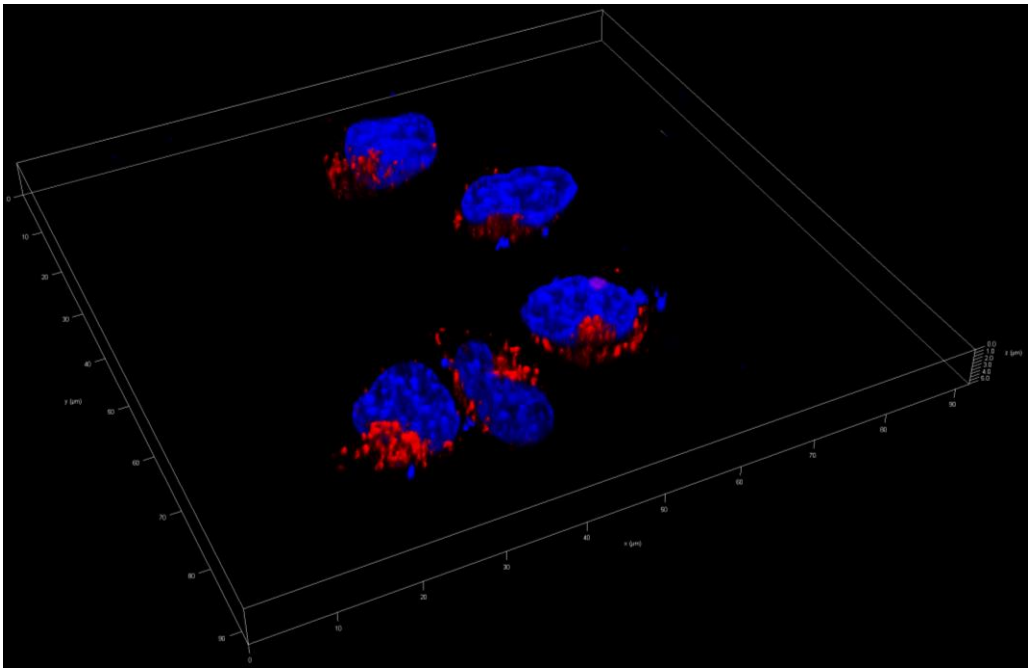

Figure 41. 3D CLSM image of live HeLa cells staining with the lysosome targeting pH activatable molecule indicate spherical lysosomal compartment (red color). Blue color designates nuclear staining by DAPI.

The ratiometric CLSM imaging (pseudocolor obtained by ImageJ software, I_{red}/I_{green}) is achieved from the two channels (Figure 43, Figure 44) showed that this ratiometric fluorescent probe is an efficient candidate to detect the live cell lysosomal pH. The real time lysosomal movement inside the live HeLa cells is also captured over the time course of 5 min using CLSM (Figure 44).

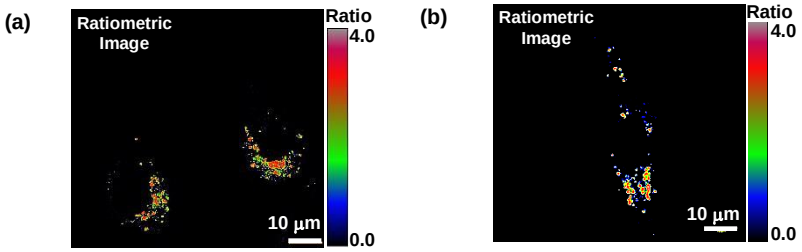

Figure 42. Pseudocolored ratiometric CLSM images of live (a) HeLa and (b) A549 carcinoma cells upon dual excitation of pH activatable probe (1 μM).

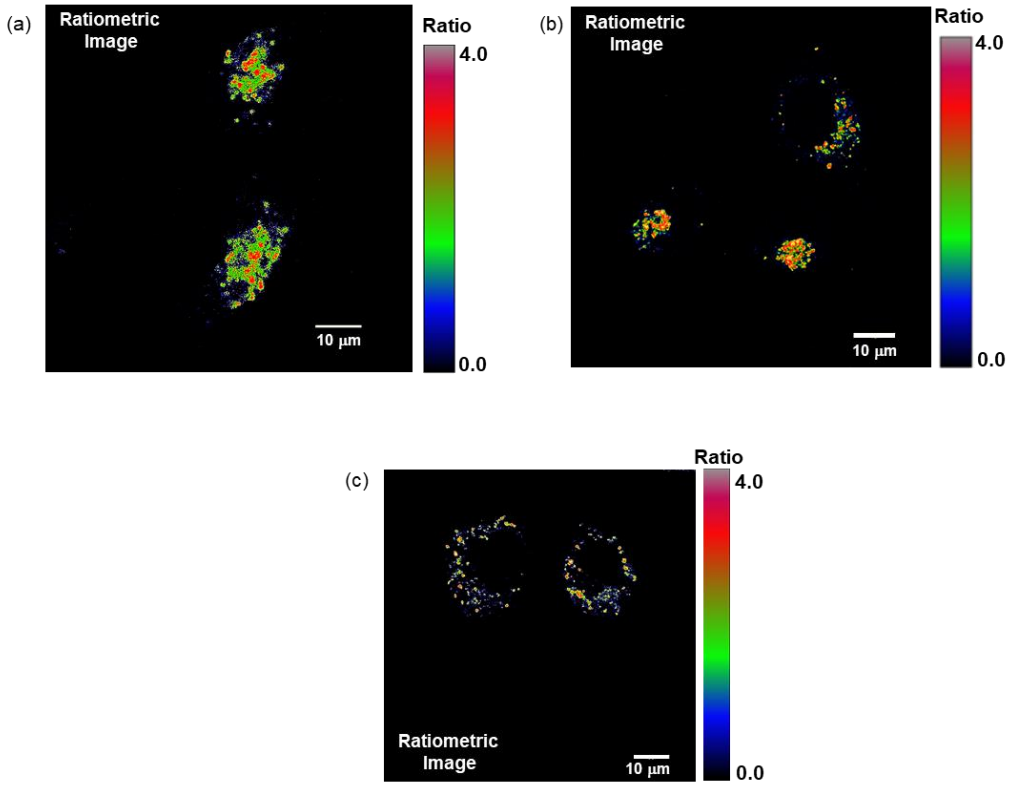

Figure 43. Pseudocolored ratiometric CLSM images of live (a, b) HeLa and (c) H9c2(2-1) cells upon dual excitation of the pH activatable probe.

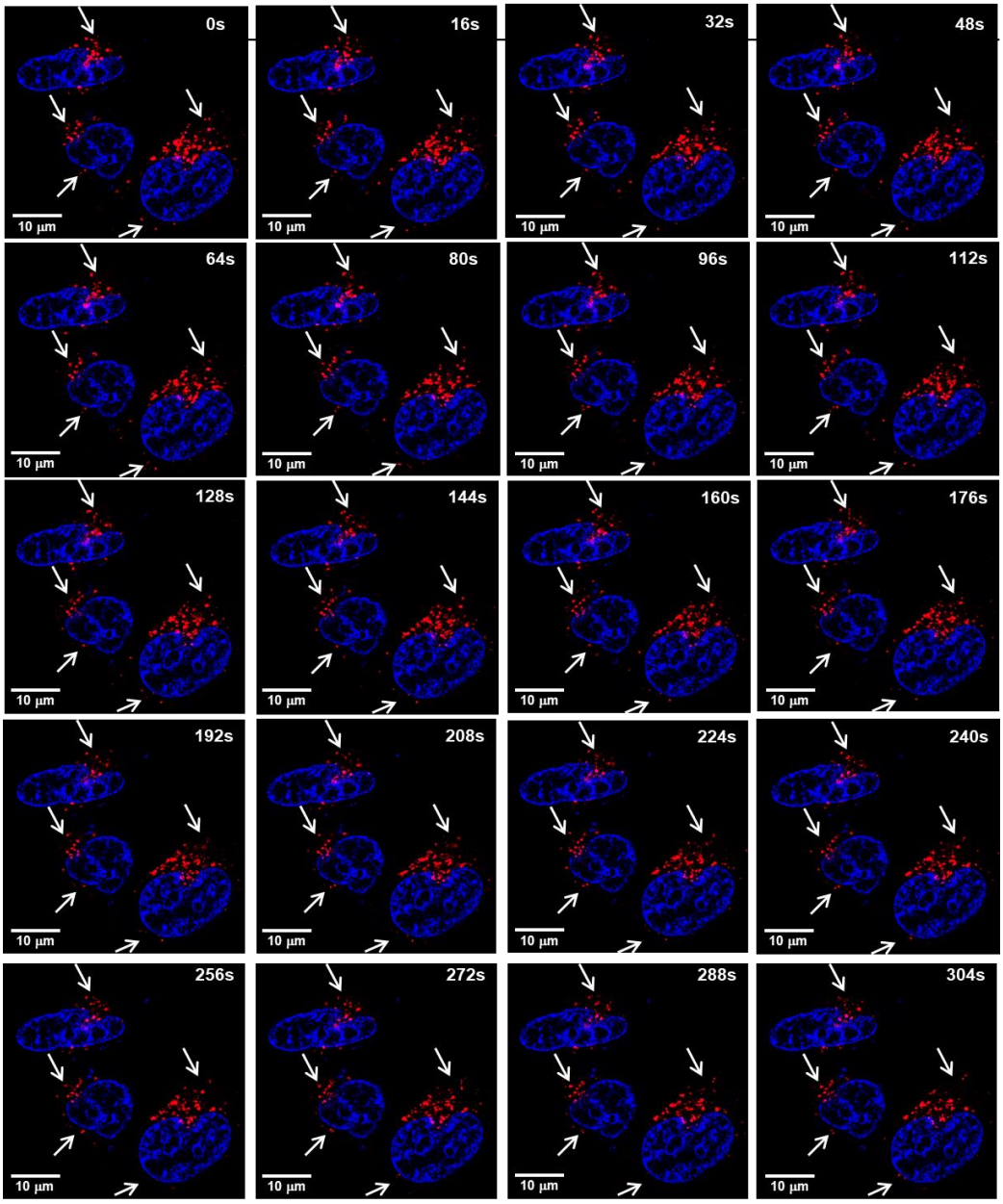

Figure 44. Real-time tracking of lysosomes inside the living HeLa carcinoma cells using pH activatable probe by confocal laser scanning microscopy. 20 frames were collected over 5 minutes.

Conclusions: We have designed and synthesized an unsymmetrical pH-switchable ratiometric organic fluorescent probe. In addition, low cytotoxicity, excellent photostability, reversible pH switching ability, acidic pH activatable narrow NIR absorption/emission with high molar extinction coefficient, ideal pK_a values in the pH_{lys} range, easier cellular penetration, high lysosomal selectivity, OFF-to-ON NIR fluorescence inside the acidic lysosomal compartment make the dye an excellent candidate for live cell imaging of lysosomes. The shift of two emission bands ($\Delta\lambda_{em}$ = 320 nm) of the probe is large enough to minimize cross talk than the other reported probes, thus providing important tools for ratiometric imaging of live cell lysosomal pH. The probe can be efficiently used for 3D imaging and real-time tracking of live cell lysosomes. The dye has great potential for early diagnosis of pH alteration in lysosomal disorder related diseases. This ratiometric NIR fluorescent probe can be engineered with a range of target specific functional groups and biomolecules.

References:

[1] Ripstein, Z. A.; Vahidi, S.; Rubinstein, J. L.; Kay, L. E. *J. Am. Chem. Soc.* **2020**, *142*, 20519–20523.

[2] Thompson, I. A. P.; Zheng, L.; Eisenstein, M.; Soh, H. T. *Nat. Commun.* **2020**, *11*, 2946.

[3] Leung, K.; Chakraborty, K.; Saminathan, A.; Krishnan, Y. *Nat. Nanotechnol.* **2019**, *14*, 176–183.

[4] Grunder, S.; McGrier, P. L.; Whalley, A. C.; Boyle, M. M.; Stern, C.; Stoddart, J. F. *J. Am. Chem. Soc*. **2013**, *135*, 17691–17694.

[5] Wang, L.; Xiao, L.; Tian, W.; Deng, L. *J. Am. Chem. Soc.* **2013**, *135*, 2903–2906.

[6] Parks, F. C.; Liu, Y.; Debnath, S.; Stutsman, S. R.; Raghavachari, K.; Flood, A. H. *J. Am. Chem. Soc*. **2018**, *140*, 17711−17723.

[7] Landge, S. M.; Aprahamian, I. *J. Am. Chem. Soc.* **2009**, *131*, 18269−18271.

[8] Gottlieb, R. A.; Nordberg, J.; Skowronski, E.; Babior, B. M. *Proc. Natl. Acad. Sci. U. S. A.* **1996**, *93*, 654−658.

[9] DeBerardinis, R. J.; Lum, J. J.; Hatzivassiliou, G.; Thompson, C. B. *Cell Metab*. **2008**, *7*, 11−20.

[10] Lee, M. H.; Han, J. H.; Lee, J. H.; Park, N.; Kumar, R.; Kang, C.; Kim, J. S. *Angew. Chem. Int. Ed.* **2013**, *52*, 6206–6209.

[11] Ohkuma, S.; Poole, B. *Proc. Natl. Acad. Sci. U. S. A*. **1978**, *75*, 3327–3331.

[12] Webb, B. A.; Chimenti, M.; Jacobson, M. P.; Barber, D. L. *Nat. Rev. Cancer* **2011**, *11*, 671–677.

[13] Casey, J. R.; Grinstein. S.; Orlowski, J. *Nat. Rev. Mol. Cell Biol.* **2010**, *11*, 50–61.

[14] Trombetta, E. S.; Ebersold, M.; Garrett, W.; Pypaert, M.; Mellman, I. *Science* **2003**, *299*, 1400–1403.

[15] Bonam, S. R.; Wang, F.; Muller, S. *Nat. Rev. Drug Discovery* **2019** *18*, 923–948.

[16] Fraldi, A.; Klein, A. D.; Medina, D. L.; Settembre, C. *Annu. Rev. Neurosci*. **2016**, *39*, 277–295.

[17] Kroemer, G.; Jäättelä, M. Lysosomes and autophagy in cell death control. *Nat. Rev. Cancer* **2005**, *5*, 886–897.

[18] Futerman, A. H.; Meer, G. V. *Nat. Rev. Mol. Cell Biol*. **2004**, *5*, 554–565.

[19] Grossi, M.; Morgunova, M.; Cheung, S.; Scholz, D.; Conroy, E.; Terrile, M.; Panarella, A.; Simpson, J. C.; Gallagher, W. M.; O'Shea, D. F. *Nat. Commun.* **2016**, *7*, 10855.

[20] Hashimoto, R.; Minoshima, M.; Kikuta, J.; Yari, S.; Bull, S. D.; Ishii, M.; Kikuchi, K. *Angew. Chem. Int. Ed.* **2020**, *59*, 20996–21000.

[21] Urano, Y.; Asanuma, D.; Hama, Y.; Koyama, Y.; Barrettt, T.; Kamiya, M.; Nagano, T.; Watanabe, T.; Hasegawa, A.; Choyke, P. L.; Kobayashi, H. *Nat. Med.* **2009**, *15*, 104–109.

[22] Wan, Q.; Chen, S.; Shi, W.; Li, L.; Ma, H. *Angew. Chem. Int. Ed.* **2014**, *53*, 10916–10920.

[23] Han, J.; Burgess, K. Fluorescent Indicators for Intracellular pH. *Chem. Rev.* **2010**, *110*, 2709–2728.

[24] Steinegger, A.; Wolfbeis, O. S.; Borisov, S. M. Optical Sensing and Imaging of pH Values: Spectroscopies, Materials, and Applications. *Chem. Rev.* **2020**, *120*, 12357–12489.

[25] Takahashi, S.; Kagami, Y.; Hanaoka, K.; Terai, T.; Komatsu, T.; Ueno, T.; Uchiyama, M.; Koyama-Honda, I.; Mizushima, N.; Taguchi, T.; Arai, H.; Nagano, T.; Urano, Y. *J. Am. Chem. Soc.* **2018**, *140*, 5925–5933.

[26] Usama, S. M.; Inagaki, F.; Kobayashi, H.; Schnermann, M. J. *J. Am. Chem. Soc.* **2021**, *143*, 5674–5679.

[27] Li, J.; Yin, X.; Li, B.; Li, X.; Pan, Y.; Li, J.; Guo, Y.*Anal. Chem.* **2019**, *91*, 5354–5361.

[28] Li, J.; Li, X.; Jia, J.; Chen, X.; Lv, Y.; Guo, Y.; Li, J. *Dyes Pigm.* **2019**, *166*, 433–442.

[29] Gao, Y.; Hu, Y.; Liu, Q.; Li, X.; Li, X.; Kim, C.-Y.; James, T. D.; Li, J.; Chen, X.; Guo, Y. *Angew. Chem. Int. Ed.* **2021**, *60*, 10756–10765.

[30] Raymo, F. M.; Giordani, S. *J. Am. Chem. Soc.* **2001**, *123*, 4651–4652.

[31] Guerrin, C.; Aidibi, Y.; Sanguinet, L.; Leriche, P.; Aloise, S.; Orio, M.; Delbaere, S. *J. Am. Chem. Soc.* **2019**, *141*, 19151−19160.

[32] Miki, K.; Kojima, K.; Oride, K.; Harada, H.; Morinibu, A.; Ohe, K. *Chem. Commun.* **2017**, *53*, 7792−7795.

[33] Fujioka, H.; Uno, S.-n.; Kamiya, M.; Kojima, R.; Johnsson, K.; Urano, Y. *Chem. Commun.* **2020**, *56*, 56175−620.

[34] Mazi, W.; Yan, Y.; Zhang, Y.; Xia, S.; Wan, S.; Tajiri, M.; Luck, R. L.; Liu, H. A *J. Mater. Chem. B* **2021**, *9*, 857–863.

[35] Samanta, A.; Vendrell, M.; Das, R.; Chang, Chem. Commun. **2010**, 46, 7406–7408.

[36] Saha, P. C.; Das, R. S.; Chatterjee, T.; Bhattacharyya, M.; Guha, S. *Bioconjugate Chem.* **2020**, *31*, 1301–1306.

[37] Alabugin, I. V.; Gilmore, *Chem. Commun.* **2013**, *49*, 11246−11250.

[38] Chatgilialoglu, C.; Ferreri, C.; Guerra, M.; Timokhin, V.; Froudakis, G.; Gimisis, T. *J. Am. Chem. Soc.* **2002**, *124*, 10765−10772.

Chapter 4

Acidic pH-Triggered Live-Cell Lysosome Specific Tracking, Ratiometric pH Sensing, and Multicolor Imaging by Visible to NIR Switchable Cy-7 Dyes

Introduction

pH is a critical intracellular factor that regulates the activities of live cell organelles including cellular proliferation, enzymatic function, muscle contraction, apoptosis, ion transport etc.[1-3] Various subcellular parts of live cells have different pH allocation, for instance cytoplasm is nearly neutral (pH 7.2), mitochondria is weakly basic (pH 8), whereas the endosomes (pH 5-6) and lysosomes (pH 4-5) are acidic.[4,5] It is irrefutable that the upholding of precise pH in the discrete intracellular organelles is of supreme concern for their regular functions. All the mammalian cells possess lysosomes which are membrane-enclosed acidic organelles, encompass a series of enzymes responsible for the breaking down of sugars, proteins, fats, and nucleic acids as well as involve in endocytosis.[6,7] Lysosomal acidic lumen (pH 4-5) is primarily preserved by the proton-pumping vacuolar ATPases.[8] Anomalies in the pH values of lysosomes are liable for their dysfunction that cause lysosomal storage disorders, cancer, neurodegenerative disorders, cell necrosis and apoptosis.[9-11] Therefore it is indispensable to precisely image the pH in lysosomes with spatiotemporal resolution in live cells to understand lysosome-related biological processes and diseases. Though, it is extremely difficult to execute and monitor organic chemical transformation in the living cells owing to the intricacy in live cell environment. It is pivotal to construct *in situ* organelle activatable probe for specific staining and real-time monitoring of lysosomes with fast response.[12-14] It is also important to design *in situ* lysosomal pH-activatable ratiometric fluorescent dyes wherein the emission must shift from visible to near-infrared (NIR) window with signal augmentation at decreasing pH and reduce the spectral cross talk at lysosomal lumen. Stimuli responsive targeted organelle activated NIR fluorescent probes (750−950 nm) hold a significant advantage as cellular or tissue constituents

possess trivial absorption and minimal autofluorescence in the NIR window; consequently, exceptionally delicate, weakly dispersed, accurate detection, and real-time monitoring of lysosomes are possible when acidic pH-activatable NIR chromophore will be exogenously incorporated.[15-17] It is highly desirable that the probe should selectively target acidic lysosomes and exhibits off-to-on strong NIR fluorescence while insignificant NIR emission is expected from off-targeted neutral and basic intracellular organelles; therefore, interference in contrary to background emission apart from the area of concern would be negligible. It is crucial when lysosome tracking dyes exhibit good feedback with an appropriate pK_a value when pH varies between 4 to 6.[18,19] Current lysosome tracking ratiometric probes possess substantial restrictions, such as improper pK_a in the lysosomal pH span, insufficiently long excitation/emission wavelengths, insignificant emission spectral shift with considerable spectral cross-talk at neutral and acidic pH, shallow brightness at lysosomal pH, high photobleaching, cytotoxicity, and these are the downsides for the ratiometric imaging of living cell lysosomal pH.[20-22] Furthermore, in the live cell environment, the probe should overcome several obstacles to arrive at the anticipated location and preferably accumulate inside the lysosomes.

To conquer these downsides, we have efficiently constructed an intermediate to synthesize unsymmetrical probe comprising an acid-activatable openable oxazolidine ring and lysosome specific morpholine moiety to endorse the dye exclusively in the lysosome. The designed probe (closed form of Cy-7) is dormant in the NIR window at pH ≥ 7.2, nevertheless, extremely NIR emissive (open form of Cy-7) in the acidic lysosomal lumen owing to its pK_a value 5, and has been effectively utilized for real-time tracking of lysosomes, 3D imaging, and ratiometric fluorescence imaging of the lysosomal pH in live cells. Fluorescence intensity in two well-separated wavelengths (visible λ_{em} 478

and NIR λ_{em} 800 nm) with ~ 322 nm bathochromic shift that minimizes cross talk and permits auto-correction, therefore deviations in signal owing to investigational artifacts like dye concentration, laser power and quenching are avoided, providing precise quantification and ratiometric fluorescence imaging of pH inside the live-cell lysosomes. Moreover, multicolor imaging in live cells has been accomplished by utilizing the synthesized probe blending with other organelle staining probes with discrete excitation/emission bands.[23-25]

Experimental Methods:

Synthesis:

All the compounds were synthesized under inert condition using dry solvents. Analytical thin layer chromatography (TLC) was achieved on TLC silica gel 60 F_{254} with suitable solvents and spots was detected by naked eye or UV lamp. The desired compounds were purified through column chromatography using silica gel 100-200 and 60-120 mesh. The distilled solvents used for column chromatography.

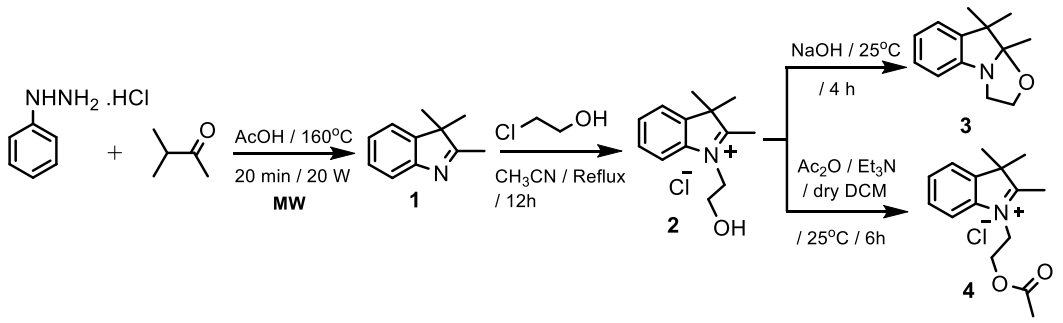

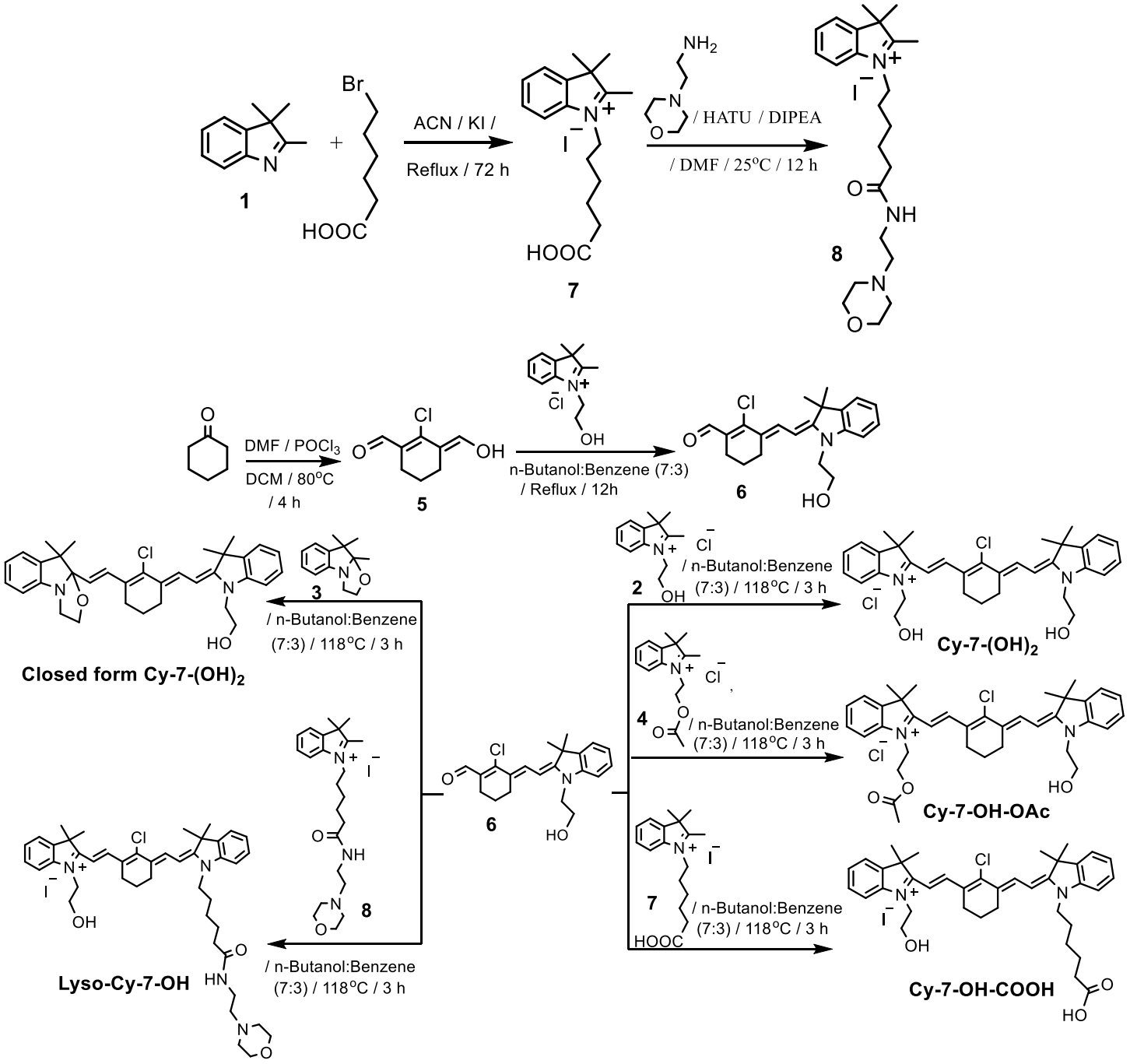

Figure 1. Synthesis of the intermediate 6 and the compounds Cy-7-$(OH)_2$, Cy-7-OH-OAc, Cy-7-OH-COOH, and Lyso-Cy-7-OH.

1-(2-hydroxyethyl)-2,3,3-trimethyl-3H-indol-1-ium chloride (2): The compound 2,3,3-trimethylindolenine (0.80 g, 5 mmol) and 2-chloroethanol (0.81 g, 10 mmol) were taken in a round bottomed flask and heated to reflux for 24 h under an inert atmosphere. The reaction mixture was cooled and washed with EtOAc for numerous times (5 × 30 mL). The precipitate was filtered off, washed with EtOAc (3 × 20 mL) and dried under vacuum to obtain the pure product **2** as a pink solid.[26] Yield: 0.82 g (68%).

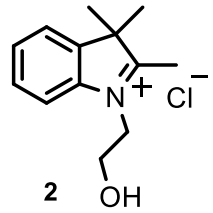

2

^{1}H NMR (300 MHz, DMSO-d_6, 25°C): δ = 7.99 (dd, J = 5.7, 3.3 Hz, 1H), 7.85 (dd, J = 5.9, 2.9 Hz, 1H), 7.62 (dd, J = 5.8, 3.1 Hz, 2H), 4.61 (t, J = 5.1 Hz, 2H), 3.87 (t, J = 5.0 Hz, 2H), 3.59 (br, 1H), 2.85 (s, 3H), 1.56 (s, 6H) ppm.^{13}C NMR (75 MHz, $CDCl_3$, 25°C): δ = 198.3, 142.4, 141.8, 129.8, 129.4, 124.0, 116.3, 58.3, 54.8, 51.1, 22.7, 15.2 ppm.

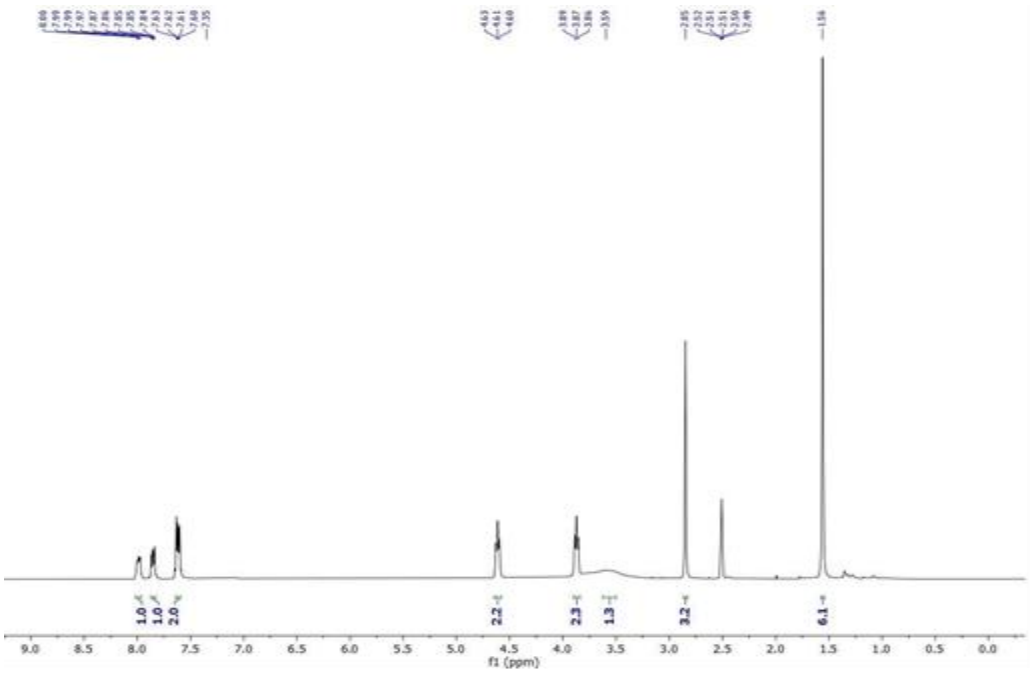

Figure 2a. ^{1}H NMR spectrum (300 MHz, DMSO-d_6, 298 K)

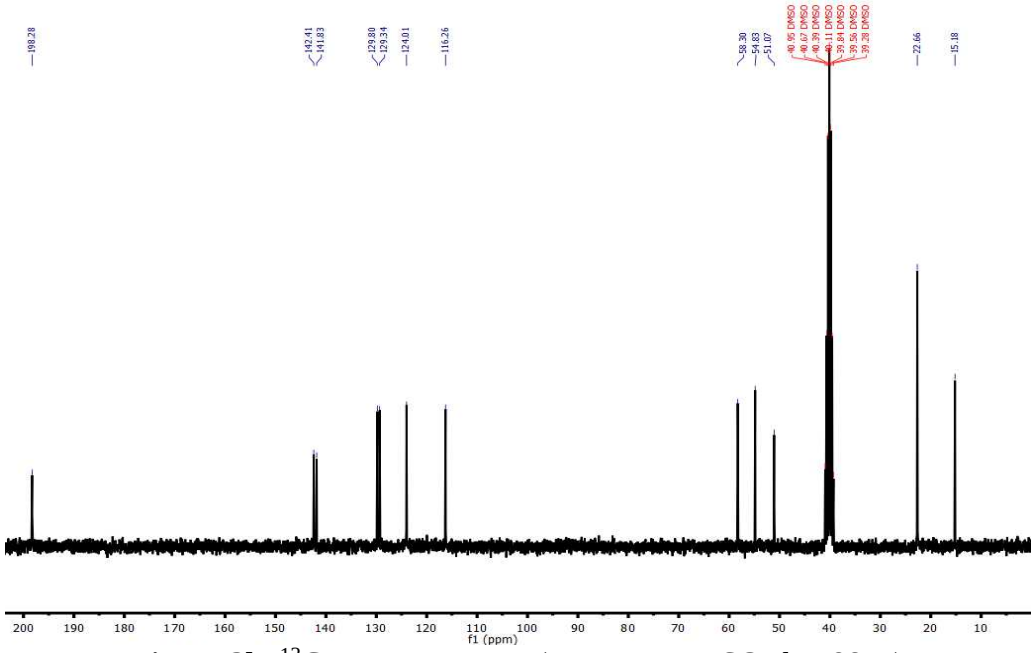

Figure 2b. ^{13}C NMR spectrum (75 MHz, DMSO-d_6, 298 K)

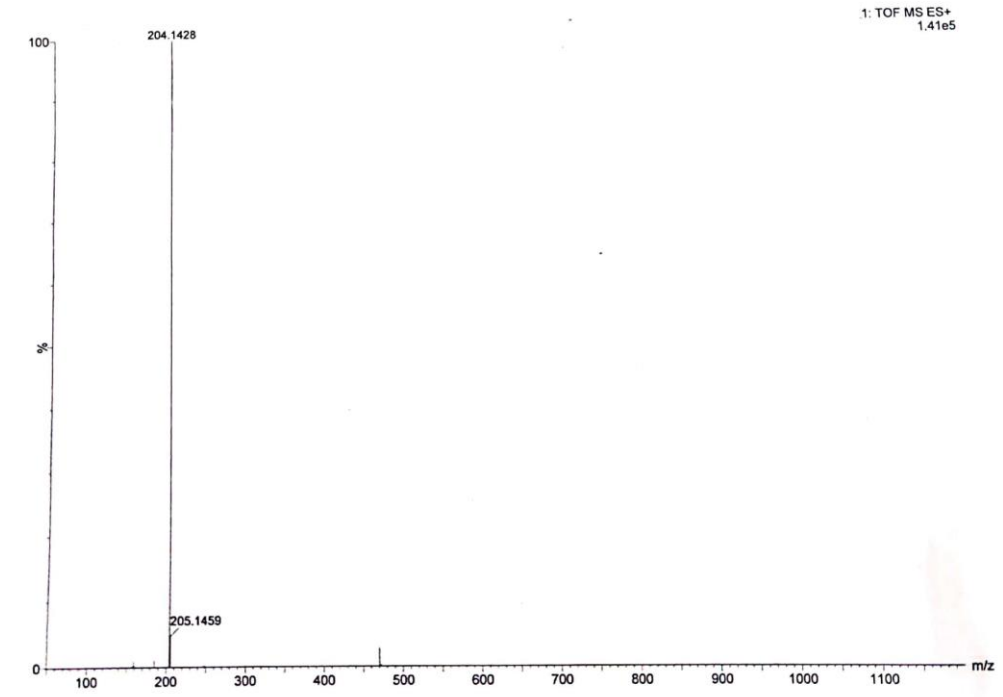

Figure 3. HRMS (ESI +ve) spectrum.

9,9,9a-Trimethyl-2,3,9,9a-tetrahydrooxazolo[3,2-*a*]indole (3): To a suspension of 2 (0.24 g, 1 mmol) in H_2O (25 mL) a solution of NaOH (0.3 g) in H_2O (15 mL) was added and the mixture was stirred at room temperature for 30 min. The reaction mixture was extracted with Et_2O (3 × 20 mL). The organic layer was washed with H_2O (2 × 20 mL), brine (1 × 20 mL), and dried over anhydrous Na_2SO_4. The organic layer was concentrated under reduced pressure to obtain the pure product **3** as a yellow oil.[26] The next step was carried out without further purification.Yield: 0.16 g (84%). ^{1}H NMR (300 MHz, DMSO-d_6, 25°C): δ = 7.12–7.06 (m, 2H), 6.87–6.78 (m, 2H), 3.77–3.67 (m, 2H), 3.53–3.43 (m, 1H), 3.38–3.30 (m, 1H), 1.35 (s, 3H), 1.29 (s, 3H), 1.10 (s, 3H) ppm. ^{13}C NMR (75 MHz, $CDCl_3$, 25°C): δ = 150.7, 141.3, 127.6, 122.3, 121.9, 110.2, 108.3, 63.8, 50.2, 46.5, 28.4, 20.5 ppm.

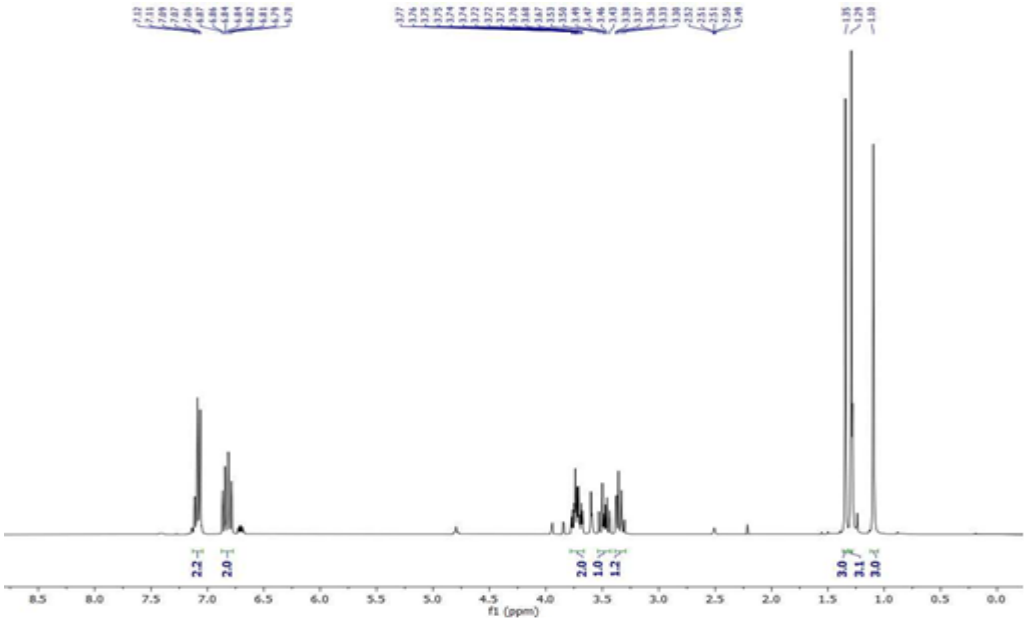

Figure 4a. ^{1}H NMR spectrum (300 MHz, DMSO-d_6, 298 K)

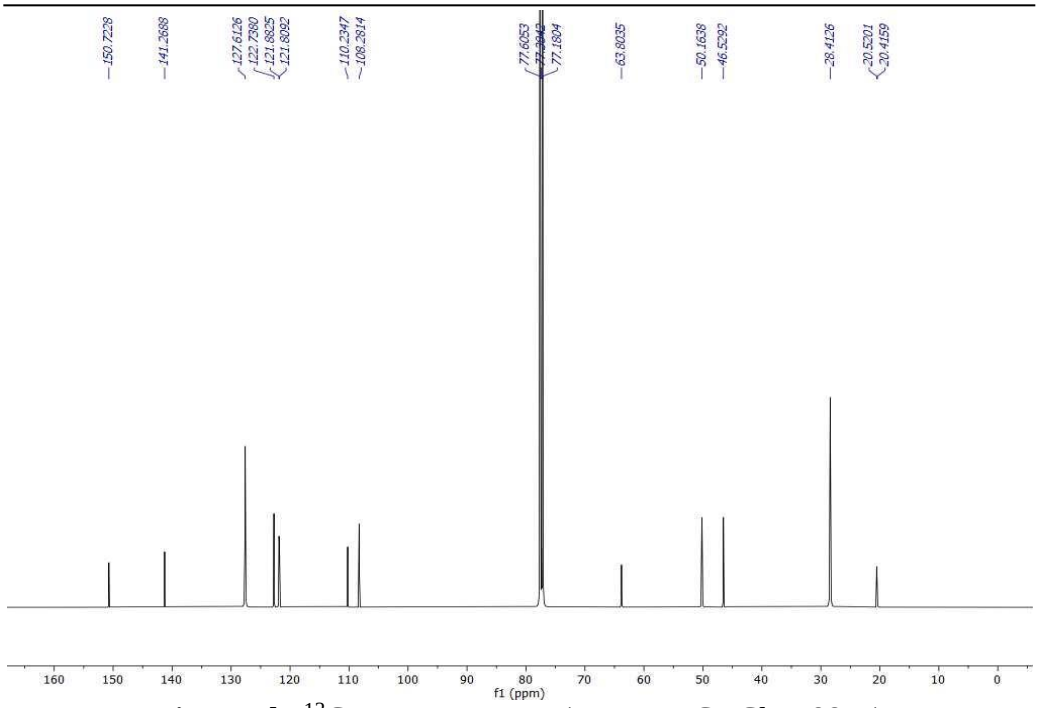

Figure 4b. ^{13}C NMR spectrum (75 MHz, $CDCl_3$, 298 K).

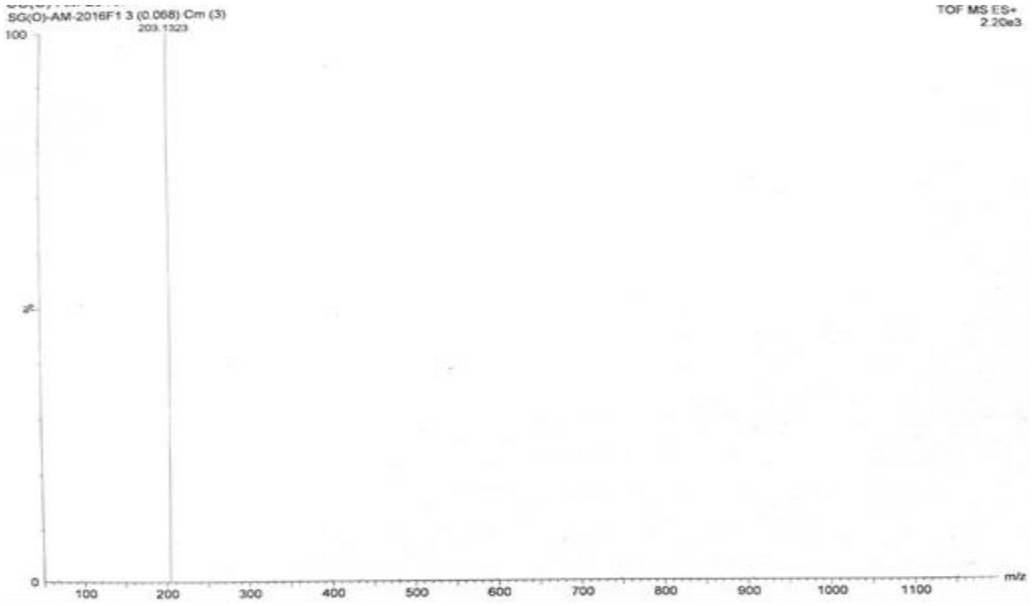

Figure 5. HRMS (ESI +ve) spectrum.

(acetoxyethyl)-2,3,3-trimethyl-3*H*-indol-1-ium chloride (4): Compound 2 (0.36 g, 1.5 mmol) was dissolved in dry DCM (10 mL) in a round bottomed flask. Et_3N (0.28 mL, 2 mmol) and Ac_2O (0.21 mL, 2 mmol) were added sequentially to the reaction mixture. The reaction mixture was stirred at room temperature for 12 h. After completion (12 h) of the reaction the color of the reaction turned into deep red from red. This reaction mixture was poured into H_2O and extracted with DCM. The organic layer was collected, dried over anhydrous Na_2SO_4, and concentrated under reduced pressure. The crude product was purified by column chromatography on silica gel (Hexane:EtOAc 70:30) to afford a reddish brown solid pure product.

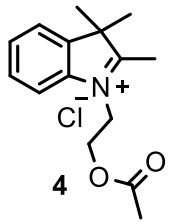

4

Yield: 0.33 g (79%).

^{1}H NMR (300 MHz, $CDCl_3$, 25°C): δ = 7.44–7.39 (m, 2H), 7.29–7.17 (s, 1H), 6.95 (d, J = 8.7 Hz, 1H), 4.24 (t, J = 7.5 Hz, 1H), 4.06 (t, J = 7.5 Hz, 1H), 2.36 (s, 3H), 1.74 (s, 6H), 1.71 (s, 3H) ppm.

^{13}C NMR (75 MHz, $CDCl_3$, 25°C): δ = 197.4, 170.9, 150.7, 141.3, 127.7, 125.5, 122.5, 108.3, 63.3, 50.0, 44.1, 40.5, 20.9, 14.8, 9.7 ppm.

HRMS (ESI +ve) *m*/*z*: Observed for $C_{15}H_{20}NO_2^+$ $[M+H]^+$ = 246.1479, $[M+H]^+$ calcd = 246.1489.

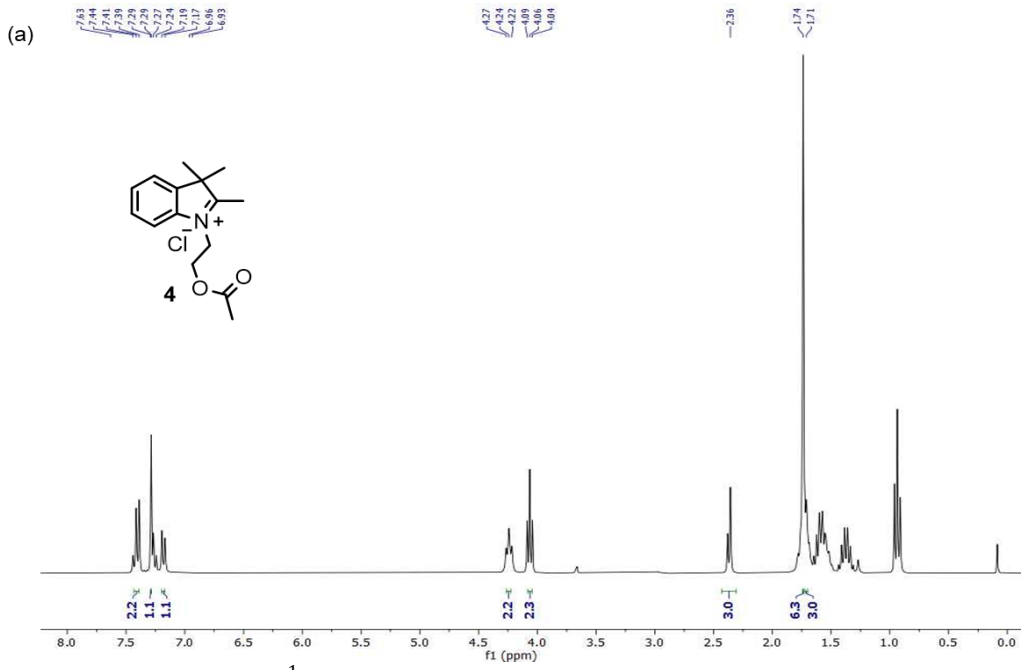

Figure 6a. ^{1}H NMR spectrum (300 MHz, $CDCl_3$, 298 K)

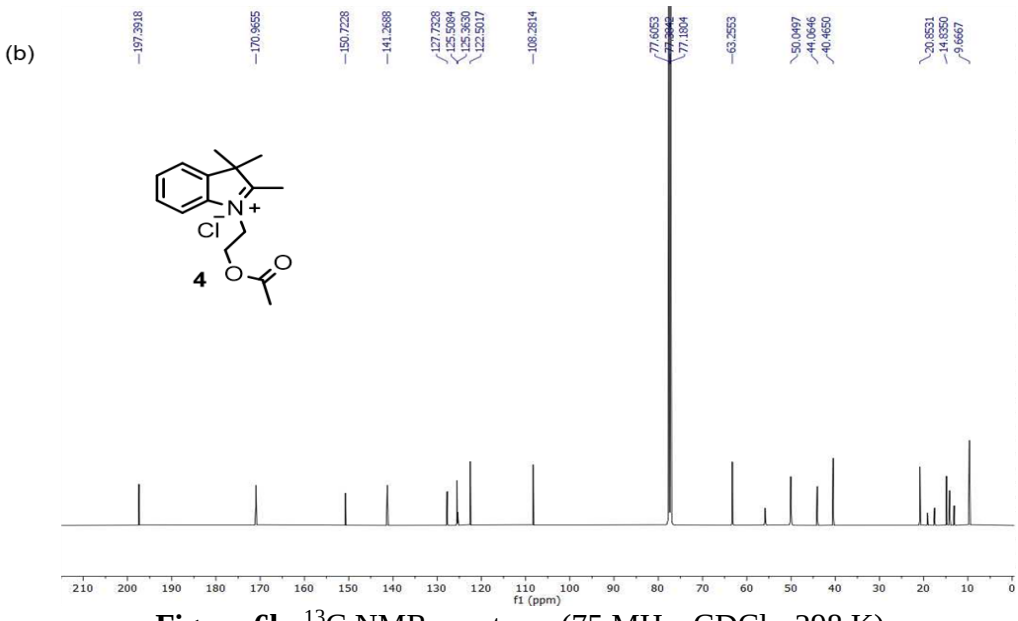

Figure 6b. ^{13}C NMR spectrum (75 MHz, $CDCl_3$, 298 K)

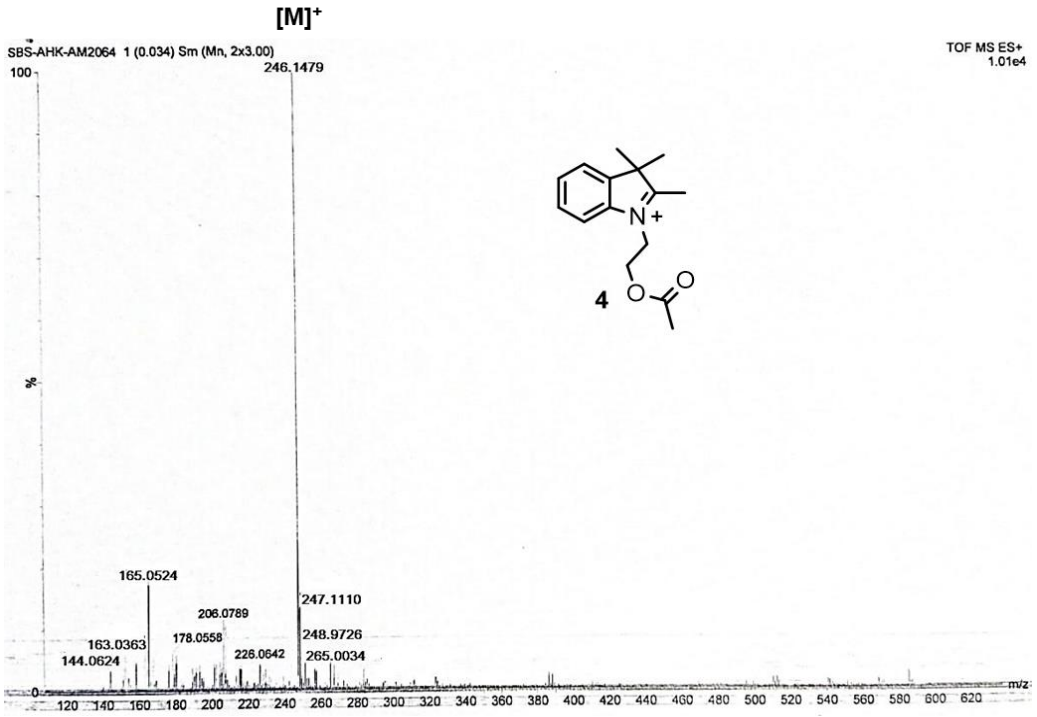

Figure 7. HRMS (ESI +ve) spectrum

1-(5-carboxypentyl)-2,3,3-trimethyl-3*H*-indol-1-ium iodide (7): 2,3,3-Trimethylindolenine (0.30 g, 1.89 mmol) was dissolved in 20 mL CH_3CN in a round bottomed flask. 6-Bromohexanoic acid (1.47 g, 7.56 mmol) and KI (1.25 g, 7.56 mmol) was added to the mixture. The reaction mixture was heated to reflux for 72 h. After that the precipitate was filtered out and the filtrate was concentrated under the reduced pressure. A red colored gummy product was observed. This red gummy crude product was washed with EtOAc for several times until grey colored solid product was obtained. The next step was carried out without further purification. Yield : 0.51 g (67%)

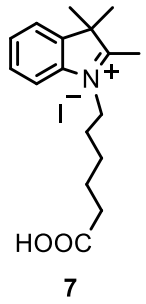

7

^{1}H NMR (400 MHz, DMSO-d_6, 25°C): δ = 8.01–7.99 (m, 1H), 7.88–7.82 (m, 1H), 7.62 (dt, *J* = 7.7, 3.9 Hz, 2H), 4.47 (t, *J* = 7.7 Hz, 2H), 2.86 (s, 3H), 2.24–2.18 (m, 2H), 1.85 (p, *J* = 7.8 Hz, 2H), 1.55 (s, 6H), 1.47–1.40 (m, 4H) ppm.

^{13}C NMR (101 MHz, DMSO-d_6, 25°C): δ = 196.9, 174.8, 142.3, 141.5, 129.9, 129.4, 124.1, 116.0, 54.7, 48.1, 33.9, 27.5, 25.9, 24.5, 22.5, 14.9 ppm.

HRMS (ESI +ve) *m*/*z*: Observed for $C_{17}H_{24}NO_2^+$ $[M]^+$ = 274.1807, $[M]^+$calcd = 274.1802

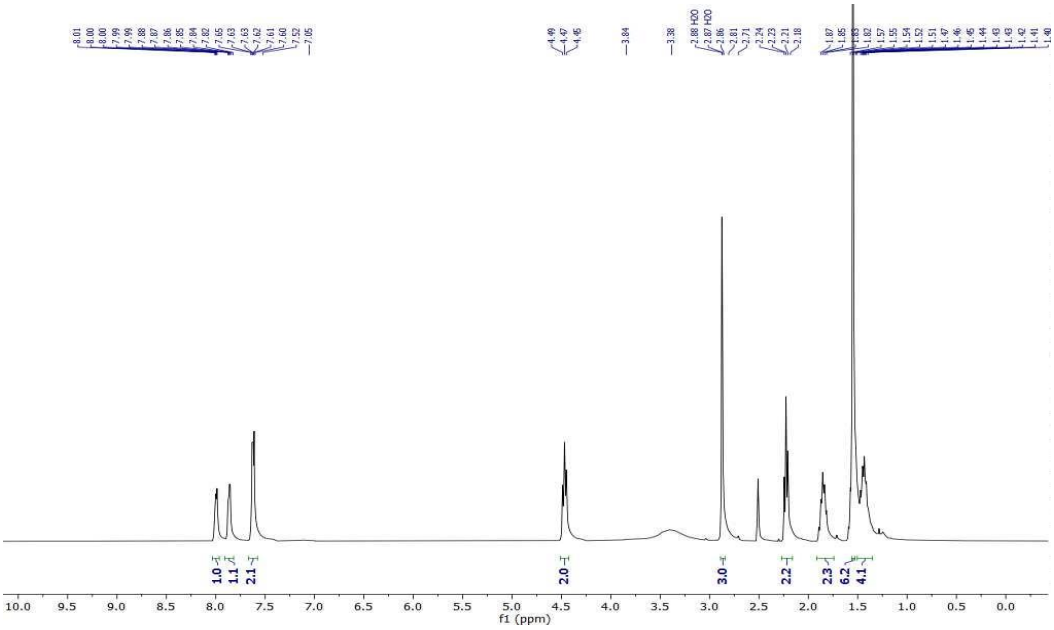

Figure 8a. ^{1}H NMR spectrum (400 MHz, $CDCl_3$, 298 K)

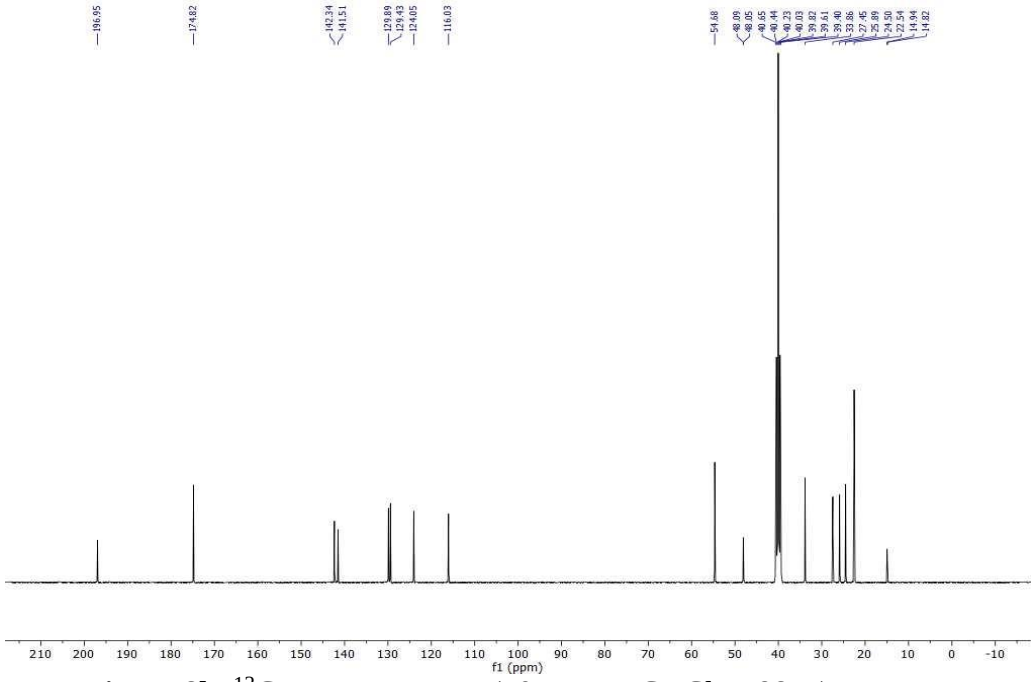

Figure 8b. ^{13}C NMR spectrum (101 MHz, $CDCl_3$, 298 K).

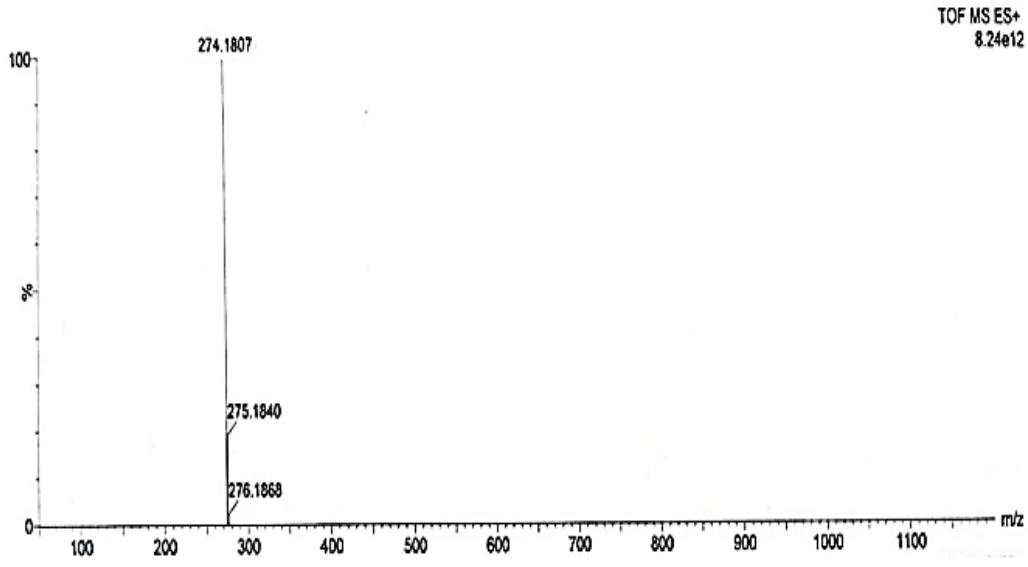

Figure 9. ESI-HRMS spectrum.

2,3,3-Trimethyl-1-(6-((2-morpholinoethyl)amino)-6-oxohexyl)-3*H*-indol-1-ium iodide (8): Compound 7 (0.5 g, 1.25 mmol) was added in chilled DMF (2 mL) at 0°C. HATU (0.57 g, 1.5 mmol) was added to the solution under continuous stirring. After 30 min 4-(2 amino ethyl) morpholine (0.26 g, 2 mmol) and DIPEA (0.26 g, 2 mmol) was added drop wise to the reaction mixture. The reaction was stirred at r.t. for 18 h. After completion of the reaction the product was extracted with EtOAc and washed with cold H_2O for three times. The organic layer was collected and the solvent was evaporated under the reduced pressure. The crude product was purified by column chromatography using 3% $CHCl_3$/MeOH as eluent. A brown colored pure solid product 8 was obtained.

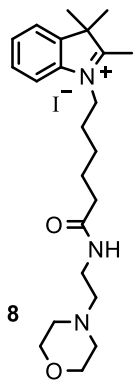

8

Yield: 0.33 g (51%) ^{1}H NMR (400 MHz, $CDCl_3$, 25°C): δ = 7.75–7.72 (m, 1H), 7.56–7.54 (m, 1H), 7.02–7.00 (m, 2H), 5.86–5.79 (m, 1H), 4.33 (t, *J* = 7.7 Hz, 2H), 4.19–4.07 (m, 4H), 3.66 (t, *J* = 6.7 Hz, 2H), 3.51 (s, 3H), 2.91–2.83 (m, 4H), 2.65–2.59 (m, 2H), 2.11–2.03 (m, 2H), 1.71–1.61 (m, 6H), 1.50 (s, 6H) ppm.

^{13}C NMR (101 MHz, $CDCl_3$, 25°C): δ = 177.1, 173.4, 150.1, 142.8, 129.1, 126.6, 122.2, 112.6, 109.3, 106.2, 64.4, 58.7, 50.3, 48.4, 43.7, 33.9, 30.7, 26.5, 24.6, 19.1, 13.7 ppm.

HRMS (ESI +ve) *m*/*z*: Observed for $C_{23}H_{37}N_3O_2^{2+}$ $[M+H]^{2+}$ = 193.6445, $[M+H]^{2+}$calcd = 193.6437

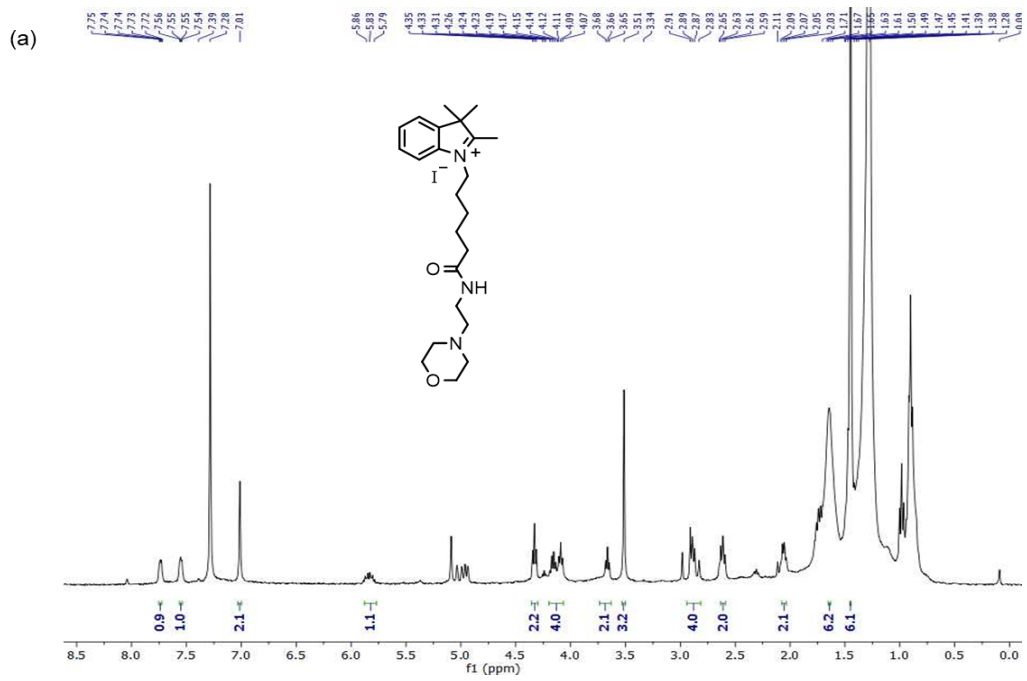

Figure 10a. ^{1}H NMR spectrum (400 MHz, $CDCl_3$, 298 K)

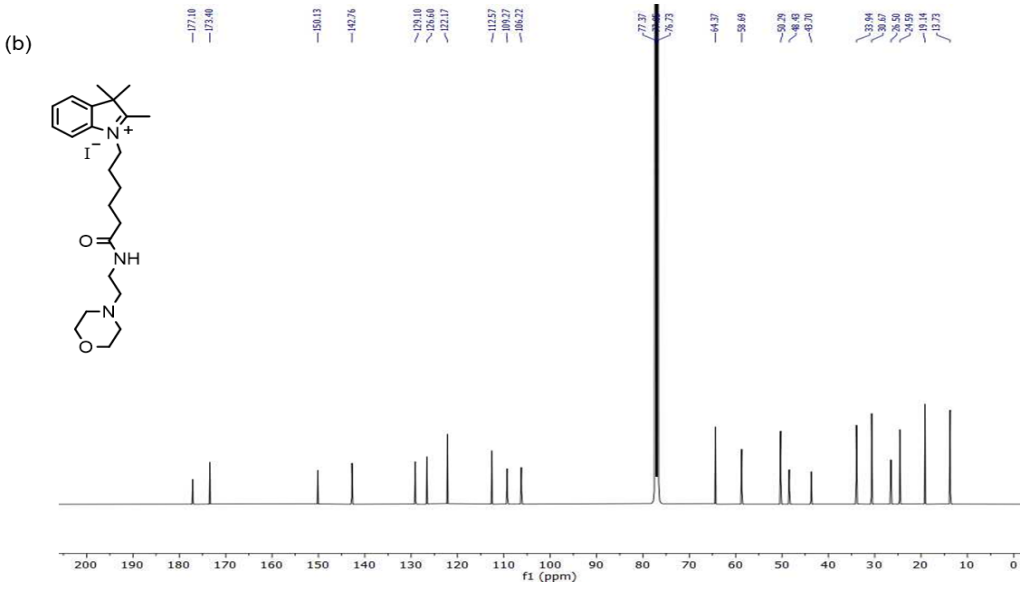

Figure 10b. ^{13}C NMR spectrum (101 MHz, $CDCl_3$, 298 K).

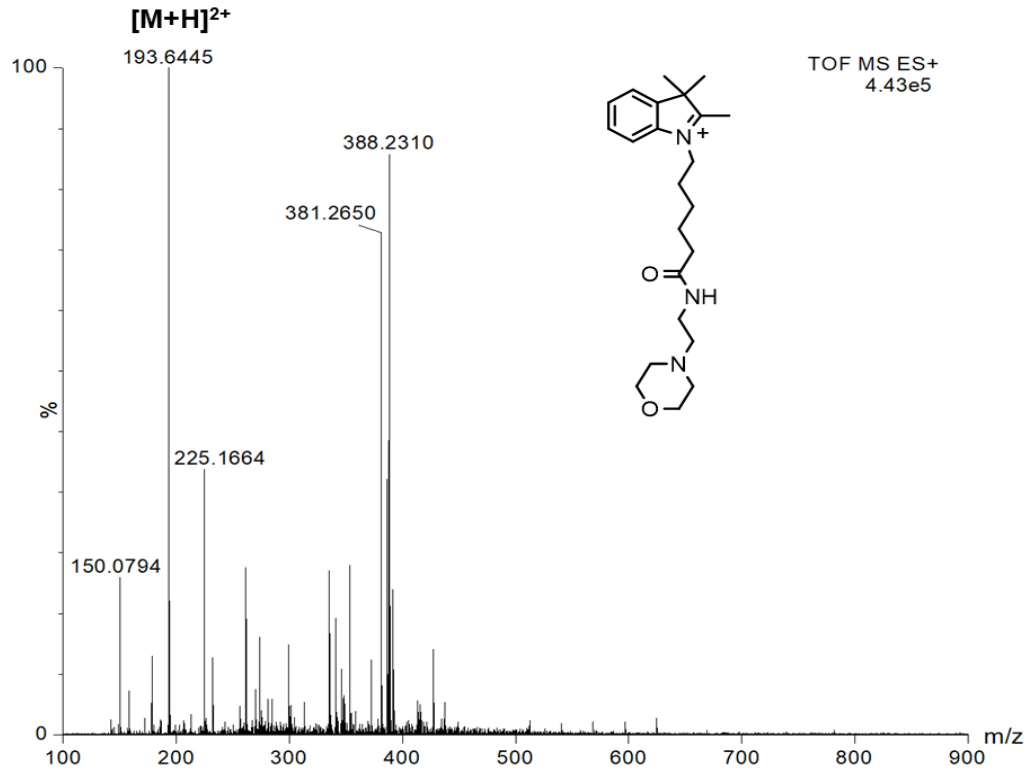

Figure 11: ESI-HRMS spectrum

(*E*)-2-chloro-3-(hydroxymethylene)cyclohex-1-ene-1-carbaldehyde (5): To a chilled solution of DMF (5 mL, 136.5 mmol, 5.4 eqv) in 5 mL DCM under N_2 atmosphere $POCl_3$ (4.5 mL, 57.5 mmol, 2.3 eqv) and 0.8 mL DCM were added simultaneously drop wise for 30 min under an ice bath. After 30 min cyclohexanone was added (1.2 mL, 25 mmol, 1eqv) and the resulting mixture was heated to reflux for 3 h at 80ºC. The solution color was changed from yellow to deep red during reflux. The reaction mixture was cooled and poured into ice-cold H_2O and kept it 24 h in a freezer.

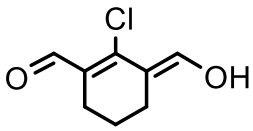

5

The yellow residue was filtered, washed with cold H_2O and purified by column chromatography [R_f: 0.5 in EtOAc/Hexane (10/90)] to acquire the pure compound 5 as a yellow solid.[26]

Yield: 3.5 g (81%)

^{1}H NMR (300 MHz, $CDCl_3$, 25°C): δ = 10.27 (s, 1H), 9.5 (s, 1H), 4.11 (br, 1H), 2.65–2.55 (m, 2H), 2.35–2.24 (m, 2H), 2.01–1.95 (m, 2H), ppm.

^{13}C NMR (101 MHz, $CDCl_3$, 25°C): δ = 197.2, 190.5, 144.5, 138.0, 79.7, 32.3, 24.3, 17.0 ppm.

HRMS (ESI +ve) *m/z*: Observed for $C_8H_{10}ClO_2^+$ $[M+H]^+$ = 173.0553, $[M+H]^+$calcd = 173.0364

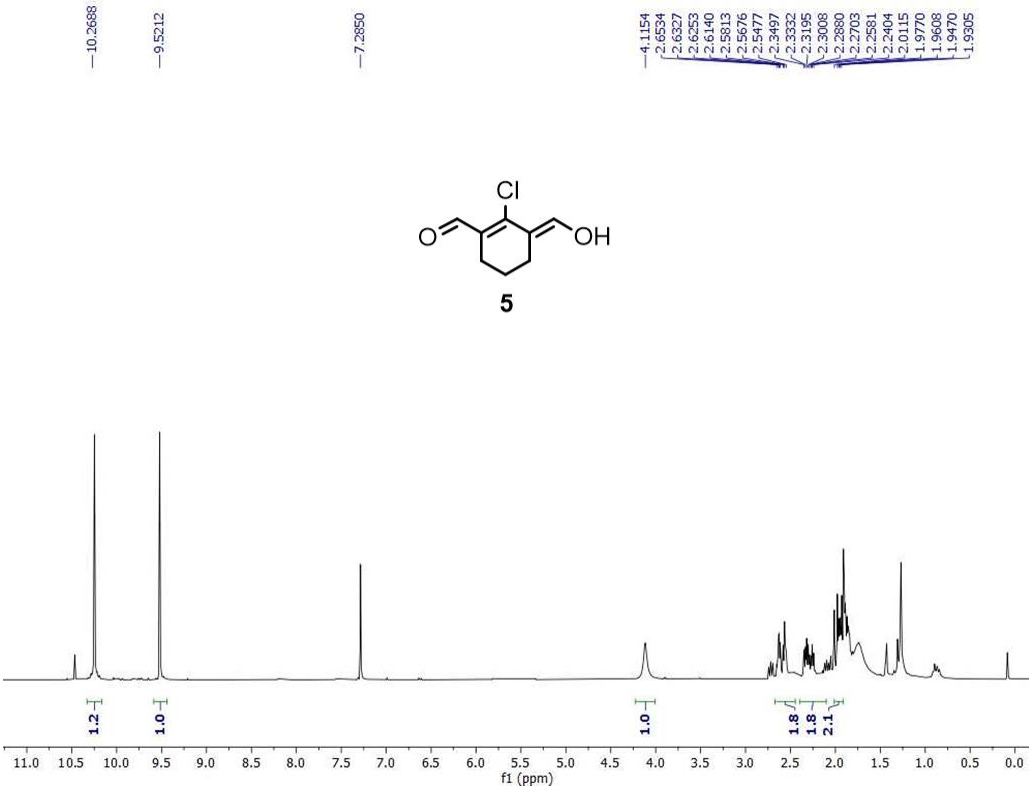

Figure 12a. ^{1}H NMR spectrum (300 MHz, $CDCl_3$, 298 K)

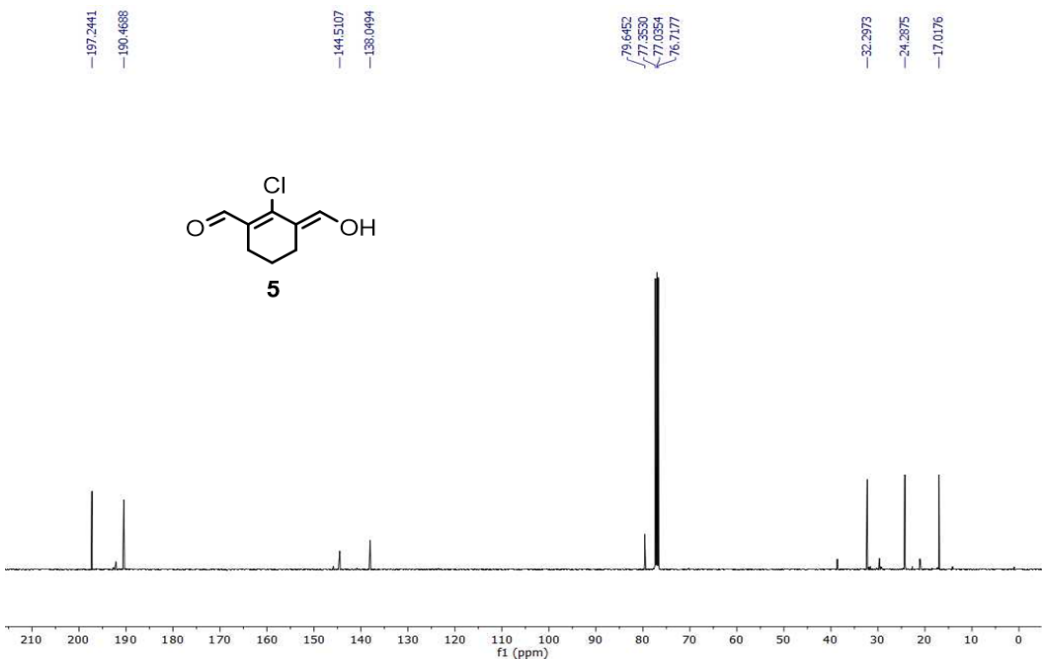

Figure 12b. ^{13}C NMR spectrum (101 MHz, $CDCl_3$, 298 K).

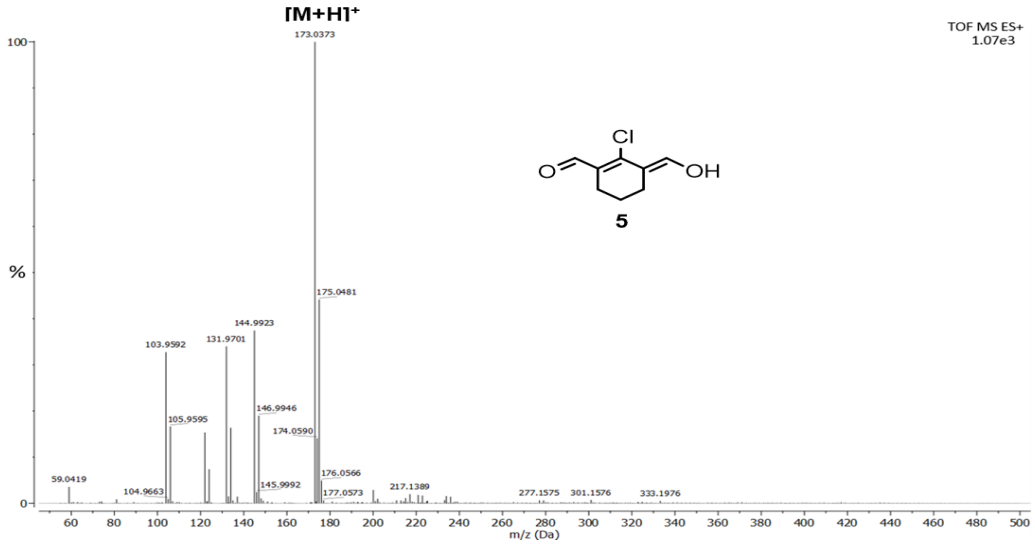

Figure 13: HRMS (ESI +ve) spectrum.

(*E*)-2-chloro-3-(2-((*E*)-1-(2-hydroxyethyl)-3,3-dimethylindolin-2-ylidene)ethylidene)cyclohex-1-ene-1-carbaldehyde (6): Compound 2 (0.59 g, 2.45 mmol) and compound 5 (0.41 g, 2.4 mmol) were dissolved in 20 mL of a mixture of 1-butanol and benzene (7:3) in a round bottomed flask. The mixture was heated to reflux with constant stirring for 12 h. The progress of the reaction was monitored by the TLC. After 12 h the reaction was completed and the color of the reaction turned into deep red from reddish brown. The crude product was purified by column chromatography [R_f: 0.6 in EtOAc/Hexane (5/95)] to afford a red colored pure solid 6.

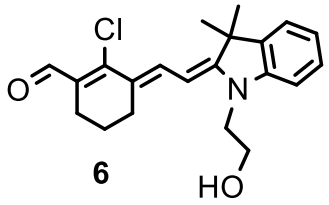

6

Yield: 0.42 g (49%).

^{1}H NMR (300 MHz, $CDCl_3$, 25°C): δ = 10.27 (s, 1H), 7.84 (d, *J* = 12.7 Hz, 1H), 7.22 (d, *J* = 7.1 Hz, 2H), 6.98 (t, *J* = 7.4 Hz, 1H), 6.84 (d, *J* = 8.0 Hz, 1H), 5.65 (d, *J* = 12.8 Hz, 1H), 4.01–3.91 (m, 4H), 2.59 (t, *J* = 6.6 Hz, 2H), 2.49 (t, *J* = 6.1 Hz, 2H), 1.82–1.74 (m, 2H), 1.68 (s, 6H) ppm.

^{13}C NMR (75 MHz, $CDCl_3$, 25°C): δ = 191.1, 162.5, 148.8, 144.5, 139.2, 131.1, 129.0, 128.1, 123.8, 122.0, 121.3, 107.4, 93.3, 59.7, 46.7, 45.3, 28.6, 26.9, 24.7, 21.0 ppm.

HRMS (ESI +ve) *m*/*z*: Observed for $C_{21}H_{25}NO_2Cl^+$ $[M+H]^+$ = 358.1540, $[M+H]^+$calcd = 358.1568.

Single crystal X-ray structure confirmed the formation of the compound 6.

^{13}C NMR (75 MHz, $CDCl_3$, 25°C): δ = 170.8, 149.9, 144.5, 141.7, 141.1, 138.8, 136.7, 133.3, 131.0, 127.9, 127.7, 127.6, 122.4, 121.7, 119.9, 111.9, 109.8, 106.0, 64.2, 63.3, 60.2, 52.9, 50.8, 50.2, 48.1, 31.9, 29.7, 28.4, 28.1, 24.5, 21.4 ppm.

HRMS (ESI +ve) *m*/*z*: Observed for $C_{34}H_{40}ClN_2O_2^+$ $[M+H]^+$ = 543.2711, $[M+H]^+$ calcd = 543.2773.

Photophysical properties in DMSO λ_{abs}= 418 nm, λ_{em}= 471 nm, Stokes shift ($\Delta\lambda$) = 53 nm, ε = 1.23 ×10^5 M^{-1} cm^{-1}, Φ_f = 0.09 in EtOH [Φ_f of the reference compound coumarin 6 is 0.78 in absolute EtOH].

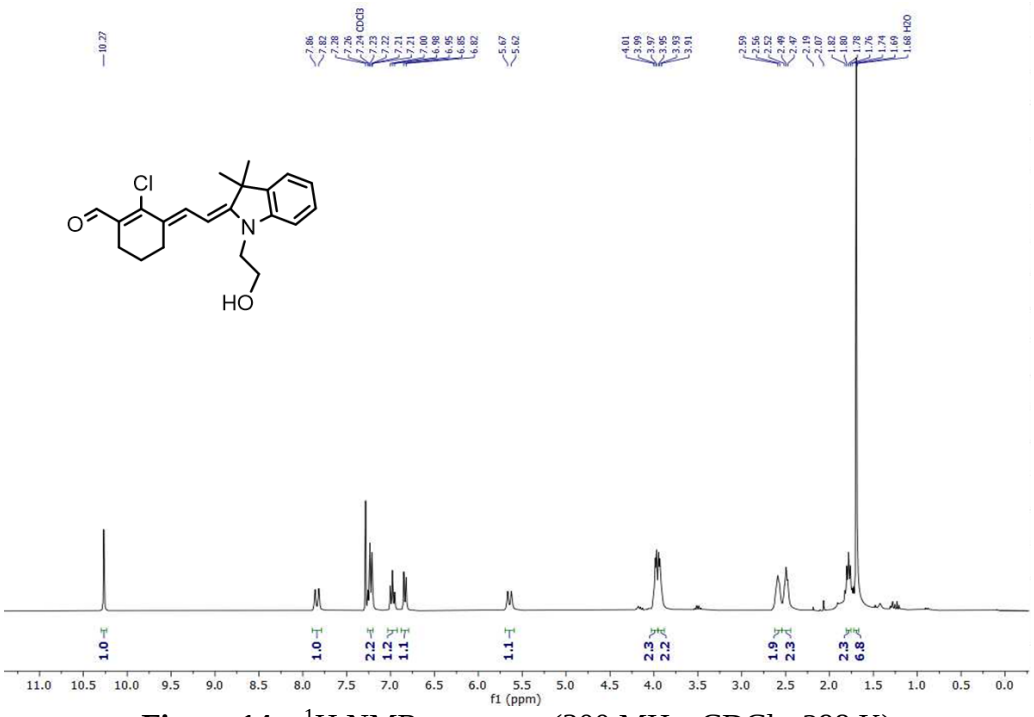

Figure 14a. ^{1}H NMR spectrum (300 MHz, $CDCl_3$, 298 K)

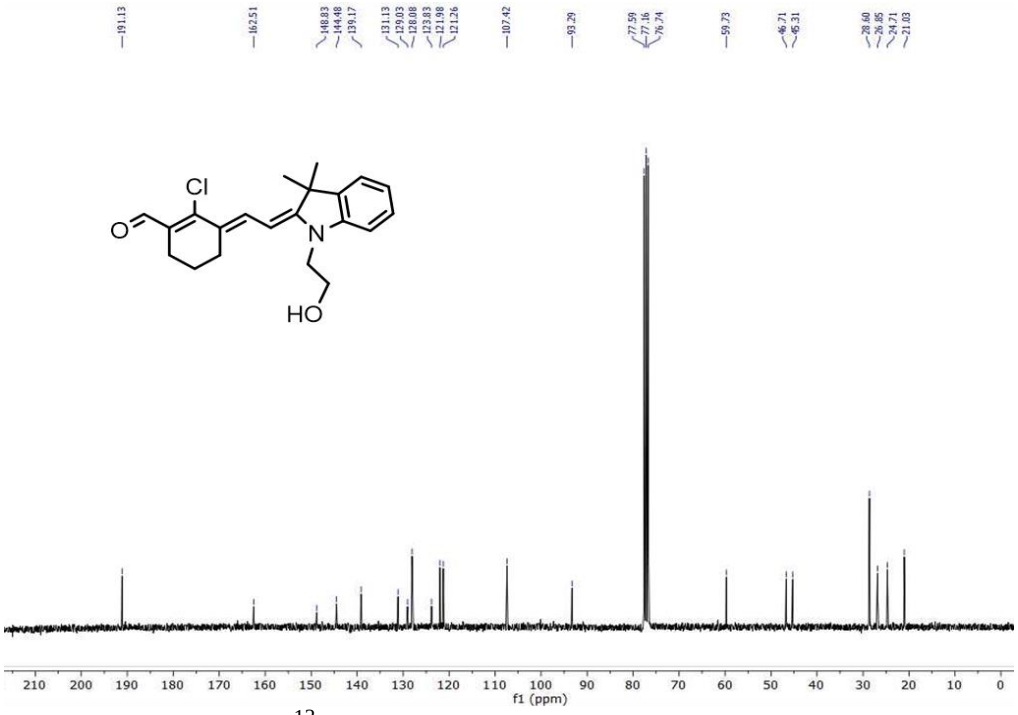

Figure 14b. ^{13}C NMR spectrum (75 MHz, $CDCl_3$, 298 K)

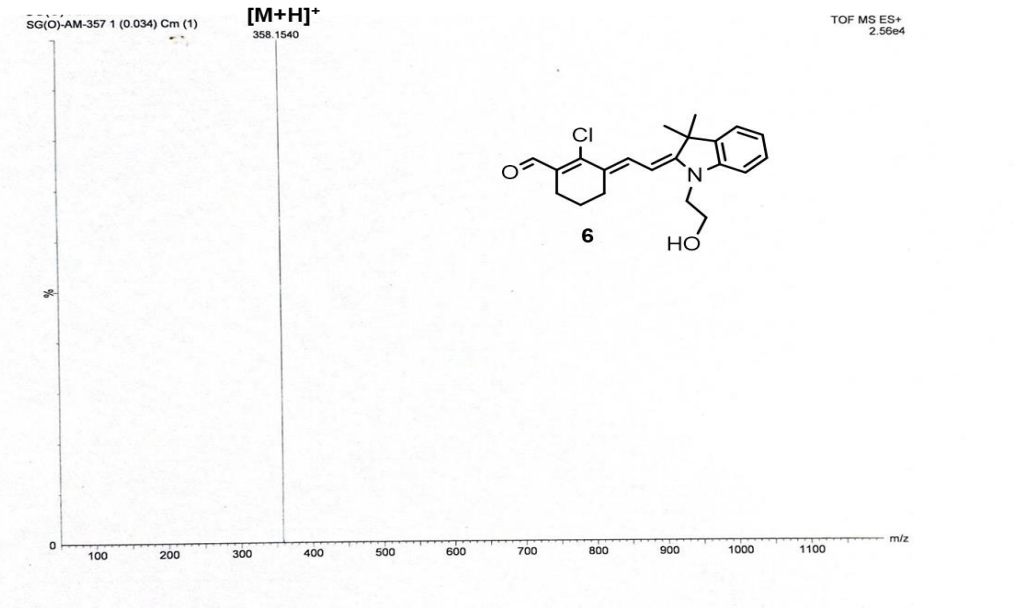

Figure 15. ESI-HRMS spectrum.

2-((*E*)-2-((*E*)-2-chloro-3-(2-((*E*)-1-(2-hydroxyethyl)-3,3-dimethylindolin-2-ylidene)ethylidene)cyclohex-1-en-1-yl)vinyl)-1-(2-hydroxyethyl)-3,3-dimethyl-3*H*-indol-1-ium chloride [Open form Cy-7-(OH)$_2$] : Compounds 6 (1.75 g, 4.9 mmol) and 2 (1.1 g, 4.9 mmol) were dissolved in 30 mL of a mixture of 1-butanol and benzene (7:3) in a round bottomed flask. The mixture was heated to reflux with constant stirring for 8 h. The progress of the reaction was monitored by the TLC. After 3 h the color of the solution turned into reddish brown and at the end of the reaction the color of the mixture turned into deep green. The crude material was purified by column chromatography [R_f : 0.5 in DCM/MeOH(97:3)] to obtain the pure open form of Cy-7-(OH)$_2$ as a green solid.

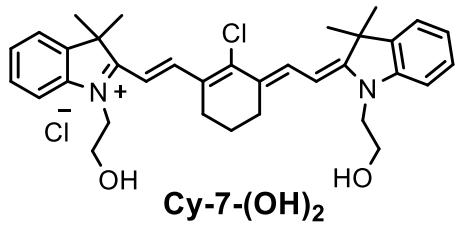

Cy-7-(OH)$_2$

Yield : 2.1 g (74%)

^{1}H NMR (300 MHz, $CDCl_3$, 25°C): δ = 8.32 (d, J = 14.1 Hz, 2H), 7.59–7.55 (m, 2H), 7.39–7.32 (m, 4H), 7.24–7.18 (m, 2H), 6.49 (d, J = 14.1 Hz, 2H), 4.83 (t, J = 4.8 Hz, 1H), 4.34 (t, J = 6.1 Hz, 4H), 4.20 (br, 1H,), 4.04 (t, J = 5.7 Hz, 4H), 2.82 (t, J = 6.0 Hz, 4H), 1.97–1.93 (m, 2H), 1.71 (s, 12H) ppm.

^{13}C NMR (75 MHz, $CDCl_3$, 25°C): δ = 197.5, 173.2, 150.4, 144.6,142.5, 141.5, 141.0, 130.1, 129.5, 128.8, 128.1, 125.1, 123.3, 122.0, 115.7, 111.4, 102.3, 58.6, 58.0, 54.8, 52.0, 49.3, 47.2, 28.3, 27.4, 23.4, 20.7, 16.8 ppm.

HRMS (ESI +ve) *m*/*z*: Observed for $C_{34}H_{40}ClN_2O_2^+$ $[M]^+$ = 543.2772, $[M]^+$calcd = 543.2773.

Photophysical properties in DMSO λ_{abs}= 780 nm, λ_{em}= 800 nm, Stokes shift ($\Delta\lambda$) = 20 nm, ε = 4.24 ×10^5 M^{-1} cm^{-1}, Φ_f = 0.12 in DMSO [Φ_f of the reference compound ICG in DMSO is 0.12].

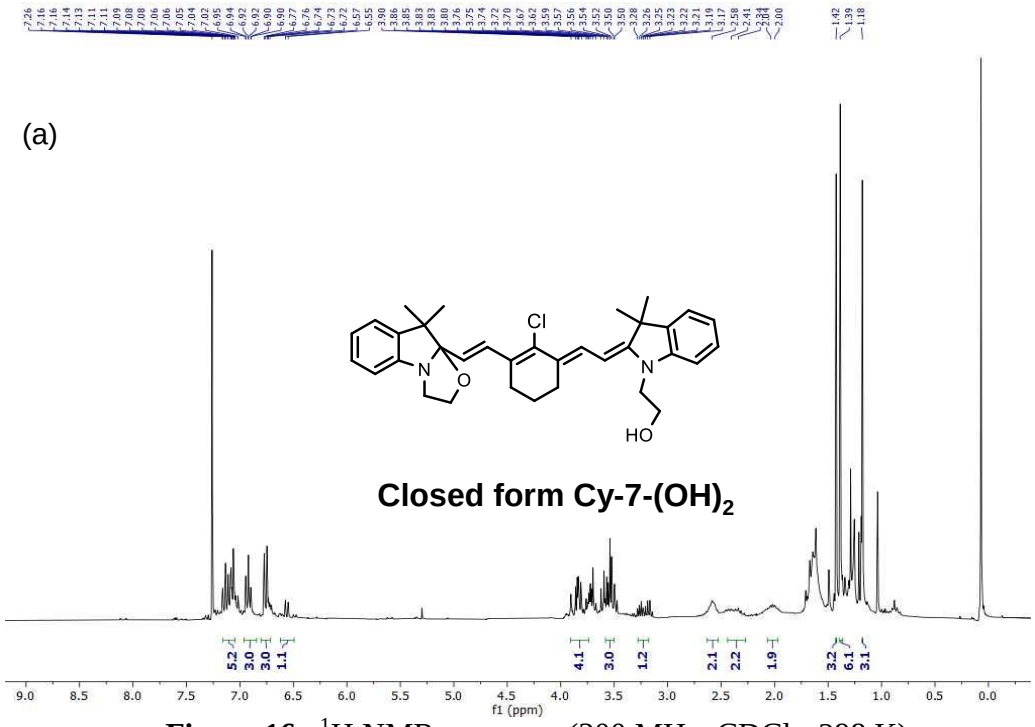

Figure 16a ^{1}H NMR spectrum (300 MHz, $CDCl_3$, 298 K)

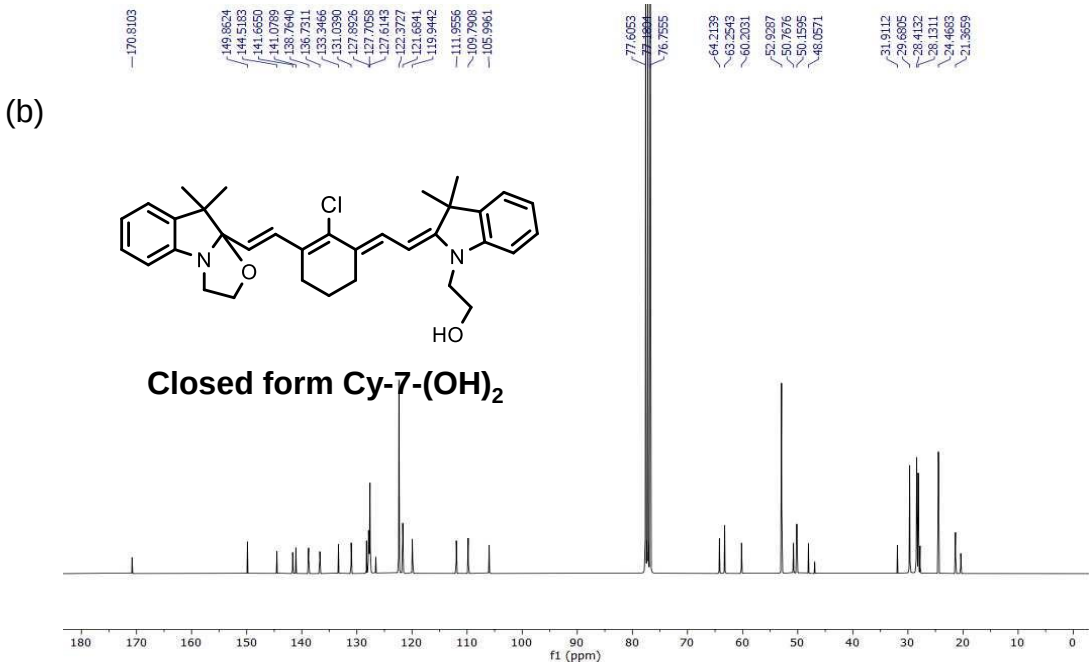

Figure 16b ^{13}C NMR spectrum (101 MHz, $CDCl_3$)

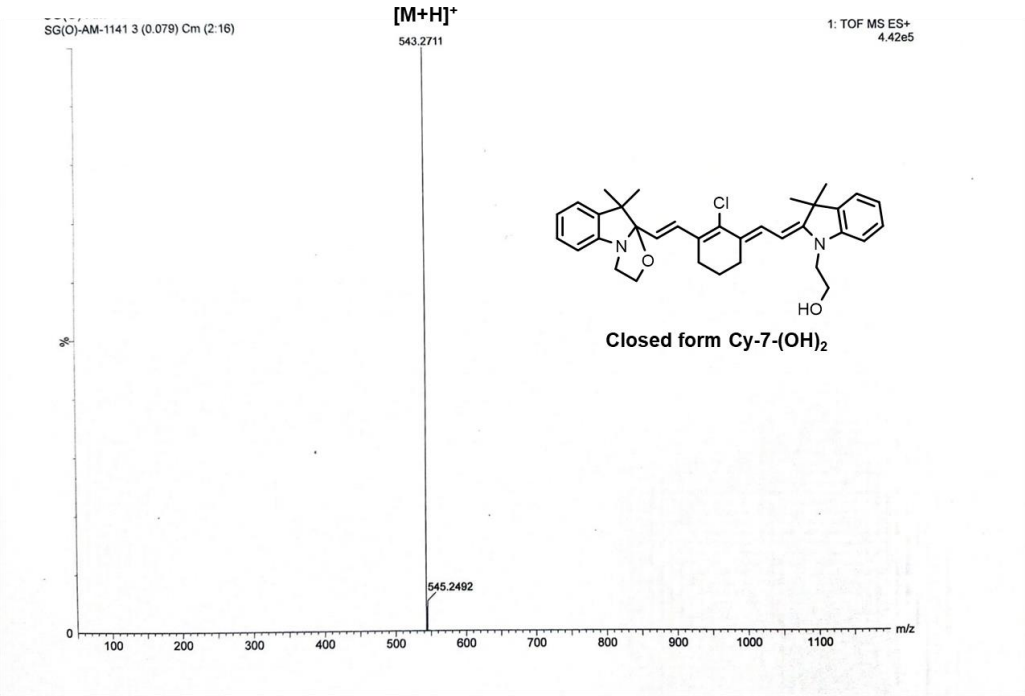

Figure 17: ESI-HRMS spectrum.

1-(2-acetoxyethyl)-2-((*E*)-2-((*E*)-2-chloro-3-(2-((*E*)-1-(2-hydroxyethyl)-3,3-dimethylindolin-2-ylidene)ethylidene)cyclohex-1-en-1-yl)vinyl)-3,3-dimethyl-3*H*-indol-1-ium chloride (Cy-7-OH-OAc): Compounds 6 (1.47 g, 4.12 mmol), compound 4 (1.16 g,4.12 mmol) were dissolved in 30 mL of a mixture of 1-butanol and benzene (7:3) in a round bottomed flask. The mixture was heated to reflux with constant stirring for 8 h. The progress of the reaction was monitored by the TLC. After 3 h the color of the solution turned into reddish brown and at the end of the reaction the color of the mixture turned into deep green. The crude material was purified by column chromatography [R_f : 0.6 in

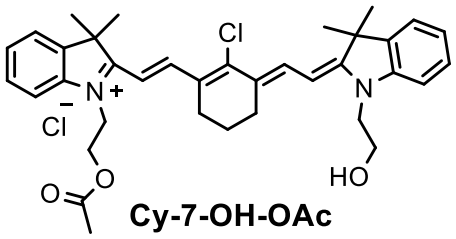

DCM/MeOH(98:2)] to obtain the pure compound **Cy-7-OH-OAc** as a green solid..

Yield: 1.9 g (74%)

^{1}H NMR (300 MHz, $CDCl_3$, 25°C): δ = 8.55 (d, *J* = 14.8 Hz, 1H), 8.12 (d, *J* = 13.3 Hz, 1H), 7.45–7.41 (m, 2H), 7.39–7.31 (m, 2H), 7.13 (d, *J* = 7.3 Hz, 1H), 7.09–7.02 (m, 1H), 6.96 (d, *J* = 7.6 Hz, 1H), 6.74 (d, *J* = 8.7 Hz, 1H), 5.95 (d, *J* = 14.7 Hz, 1H), 4.62 (t, *J* = 5.4 Hz, 2H), 4.45 (t, *J* = 5.7 Hz, 2H), 4.20–4.09 (m, 4H), 2.97 (t, *J* = 5.7 Hz, 2H), 2.65 (t, *J* = 7.1 Hz, 2H), 2.06–2.00 (m, 2H), 1.96 (s, 3H), 1.77 (s, 6H), 1.69 (s, 6H) ppm.

^{13}C NMR (101 MHz, $CDCl_3$, 25°C): δ = 173.2, 150.4, 144.6, 142.6, 141.0, 128.7, 128.0, 125.1, 122.0, 111.3, 102.3, 70.4, 60.1, 58.7, 49.3, 47.2, 33.9, 29.7, 28.3, 25.0, 22.7, 20.7 ppm.

HRMS (ESI +ve) *m*/*z*: Observed for $C_{36}H_{42}N_2O_3Cl^+$ $[M]^+$ = 585.2852, $[M]^+$ calcd = 585.2878.

Photophysical properties in DMSO λ_{abs}= 780 nm, λ_{em}= 800 nm, Stokes shift ($\Delta\lambda$) = 20 nm, ε = 4.2 ×10^5 M^{-1} cm^{-1}, Φ_f = 0.12 in DMSO [Φ_f of the reference compound ICG in DMSO is 0.12].

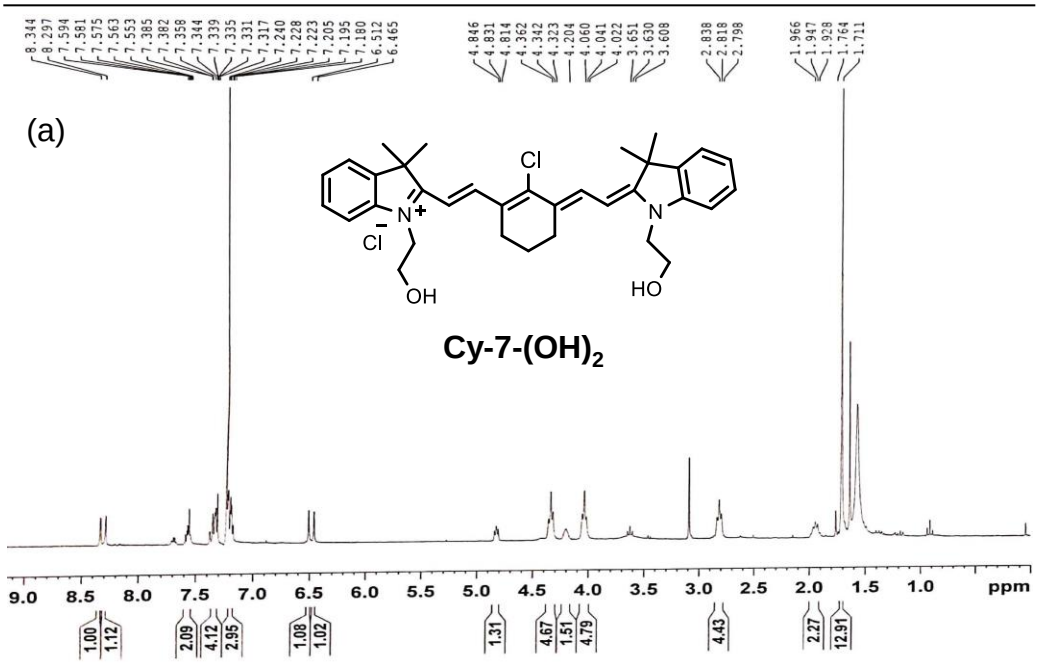

Figure 18a. ^{1}H NMR spectrum (300 MHz, $CDCl_3$, 298 K)

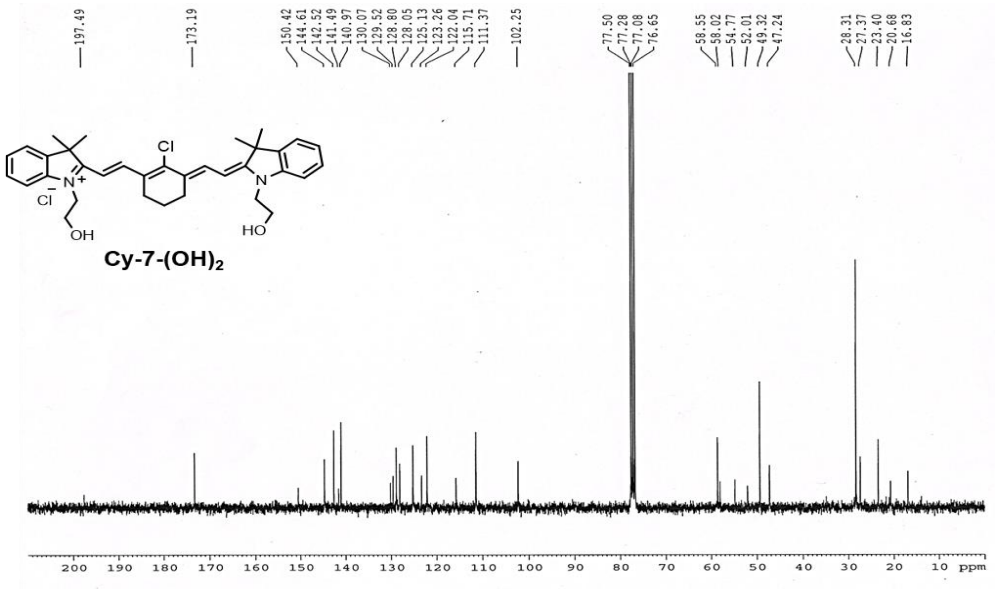

Figure 18b. ^{13}C NMR spectrum (75 MHz, $CDCl_3$)

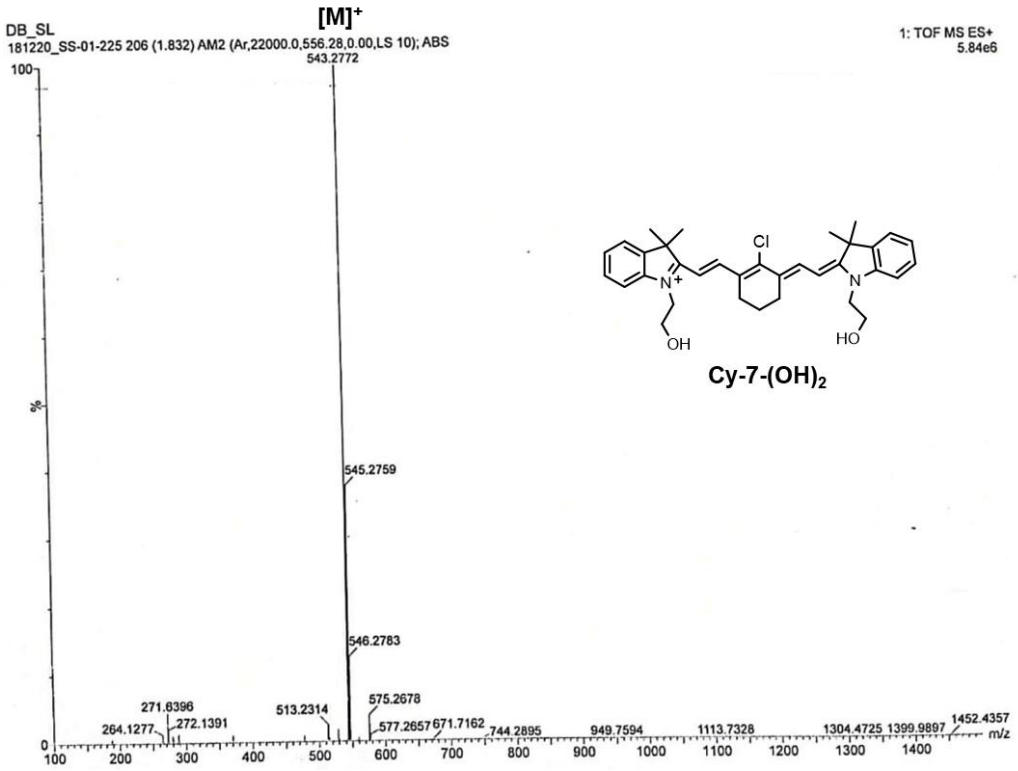

Figure 19: ESI-HRMS spectrum of the open form of Cy-7-$(OH)_2$

2-((*E*)-2-((*E*)-2-(2-chloro-3-((*E*)-2-(9,9-dimethyl-2,3-dihydrooxazolo[3,2-*a*]indol-9a(9*H*)-yl)vinyl)cyclohex-2-en-1-ylidene)ethylidene)-3,3-dimethylindolin-1-yl)ethyl acetate (Closed form of Cy-7-OH-OAc): Compound Cy-7-OH-OAc (0.62 g, 1 mmol) was dissolved 25 mL MeOH and 50% NaOH (20 mL) was added to it and stirred for 6 h. A brown yellow colored precipitate was formed. MeOH was evaporated and the solution was extracted with $CHCl_3$. The crude product was purified by column

chromatography using (DCM:MeOH 97:3, 0.5% Et_3N was mixed with silica gel solvent mixture) as eluent to obtain the basic closed form of Cy-7-OH-OAc. Yield: 0.33 g (56%)

^{1}H NMR (300 MHz, $CDCl_3$, 25°C): δ = 7.64–7.59 (m, 2H), 7.38 (d, *J* = 15.3 Hz, 2H), 7.19 (t, *J* = 7.6 Hz, 1H), 7.10 (d, *J* = 8.1 Hz, 1H), 6.96 (t, *J* = 7.4 Hz, 1H), 6.82 (d, *J* = 8.6 Hz, 1H), 6.75–6.73 (m, 1H), 6.61 (d, *J* = 9.7 Hz, 1H), 5.83 (d, *J* = 15.9 Hz, 1H), 5.49 (d, *J* = 12.2 Hz, 1H), 3.77–3.75 (m, 4H), 3.67–3.56 (m, 4H), 2.68–2.50 (m, 4H), 2.09 (s, 3H), 1.91–1.87 (m, 2H), 1.68 (s, 6H), 1.46 (s, 3H), 1.16 (s, 3H) ppm.

^{13}C NMR (100 MHz, $CDCl_3$, 25°C): δ = 171.0, 149.9, 149.4, 144.5, 142.1, 141.7, 139.4, 139.2, 138.8, 138.4, 136.7, 135.6, 133.2, 131.2, 129.5, 128.8, 128.3, 127.8, 127.7, 127.5, 126.6, 125.6, 125.5, 124.0, 121.9, 119.9, 114.1, 109.8, 108.2, 106.0, 64.2, 60.2, 52.9, 50.2, 48.1, 47.8, 45.7, 30.0, 26.8, 24.5, 19.1, 14.8 ppm.

HRMS (ESI +ve) *m*/*z*: Observed for $C_{36}H_{42}N_2O_3Cl^+$ $[M+H]^+$ = 585.2862, $[M+H]^+$ calcd = 585.2878.

Photophysical properties in DMSO λ_{abs}= 418 nm, λ_{em}= 478 nm, Stokes shift ($\Delta\lambda$) = 60 nm, ε = 1.23 ×10^5 M^{-1} cm^{-1}, Φ_f = 0.09 in EtOH [Φ_f of the reference compound coumarin 6 is 0.78 in absolute EtOH].

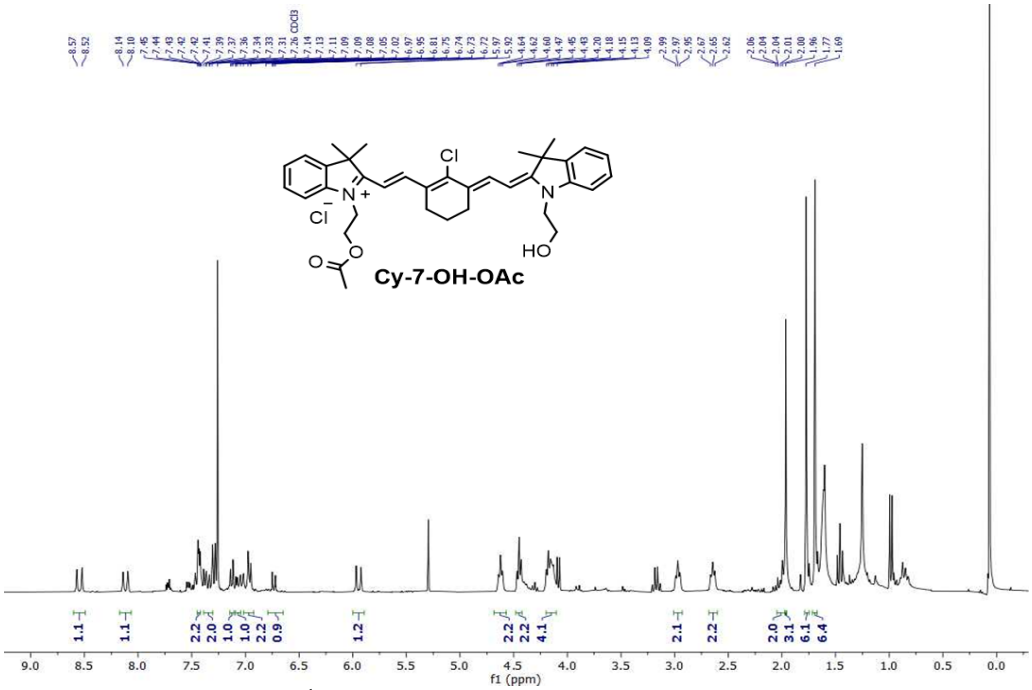

Figure 20a. ^{1}H NMR spectrum (300 MHz, $CDCl_3$, 298 K)

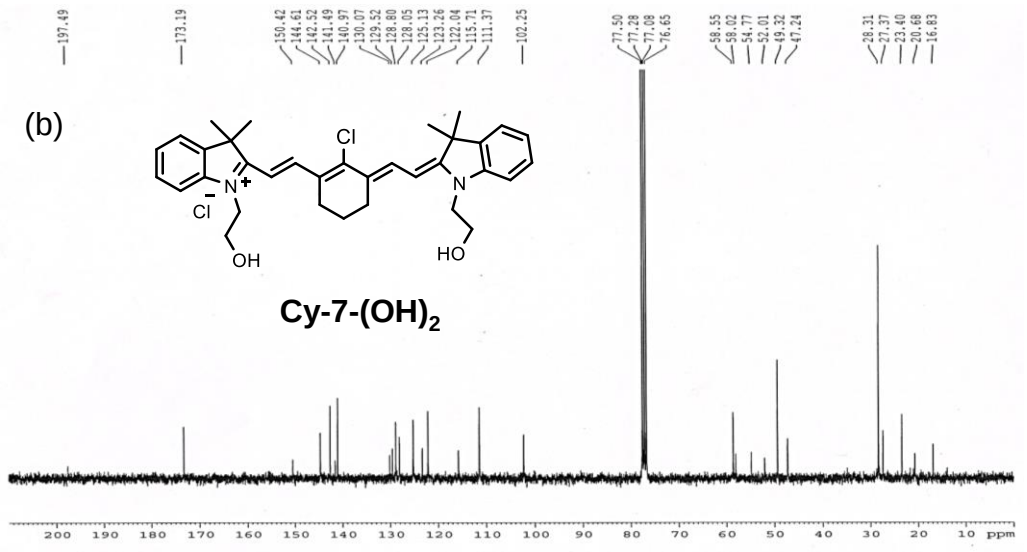

Figure 20b. ^{13}C NMR spectrum (101 MHz, $CDCl_3$)

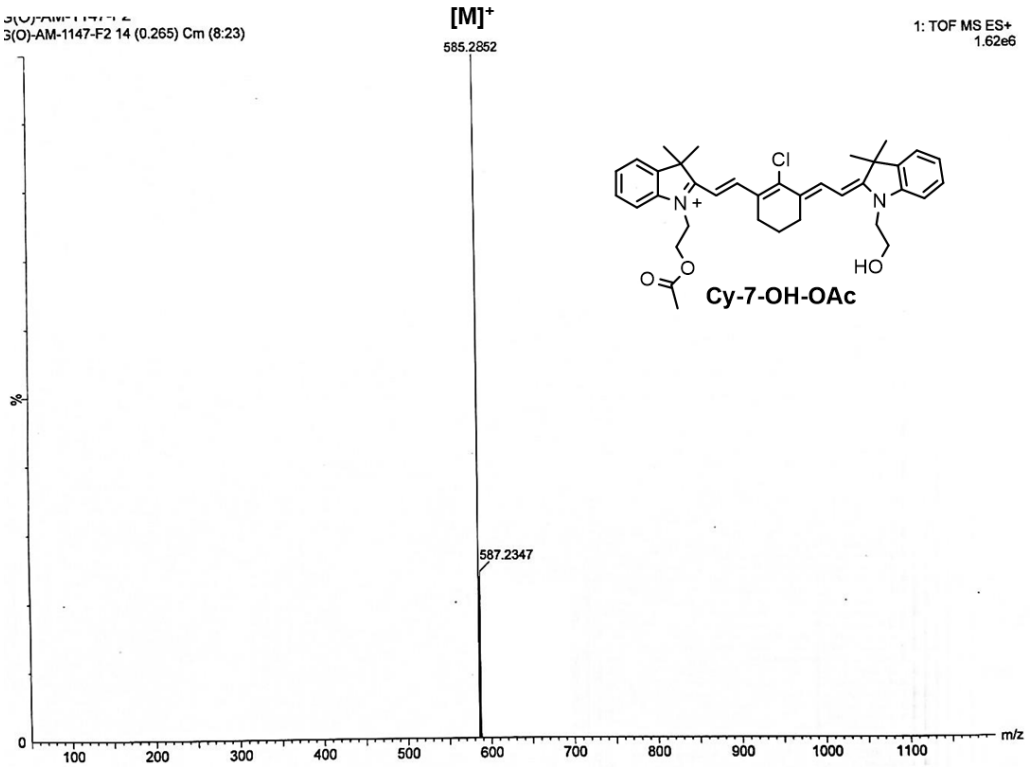

Figure 21. ESI-HRMS spectrum of the open form of Cy-7-OH-OAc

1-(2-acetoxyethyl)-2-((*E*)-2-((*E*)-3-(2-((*E*)-1-(2-acetoxyethyl)-3,3-dimethylindolin-2-ylidene)ethylidene)-2-chlorocyclohex-1-en-1-yl)vinyl)-3,3-dimethyl-3*H*-indol-1-ium chloride [**Cy-7-(OAc)$_2$**]: Cy-7-(OH)$_2$ (0.12 g, 0.2 mmol), AcOH (0.012 mL, 0.2 mmol), DCC (0.041 g, 0.2 mmol), and TsOH (0.007 g, 0.04 mmol) were dissolved in 15 mL DCM. The mixture was stirred at room temperature for 24 h. The reaction mixture was extracted with DCM and H_2O and the organic layer was combined,

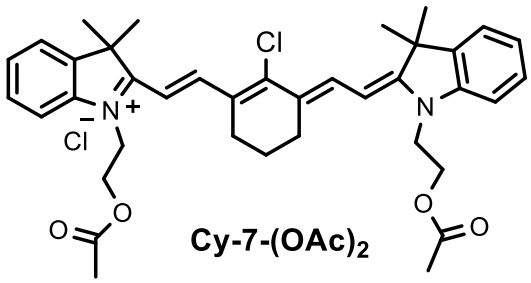

dried over anhydrous Na_2SO_4, filtered, and evaporated the solvent under the reduced pressure. The crude material was purified by column chromatography, R_f : 0.4 in DCM/MeOH(96:4) to obtain the pure product **Cy-7-(OAc)$_2$** as a green solid.

Yield: 0.06 g (45%)

^{1}H NMR (300 MHz, $CDCl_3$, 25°C): δ = 8.36 (d, J = 14.7 Hz, 2H), 7.40–7.35 (m, 4H), 7.27–7.21 (m, 4H), 6.35 (d, J = 14.1 Hz, 2H), 4.59–4.56 (m, 8H), 2.75 (t, J = 5.7 Hz, 4H), 2.00–1.93 (m, 2H), 1.87 (s, 6H), 1.71 (s, 12H) ppm.

^{13}C NMR (75 MHz, $CDCl_3$, 25°C): δ = 173.0, 170.7, 147.9, 144.6, 142.4, 141.0, 137.8, 128.8, 128.6, 125.5, 122.3, 112.2, 110.9, 103.8, 102.2, 60.6, 51.9, 49.5, 44.3, 29.8, 28.2, 27.1, 20.8, 19.2 ppm.

HRMS (ESI +ve) *m*/*z*: Observed for $C_{38}H_{44}N_2O_4Cl^+$ $[M]^+$ = 627.2793, $[M]^+$ calcd = 627.2984.

Photophysical properties in DMSO λ_{abs}= 780 nm, λ_{em}= 800 nm, Stokes shift ($\Delta\lambda$) = 20 nm, ε = 4.28 ×10^5 M^{-1} cm^{-1}, Φ_f = 0.13 in DMSO [Φ_f of the reference compound ICG in DMSO is 0.12].

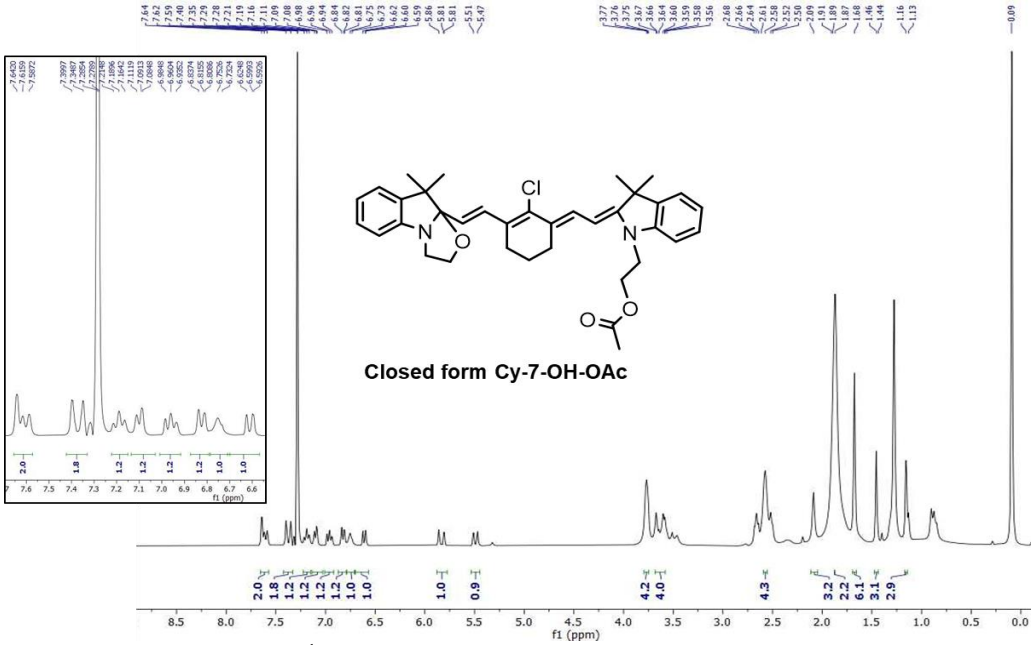

Figure 22a. ^{1}H NMR spectrum (300 MHz, $CDCl_3$, 298 K)

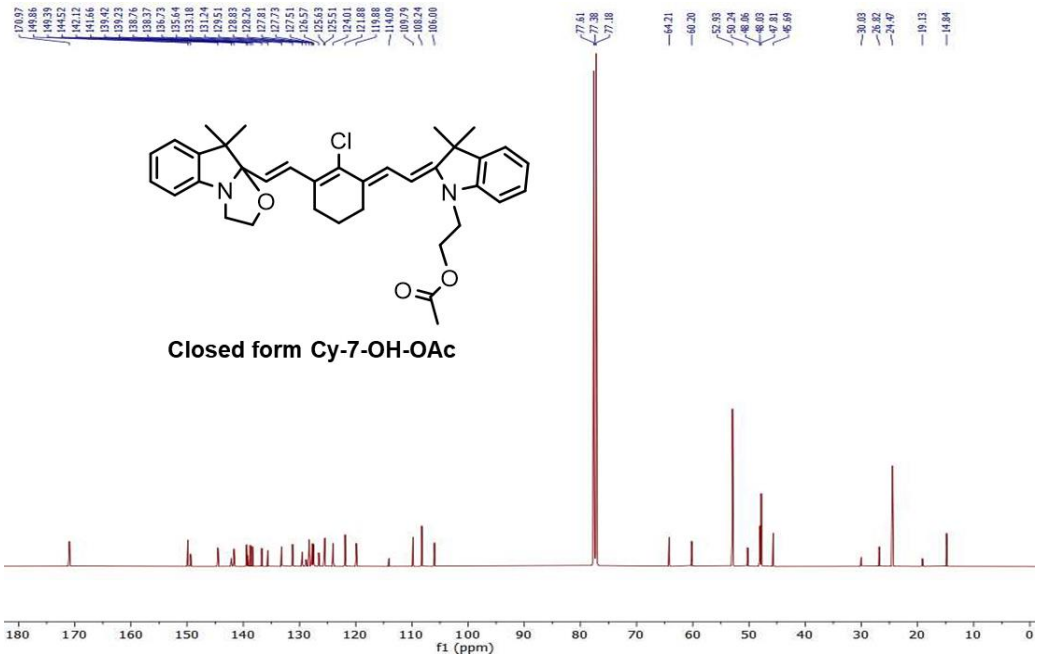

Figure 22b. ^{13}C NMR spectrum (100 MHz, $CDCl_3$).

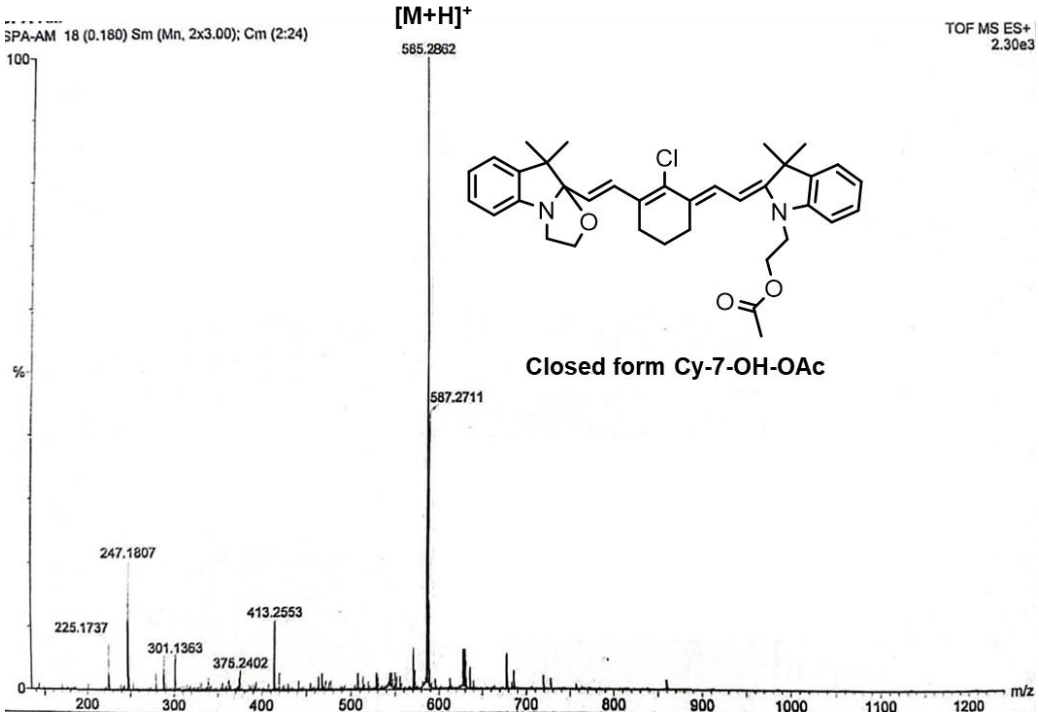

Ac.

Figure 23: ESI-HRMS spectrum of the closed form of Cy-7-OH-OAc.

2-((*E*)-2-((*E*)-3-(2-((*E*)-1-(5-carboxypentyl)-3,3-dimethylindolin-2-ylidene)ethylidene)-2-chlorocyclohex-1-en-1-yl)vinyl)-1-(2-hydroxyethyl)-3,3-dimethyl-3*H*-indol-1-ium (Cy7-OH-COOH): Compounds 6 (1.47 g, 4.12 mmol) and 7 (1.65 g, 4.12 mmol) were dissolved in 30 mL of a mixture of 1-butanol and benzene (7:3) in a round bottomed flask. The mixture was heated to reflux for 8 h with constant stirring. The progress of the reaction was monitored by TLC. After 3 h the color of the solution was turned into brown and after 8 h the

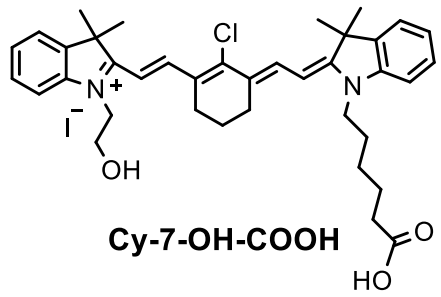

color of the reaction mixture turned into deep green. The crude product was purified by column chromatography using DCM/MeOH (97:3) as eluent to obtain the pure product **Cy7-OH-COOH** as a green solid.

Yield: 2.64 g (87%)

^{1}H NMR (300 MHz, $CDCl_3$, 25°C): δ = 8.41 (d, *J* = 14.4 Hz, 1H), 8.19 (d, *J* = 13.7 Hz, 1H), 7.43–7.28 (m, 5H), 7.23 (t, *J* = 7.3, 1H), 7.13 (t, *J* = 7.5, 1H), 7.03 (d, *J* = 8.1 Hz, 1H), 6.60 (d, *J* = 14.4 Hz, 1H), 5.92 (d, *J* = 13.7 Hz, 1H), 4.72 (br, 1H), 4.44 (t, *J* = 6.0 Hz, 2H), 4.05 – 3.95 (m, 4H), 2.80 (t, *J* = 6.1 Hz, 2H), 2.60 (t, *J* = 7.2 Hz, 2H), 1.95–1.87 (m, 2H), 1.85–1.75 (m, 2H), 1.70 (s, 6H) 1.65 (s, 6H), 1.55–1.26 (m, 6H) ppm.

^{13}C NMR (101 MHz, $CDCl_3$, 25°C): δ = 177.1, 173.4, 168.5, 150.1, 147.9, 142.8, 141.9, 140.7, 140.3, 129.4, 129.1, 128.5, 126.8, 126.6, 123.8, 122.2, 112.6, 109.3, 106.2, 97.9, 64.4, 58.7, 50.3, 48.4, 43.7, 33.9, 30.7, 28.3, 27.8, 26.7, 24.6, 20.7, 19.1, 13.7 ppm.

HRMS (ESI +ve) *m*/*z*: Observed for $C_{38}H_{46}N_2O_3Cl^+$ $[M]^+$ = 613.3177, $[M]^+$ calcd = 613.3191.

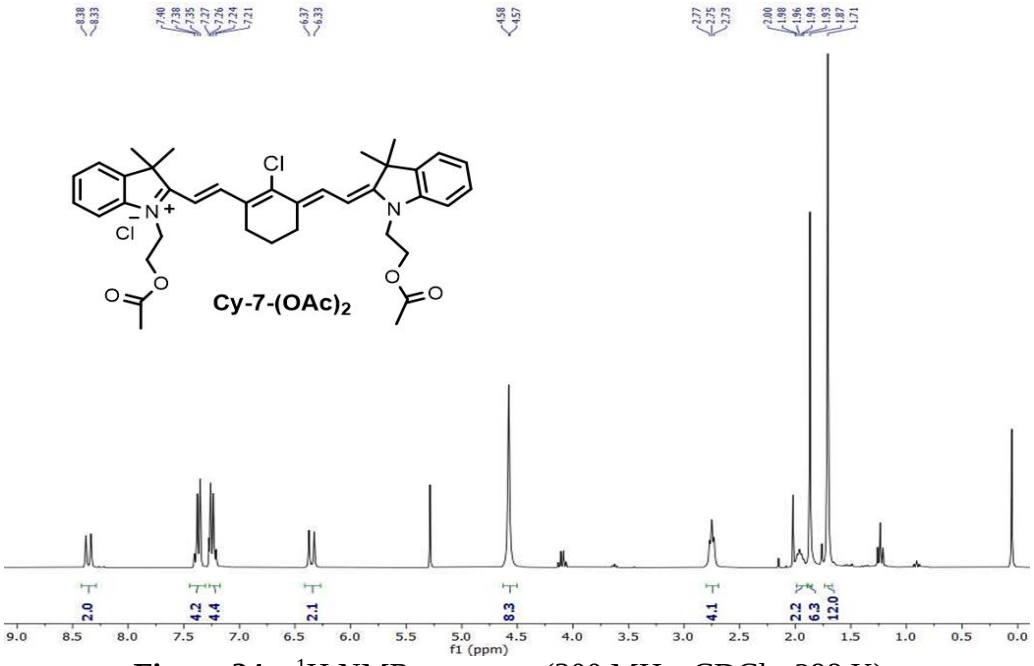

Figure 24a. ^{1}H NMR spectrum (300 MHz, $CDCl_3$, 298 K)

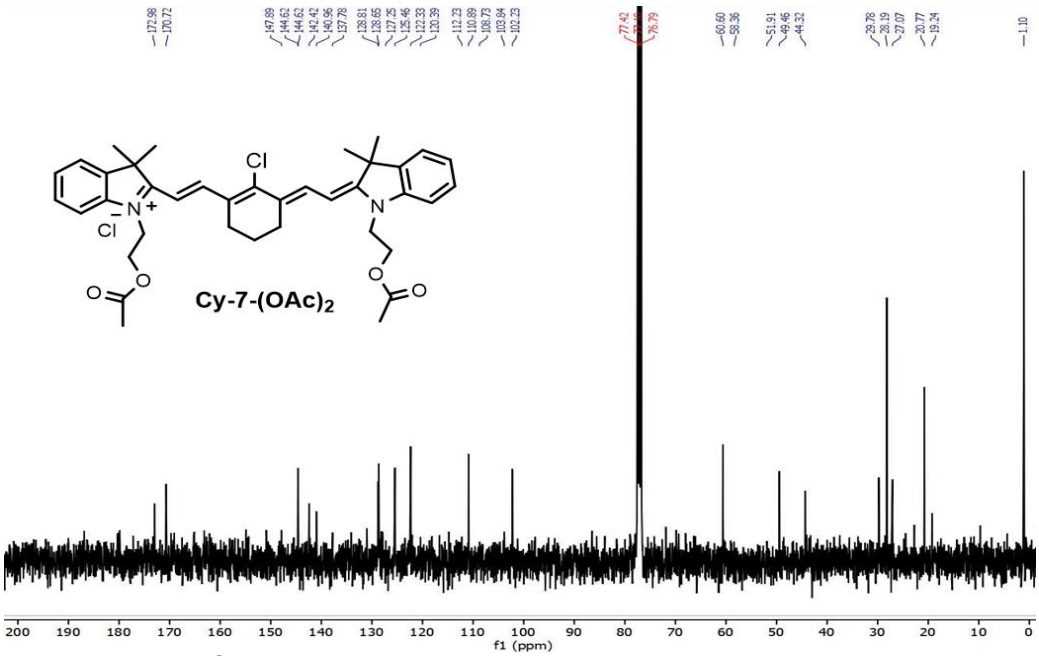

Figure 24b. ^{13}C NMR spectrum (75 MHz, $CDCl_3$, 298 K) of Cy-7-$(OAc)_2$.

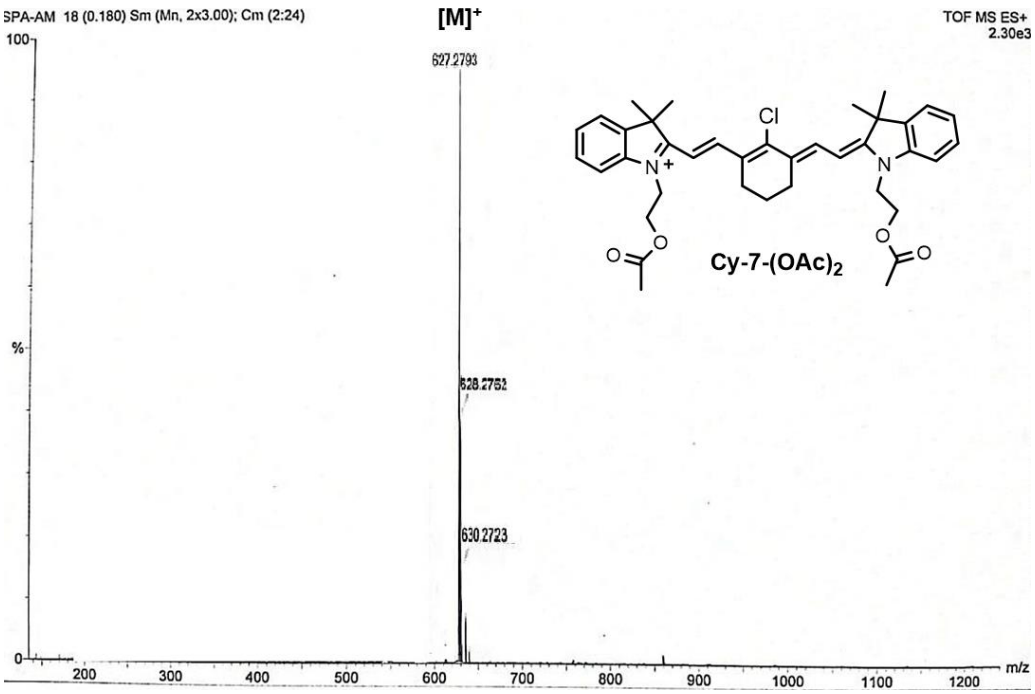

Figure 25. ESI-HRMS spectrum of Cy-7-$(OAc)_2$.

2-((*E*)-2-((*E*)-3-(2-((*E*)-1-(5-carboxypentyl)-3,3-dimethylindolin-2-ylidene)ethylidene)-2-chlorocyclohex-1-en-1-yl)vinyl)-1-(2-hydroxyethyl)-3,3-dimethyl-3*H*-indol-1-ium (Cy7-OH-COOH): Compounds 6 (1.47 g, 4.12 mmol) and 7 (1.65 g, 4.12 mmol) were dissolved in 30 mL of a mixture of 1-butanol and benzene (7:3) in a round bottomed flask. The mixture was heated to reflux for 8 h with constant stirring. The progress of the reaction was monitored by TLC. After 3 h the color of the solution was turned into brown and after 8 h the color of the reaction mixture turned into deep green. The crude product was

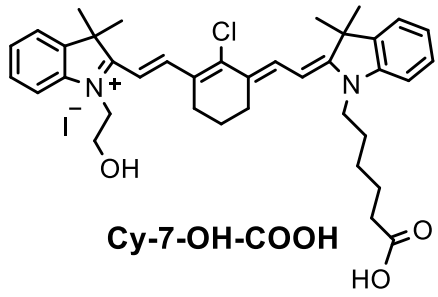

purified by column chromatography using DCM/MeOH (97:3) as eluent to obtain the pure product **Cy7-OH-COOH** as a green solid.

Yield: 2.64 g (87%)

^{1}H NMR (300 MHz, $CDCl_3$, 25°C): δ = 8.41 (d, *J* = 14.4 Hz, 1H), 8.19 (d, *J* = 13.7 Hz, 1H), 7.43–7.28 (m, 5H), 7.23 (t, *J* = 7.3, 1H), 7.13 (t, *J* = 7.5, 1H), 7.03 (d, *J* = 8.1 Hz, 1H), 6.60 (d, *J* = 14.4 Hz, 1H), 5.92 (d, *J* = 13.7 Hz, 1H), 4.72 (br, 1H), 4.44 (t, *J* = 6.0 Hz, 2H), 4.05 – 3.95 (m, 4H), 2.80 (t, *J* = 6.1 Hz, 2H), 2.60 (t, *J* = 7.2 Hz, 2H), 1.95–1.87 (m, 2H), 1.85–1.75 (m, 2H), 1.70 (s, 6H) 1.65 (s, 6H), 1.55–1.26 (m, 6H) ppm.

^{13}C NMR (101 MHz, $CDCl_3$, 25°C): δ = 177.1, 173.4, 168.5, 150.1, 147.9, 142.8, 141.9, 140.7, 140.3, 129.4, 129.1, 128.5, 126.8, 126.6, 123.8, 122.2, 112.6, 109.3, 106.2, 97.9, 64.4, 58.7, 50.3, 48.4, 43.7, 33.9, 30.7, 28.3, 27.8, 26.7, 24.6, 20.7, 19.1, 13.7 ppm.

HRMS (ESI +ve) *m*/*z*: Observed for $C_{38}H_{46}N_2O_3Cl^+$ $[M]^+$ = 613.3177, $[M]^+$ calcd = 613.3191.

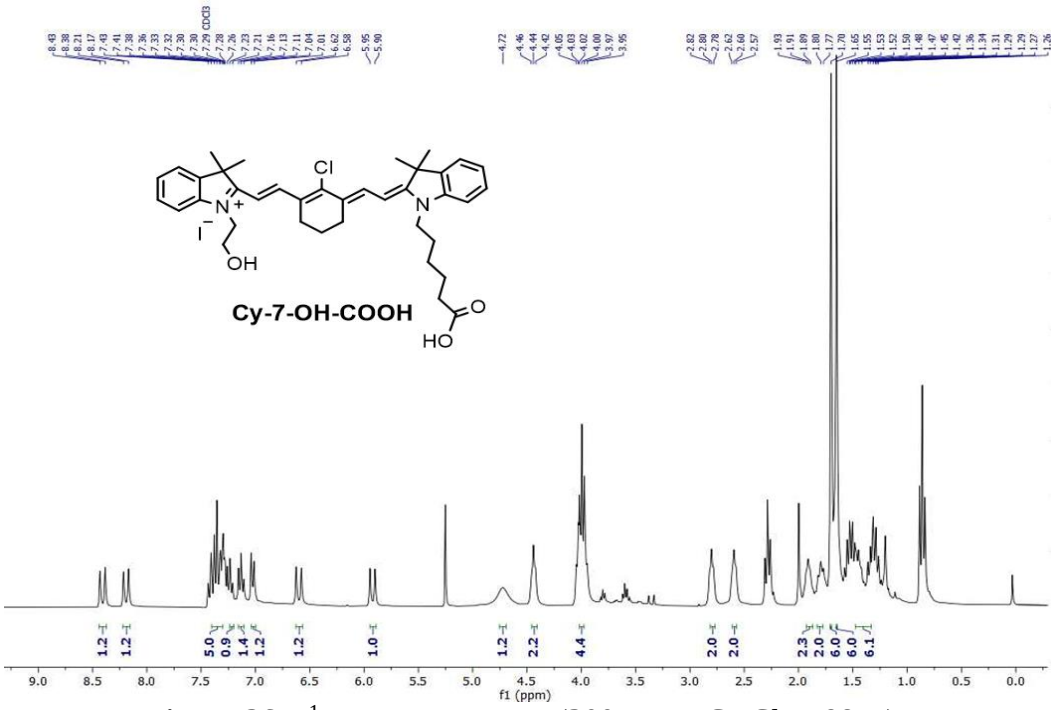

Figure 26a. ^{1}H NMR spectrum (300 MHz, $CDCl_3$, 298 K)

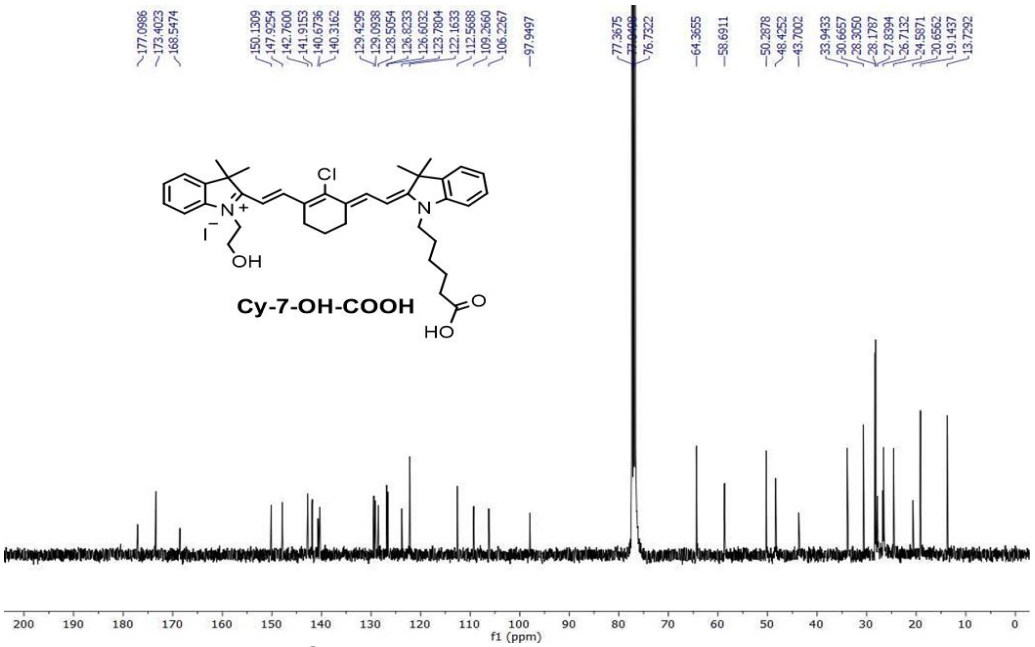

Figure 26b. ^{13}C NMR spectrum (101 MHz, $CDCl_3$, 298 K).

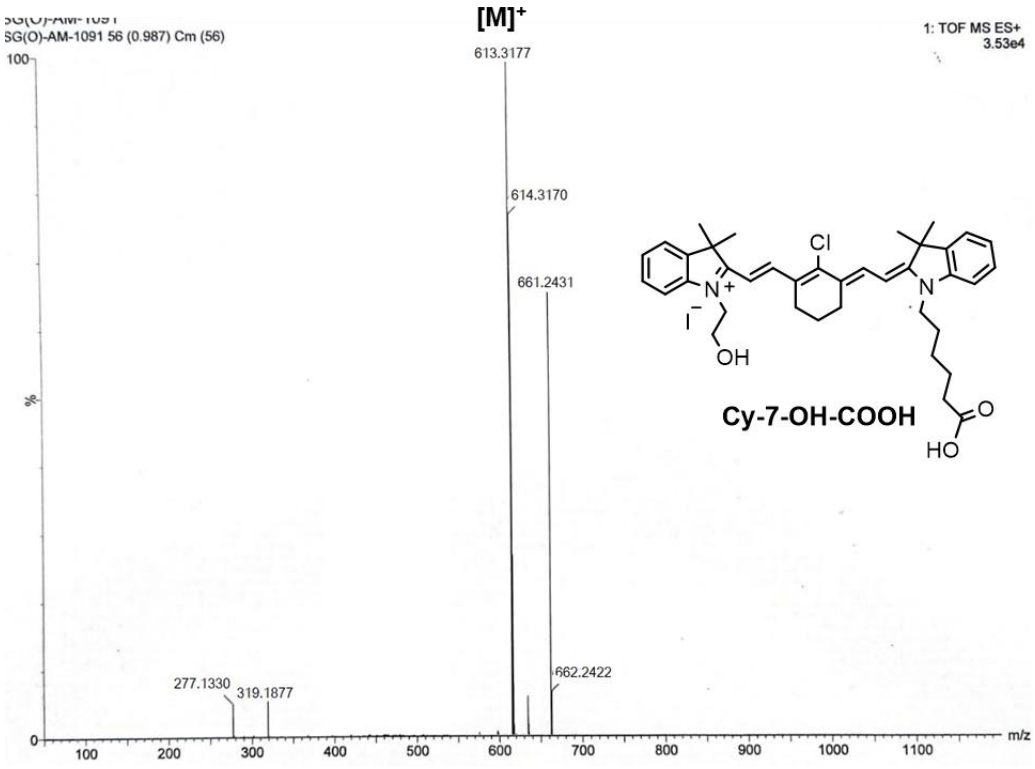

Figure 27. ESI-HRMS spectrum of Cy-7-OH-COOH.

Open form of Lyso-Cy-7-OH: Compounds 6 (0.36 g, 1 mmol) and 8 (0.51 g, 1 mmol) were taken in a round bottomed flask. 14 mL n-Butanol and 6 mL of benzene (7:3 ratio) were added to it and the mixture was heated to reflux for 12 h. The color of the reaction mixture was turned into red. The solvent was removed under the reduced pressure. The crude product was purified by column chromatography using 3%

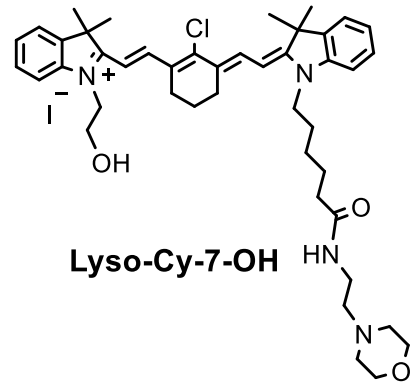

DCM/MeOH as eluent. A green colored solid of the open form of Lyso-Cy-7-OH was obtained.

Yield: 0.59 g (69%)

^{1}H NMR (300 MHz, $CDCl_3$, 25°C): δ = 8.52 (d, *J* = 14.6 Hz, 1H), 8.19 (d, *J* = 13.5 Hz, 1H), 7.49–7.42 (m, 3H), 7.39–7.35 (m, 2H), 7.17 (t, *J* = 7.5 Hz, 2H), 6.98 (d, *J* = 7.8 Hz, 1H), 6.89 (d, *J* = 14.7 Hz, 1H), 5.90 (d, *J* = 13.6 Hz, 1H), 4.59 (t, *J* = 5.8 Hz, 2H), 4.13 (t, *J* = 5.7 Hz, 2H), 4.08 (t, *J* = 6.7 Hz, 4H), 3.94 (t, *J* = 7.5 Hz, 2H), 3.73 (t, *J* = 4.6 Hz, 2H), 2.96 (t, *J* = 6.2 Hz, 2H), 2.64 (t, *J* = 5.8 Hz, 2H), 2.58–2.56 (m, 2H), 2.02–1.98 (m, 2H), 1.89–1.84 (m, 2H), 1.82–1.81 (m, 2H), 1.78 (s, 6H), 1.71 (s, 6H), 1.66–1.59 (m, 4H), 1.54–1.48 (m, 2H), 1.42–1.35 (m, 2H) ppm.

^{13}C NMR (100 MHz, $CDCl_3$, 25°C): δ = 177.1, 173.4, 168.6, 150.1, 147.9, 142.8, 141.9, 141.8, 140.7, 140.3, 129.4, 129.1, 128.5, 126.8, 126.6, 123.8, 122.2, 112.6, 109.3, 106.2, 97.9, 64.4, 58.7, 50.3, 48.4, 43.7, 33.9, 30.7, 28.3, 28.2, 27.8, 26.7, 26.6, 26.5, 24.6, 20.7, 19.1, 13.7 ppm.

HRMS (ESI +ve) *m*/*z*: Observed for $C_{44}H_{59}N_4O_3Cl^{2+}$ $[M+H]^{2+}$ = 363.2120, $[M+H]^{2+}$ calcd = 363.2132.

Photophysical properties in DMSO λ_{abs}= 780 nm, λ_{em}= 800 nm, Stokes shift ($\Delta\lambda$) = 20 nm, ε = 4.16 ×10^5 M^{-1} cm^{-1}, Φ_f = 0.13 in DMSO [Φ_f of the reference compound ICG in DMSO is 0.12].

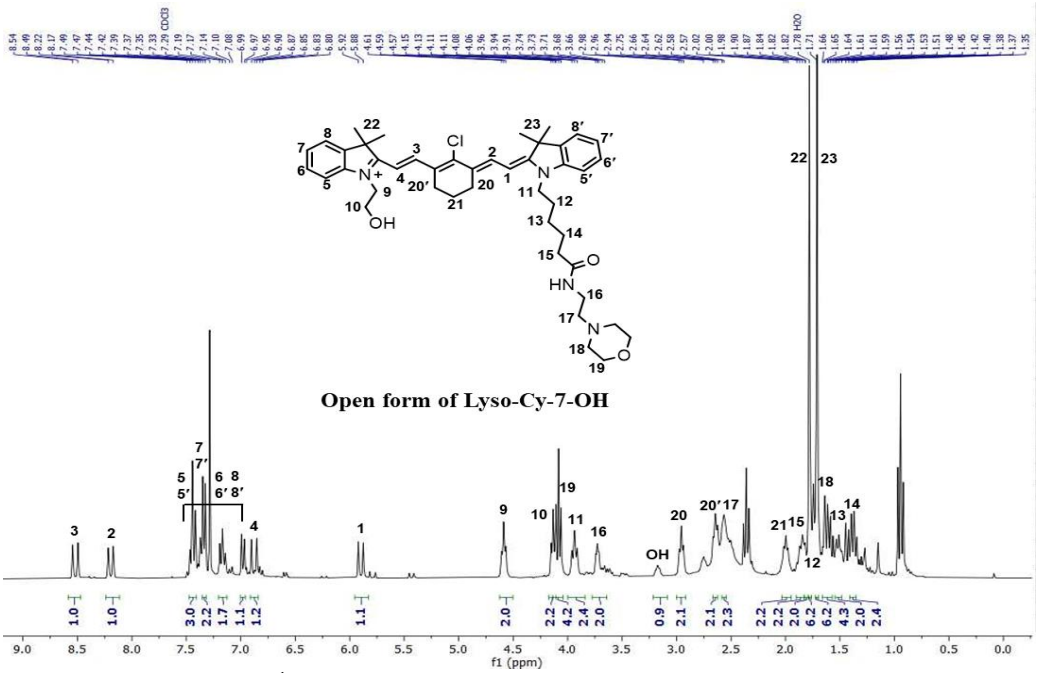

Figure 28a. ^{1}H NMR spectrum (300 MHz, $CDCl_3$, 298 K)

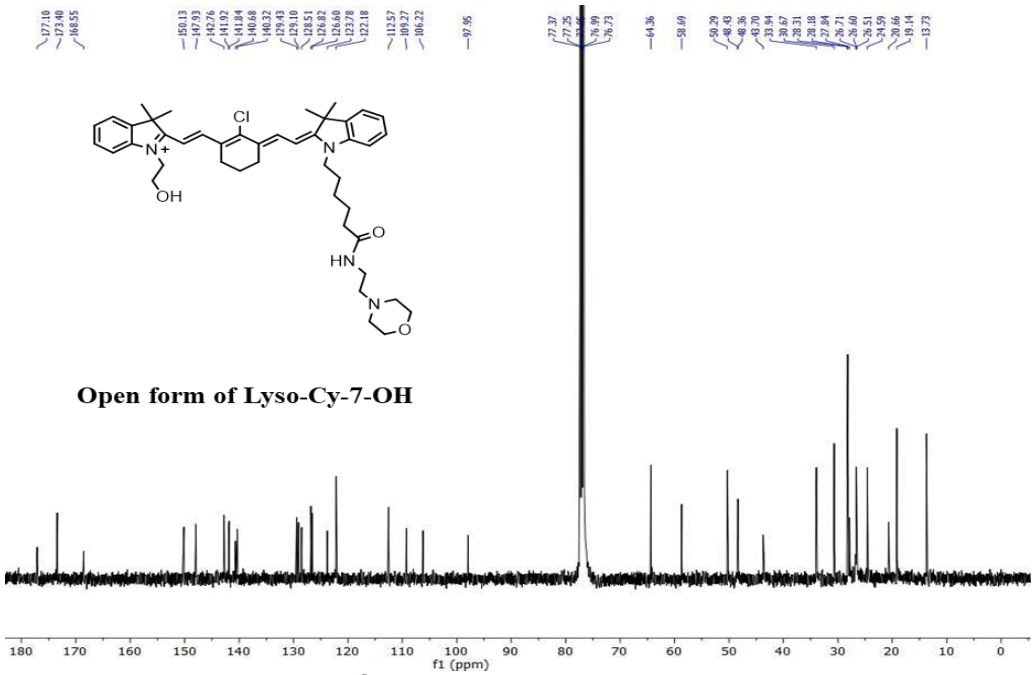

Figure 28b. ^{13}C NMR spectrum (100 MHz, $CDCl_3$)

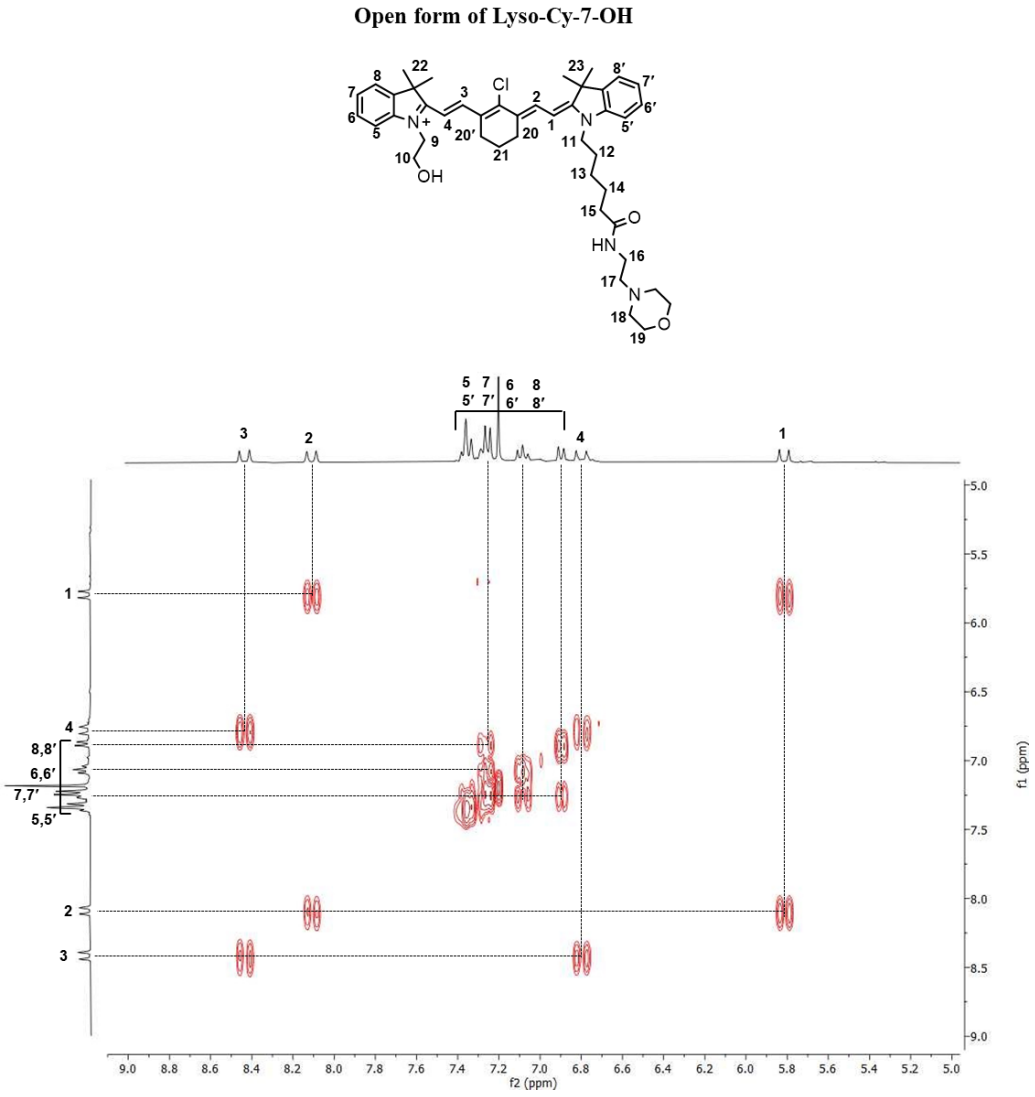

Figure 29a. Partial ^{1}H-^{1}H gCOSY (Gradient-selected Correlation Spectroscopy) NMR (300 MHz, $CDCl_3$, 25°C) spectrum of the open form of Lyso-Cy-7-OH.

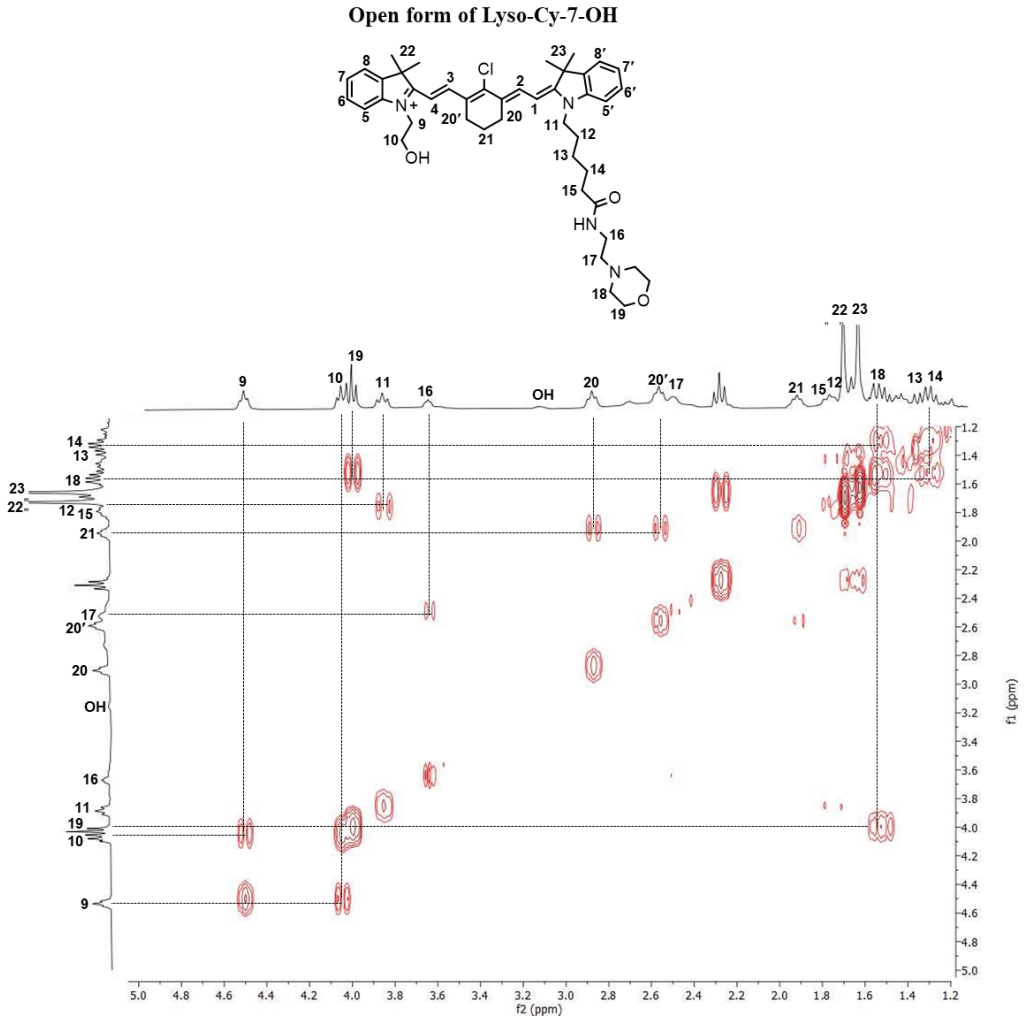

Figure 29b. Partial ^{1}H-^{1}H gCOSY (Gradient-selected Correlation Spectroscopy) NMR (300 MHz, $CDCl_3$, 25°C) spectrum of the open form of Lyso-Cy-7-OH

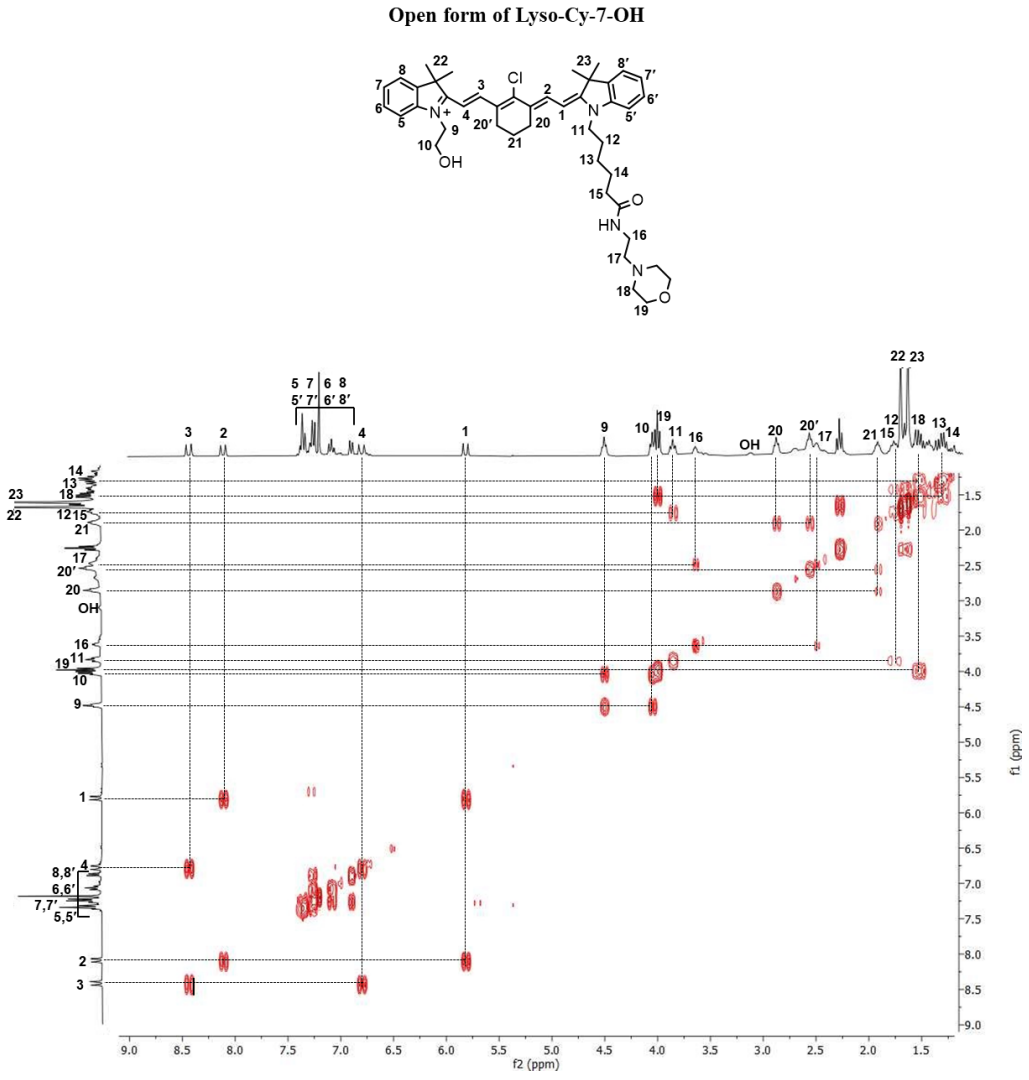

Figure 29c. ^{1}H-^{1}H gCOSY (Gradient-selected Correlation Spectroscopy) NMR (300 MHz, $CDCl_3$, 25°C) spectrum of the open form of Lyso-Cy-7-OH.

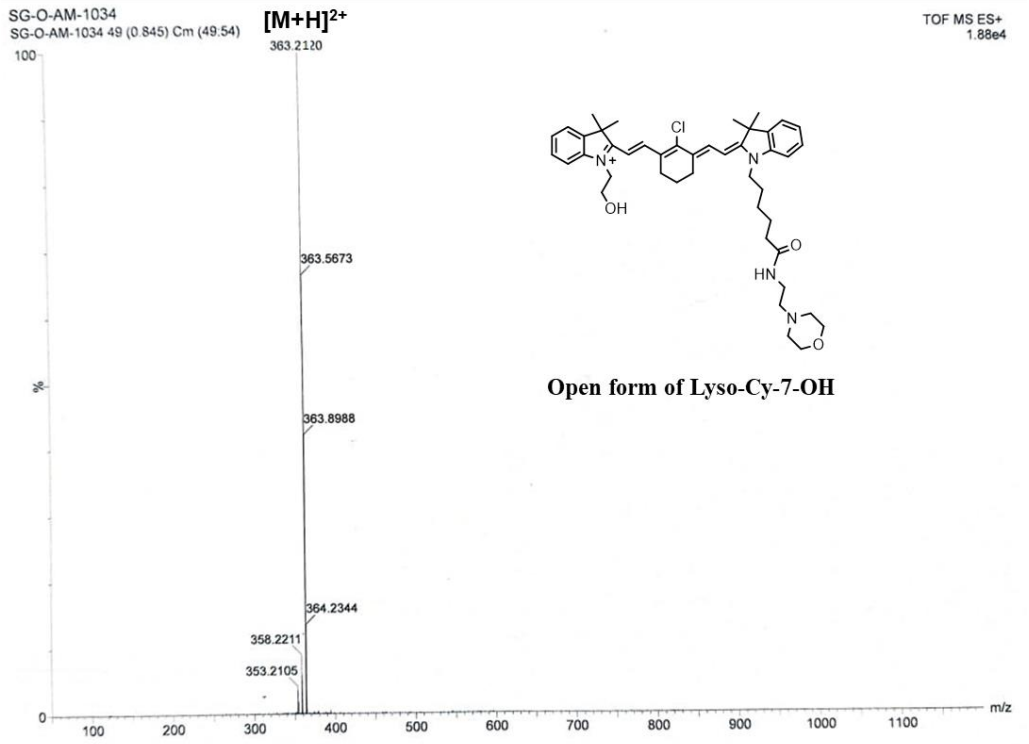

Figure 30. ESI-HRMS spectrum of the open form of Lyso-Cy-7-OH

Closed form of Lyso-Cy-7-OH: Open form of Lyso-Cy-7-OH (0.85 g, 1 mmol) was dissolved in 25 mL MeOH and 50% NaOH (20 mL) was added to it and stirred for 6 h. A brown yellow colored precipitate was formed. Methanol was evaporated and the solution was extracted with $CHCl_3$. The organic layer was dried over anhydrous Na_2SO_4, filtered, and evaporated under reduced pressure. The crude material was purified by column chromatography using (DCM:MeOH 97:3, 0.5% Et_3N was mixed with silica gel solvent mixture) as eluent to obtain the pure **closed form of Lyso-Cy-7-OH** as a red solid.

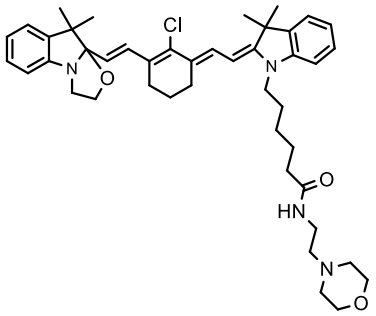

Yield: 0.66 g (11%)

^{1}H NMR (400 MHz, $CDCl_3$, 25°C): δ = 7.77 (d, *J* = 7.9 Hz, 1H), 7.41–7.35 (m, 2H), 7.22–7.18 (m, 2H), 7.09 (d, *J* = 7.3 Hz, 1H), 6.96 (t, *J* = 7.3 Hz, 1H), 6.88 (t, *J* = 7.3 Hz, 1H), 6.82 (d, *J* = 7.7 Hz, 1H), 6.73 (d, *J* = 8.2 Hz, 1H), 6.58 (d, *J* = 14.0 Hz, 1H), 5.81 (d, *J* = 15.7 Hz, 1H), 5.57 (d, *J* = 12.3 Hz, 1H), 4.36–4.34 (m, 2H), 4.05 (t, *J* = 5.7 Hz, 2H), 3.96–3.93 (m, 2H), 3.87–3.78 (m, 2H), 3.67 (t, *J* = 4.7 Hz, 4H), 3.05 (t, *J* = 5.8 Hz, 2H), 2.82–2.81 (m, 2H), 2.62–2.59 (m, 4H), 2.51–2.46 (m, 4H), 1.96–1.94 (m, 2H), 1.86–1.84 (m, 2H), 1.75 (s, 6H), 1.67 (s, 3H), 1.65–1.63 (m, 4H), 1.45 (s, 3H) ppm.

^{13}C NMR (100 MHz, $CDCl_3$, 25°C): δ = 181.6, 170.9, 150.6, 149.4, 144.5, 138.4, 136.7, 133.2, 131.2, 127.8, 126.6, 125.8, 125.5, 119.9, 114.1, 112.6, 109.8, 108.2, 106.0, 65.6, 64.2, 63.7, 58.2, 55.8, 52.9, 50.8, 50.1, 48.1, 47.3, 41.1, 40.5, 40.1, 34.4, 30.7, 28.1, 27.8, 27.2, 26.4, 24.5, 23.3, 21.4, 20.5, 14.8 ppm.

HRMS (ESI +ve) *m*/*z*: Observed for $C_{44}H_{57}N_4O_3Cl^+$ $[M]^+$ = 724.4108, $[M]^+$ calcd = 724.4119.

Photophysical properties in DMSO λ_{abs}= 418 nm, λ_{em}= 478 nm, Stokes shift ($\Delta\lambda$) = 60 nm, ε = 1.24 ×10^5 M^{-1} cm^{-1}, Φ_f = 0.09 in EtOH [Φ_f of the reference compound coumarin 6 is 0.78 in absolute EtOH].

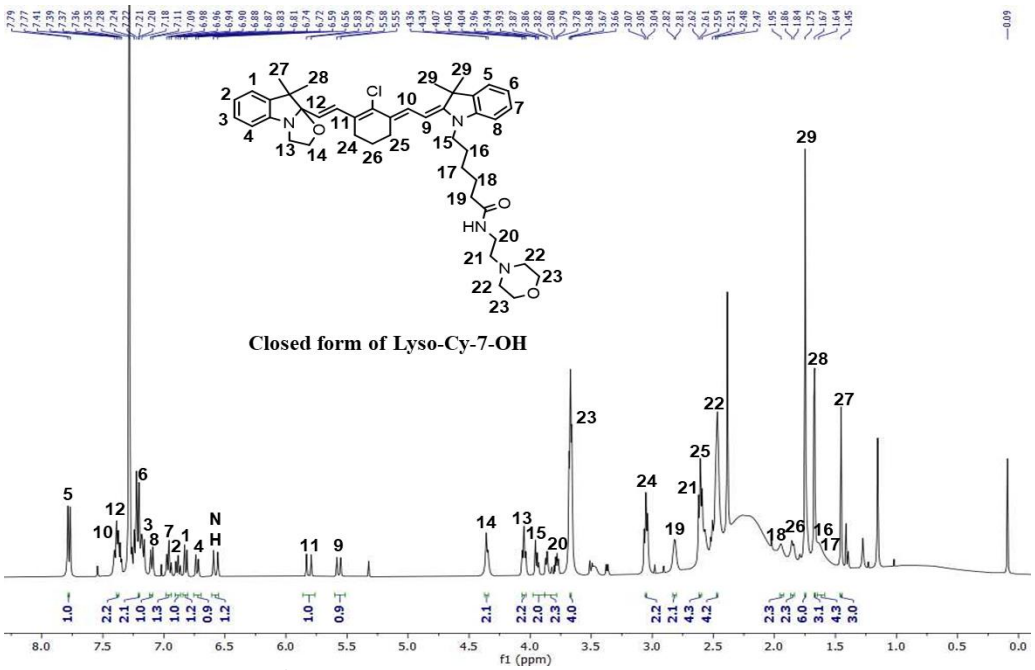

Figure 31a. ^{1}**H** NMR spectrum (400 MHz, $CDCl_3$, 298 K)

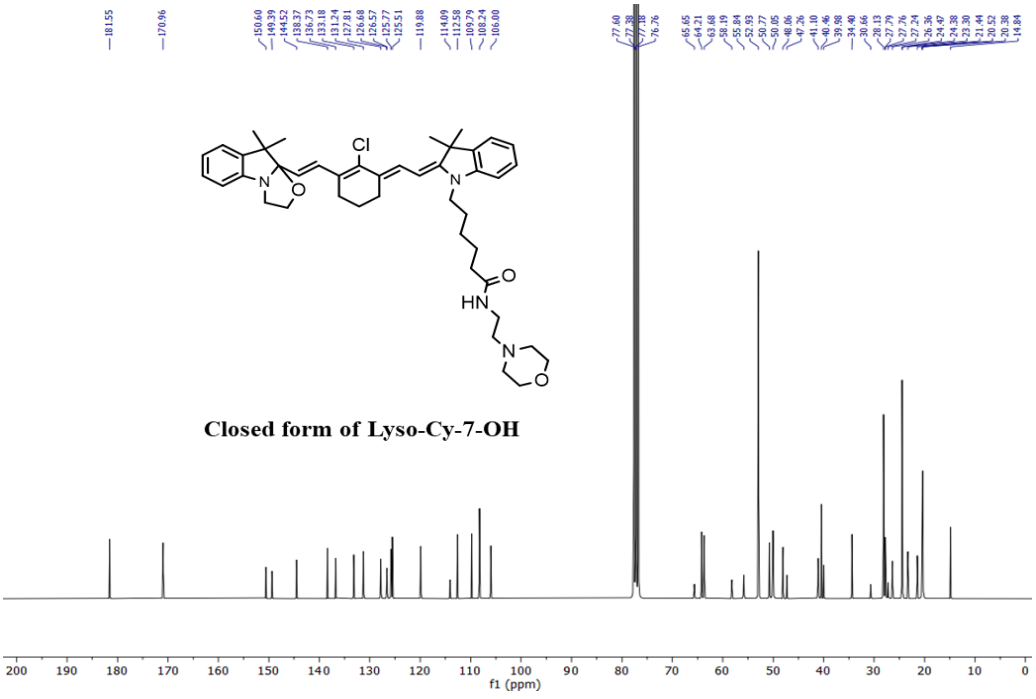

Figure 31b. ^{13}C NMR spectrum (100 MHz, $CDCl_3$)

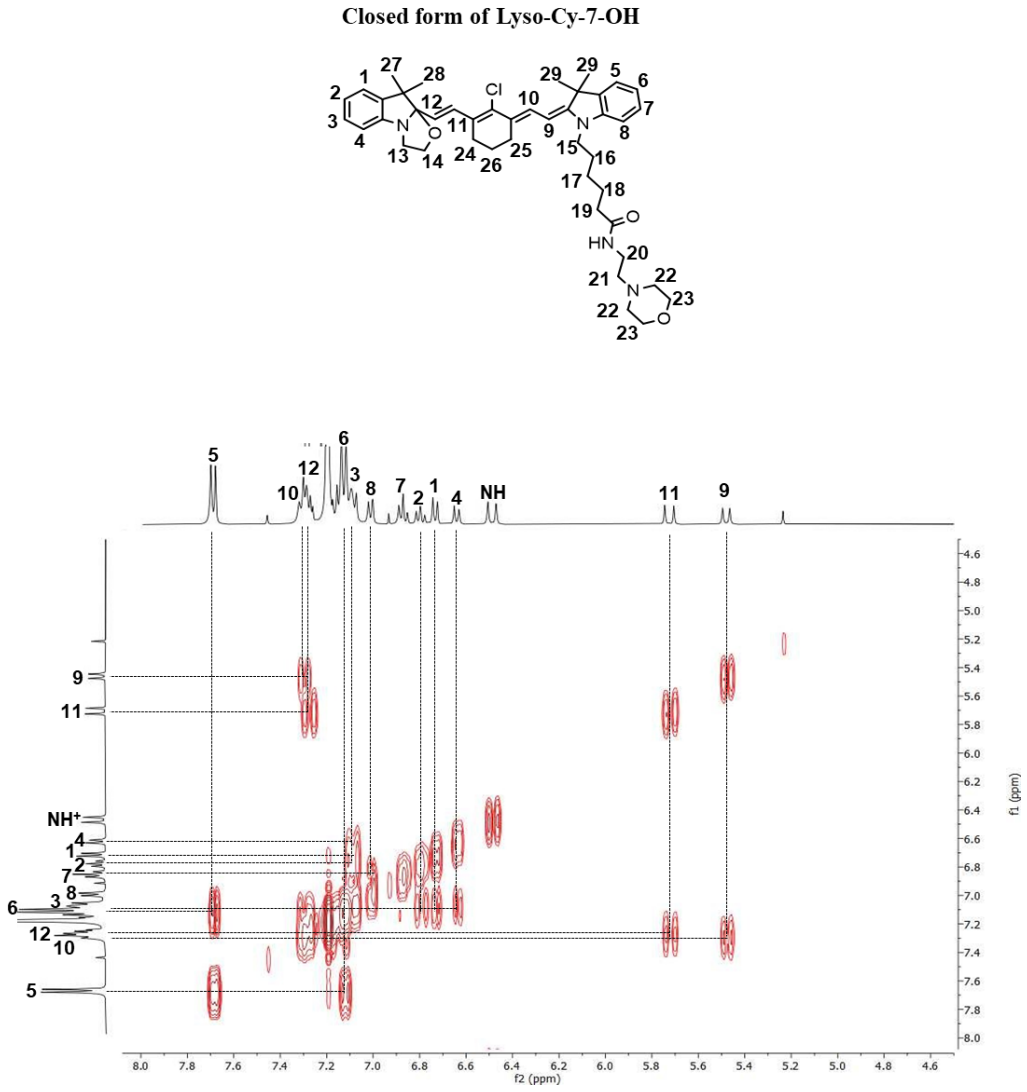

Figure 32a. Partial ^{1}H-^{1}H gCOSY (Gradient-selected Correlation Spectroscopy) NMR (300 MHz, $CDCl_3$, 25°C) spectrum of the closed form of Lyso-Cy-7-OH.

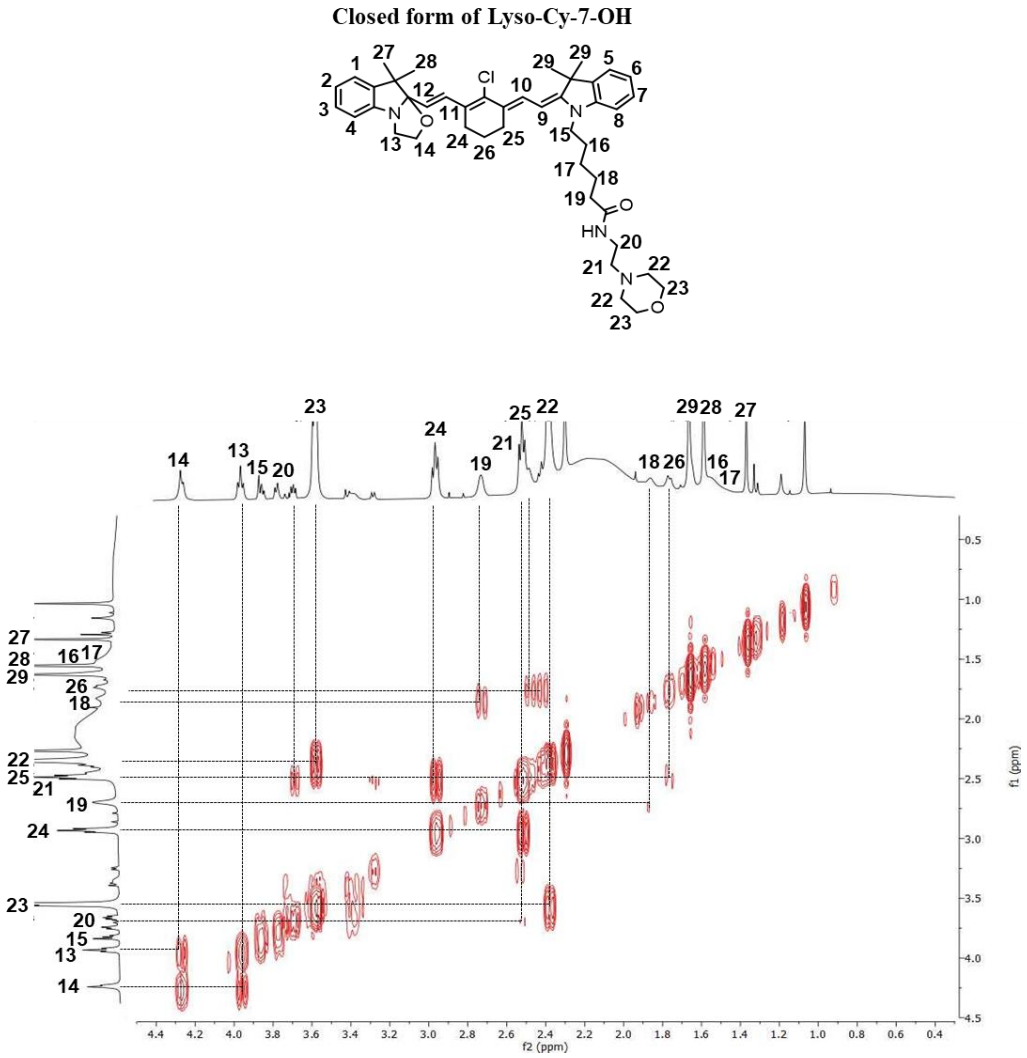

Figure 32b. Partial ^{1}H-^{1}H gCOSY (Gradient-selected Correlation Spectroscopy) NMR (300 MHz, $CDCl_3$, 25°C) spectrum of the closed form of Lyso-Cy-7-OH.

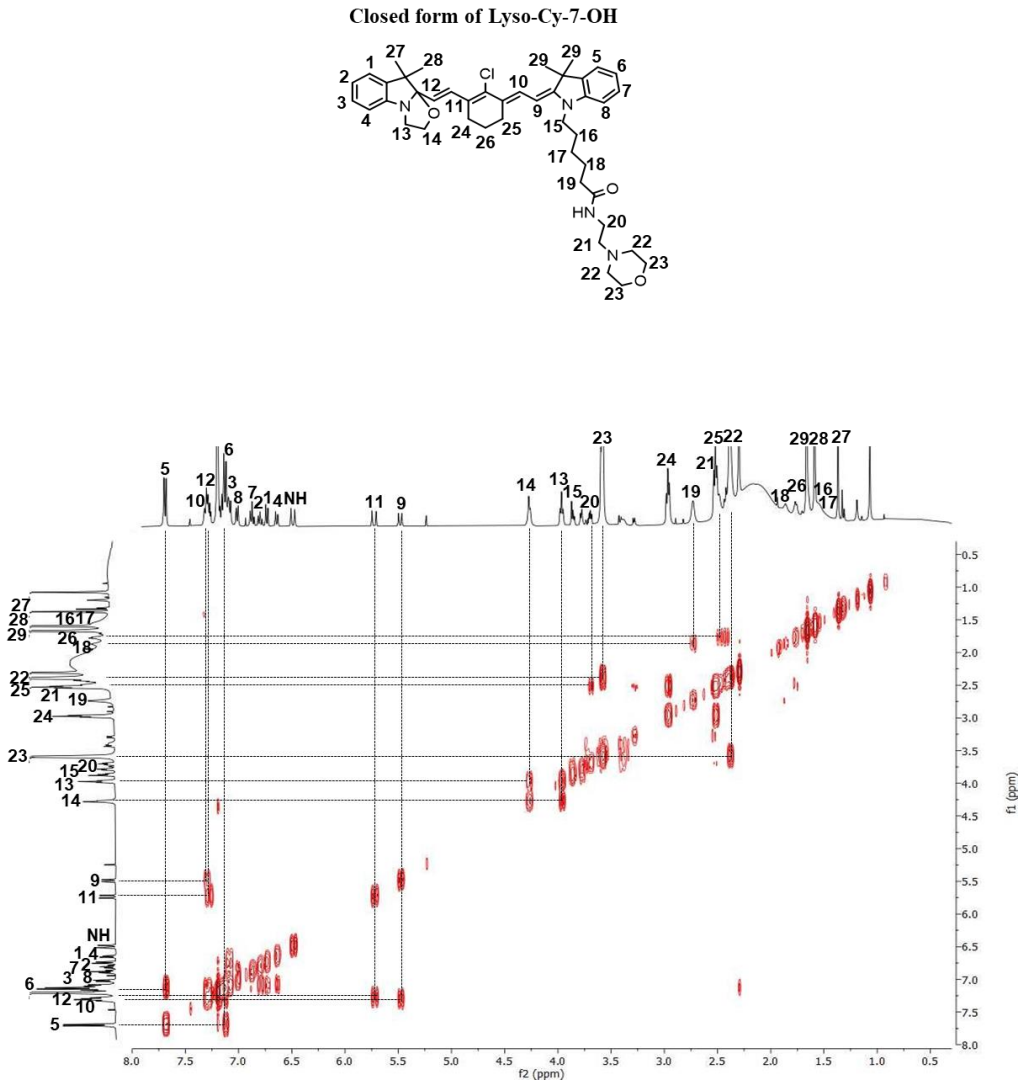

Figure 32c. ^{1}H-^{1}H gCOSY (Gradient-selected Correlation Spectroscopy) NMR (300 MHz, $CDCl_3$, 25°C) spectrum of the closed form of Lyso-Cy-7-OH.

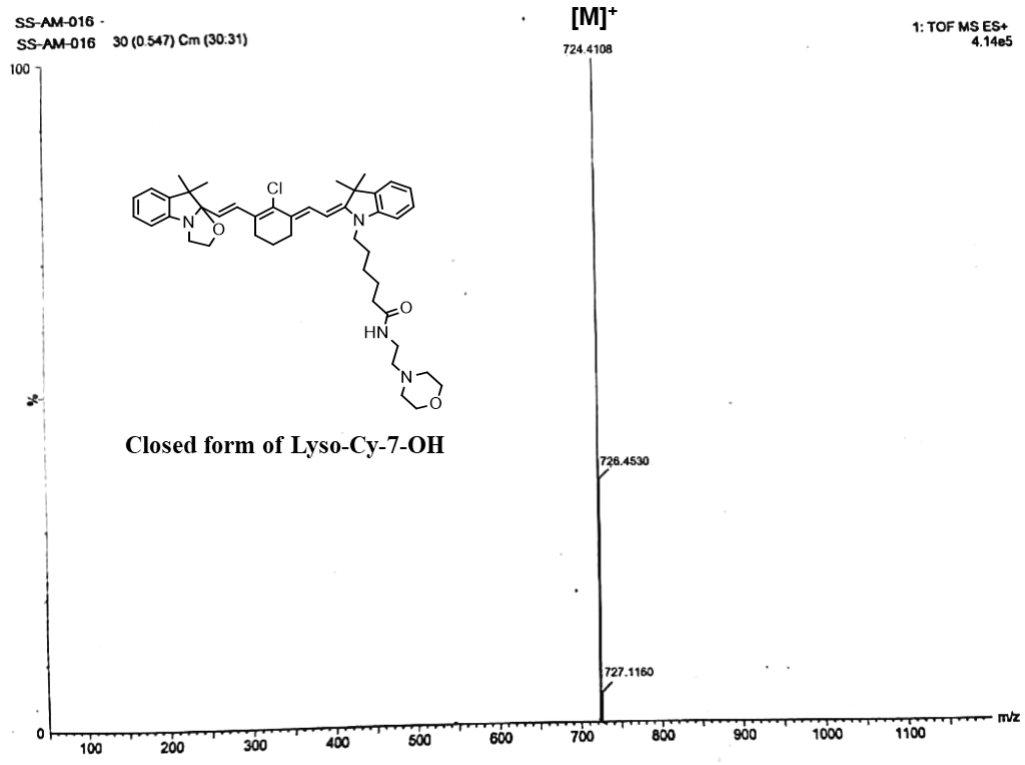

Figure 33: ESI-HRMS spectrum of the closed form of Lyso-Cy-7-OH.

Methods:

Single Crystal X-Ray Diffraction: Single crystals appropriate for X-ray diffractions were accomplished by slow evaporation method. A micro focus Single Crystal X-ray Diffraction instrument (Model: D8 Quest, Make: Bruker) with MoKα radiation (a graded multilayer mirror monochromator, λ = 0.71073 Å) at 293 K was used to collect the diffraction data. A PHOTON-100 CMOS detector was used. Structures of the compounds were solved by direct methods using the SHELXT 2014/5 program.[27,28] Refinements were performed with a

full-matrix least squares method against F^2 using SHELXL-2018/3[27,28] incorporated in Olex2[29] crystallographic collective package. The non-hydrogen atoms were refined with anisotropic thermal parameters.

Intermediate of Cy-7 (6): Reddish orange crystals were obtained by slow evaporation from MeOH. Formula sum = C21 H24 Cl N O2, formula weight = 357.86, crystal system = monoclinic, space group = *P* 2_1/c, *a* = 10.557(5) Å, *b* = 15.898(12) Å, *c* = 11.829(8) Å, β = 102.75(4)°, *V* = 1936(2) Å^3, Z = 4, D_{calcd} = 1.228 g cm^{-3}, μ = 0.211 mm^{-1}. The final R value was R_1 = 0.0852 and wR_2 = 0.2236 for reflections with I > 2ζ(I). CCDC number 2182669.

Cy-7-(OH)$_2$: The compound was dissolved in MeOH and stirred with NH_4PF_6 to obtain PF_6^- counter anion of the molecule **Cy-7-(OH)$_2$**. The solvent was evaporated and the residue was washed with cold water. The compound was dissolved in MeOH and after 7 days green colored block shaped crystals were obtained by slow evaporation from MeOH. Formula sum = C34 H40 Cl N2 O2, F6 P, formula weight = 689.10, crystal system = monoclinic, space group = *P* n, *a* = 7.9611(7) Å, *b* = 12.5732(11) Å, *c* = 17.6749(15) Å, β = 101.651(2)°, *V* = 1732.7(3) Å^3, Z = 2, D_{calcd} = 1.321 g cm^{-3}, μ = 0.221 mm^{-1}. The final R value was R_1 = 0.0994 and wR_2 = 0.2099 for reflections with I > 2ζ(I). CCDC number 2182670.

High-Resolution Electrospray Ionization Mass Spectrometry (HRMS-ESI): HRMS-ESI in positive mode was acquired on a Q-Tofmicro (Waters Corporation) mass spectrometer. The data were recorded and processed by manufacturers' supplied mass application software MassLynx V4.1.

NMR Spectroscopy: ^{1}H NMR, ^{13}C NMR, and ^{1}H-^{1}H gCOSY were recorded on Bruker DPX300 MHz and DPX400 MHz spectrometers at 298 K in suitable

deuterated solvents. Manufacturers' supplied Bruker TopSpin 3.6.2 software was used to process the data.

UV/vis Spectroscopy: Absorption spectra were obtained on a JASCO V-730 double-beam spectrophotometer with wavelength range from 200 to 1100 nm. All the measurements were carried out using a quartz cuvette of 1 cm path length. The data were processed by manufacturers' supplied Spectra Manager Version 2 software and controlled by a PC. The absorption ratio (I_{780}/I_{418}) was obtained from the absorption intensities at 780 nm and 418 nm.

Fluorescence Spectroscopy: Horiba Jobin Yvon FluoroMax-4 spectrofluorometer (Horiba Scientific) operated by a FluorEssence Version 3.9.0.1 software was used to obtain fluorescence spectra. 5 nm excitation and emission slit widths were used. The fluorescence ratio (I_{800}/I_{480}) was obtained from the fluorescence intensities at 800 nm and 480 nm.

Time-Correlated Single Photon Counting (TCSPC) Experiment: Fluorescence lifetime (τ) of closed basic oxazolidine form and open acidic Cy-7 form were measured in solution by a Horiba DeltaFlex lifetime machine (Horiba Jobin Yvon IBH Ltd, UK) using time-correlated single photon counting (TCSPC) method. 415 nm (Model: DD-415L, Horiba Scientific) and 785 nm (Model: DD-785L, Horiba Scientific) delta diode laser excitation sources were used to measure the τ of the closed oxazolidine form and open Cy-7 form, respectively, in DMSO. Horiba EzTime decay analysis software was utilized to analyses the τ data.

pH Titrations: Mettler Toledo pH meter was used to make the buffer solutions of various pH values and the instrument was calibrated with the authentic buffer solutions of pH 4.01 ± 0.01, 7.00 ± 0.01, and 10.00 ± 0.01 at 25°C. For the pH titration Britton–Robinson universal buffer solution of various pH values were prepared. All aqueous buffered solutions were freshly prepared and

kept in a refrigerator (used within one week). A concentrated stock solution (75 μM) of the closed oxazolidine form in DMSO was prepared. Aliquot of the stock solution was quantitatively added to the aqueous buffer solutions of various pH values to achieve the final concentration of the probe of 2 μM. The solutions were stirred before recording the spectra. Absorption and emission pH titration plots were measured in triplicate and the consequences were expressed as the mean ± standard deviation.

Fluorescence Quantum Yields of Basic Closed Oxazolidine State and Acidic Open Cy-7 Form: Fluorescence quantum yields (Φ_f) of basic closed oxazolidine and acidic open Cy-7 forms were measured by relative method. Concentrations of the probes were adjusted such a way that the λ_{max} was less than 0.1 to avoid inner filter effect. Here, the integrated fluorescence intensities of basic closed oxazolidine and open acidic Cy-7 forms were compared with the emission intensities of standard fluorophores using the successive equation (Table S3):

Φ_f (u) = Φ_f (st) × [(A_{st} × F_u × η_u^2) /(A_u × F_{st} × η_{st}^2)]

Φ_f(st): Fluorescence quantum yield of the reference fluorophore

Φ_f(u): Fluorescence quantum yield of the synthesized closed oxazolidine form or open Cy-7 form

A_{st} and A_u: Absorbance of reference and synthesized compounds at the excitation wavelength, respectively

F_{st} and F_u: Integrated fluorescence areas under the adjusted fluorescence spectra for the reference and synthesized compounds, respectively

η_{st} and η_u: Refractive indices of the solvent where the reference and synthesized molecules were studied, respectively

"u" refers to the unknown molecule and "st" stands for the standard molecule

Φ_f (s) of Coumarin 6 in absolute EtOH is 0.78 and used as the reference for closed oxazolidine form.

Φ_f (s) of ICG in DMSO is 0.12 and used as the reference for open Cy-7 form.

Cell Culture: Human cervix adenocarcinoma epithelial HeLa and lung adenocarcinoma A549 cell lines were independently cultured in Dulbecco's modified Eagle medium (DMEM, pH 7.4) supplemented with 10% fetal bovine serum (FBS) and antibiotic-antimycotic solution 100×(containing 10000 units penicillin, 10 mg streptomycin, and 25 μg amphotericin B per mL in 0.9% normal saline) in an air-jacketed 5% CO_2 incubator at 37°C and was routinely passaged.

Cell Viability Assay: The cytotoxicity of the pH activatable probe on HeLa and A549 cell lines were tested by 3-(4,5-dimethylthiazol-2-yl)-2,5-diphenyltetrazolium bromide (MTT) assay. HeLa and A549 cell lines were individually seeded at a density of ~10^4 cells in a 96-well plate and incubated for 24 h in DMEM. After 24 h incubation, closed oxazolidine and open Lyso-Cy-7-OH forms were independently treated at various doses (1, 2, 5, 10, 15, and 20 μM per well) for 24 h at 37°C. HeLa and A549 cell lines were then individually incubated with 10 μL MTT solution (5 mg mL^{-1} in PBS) for 4 hour in darkness at 37°C. Formazan crystals (dark blue) were dissolved in DMSO and the absorbance (*A*) at 575 nm was measured (recorded in triplicate) by an ELISA plate reader. The results were expressed by the following equation:

Cell Viability (%) = (*A* of treated cells / *A* of untreated cells) × 100

Live Cell Confocal Laser Scanning Microscopy: A Leica STELLARIS 5 with white light laser (WLL) combined with Acousto-Optical Beam Splitter (AOBS) and HyD S detectors was used for the live cell confocal laser scanning

microscopy (CLSM). It was equipped with a 100x /1.40 (Specification: HC PL APO 100x/1.40 OIL CS2) oil plan apochromatic objective. A unique set-up for the live cell confocal microscopy instrument maintaining 37°C and 5% CO_2 atmosphere is shown. Confocal microscopic images were analyzed and processed by Leica Application Suite X (LAS X 4.3.0.24308) software. HeLa and A549 cell lines were independently seeded in a 35 mm glass bottomed cell culture confocal dishes (SPL Lifesciences) at a density of 10^4 cells/mL and permitted to grow in DMEM for 24 h at 37°C in a humidified 5% CO_2 incubator. Later the cells were washed with 1x PBS (three times). Subsequently, HeLa and A549 live cells were separately incubated with oxazolidine state of Lyso-Cy-7-OH (1.0 μM) in media for 15 min in 5% CO_2 atmosphere at 37°C and then rinsed with 1x PBS three times. According to the manufacturer's protocol the cells were incubated with LysoTracker Green DND-26 (75 nM) at 37°C for 30 min in 5% CO_2 atmosphere. The cell lines were finally incubated with Hoechst (1.5 μg/mL) for 20 min and washed in the similar protocol. Before CLSM imaging the cells were washed with 1x PBS (three times) and phenol red free media was added. All over the live cell CLSM imaging 37°C and 5% CO_2 atmosphere was preserved.

For Hoechst: laser excitation wavelength = 405 nm (blue channel, detection range of emission wavelength 415–490 nm); LysoTracker Green DND-26 (LTG): laser excitation wavelength = 498 nm (green channel, detection range of emission wavelength 500–572 nm); pH activatable Lyso-Cy-7-OH probe: laser excitation wavelength 670 nm (red channel, detection range of emission wavelength 700–780 nm).

Pearson's Correlation Coefficient (PCC): Pearson's correlation coefficient (PCC) is one of the typical statistical analysis in pattern recognition for

matching one CLSM image (green channel defines LysoTracker Green DND-26 staining) with another (red channel designates acidic pH activatable Lyso-Cy-7-OH probe). PC graph can elucidate the extent of overlapping between two patterns in a colocalization image. PCC was calculated by the LAS X software by Quantify tool.

PCC was calculated (image including red and green channels) by the subsequent equation:

$$PCC = \frac{\sum_i (S1_i - S1_{avg}) * (S2_i - S2_{avg})}{[\sum_i (S1_i - S1_{avg})^2 * \sum_i (S2_i - S2_{avg})^2]^{(1/2)}}$$

S1 = signal intensity of pixels (pixel i) in the green channel

S2 = signal intensity of pixels (pixel i) in the red channel.

$\mathbf{S1_{avg}}$ = mean values of pixels in the green channel

$\mathbf{S2_{avg}}$ = mean values of pixels in the red channel.

Live Cells 3D Confocal Images using Synthesized Acidic pH Activatable Lyso-Cy-7-OH Probe: To obtain the 3D view of lysosomal staining, Z-stack images of live HeLa as well as A549 cells stained with Hoechst (nuclear staining dye) and the synthesized acidic pH activatable Lyso-Cy-7-OH probe were acquired by a Leica STELLARIS 5 confocal microscope. For the live cell 3D CLSM image production, the images were harvested every 0.4 μm on the Z-axis. Eighteen different frames for each channel were snapped over a time period of 6 min and finally reconstructed with the help of LAS X software to obtain the 3D CLSM image. This 3D reconstructed CLSM images designates the spherical lysosomes inside the live HeLa and A549 cells.

Ratiometric Confocal Microscopic Images using Acidic pH-Activatable Lyso-Cy-7-OH Dye: The cultured HeLa and A549 cells were incubated separately with acidic pH activatable closed form of Lyso-Cy-7-OH (1 μM) for 15 min in 5% CO_2 atmosphere at 37°C in a glass bottomed culture dishes without adding any other staining agent. After washing the cells with 1X PBS, ratiometric confocal microscopic images of live HeLa as well as A549 cells were acquired by dual channel excitation (green channel and red channel), respectively. The exposure times for each filter were kept constant. To get pixel based ratiometric imaging, confocal images captured by a Leica STELLARIS 5 confocal microscope were processed by ImageJ software (ImageJ 2.1.0; Java 1.8.0_172) with a preinstalled Ratio_Plus.class plugin (downloaded from Ratio_Plus.java source and installed in the plugins folder or subfolder). Before ratiometric imaging, both channel 1 (red) and channel 2 (green) single images of the same width and height and of the same type (8 or 16 or 32 bit) were taken. Then background subtraction was carried out for each channel [channel 1 (red) and channel 2 (green)] and ratiometric images were generated by selecting following operations:

Select menu bar ⇨ Process ⇨ Calculator Plus ⇨ Select Channel 1 and Channel 2 ⇨ Select operation for Channel 1 and Channel 2 ratio.

Selected operation, intR= $(i_1/i_2)*K_1+K_2$, where i_1= intensity of Channel 1 (red channel) after subtraction of constant background value, i_2= intensity of Channel 2 (green Channel) after subtraction of constant background value. K_1 arbitrary multiplication factor which is taken as 1 and K_2= 0.

The constructed pseudocolored ratiometric images (I_{red}/I_{green}) represent the pH values of the exact positions.

Real-Time Tracking of Lysosomes in Live Cells by Synthesized Acidic pH-Activatable Lyso-Cy-7-OH Dye: Lysosomal movement in the live HeLa and A549 cells were monitored by a Leica STELLARIS 5 instrument using the synthesized lysosome targeting acidic pH activatable Lyso-Cy-7-OH probe over a time course of 70-83 seconds. 10 frames were captured over 70 seconds for HeLa and 83 seconds for A549 cells to make separate real-time movies using LAS X software.

Multicolor Confocal Imaging of Live Cells: Multicolor imaging of intracellular organelles in the same live cell was acquired by a mixture of suitable organelle targeting probes with distinct excitation/emission bands. MitoTracker Green (MTG, green emitting) was used to specifically stain the mitochondria, blue-fluorescent Hoechst to label the nucleus, and the synthesized acidic pH activatable Lyso-Cy-7-OH probe to stain the lysosomes of live A549 and HeLa cells.

Multicolor confocal imaging of live A549 and HeLa cell lines were captured by using appropriate filters.

For MTG, laser excitation wavelength = 488 nm (green channel, detection range of emission wavelength 499–544 nm).

Hoechst, laser excitation wavelength = 405 nm (blue channel, detection range of emission wavelength 415–490 nm).

Synthesized acidic pH activatable Lyso-Cy-7-OH probe, laser excitation wavelength = 670 nm (red channel, detection range of emission wavelength 700–780 nm).

Synthesis, Purification, and Characterization of the Compounds: Symmetrical and unsymmetrical closed and open form of Cy-7 dyes and their precursor molecules were synthesized by an effective method with reasonable yield from easily accessible low-cost starting materials. Analytical TLC (TLC

silica gel 60 F_{254}) was accomplished on silica gel covered aluminum sheets with suitable solvent mixtures and identified by naked eye or UV lamp. The synthesized molecules were purified through column chromatography by silica gel 100-200 mesh. The solvents used for chromatography were distilled prior to their use. The compound 2,3,3-Trimethylindolenine (1) was synthesized by our previously reported procedure.[30]

Results and Discussion

Design and Synthesis: The synthetic methods permitted us to covalently link the nitrogen of 2,3,3-trimethylindolenine with 2-hydroxyethyl (**2**), fused oxazolidine ring (pH switchable group, **3**), 2-acetoxyethyl (OH is protected as acetyl group, **4**), and carboxylic (–COOH, **7**, to conjugate with NH_2 functionality of the lysosome targeting moiety, **8**) functionality by suitable alkylating agents (Figures 2-11). Synthesis of unsymmetrical probe is more challenging and essential than symmetrical probe. We have efficiently constructed the intermediate (*E*)-2-chloro-3-(2-((*E*)-1-(2-hydroxyethyl)-3,3-dimethylindolin-2-ylidene)ethylidene)cyclohex-1-ene-1-carbaldehyde **(6)** from cyclohexanone by Vilsmeier-Haack synthesis followed by condensation reaction with indolium salt **2** (Figures 1, 12-15). The compounds Cy-7-$(OH)_2$ (closed and open form), Cy-7-OH-OAc (closed and open form), Cy-7-OH-COOH, Cy-7-$(OAc)_2$, and Lyso-Cy-7-OH (closed and open form) are synthesized from the intermediate **6** by condensation with suitable quaternized heterocycles in *n*-butanol/benzene (7:3) (Figures 1, 16-33). The basic closed Lyso-Cy-7-OH form contains lysosome-targeting 4-(2-aminoethyl)morpholine moiety and acidic pH openable oxazolidine functionality (Figure 34).[26,27] The unsymmetrical closed and open Lyso-Cy-7-OH states are obtained in decent yield and characterized by NMR (1D and 2D) spectroscopy and HRMS (Figure

28-33). In the closed state multiplets obtained between 4.3–3.9 ppm due to the $-CH_2-CH_2-$ protons of the fused oxazolidine ring which is downfield shifted at 4.6 and 4.1 ppm as two triplets (J = 5.8 Hz) after acidification, are characteristic ^{1}H NMR peaks for $-CH_2-CH_2-$

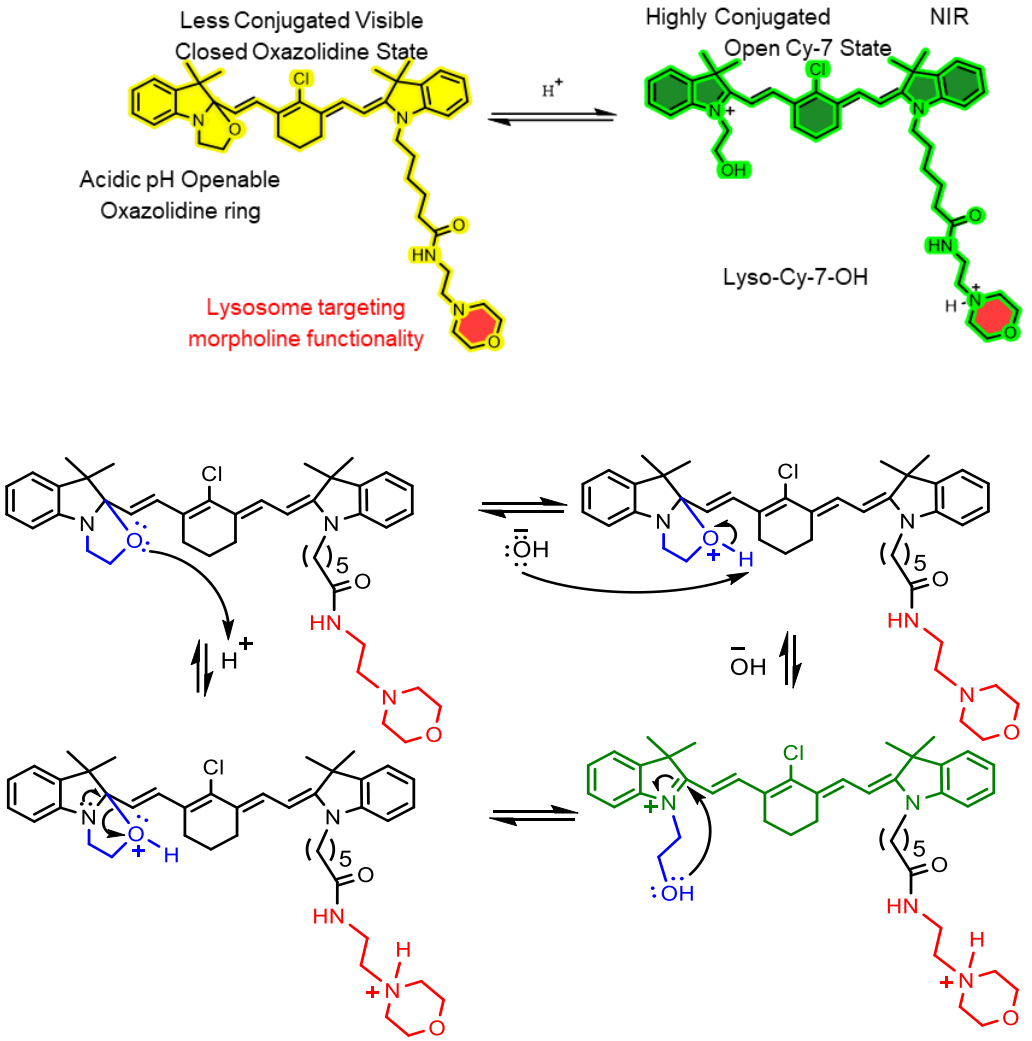

Figure 34. Basic closed and acidic open Cy-7 state and their interconversion.

protons of pendant hydroxyethyl moiety of the open state Lyso-Cy-7-OH (Figures 35, 28a, 31a).[31-33] In addition after acidification four doublets with *J* ~ 14.2 Hz proved the conjugated all *trans* double bond configuration of unsymmetrical open Lyso-Cy-7-OH form (Figure 35).

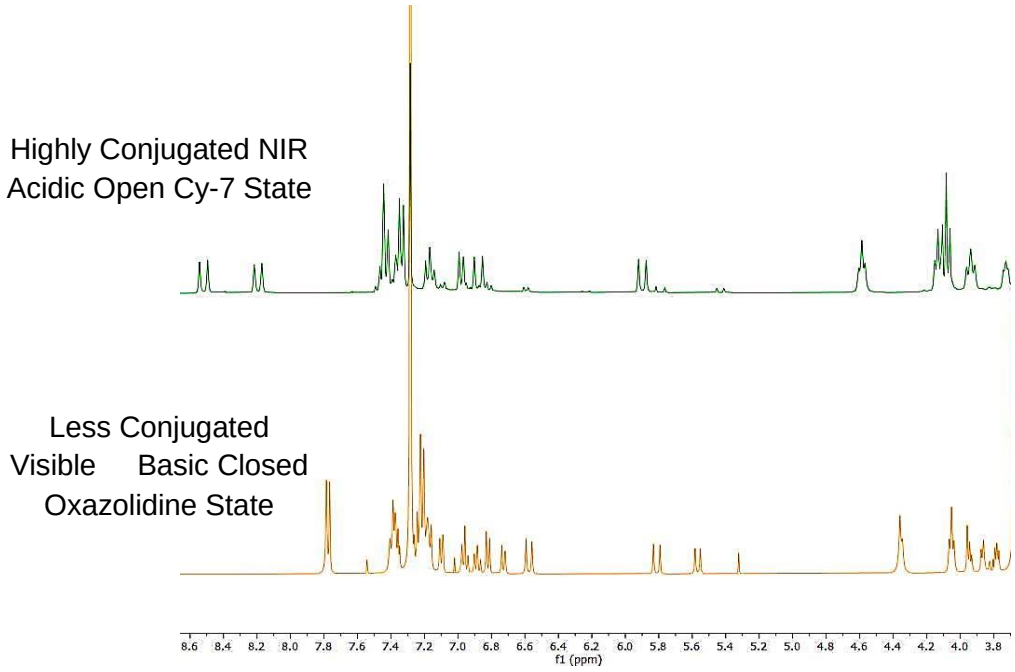

Figure 35. Partial ^{1}H NMR (300 MHz, $CDCl_3$, 25°C) stacking plot of the basic closed and acidic open Cy-7 state of Lyso-Cy-7-OH.

X-Ray Crystal Structures: Single crystals of the active intermediate **6** (reddish orange crystals) and the open form of Cy-7-$(OH)_2$ (green crystals) appropriate for X-ray diffractions are accomplished by slow evaporation from MeOH solution at room temperature (Figure 36a,b and Table1). The intermediate 6 crystallizes in the noncentrosymmetric monoclinic *P* 2_1/c space group. With PF_6^- counter anion [methanol solution of the compound is stirred with NH_4PF_6 to obtain PF_6^- counter anion containing cationic molecule Cy-7-

$(OH)_2$] the cationic open form of Cy-7-$(OH)_2$ crystallizes in a monoclinic *P* n space group containing a half-chair puckering conformation of the central six membered ring. Single crystal X-ray structures confirm all *trans* conjugated double bond conFigureurations of **6** and the open form of Cy-7-$(OH)_2$ that is also in fair agreement with the *J* values obtained in solution state ^{1}H NMR. Moreover, *syn* orientations of the indoline residues are observed in the crystal structure of the open form of Cy-7-$(OH)_2$. Crystal structure of Cy-7-$(OH)_2$ reveals that the two indoline N atoms and the nine sp^2-hybridized conjugated C linkages lie in an almost same plane (Figure 36b).

(a)

(b)

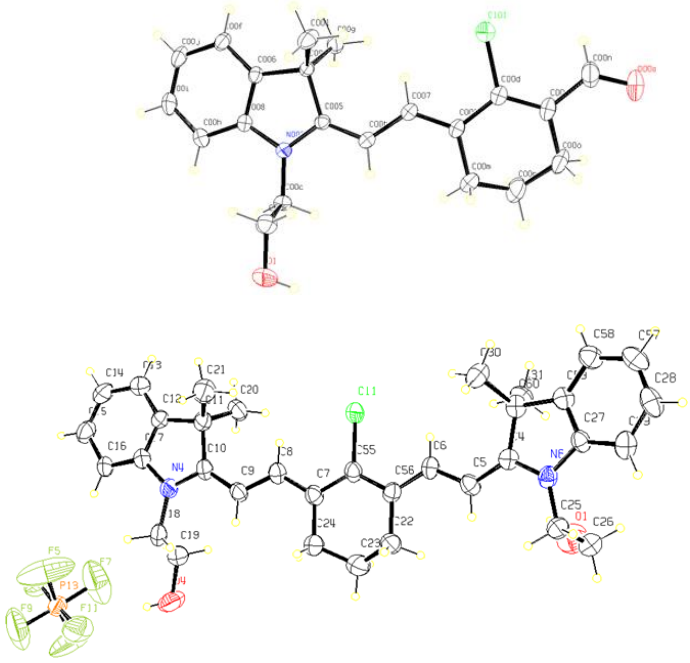

Figure 36. Lyso-Cy-7-OH. Single crystal X-ray structures (ORTEP diagrams) of (a) the intermediate compound 6 and (b) the acidic open form of Cy-7-$(OH)_2$.

Description	Intermediate of Cy-7 (Compound 6)	Cy-7-$(OH)_2$
formula sum	C21 H24 Cl N O2	C34 H40 Cl N2 O2, F6 P
formula weight	357.86	689.10
crystal system	monoclinic	monoclinic
space group	$P\ 2_1/c$	$P\ n$
a (Å)	10.557(5)	7.9611(7)
b (Å)	15.898(12)	12.5732(11)
c (Å)	11.829(8)	17.6749(15)
α (°)	90	90
β (°)	102.75(4)	101.651(2)
γ (°)	90	90
V (Å^3)	1936(2)	1732.7(3)
Z	4	2
D_{calcd} (g cm^{-3})	1.228	1.321
μ (mm^{-1})	0.211	0.221
T (K)	293K	273 K
λ (Å)	0.71073	0.71073
R_1	0.0852	0.0994
wR_2	0.2236	0.2099
CCDC No.	2182669	2182670

Table 1. Crystallographic data of the compounds.

This leads to the possibility of a strong charge delocalization along the 11-membered push pull system. Moreover, the two aromatic rings are also in the same plane with respect to the extended π-conjugated molecular plane. The C–C (~1.39 Å) and C–N (~1.35 Å) bond lengths of the push-pull system have intermediate values between those of single and double bonds which confirm

Compound	Bond	Bond length (Å)
Intermediate of Cy-7 (Compound 6)	C_{00n}-O_{00a}	1.214
	C_{00n}-C_{00e}	1.451
	C_{00e}-C_{00d}	1.357
	C_{00d}-C_{009}	1.437
	C_{009}-C_{007}	1.36
	C_{007}-C_{00b}	1.413
	C_{00b}-C_{005}	1.359
	C_{005}-N_{002}	1.372
Compound	**Bond**	**Bond length (Å)**
$Cy\text{-}7\text{-}(OH)_2$	C_{10}-N_4	1.341
	C_{10}-C_9	1.397
	C_9-C_8	1.383
	C_8-C_7	1.39
	C_7-C_{55}	1.414
	C_{55}-C_{56}	1.409
	C_{56}-C_6	1.387
	C_6-C_5	1.392
	C_5-C_4	1.378
	C_4-N_6	1.356

Table 2. Bond lengths along the push-pull polymethine chain of the intermediate compound 6 and the open form of $Cy\text{-}7\text{-}(OH)_2$.

that the Cy-7-$(OH)_2$ owns a delocalized cationic charge with insignificant bond-length alternation through the heptamethine chain (Table 2).

Photophysical Property: The distinctive changes of the Cy-7-$(OH)_2$ as well as Cy-7-OH-OAc structures at low and high pH are detected owing to the H^+ activated oxazolidine ring-opening to build a highly conjugated push-pull Cy-7 form, consequently red shift in the λ_{abs} / λ_{em} from visible to the NIR region are observed (Figures 37-41).

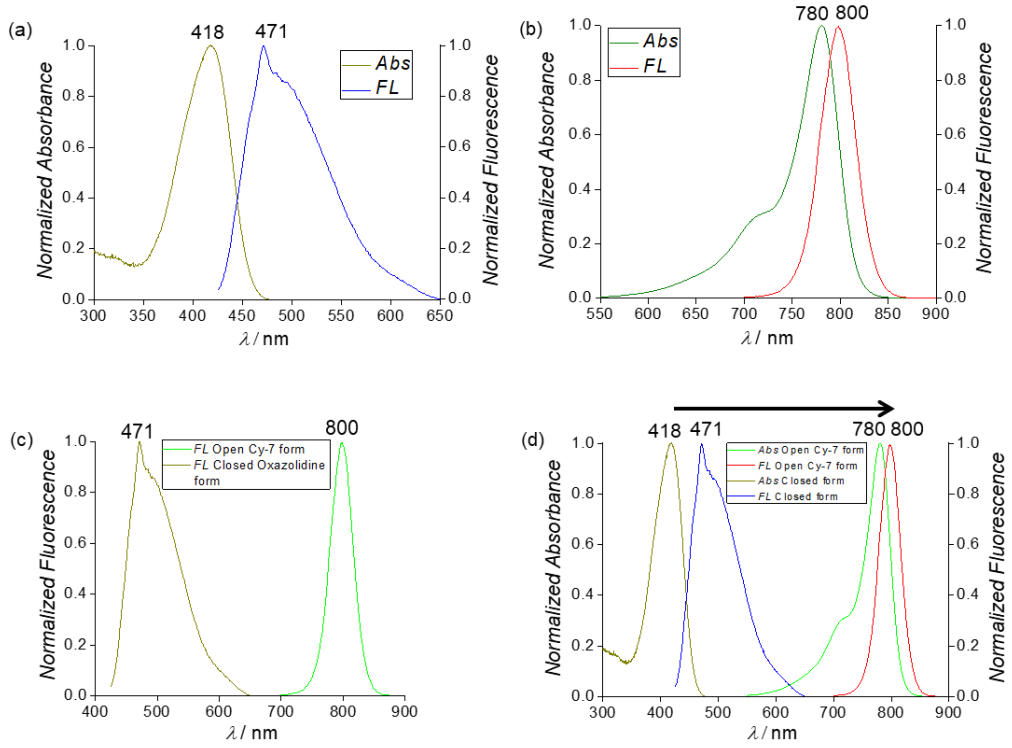

Figure 37. (a) Normalized UV/vis absorption and fluorescence merge plot of the closed form of Cy-7-$(OH)_2$ (2 μM) in DMSO. (b) Normalized UV/vis absorption and fluorescence merge plot of the open form of Cy-7-$(OH)_2$ (2 μM) in DMSO. (c) Normalized emission plot of both the open and closed form of

Cy-7-$(OH)_2$ (2 μM) in DMSO. (d) Normalized absorption and fluorescence merge plot of both the open and closed form of Cy-7-$(OH)_2$ in DMSO.

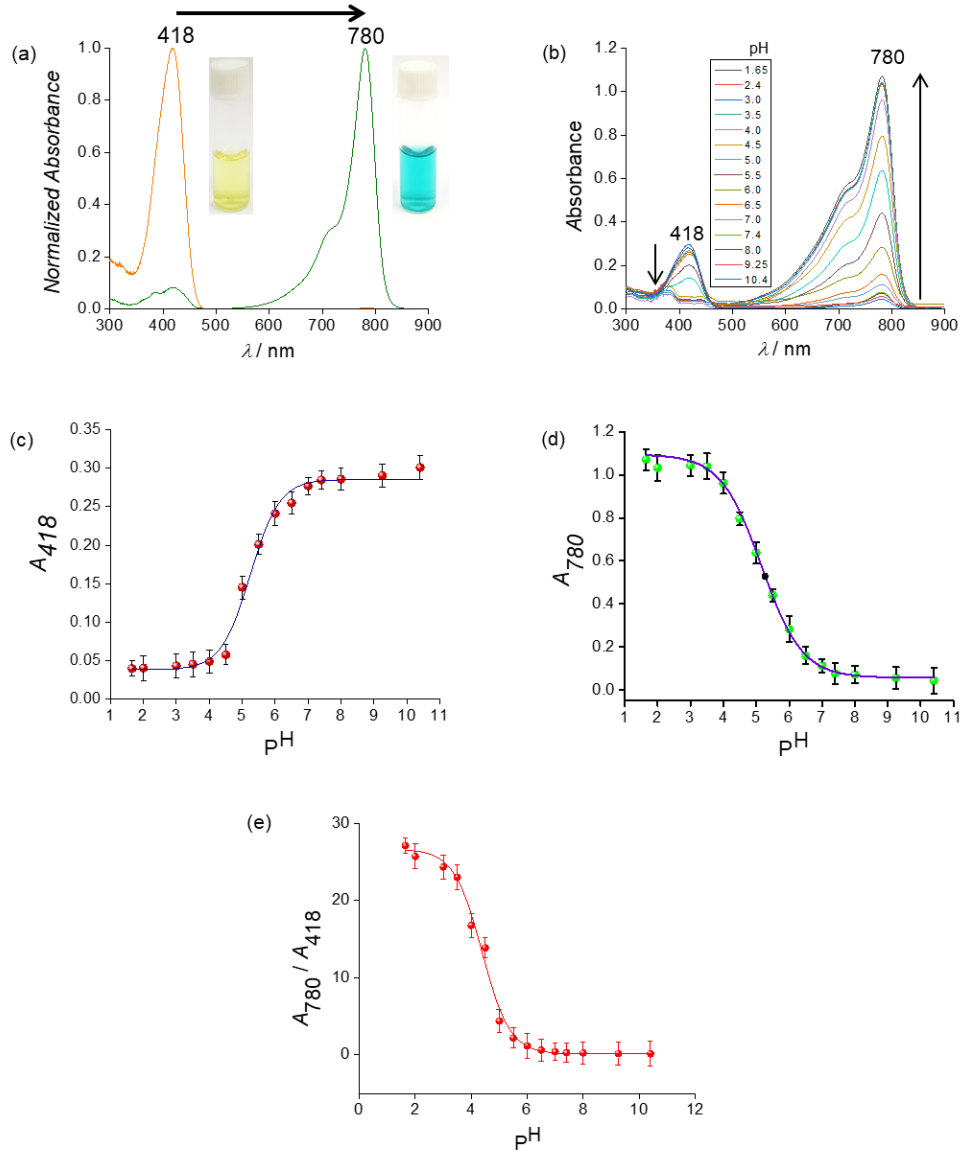

Figure 38. (a) Normalized absorption plot for the open and closed form of Cy-7-$(OH)_2$ (2 μM) in DMSO. (b) pH titration plot of Cy-7-$(OH)_2$ in buffer

solutions. (c) Absorbance (418 nm) vs pH plot. (d) Absorbance at 780 nm vs pH changes. (e) Ratiometric absorbance (A_{780}/A_{418}) vs pH plot.

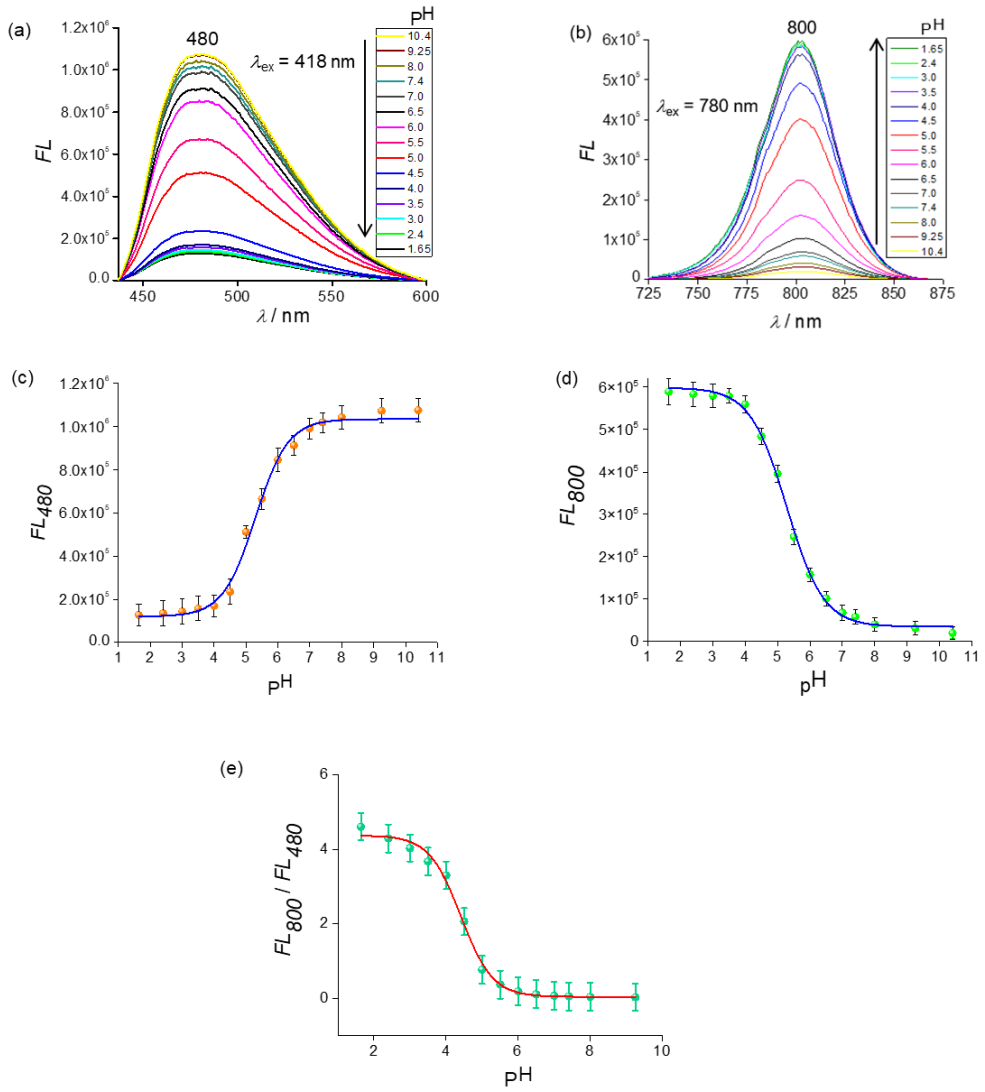

Figure 39. (a) Fluorescence emission plot of Cy-7-$(OH)_2$ (2 μM) at λ_{em} 480 nm (λ_{ex} 418 nm) in buffer solutions at different pH. (b) Fluorescence emission plot for Cy-7-$(OH)_2$ at λ_{em} 800 nm (λ_{ex} 780 nm) in buffer solutions at different pH. (c) Emission at 480 nm (λ_{ex} = 418 nm) vs pH changes. (d) Emission at 800 nm

(λ_{ex} = 780 nm) vs pH changes. (e) Ratiometric fluorescence emission (FL_{800}/FL_{480}) plot vs pH.

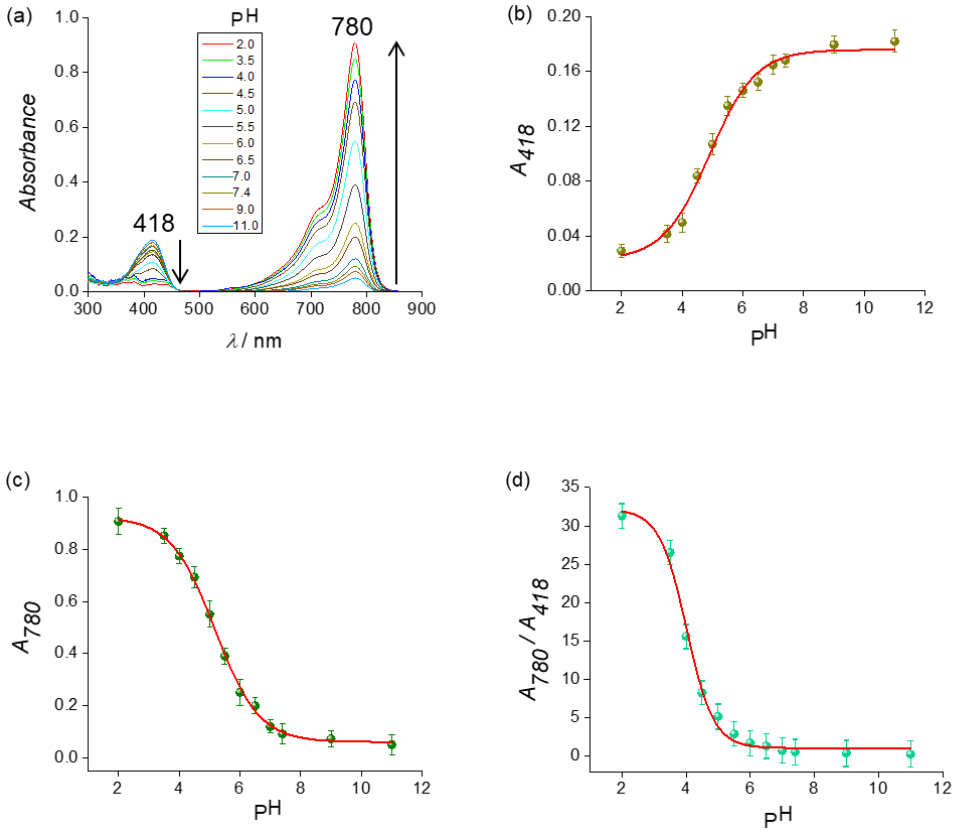

Figure 40. (a) Absorption plot of Cy-7-OH-OAc (2 μM) at various pH. (b) Absorption at 418 nm vs pH plot for Cy-7-OH-OAc. (c) Absorption at 780 nm vs pH plot for Cy-7-OH-OAc. (e) Ratiometric absorption (A_{780}/A_{418}) plot at various pH.

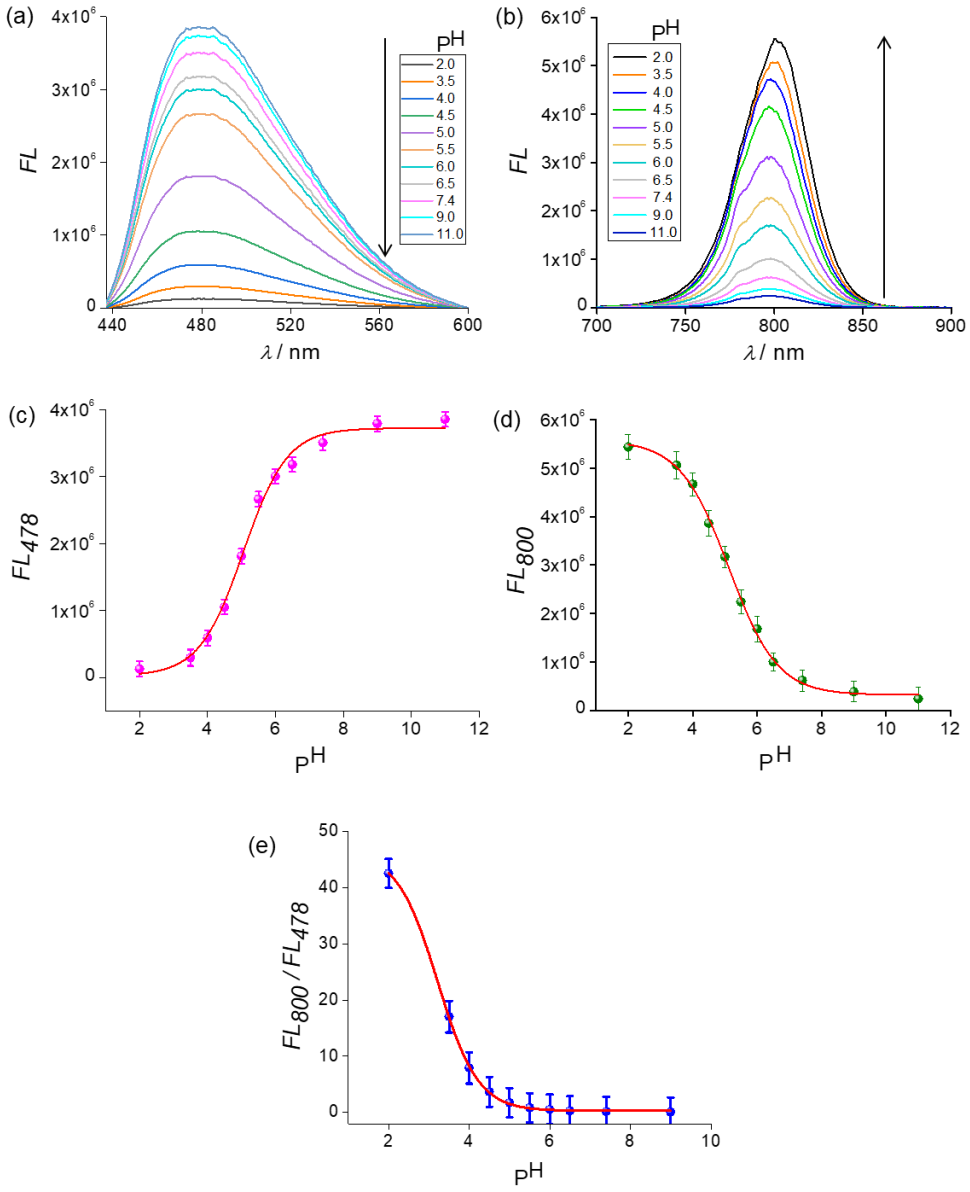

Figure 41. (a) Fluorescence emission plot at λ_{ex} = 418 nm of Cy-7-OH-OAc (2 μM) at various pH. (b) Fluorescence emission plot at λ_{ex} = 780 nm of Cy-7-OH-OAc (2 μM) at various pH. (c) Fluorescence emission at 478 nm vs pH curve. (d) Fluorescence emission at 800 nm vs pH curve. (e) Ratiometric fluorescence (FL_{800}/FL_{478}) plot at various pH values.

A reversible pH-triggered absorption/emission spectral shift are detected owing to the hydroxyl group attacks the sp^2 carbon of the indolium residue to form a 5 membered ring by 5-endo-trig cyclization and that the generated acidic proton is taken by a base to form the fused oxazolidine ring, thus extended conjugation in heptamethine chain is broken and blue shift is perceived (Figure 34). Absorption and fluorescence pH titrations are executed in different pH buffer solutions at a dye concentration of 2.0 μM. Yellow colored basic closed oxazolidine state of Cy-7-$(OH)_2$ or Cy-7-OH-OAc displays λ_{abs} at 418 nm in the visible region and during the pH titration a green colored highly conjugated open Cy-7 form of Cy-7-$(OH)_2$ or Cy-7-OH-OAc is generated at acidic pH and a new λ_{abs} peak at 780 nm started to form and augmented with simultaneous diminution of the 418 nm peak with an isosbestic point at ~500 nm (Figures 38b, 40a). The λ_{em} peaks and intensities in closed oxazolidine state and open Cy-7-$(OH)_2$ state are drastically different. At basic pH emission of the closed oxazolidine state is detected in the visible region ($\lambda_{ex}/\lambda_{em}$ 418 nm/480 nm) and during pH titration the emission intensity at 480 nm progressively reduces alongside a new NIR λ_{em} peak at 800 nm (λ_{ex} 780 nm) is turned on and undergone simultaneous augmentation with diminishing pH owing to the switching on open Cy-7 state (Figures 39, 41). Both the molecules Cy-7-$(OH)_2$ and Cy-7-OH-OAc, where two and one OH functionality are present, respectively, exhibited reversible pH-switching property, however, the molecule Cy-7-$(OAc)_2$ where OH are protected by acetyl group does not exhibit pH switching property (Figure 42a,b).

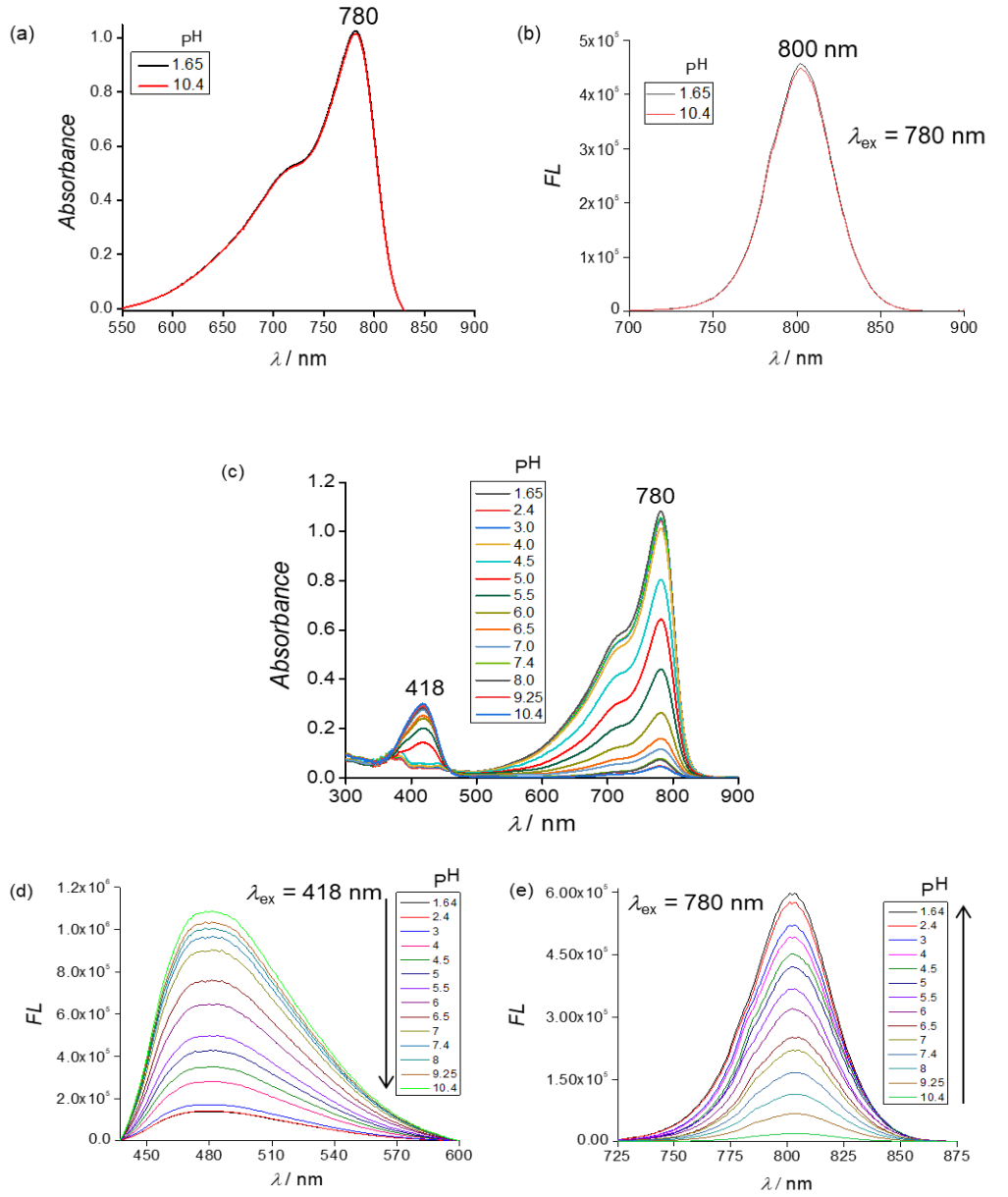

Figure 42. (a) Absorption and (b) fluorescence emission plots of Cy-7-$(OAc)_2$ showing negligible change in response to pH. Esterase activated pH switching. (c) absorption and (d,e) emission behavior is notices after the treatment of Cy-7-$(OAc)_2$ (2 μM) probe with 10.0 U/mL easterase.

However, the pH insensitive diester molecule Cy-7-$(OAc)_2$ exhibits esterase enzyme activated pH switching behavior (Figure 42c-e).[32] The morpholine functionalized closed form of Lyso-Cy-7-OH displays massive absorption ($\Delta\lambda_{abs}$ 362 nm) and emission ($\Delta\lambda_{em}$ 322 nm) bathochromic shifts from pH values 10 to 3 with colorimetric response (Figures 43a,b and 45).

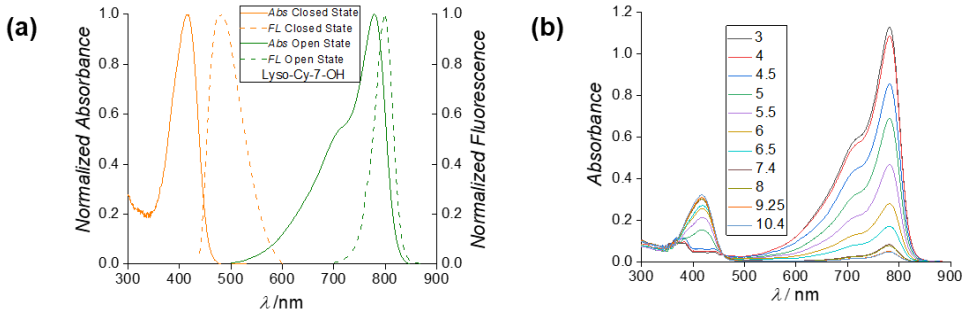

Figure 43. (a) Normalized absorbance and emission plot of closed and open state of Lyso-Cy-7-OH in DMSO. (b) Color change of Lyso-Cy-7-OH in buffer solutions at different pH values. UV/vis titration plot of closed oxazolidine (2 μM) form in buffer at various pH values exhibits 362 nm bathochromic shifts at acidic pH owing to the formation of open Lyso-Cy-7-OH form.

However, the pH insensitive diester molecule Cy-7-$(OAc)_2$ exhibits esterase enzyme activated pH switching behavior (Figure 42c-e).[32]

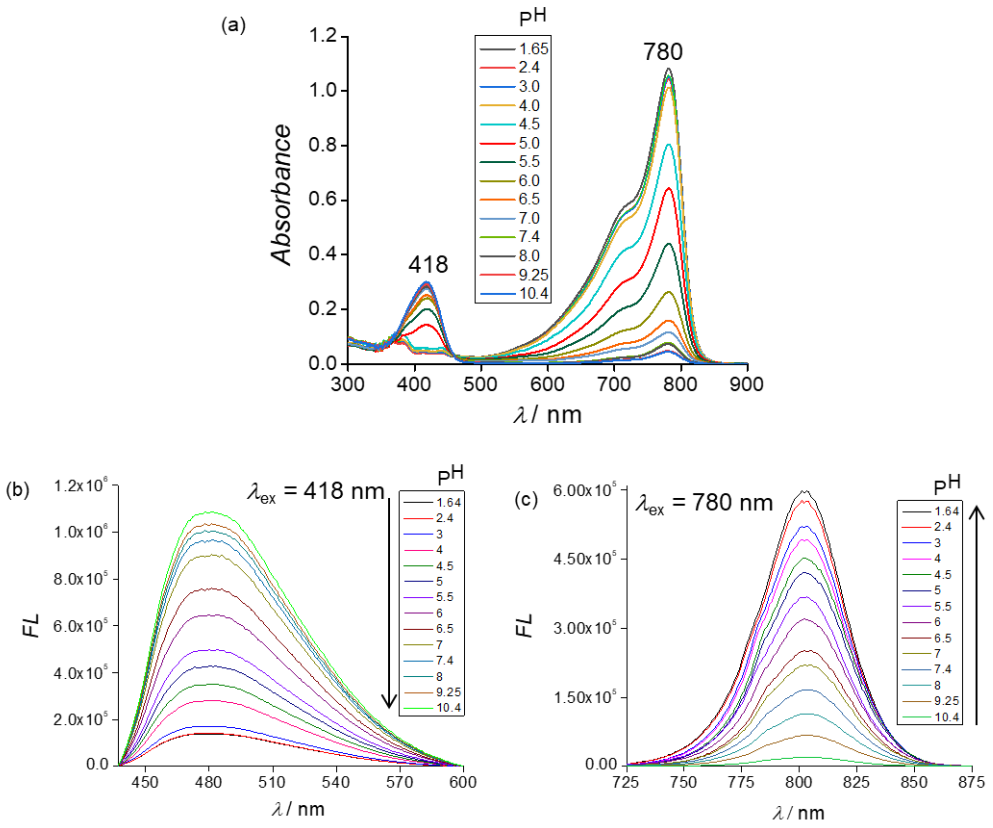

Figure 44. (a) absorption and (b,c) emission behavior is notices after the treatment of Cy-7-$(OAc)_2$ (2 μM) probe with 10.0 U/mL easterase.

The morpholine functionalized closed form of Lyso-Cy-7-OH displays massive absorption ($\Delta\lambda_{abs}$ 362 nm) and emission ($\Delta\lambda_{em}$ 322 nm) bathochromic shifts from pH values 10 to 3 with colorimetric response (Figures 43a,b).

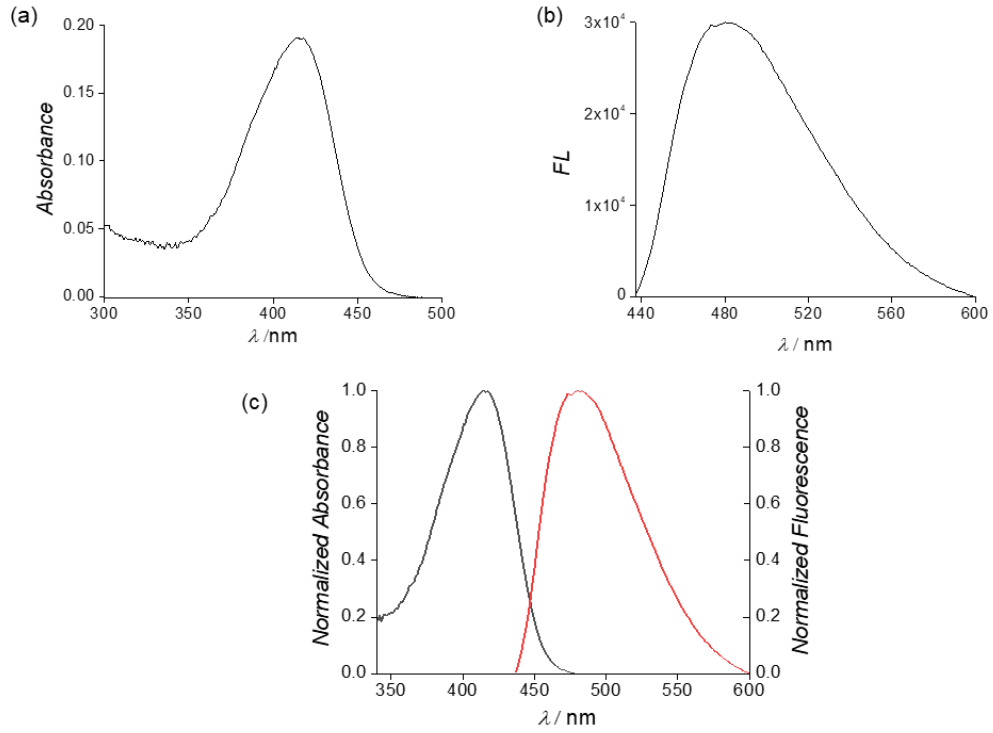

Figure 45. (a) UV/vis absorption spectrum and (b) fluorescence spectrum of the closed form of Lyso-Cy-7-OH (2 μM) in DMSO. (c) Normalized absorption and fluorecence plot of the closed form of Lyso-Cy-7-OH in DMSO (λ_{ex} = 418 nm).

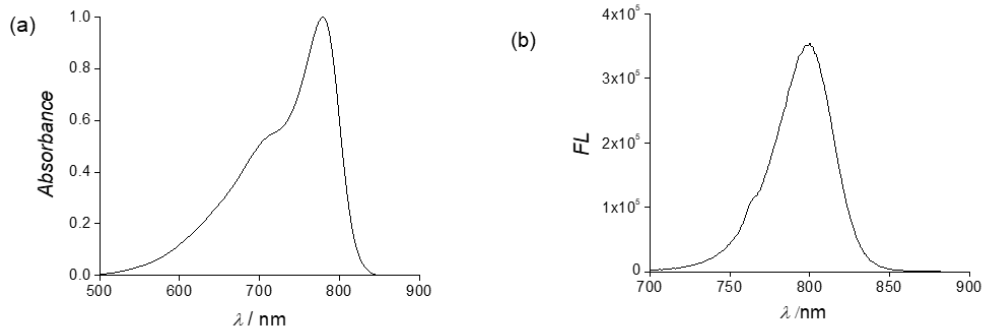

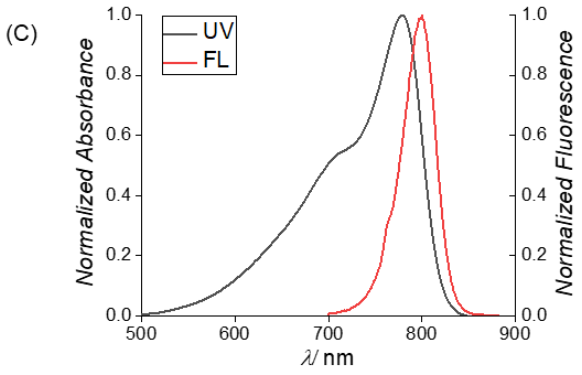

Figure 46. (a) UV/vis absorption spectrum and (b) fluorescence spectrum of the open form of Lyso-Cy-7-OH (2 μM) in DMSO. (c) Normalized absorption and fluorecence plot (λ_{ex} = 780 nm) of the open form of Lyso-Cy-7-OH in DMSO.

The pK_a of Lyso-Cy-7-OH is measured to be 5 using the sigmoidal curve fitting from the absorption and emission titration plots at numerous pH values and also revealed an outstanding linearity in the pH scale 4–6 (Figures 46a,b and 47).

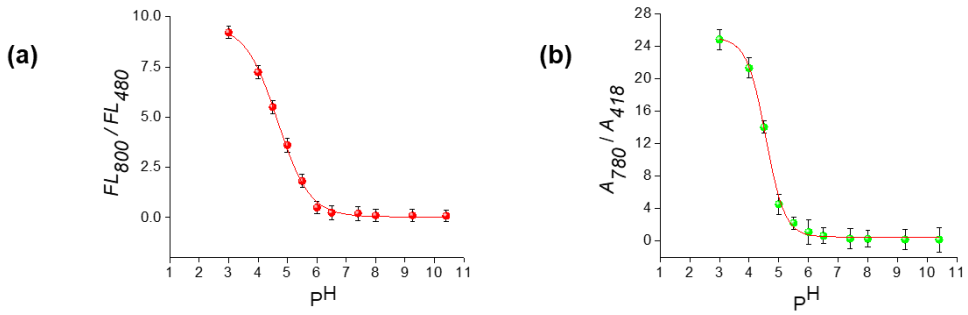

Figure 46. (a) Ratiometric absorption (A_{780}/ A_{418}) vs pH plot. (b) Ratiometric fluorescence emission (FL_{800}/FL_{480}) vs pH plot.

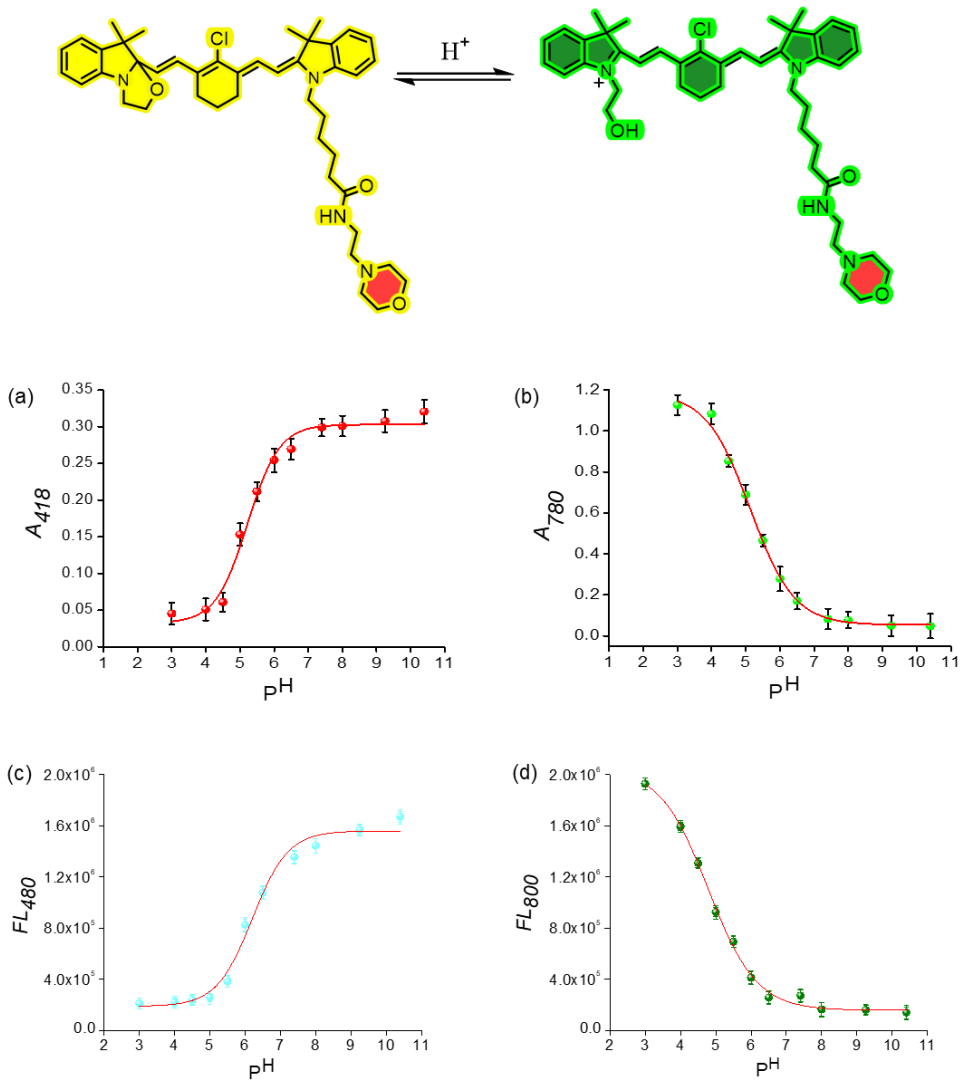

Figure 47. pH vs absorbance intensity at (a) 418 nm and (b) 780 nm plots of closed oxazolidine (2 μM) form of Lyso-Cy-7-OH with sigmoidal curve fitting. Error bars indicate the mean±standard deviation of three independent analyzes. (b) pH vs fluorescence intensity at (c) 480 nm and (d) 800 nm plots of open form of Lyso-Cy-7-OH with sigmoidal curve fitting. Error bars represent the mean±standard deviation of three independent tests.

The pK_a value of the probe Lyso-Cy-7-OH is perfect for the imaging of intracellular acidic compartments. The fluorescence intensity ratio (I_{800}/I_{480}) augmented >35-fold from pH 7.4 to 4 owing to off-to-on NIR fluorescence of the dye. We perceived fully reversible pH switching behavior of the closed oxazolidine and open Cy-7 forms of Lyso-Cy-7-OH with extreme structural alteration deprived of any degradation or aggregation of the probes. Sharp fluctuations at two well separated emission wavelengths in small pH alterations with 320 nm red shift ($\Delta\lambda_{FL}$) and the turn-on NIR Cy-7 fluorescence at acidic pH make the probe an efficient choice for ratiometric pH sensing and real-time lysosomal imaging. Moreover, due to the narrow excitation/emission bands the dye could be utilized in multicolor cellular imaging application. Furthermore, at acidic pH the open form of Lyso-Cy-7-OH reveals high molar extinction

Compound	Solvent	λ_{max} (nm)	λ_{em} (nm)	Stokes shift ($\Delta\lambda$)	$\varepsilon \times 10^5$ (M^{-1} cm^{-1})	Quantum Yield
Cy-7-$(OH)_2$ Closed form	DMSO	418	471	53	1.23×10^5	0.088 in EtOH
Cy-7-$(OH)_2$ Open form	DMSO	780	800	20	2.69×10^5	0.12 in DMSO
Cy-7-OH-OAc Closed form	DMSO	418	478	60	1.23×10^5	0.088 in EtOH
Cy-7-OH-OAc Open form	DMSO	780	800	20	2.55×10^5	0.121 in DMSO
Cy-7-$(OAc)_2$	DMSO	780	800	20	2.7×10^5	0.132 in DMSO
Lyso-Cy-7-OH Closed form	DMSO	418	478	60	1.24×10^5	0.09 in EtOH
Lyso-Cy-7-OH Open form	DMSO	780	800	20	2.52×10^5	0.13 in DMSO

Table 3. Photophysical data of the compounds

coefficient (ε = 2.52 ×10^5 M^{-1}cm^{-1}), high fluorescence quantum yield (Φ_f = 0.13), and greater fluorescence lifetime [time correlated single photon counting (TCSPC), τ = 0.97 ns] in comparison to the basic closed oxazolidine form (ε = 1.24 ×10^5 M^{-1}cm^{-1}, Φ_f = 0.09, τ = 0.51 ns) (Figure 48, Table S3, S4).

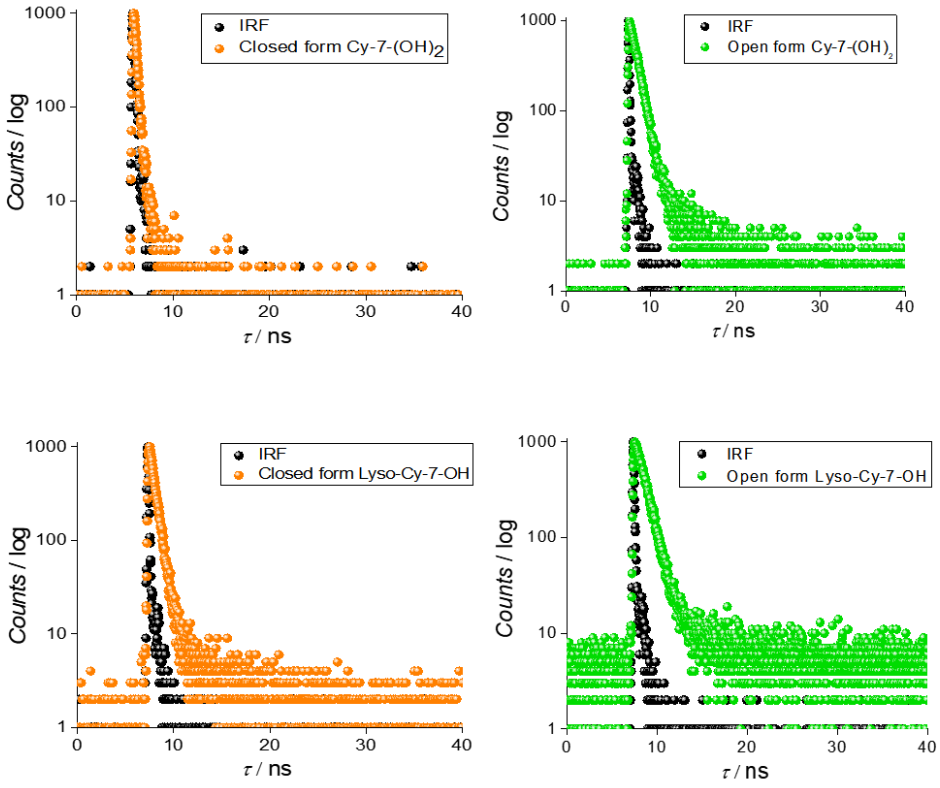

Figure 48. TCSPC plots of (a) closed Cy-7-(OH)$_2$, (b) open Cy-7-(OH)$_2$, (c) closed Lyso-Cy-7-OH, and (d) open Lyso-Cy-7-OH forms. The fluorescence lifetime (τ) is calculated to be 0.159115 ± 0.012424 ns, 0.789989 ± 0.017295 ns, 0.507359 ± 0.01398 ns, and 0.966673 ± 0.019312 ns, for the closed Cy-7-(OH)$_2$, open Cy-7-(OH)$_2$, closed Lyso-Cy-7-OH, and open Lyso-Cy-7-OH forms, respectively. IRF = instrument response function.

Compound	Florescence lifetime (τ)
Closed form Cy-7$(OH)_2$	0.159115 ± 0.012424 ns
Open form Cy-7$(OH)_2$	0.789989 ± 0.017295 ns
Closed form Lyso-Cy-7-OH	0.507359 ± 0.01398 ns
Open form Lyso-Cy-7-OH	0.966673 ± 0.019312 ns

Table 4. Fluorescence lifetime (τ) of the compounds.

Biocompatibility and Cell Viability Assay: Extensive biocompatibility of a pH switching dye is a fundamental prerequisite for its intracellular and *in vivo* utilization. The pH switching behavior of the dye (2 μM) is examined by monitoring the emission signal ratio 800/480 during 24 h at pH 8.0, 7.2, 5.0, and 4.0 in DMEM comprising 10% FBS at 37°C (Figure 49). The experiment indicates that the fluorescence ratio 800/480 remains almost unaltered over time at various pH values at 37°C. The probable interfering from biological milieu by numerous cations (Na^+, K^+, Ca^{2+}, Mg^{2+}, Zn^{2+} etc.) and anions (Cl^-, I^-, HCO_3^-, NO_3^- , NO_2^-, CO_3^-, and SO_4^-) are investigated in buffer solution at pH 7.2 at 37°C over 24 h. No noteworthy fluorescence deviations are detected in the presence of these biologically relevant cations and anions (Figure 50a-f).

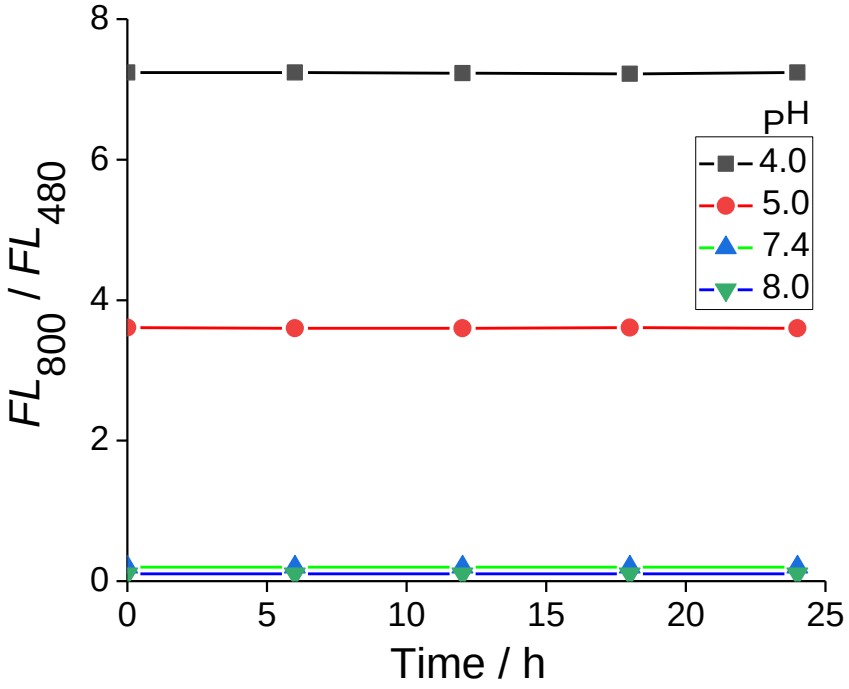

Figure 49. No noticeable ratiometric emission (FL_{800}/FL_{480}) signal change has been detected for Lyso-Cy-7-OH (2 μM) at pH 8.0, 7.2, 5.0, and 4.0 in DMEM comprising 10% FBS (w/w) at 37°C over 24 h.

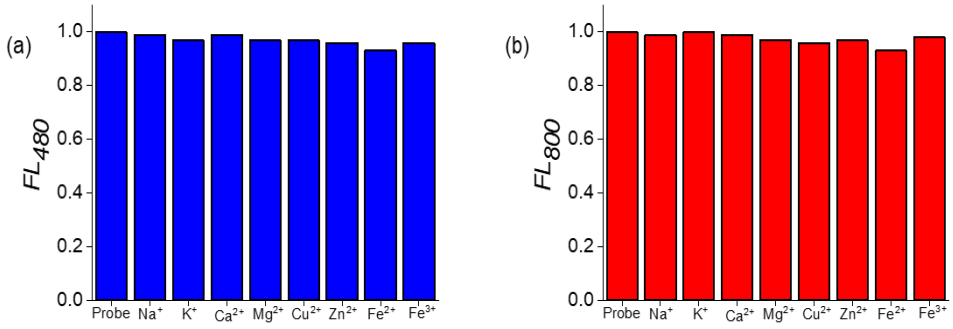

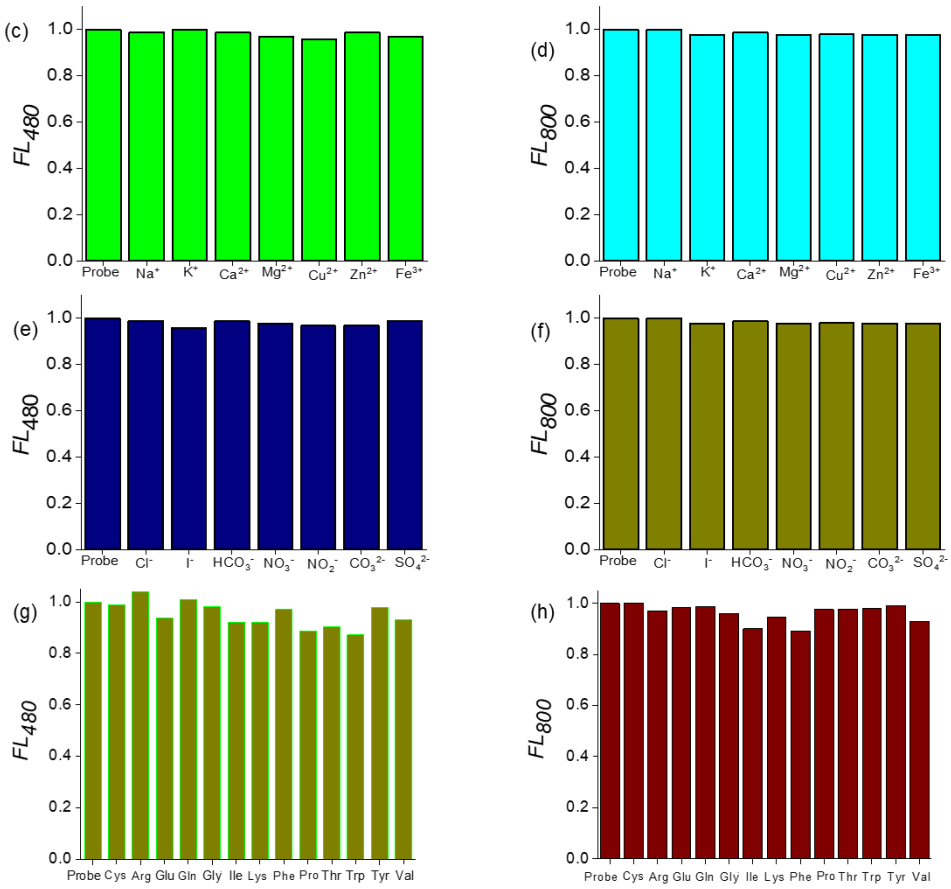

Figure 50A. No significant fluctuations are observed in the fluorescence signal of the Lyso-Cy-7-OH probe (2 μM) at 480 nm and 800 nm in presence of various cations [10 mM Na^{+}, 10 mM K^{+} and 200 μM for Ca^{2+}, Mg^{2+}, Cu^{2+}, Zn^{2+}, Fe^{2+}, and Fe^{3+}] as (a,b) chloride and (c,d) nitrate salts; (e,f) different anions (200 μM for Cl^{-}, I^{-}, HCO_3^{-},NO_3^{-}, NO_2^{-}, CO_3^{2-}, and SO_4^{2-} as Na^{+} salts) under physiological conditions (37°C, pH 7.2, 24 h). (g,h) No noticeable emission signal fluctuations are detected in presence of various amino acids like Cys, Arg, Glu, Gln, Gly, Ile, Lys, Phe, Pro, Thr, Trp, Tyr, Val at 5 mM concentration under physiological conditions (37°C, pH 7.2, 48 h).

Furthermore, Lyso-Cy-7-OH is extremely stable in presence of bioactive compounds such as GSH (5 mM), Cys (5 mM), and other amino acids (5 mM) as well as H_2O_2 (1 mM) in PBS (pH 7.2) at 37°C over 48 h (Figure 50g,h).

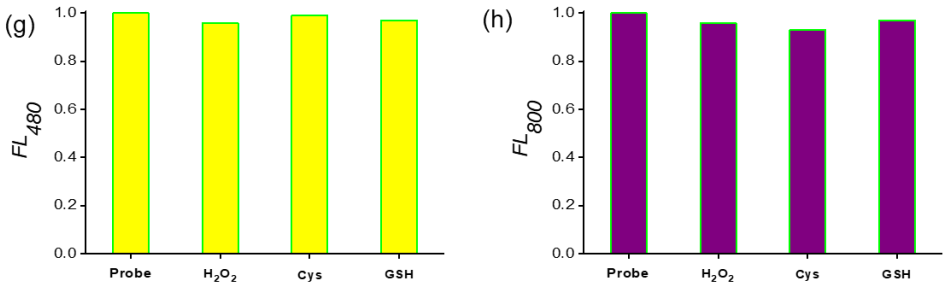

Figure 50B. (g,h) No noticeable emission signal fluctuations are detected in presence of bioactive small molecules like glutathione (GSH, 5 mM), cysteine (Cys, 5 mM), and H_2O_2 (1 mM) under physiological conditions (37°C, pH 7.2, 48 h).

Lyso-Cy-7-OH showed an exceptional reversibility with quick OFF/ON switching of absorbance from A_{418} to A_{780} and emission from FL_{480} to FL_{800} when the pH is adjusted forth and back between 10.4 and 3.0 at least for five cycles (Figure 51). No degradation or aggregation is noticed proving the robustness of the systems. The probe has high specificity towards H^+ and can be considered an effective lysosomal dye for investigating pH-associated cellular processes deprived of intervention from the biological milieu. Cell viability assay shows that the dye is non-cytotoxic to HeLa and A549 cell lines (Figure 52). This outcome suggests that Lyso-Cy-7-OH dye has the potentiality to be utilized as an effective biocompatible fluorescent probe for monitoring pH changes inside lysosome in live cells.

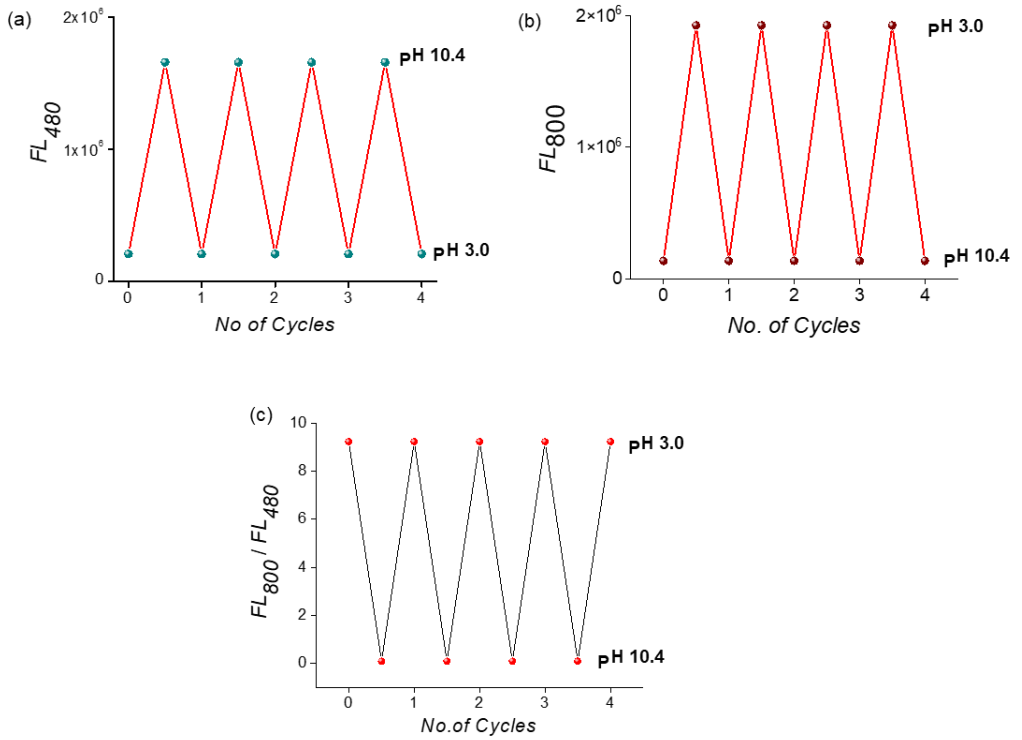

Figure 51. Reversible fluorescence switching between pH 10.4 and 3.0 for four cycles at (a) 480 nm and (b) 800 nm emission of Lyso-Cy-7-OH. (c) Ratiometric (FL_{800}/FL_{480}) pH switching (pH 10.4 and 3.0) for four cycles of Lyso-Cy-7-OH.

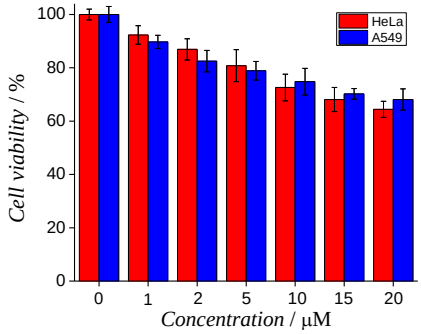

Figure 52. Cell viability assay against HeLa (red color) and A549 (blue color) cell lines over 24 h at various concentrations of acidic pH activable probe Lyso-Cy-7-OH.

Live Cell Lysosome Targeted Imaging Using Confocal Laser Scanning Microscopy:

We first investigated the live cell membrane permeability and targeted in situ organelle activated imaging using our closed form of lysosomal probe Lyso-Cy-7-OH. Confocal laser scanning microscopic (CLSM) images reveal that, after incubation of the live cells for 15 min, the closed form of Lyso-Cy-7-OH entered cells efficiently, localized, and activated into punctate vesicular compartments. To confirm the lysosomal selectivity of our synthesized closed form of Lyso-Cy-7-OH, colocalization assay are performed in HeLa and A549 carcinoma as well as healthy mouse myoblast C2C12 live cells with a commercially available lysosome tracker, LysoTracker Green DND-26 (LTG, $\lambda_{ex}/\lambda_{em}$ 504/511). The probe Lyso-Cy-7-OH exhibited decent colocalization with LTG in the CLSM (Pearson's correlation coefficient, PCC 0.79 for HeLa, 0.76 for A549 and 0.60 for C2C12 cells) (Figures 53, 54).

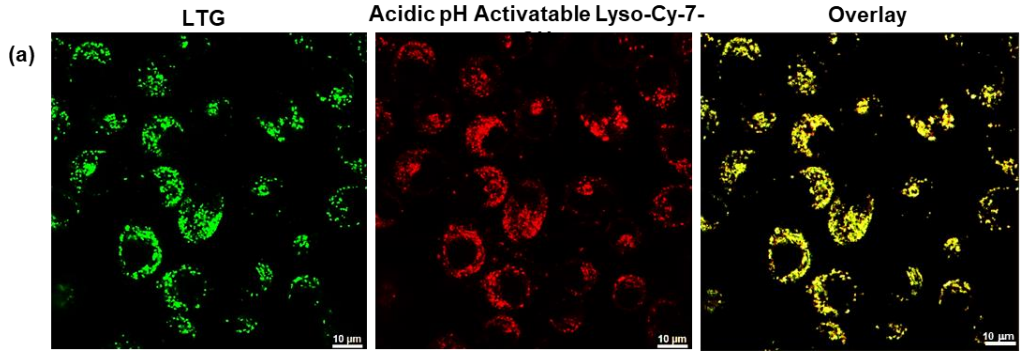

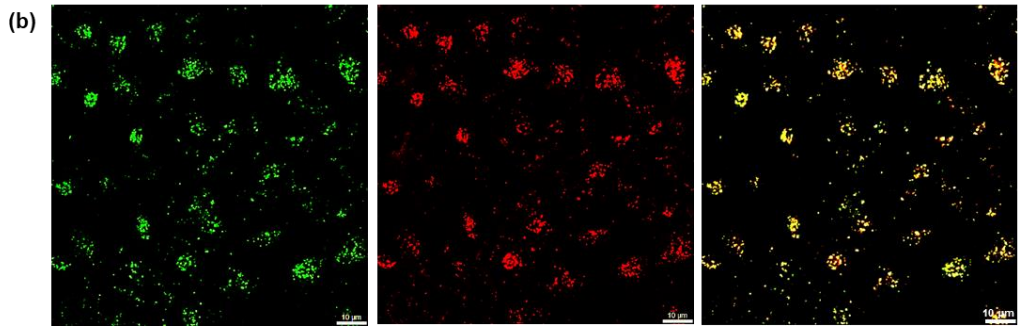

Figure 53. (a,b) CLSM images of live (a) A549 and (b) HeLa cells staining with the pH activatable probe Lyso-Cy-7-OH colocalized with LysoTracker Green DND-26 (LTG).

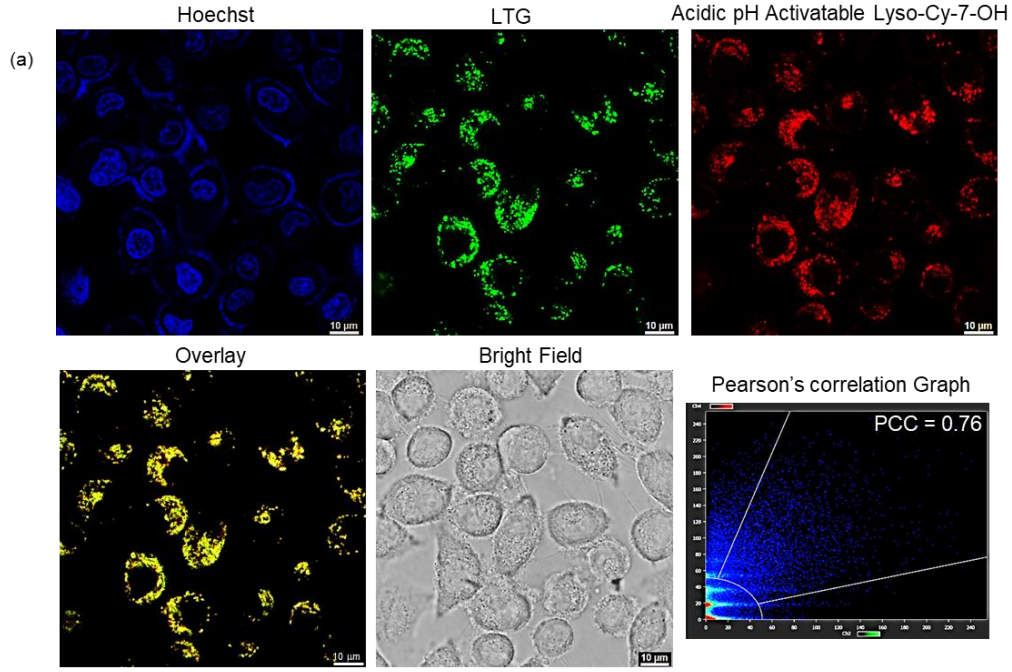

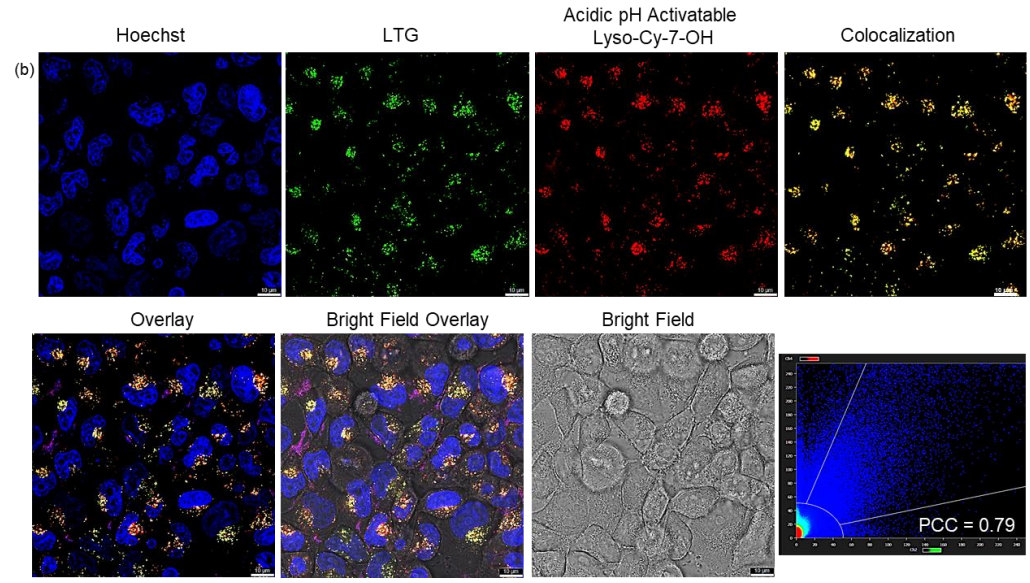

Figure 54A. CLSM images of live (a) A549 and (b) HeLa cells staining with the pH activatable probe Lyso-Cy-7-OH colocalized with LysoTracker Green DND-26 (LTG). Overlay images indicate high colocalization in live cell lysosomes. Colocalization scatter plots display Pearson's correlation coefficient (PCC) of 0.76 and 0.79 for A549 and HeLa cells, respectively.

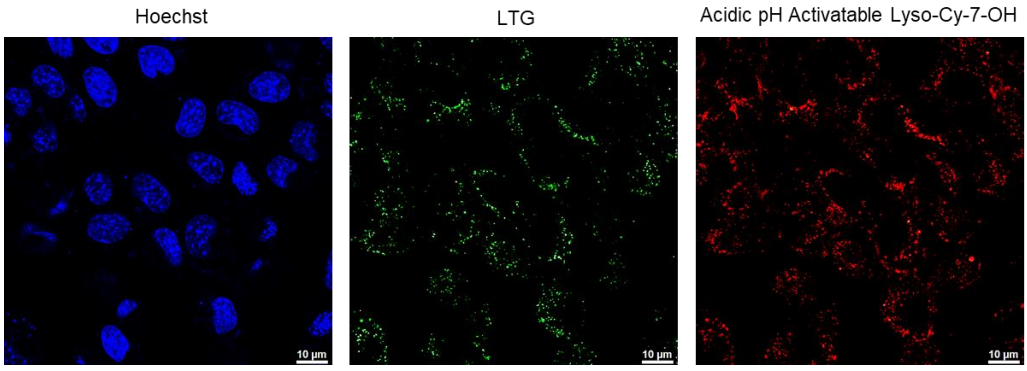

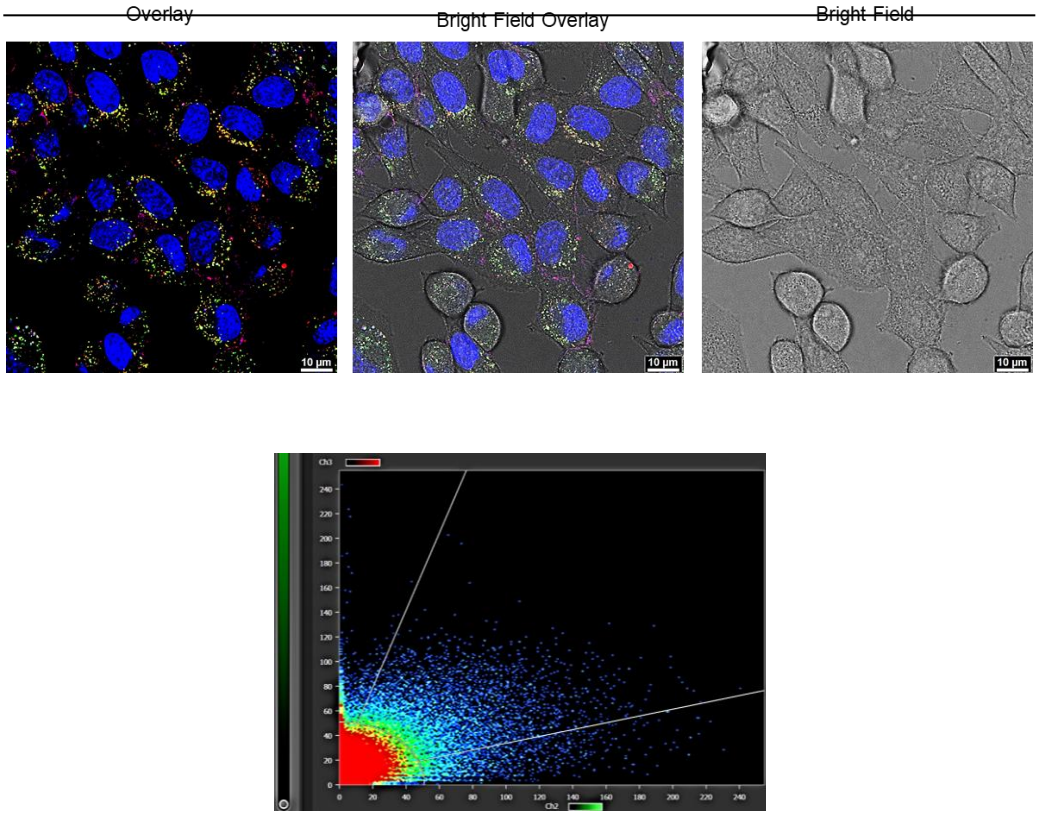

Figure 54B. CLSM images of healthy mouse myoblast C2C12 live cells staining with the pH activatable probe Lyso-Cy-7-OH colocalized with LysoTracker Green DND-26 (LTG). Colocalization scatter plot display Pearson's correlation coefficient (PCC) of 0.6.

However, in case of control dyes Cy-7-$(OH)_2$, Cy-7-OH-OAc, and Cy-7-$(OAc)_2$ lacking the lysosome targeting morpholine functionality we observed weak colocalization with LTG (low PCC) in both the A549 and HeLa cells (Figure 55-57). It indicates that conjugation of morpholine functionality to the pH-activated probe is necessary to target lysosomes.

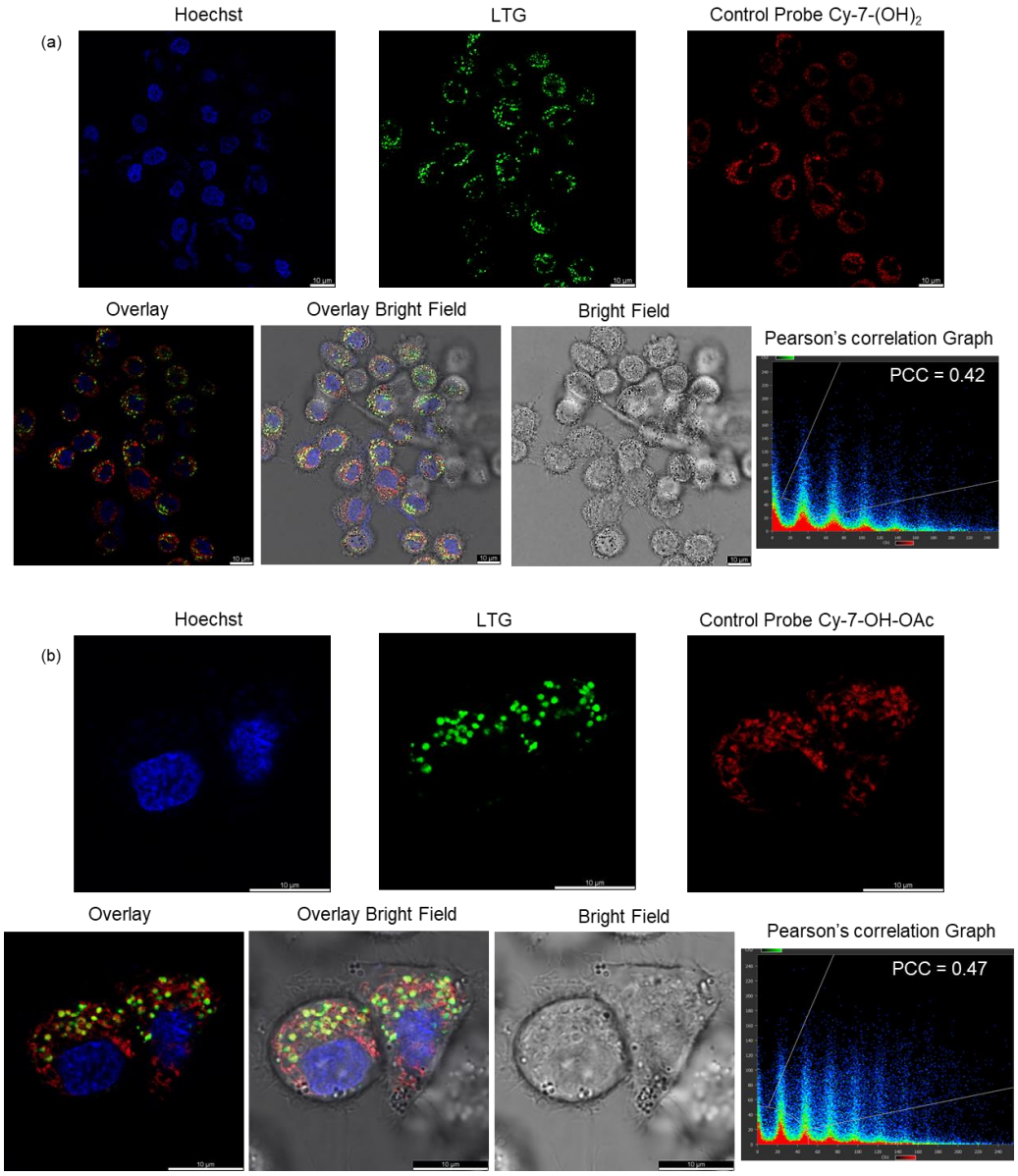

Figure 55. Confocal microscopic images of pH-switchable closed oxazolidine state of the control dyes (a) Cy-7-$(OH)_2$ and (b) Cy-7-OH-OAc lacking the

lysosome targeting morpholine moiety colocalized with LysoTracker Green (LTG) in live A549 cells. Hoechst (blue channel), LTG (green channel), and lysosome targeting morpholine moiety colocalized with LysoTracker Green (LTG) in live HeLa cells. Hoechst (blue channel), LTG (green channel), and Cy-7-$(OH)_2$ or Cy-7-OH-OAc (red channel). Overlay images designate poor

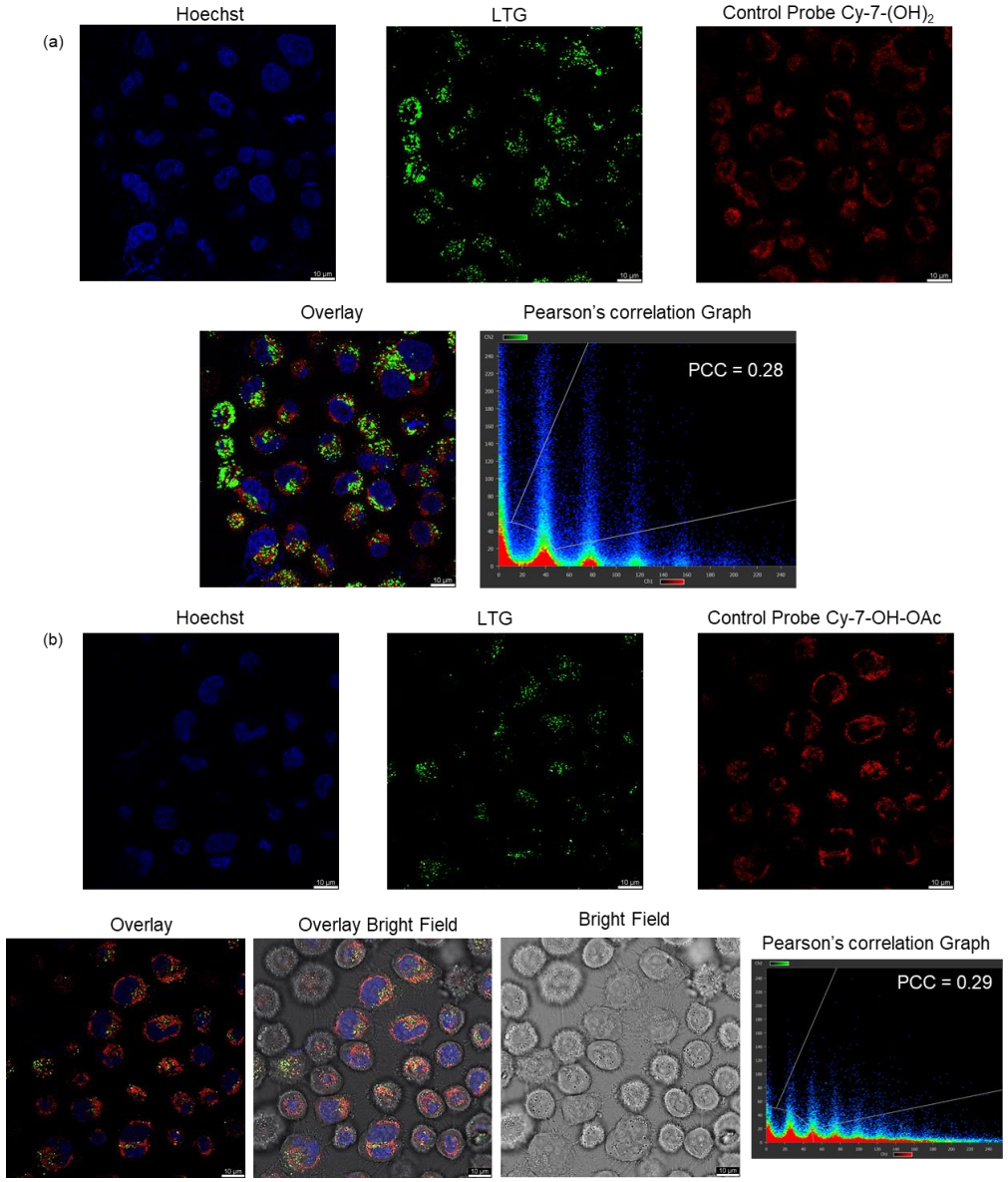

Figure 56: Confocal microscopic images of pH-switchable closed oxazolidine

state of the control dyes (a) Cy-7-$(OH)_2$ and (b) Cy-7-OH-OAc lacking the colocalization with LTG. Colocalization scatter plots display PCC of 0.28 and 0.29 for Cy-7-$(OH)_2$ and Cy-7-OH-OAc, respectively in HeLa cells.

Cy-7-$(OH)_2$ or Cy-7-OH-OAc (red channel). Overlay images designate poor colocalization with LTG. Colocalization scatter plots display PCC of 0.42 and 0.47 for Cy-7-$(OH)_2$ and Cy-7-OH-OAc, respectively in A549 cells.

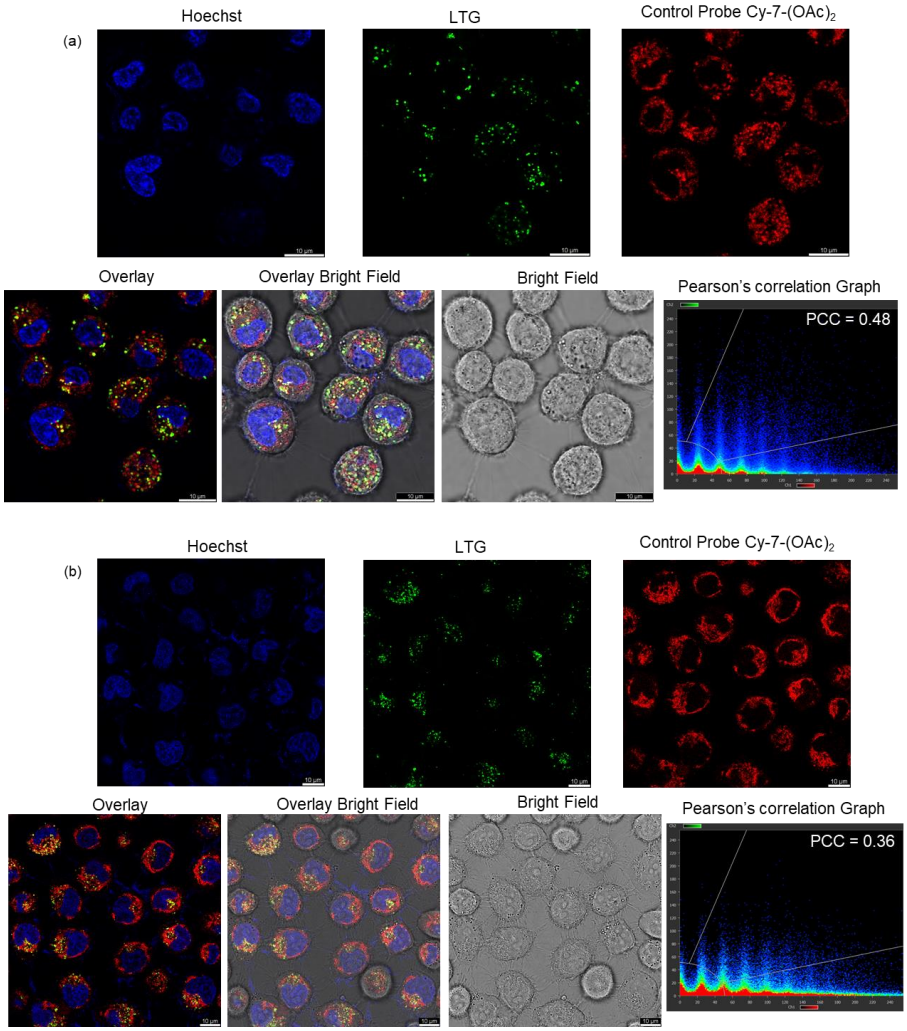

Figure 57: Confocal microscopic images of pH-insensitive control dye Cy-7-$(OAc)_2$ lacking the lysosome targeting morpholine moiety colocalized with

LysoTracker Green (LTG) in live (a) A549 and (b) HeLa cells. Hoechst (blue channel), LTG (green channel), and Cy-7-$(OAc)_2$ (red channel). Overlay images designate poor colocalization with LTG. Colocalization scatter plots display PCC of 0.48 and 0.36 for Cy-7-$(OAc)_2$ in A549 and HeLa cells, respectively.

Live Cell Ratiometric Fluorescence Imaging: Live cell ratiometric CLSM imaginings in HeLa and A549 cell lines are accomplished using dual channel excitation by treatment with the oxazolidine form of Lyso-Cy-7-OH. The fluorescence emission in Channel 1 (open Cy-7 form, 800 nm) is higher than the fluorescence in Channel 2 (closed oxazolidine form, 480 nm), designating *in situ* lysosomal pH triggered transformation of the probe with insignificant cross talk among the two emission channels. Ratiometric confocal imagings (I_{red}/I_{green}, pseudocolor produced by ImageJ software) are acquired using the two channels that showed that this ratiometric fluorescent dye is an effective molecule for real time monitoring and imaging of live cell lysosomes (Figures 58, 59).

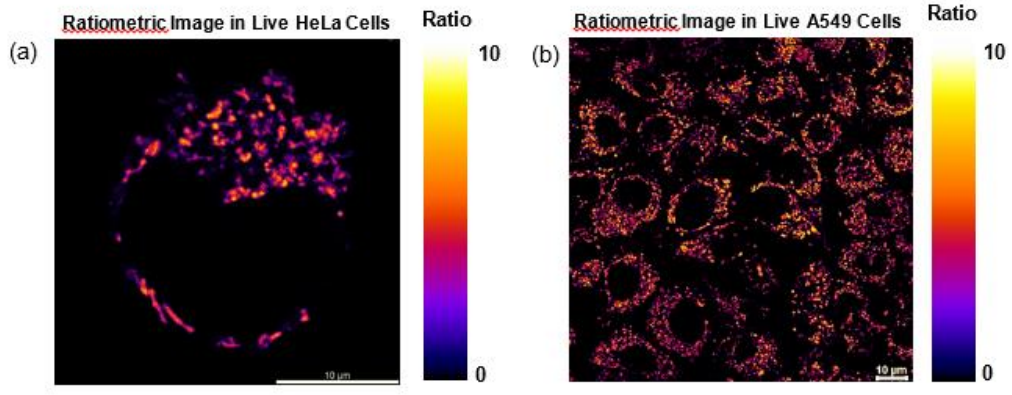

Figure 58: Ratiometric CLSM images (I_{red}/I_{green}, pseudocolor produced by ImageJ

software) of live (a) HeLa and (b) A549 cell lines upon dual excitation of the pH activatable probe Lyso-Cy-7-OH.

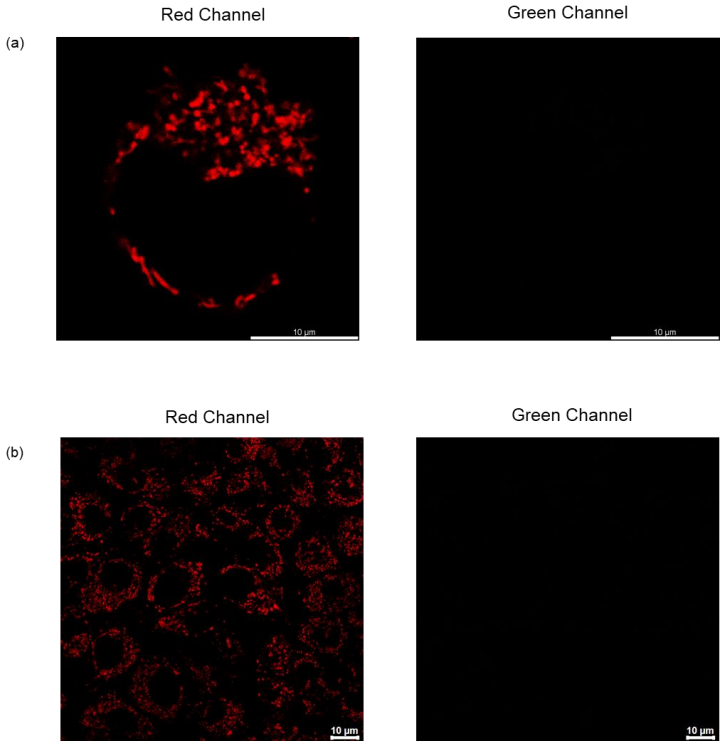

Figure 59: CLSM images in channel 1 (red channel) and channel 2 (green channel) of live (a) HeLa and (b) A549 cell lines upon dual channel excitation of the pH activatable probe Lyso-Cy-7-OH.

Real-Time Tracking of Living Cell Lysosomes, 3D and Multicolor Imaging:

CLSM is used to scan various layers through the z axis to acquire 3D info of the live cells stained with the Lyso-Cy-7-OH dye. The 3D rebuilding of the CLSM images indicate the spherical lysosomal compartments in the living HeLa and A549 cells incubated with the pH-switchable dye Lyso-Cy-7-OH (Figure 60).

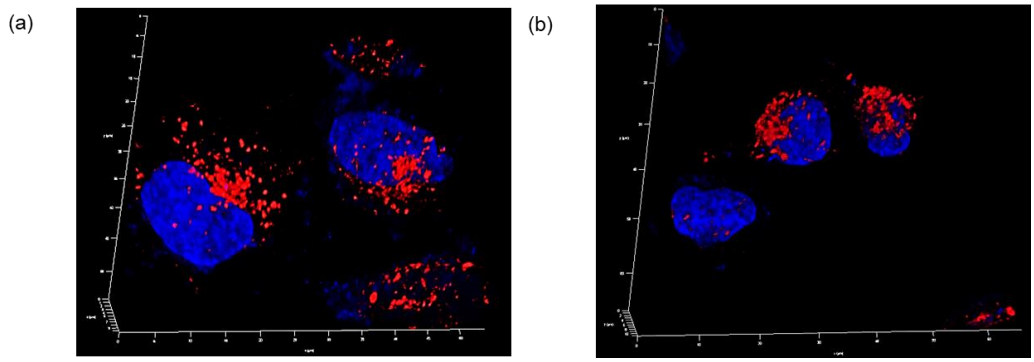

Figure 60: 3D CLSM images of live (a) HeLa and (b) A549 carcinoma cells staining with the lysosome targeting pH activatable probe Lyso-Cy-7-OH indicate spherical lysosomal compartment (red color). Blue color designates nuclear staining by Hoechst.

The real-time lysosomal movement over the time span of 70-85 seconds inside the living cells is also monitored using CLSM (Figures 62, 63). Furthermore, multicolor confocal images of living A549 and HeLa cell lines are captured in amalgamation with organelle targeting biomarkers with discrete $\lambda_{ex}/\lambda_{em}$, like blue-fluorescent Hoechst to stain the nucleus, green emitting MitoTracker Green (MTG) to selectively image the mitochondria, and the synthesized pH-activatable probe Lyso-Cy-7-OH with narrow excitation/emission bands to image the lysosomes (Figures 61 and 64,65). The real-time movement of numerous cellular organelles over time inside the living A549 and HeLa cells using pH-activatable probe Lyso-Cy-7-OH in combination with other organelle specific staining agents is also monitored using multicolor CLSM (Figure 65).

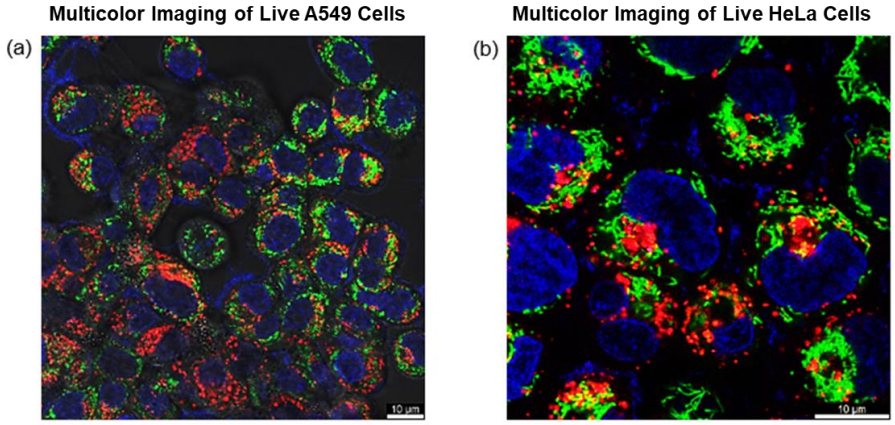

Figure 61. Multicolor CLSM images of living (a) A549 and (b) HeLa cells stained with blue-fluorescent Hoechst to target nucleus (blue color), green emitting MTG to stain mitochondria (green color), and acidic pH-activated NIR emitting Lyso-Cy-7-OH to specifically track lysosomes (red color).

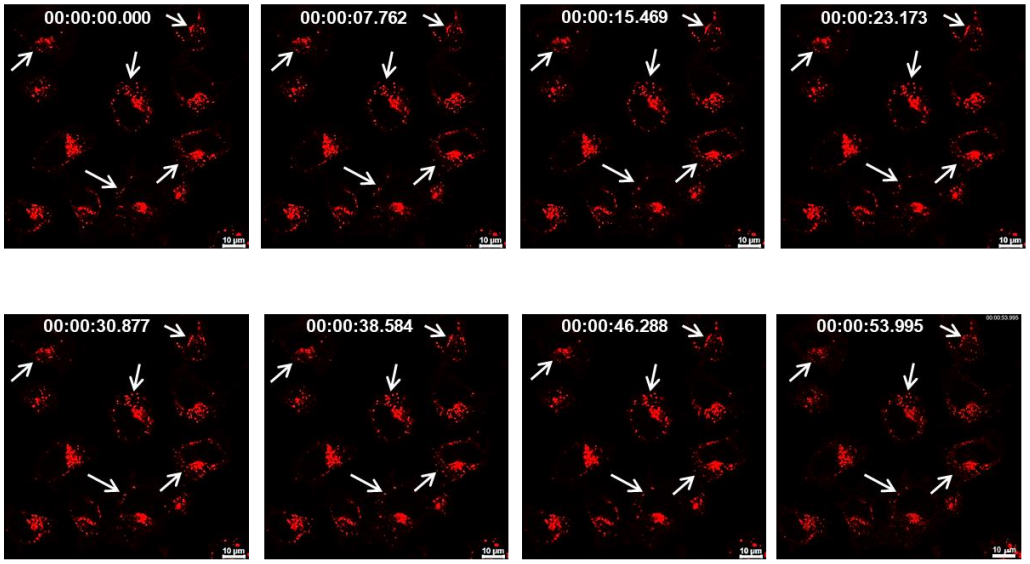

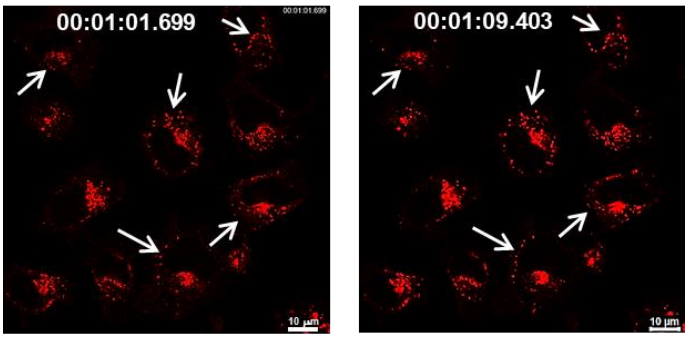

Figure 62. Real-time tracking of lysosomes inside the living HeLa carcinoma cells using pH activatable probe Lyso-Cy-7-OH by confocal laser scanning microscopy. 10 frames were collected over 70 seconds.

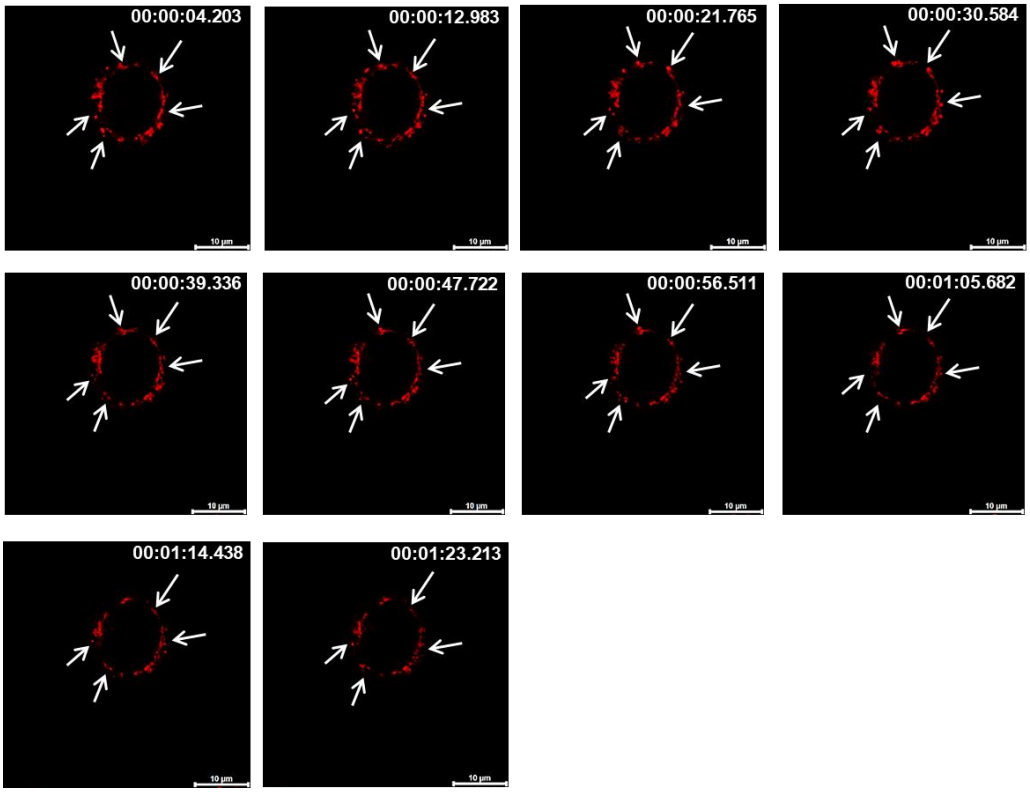

Figure 63. Real-time tracking of lysosomes inside the living A549 carcinoma cells using pH activatable probe Lyso-Cy-7-OH by confocal laser scanning microscopy. 10 frames were collected over 83 seconds.

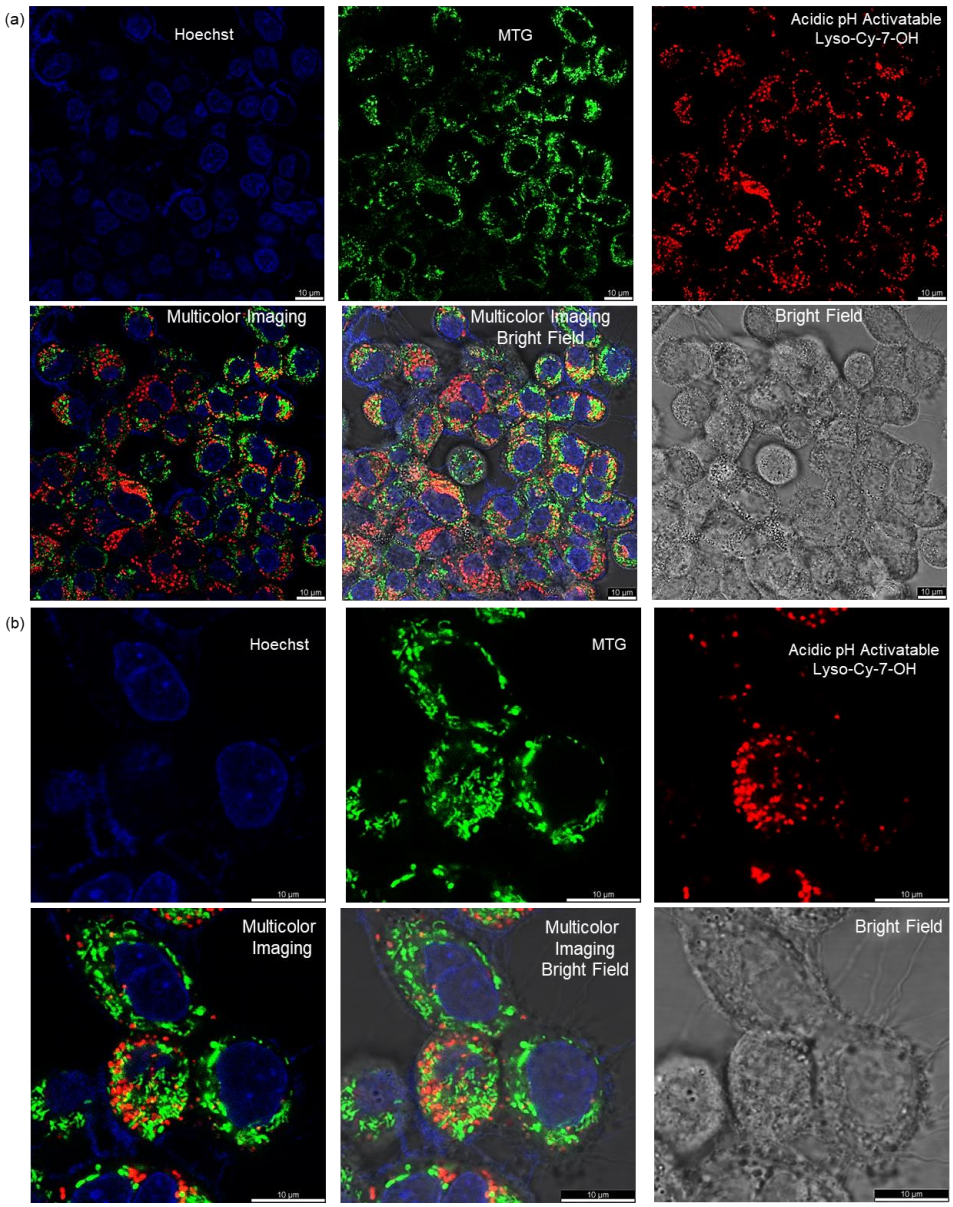

Figure 64. (a,b) Multicolor CLSM images of living A549 cells stained with blue-fluorescent Hoechst to target nucleus (blue color), green emitting MTG to stain mitochondria (green color), and acidic pH-activated NIR emitting Lyso-Cy-7-OH to specifically track lysosomes (red color).

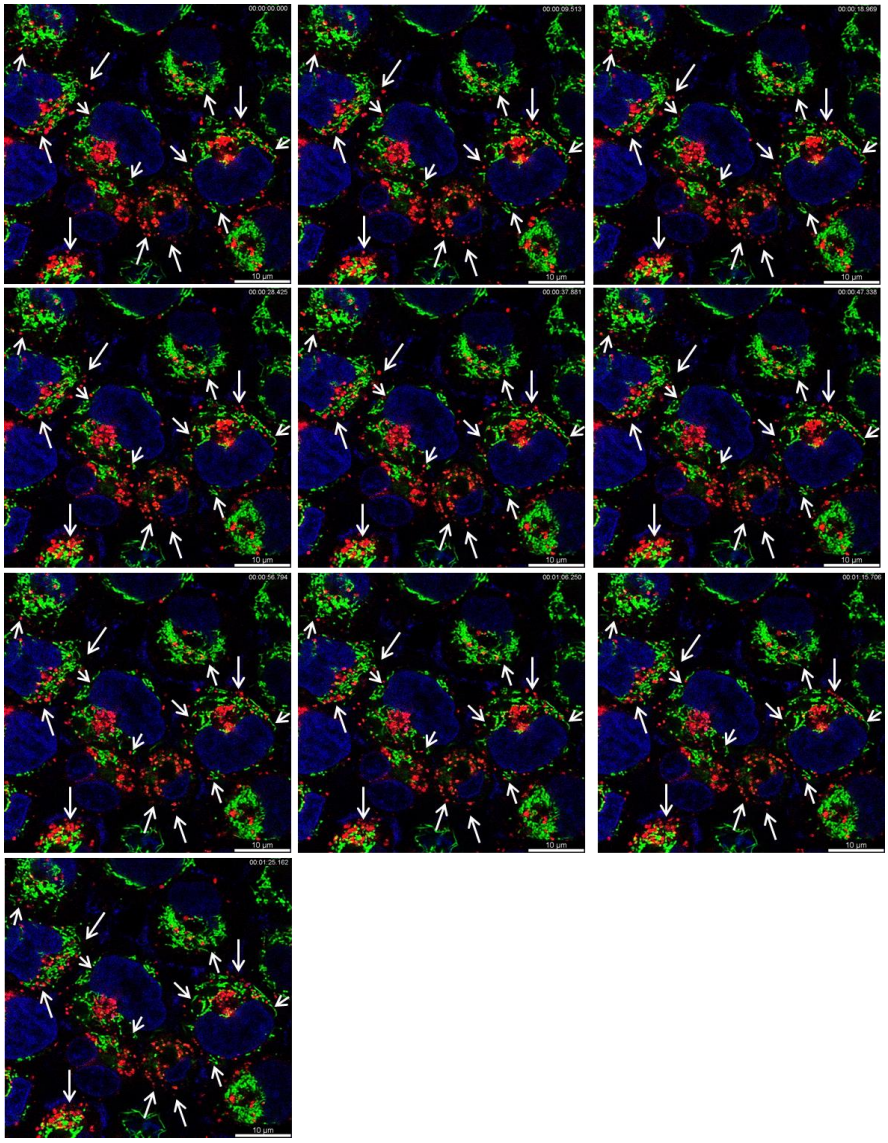

Figure 65: Real-time tracking of numerous cellular organelles such as nucleus, mitochondria, and lysosomes by confocal laser scanning microscopy inside the living HeLa cells using pH activatable probe Lyso-Cy-7-OH in combination with Hoechst and MTG. 10 frames were collected over 1 minute 25 seconds.

Conclusions:

In conclusion, we have efficiently constructed an intermediate to synthesize ratiometric pH sensors along with pH-switchable cell membrane penetrating lysosome targeting organic ratiometric fluorescent probes. In addition, high lysosomal selectivity, fine reversibility with huge fluorescence spectral shift; ideal pK_a values in the pH_{lys} range, turned on NIR fluorescence at acidic lysosomal pH and low cytotoxicity, further make the probe a marvelous candidate for lysosome targeted ratiometric imaging. The confocal microscopic images of the probe colocalized with LTG in live cells are accomplished effectively, signifying that the dye has good cell membrane penetrating ability and specifically illuminate at acidic lysosomal lumen in live cells. Huge bathochromic shift from physiological to acidic pH ($\Delta\lambda$ 322 nm) with narrow excitation and emission bands provide important tools for dual-channel CLSM, 3D imaging, multicolor imaging, and might contribute to the ratiometric imaging and real time monitoring of lysosomes in living cells. This acidic pH activatable ratiometric probe can be effortlessly engineered with a diversity of target specific functionalities.

References:

[1] Donahue, C. E. T.; Siroky, M. D.; White, K. A. *J. Am. Chem. Soc.* **2021**, *143*, 18877–18887.

[2] Wang, K.; Yan, S.; Han, T.; Wu, Q.; Yan, N.; Kang, M.; Ge, J.; Wang, D.; Tang, B. Z.. *J. Am. Chem. Soc.* **2022**, *144*, 11788–11801.

[3] Han, J.; Burgess, K. *Chem. Rev.* **2010**, *110*, 2709–2728.

[4] Aref, M.; Ranjbari, E.; García-Guzmán, J. J.; Hu, K.; Lork, A.; Crespo, G. A.; Ewing, A. G.; Cuartero, M. *Anal. Chem.* **2021**, *93*, 15744–15751.

[5] Casey, J. R.; Grinstein, S.; Orlowski, J. *Nat. Rev. Mol. Cell Biol.* **2010**, *11*, 50–61.

[6] Bonam, S. R.; Wang, F.; Muller, S. *Nat. Rev. Drug Discov.* **2019**, *18*, 923–948.

[7] Cui, C.; Chakraborty, K.; Tang, X. A.; Schoenfelt, K. Q.; Hoffman, A.; Blank, A.; McBeth, B.; Pulliam, N.; Reardon, C. A.; Kulkarni, S. A.; Vaisar, T.; Ballabio, A.; Krishnan, Y.; Becker, L.. *Nat. Nanotechnol.* **2021**, *16*, 1394–1402.

[8] Chin, M. Y.; Patwardhan, A. R.; Ang, K. H.; Wang, A. L.; Alquezar, C.; Welch, M.; Nguyen, P. T.; Grabe, M.; Molofsky, A. V.; Arkin, M. R.; Kao, A. W. *ACS. Sens.* **2021**, *6*, 2168–2180.

[9] Lambeth, T. R.; Riggs, D. L.; Talbert, L. E.; Tang, J.; Coburn, E.; Kang, A. S.; Noll, J.; Augello, C.; Ford, B. D.; Julian, R. R. *A.C.S. Cent. Sci.* **2019**, *5*, 1387–1395.

[10] Futerman, A. H.; van Meer, G. *Nat. Rev. Mol. Cell Biol.* **2004**, *5*, 554–565.

[11] Fraldi, A.; Klein, A. D.; Medina, D. L.; Settembre, C. *Annu. Rev. Neurosci.* **2016**, *39*, 277–295.

[12] Grossi, M.; Morgunova, M.; Cheung, S.; Scholz, D.; Conroy, E.; Terrile, M.; Panarella, A.; Simpson, J. C.; Gallagher, W. M.; O'Shea, D. F. *Nat. Commun.* **2016**, *7*, 10855.

[13] Ning, P.; Hou, L.; Feng, Y.; Xu, G.; Bai, Y.; Yu, H.; Meng, X. *Chem. Commun.* **2019**, *55* , 1782–1785.

[14] Qiao, Q.; Liu, W.; Zhang, Y.; Chen, J.; Wang, G.; Tao, Y.; Miao, L.; Jiang, W.; An, K.; Xu, Z. *Angew. Chem. Int. Ed.* **2022**, *61*, e202202961.

[15] Song, G.; Heng, H.; Wang, J.; Liu, R.; Huang, Y.; Lu, H.; Du, K.; Feng, F.; Wang, S. *Angew. Chem. Int. Ed.* **2021**, *60*, 16889–16893.

[16] Wan, Q.; Chen, S.; Shi, W.; Li, L.; Ma, H. *Angew. Chem. Int. Ed.* **2014**, *53*, 10916–10920.

[17] Zhang, Y.; Xia, S.; Fang, M.; Mazi, W.; Zeng, Y.; Johnston, T.; Pap, A.; Luck, R. L.; Liu, H. *Chem. Commun.* **2018**, *54*, 7625–7628.

[18] Roy, S.; Zhu, D.; Parak, W. J.; Feliu, N. *ACS. Nano* **2020**, *14*, 8012–8023.

[19] Mukherjee, A.; Saha, P. C.; Das, R. S.; Bera, T.; Guha, S. *ACS. Sens.* **2021**, *6*, 2141–2146.

[20] Chen, X.; Bi, Y.; Wang, T.; Li, P.; Yan, X.; Hou, S.; Bammert, C. E.; Ju, J.; Gibson, K. M.; Pavan, W. J.; Bi, L. *Sci. Rep.* **2015**, *5*, 9004.

[21] Pierzyńska-Mach, A.; Janowski, P. A.; Dobrucki, J. W. *Cytometry* **2014**, *85*, 729–737.

[22] Qiu, K.; Huang, H.; Liu, B.; Liu, Y.; Huang, Z.; Chen, Y.; Ji, L.; Chao, H. *ACS. Appl. Mater. Interfaces* **2016**, *8*, 12702–12710.

[23] Collot, M.; Fam, T. K.; Ashokkumar, P.; Faklaris, O.; Galli, T.; Danglot, L.; Klymchenko, A. S. *J. Am. Chem. Soc.* **2018**, *140* , 5401–5411.

[24] Das, R. S.; Mukherjee, A.; Kar, S.; Bera, T.; Das, S.; SenGupta, A.; Guha, S. *Org. Lett.* **2022**, *24*, 5907–5912.

[25] Wang, L.; Tran, M.; D'Este, E.; Roberti, J.; Koch, B.; Xue, L.; Johnsson, K. *Nat. Chem.* **2020**, *12* (2), 165–172.

[26] Miki, K.; Kojima, K.; Oride, K.; Harada, H.; Morinibu, A.; Ohe, K. *Chem. Commun. (Camb)* **2017**, *53* (55), 7792–7795.

Mukherjee, A.; Saha, P. C.; Das, R. S.; Bera, T.; Guha, S. *ACS Sens.* **2021**, *6*, 2141–2146.

[27] Sheldrick, G. M. *Acta Cryst.* **2015**, *A71*, 3–8.

[28] Sheldrick, G. M. *Acta Cryst.* **2015**, *C71*, 3–8.

[29] Dolomanov, O. V.; Bourhis, L. J.; Gildea, R. J.; Howard, J. A. K.; Puschmann, H. *J. Appl. Cryst.* **2009**, *42*, 339–341.

[30] Das, R. S.; Mukherjee, A.; Kar, S.; Bera, T.; Das, S.; Sengupta, A.; Guha, S. *Org. Lett.* **2022**, *24*, 5907–5912.

[31] Raymo, F. M.; Giordani, S. *J. Am. Chem. Soc.* **2001**, *123*, 4651–4652.

[32] Zheng, Y.; Meana, Y.; Mazza, M. M. A.; Baker, J. D.; Minnett, P. J.; Raymo, F. M.. *J. Am. Chem. Soc.* **2022**, *144*, 4759–4763.

[33] Guerrin, C.; Aidibi, Y.; Sanguinet, L.; Leriche, P.; Aloise, S.; Orio, M.; Delbaere, S. *J. Am. Chem. Soc.* **2019**, *141*, 19151–19160.

Chapter 5

Dual Targeting Acidic pH-Activatable NIR Convertible Ratiometric Fluorescent Probe-Peptide Conjugate for Living Cancer Cell Specific Active Targeting Subsequently Selective Tracking of Lysosomes

Introduction

A logically designed acidic pH stimulated visible-to-NIR convertible ratiometric organic fluorescent molecule for active targeting of living carcinoma cells consequently cell penetration and selective staining of organelle are an emerging field of contemporary research.[1-4] In contrast to UV and Vis light, NIR light (700−1000 nm) excitation has least extent of photodamage, deep tissue infiltration, high signal-to-background ratio with spatiotemporal resolution that proffers effectual device for live cells fluorescence imaging.[4-6] Furthermore, NIR fluorescence bioimaging has certain benefits such as high sensitivity at the molecular level, no radiation exposure, cost effective, non-invasive, and real-time monitoring in comparison to other molecular imaging techniques.[7,8] A critical biological parameter is intracellular pH and it serves as a crucial internal reference for health assessment.[9-11] pH of the cancer cells is weakly acidic (pH 6.5-7.2) contrary to the healthy cells (pH 7.4).[9] Furthermore, different pH values are found in various intracellular organelles e.g. endosomes (pH 5-6) and lysosomes (pH 4-5) are acidic, mitochondria are alkaline (pH 8.0), whereas cytoplasm is neutral (pH 7.2).[10,11] An aberrant pH level is the sign of malfunction and are connected with organelle related deadly diseases.[12,13] It is imperative to design functional probes for targeting and activated staining of cancer cell specific acidic organelles. Cancer is the foremost threat for human life; however, it is very tough to target cancer. Various receptors are overexpressed at the cancer cell surface e.g., $\alpha_V\beta_3$ integrin and it is essential to design appropriate molecules to target the overexpressed cell surface receptors through molecular recognition.[14,15] Unequivocal targeting and monitoring of malignant cell acidic lysosomes are the important steps for early diagnosis of cancers.[16,17]Lysosomes are the membrane enclosed organelles having acidic

pH and comprise a diversity of enzymes that are accountable for the degradation of nucleic acids, fats, proteins etc. besides liable for cellular signalling and immunologic defense.[18,19] Lysosomes are proton-pumping vacuolar ATPases that is answerable to retain the inner acidic pH milieu. Anomalies in lysosomes are liable for lysosomal storage disorders, Alzheimer's, and cancer.[20-22] he current live cancer cell specific lysosome targeting organic probes have several limitations, including poorer water solubility, less cancer cell lysosome target selectivity, broader and lower ex/em bands, spectral overlap, inappropriate pK_a, shallow brightness inside the acidic malignant lysosome, and cytotoxicity.[23-25] There is an unmet need to design *in situ* live cancer cell targeted acidic lysosomal pH activatable water-soluble visible-to-NIR switchable ratiometric fluorescent probe-peptide conjugates.[26–28] Despite this, the intricacy of the live cancer cells lysosomal environment makes it hard to execute targeted pH sensitive organic chemical switching. The designed functional probe-peptide conjugate has four distinct structural features: (a) an acidic pH-activatable visible-to-NIR switchable live-cell permeable spiro-lactam moiety containing Changsha probe for the ratiometric response inside the complex living cells,[29,30] (b) Arg-Gly-Asp-Ser (RGDS) peptide conjugated with the Changsha probe using Fmoc-SPPS protocol on resin to enhance water solubility, dynamic spiro-lactam ring formation and opening through Arg amide NH residue, and to target heterodimeric transmembrane domain containing cancer cell surface overexpressed receptor $\alpha_V\beta_3$ integrin, and (c) morpholine functionality tethered at the xantheneindolium residue to enhance the probe hydrophilicity, reduce the pK_a value, and to target malignant lysosomes. The synthesized carboxylic acid functionalized Changsha chromophore is conjugated with cancer cell specific RGDS peptide by Fmoc-SPPS protocol on the Rink amide AM resin to develop

the ratiometric probe-peptide conjugate. An intramolecular nucleophilic cyclization reaction i.e., spirolactamization between the Arg amide NH of RGDS peptide residue with the meso-C of the xanthene scaffold yields non-NIR (visible) fluorescent spiro-lactam form in physiological pH 7.4 and basic pH. The non-NIR fluorescent spiro-lactam form is switched on to the highly conjugated NIR open amide form through ring opening of the spiro-lactam moiety at acidic lysosomal lumen. The NIR fluorescence OFF-ON switching of the probe-peptide conjugate is in dynamic equilibrium which is manipulated by pH. Active targeting of living carcinoma cells successively cell penetration and high-contrast selective staining of lysosomes by the ratiometric probe-peptide conjugate is established by confocal laser scanning microscopy (CLSM) and contrasted with a control molecule. Real-time tracking of living carcinoma cell lysosomes along with 3D and multicolor imaging is also attained. Until further notice, this is the first account of a water-soluble, biocompatible, noncytotoxic, live-cell permeable, photostable, visible-to-NIR switchable, ultrabright, dual targeting ratiometric probe-peptide conjugate where cancer cell targeting RGDS tetrapeptide is bioconjugated with the benzoic acid functionality of the Changsha probe and lysosome targeting morpholine group is linked at the xantheneindolium moiety for active targeting of living carcinoma cells subsequently selective cell penetration and activated ratiometric imaging of lysosomes in addition to real-time monitoring, 3D, and multicolor live-cell imaging applications.

Synthesis, Purification, and Characterization of the Compounds:

With a descent yield and an efficient approach, the dyes and their precursor molecules were synthesised from readily available, inexpensive starting materials. On aluminium sheet coated with silica gel, analytical TLC (TLC silica gel 60 F_{254}) was carried out with the appropriate solvent combinations,

and the results were detected using the naked eye or a UV lamp. By using silica gel with a mesh size of 100–200, the synthesised compounds were purified using column chromatography. Prior to usage, the chromatography solvents were distilled. Our previously reported method was used to construct the material 2,3,3-trimethylindolenine.[31]

Synthesis:

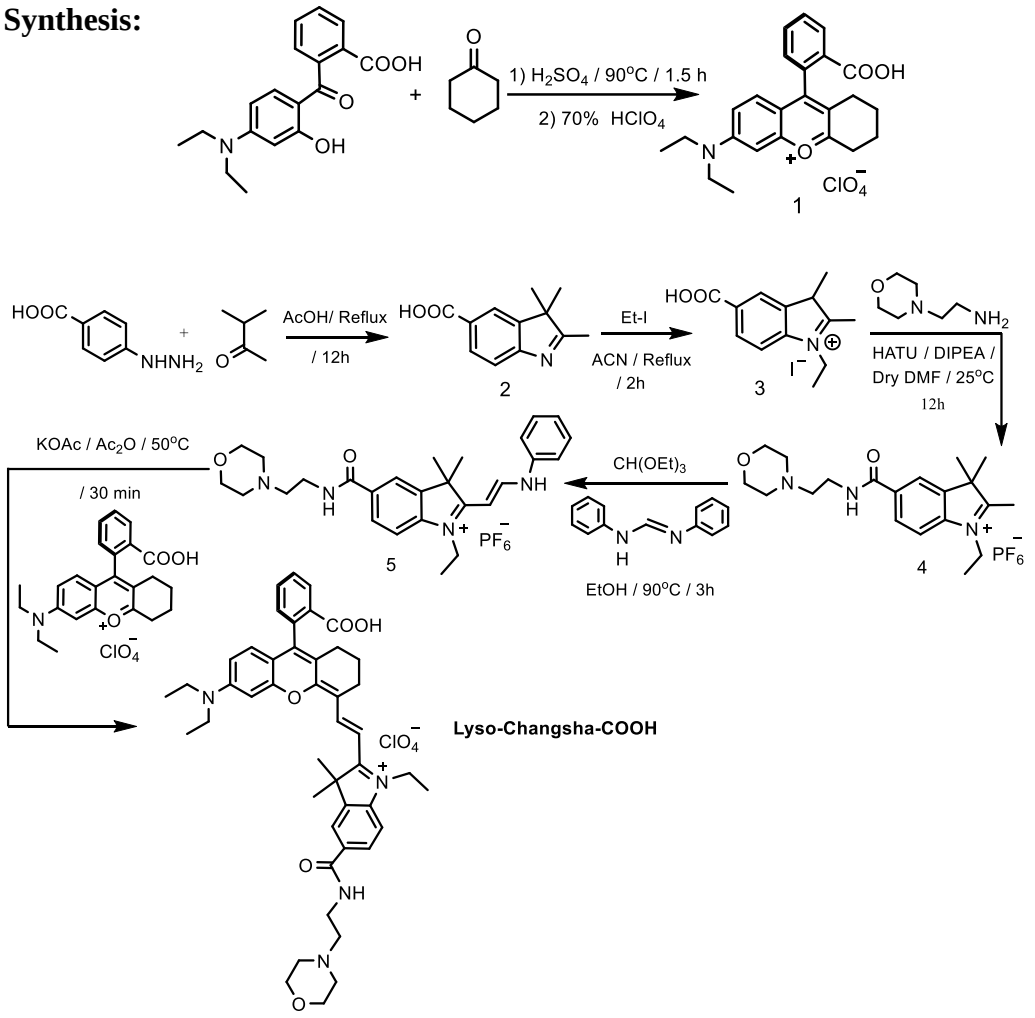

Figure 1. Synthesis of the compounds 1-5 and Lyso-Changsha-COOH.

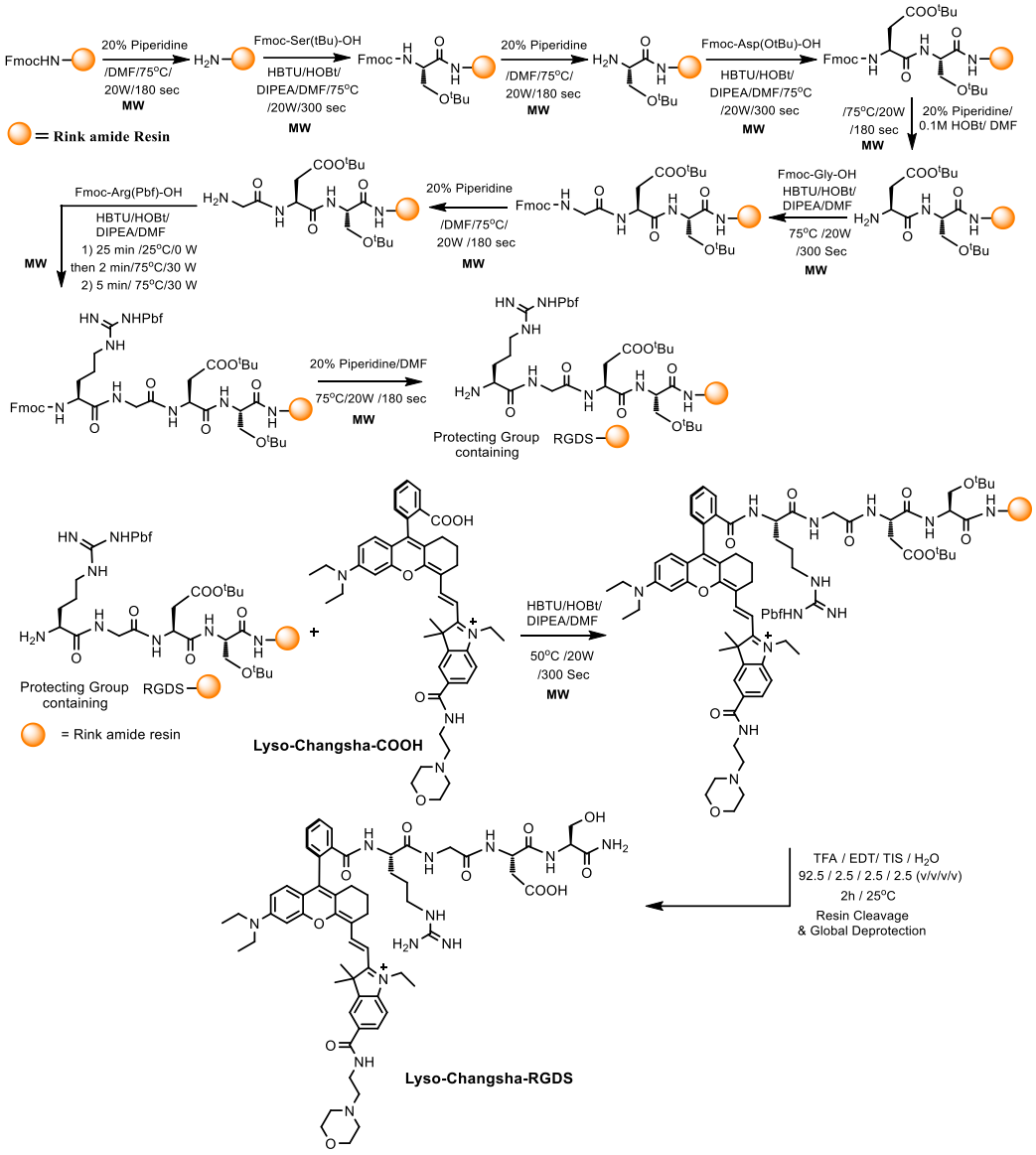

Figure 2. Synthesis of RGDS peptide and Lyso-Changsha-RGDS conjugate using Fmoc-SPPS protocol on the Rink amide AM resin.

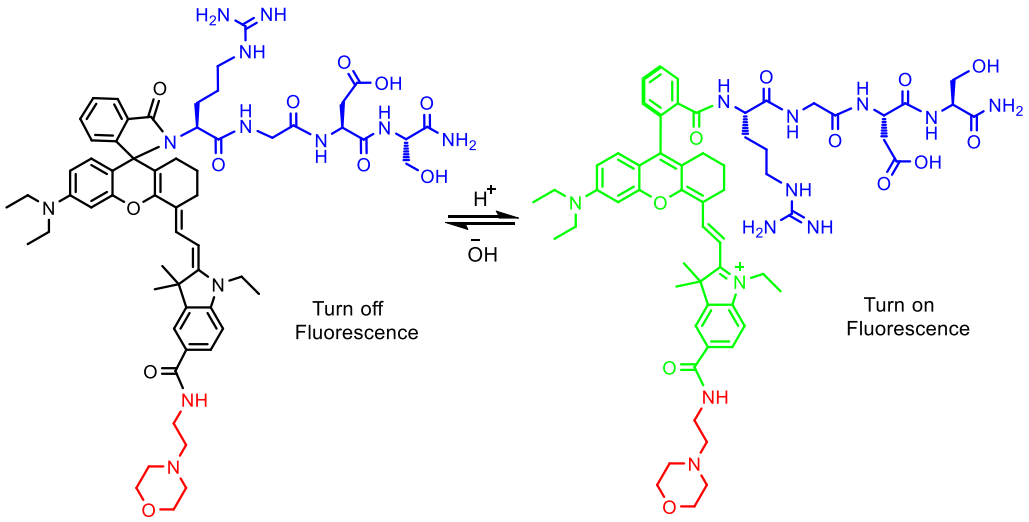

Figure 3. Dynamic pH switching of the closed and open form of Lyso-Changsha-RGDS.

Synthesis of 9-(2-carboxyphenyl)-6-(diethylamino)-1,2,3,4-tetrahydroxanthylium perchlorate (Compound 1) Freshly distilled cyclohexanone (6.6 mL, 63.7 mmol) was added drop wise to concentrated H_2SO_4 (70 mL) and cooled down to 0°C. Then, compound 2-(4-(diethylamino)-2-hydroxybenzoyl) benzoic acid (10.027 g, 32 mmol) was added in portions with vigorous stirring. The reaction mixture was heated at 90°C for 1.5 h, cooled down to room temperature, and poured into crushed ice. Perchloric acid (70%, 7 mL) was then added, and the resulting precipitate was filtered and washed with cold water (100 mL). A red solid pure compound 1 was obtained.

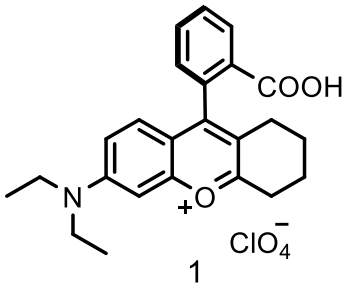
1

Yield: 11.88 g (78%).

^{1}H NMR (300 MHz, $CDCl_3$, 298 K): δ = 8.28 (d, J = 7.7 Hz, 1H), 7.79–7.63 (m, 2H), 7.20 (d, J = 7.5 Hz, 1H), 7.12–7.04 (m, 2H), 6.88 (s, 1H), 3.63 (q, J = 7.2 Hz, 4H),

2.38–2.26 (m, 2H), 2.03–1.90 (m, 2H), 1.86–1.70 (m, 4H), and 1.32 (t, J = 7.1 Hz, 6H) ppm. ^{13}C NMR (75 MHz, $CDCl_3$, 298 K): δ = 194.84, 166.07, 158.00, 153.00, 134.04, 132.56, 130.69, 128.68, 128.06, 122.67, 121.92, 118.08, 117.56, 46.68, 29.44, 25.13, 23.55, 21.43, 21.00, and 12.55 ppm. HRMS (ESI +ve) *m*/*z*: Observed for $C_{24}H_{26}NO_3^+$ $[M]^+$ = 376.1902, $[M]^+_{calcd}$ = 376.1907.

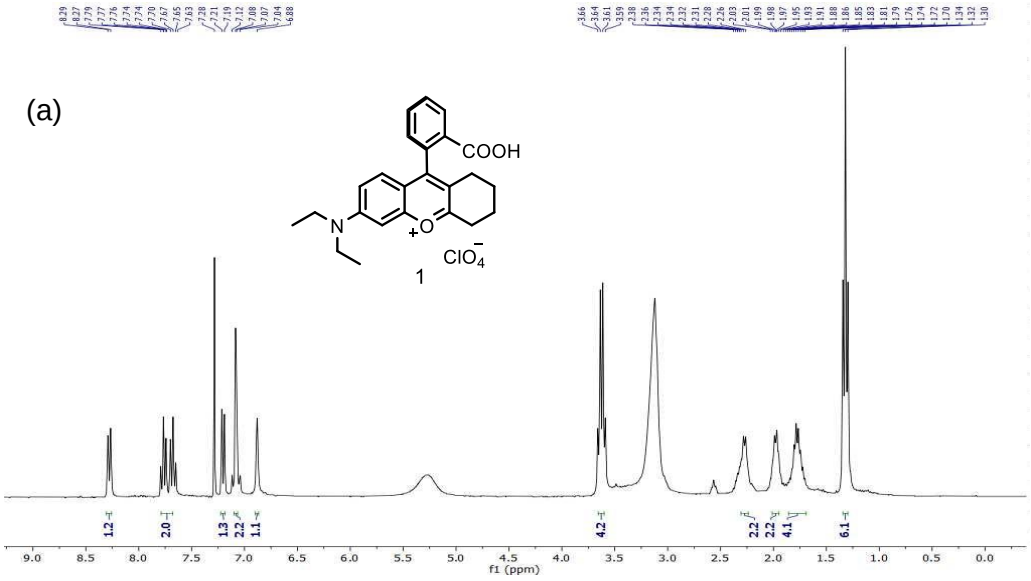

Figure 4a. ^{1}H NMR spectrum (300 MHz, $CDCl_3$, 298**)**

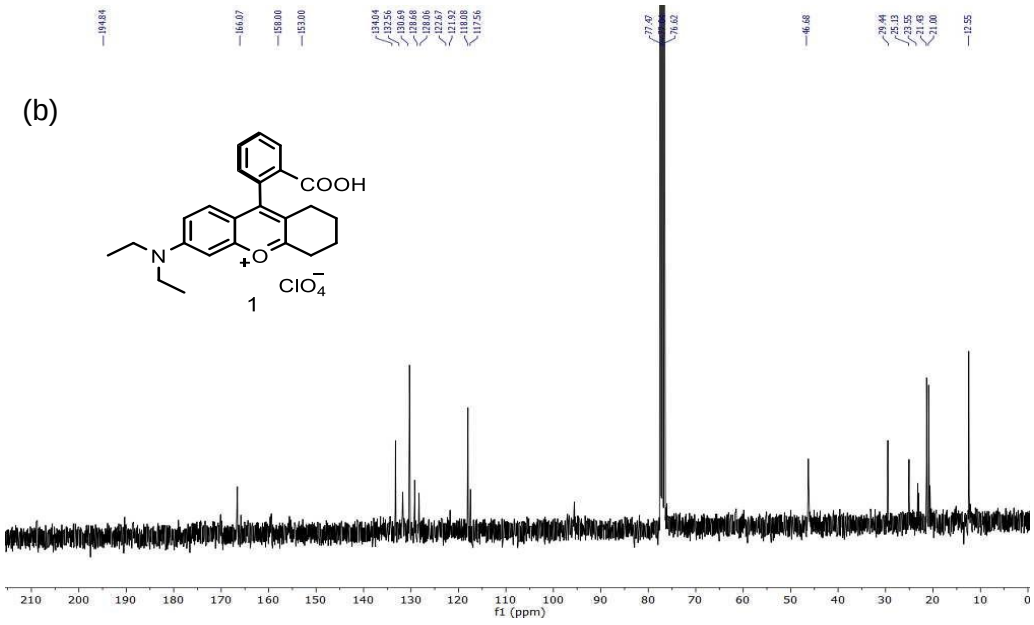

Figure 4b. ^{13}C NMR spectrum (75 MHz, $CDCl_3$, 298 K).

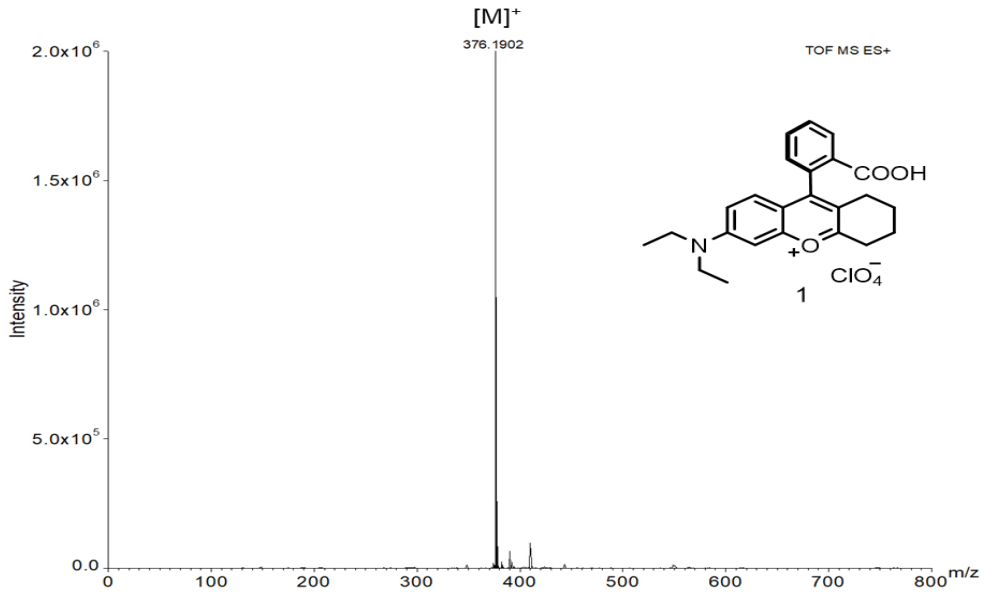

Figure 5. HRMS (ESI +ve) spectrum.

Synthesis of 2,3,3-trimethyl-3*H*-indole-5-carboxylic acid (Compound 2): Compound 2 was synthesised using our previously reported procedure.[34] 3-Methyl-2-butanone (2 mL, 32 mmol) was added into the glacial AcOH (30 mL) solution of 4-hydrazinobenzoic acid (1.83 g, 12 mmol). The solution was refluxed for 12 h and then cooled to room temperature. The solvent was removed under decreased pressure. By using column chromatography (50% EtOAc/Hexane), the crude product was further purified to yield the pure chemical as a light yellow solid (R_f = 0.4, 50% EtOAc/Hexane). Yield: 1.54 g (63%).

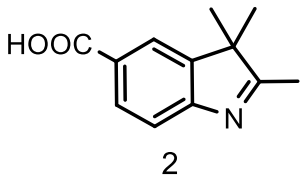

2

^{1}H NMR (300 MHz, DMSO-d_6, 298K): δ = 12.74 (br, 1H), 7.97 (d, J = 1.3 Hz, 1H), 7.90 (dd, J = 1.6 Hz and J = 8.0 Hz, 1H), 7.48 (d, J = 8.1 Hz, 1H), 2.24 (s, 3H), and 1.26 (s, 6H) ppm.

^{13}C NMR (101 MHz, DMSO-d_6, 298K): δ = 192.17, 168.03, 157.93, 146.62, 130.16, 127.83, 123.24, 119.64, 53.98, 22.78, and 15.84 ppm.

HRMS (ESI +ve) *m*/*z*: Observed for $C_{12}H_{14}NO_2^+$ $[M+H]^+$ = 204.1016, $[M]^+$ calcd = 204.1019.

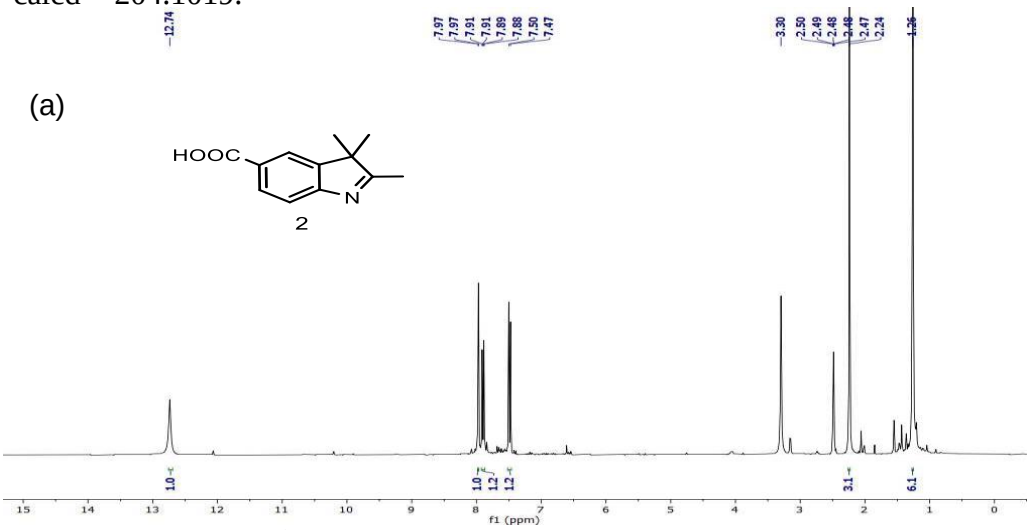

Figure 6a. ^{1}H NMR spectrum (300 MHz, DMSO-d_6, 298 K).

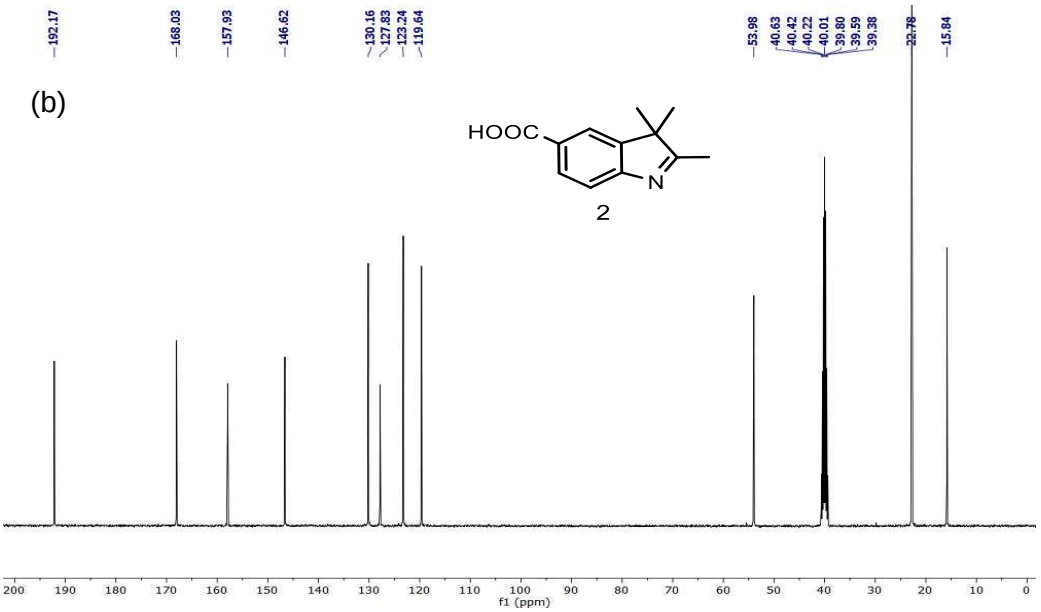

Figure 6b. ^{13}C NMR spectrum (101 MHz, DMSO-d_6, 298 K).

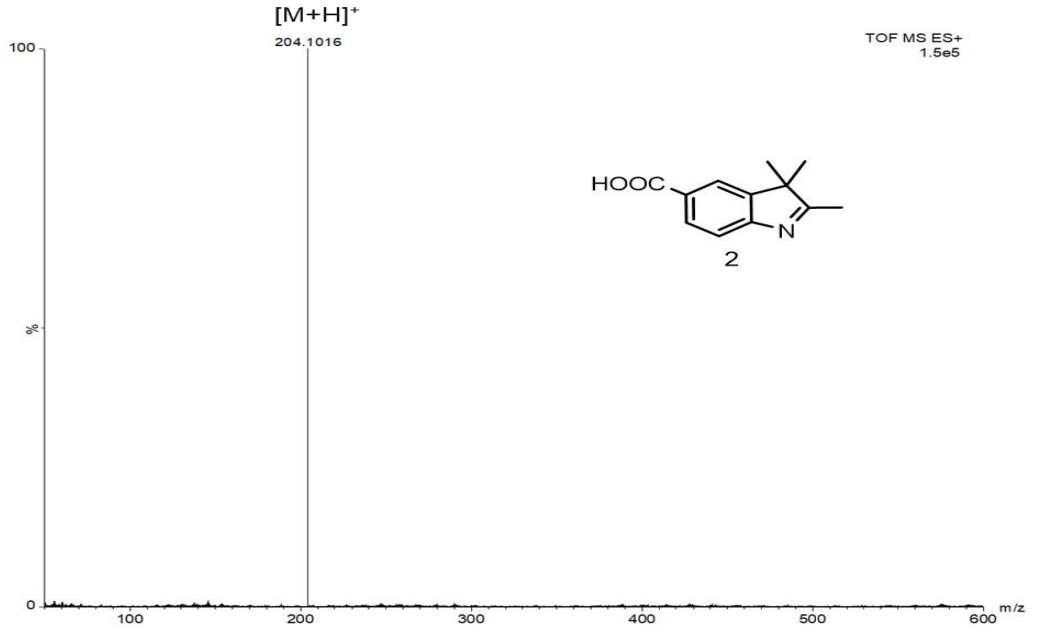

Figure 7. HRMS (ESI +ve) spectrum.

Synthesis of 5-carboxy-1-ethyl-2,3,3-trimethyl-3*H*-indol-1-ium iodide (Compound 3): Compound 2 (0.5 g, 2.46 mmol) and C_2H_5I (1.25 g, 8.0 mmol) were dissolved in CH_3CN (10 mL) and refluxed for 3 h. After the reaction was completed, it was cooled to room temperature and Et_2O was added to the solution. A deep brown precipitate was formed and it was filtered. The residue was repeatedly washed with Et_2O (5×25 mL) to obtain a pure light brown solid compound 3.

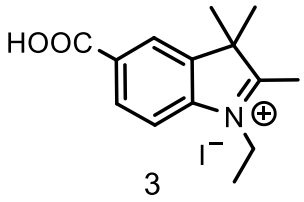

3

Yield: 0.064 g (72%)

^{1}H NMR (300 MHz, DMSO-d_6, 298 K): δ = 8.40 (s, 1H), 8.19 (d, J = 8.5 Hz, 1H), 8.09 (d, J = 8.3 Hz, 1H), 4.53 (q, J = 7.7 Hz, 2H), 2.88 (s, 3H), 1.58 (s, 6H), and 1.46 (t, J = 7.3 Hz, 3H) ppm.

^{13}C NMR (75 MHz, DMSO-d_6, 298 K): δ = 199.51, 166.77, 146.24, 143.62, 131.94, 131.02, 124.86, 118.40, 57.13, 44.45, 22.23, 15.11, and 13.73 ppm.

HRMS (ESI +ve) *m*/*z*: Observed for $C_{14}H_{18}NO_2^+$ $[M]^+$ = 232.1335, $[M]^+$ calcd = 232.1332.

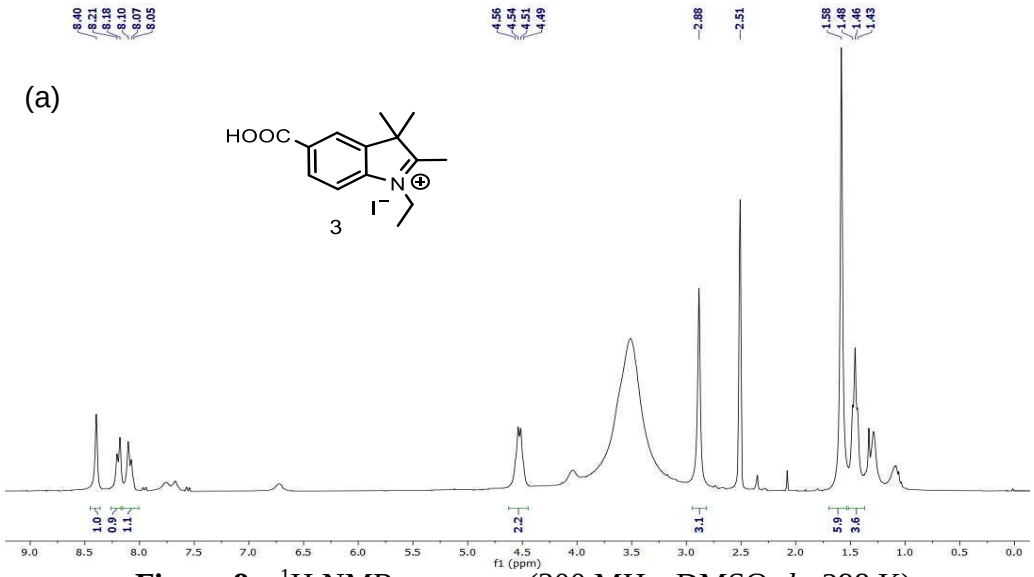

Figure 8a. ^{1}H NMR spectrum (300 MHz, DMSO-d_6, 298 K).

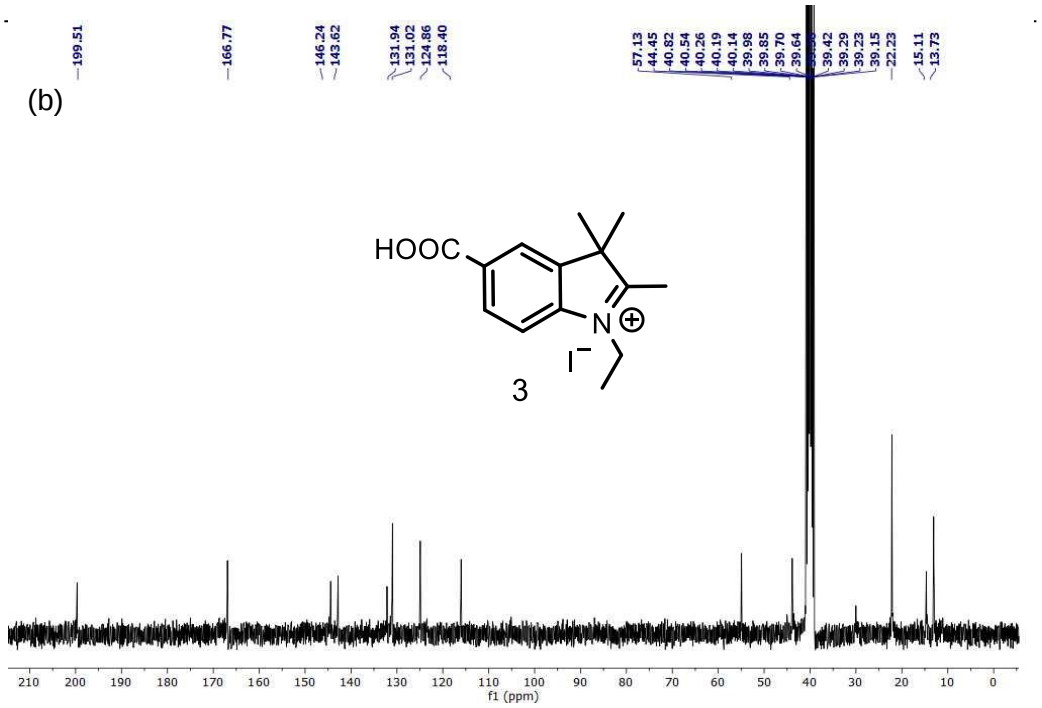

Figure 8b. ^{13}C NMR spectrum (75 MHz, DMSO-d_6, 298 K).

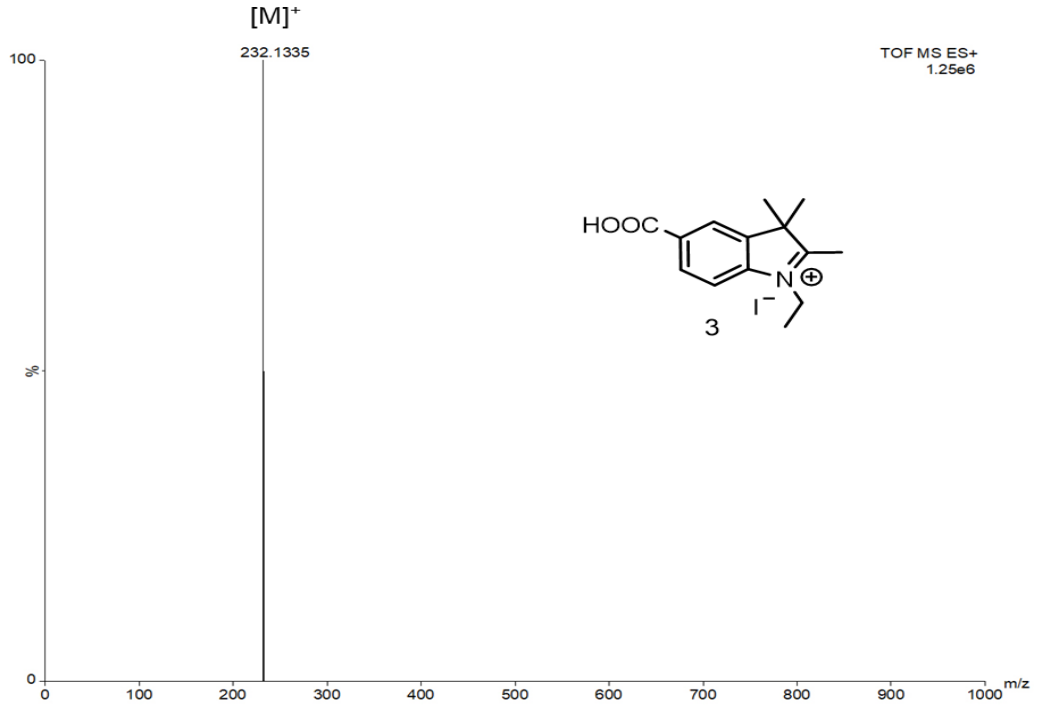

Figure 9. HRMS (ESI +ve) spectrum of compound 3.

Synthesis of 1-ethyl-2,3,3-trimethyl-5-((2-morpholinoethyl)carbamoyl)-3*H*-indol-1-ium hexafluorophosphate(V) (Compound 4): Under stirring conditions, compound 3 (0.83 g, 2.29 mmol) was added to ice-cold DMF (3 mL). Next, DIPEA (0.87 mL, 5 mmol) and HATU (0.96 g, 2.52 mmol) were added to the mixture. After 30 minutes, 4-(2-aminoethyl)morpholine (0.65 mL, 5 mmol) was added and the reaction was stirred for 18 h. Cold distilled water was added to the reaction mixture and extracted with DCM. The organic layer was collected, dried over anhydrous Na_2SO_4, and concentrated under reduced pressure. Column chromatography was used to separate the pure product 4, which was obtained as a pink gummy solid.

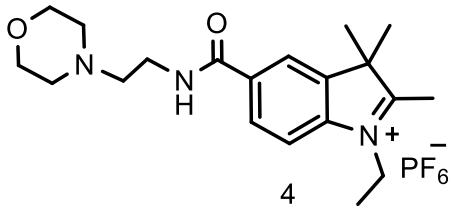

4

Yield: 0.85 g (76%)

^{1}H NMR (300 MHz, $CDCl_3$, 298 K): δ = 7.61–7.55 (m, 2H), 6.98 (t, J = 6.3 Hz, 1H), 6.47–6.41 (m, 1H), 3.76–3.73 (m, 6H), 3.62–3.55 (m, 2H), 2.69 (s, 3H), 2.59–2.56 (m, 6H), 1.40 (t, J = 6.4 Hz, 3H), and 1.25 (s, 6H) ppm.

^{13}C NMR (75 MHz, DMSO-d_6, 298 K): δ = 196.93, 174.82, 142.33, 141.50, 129.88, 129.42, 124.06, 116.05, 54.68, 48.11, 33.86, 27.47, 25.89, 24.50, 22.55, and 14.97 ppm.

HRMS (ESI +ve) *m*/*z*: Observed for $C_{20}H_{31}N_3O_2^{2+}$ $[M+H]^{2+}$ = 172.6208, $[M+H]^{2+}$ calcd = 172.6203 (*m*/*z*, *z* = 2).

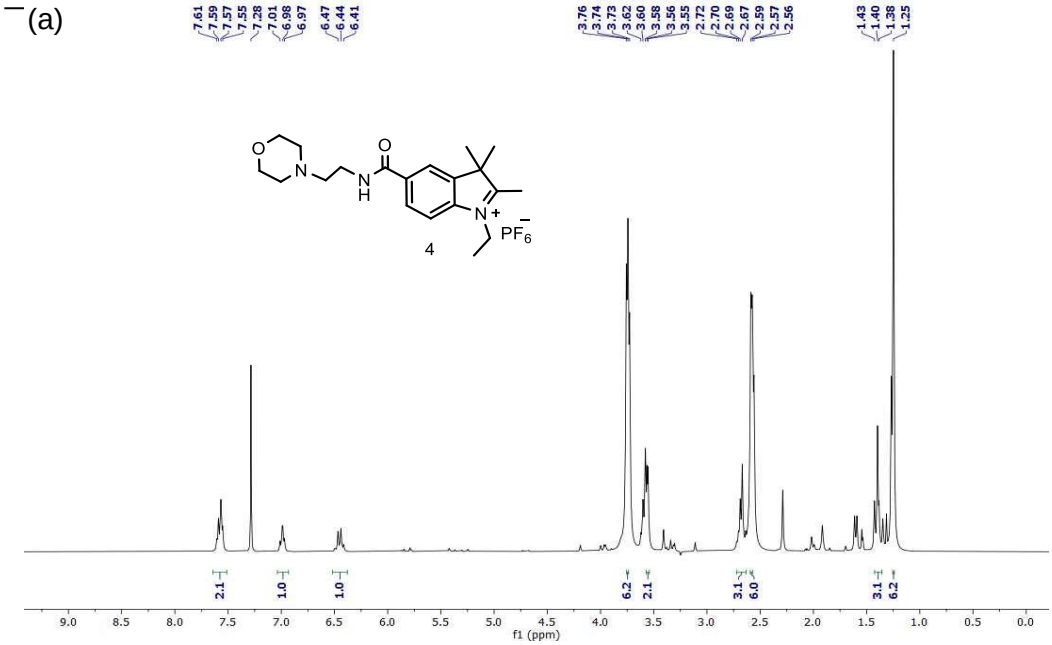

Figure 10a. ^{1}H NMR spectrum (300 MHz, $CDCl_3$, 298 K).

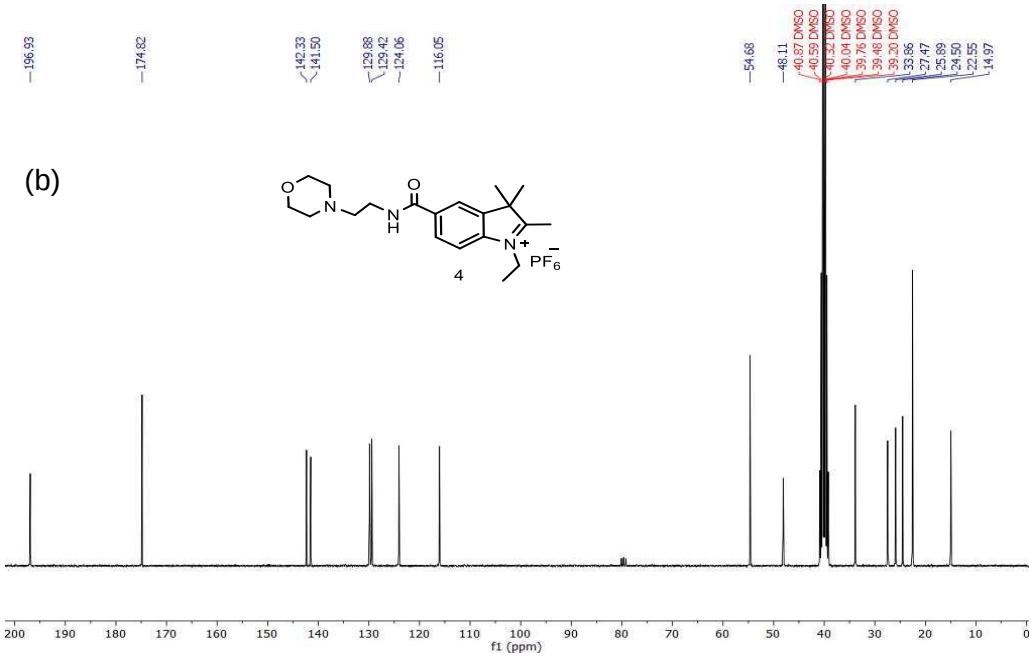

Figure 10b. ^{13}C NMR spectrum (75 MHz, DMSO-d_6, 298 K).

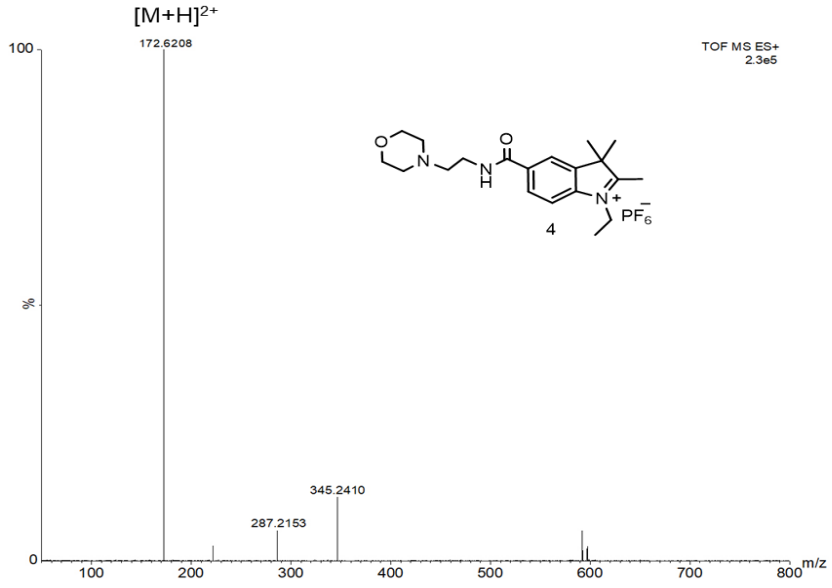

Figure 11. HRMS (ESI +ve) spectrum.

Synthesis of Compound (*E*)-1-ethyl-3,3-dimethyl-5-((2-morpholinoethyl)carbamoyl)-2-(2-(phenylamino)vinyl)-3H-indol-1-ium hexafluorophosphate(V) (Compound 5): Compound 4 (4.89 g, 10 mmol), triethyl orthoformate (1.32 mL, 10 mmol), and N,N'-bis-phenylformamidine (1.96 g, 10 mmol) were dissolved in 10 mL of EtOH. The mixture was heated to reflux for 2 h. The resulting mixture was cooled to room temperature and then poured into 50 g of crushed ice. The product was separated by filtration and the residue was washes with ice-cold diethyl ether to afford the pure compound 5 as a red solid.

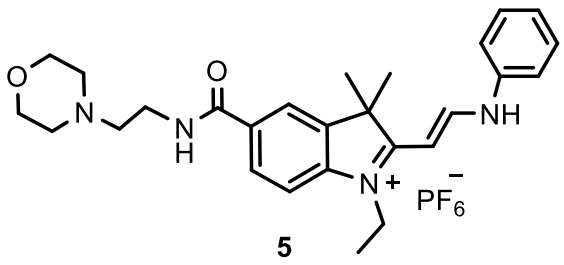

Yield: 4.6 g (76%)

^{1}H NMR (300 MHz, $CDCl_3$, 298 K): δ = 8.53 (d, J = 14.9 Hz, 1H), 8.21 (s, 1H), 7.55–7.51 (m, 2H), 7.42–7.36 (m, 1H), 7.22 (t, J = 7.4 Hz, 1H), 7.08–7.05 (m, 2H), 6.87 (d, J = 6.1 Hz, 1H), 6.66–6.60 (m, 2H), 5.96 (d, J = 14.4 Hz, 1H), 4.10–4.08 (m, 2H), 3.57–3.49 (m, 6H), 2.65–2.29 (m, 6H), 1.45 (t, J = 6.4 Hz, 3H), and 1.28 (s, 6H) ppm.

^{13}C NMR (75 MHz, $CDCl_3$, 298 K): δ = 171.01, 163.75, 156.41, 152.25, 142.26, 141.13, 132.66, 128.80, 124.94, 122.29, 116.92, 114.22, 111.93, 109.21, 98.09, 95.74, 68.69, 49.07, 45.79, 39.27, 29.60, 28.55, 26.73, 24.40, 20.72, 13.77, and 12.10 ppm.

HRMS (ESI +ve) *m/z*: Observed for $C_{27}H_{36}N_4O_2^{2+}$ $[M+H]^{2+}$ = 224.1410, $[M+H]^{2+}$ calcd = 224.1414.

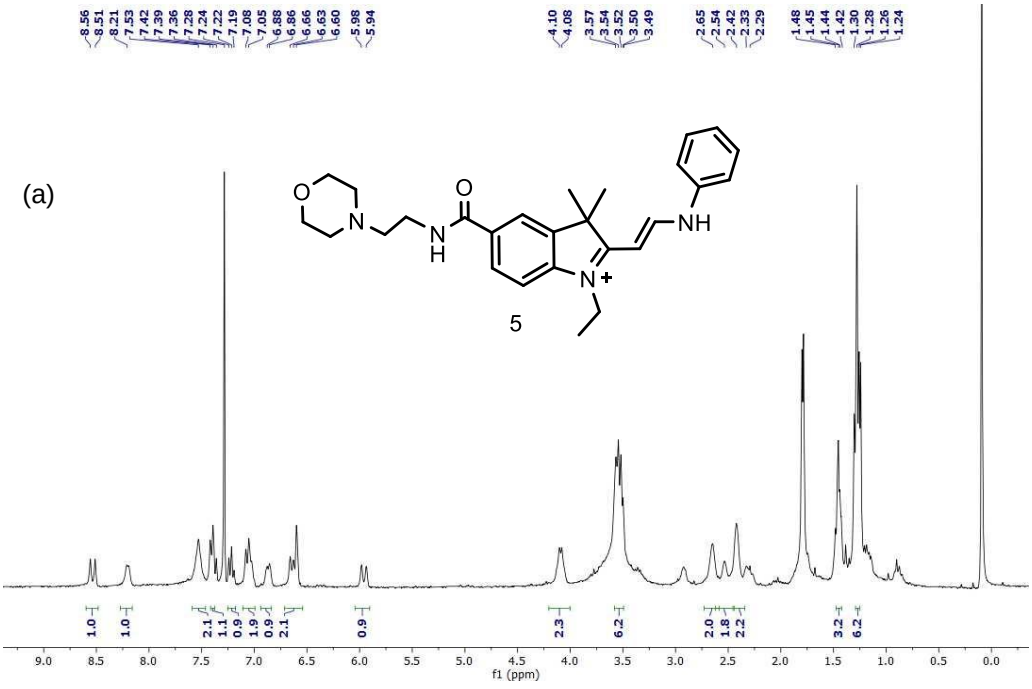

Figure 12a. ^{1}H NMR spectrum (300 MHz, $CDCl_3$, 298 K).

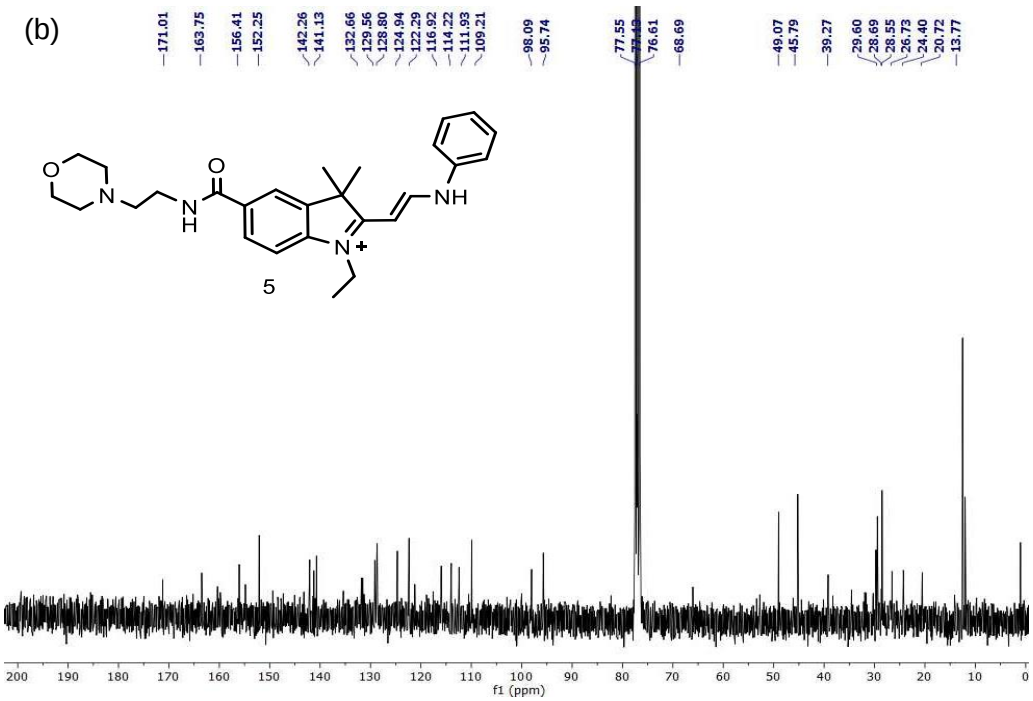

Figure 12b. ^{13}C NMR spectrum (75 MHz, $CDCl_3$, 298 K).

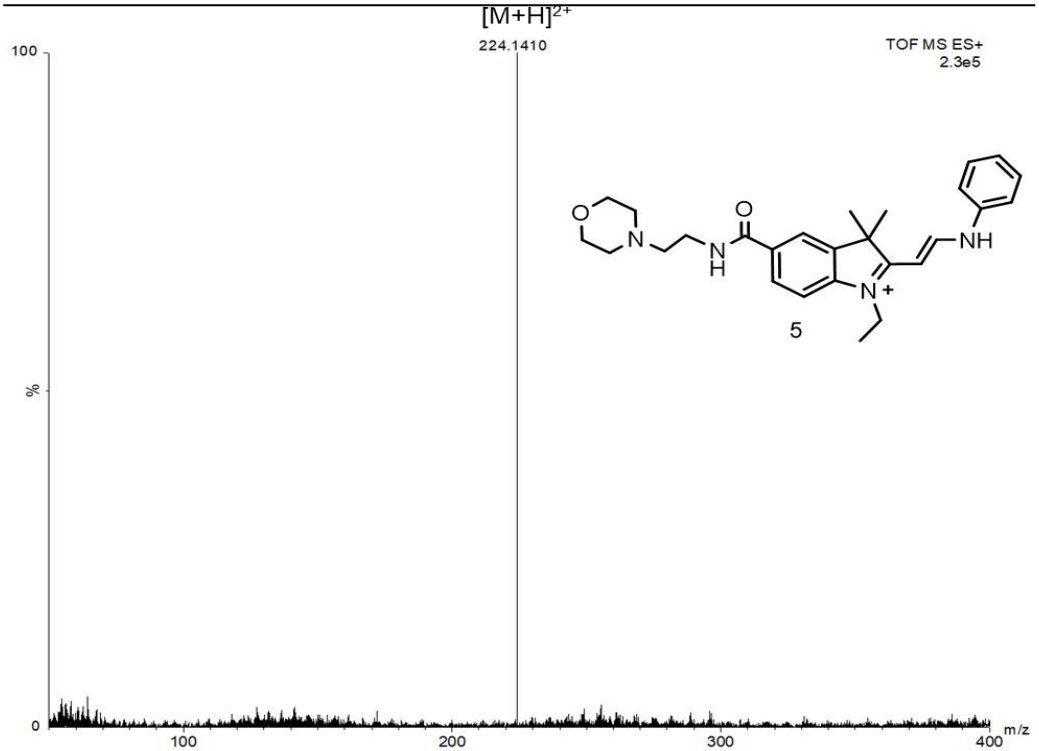

Figure 13. HRMS (ESI +ve) spectrum.

Synthesis of compound (*E*)-2-(2-(9-(2-carboxyphenyl)-6-(diethylamino)-2,3-dihydro-1*H*-xanthen-4-yl)vinyl)-1-ethyl-3,3-dimethyl-5-((2-morpholinoethyl)carbamoyl)-3*H*-indol-1-ium perchlorate (Lyso-Changsha-COOH): The freshly synthesized compound 9-(2-carboxyphenyl)-6-(diethylamino)-1,2,3,4-tetrahydroxanthylium perchlorate (Compound 1, 0.95 g, 2.0 mmol), compound 5 (1.2 g, 2.0 mmol), and KOAc (0.22 g, 2.2 mmol) were dissolved in 15 mL Ac_2O. The mixture was heated to 50°C for 30 min and the solution turned green. After vigorous stirring for 10 min at room temperature, the mixture was added into 100 mL water. The crude product was filtered and thoroughly cleaned with water (3 × 25 mL) and diethyl

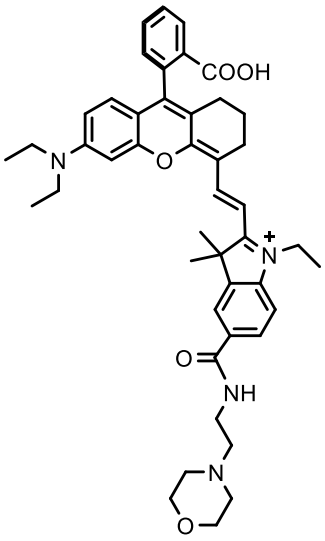

Lyso-Changsha-COOH

ether (3 × 25 mL). Crude material was purified by column chromatography using DCM/MeOH (40:1) mixture as the eluent. The green component was collected to afford the pure compound Lyso-Changsha-COOH as a green solid. Yield: 1.16 g (70%).

^{1}H NMR (400 MHz, $CDCl_3$, 298 K): δ = 8.56 (d, J = 13.8 Hz, 1H), 8.21–8.17 (m, 1H), 7.58–7.57 (m, 2H), 7.40 (t, J = 7.9 Hz, 2H), 7.28–7.24 (m, 1H), 7.22–7.07 (m, 2H), 6.89 (d, J = 9.3 Hz, 1H), 6.62–6.58 (m, 2H), 5.98 (d, J = 13.8 Hz, 1H), 4.11–4.09 (m, 2H), 3.76–3.72 (m, 6H), 3.38–3.35 (m, 4H), 2.66–2.64 (m, 4H), 2.61–2.49 (m, 4H), 1.81–1.79 (m, 2H), 1.71–1.67 (m, 2H), 1.45 (t, J = 5.9 Hz, 3H), 1.28 (s, 6H), and 1.19–1.15 (m, 6H) ppm.

^{13}C NMR (101 MHz, $CDCl_3$, 298 K): δ = 169.62, 161.40, 156.05, 152.74, 152.16, 150.00, 143.23, 142.07, 134.78, 131.32, 131.19, 128.82, 127.89, 127.57, 122.43, 122.32, 122.23, 116.06, 112.54, 109.76, 108.17, 97.76, 66.55, 66.21, 64.07, 56.79, 53.08, 48.97, 45.22, 44.68, 43.50, 34.54, 31.92, 30.27, 29.69, 29.43, 28.62, 28.35, 24.36, 22.68, 14.10, 12.51, and 11.96 ppm.

HRMS (ESI +ve) *m*/*z*: Observed for $C_{45}H_{54}N_4O_5^{2+}$ $[M+H]^{2+}$ = 365.2048, $[M+H]^{2+}$ calcd = 365.2042 (*m*/*z*, *z* = 2).

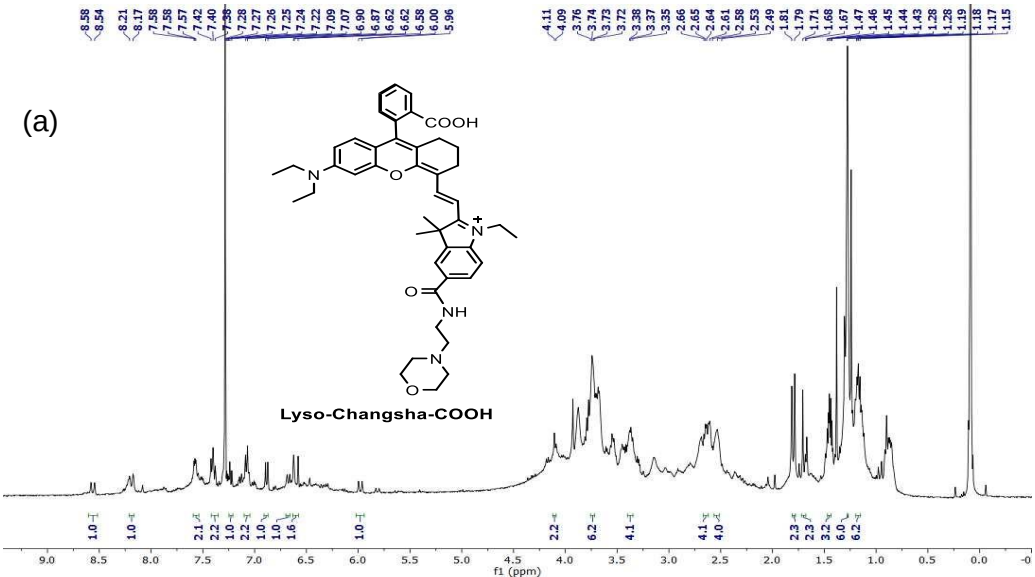

Figure 14a. ^{1}H NMR spectrum (300 MHz, $CDCl_3$, 298 K)

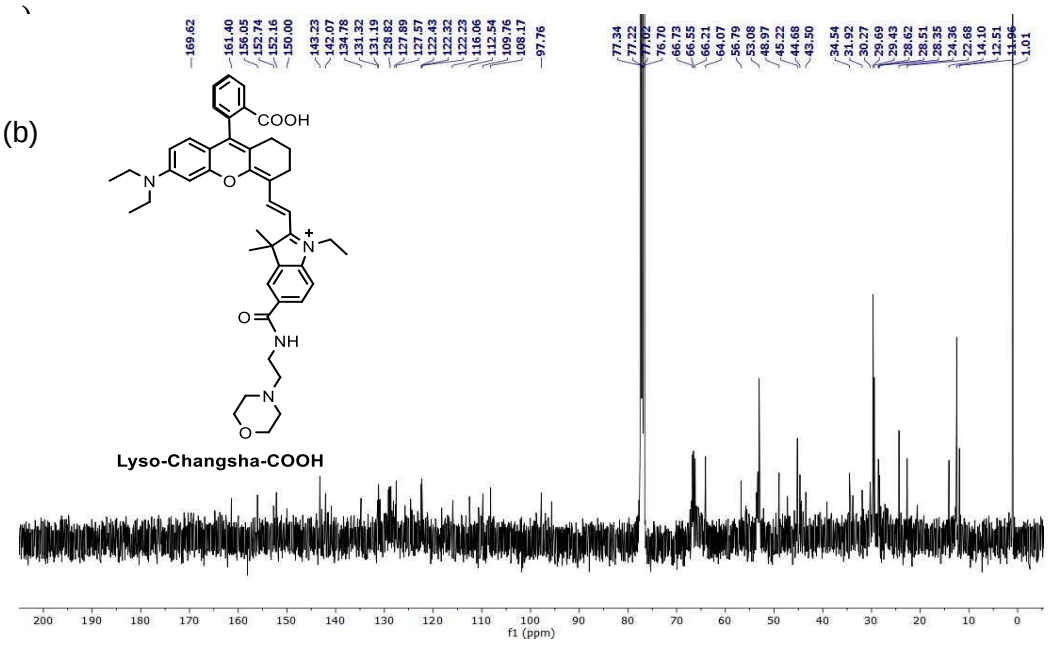

Figure 14b. ^{13}C NMR spectrum (75 MHz, $CDCl_3$, 298 K).

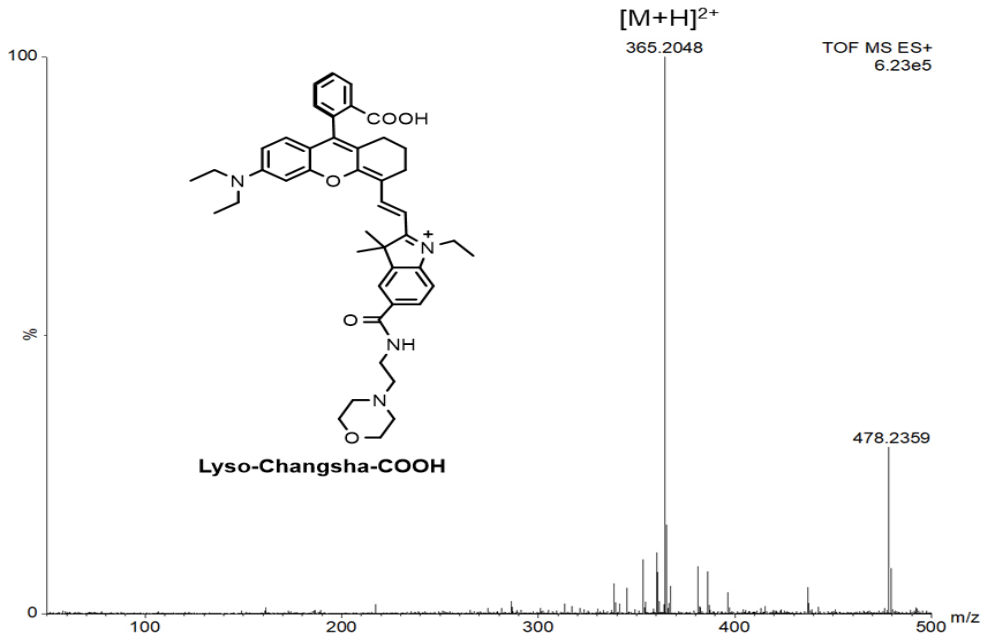

Figure 15. HRMS (ESI +ve) spectrum.

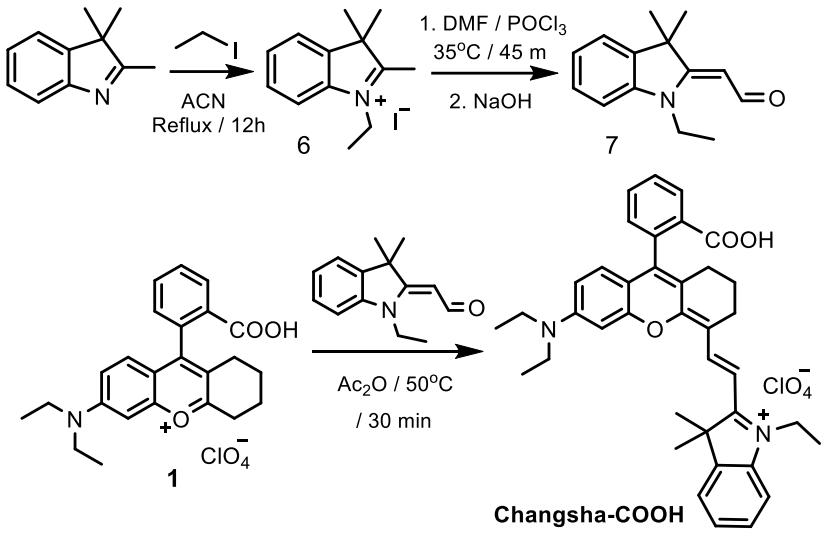

Figure 16. Synthesis of the compounds 6, 7, and Changsha-COOH.

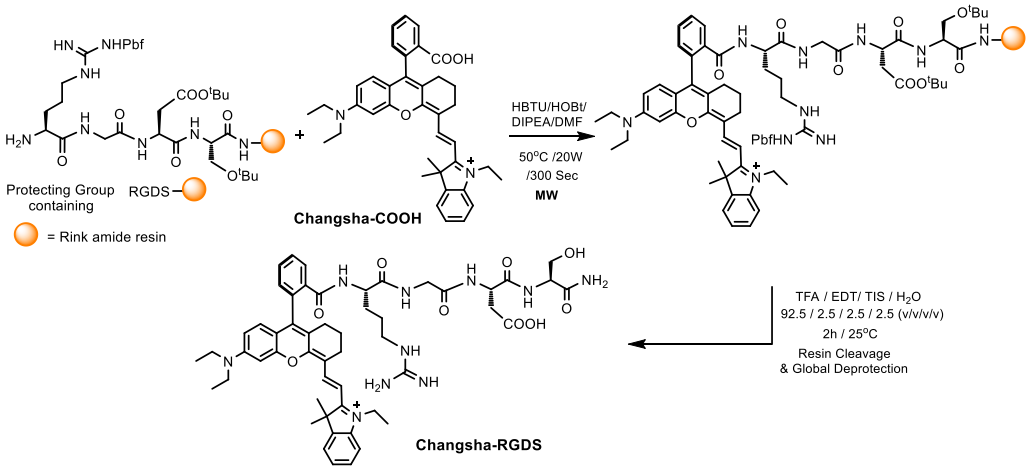

Figure 17. Solid phase synthesis of Changsha-RGDS conjugate on the Rink amide AM resin using Fmoc-SPPS protocol.

Synthesis of compound 1-ethyl-2,3,3-trimethyl-3*H*-indol-1-ium iodide (Compound 6): 2,3,3-trimethylindolenine (0.48 g, 3 mmol) and ethyl iodide (0.78 g, 5 mmol) were taken in a round bottom flask filled with 25 mL acetronitrile. The reaction mixture was heated to reflux for 12 h. After 12 h the color of the reaction mixture was turned into deep red from light orange color. The solvent was evaporated to get the crude product as a brown solid. The crude product was purified through column chromatography using 98:2 DCM/MeOH as eluent to obtain the pure product **6** as a brown solid.

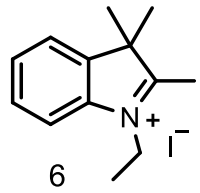

6

Yield: 0.63 g (66%)

^{1}H NMR (300 MHz, $CDCl_3$, 298 K): δ = 7.78–7.73 (m, 1H), 7.63–7.59 (m, 3H), 4.76 (m, 2H), 3.16 (s, 3H), 1.67 (s, 6H), and 1.63 (m, 3H) ppm.

^{13}C NMR (101 MHz, $CDCl_3$, 298 K): δ = 195.43, 141.72, 140.62, 130.20, 129.62, 123.42, 115.37, 54.68, 45.49, 23.20, 17.01, and 13.65 ppm.

HRMS (ESI +ve) *m*/*z*: Observed for $C_{13}H_{18}N^+$ $[M]^+$ = 188.1426, $[M]^+_{calcd}$ = 188.1434

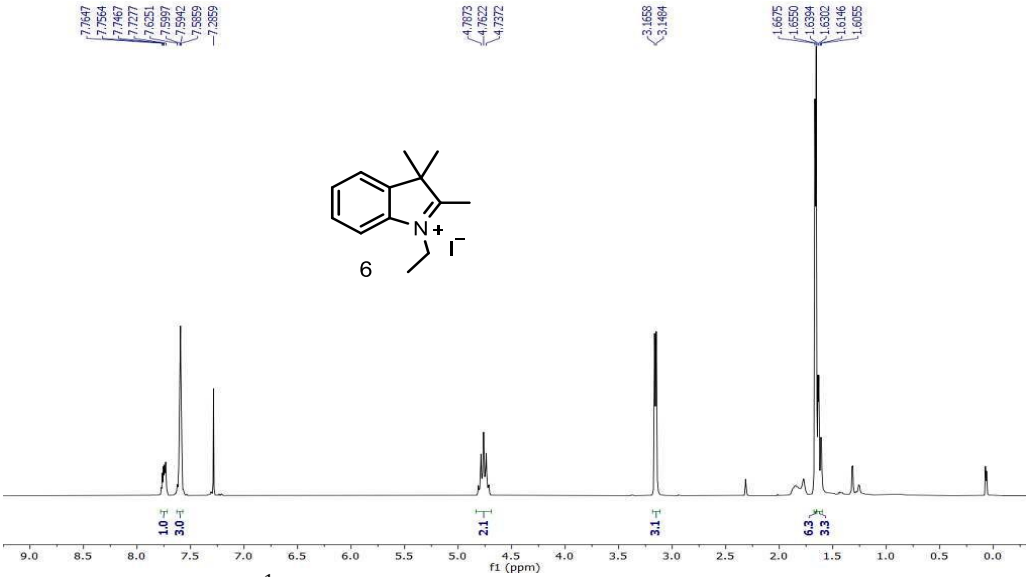

Figure 18. ^{1}H NMR spectrum (300 MHz, $CDCl_3$, 298 K).

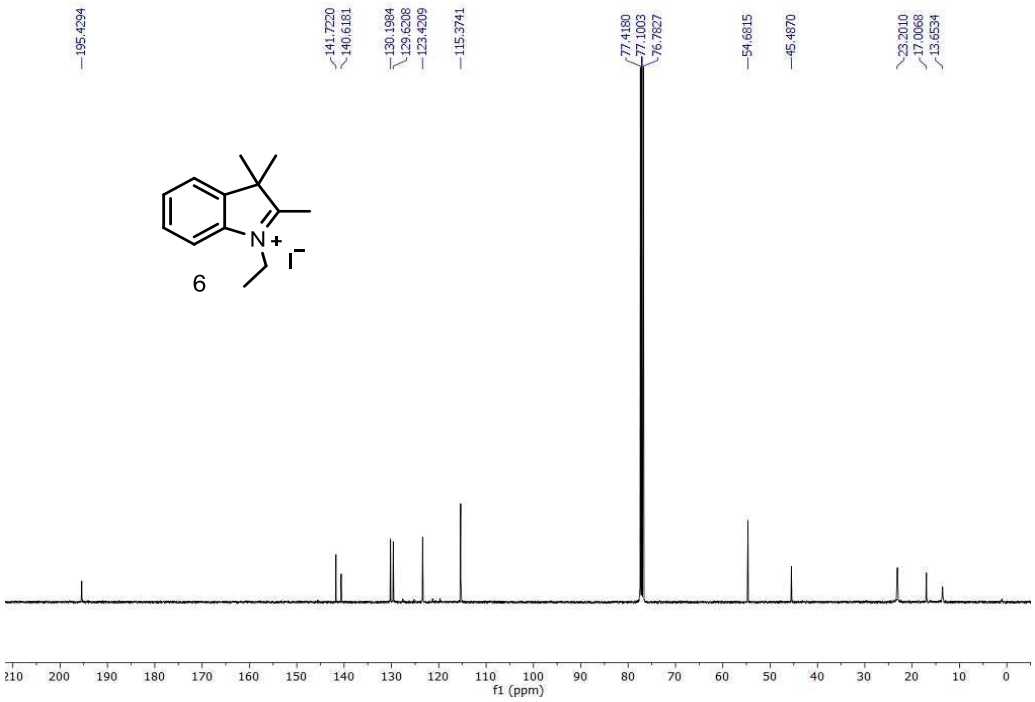

Figure 19. ^{13}C NMR spectrum (101 MHz, $CDCl_3$, 298 K).

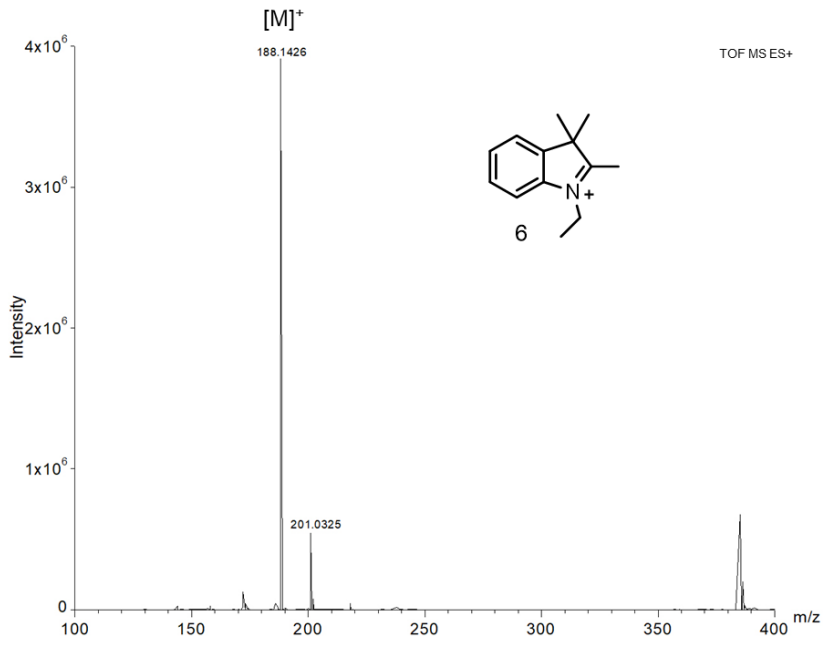

Figure 20. HRMS (ESI +ve) spectrum.

Synthesis of (*Z*)-2-(1-ethyl-3,3-dimethylindolin-2-ylidene)acetaldehyde (Compound 7): $POCl_3$ (6 mL) was added drop wise to cold DMF (19 mL) under stirring in an inert N_2 atmosphere, and the temperature was kept below 10°C for 30 min using an ice bath. After 30 min a mixture of compound 6 (11 g, 58.42 mmol) in DMF (4.8 mL) was added drop wise to the reaction vessel at this temperature and the solution was heated at 35°C for 45 min. Next the reaction solution was poured into ice-water and the mixture was basified to pH 10.0 using NaOH solution. The resulting solution was heated to boiling for 30 minutes and cooled to room temperature. The product

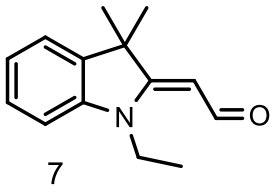

7

was precipitated out and it was filtered off and washed with cold water to afford red crystals of compound 7.

Yield: 7.5 g (60%)

^{1}H NMR (300 MHz, $CDCl_3$, 298 K): δ = 10.01 (d, J = 9.0 Hz, 1H), 7.31–7.25 (m, 2H), 7.08 (t, J = 7.4 Hz, 1H), 6.87 (d, J = 7.8 Hz, 1H), 5.45 (d, J = 8.97 Hz, 1H), 3.78 (q, J = 7.2 Hz, 2H), 1.66 (s, 6H), and 1.29 (t, J = 7.2 Hz, 3H) ppm.

^{13}C NMR (75 MHz, $CDCl_3$, 298 K): δ = 186.64, 172.62, 143.77, 139.55, 128.19, 122.43, 121.87, 108.14, 98.55, 47.53, 37.84, 29.54, and 11.22 ppm.

HRMS (ESI +ve) *m/z*: Observed for $C_{14}H_{18}NO^+$ $[M+H]^+$ = 216.1376, $[M+H]^+_{calcd}$ = 216.1383.

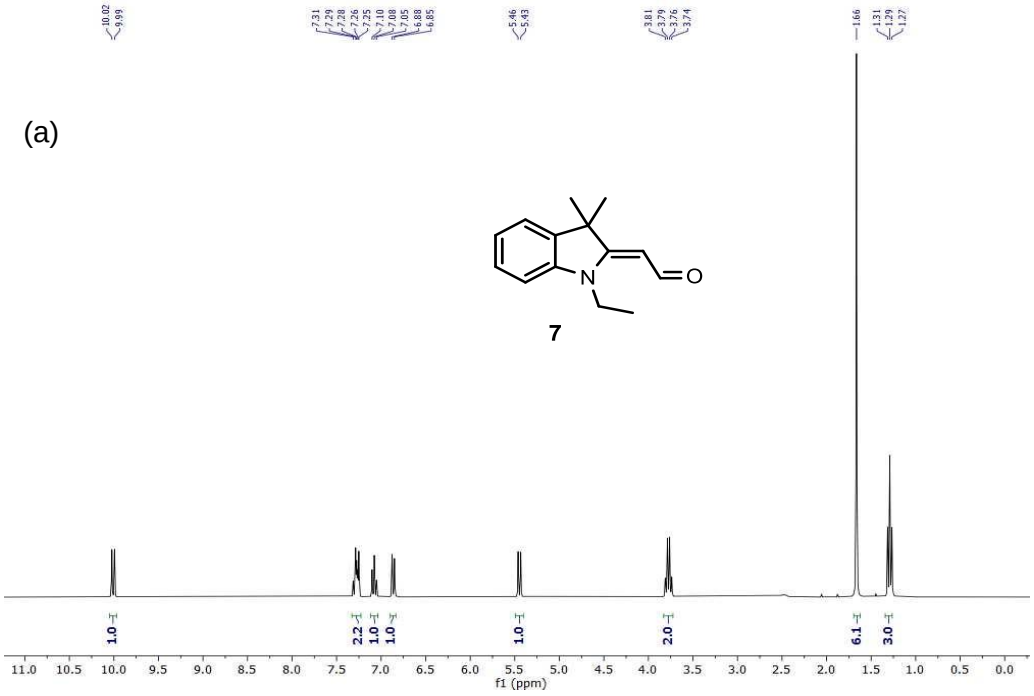

Figure 21a. ^{1}H NMR spectrum (300 MHz, $CDCl_3$, 298 K).

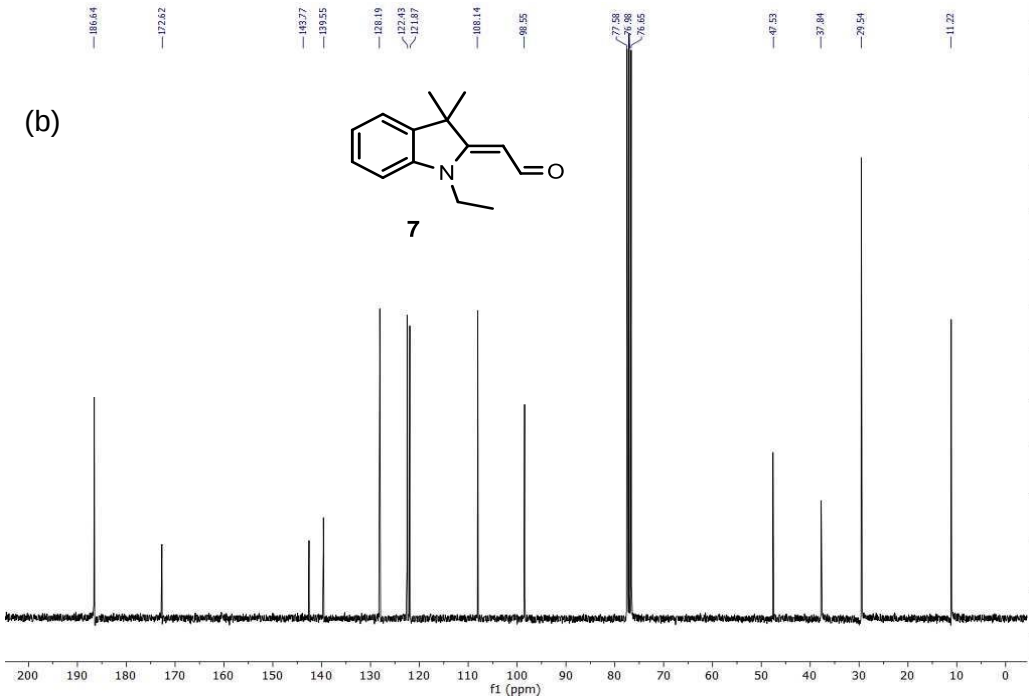

Figure 21. (b) ^{13}C NMR spectrum (75 MHz, $CDCl_3$, 298 K) of compound **7**.

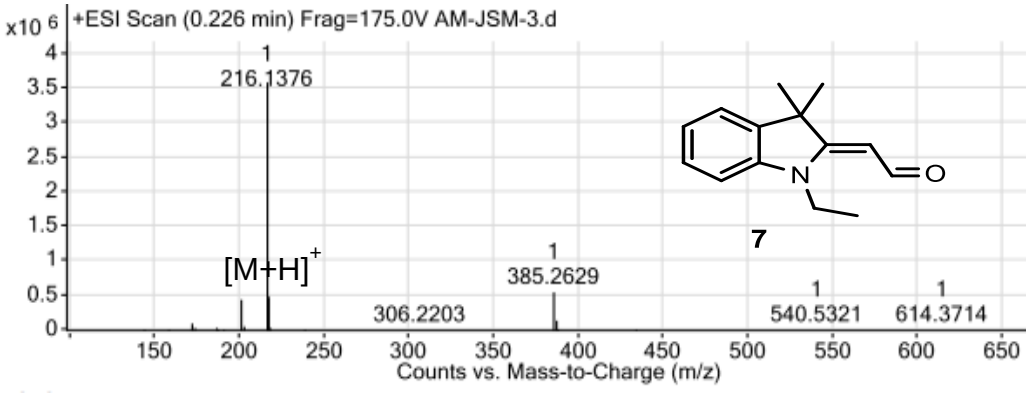

Figure 22. HRMS (ESI +ve) spectrum.

Synthesis of (*E*)-2-(2-(9-(2-carboxyphenyl)-6-(diethylamino)-2,3-dihydro-1*H*-xanthen-4-yl)vinyl)-1-ethyl-3,3-dimethyl-3*H*-indol-1-ium perchlorate (Changsha-COOH) : Compounds 1 (0.47 g, 0.22 mmol) and 7 (0.112 g, 0.21 mmol) were dissolved in acetic anhydride (8 mL), and the reaction mixture was heated to 50°C under stirring condition for 30 min. Next, water (8 mL) was added to the reaction mixture to quench the reaction. The solvent was removed on a rotary evaporator to give the crude product, which was purified by column chromatography using DCM/MeOH (20.0:0.1 to 2.0:0.1) as eluent to afford the pure compound Changsha-COOH as a green solid**.** Yield: 0.07 g (45%).

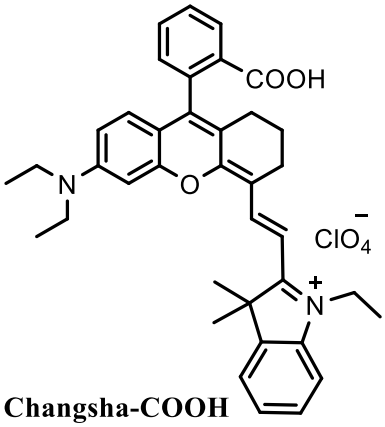

Changsha-COOH

^{1}H NMR (300 MHz, $CDCl_3$, 298 K): δ = 8.48 (d, *J* = 13.9 Hz, 1H), 8.27 (d, *J* = 7.6 Hz, 1H), 7.58–7.46 (m, 2H), 7.42–7.36 (m, 2H), 7.21 (t, *J* = 7.5 Hz, 1H), 7.06 (dd, *J* = 12.7, 7.6 Hz, 2H), 6.84 (d, *J* = 9.2 Hz, 1H), 6.62 (d, *J* = 9.2 Hz, 1H), 6.54 (d, *J* = 2.5 Hz, 1H), 5.93 (d, *J* = 13.8 Hz, 1H), 4.08 (q, *J* = 6.9 Hz, 2H), 3.51 (q, *J* = 7.1 Hz, 4H), 2.64–2.50 (m, 2H), 2.48–2.40 (m, 1H), 2.32–2.22 (m, 1H), 2.06–2.00 (m, 2H), 1.78 (s, 6H), 1.45 (t, *J* = 7.2 Hz, 3H), and 1.27 (t, *J* = 7.1 Hz, 6H) ppm.

^{13}C NMR (75 MHz, $CDCl_3$, 298 K): δ = 170.30, 168.39, 163.55, 156.55, 156.28, 152.19, 142.23, 140.74, 140.21, 135.16, 134.05, 131.63, 130.96, 129.28, 128.83, 128.60, 128.09, 124.16, 122.34, 121.33, 116.50, 114.70, 112.46, 110.01, 97.34, 95.30, 48.79, 45.28, 39.08, 28.82, 28.50, 26.37, 24.37, 20.45, 12.48, and 11.89 ppm.

HRMS (ESI +ve) *m*/*z*: Observed for $C_{38}H_{41}N_2O_3^+$ $[M]^+$ = 573.3098, $[M]^+$ calcd = 573.3112.

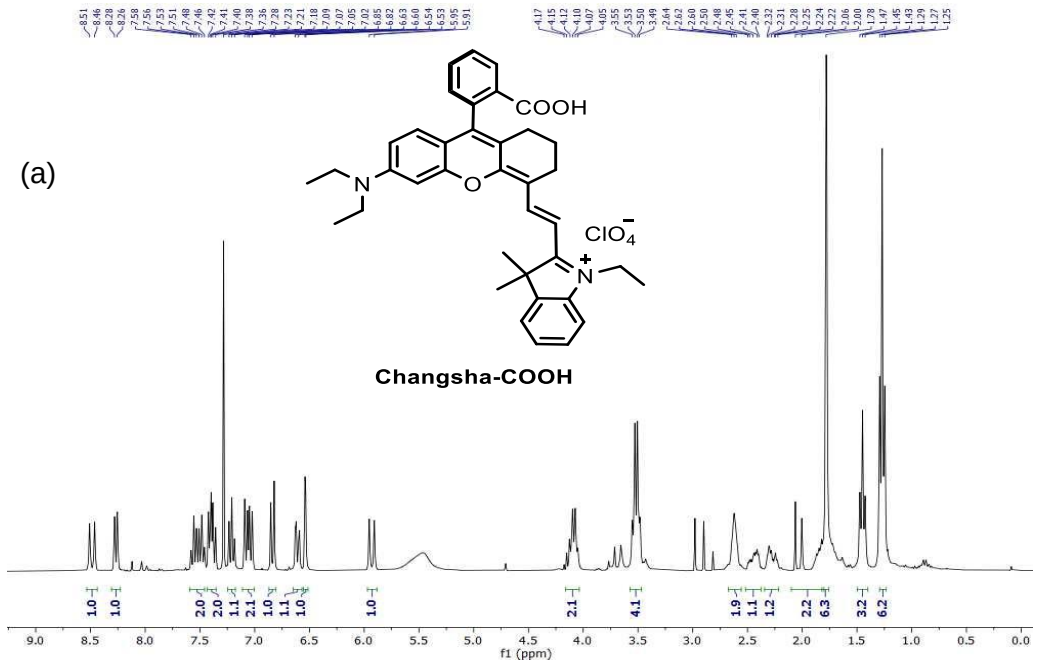

Figure 23a. ^{1}H NMR spectrum (300 MHz, $CDCl_3$, 298 K)

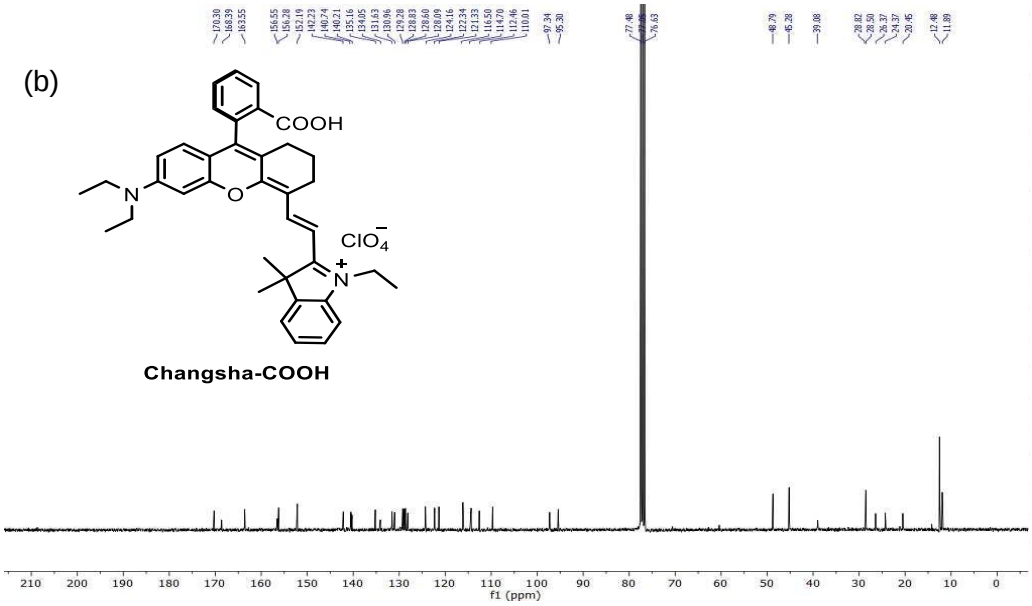

Figure 23b. ^{13}C NMR spectrum (75 MHz, $CDCl_3$, 298 K).

Manual Microwave Assisted Solid-Phase Peptide Synthesis (SPPS):

A manual microwave (MW)-assisted Fmoc-SPPS process was used to construct Arg-Gly-Asp-Ser (RGDS) tetrapeptide, Lyso-Changsha-RGDS conjugate, and Changsha-RGDS conjugate on a MW peptide synthesiser (CEM, Discover Bio). The RGDS tetrapeptide, Lyso-Changsha-RGDS conjugate, and Changsha-RGDS conjugate were synthesised using Fmoc-SPPS protocol on Rink Amide AM resin (LL, 0.26 mmol/g loading density, 100-200 mesh) from the C-termini to N-termini. Fmoc-amino acid building blocks Fmoc-Arg(Pbf)-OH, Fmoc-Gly-OH, Fmoc-Asp(OtBu)-OH, and Fmoc-Ser(tBu)-OH were used.

First Amino Acid [Fmoc-Ser(tBu)-OH] Loading on Rink Amide AM Resin (LL): The Rink amide AM resin (0.1 mmol) was swollen in DMF (2 mL) for 2 hour, the solvent was drained off and the resin was washed with 2 mL DMF. Fmoc of the Rink amide AM resin was deprotected by 20% piperidine/DMF; time 210 (or 180) sec, power 20 W, temperature 75ºC, delta temperature 5ºC on a manual microwave solid phase peptide synthesizer. The solvent was drained and the resin was washed with DMF (4×), DCM (4×), DMF (4×) to remove the dibenzofulvene by-product. Fmoc-Ser(tBu)-OH (5 eq), 0.5 M HBTU (4.9 eq), and 0.5 M HOBt (5 eq) were dissolved in 2 mL DMF, subsequently 2M DIPEA (10 eq.) was added and the mixture were taken into the MW reactor cartridge containing the Fmoc-deprotected Rink amide AM resin and MW reaction was performed for 300 sec (power 20 W, temperature: 75ºC, delta temperature: 5ºC) under N_2 bubbling. The solvent was drained and the resin was sequentially washed with DMF (3×), DCM (3×), DMF (3×). The loading density of Rink amide AM resin after Fmoc-Ser(tBu)-OH loading was assessed by UV/vis spectroscopy of the Fmoc-dibenzofulvene deprotection product.

Assessment of the First Amino Acid Fmoc-Ser(tBu)-OH Loading on the Rink Amide AM Resin (LL): In a 10 mL volumetric flask 5 mg Fmoc-Ser(tBu)-Rink amide AM resin, 2 mL 1,8-diazabicyclo[5.4.0]undec-7-en (DBU) in NMP (2% in NMP) were taken. After being shaken for 30 minutes in a shaker, CH_3CN was added up to the mark of the 10 mL volumetric flask. The solution was transferred to a UV quartz cuvette (path length = 1 cm) after being diluted with CH_3CN (1/12.5). The absorption of cleaved dibenzofulvene was monitored at 304 nm (ε_{304} = 7624 L mol^{-1} cm^{-1}) and adjusted against the reference. The Lambert-Beer's law was used to calculate the first amino acid loading on the Rink amide AM resin.

ρ(mmol/g) = $163.96\times(A - A_0)/m$

ρ = loading density of the Rink amide AM resin.

A = absorption of the sample

A_0 = absorption of the reference

m = mass of the analyzed Rink amide AM resin in mg.

MW-Assisted Fmoc-SPPS of RGDS Peptide, Lyso-Changsha-RGDS conjugate, and Changsha-RGDS conjugate on Rink Amide AM Resin: The synthesis of RGDS peptide, Lyso-Changsha-RGDS conjugate, and Changsha-RGDS conjugate were performed using MW assisted Fmoc-SPPS protocol on Rink amide AM resin at a 0.1 mmol scale.

Protocols for MW-Assisted Fmoc-SPPS:

1. Bubbling during the MW-assisted synthesis for all Steps: on 3 sec; off 7 sec.

2. **Fmoc Deprotection**: 20% piperidine/DMF; time 210 sec, power 20 W, temperature 75ºC, delta temperature 5ºC.

To avoid aspartimide creation through the Fmoc deprotection stage of Asp comprising RGDS sequence, 0.1 M HOBt in the Fmoc deprotection solution (20% piperidine/0.1 M HOBt/DMF) was used to diminish aspartimide development.

Washing After Fmoc-Deprotection: DMF (4×), DCM (4×), DMF (4×) to eradicate dibenzofulvene by-product.

3. **Coupling**: 0.5 M HBTU/0.5 M HOBt/2 M DIPEA/DMF;

General protocol: time 300 sec, power 20 W, temperature: 75ºC, delta temperature: 5ºC.

Arg (R) is vulnerable to γ-lactam creation therefore significantly reduces the coupling productivity. Special attention was taken in case of Arg coupling to diminish the side reactions. A modified double coupling was performed for Arg. 1st coupling: 25 min at 25°C (MW Power 0 W), subsequently 2 min at 75°C (MW Power 30 W); 2nd coupling: 5 min at 75°C (MW Power 30 W).

Washing after Coupling: DMF (3×), DCM (3×), DMF (3×)

After the final step, the resin was transferred into a SPE cartridge with frit and washed with DMF (5×), DCM (5×), MTBE (5×), and finally with MeOH (5×). The resins were dried in vacuum and stored at −18°C.

Test Cleavage from Rink Amide AM Resin: To a pinch of the resin 2 mL solution of TFA/EDT/TIS/H_2O (92.5/2.5/2.5/2.5 *v/v/v/v*) was added and the cleavage reaction was performed by shaking the resin for 2 h at 25°C. Next the resin beads were filtered off and the solvent was evaporated under N_2 stream. The RGDS peptide was precipitated by adding cold MTBE. The MTBE suspension was centrifuged at −5°C. The supernatant was discarded and the residue was washed with cold MTBE (3×) through centrifugation and dried to acquire the desired product RGDS, Lyso-Changsha-RGDS conjugate, and Changsha-RGDS conjugate.

MW assisted Fmoc-SPPS protocol on the Rink Amide AM resin for the construction of RGDS, Lyso-Changsha-RGDS conjugate, and Changsha-RGDS conjugate

Working Steps	Reagents	Reaction condition

Coupling	HBTU/HOBt/DIPEA/DMF	300 sec/75°C/20 W Special care for Arg coupling: 1) 25 min/25°C/0 W then 2 min/75°C/30 W 2) 5 min/75°C/30 W
Washing after coupling	DMF(5×), DCM(5×), DMF(5×)	
Fmoc deprotection	20% piperidine/DMF Special care for Asp Fmoc-deprotection step: 20% piperidine/DMF with 0.1 M HOBt monohydrate	210 sec/75ºC/20 W
Washing after deprotection	DMF (4×), DCM (4×), DMF (4×)	
Washing after final coupling	DMF(5×), DCM(5×), MTBE(5×), MeOH(5×)	
Test Cleavage	TFA/EDT/TIS/H_2O (92.5/2.5/2.5/2.5 *v/v/v/v*)	2 h/25°C

C-Terminal Amide Containing RGDS Peptide:

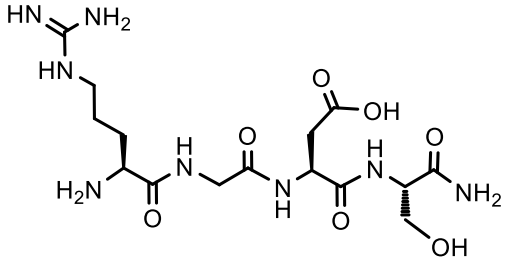

HRMS (ESI +ve) *m/z*: Observed for $C_{15}H_{29}N_8O_7^+$ $[M+H]^+$ = 433.2150, $[M+H]^+$calcd = 433.2154.

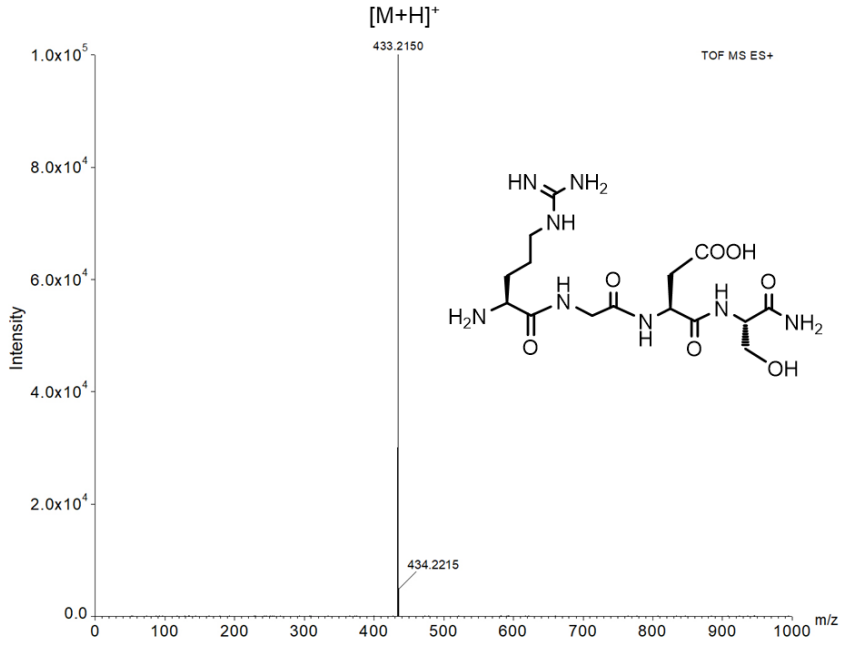

Figure 24. HRMS (ESI +ve) spectrum

Spirolactam State of Lyso-Changsha-RGDS Conjugate: ^{1}H NMR (300 MHz, CD_3OD) δ 7.99 (s, 1H), 7.90 (d, *J* = 3.2 Hz, 1H), 7.87 (s, 1H), 7.63 (q, *J* = 7.9 Hz, 3H), 7.56 (d, *J* = 6.1 Hz, 2H), 7.52 (s, 1H), 7.27 – 7.22 (m, 2H), 7.19 (d, *J* = 2.8 Hz, 1H), 7.17 – 7.13 (m, 1H), 6.84 (t, *J* = 7.5 Hz, 2H), 6.73 – 6.68 (m,

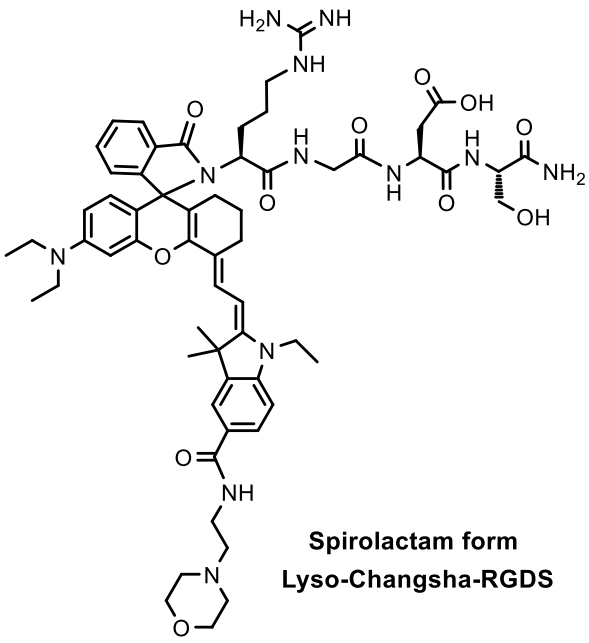

Spirolactam form
Lyso-Changsha-RGDS

1H), 6.46 – 6.37 (m, 2H), 6.35 (s, 1H), 6.32 – 6.26 (m, 1H), 4.61 (s, 1H), 4.38 (d, *J* = 4.7 Hz, 4H), 4.04 (dd, *J* = 16.5, 7.8 Hz, 3H), 3.97 – 3.87 (m, 7H), 3.85 (d, *J* = 7.2 Hz, 3H), 3.80 – 3.72 (m, 4H), 3.42 (d, *J* = 6.9 Hz, 6H), 3.16 (s, 2H), 3.07 (d, *J* = 6.8 Hz, 2H), 2.56 (s, 6H), 1.69 (s, 6H), 1.43 (d, *J* = 7.8 Hz, 2H), 1.38 – 1.33 (m, 3H), 1.30 (s, 2H), 1.24 (s, 6H).

13C NMR (101 MHz, CD_3OD) δ 175.19, 174.04, 173.63, 172.37, 170.89, 170.57, 168.48, 157.99, 155.96, 154.84, 152.60, 151.82, 141.68, 140.89, 131.09, 129.51, 129.42, 128.44, 127.74, 127.29, 125.64, 122.13, 121.66, 115.44, 115.24, 113.83, 112.57, 111.46, 105.99, 103.40, 95.36, 78.17, 77.51, 73.13, 61.54, 57.82, 55.06, 54.49, 52.64, 50.12, 48.31, 48.07, 47.86, 47.65, 47.43, 47.22, 47.08, 44.63, 44.35, 42.57, 42.03, 40.43, 35.55, 35.06, 33.51, 28.09, 27.28, 25.84, 23.67, 22.83, 21.48, 11.42, 11.02. HRMS (ESI +ve) *m*/*z*: Observed for $C_{60}H_{81}N_{12}O_{11}^{3+}$ $[M+2H]^{3+}$ = 381.8770, $[M+H]^{3+}$ calcd = 381.8716 (*m*/*z*, *z* = 3). Photophysical properties in PBS, pH 10: λ_{abs}= 378 nm, λ_{em}= 470 nm, Stokes shift ($\Delta\lambda$) = 92 nm, ε = 0.61 ×10^5 $M^{-1}cm^{-1}$, Φ_f = 0.13, brightness = 7930 $M^{-1}cm^{-1}$. Fluorescence lifetime (τ) = 2.405 ns in PBS, pH 10.

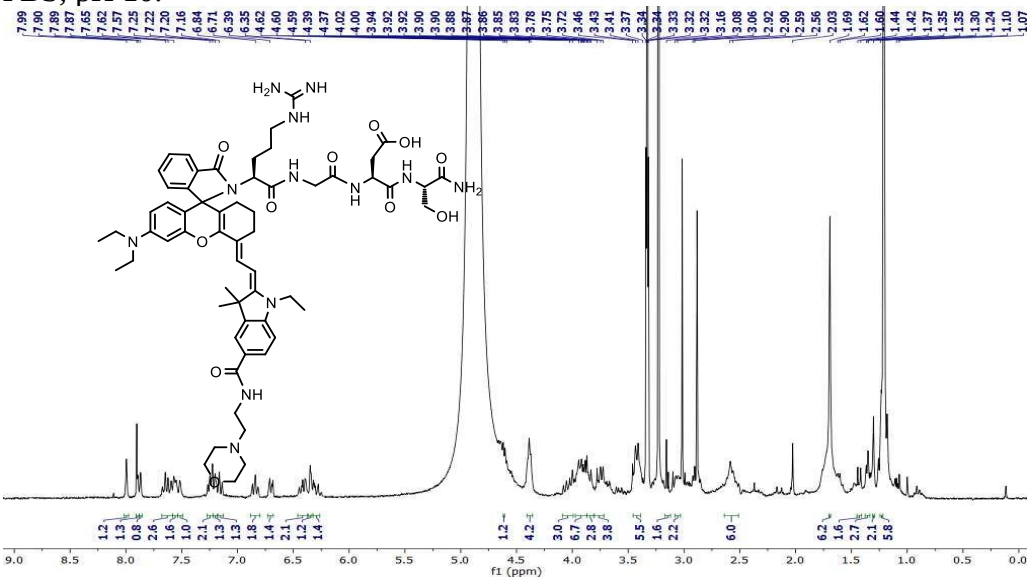

Figure 25a. ^{1}H NMR spectrum (400 MHz, CD_3OD, 298 K).

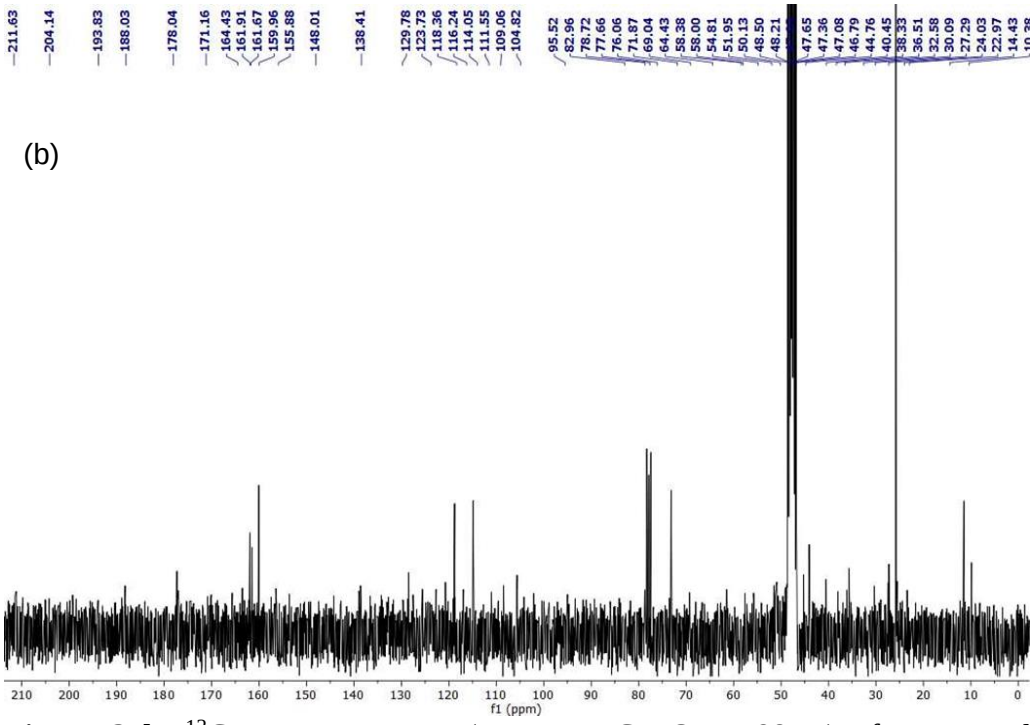

Figure 25b. ^{13}C NMR spectrum (75 MHz, CD_3OD, 298 K) of compound Changsha-COOH.

Open Amide State of Lyso-Changsha-RGDS Conjugate: ^{1}H NMR (400 MHz, CD_3OD, 298 K) δ 8.70 (d, J = 12 Hz 1H), 8.00 (s, 1H), 7.94 (t, J = 6.9 Hz, 2H), 7.71 (d, J = 25.6 Hz, 3H), 7.58 (d, J = 7.4 Hz, 2H), 7.47 (t, J = 7.8 Hz, 2H), 7.34 (dd, J = 15.6, 7.4 Hz, 5H), 6.88 – 6.85 (m, 1H), 6.80 (s, 1H), 6.73 (s, 1H), 6.27 (d, J =

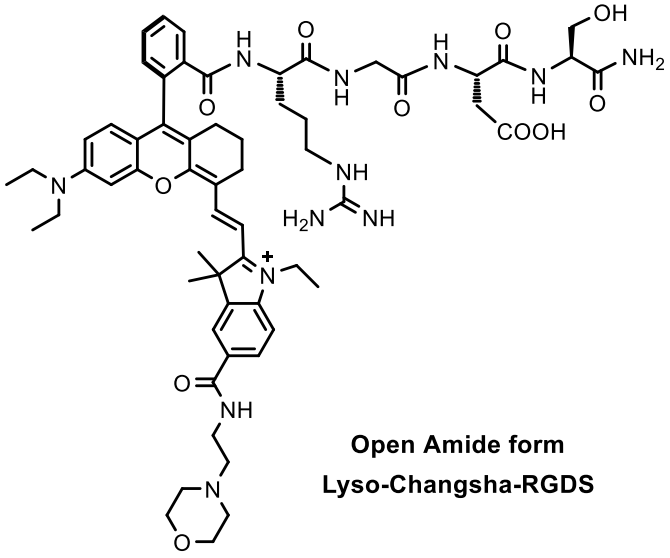

14.6 Hz, 1H), 4.67 (t, *J* = 5.6 Hz, 1H), 4.42 (s, 1H), 4.33 (s, 1H), 4.25 (s, 1H), 4.09 (d, *J* = 16.5 Hz, 2H), 3.99 (t, *J* = 6.3 Hz, 2H), 3.94 (d, *J* = 4.3 Hz, 2H), 3.88 (d, *J* = 6.3 Hz, 4H), 3.79 (t, *J* = 5.1 Hz, 2H), 3.59 (d, *J* = 7.6 Hz, 4H), 3.27 (d, *J* = 7.4 Hz, 4H), 3.15 (t, *J* = 5.8 Hz, 2H), 3.11 (s, 2H), 2.92 (d, *J* = 5.6 Hz, 2H), 2.83 (d, *J* = 6.7 Hz, 2H), 2.72 (s, 1H), 2.41 (s, 2H), 1.97 (d, *J* = 7.4 Hz, 2H), 1.86 (s, 2H), 1.83 (d, *J* = 3.9 Hz, 6H), 1.71 (s, 2H), 1.46 (s, 3H), 1.36 (s, 2H), and 1.28 (s, 6H) ppm.

^{13}C NMR (101 MHz, CD_3OD, 298 K) δ 175.19, 174.04, 173.63, 172.37, 170.89, 170.57, 168.48, 157.99, 155.96, 154.84, 152.60, 151.82, 141.68, 140.89, 131.09, 129.51, 129.42, 128.44, 127.74, 127.29, 125.64, 122.13, 121.66, 115.44, 115.24, 113.83, 112.57, 111.46, 105.99, 103.40, 95.36, 78.17, 77.51, 73.13, 61.54, 57.82, 55.06, 54.49, 52.64, 50.12, 44.63, 44.35, 42.57, 42.03, 40.43, 36.27, 35.06, 34.24, 28.09, 27.28, 25.84, 23.67, 22.11, 20.32, 11.42, and 11.02 ppm.

HRMS (ESI +ve) *m*/*z*: Observed for $C_{60}H_{81}N_{12}O_{11}^{3+}$ $[M+2H]^{3+}$ = 381.8770, $[M+H]^{3+}$ calcd = 381.8716 (*m*/*z*, *z* = 3).Photophysical properties in PBS, pH 2: λ_{abs}= 714 nm, λ_{em}= 735 nm, Stokes shift ($\Delta\lambda$) = 21 nm, ε = 1.2 ×10^5 $M^{-1}cm^{-1}$, Φ_f = 0.37, brightness = 44400 $M^{-1}cm^{-1}$. Fluorescence lifetime (τ) = 2.93 ns in PBS, pH 2

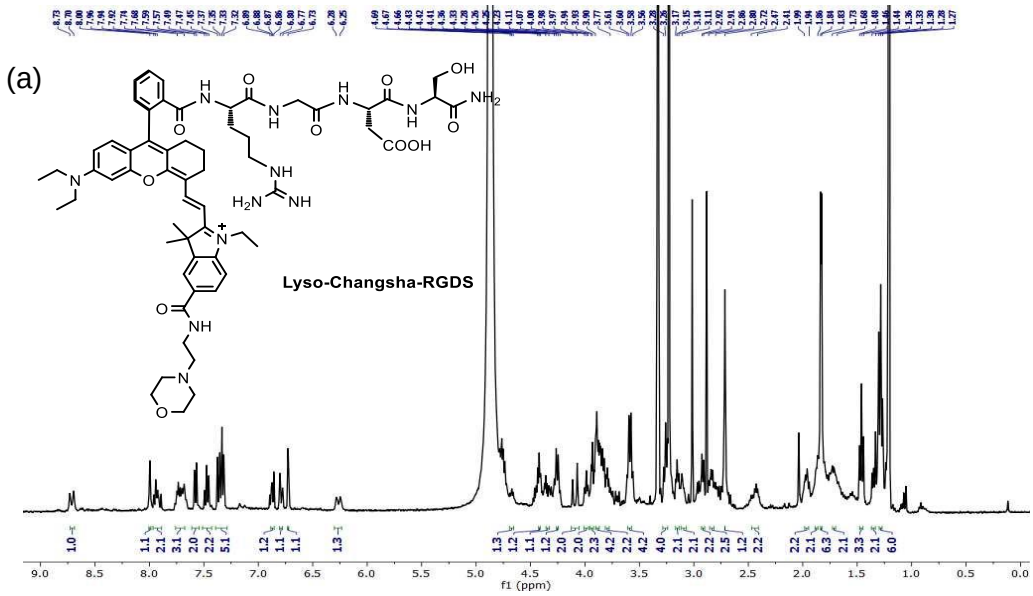

Figure 26a. ^{1}H NMR spectrum (400 MHz, CD_3OD, 298 K).

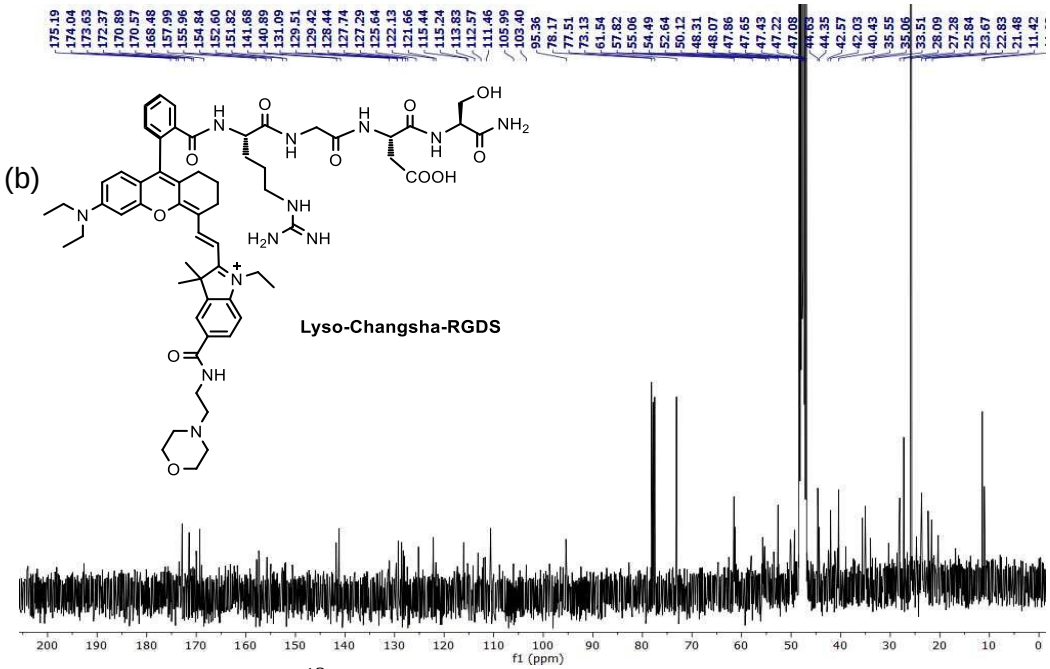

Figure 26b. ^{13}C NMR spectrum (101 MHz, CD_3OD, 298 K).

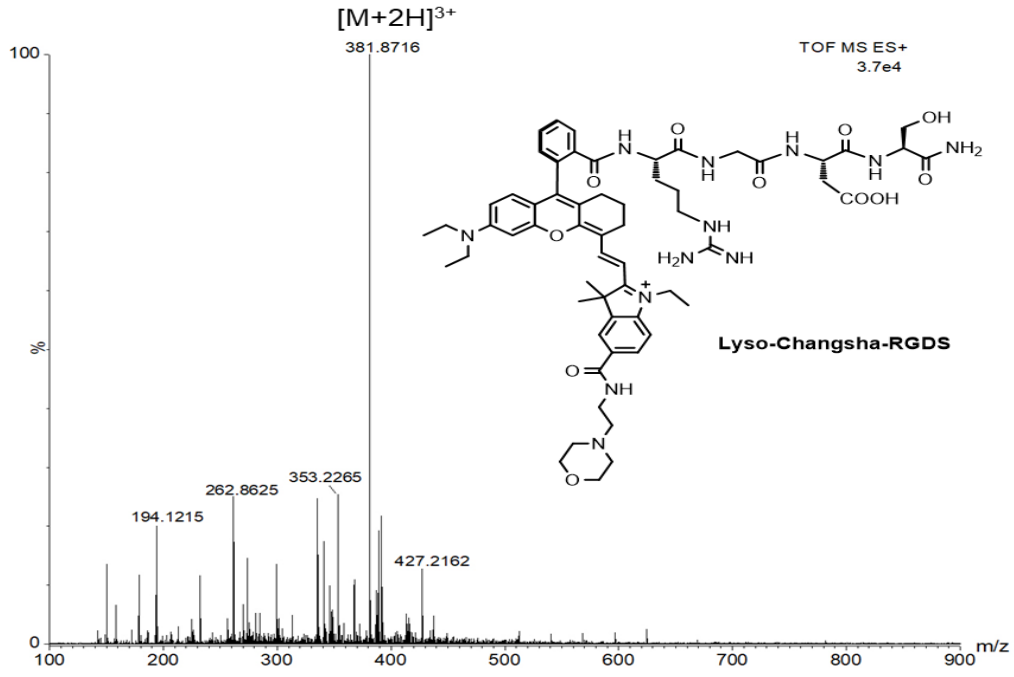

Figure 27. HRMS (ESI +ve) spectrum of compound Lyso-Changsha-RGDS.

Spirolactam State of Changsha-RGDS Conjugate: HRMS (ESI +ve) *m*/*z*: Observed for $C_{53}H_{69}N_{10}O_9^{3+}$ $[M+2H]^+$= 329.8416, $[M+2H]^+$ calcd = 329.8411 (*m*/*z*, *z* = 3). Photophysical properties in PBS, pH 10: λ_{abs}= 377 nm, λ_{em}= 458 nm, Stokes shift ($\Delta\lambda$) = 81 nm, ε = 0.57 $\times 10^5$ $M^{-1}cm^{-1}$, Φ_f = 0.14, brightness = 7980 $M^{-1}cm^{-1}$.

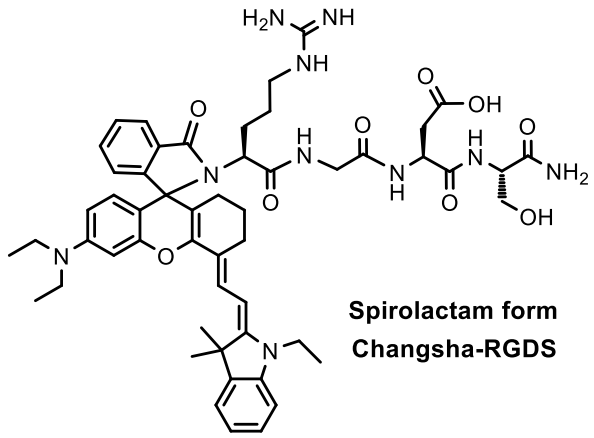

Open Amide State of Changsha-RGDS Conjugate: HRMS (ESI +ve) *m*/*z*: Observed for $C_{53}H_{69}N_{10}O_9^{3+}$ $[M+2H]^+$ =329.8416, $[M+2H]^+$calcd = 329.8411 (*m*/*z*, *z* = 3). Photophysical properties in PBS, pH 2: λ_{abs}= 713 nm, λ_{em}= 733 nm, Stokes shift ($\Delta\lambda$) = 20 nm, ε = 1.1 $\times 10^5$ $M^{-1}cm^{-1}$, Φ_f = 0.35, brightness = 38500 $M^{-1}cm^{-1}$.

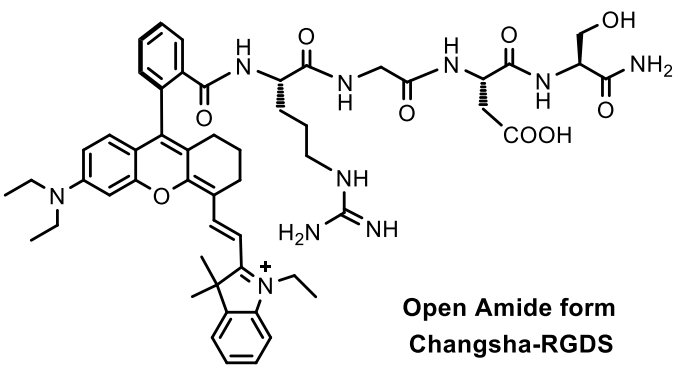

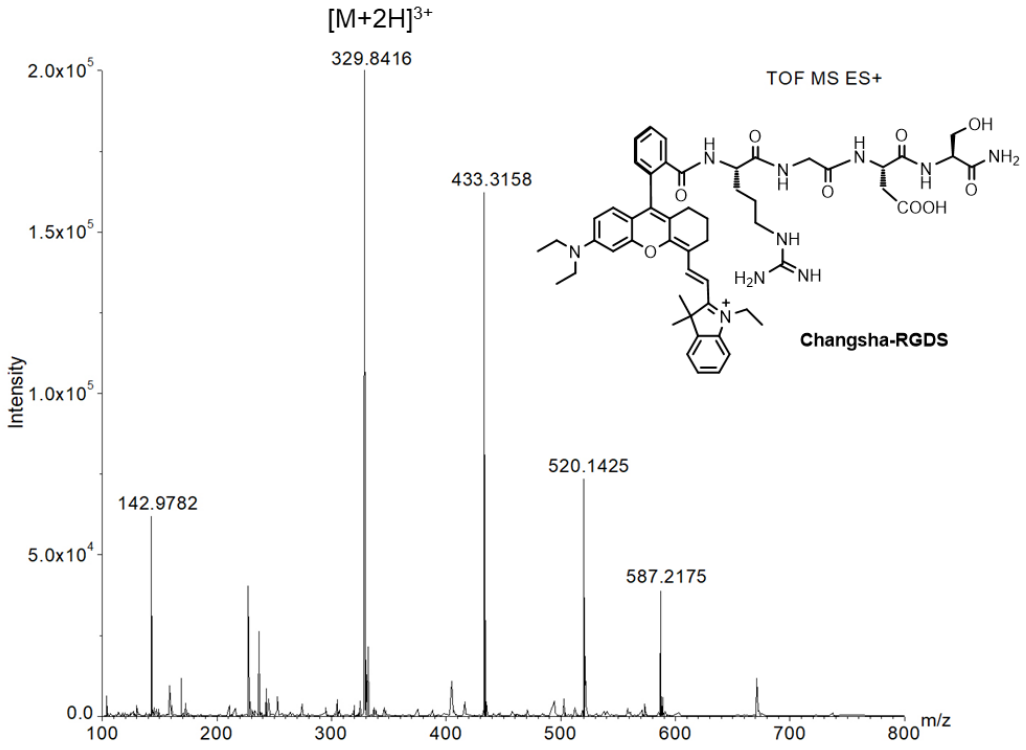

Figure 28. HRMS (ESI +ve) spectrum of compound Changsha-RGDS.

Experimental Section

Materials: We have procured the following materials from Merck: 4-Hydrazinobenzoic acid, 3-methyl-2-butanone, iodoethane, cyclohexanone, 4-(2-aminoethyl)morpholine, Rink Amide AM resin (LL, 0.26 mmol/g loading density, 100-200 mesh), Fmoc-amino acid building blocks [Fmoc-Arg(Pbf)-OH, Fmoc-Gly-OH, Fmoc-Asp(OtBu)-OH, and Fmoc-Ser(tBu)-OH], 2-(1HBenzotriazole-1-yl)-1,1,3,3-tetramethyluroniumhexafluorophosphate (HBTU), 1-Hydroxybenzotriazole (HOBt) hydrate, 1-[Bis(dimethylamino)methylene]-1*H*-1,2,3-triazolo[4,5-*b*]pyridinium 3-oxide hexafluorophosphate (HATU), DMF (anhydrous, 99.8%), N,N-

diisopropylethylamine (DIPEA), trifluoroacetic acid (TFA), triisopropylsilane (TIS), piperidine, Hoechst 33342, acetonitrile, acetic acid, perchloric acid, 1,2-ethanedithiol, triethyl orthoformate, potassium acetate, indocyanine green (ICG), 2-amino pyridine, dichloromethane, and TLC silica gel 60 F_{254}. Phosphorus(V) oxyvhloride was purchased from Spectrochem. Deuterated NMR solvents e.g. $CDCl_3$, DMSO-d_6, and CD_3OD were acquired from Cambridge Isotope Laboratories, Inc. For the UV/vis and fluorescence investigations spectroscopic grade solvents were used. Human epithelioid cervix carcinoma HeLa, lung adenocarcinoma A549 and a mouse myoblast C2C12 cell lines were bought from the National Centre for Cell Science, India. MTT, DMEM, Trypsin-EDTA mixture, FBS, and Antibiotic Antimycotic Solution were acquired from HiMedia Laboratories. Commercially available lysosome staining probe LysoTracker Green DND-26 was obtained from Cell Signaling Technology. *Millipore* ultra-pure H_2O was used for all the experiments.

METHODS:

Microwave Synthesizer: RGDS peptide, Lyso-Changsha-RGDS conjugate, and Changsha-RGDS conjugate were synthesized on a manual microwave solid phase peptide synthesizer (CEM corporation, USA make, model discover bio, precise temperature is controlled by fiber optic) with decent overall yield from easily available low cost starting materials.

Single Crystal X-Ray Diffraction: The vapour diffusion approach was used to create single crystals suitable for the X-ray diffractions. The diffraction data were obtained using a micro focus Single Crystal X-ray Diffraction equipment (Model: D8 Quest, Make: Bruker) with MoKα radiation (a graded multilayer mirror monochromator, λ = 0.71073) at 293 K. The

detector was a PHOTON-100 CMOS device. The SHELXT 2014/15 programme was used to directly solve the crystal structure of the compound Changsha-COOH.[31,32] Full-matrix least squares adjustments were made using SHELXL-2018/3 included in the Olex2[33] crystallographic collective package against F^2.[31,32] With the use of anisotropic thermal parameters, the non-hydrogen atoms were refined.

The compound Changsha-COOH was dissolved in MeOH in a glass vial. Then the glass vial was inserted into a 100 mL container filled with 20 mL diethyl ether. After two days the ether diffuses into the methanolic solution of the compound 5 at room temperature and the small shiny green needle like crystals were obtained. The formula sum = $C_{75.5}$ $H_{81.5}$ Cl_2 N_4 O_{14}, formula weight = 1339.82, crystal system = triclicnic, space group = *P* 1, a = 12.435(8) Å, b = 12.992(9) Å, c = 13.111(9) Å, α = 107.577(18)°, β = 92.181(19)°, γ = 117.895(17)°, V = 1744(2) Å^3. Z = 1, D_{calcd} = 1.276 g cm^{-3}, μ = 0.161 mm^{-1}. R_1 = 0.0988 and *wR*2 = 0.2506 were the final R values for reflections with I > 2(I). CCDC number = 2279345.

Crystallographic data were deposited at Cambridge Crystallographic Data Centre (CCDC). These data can be obtained free of charge from the Cambridge Crystallographic Data Centre, www.ccdc.cam.ac.uk/structures.

High-Resolution Electrospray Ionization Mass Spectrometry (HRMS-ESI): On a Q-Tofmicro mass spectrometer instrument from the Waters Corporation, HRMS-ESI data were collected in positive mode. MassLynx V4.1 mass application software provided by the makers was used to record and process the data.

NMR Spectroscopy: On Bruker DPX300 MHz and DPX400 MHz spectrometers at 298 K in suitable deuterated solvents, ^{1}H NMR and ^{13}C NMR

measurements were done. The data was processed using the Bruker TopSpin 3.6.2 software that was provided by the manufacturers.

UV/vis Spectroscopy: A JASCO V-730 double-beam spectrophotometer with a 200–1100 nm wavelength range was used to produce the absorption spectra. A quartz cuvette with a 1 cm path length was used for all the measurements. Spectra Manager Version 2 software, provided by the manufacturers was used to process the data under the direction of a PC. The absorption intensities at 714 nm and 378 nm were used to calculate the absorption ratio (A_{714}/A_{378}).

Fluorescence Spectroscopy: Fluorescence spectra were obtained using a Horiba Jobin Yvon FluoroMax-4 spectrofluorometer (Horiba Scientific) operated through Fluor Essence Version 3.9.0.1 software using PC. We have used 5 nm excitation and emission slit widths. The fluorescence intensities at 735 nm and 470 nm were used to calculate the fluorescence ratio (FL_{735}/FL_{470}).

Fluorescence Quantum Yields of Basic Closed Form and Acidic Open Form: By using a relative technique, the fluorescence quantum yields Φ_f(u) of the basic spirolactam state and acidic open amide state of Lyso-Changsha-RGDS and Changsha-RGDS conjugates were determined. To prevent the inner filter effect, the probe concentrations were changed so that the max absorbance was less than 0.1. Here, the emission intensities of standard fluorophores were compared with the integrated fluorescence intensities of basic spirolactam and acidic open amide forms of Lyso-Changsha-RGDS and Changsha-RGDS conjugates using the following equation (Table S3):

$$\Phi_f(\mathrm{u}) = \Phi_f(\mathrm{st}) \times [(A_{\mathrm{st}} \times F_{\mathrm{u}} \times \eta_{\mathrm{u}}^2) / (A_{\mathrm{u}} \times F_{\mathrm{st}} \times \eta_{\mathrm{st}}^2)]$$

Φ_f(st): Fluorescence quantum yield of the reference fluorophore

Φ_f (u): Fluorescence quantum yield of the open amide state or spirolactam state of Lyso-Changsha-RGDS and Changsha-RGDS conjugates

A_{st} and A_u: Absorbance of the reference fluorophore and open amide state or spirolactam state of Lyso-Changsha-RGDS and Changsha-RGDS conjugates at λ_{ex}, respectively.

F_{st} and F_u: Integrated fluorescence areas for the reference fluorophore and and open amide state or spirolactam state of Lyso-Changsha-RGDS and Changsha-RGDS conjugates, respectively, under the modified fluorescence spectra.

η_{st} and η_u: Refractive indices of the solvent used to study the reference fluorophore and open amide state or spirolactam state of Lyso-Changsha-RGDS and Changsha-RGDS conjugates.

"st" indicates for the standard molecule, and "u" stands for the unknown molecule.

Φ_f(st) of Quinine Sulphate in absolute 0.1(M) H_2SO_4 is 0.54 and used as the reference for the spirolactam form of Lyso-Changsha-RGDS and Changsha-RGDS conjugates.

Φ_f (st) of ICG in DMSO is 0.12 and used as the reference for the open amide form of Lyso-Changsha-RGDS and Changsha-RGDS conjugates.

Time-Correlated Single Photon Counting (TCSPC) Experiment: Using the TCSPC approach on a Horiba DeltaFlex lifetime machine (Horiba Jobin Yvon IBH Ltd, UK) the fluorescence lifetime (τ) of the basic spirolactam form and the acidic open amide form were determined in solution. We have measured the τ in PBS using delta diode laser excitation sources 375 nm (Model: DD-375L, Horiba Scientific) and 730 nm (Model: DD-730L, Horiba Scientific) for the closed state and open state, respectively. The data were analysed using Horiba EzTime decay analysis software.

pH Titrations: The pH solutions of the specific pH values were made using a Mettler Toledo pH metre, and the device was calibrated using standard

buffer solutions with pH values of 4.01, 7.00, and 10 at 25°C. Britton-Robinson universal buffer solutions with a range of pH values were made for the pH titration. All the aqueous buffered solutions were freshly prepared and stored in a refrigerator until they were needed (used within a week). In DMSO, a 75 μM concentrated stock solution of the spirolactam form was made. To acquire the final concentration of the probe of 2 μM, aliquots of the stock solution were quantitatively added to the aqueous buffer solutions of various pH values. The solutions were mixed before the absorption/emission spectra were recorded. pH titration plots for absorption and emission were measured in triplicate and the values were expressed as the mean ± standard deviation.

Cell Culture: The human cervix adenocarcinoma HeLa, lung adenocarcinoma A549, and healthy mouse myoblast C2C12 cell lines were cultured separately in DMEM (pH 7.4) supplemented with 10% FBS and antibiotic-antimycotic solution 100× (having 10000 units mL^{-1} penicillin, 10 mg mL^{-1} streptomycin, and 25 μg mL^{-1} amphotericin B in 0.9% sodium chloride). The cells were upheld in a 5% CO_2 incubator at 37°C and were routinely passaged.

Cell Viability Assay: The 3-(4,5-dimethylthiazol-2-yl)-2,5-diphenyltetrazolium bromide (MTT) assay was used to determine the cytotoxicity of the pH-activatable probe on HeLa and A549 carcinoma and C2C12 healthy cell lines. In a 96-well plate, HeLa, A549, and C2C12 cell lines were each seeded at a population of about 10^4 cells per well in DMEM and cultured for 24 h at 37°C with 5% CO_2 incubation. Following a 24-hour incubation period, Lyso-Changsha-RGDS was treated for an additional 24-hour period at varied doses of 1, 2, 5, 10, 15, and 20 μM per well at 37°C. Then the HeLa, A549, and C2C12 cell lines were independently incubated for 4 h in the dark at 37°C with MTT (10 μL) reagent (5 mg mL^{-1} in PBS). After 4 h

incubation, DMSO was mixed to each well to dissolve the purple formazan crystals and the absorption (*A*) at 570 nm was recorded (verified in triplicate) by an ELISA plate reader. The results (performed the assay in triplicates) were expressed by the following equation:

Viable cells (%) = (*A* of treated cells / *A* of untreated cells) × 100.

Live-Cell Confocal Laser Scanning Microscopy: For the live-cell confocal laser scanning microscopy (CLSM), a Leica STELLARIS 5 platform with a white light laser (WLL), an Acousto-Optical Beam Splitter (AOBS), and HyD S detectors was employed. It had a 100×/1.40 oil plan apochromatic objective (Specification: HC PL APO 100×/1.40 OIL CS2). Figure S57 depicts the special setup for the live-cell confocal microscopy device that maintains a 37°C and 5% CO_2 atmosphere. Leica Application Suite X (LAS X 4.3.0.24308) software was used to analyse and process the CLSM pictures. For the living cell CLSM imaging HeLa and A549 cell lines at a density of ~10^4 cells/mL were independently seeded in 35 mm glass bottom confocal dish (SPL Lifesciences, catalogue no. 200350) and allowed to grow ~80% confluency in DMEM for 24 h at 37°C in 5% CO_2 incubator. The cells were then rinsed three times with 1× PBS. HeLa and A549 live cells were then treated individually with the spirolactam state of Lyso-Changsha-RGDS (1.0 μM) in medium for 24 h in a 5% CO_2 environment at 37°C. Next the media was removed carefully and washed gently with 1× PBS. Subsequently the cells were treated with LysoTracker Green DND-26 (75 nM) at 37°C for 5 min in a 5% CO_2 environment in accordance with the manufacturer's instructions. The cell lines were then washed continuing the same protocol and treated with Hoechst 33342 (0.1 μg mL^{-1}) for 15 min. The cells were rinsed three times with 1× PBS prior

to CLSM imaging, and phenol red-free medium was added. 37°C and 5% CO_2 environment was maintained during the live cell CLSM imaging.

For Hoechst 33342: laser excitation wavelength = 405 nm (blue channel, detection range of emission wavelength 415-490 nm); LysoTracker Green DND-26 (LTG): laser excitation wavelength = 488 nm (green channel, detection range of emission wavelength 500-572 nm); pH activatable Lyso-Changsha-RGDS conjugate: laser excitation wavelength 670 nm (red channel, detection range of emission wavelength 700-780 nm).

Pearson's Correlation Coefficient (PCC): One common statistical analysis used in pattern recognition is Pearson's correlation coefficient (PCC), which is used to compare two CLSM images where the green channel denotes LysoTracker Green DND-26 staining and the red channel designates the acidic pH activatable Lyso-Changsha-RGDS conjugate staining. The degree of overlap between two patterns in a colocalization image can be clarified using a PC graph. PCC was measured by the LAS X software using Quantify tool.

PCC was calculated (images including red and green channels) by the subsequent equation:

$$PCC = \frac{\sum_i (S1_i - S1_{avg}) * (S2_i - S2_{avg})}{[\sum_i (S1_i - S1_{avg})^2 * \sum_i (S2_i - S2_{avg})^2]^{(1/2)}}$$

S1 = signal intensity of pixels (pixel i) in the green channel

S2 = signal intensity of pixels (pixel i) in the red channel.

$S1_{avg}$ = mean values of pixels in the green channel

$\mathbf{S2_{avg}}$ = mean values of pixels in the red channel.

Live Cells 3D Confocal Images using Synthesized Acidic pH Activatable Lyso-Changsha-RGDS Conjugate:

A Leica STELLARIS 5 confocal microscope was used to take Z-stack pictures of live HeLa and A549 cancer cells labelled with Hoechst 33342 (a nuclear staining dye) and the synthesized acidic pH activatable Lyso-Changsha-RGDS conjugate in order to obtain the 3D view of the cancer cell lysosomes. The pictures were harvested every 0.14 μm on the Z-axis for the live cancer cell 3D CLSM image creation. The 3D CLSM image was created by reconstructing 18 separate frames for each channel over the course of 6 minutes using the LAS X software. The spherical lysosomes located inside the living HeLa and A549 carcinoma cells were identified in the 3D reconstructed CLSM pictures.

Ratiometric Confocal Microscopic Images using Acidic pH-Activatable Lyso-Changsha-RGDS Conjugate: The cultured HeLa and A549 cells were treated individually for 24 h at 37°C in a 5% CO_2 environment with an acidic pH activatable closed form of Lyso-Changsha-RGDS conjugate (1 μM) without using any additional staining agents. After the cells had been cleaned with 1× PBS the ratiometric CLSM pictures of live HeLa and A549 cells were obtained by dual channel excitation (green channel and red channel). Each filter's exposure periods were maintained consistent. In order to obtain pixel-based ratiometric imaging, CLSM images captured with a Leica STELLARIS 5 confocal microscope were processed using ImageJ software (ImageJ 2.1.0; Java 1.8.0_172) with a preinstalled Ratio_Plus.class plugin (downloaded from Ratio_Plus.java source and installed in the plugins folder or subfolder). Prior to ratiometric imaging, single images of the same type (8 or 16 or 32 bit), width, and height were taken for both the channel 1 (red) and channel 2 (green). Next, background subtraction was performed for each

channel (Channels 1 and 2, red and green, respectively) and ratiometric images were developed by choosing the subsequent operations:

Select menu bar ⇨ Process ⇨ Calculator Plus ⇨ Select Channel 1 and Channel 2 ⇨ Select operation for Channel 1 and Channel 2 ratio.

The chosen operation was $intR=(i_1/i_2)*K_1+K_2$, where i_1 is the intensity of Channel 1 (the red channel) after subtracting a constant background value and i_2 is the intensity of Channel 2 (the green channel) after subtracting a constant background value. K_1 is an arbitrary multiplication factor that is assumed to be 1, and K_2 is equal to 0. Pseudocolored ratiometric images (I_{red}/I_{green}) that were created represent the precise pH values of those locations.

Real-Time Tracking of Lysosomes in Live Carcinoma Cells by Synthesized Acidic pH-Activatable Lyso-Changsha-RGDS Conjugate: Real-time lysosomal tracking inside the live carcinoma HeLa and A549 cells were monitored by a Leica STELLARIS 5 microscope utilizing the synthesized lysosome targeting acidic pH activatable Lyso-Changsha-RGDS conjugate over a few minutes time course. To create separate real-time videos using the LAS X software, 27 frames were captured over 2 min 15 sec for HeLa and 12 frames were collected over 2 min 19 sec for A549 carcinoma cells.

Multicolor Confocal Imaging of Live Carcinoma Cells: A combination of appropriate organelle targeting fluorescent dyes with unique excitation/emission bands were used to capture multicolor imaging of intracellular organelles in the same live cell. The mitochondria of live A549 and HeLa cells were specifically stained with MitoTracker Green (MTG, green emitting), the nucleus was labelled with blue-fluorescent Hoechst 33342, and the lysosomes were stained with our synthesized acidic pH activatable Lyso-

Changsha-RGDS conjugate. Using the appropriate filters, multicolor CLSM images of live A549 and HeLa cell lines were obtained.

For MTG, the detection range of the emission wavelength was between 499 to 544 nm (laser excitation wavelength = 488 nm, green channel). Hoechst 33342, detection range of emission wavelength was between 415 to 490 nm (laser excitation wavelength = 405 nm. blue channel). Synthesised acidic lysosomal pH activated Lyso-Changsha-RGDS conjugate, the detection range of the emission wavelength was between 700 to 780 nm (laser excitation wavelength = 670 nm, red channel).

Synthesis, Purification, and Characterization of the Compounds: With a descent yield and an efficient approach, the dyes and their precursor molecules were synthesised from readily available, inexpensive starting materials. On aluminium sheet coated with silica gel, analytical TLC (TLC silica gel 60 F_{254}) was carried out with the appropriate solvent combinations, and the results were detected using the naked eye or a UV lamp. By using silica gel with a mesh size of 100–200, the synthesised compounds were purified using column chromatography. Prior to usage, the chromatography solvents were distilled. Our previously reported method was used to construct the material 2,3,3-trimethylindolenine (1).[35]

Result and Discussion:

Synthesis of targeted and stimuli-activated unsymmetrical fluorescent probe-peptide conjugate is challenging. Condensation of compound 2-(4-(diethylamino)-2-hydroxybenzoyl) benzoic acid with cyclohexanone under acidic medium afford the intermediate **1** (Figures 1-5). The synthesized 5-carboxy-1-ethyl-2,3,3-trimethyl-3*H*-indol-1-ium iodide (**3**) is tethered with

lysosome targeting 4-(2-aminoethyl)morpholine using amide coupling protocol to acquire compound **4** which is treated with N,N'-bis-phenylformamidine in triethyl orthoformate to obtain compound **5** (Figures 6-13). Compound **1** is then condensated with compound **5** in Ac_2O to acquire the carboxylic acid group containing probe Lyso-Changsha-COOH as a green solid with a decent yield (Figures 14-15). A control probe Changsha-COOH lacking the lysosome targeting morpholine functionality is also synthesized by the same protocol (Figures 16-23). Single crystal X-ray structure of Changsha-COOH indicates that the benzoic acid residue is twisted and orthogonal to the xanthene scaffold having a dihedral angle of ca. 90° and electronically decoupled (Figure 29 and Table 1).

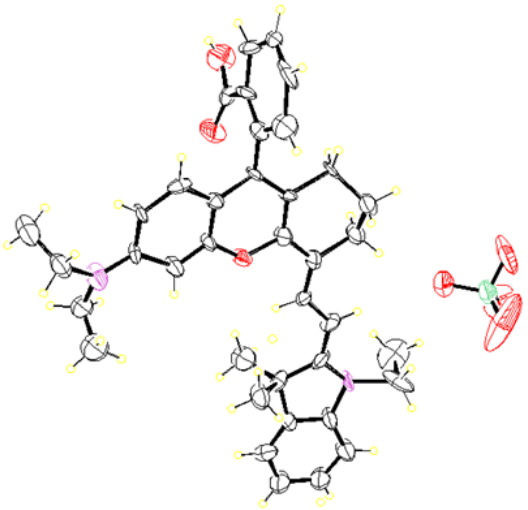

Figure 29. Single crystal X-ray structure of the compound Changsha-COOH**.** Ellipsoids are shown at 30% probability level (ORTEP diagram).

Formula sum	$C_{75.5}\ H_{81.5}\ Cl_2\ N_4\ O_{14}$
Formula weight	1339.82
Color	Green
Crystal system	Triclinic
Space group	*P* 1
a (Å)	12.435(8)
b (Å)	12.992(9)
c (Å)	13.111(9)
α (°)	107.577(18)
β (°)	92.181(19)
γ (°)	117.895(17)
V (Å^3)	1744(2)
Z	1
$D_{calculated}$ (g cm^{-3})	1.276
μ (mm^{-1})	0.161
T (K)	273 K
λ	0.71073
*R*1	0.0988
*wR*2	0.2506
Goodness of fit	0.9501
CCDC number	2279345

Table 1. Crystallographic data of the compound Changsha-COOH.

In contrary, the indolium residue is coplanar and highly conjugated with the xanthene scaffold. All the C−C bond lengths of the push-pull xantheneindolium

backbone are comparable with an average length of 1.40 Å which is between the C−C single (1.54 Å) and double (1.34 Å) bonds, ascribed to the strong electronic delocalization along the push-pull π-conjugated system. Strong electronic delocalization of xantheneindolium backbone is additionally supported by the inspection of the terminal two N−C bond lengths of the push-pull π-electronic compound. The N–C bond length of Et_2N–C and iminium N–C are 1.38 Å (for other unit cell molecule Et_2N–C is 1.33 Å) and 1.39 Å (for other unit cell molecule iminium N–C is 1.33 Å), respectively, that are in-between the lengths of N−C single (~1.47 Å) and the iminium N=C double bonds (~1.28 Å). The Lyso-Changsha-COOH probe is conjugated with cancer cell targeting tetrapeptide RGDS by Fmoc-SPPS protocol on Rink amide AM resin to construct the Lyso-Changsha-RGDS conjugate. Here, the Lyso-Changsha-RGDS conjugate consists of a Changsha chromophore conjugated with a morpholine functionality at the indolium residue for lysosome targeting and RGDS peptide tethered at the benzoic acid of the xanthene scaffold to improve water solubility and to target cancer cell overexpressed $\alpha_V\beta_3$ integrin receptor. An intramolecular nucleophilic cyclization reaction i.e., spirolactamization between the Arg amide NH of RGDS peptide residue with the meso-C of the xantheneindolium scaffold yields spiro-lactam form in basic pH. The spiro-lactam form is switched on to the highly conjugated NIR open amide form via ring opening of the spiro-lactam form at acidic pH (Figure 3). The closed and open states of Lyso-Changsha-RGDS conjugate are characterized by innumerable spectroscopic techniques (Figures 25-27). A control probe-peptide conjugate Changsha-RGDS lacking the lysosome targeting morpholine fuctionality is also synthesized using the same protocol on Rink amide AM resin (Figures 16-17).

^{1}H NMR spectrum of the spirolactam form of Lyso-Changsha-RGDS conjugate is characterized by the multiplets between 6.28-6.35 ppm originating from the olefinic two protons of the xantheneindolium backbone (Figure 25a). Upon addition with excess dil HCl full switching of colorless spirolactam form to green colored highly conjugated open amide form of Lyso-Changsha-RGDS conjugate is achieved (Figures 3, 25-27) which exhibits charateristic two new doublets in ^{1}H NMR where one olefinic proton is highly deshielded (8.72 ppm, d, J = 12.0 Hz) compared to the other olefinic proton (6.27 ppm, d, J = 14.6 Hz) with *trans* coupling in the open amide state (Figure 26a). The characteristic change of the probe-peptide conjugate Lyso-Changsha-RGDS at low pH is detected owing to the acidic pH-stimulated spirolactam ring-opening to yield a highly conjugated π electronic push-pull amide system.

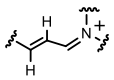

UV/vis and fluorescence spectroscopies are used to monitor dynamic pH switching behavior of the Lyso-Changsha-RGDS conjugate. A pH-sensitive absorption and emission spectral shift arises due to the nucleophilic attack of Arg amide NH i.e., spirotactamization at the electron-deficient meso-C of xantheneindolium scaffold by 5-exo-trig cyclization and electronic pulling through an indolenine iminium moiety at basic pH (Figure 3). Therefore push-pull effect of Changsha molecule disrupts and blue shift is perceived. At alkaline and physiological pH the colorless predominating spirolactam state with smaller π-conjugation displays λ_{abs} at 378 nm in the UV region (Figure 30a). At acidic pH due to spirolactam ring opening, a highly conjugated green colored open amide form at λ_{abs} 714 nm is begun with allied diminution of the absorbance at 378 nm and a isosbestic point at 424 nm (Figures 31).

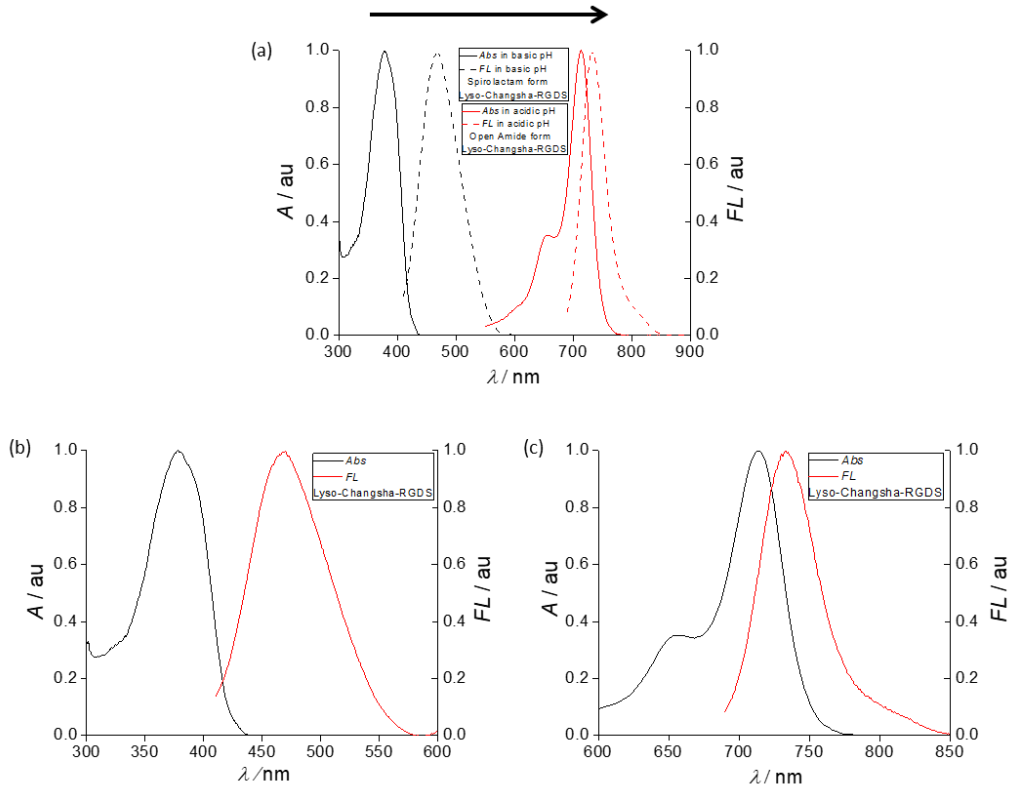

Figure 30. (a) Normalized absorption and fluorescence merge plot for the closed spirolactam and open amide state of Lyso-Changsha-RGDS conjugate in PBS at pH 10 and 2, respectively. (b) Normalized absorption and fluorescence merge plot for the spirolactam form of Lyso-Changsha-RGDS conjugate in PBS, pH 10. (c) Normalized absorption and fluorescence merge plot for the open amide form of Lyso-Changsha-RGDS conjugate in PBS, pH 2.

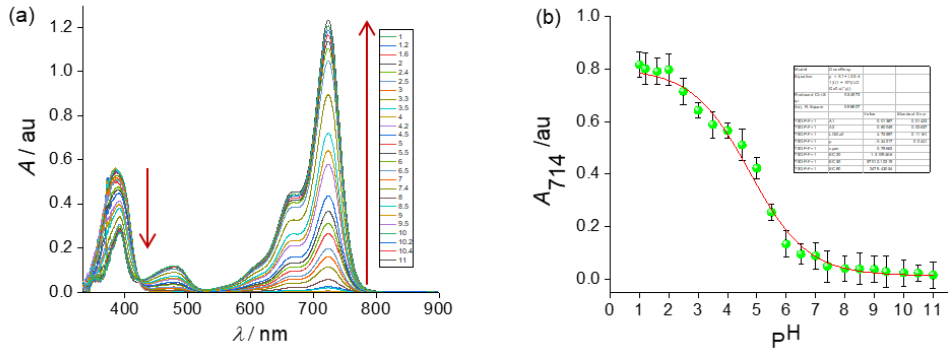

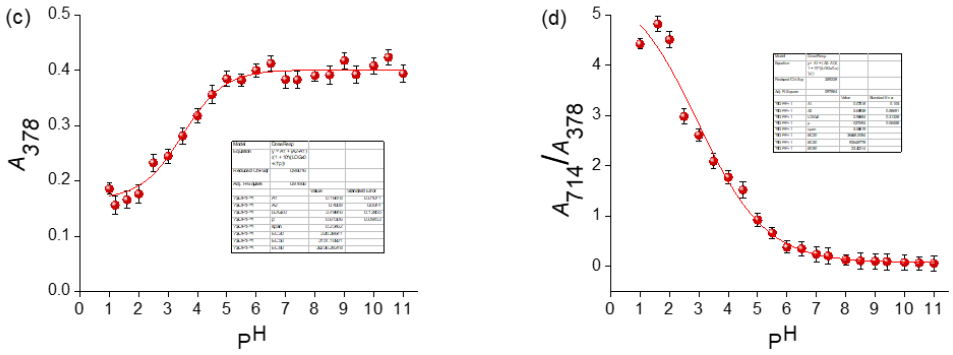

Figure 31. (a) pH titration plot Lyso-Changsha-RGDS in buffer solutions. (b) Absorbance (714 nm) vs pH plot. (c) Absorbance at 378 nm vs pH changes. (d) Ratiometric absorbance (A_{714}/A_{378}) vs pH plot.

A reversible dynamic switching of the Lyso-Changsha-RGDS conjugate absorption between a basic spirolactam state and an acidic open amide state for numerous cycles are detected (Figure 32).

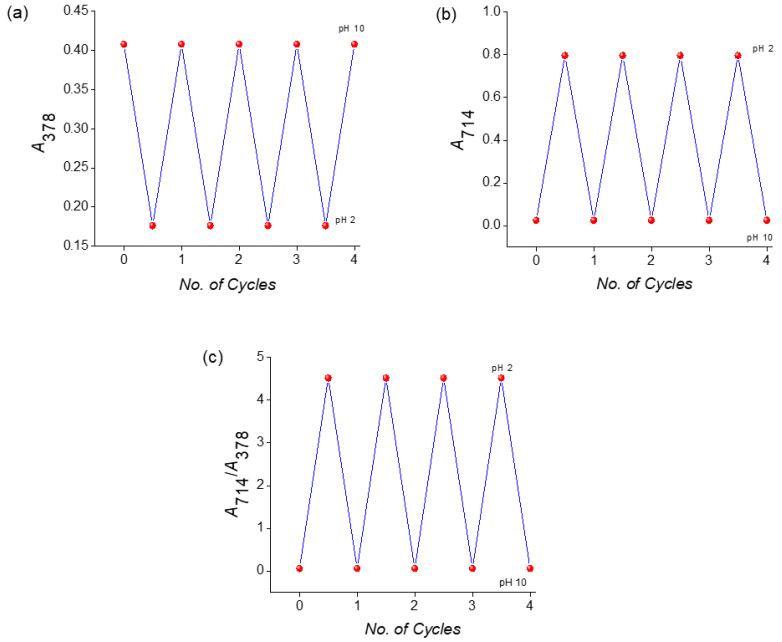

Figure 32. Reversible absorbance switching between pH 10 and 2 for four cycles at (a) 378 nm and (b) 714 nm absorption for Lyso-Changsha-RGDS

conjugate. (c) Ratiometric (A_{714}/A_{378}) pH switching (pH 10 and 1) for four cycles of Lyso-Changsha-RGDS conjugate.

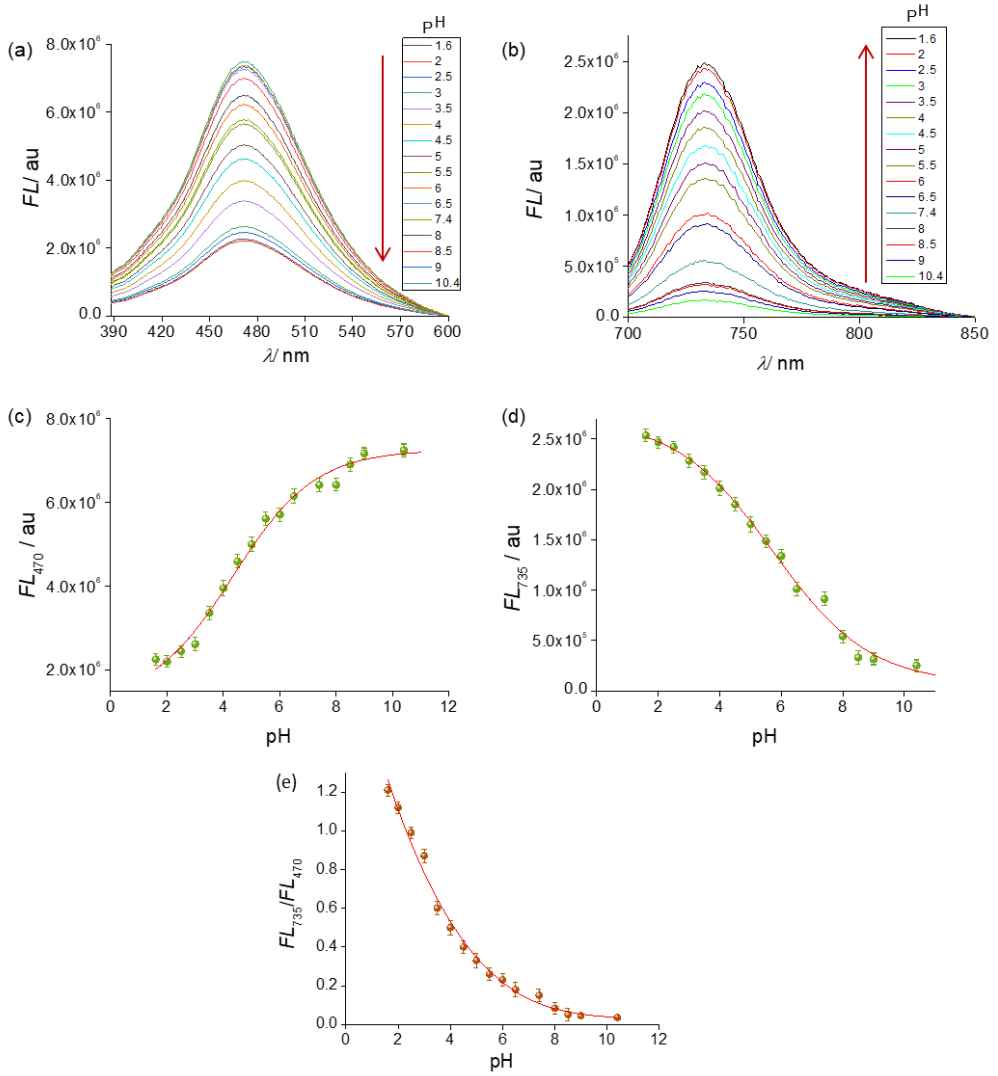

Figure 33. (a) Fluorescence emission plot of Lyso-Changsha-RGDS (2 μM) at λ_{em} 470 nm (λ_{ex} 378 nm) in buffer solutions at different pH. (b) Fluorescence emission plot for Lyso-Changsha-RGDS at λ_{em} 735 nm (λ_{ex} 714 nm) in buffer solutions at different pH. (c) Emission at 470 nm (λ_{ex} = 378 nm) vs pH changes. (d) Emission at 735 nm (λ_{ex} = 714 nm) vs pH changes. (e) Ratiometric fluorescence emission (FL_{735}/FL_{470}) plot vs pH.

A striking spectral characteristic is the narrow NIR bandwidth with massive molar extinction coefficient (ε) augmentation at acidic pH. The λ_{em} of spirolactam and open amide states of Lyso-Changsha-RGDS are significantly distinct. Absorption/emission pH titrations are accomplished in buffered solution with numerous pH. At basic pH the spirolactam state emits at 470 nm (λ_{ex} 378 nm) while pH titration the intensity at 470 nm progressively diminishes and a new NIR fluorescence band [$(\lambda_{em})_{acidic}$ 735 nm, $(\lambda_{ex})_{acidic}$ 714 nm)] turned on and steadily augmented with diminishing pH owing to the construction of push-pull open amide state of Lyso-Changsha-RGDS (Figure 31). An enormous red shift in absorption ($\Delta\lambda_{abs}$ 336 nm) and fluorescence ($\Delta\lambda_{em}$ 265 nm) is perceived from basic spirolactam state to acidic open amide state of Lyso-Changsha-RGDS. The pK_a value of Lyso-Changsha-RGDS conjugate is determined to be 5.1 using the sigmoidal curve fitting from pH titration utilizing the ratiometric data acquired from A_{714}/A_{378} and FL_{735}/FL_{470} (Figures 31d and 33d). The pK_a value of Lyso-Changsha-RGDS is perfect for the activated imaging of acidic cellular lysosomes. Additionally, owing to OFF-to-ON NIR emission switching the emission peak at 735 nm amplified 19-fold from pH 10.4 to 1.6 for Lyso-Changsha-RGDS (Figure 33b). Drastic fluorescence alterations at two well separated emission λ_{em} (470 nm and 735 nm, $\Delta\lambda_{FL}$ 265 nm) diminishes cross talk and permits self-calibration. The probe-peptide conjugate undergo multiple cycles of ratiometric fluorescence switching in a wide range of pH 2–10 and exhibits stable and reproducible dynamic pH dependence switching performance. Subsequently abnormalities in intensity owing to investigational artifacts e.g., probe-peptide concentration; detector sensitivity, laser power, and bleaching are avoided. At acidic pH the open amide state of Lyso-Changsha-RGDS conjugate exhibits admirable

photophysical properties including high molar extinction coefficient (ε = 1.2×10^5 $M^{-1}cm^{-1}$), adequate fluorescence quantum yield (Φ_f = 0.37) along with high brightness ($\varepsilon \times \Phi_f$ = 44400 $M^{-1}cm^{-1}$) (Table 2).

Compound	Solvent	λ_{max} (nm)	λ_{em} (nm)	Stokes shift ($\Delta\lambda$)	$\varepsilon \times 10^5$ (M^{-1} cm^{-1})	Quantum Yield	Brightness (M^{-1} cm^{-1})
Changsha-RGDS Spirolactam form	PBS pH 10	377	458	81	0.57×10^5	0.14 PBS pH 10	7980 PBS pH 10
Changsha-RGDS Open amide form	PBS pH 2	713	733	20	1.1×10^5	0.35 PBS pH 2	38500 PBS pH 2
Lyso-Changsha-RGDS Spirolactam form	PBS pH 10	378	470	92	0.61×10^5	0.13 PBS pH 10	7930 PBS pH 10
Lyso-Changsha-RGDS Open amide form	PBS pH 2	714	735	21	1.2×10^5	0.37 PBS pH 2	44400 PBS pH 2

Table 2. Photophysical data of Changsha-RGDS and Lyso-Changsha-RGDS conjugates in closed spirolactam and open amide states in aqueous PBS.

The brightness of Lyso-Chansha-RGDS conjugate decreases significantly as pH values increases. Moreover, turn-on NIR fluorescence with 21 nm Stokes shift at acidic pH with narrow bandwidth make Lyso-Changsha-RGDS conjugate a potential probe for ratiometric fluorescence sensing of pH.

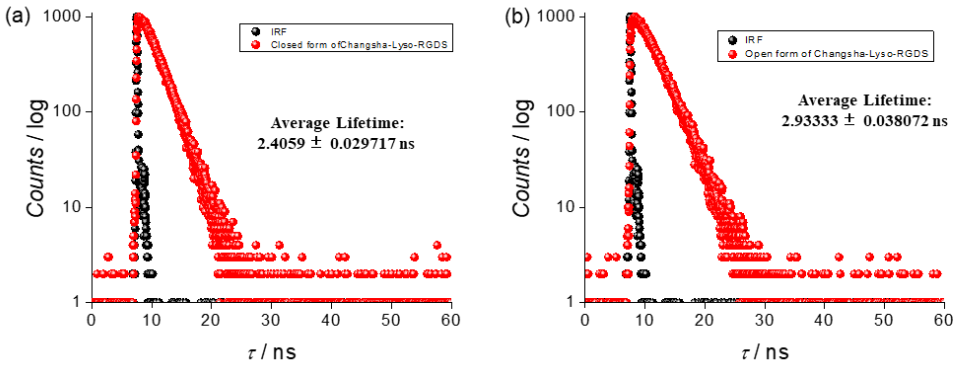

Figure 34: TCSPC plots of (a) closed state and (b) open state of the compound. The fluorescence lifetime (τ) is measured to be **2.4059 ± 0.029717** ns and

2.93333 ± 0.038072 ns, for the closed **s**tate and open state, respectively. IRF = instrument response function.

Fluorescence lifetime (τ) of the open amide state of Lyso-Changsha-RGDS (τ = 2.93 ns) at pH 2 is observed higher than the spirolactam state (τ = 2.406 ns) at basic pH 10.4 in PBS using time-correlated single photon counting (TCSPC) experiment (Table 2, Figure 34). The spirolactam form of Lyso-Changsha-RGDS conjugate predominantly exists in physiological pH 7.4 and exhibits a very low molar extinction coefficient in PBS, pH 10 (0.61×10^5 M^{-1} cm^{-1}), low fluorescence quantum yield (Φ_f = 0.13), low brightness (7930 M^{-1} cm^{-1}), and

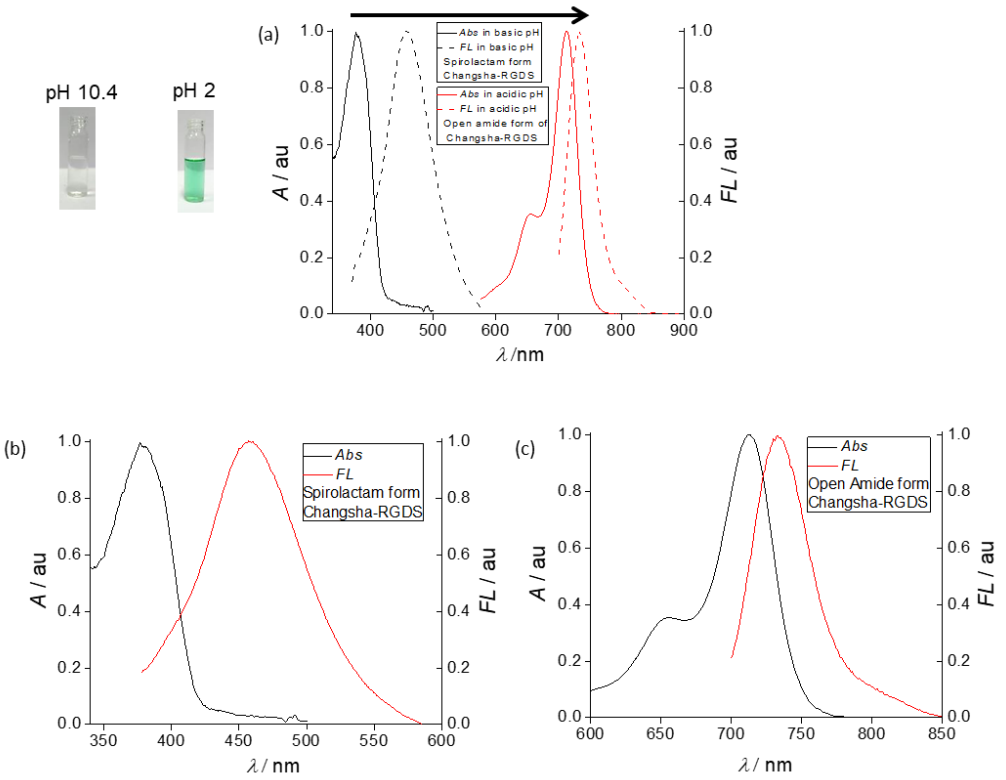

Figure 35. (a) Normalized absorption and fluorescence merge plot for the closed spirolactam and open amide state of Changsha-RGDS conjugate in PBS at pH 10 and 2, respectively. (b) Normalized absorption and fluorescence merge plot for the spirolactam form of Changsha-RGDS in PBS, pH 10. (C)

Normalized absorption and fluorescence merge plot for the open amide form of Changsha-RGDS conjugate in PBS, pH 2.

poor fluorescence lifetime (τ = 2.405 ns) which might be ascribed to the short π-conjugation of the spirolactam state. Similar type of pH-sensitive dynamic molecular OFF/ON switching between the spirolactam and open amide states are also detected for control Changsha-RGDS conjugate lacking the lysosome targeting morpholine functionality (Figure 35-37).

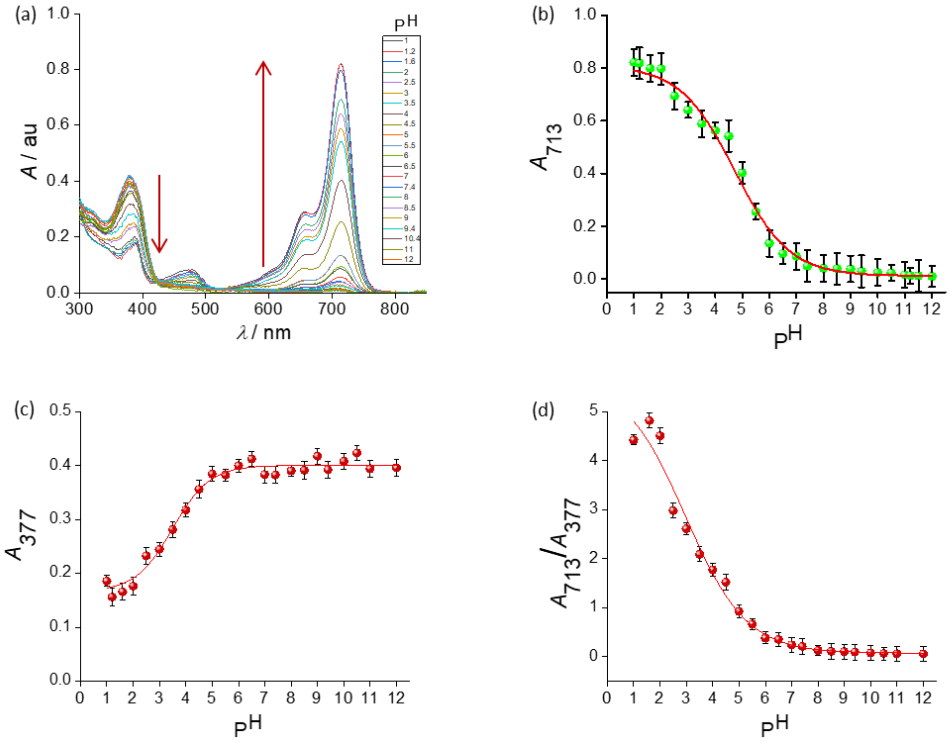

Figure 36. (a) pH titration plot of Changsha-RGDS in buffer solutions. (b) Absorbance (713 nm) vs pH plot. (c) Absorbance at 377 nm vs pH changes. (d) Ratiometric absorbance (A_{713}/A_{377}) vs pH plot.

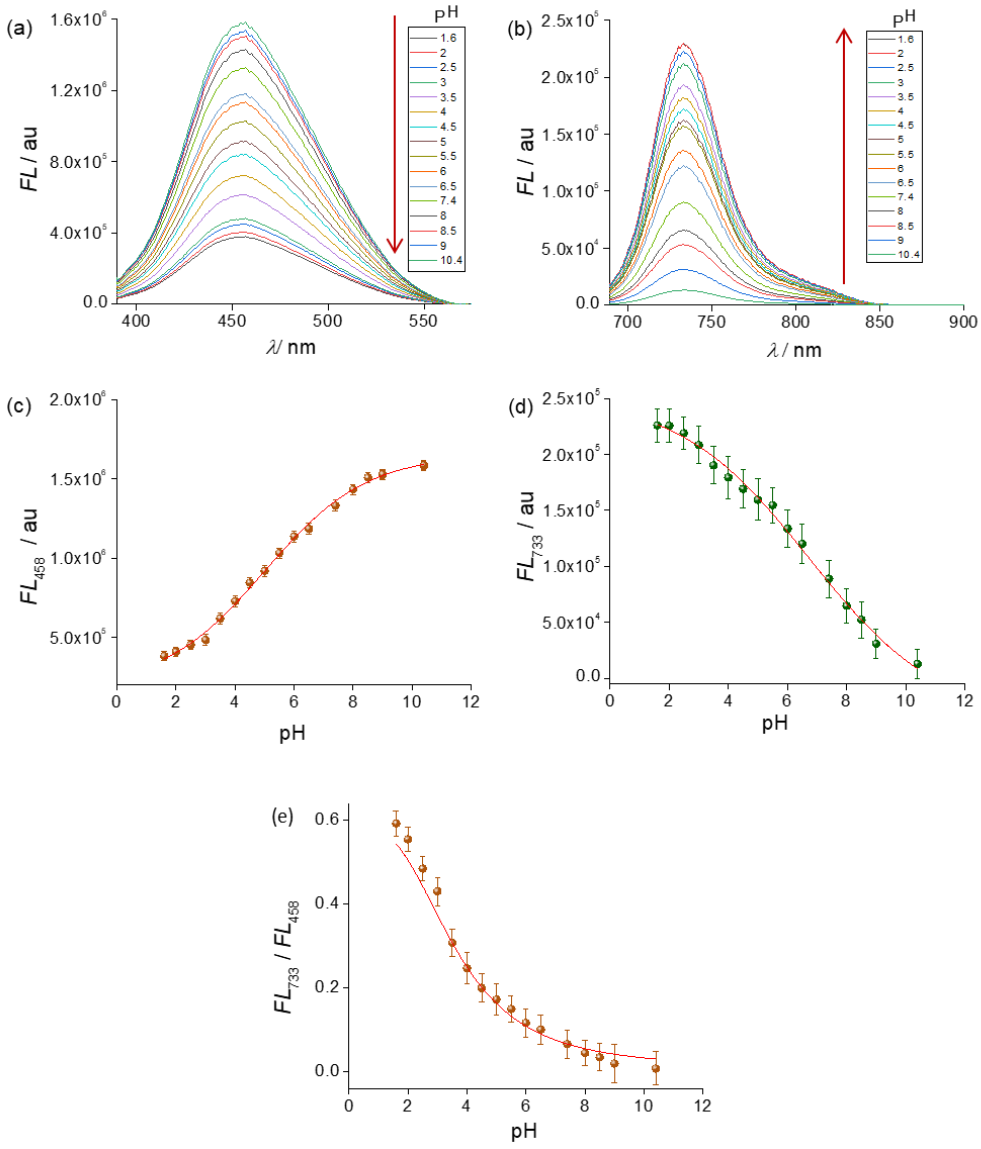

Figure 37. (a) Fluorescence emission plot of Changsha-RGDS conjugate (2 μM) at λ_{em} 458 nm (λ_{ex} 377 nm) in buffer solutions at different pH. (b) Fluorescence emission plot for Changsha-RGDS conjugate at λ_{em} 733 nm (λ_{ex} 713 nm) in buffer solutions at different pH. (c) Emission at 458 nm (λ_{ex} = 377 nm) vs pH changes. (d) Emission at 733 nm (λ_{ex} = 713 nm) vs pH changes. (e) Ratiometric fluorescence emission (FL_{733}/FL_{458}) plot vs pH.

Prolonged durability of the pH activated Lyso-Changsha-RGDS conjugate is an indispensible requirement for its high performance bioimaging applications. The fluorescence assay shows that the ratio of the emission intensities (FL_{735} / FL_{470}) of Lyso-Changsha-RGDS conjugate is steady in pH 4.0 and 7.4 at 37°C over 24 h in DMEM comprising 10% FBS (w/w) (Figure 38). Furthermore, the Lyso-Changsha-RGDS conjugate displays dynamic reversible switching with quick response when the pH is swapped to-and-fro 10 and 2 as a minimum four rounds (Figure 3d). The dynamic ON/OFF switching of A_{714}/A_{378} and FL_{735}/FL_{470} ratios are witnessed deprived of noteworthy alteration. Additionally, no aggregation or degradation is noticed at various pH demonstrating the robustness of Lyso-Changsha-RGDS conjugate. Insignificant fluctuations are perceived in the emission of Lyso-Changsha-RGDS conjugate (2 μM) at 470 nm and 735 nm in presence of innumerable metal ions and anions at physiological settings (pH 7.4, 37°C) over 24 h (Figure 38). Furthermore, probe-peptide conjugate is highly stable in presence of numerous amino acids at physiological environments (PBS, pH 7.4, 37°C, 24 h) (Figure 39). Cell viability assay show that the Lyso-Changsha-RGDS conjugate is non-cytotoxic to human epithelioid cervix carcinoma HeLa and lung adenocarcinoma A549 cancerous cells along with healthy mouse myoblast

C2C12 cell line (Figure 40). In view of this, we propose that the dual targeting acidic pH-activatable Lyso-Changsha-RGDS conjugate has the potentiality to be utilized as a harmless probe-peptide conjugate for the living cancer cell specific active targeting followed by cell penetration and selective tracking of acidic lysosomes.

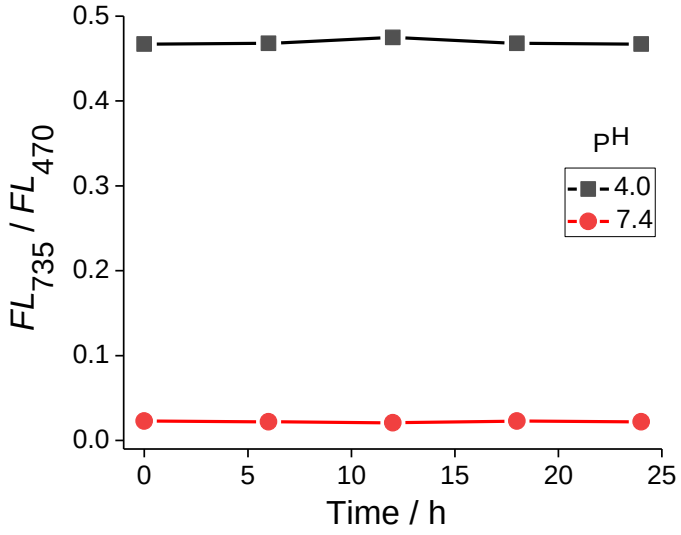

Figure 38. Insignificant ratiometric fluorescence (FL_{735}/FL_{470}) signal variation are detected for Lyso-Changsha-RGDS conjugate (2 μM) at pH 4.0 and 7.4 in DMEM containing 10% FBS (w/w) at 37°C over 24 h.

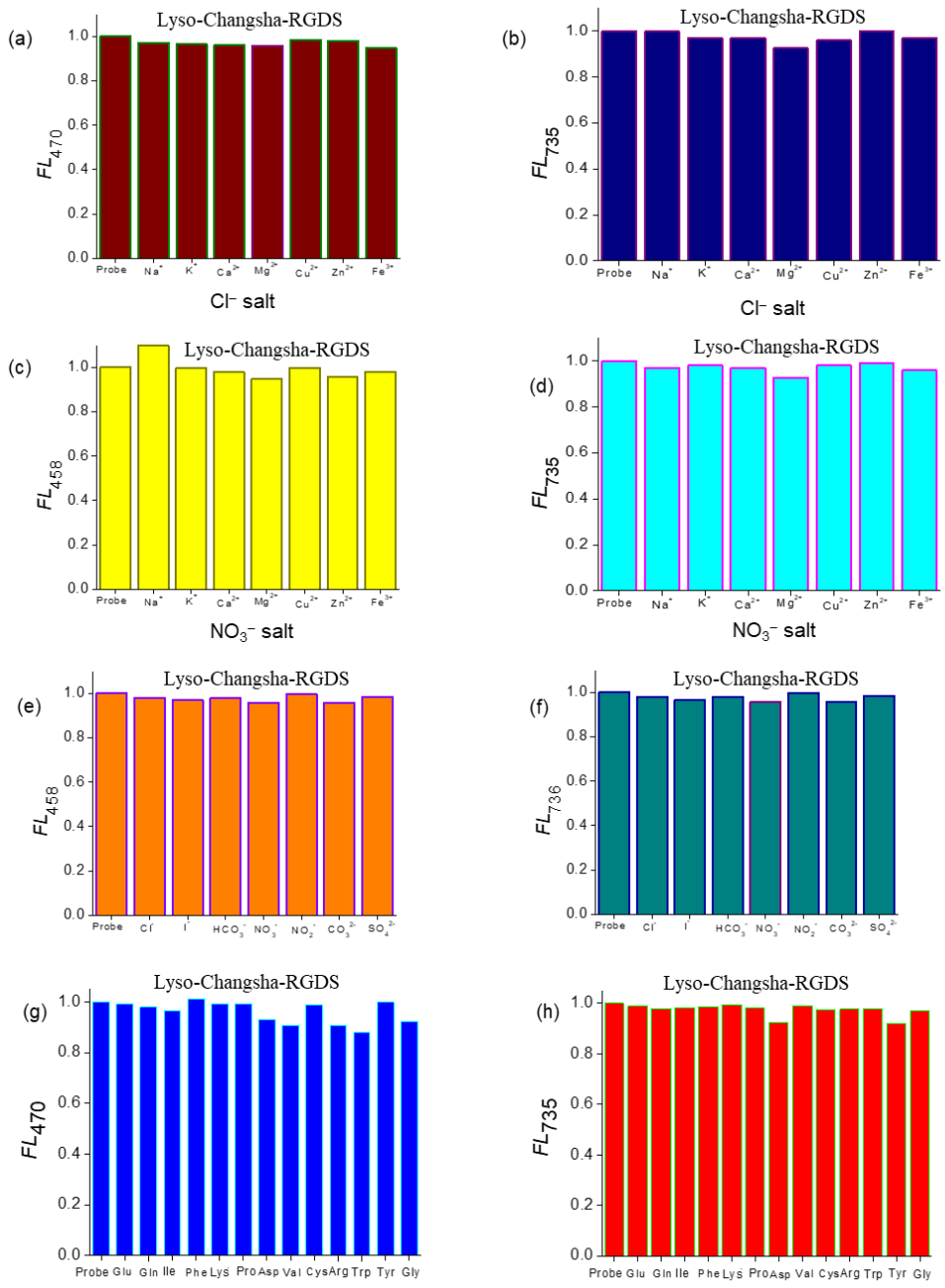

Figure 39. Insignificant fluctuations are observed in the fluorescence signal of the Lyso-Changsha-RGDS conjugate (2 μM) at (a) 470 nm and (b) 735 nm in presence of innumerable cations [10 mM Na^+, 10 mM K^+ and 200 μM for Ca^{2+}, Mg^{2+}, Cu^{2+}, Zn^{2+}, Fe^{2+}, and Fe^{3+}] as chloride and (c,d) nitrate salts. Trivial fluctuations of the fluorescence signal of the Lyso-Changsha-RGDS conjugate

at (e) 470 nm and (f) 735 nm in presence of different anions (200 μM for Cl^-, I^-, HCO_3^-,NO_3^-, NO_2^-, CO_3^{2-}, and SO_4^{2-} as Na^+ salts) under physiological conditions (pH 7.4, 37°C, 24 h). (g,h) Insignificant fluorescence signal fluctuations are detected in presence of various amino acids like Glu, Gln, Ile, Phe, Lys, Pro, Asp, Val, Cys, Arg, Trp, Tyr, and Gly under physiological conditions (pH 7.4, 37°C, 24 h).

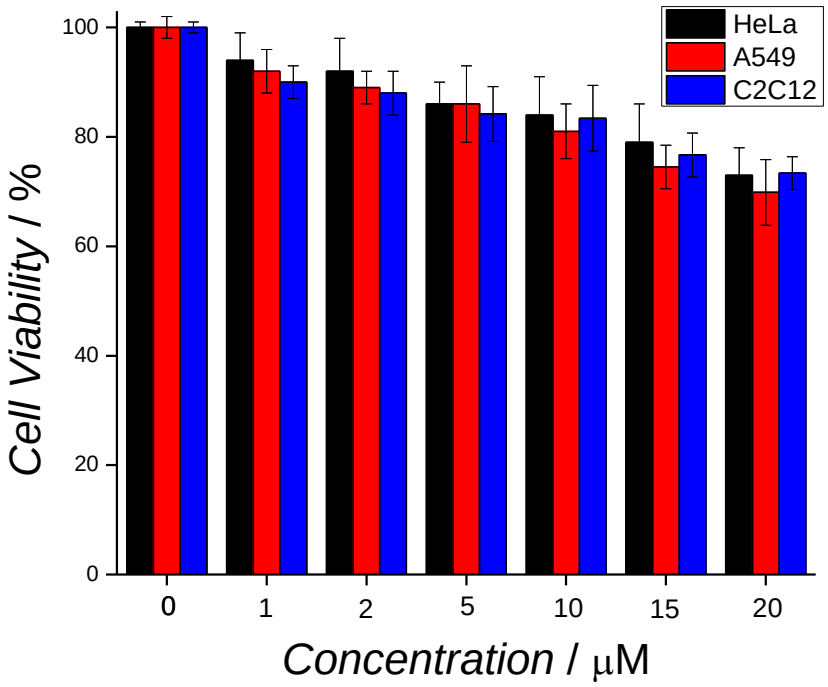

Figure 40. Cell viability assay against A549 and HeLa carcinoma and C2C12 healthy cell lines over 24 h at different doses of Lyso-Changsha-RGDS conjugate.

Confocal experiments disclose that, afterward incubation with the living cancer HeLa and A549 cell lines for 30 min, the spirolactam state of Lyso-Changsha-RGDS conjugate internalized live cancer cells efficiently, selectively

accumulates inside the acidic malignant lysosomal milieu, switched on to the highly conjugated push-pull open amide state, and displays a punctate vesicular shape. To confirm lysosomal selectivity of Lyso-Changsha-RGDS conjugate, colocalization experiments are accomplished in live HeLa and A549 carcinoma cell lines with a commercially obtainable LysoTracker Green DND-26 (LTG, $\lambda_{ex}/\lambda_{em}$ 504/511) (Figure 41). The Lyso-Changsha-RGDS conjugate exhibits decent colocalization with LTG inside the A549 and HeLa live cancer cells that is endorsed by CLSM with a high Pearson's correlation coefficient (PCC) of 0.79 and 0.73, respectively (Figures 41,42). CLSM is utilized to scan innumerable layers of the living cancer cells on the *z* axis to capture 3D info. The 3D rebuilding of the CLSM picture displays the spherical lysosomal part in the living A549 and HeLa cancer cells highlighted with the Lyso-Changsha-RGDS conjugate (Figure 43). It designates that the spirolactam form of the probe-peptide conjugate Lyso-Changsha-RGDS has decent cell membrane penetrating ability and after internalization thru the plasma membrane it accumulates inside the acidic lysosomal compartment. The probe-peptide conjugate displays living cancer cells lysosome targeted activation and turned-on NIR emission. Additionally, ratiometric CLSM images of HeLa and A549 live cancer cells incubated with the pH sensitive Lyso-Changsha-RGDS conjugate using dual channel excitation are also accomplished (Figure 44).

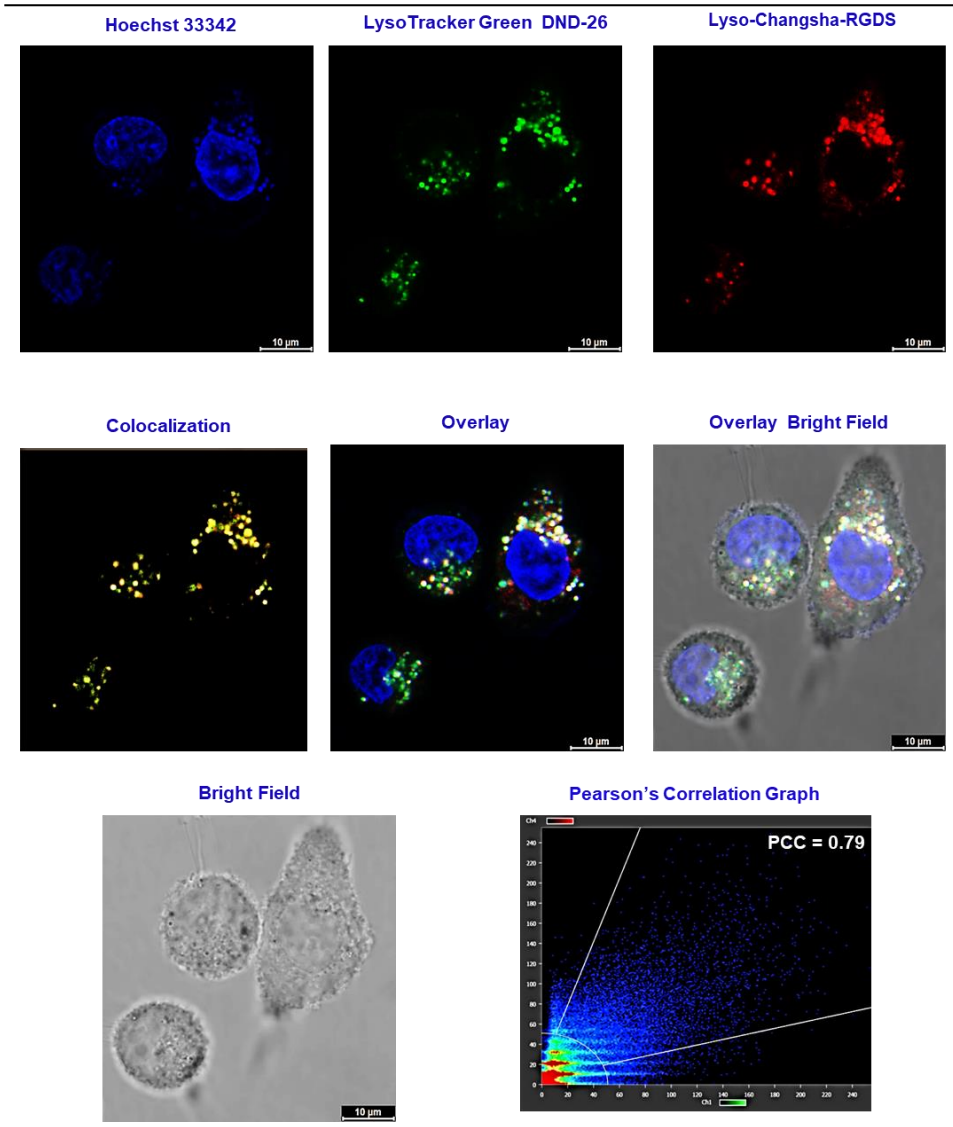

Figure 41. Confocal microscopic images of Lyso-Changsha-RGDS conjugate colocalized with LysoTracker Green DND-26 (MTG) in live A549 carcinoma cells. Hoechst (blue channel), LTG (green channel), and Lyso-Changsha-RGDS conjugate (red channel). Colocalization scatter plot displays Pearson's correlation coefficient (PCC) of 0.79.

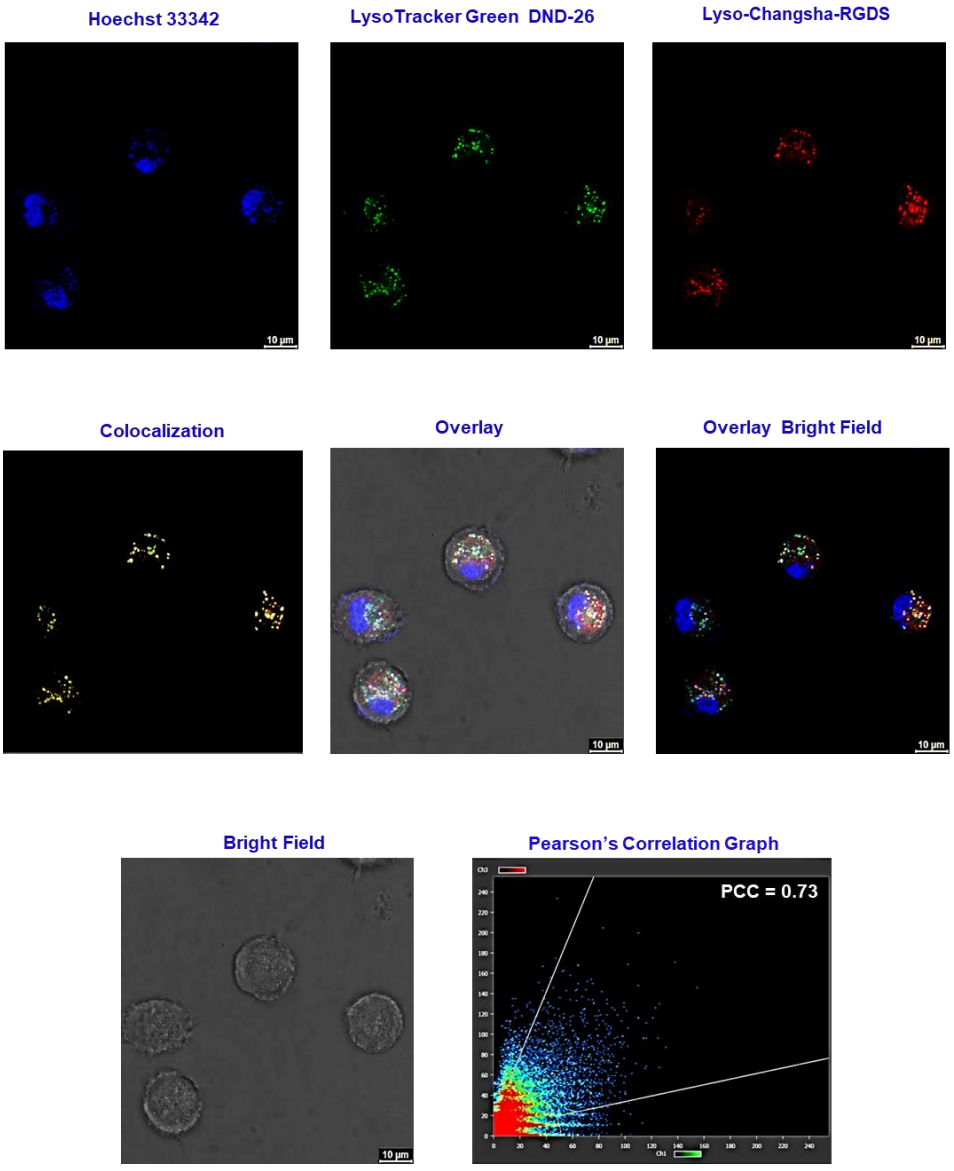

Figure 42. Confocal microscopic images of Lyso-Changsha-RGDS conjugate colocalized with LysoTracker Green DND-26 (MTG) in live HeLa carcinoma cells. Hoechst (blue channel), LTG (green channel), and Lyso-Changsha-RGDS conjugate (red channel). Colocalization scatter plot displays Pearson's correlation coefficient (PCC) of 0.73.

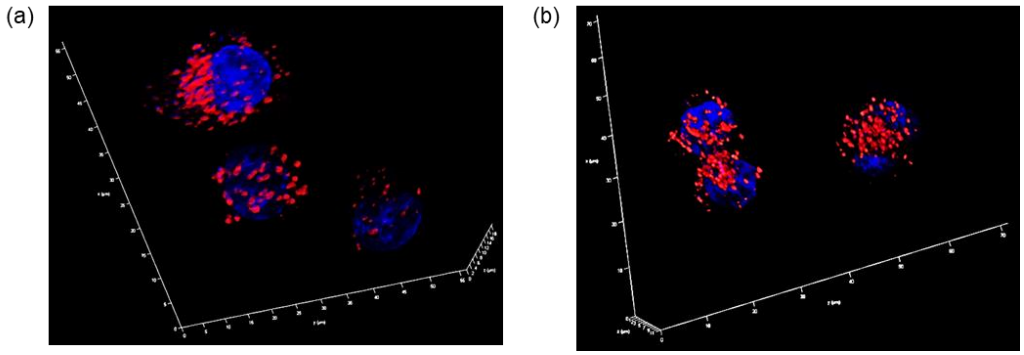

Figure 43. 3D CLSM images of the live (a) A549 and (b) HeLa carcinoma cell lines stained with lysosome targeting Lyso-Changsha-RGDS conjugate (red color). Blue color indicates nuclear staining by Hoechst 33342.

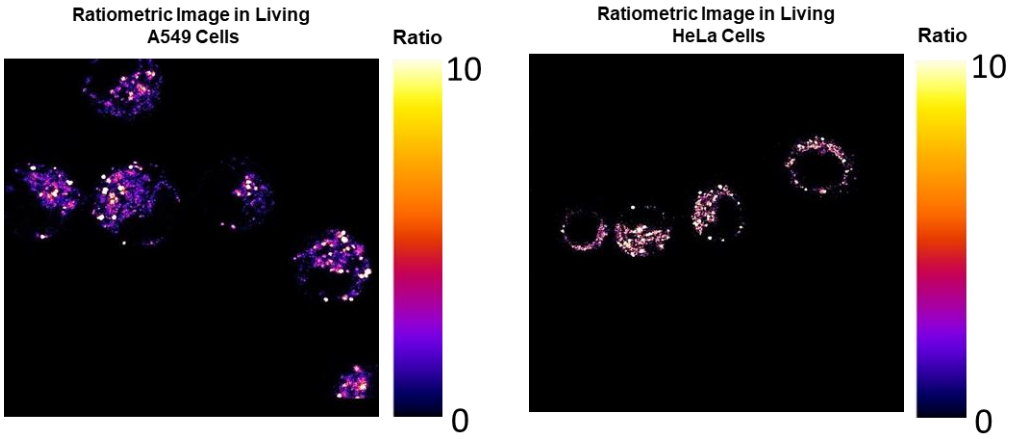

Figure 44. Ratiometric CLSM images (I_{red}/I_{green}, pseudocolor produced by ImageJ software) of live (a) A549 and (b) HeLa carcinoma cells upon dual excitation of the pH activatable Lyso-Changsha-RGDS conjugate.

The fluorescence emission intensity in red channel is enough separated to green channel, indicating insignificant cross talk among these two channels. The

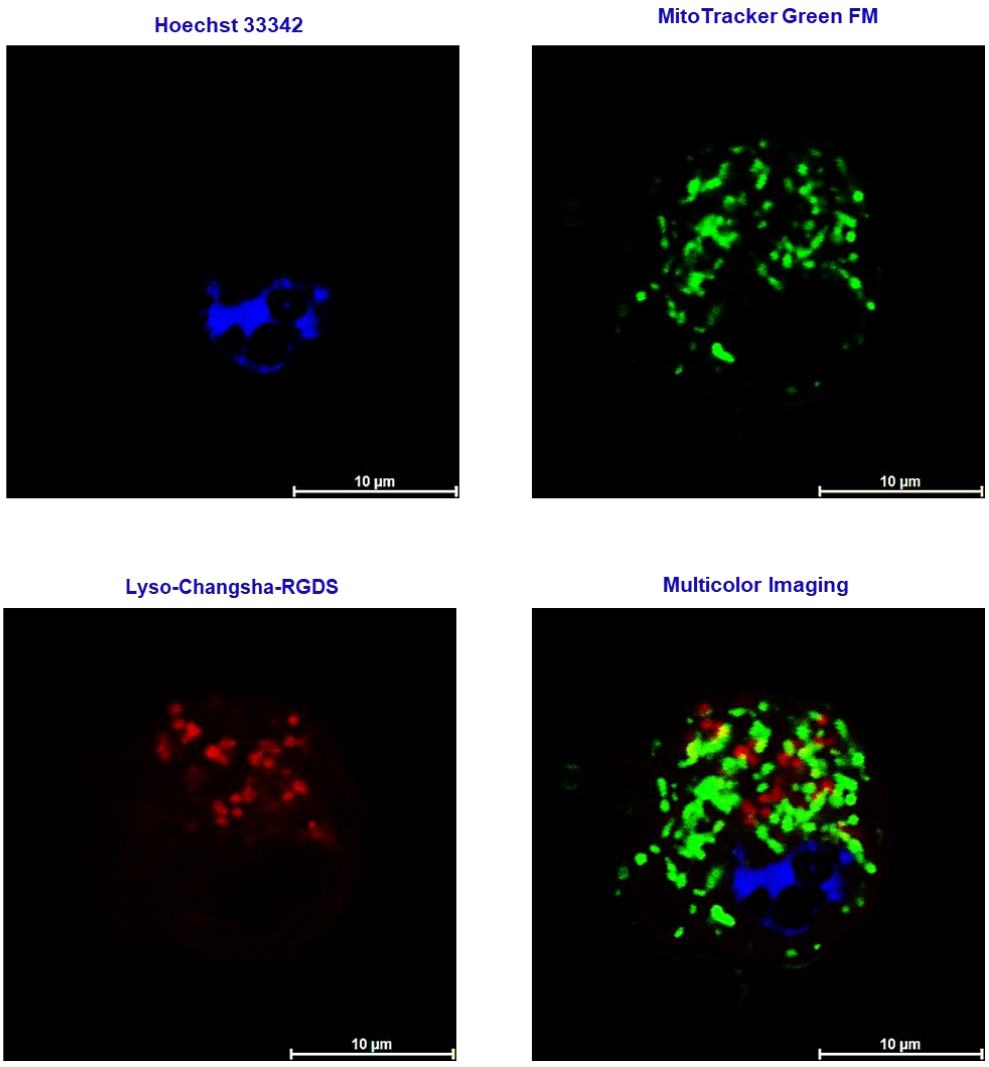

Figure 45. Multicolor CLSM images of living A549 cells stained with blue-fluorescent Hoechst 33342 to stain nucleus (blue color), green emitting MitoTracker Green FM (MTG) to target mitochondria (green color), and acidic pH-activatable NIR emitting Lyso-Changsha-RGDS to specifically track lysosomes (red color).

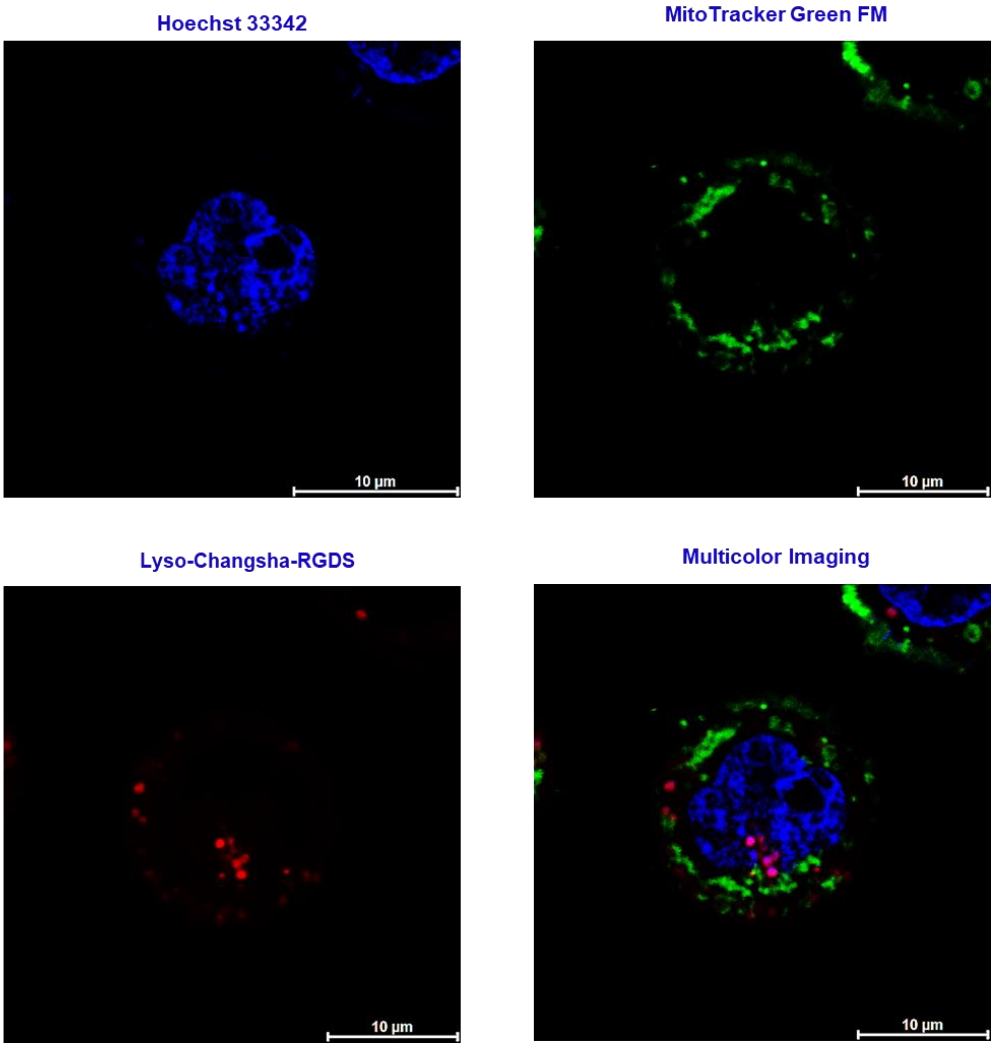

Figure 46. Multicolor CLSM images of living HeLa cells stained with blue-fluorescent Hoechst 33342 to stain nucleus (blue color), green emitting MitoTracker Green FM (MTG) to target mitochondria (green color), and acidic pH-activatable NIR emitting Lyso-Changsha-RGDS to specifically track lysosomes (red color).

ratiometric pseudocolor (I_{red}/I_{green}) CLSM images acquired through ImageJ software is achieved from the two channels show that the ratiometric Lyso-Changsha-RGDS conjugate is an effectual probe-peptide conjugate to observe the live cancer cells lysosomes. The CLSM experiments show ratiometric imaging with enhanced selectivity of acidic lysosomes although diminishing fluorescence at NIR window from nontargeted neutral/basic organelles in living cancer cells is detected. The real time lysosomes tracking in the living A549 and HeLa carcinoma cells are also taken over the time period of 5 min by CLSM . Furthermore, multicolor imaging of living A549 and HeLa cancer cells are acquired by targeted dyes with diverse $\lambda_{ex}/\lambda_{em}$ e.g., Hoechst 33342, MitoTracker Green FM (MTG), and our designed Lyso-Changsha-RGDS conjugate to stain live cancer cells nucleus (blue color), mitochondria (green color), and lysosomes (red color), respectively (Figures 45, 46). On contrary the control molecule Changsha-RGDS conjugate lacking the lysosome targeting morpholine functionality exhibits poorer lysosomal selectivity with low PCC of 0.61. It confirms that the Lyso-Changsha-RGDS might be an effectual ratiometric probe-peptide conjugate for targeted living carcinoma cell lysosomal imaging.

Conclusions: We have designed and constructed acidic pH-stimulated visible-to-NIR convertible ratiometric organic fluorescent probe-peptide conjugate.

Water-soluble, noncytotoxic, photostable, ultra-bright, dual targeting, live cancer cell penetrating, dynamic pH switching, acidic pH activated narrow NIR abs/em with huge molar absorptivity, perfect pK_a, high cancer cell lysosome targeting ability, OFF-to-ON NIR emission in the acidic lysosomal lumen create the Lyso-Changsha-RGDS conjugate an outstanding molecule for living cancer cell ratiometric imaging of lysosomes. The shift of two fluorescence wavelengths ($\Delta\lambda_{em}$ = 265 nm) of Lyso-Changsha-RGDS conjugate is sufficient to diminish cross talk, hence providing significant tools for ratiometric tracking of live cancer cell lysosomes. The probe-RGDS conjugate could be effectively utilized for 3D cellular mapping, real-time monitoring of living carcinoma cell lysosomes and has great potential for early diagnosis of cancer and targeted image guided surgery. This ratiometric probe-peptide conjugate could easily be engineered with a diversity of target selective functionality and biomolecules. Lyso-Changsha-RGDS might be an effectual ratiometric probe-peptide conjugate for targeted living carcinoma cell lysosomal imaging.

References:

[1] Wu, P.; Zhu, Y.; Liu, S.; Xiong, H. *ACS. Cent. Sci.* **2021**, *7*, 2039–2048.

[2] Goshisht, M. K.; Tripathi, N.; Patra, G. K.; Chaskar, M. *Chem. Sci*. **2023**, *14*, 5842–5871.

[3] Chen, C.; Tian, R.; Zeng, Y.; Chu, C.; Liu, G. *Bioconjugate Chem.* **2020**, *31*, 276–292.

[4] Siriwibool, S.; Kaekratoke, N.; Chansaenpak, K.; Siwawannapong, K.; Panajapo, P.; Sagarik, K.; Noisa, P.; Lai, R. Y.; Kamkaew, A. *Sci Rep*. **2020**, *10*, 1283.

[5] Weinstain, R.; Slanina, T.; Kand, D.; Klán, P. *Chem. Rev.* **2020**, *120*, 13135–13272.

[6] Zhang, S.; Chen, H.; Wang, L.; Qin, X.; Jiang, B.; Ji, S.; Shen, X.; Liang, H. *Angew. Chem. Int. Ed.* **2021**, *61*, e20210707.

[7] Das, R. S.; Maiti, D.; Kar, S.; Bera, T.; Mukherjee, A.; Saha, P. C.; Mondal, A.; Guha, S. *J. Am. Chem. Soc.* **2023**, *145*, 20451–20461.

[8] Hu, Z.; Fang, C.; Li, B.; Zhang, Z.; Cao, C.; Cai, M.; Su, S.; Sun, X.; Shi, X.; Li, C.; et al. *Nat. Biomed. Eng.* **2020**, *4*, 259−271.

[9] Persi, E.; Duran-Frigola, M.; Damaghi, M.; Roush, W. R.; Aloy, P.; Cleveland, J. L.; Gillies, R. J.; Ruppin, E. *Nat Commun*. **2018**, *9*, 2997.

[10] Hou, H.; Zhao, Y.; Li, C.; Wang, M.; Xu, X.; Jin, Y. *Sci Rep*. **2017**, *7*, 1759.

[11] Chen, S.; Hong, Y.; Liu, Y.; Liu, J.; Leung, C. W. T.; Li, M.; Kwok, R. T. K.; Zhao, E.; Lam, J. W. Y.; Yu, Y.; Tang, B. Z. *J. Am. Chem. Soc.* **2013**, *135*, 4926–4929.

[12] Medeiros-Silva, J.; Somberg, N. H.; Wang, H. K.; McKay, M. J.; Mandala, V. S.; Dregni, A. J.; Hong, M. *J. Am. Chem. Soc.* **2022**, *144*, 6839–6850.

[13] Tian, Y.; Viles, J. H. *Angew. Chem. Int. Ed.* **2022**, *61*, e202210675.

[14] Van Agthoven, J. F.; Xiong, J.-P.; Alonso, J. L.; Rui, X.; Adair, B. D.; Goodman, S. L.; Arnaout, M. A. *Nat. Struct. Mol.Biol.* **2014**, *21*, 383–388.

[15] Turaga, R. C.; Yin, L.; Yang, J. J.; Lee, H.; Ivanov, I.; Yan, C.; Yang, H.; Grossniklaus, H. E.; Wang, S.; Ma, C.; Sun, L.; Liu, Z.-R. *Nat. Commun.* **2016**, *7*, 11675

[16] Iulianna, T.; Kuldeep, N.; Eric, F. *Cell Death Dis*. **2022**, *13*, 509.

[17] Jana, B.; Jin, S.; Go, E. M.; Cho, Y.; Kim, D.; Kim, S.; Kwak, S. K.; Ryu, J.-H. *J. Am. Chem. Soc.***2023**, *145*, 18414–18431.

[18] Bonam, S. R.; Wang, F.; Muller, S. *Nat Rev Drug Discov.* **2019**, *18*, 923–948.

[19] Mondal, B.; Dutta, T.; Padhy, A.; Das, S.; Sen Gupta, S. *ACS Omega* **2021**, *7*, 5–16.

[20] Fraldi, A.; Klein, A. D.; Medina, D. L.; Settembre, C. *Annual Review of Neuroscience* **2016**, *39*, 277–295.

[21] Kroemer, G.; Jäättelä, M. *Nat Rev Cancer*. **2005**, *5*, 886–897.

[22] Futerman, A. H.; van Meer, G. *Nat. Rev. Mol. Cell Biol.* **2004**, 5, *554−565*.

[23] X. Chen, Y. Bi, T. Li, P. Wang, X. Yan, S. Hou, C. E. Bammert, J. Ju, K. M. Gibson, W. J. Pavan, L. Bi, *Sci. Rep*. **2015**, *5*, 9004.

[24] A. Pierzyńska-Mach, P. A. Janowski, J. W. Dobrucki, *Cytometry, Part A*. **2014**, *85*, 729−737.

[25] Qiu, K.; Huang, H.; Liu, B.; Liu, Y.; Huang, Z.; Chen, Y.; Ji, L.; Chao, H. *ACS Appl. Mater. Interfaces.* **2016**, *8*, 12702–12710.

[26] Kobayashi, H.; Choyke, P. L. *Acc. Chem. Res.* **2010**, *44*, 83–90.

[27] Li, W.; Yin, S.; Shen, Y.; Li, H.; Yuan, L.; Zhang, X.-B. *J. Am. Chem. Soc.* **2023**, *145*, 3736–3747.

[28] Liu, C.; Zhang, R.; Zhang, W.; Liu, J.; Wang, Y.-L.; Du, Z.; Song, B.; Xu, Z. P.; Yuan, J. *J. Am. Chem. Soc.* **2019**, *141*, 8462–8472.

[29] Yuan, L.; Lin, W.; Yang, Y.; Chen, H. *J. Am. Chem. Soc.* **2012**, *134*, 1200–1211.

[30] Yang, H.; Han, C.; Zhu, X.; Liu, Y.; Zhang, K. Y.; Liu, S.; Zhao, Q.; Li, F.; Huang, W. *Adv. Funct. Mater.* **2016**, *26*, 1945–1953.

[31] Sheldrick, G. M. *Acta Cryst.* **2015**, *A71*, 3–8.

[32] Sheldrick, G. M. *Acta Cryst.* **2015**, *C71*, 3–8.

[33] Dolomanov, O. V.; Bourhis, L. J.; Gildea, R. J.; Howard, J. A. K.; Puschmann, H. *J. Appl. Cryst.* **2009**, *42*, 339–341.

[34] Mukherjee, A.; Saha, P. C.; Das, R. S.; Bera, T.; Guha, S. *ACS Sens.* **2021**, *6*, 2141–2146.

[35] Das, R. S.; Saha, P. C.; Sepay, N.; Mukherjee, A.; Chatterjee, S.; Guha, S. *Org. Lett.* **2020**, *22*, 5839−5843.

Chapter 6

Summery and Outlook

An expanding area of modern study involves the selective targeting and monitoring of particular intracellular organelles, such as the nucleus, mitochondria, lysosomes, etc. However, because biological systems are so complicated, working in the cellular environment is difficult. Fluorescence microscopy is a preferred method for studying intracellular organelle-related activities in real-time. Because NIR light has a high signal-to-noise ratio, a deep tissue penetration efficiency, and less phototoxicity to living organisms, it is an efficient next-generation instrument for lighting a variety of biological activities. There are distinct changes in the pH of organelles, and pH plays a significant role in a range of pathological and physiological processes. The pH of the cytoplasm is close to neutral (7.2), that of the mitochondria is weakly basic (8.0), and that of the endosomes and lysosomes is acidic (5.0–6.0 and 4.0–5.0 respectively). An altered intracellular organelle pH is a sign of the organelle's dysfunction, which can cause significant illnesses. To accurately track organelle pH, new NIR ratiometric fluorescence sensors are needed. Several rotaxane-peptide conjugates anchoring with Lysosome selective morpholine moiety have also been developed, which selectively accumulate inside the malignant lysosome. Among the various intracellular organelles, lysosomes are the key target for all malignant cells. Lysosomes are the membrane-bound cellular organelles with low pH 4−5.They encompass a variety of degradable enzymes and are liable for the disruption of nucleic acids, lipids, proteins, etc. as well as being responsible for exocytosis

This thesis is an overview of the literature-reported synthetic methods and ratiometric fluorescence probe applications. The importance of intracellular pH as a biological parameter for controlling cellular activity and function is highlighted. The importance of NIR chromophore in light of the discussion of UV and visible probes. The emphasis of this thesis has been on cyanine dyes,

with a special emphasis on Cy-7 dyes. There has been discussion of structural scaffolds for ratiometric pH sensing. The significance of lysosomes as a cellular organelle has been highlighted. Multicolor cellular imaging, confocal laser scanning microscopy for live cell imaging, and lysosome targeting structural scaffolds have also been discussed.

The novel observations of this thesis are:

- A RGDS peptide conjugated ratiometric pH sensitive NIR fluorophore to target cancer cell lysosomes is designed and synthesised as described in this thesis. A NIR OFF/ON functional dye based on ring closing and opening mechanism is shown here. Changsha NIR fluorophores are a unique class of NIR functional fluorescent dyes with large extinction coefficients, high fluorescence quantum yields, high brightness, and pH sensitive properties that we have created and synthesised. Surprisingly, the new NIR dyes maintain the ON-OFF switching mechanism of rhodamine while outperforming the traditional rhodamine dyes in both NIR absorption and emission. In order to specifically target the lysosomes and the cancer cells, we have coupled the RGDS peptide in this NIR dye.
- I've used a MW-assisted SPPS procedure to make RGDS and Cs-RGDS peptide quickly and efficiently. To specifically target living cancer cells, RGDS peptide is conjugated at the spirocyclic connecting carboxylic acid group and a morpholine moiety is tethered with indole poart of the dye. This is followed by selective internalisation and tracking of malignant lysosomes. To create NIR dye/RGDS conjugates, I used solid phase petide synthesis chemistry on Wang resin and Rink amide resin.

List of Publications and Research Works Included in the Thesis:

As a First Author:

(1) Acidic pH-Activatable Visible to Near-Infrared Switchable Ratiometric Fluorescent Probe for Live-Cell Lysosome Targeted Imaging. **Ayan Mukherjee**, Pranab Chandra Saha, Rabi Sankar Das, Tapas Bera, and Samit Guha*. *ACS Sens.* **2021**, *6*, 2141–2146.

(2) *Acidic pH-Triggered Live-Cell Lysosome Specific Tracking, Ratiometric pH Sensing, and Multicolor Imaging by Visible to NIR Switchable Cy-7 Dyes.* **Ayan Mukherjee**, Pranab Chandra Saha, Samiran Kar, Pampa Guha, Rabi Sankar Das, Tapas Bera, and Samit Guha*. *ChemBioChem.* **2023**, *24*, e2022006.

List of Publications and Research Works That Not Included in the Thesis:

As a Co Author:

(1) Design of Water-Soluble Rotaxane Capped Superparamagnetic Ultrasmall Fe_3O_4 Nanoparticles for Targeted NIR Fluorescence Imaging in Combination with Magnetic Resonance. Rabi Sankar Das**,** Debabrata Maiti, Samiran Kar, Tapas Bera, **Ayan Mukherjee**, Pranab Chandra Saha, Aniruddha Mondal, and Samit Guha* ***J. Am. Chem. Soc*. https://doi.org/10.1021/jacs.3c06232 .**

(2) Live-Cell Mitochondrial Targeted NIR Fluorescent Covalent Labeling of Specific Proteins Using a Dual Localization Effect. Pranab Chandra Saha, Rabi Sankar Das**,** Shreya Das, Nayim Sepay, Tanima Chatterjee, **Ayan Mukherjee**, Tapas Bera, Samiran Kar, Maitree Bhattacharyya, Arunima Sengupta, and Samit Guha* ***Bioconjugate.Chem. 10.1021/acs.bioconjchem.3c00185***

(3) . Construction of Red Fluorescent Dual Targeting Mechanically Interlocked Molecules for Live Cancer Cell Specific Lysosomal Staining and Multicolor Cellular Imagin. Rabi Sankar Das, **Ayan Mukherjee**, Samiran Kar, Tapas Bera, Shreya Das, Arunima Sengupta, and Samit Guha*. ***Org. Lett.* 2022,** 24, **5907–5912**

(4) Construction of unsymmetrical bis-urea macrocyclic host for neutral molecule and chloride-ion binding. Biprajit paul, **Ayan Mukherjee,** Deepak Bhyuan, Samit Guha* ***J Heterocyclic Chem*.2021; 58:2033–2038.**

(5) Design and Synthesis of Near-Infrared Mechanically Interlocked Molecules for Specific Targeting of Mitochondria. Rabi Sankar Das, Pranab Chandra Saha, Nayim Sepay, **Ayan Mukherjee**, Sudipta Chatterjee, and Samit Guha*****. ***Org. Lett.* 2020, *22*, 5839–5843**

(6) Targeting and Imaging of Mitochondria Using Near-Infrared Cyanine Dye and Its Application to Multicolor Imaging. Pranab Chandra Saha, Tanima Chatterjee, Rudradip Pattanayak, Rabi Sankar Das, **Ayan Mukherjee**, Maitree Bhattacharyya, and Samit Guha*. ***ACS Omega,* 2019*, 4,* 14579-14588**

PRESENTATION/PARTICIPATION IN INTERNATIONAL/NATIONAL/SYMPOSIUM/ CONFERENCES:

1. Poster presentation "***Acidic pH-Activatable Visible to Near-Infrared Switchable Ratiometric Fluorescent Probe for Live-Cell Lysosome Targeted Imaging."***. Ayan Mukherjee, and Samit Guha*. One Day Symposium in Chemical Sciences, National Conference on Chemistry Organized by Chemical Reserch Society of India (CRSI-2022) held at Indian Association for The Cultivation of Science (IACS), Kolkata, India, 4th June, 2022.

2. Poster presentation ***"Designing and synthesis of a near infrared cy-PH switchable dye to target and image Lysosome***" presented at International Seminar on Recent Advances in Chemistry and Materials Sciences (RACMS-2022) organised by INDIAN CHEMICAL SOCIETY (ICS). (Date-30-31 July and 2-3August). Ayan Mukherjee, and Samit Guha*. International Seminar on Recent Advances in Chemistry and Material Science (RACMS-2022) held at Department of Chemistry, Jadavpur University (JU), Kolkata, India, During July 30-31 and August 02-03, 2022**.**

3. Poster presentation "***Amyloid-β Peptide Fragment Conjugated with Near-Infrared Chromophore for Selective Targeting and Imaging of Mitochondria*"**.** Pranab Chandra Saha, Rabi Sankar Das, Ayan Mukherjee, Tapas Bera, and Samit Guha*. National Seminar on Emerging Trends in Chemical Sciences under Centre for Advanced Studies II Program, Organized by Department of Chemistry, Jadavpur University, Kolkata-700032 on January 07, 2020.